2009-06-10

A Model to Describe Spatial and Temporal Variation of Phosphorus Mass and Fluxes in Tree Islands of Shark River Slough in the Everglades

Marcelo E. Lago
University of Miami, mla@dhi.us

UNIVERSITY OF MIAMI

A MODEL TO DESCRIBE SPATIAL AND TEMPORAL VARIATION OF PHOSPHORUS MASS AND FLUXES IN TREE ISLANDS OF SHARK RIVER SLOUGH IN THE EVERGLADES

By

Marcelo E. Lago

A DISSERTATION

Submitted to the Faculty
of the University of Miami
in partial fulfillment of the requirements for
the degree of Doctor of Philosophy

Coral Gables, Florida

June 2009

UNIVERSITY OF MIAMI

A dissertation submitted in partial fulfillment of
the requirements for the degree of
Doctor of Philosophy

A MODEL TO DESCRIBE SPATIAL AND TEMPORAL VARIATION OF PHOSPHORUS MASS AND FLUXES IN TREE ISLANDS OF SHARK RIVER SLOUGH IN THE EVERGLADES

Marcelo E. Lago

Approved:

_____ Jorge F. Willemsen, Ph.D. Professor of Applied Marine Physics	_____ Terri A. Scandura, Ph.D. Dean of the Graduate School
_____ Donald DeAngelis, Ph.D. Adjunct Professor of Biology	_____ Leonel Sternberg, Ph.D. Professor of Biology
_____ John D. Wang, Ph.D. Professor of Applied Marine Physics	_____ Fernando Miralles-Wilhelm, Ph.D. Associate Professor of Civil and Environmental Engineering Florida International University

LAGO, MARCELO E. (Ph.D., Applied Marine Physics)
A Model to Describe Spatial and Temporal Variation of Phosphorus Mass and Fluxes in Tree Islands of Shark River Slough in the Everglades (June 2009)

Abstract of a dissertation at the University of Miami.

Dissertation supervised by Professor Fernando Miralles-Wilhelm.
No. of pages in text. (375)

A numerical model has been developed to study the temporal and spatial variations of Phosphorus mass and fluxes around the tree islands of Shark River Slough in the Everglades. The developed model is based on a conceptualization of physical, chemical and biological processes that consider advective and diffusive transport of dissolved Phosphorus, adsorption on to soil, input from rainfall and external sources, and Phosphorus cycling in biomass. The biomass related processes are Phosphorus uptake, release as litter, transport as suspended litter and release from the decomposition of the deposited litter. The water flow and transport of dissolved Phosphorus in the numerical model are implemented originally in the simulator MODHMS. However, the transport equations for dissolved Phosphorus were also coded separately, as well as the balance equation for suspended litter particles and deposited litter. The parameterization of the model was conducted by using the data collected by Ross et al. [2004] in three tree islands of Shark River Slough, as well as other parameters reported among the literature. The model was calibrated in three phases. Initially, Manning coefficients were adjusted from surface water velocity data collected by Bazante et al. [2004]. Then the calibration of several groundwater flow parameters was performed from water table data collected at wells by Ross et al. [2004]. In the third phase, the Phosphorus input rate from external sources and the initial concentration of Phosphorus were calibrated by assuming that the average surveyed Phosphorus concentration in soil pore water remains approximately constant over a 10 year period. The quantitative assessment of the spatial distribution and temporal variations of Phosphorus mass and fluxes around tree islands obtained from the developed model corroborate the negative effect of the rainfall events on Phosphorus accumulation in the head of the tree island. However, the possible positive effect of the

ET driven water flows on Phosphorous accumulation was found not as relevant as hypothesed by other authors in the literature. According to the model results, most of the Phosphorus transport in the tree islands occurs as suspended particles in surface water, even though the transport of dissolved Phosphorus in pore water cannot be neglected around the head of the island. The model results also suggest that an input of Phosphorus from external sources (e.g., animal activity such as bird guano and other sources) is needed to preserve the average Phosphorus levels in the head and in the whole tree island. Finally, Phosphorus accumulation and losses in certain areas of the tree island suggest changes in vegetation that need to be investigated in future work. The developed model can be used as a predicting tool to gain insight into the potential effects of restoration scenarios in tree islands environments. The model could be run for hypothetical future conditions and contribute to provide quantitative information for conservation and restoration efforts in the Everglades and similar wetlands.

Acknowledgments

This project involves a variety of data and models that could not be carried out without the kindly collaboration of several people.

Pablo Ruiz and Mike Ross who provided the transect data surveyed at tree islands and collaborated in obtaining the soil surface and bedrock elevation maps resulting from them. They shared vegetation coverage maps, aerial images, the well location of tree islands wells and data about litter production and decomposition studies. Based on their valuable field experience, they also made comments, which were very useful to better capture the reality in the model.

David Reed and Mike Ross who provided the water table elevation data measured at different wells at tree islands from 2002 to 2003. These data were used to calibrate the groundwater parameters in the model. Discussions about the data acquisition procedure were also useful.

Jose Bazante and Helena Solo-Gabriele gave the overland velocity data that was used to calibrate the Manning coefficients of the model. Discussions on data acquisition and model results were useful. Jose Bazante also read the draft of this document and made useful corrections and comments.

Roy Sonenshein supplied hourly stage and rainfall data from stations available at EDEN project and also the updated German ET data from stations up to 2003. He also delivered a gazetteer with the station coordinates and helped me to locate G-620 station.

Sorab Panday and Vivek Bedekar provided the software (MODHMS, HydroGeoLogic, Inc.) that was used to obtain the water flow as well as the Phosphorus transport in the first part of the work. They gave me training and support on this software as well as in the preprocessing tool (ViewHMS, HydroGeoLogic, Inc.). They sent me the updates and discussed the implementation of the conceptual model on it.

In addition, I thank to my dissertation committee members Donald DeAngelis, Fernando Miralles-Wilhelm, Leo Sternberg, John Wang, and Jorge Willemsen (listed in alphabetical order) for their critical comments and useful recommendations during our periodic meetings and other communications forms**.** In particular, Fernando Miralles-Wilhelm, my advisor, made numerous contributions to my work and he was always there for periodic discussion. His guidance and his continuous support were essential factors to

conclude this work.

Finally, it is worth mentioning that this work was mostly supported by the National Science Foundation through the project Biocomplexity of Hydrologically-Controlled Vegetation Dynamics: Quantitative Comparative Analysis-Everglades and Cerrado Ecosystems under Soil Moisture and Nutrient Spatiotemporal Dynamics.

Table of Contents

List of Acronyms

AD: Advection-Dispersion

BH: Black Hammock (refers to the Tree Island name) or Bayhead (refers to the vegetation type)

BHS: Bayhead Swamp forest (similar as BS)

BS: Bayhead Swamp (refers to the vegetation type)

DIN: Dissolved inorganic nitrogen

E: Evaporation

ELM: Everglades Landscape Model

ELVM: Everglades Landscape Vegetation Model

ET: Evapotranspiration

GL: Gumbo Limbo (refers to the Tree Island name)

GW: Ground water

HH: Hardwood Hammock (refers to the vegetation type)

MA: Marsh (refers to the vegetation type)

MODHMS: numerical simulator distributed by HGL, Inc. based on MODFLOW.

N: Nitrogen

Nin: external nutrient (Phosphorus) input in the soil

OL: Overland

OLF: Overland flow

P: Phosphorus

SL: Satinleaf (refers to the Tree Island name)

SRM: Spikerush marsh (refers to the vegetation type)

SRP: Soluble reactive Phosphorus

SS: Sparse Sawgrass marsh (refers to the vegetation type)

T: Transpiration

TI: Tree Island

TN: Total nitrogen

TP: Total Phosphorus

TS: Tall Sawgrass (refers to the vegetation type)

VT: Vegetation type

List of Figures

Page

List of Tables

Page

Chapter 1. Introduction

Phosphorus is a limiting nutrient for vegetation in the Everglades marsh [Miao and Sklar, 1998]. The grassy vegetation, composed mainly of *Cladium jamaicense* (sawgrass) and *Eleocharis cellulosa* (spikerush), is adapted to Phosphorus limitation, and the Phosphorus-rich water released from agricultural areas and from canals have caused the invasion of other species such as *Typha domingensis Pers* (cattail) [Sklar et al., 2001].

The grassy vegetation is not uniformly distributed in the Everglades and a ridge and slough pattern is observed oriented along the flow direction. In the ridge, the grass is denser than in the slough [Ross et al., 2006].

The view of extensive grass areas in the Everglades is occasionally interrupted by areas with trees and bushes, which are referred to as tree islands. The tree islands may have different shapes, topography, and species of trees, among other characteristics; however, Ross et al. [2004] surveyed three tree islands in Shark River Slough and found several similarities. Those tree islands are composed by a head with hammock trees in a slightly elevated soil with a short hydroperiod. In this head area, the Phosphorus concentration in soil pore water is about one hundred times higher than in the surrounding marsh. The Phosphorus concentration, the soil elevation and the vegetation height decrease toward the tail, which is oriented in the direction of the regional flow.

The fact that Phosphorus remains concentrated in the head of the tree islands has been explained qualitatively in the literature through several mechanisms [Ross et al. 2004]. The transpiration of the trees may cause groundwater advective transport of Phosphorus toward the tree island. Animal activity (mainly producing bird guano) may represent also a net input of Phosphorus in the tree island. In addition, the soil in the head of the island may retain Phosphorus due to adsorption and mineralization processes. On the other hand, there are other mechanisms that may produce losses of Phosphorus in the tree island such as the advective transport caused by rainfall and by the regional gradient. The qualitative picture about why the Phosphorus is kept concentrated in the head of the tree islands becomes more challenging if one considers the spatial and temporal variability of all those mechanisms. In other words, the variability makes more difficult an assessment about the relative importance of the different processes.

Troxler-Gann [2005] and Troxler-Gann et al. [2005] reported an estimation of the nutrient (N and P) pools and fluxes around tree islands in the C-111 basin of the Everglades. The study was mostly focused on N and presented annual averaged values. Moreover, Ross et al. [2006] reported a simple model to show the Phosphorus distribution (elongated plumes with a shape similar to tree islands) caused by enhanced ET sites in a regional gradient. However, this model has limitations since it does not consider the vegetation uptake and release of Phosphorus, the soil adsorption, the effect of the overland (OL) flow, among other phenomena.

In summary, there is a need for more detailed research of how Phosphorus is kept concentrated in the tree island head. Thus, further studies of the different mechanisms involved in this process are warranted. This knowledge would help to better understand not only the evolution of tree islands, but also how to preserve them [Sklar and van der Valk, 2002]. The research work presented herein makes a contribution to that knowledge by developing a conceptual and numerical model to simulate the spatial and temporal variations of Phosphorus mass and fluxes in tree islands of the Everglades.

This document is structured in six chapters. Chapter 1 introduces some general aspects of the tree islands, emphasizing on the Phosphorus fluxes around them. Moreover, previously developed models that are relevant for simulating the tree island processes are described. At the end of this chapter, the main objectives of the current work are stated. Chapter 2 presents the proposed conceptual model, followed by the governing equations, the numerical procedure developed and the assumption and limitations introduced. Chapter 3 contains the parameterization of the model. It contains a survey of the available data in the literature and its processing in order to estimate parameters used in the numerical model. This chapter describes the vertical layer boundaries, the transport properties in the different layers, the water source components, the lateral boundary conditions, the initial conditions, the biomass related parameters, the external fluxes, the description of the base case and the assumptions and limitations introduced during the parameterization. Chapter 4 includes the procedure followed for model calibration as well as its results. The calibration is divided in three steps: the calibration of the Manning coefficient of the model by using the available surface water velocity data, the calibration of groundwater (GW) flow parameters by using recorded water table elevation data, and

the calibration of the Phosphorus transport part of the numerical model. Chapter 5 presents a summary of the model results and further discussions based on the main objectives listed at the end of Chapter 1. The concluding chapter, Chapter 6, summarizes the model development, the main results and gives some recommendations for future work.

1.1 Characteristics of Tree Islands

This section introduces the different types of tree islands in the Everglades and the correlations among vegetation, water and nutrients reported in Shark River Slough for the surveyed tree islands. The feedback mechanisms on tree islands and the tail formation hypotheses are discussed. Phosphorus fluxes around the tree islands are described. Following this, three previous modeling efforts related to tree islands are reviewed, leading to the statement of the objectives of this dissertation.

1.1.1 Types of Tree Islands

Tree islands in the Everglades have been classified into two major groups: the pop-up, floating or battery tree islands, and the fixed tree islands [Sklar and van der Valk, 2002]. This research work is focused on fixed tree islands, which are believed to be developed from slight topographic height differences in the underlying limestone bedrock. The tallest trees and shrubs are found in the bedrock platforms, which form the head of the island. Contrary to pop-up tree islands, the fixed ones have a tail, which is typically of sedimentary origin [Ross et al. 2004], and it is oriented in the direction of the regional water flow. The structure of the fixed tree islands is detailed in the field work reported by Ross et al. [2004].

1.1.2 Correlation among Vegetation, Water and Nutrients

A correlation among the vegetation type, the water level and the nutrient content in tree islands of Shark River Slough, has been reported by Ross et al. [2006] (see Table 1 and Figure 1). The head of the island is occupied by the tallest trees (Hardwood Hammock), which requires the lowest water depth and the highest Phosphorus concentration to survive. As one moves away from the head of the island, the average water depth increases and the Phosphorus concentration decreases. The Hardwood Hammock (HH) trees cannot survive under these conditions and the vegetation type

changes gradually to Bayhead (BH), Bayhead swamp (BS), Tall Sawgrass (TS), Sparse Sawgrass (SS) and Spikerush marsh (SRM).

Vegetation type	N of sites	Mean water depth (cm)	30-day maximum water depth (cm)	Hydroperiod (days)
Spikerush marsh	78	41.2	64.0	344.1
Sparse sawgrass	182	36.9	57.8	339.3
Tall sawgrass	54	32.2	52.4	322.6
Bayhead swamp	3	13.0	33.8	262.7
Bayhead	4	−4.2	16.6	156.9
Hardwood hammock	3	−69.3	−48.4	0.2

Table 1. Mean water level and nutrient content for several vegetation types. Reproduced from Ross et al. [2006].

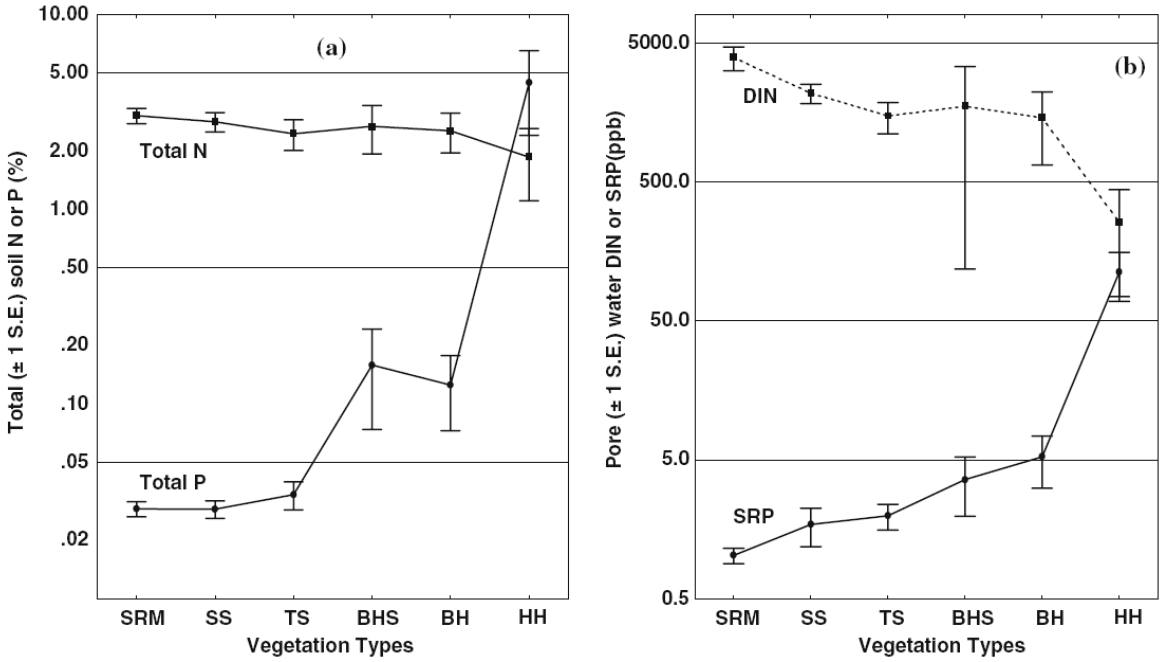

Figure 1. Average Phosphorus and nitrogen amount contained in soil (a) and dissolved in soil pore water (b) for several vegetation types. Reproduced from Ross et al. [2006].

1.1.3 Hypothesized Feedback Mechanisms

The correlations among vegetation type, mean water depth and Phosphorus content have been tentatively explained through the following feedback mechanisms:

1) The presence of trees increases soil elevation. During their life, trees produce debris, which increases the organic soil layer elevation around them. As the soil elevation increases more soil area is available for hammock tree colonization.

2) The presence of trees increases Phosphorus availability. Hammock trees have a high transpiration rate causing a depletion of the water table during the daytime. They take the nutrients dissolved in the soil water and discharge them (in the debris) to the peat layer around them. The trees also attract birds and other animals, resulting in a net input of nutrients into the island [Ross et al. 2004].

3) Soil elevation cannot be too high above the water table. During the dry season, the frequent fires in the Sawgrass may penetrate the tree island if the soil is too dry (soil level more than 2 ft above the water table), destroying the trees and consuming the peat layer up to the water table level [Wade et al. 1980]. On the other hand, the peat anaerobic (i.e., when the water table is higher) decomposition rate is lower than in aerobic (i.e., when the water table is lower) conditions [Mitsch and Gosselink, 2003]. These two mechanisms prevent the soil elevation in the tree islands from rising too high above the mean water table level.

1.1.4 Tail Formation Hypotheses

Figure 2 shows the two proposed hypotheses to explain the formation of tree island tails: the *hydrodynamic* and the *chemo-hydrodynamic* [Sklar and van der Valk, 2002]. In the hydrodynamic hypothesis, the tail is developed due to litter released from the head being deposited downstream by surface water flow. In the chemo-hydrodynamic hypothesis, the tail develops due to the release of nutrients from the head. This process was perceived by these authors as a plume of nutrients behind the head created by the surface water or shallow groundwater (also referred herein as soil water).

In the hydrodynamic hypothesis, the material suspended in surface water and transported from the head to the tail of the tree island may have different sources. The suspended material may be litter that falls directly onto the surface water, as well as litter and smaller organic particles eroded from the bottom. The litter that has fallen onto the dry soil may be transported later by a rainfall event into the surface water, or may be re-suspended when the water level rises and the soil is inundated. The deposition of the transported organic material might cause a net increase of the soil elevation by peat accumulation (peat that is richer in nutrients) downstream from the island head, especially when the conditions are more anaerobic and the decomposition rate is slower.

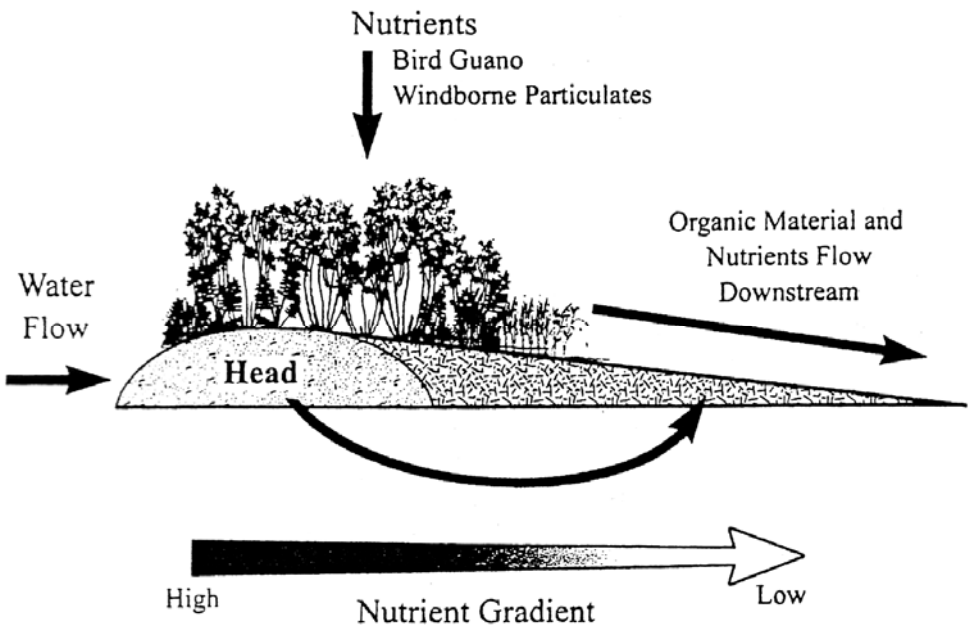

Figure 2. Schematic representation of the transport of organic matter and nutrients to the tail of the tree islands. Reproduced from Wetzel [2002].

Regarding the chemo-hydrodynamic hypothesis, it is not clear that the surface water flow contributes to the increase of the nutrient concentration in the tail. During the wet season, a low-in-nutrients surface water flow of about 1cm/s might wash away part of the dissolved nutrients from the submerged soil in the head but also from the tail region. During the dry season, however, when there is no surface water flow, the evapotranspiration rate of the vegetation in the head and tail of the island creates a soil water flow toward the island from the neighboring areas. The advective transport of nutrient through this flow and the nutrients uptake by the trees were mentioned before as a component of the feedback mechanism that likely concentrates and maintains the Phosphorus in the tree islands.

1.2 Phosphorus Fluxes around the Tree Islands

Figure 3 shows the water fluxes around a tree island. In the marsh areas, rainfall brings water in, evapotranspiration removes water and there is also a surface and groundwater flow along the regional gradient. In the head of the tree island, however, the soil surface is slightly higher and it remains dry most of the year. As explained below in further detail, the same ET and rainfall rates on both marsh and head areas may drive a

groundwater flow toward or away from the island, respectively. The effect of the regional gradient on the tree island is a flux toward the tail.

The water fluxes between the tree island and the surrounding marsh driven by ET and rainfall are sketched in Figure 4. In equilibrium, the water surface elevation (hydraulic head) is the same in the tree island as in the marsh, and there is no flow between those areas. The most common situation is when the head of the tree island remains dry (water table level is below the ground) and the marsh remains inundated. Assuming the same ET rate on both areas, the hydraulic head decreases more in the tree island due to the porosity of the soil. Thus, the hydraulic head difference causes a groundwater flow toward the tree island. On the other hand, when rainfall exceeds the ET rate, the hydraulic head in the tree island becomes higher than in the marsh due to the porosity of the soil and groundwater flow in the opposite direction is generated. If the rain is heavy enough to exceed the infiltration rate, an overland flow (runoff) from the tree island toward the marsh may also occur.

The Phosphorus fluxes around a tree island are also sketched in Figure 3. In the marsh areas, there is an input of available Phosphorus through the rainfall, an advective transport due to the regional gradient flow, and Phosphorus cycling in the biomass. Live biomass takes up dissolved Phosphorus and releases litter containing it. Surface flow due to the regional gradient or due to the rainfall may transport the litter while it is suspended. The litter decomposition returns the Phosphorus into the solution.

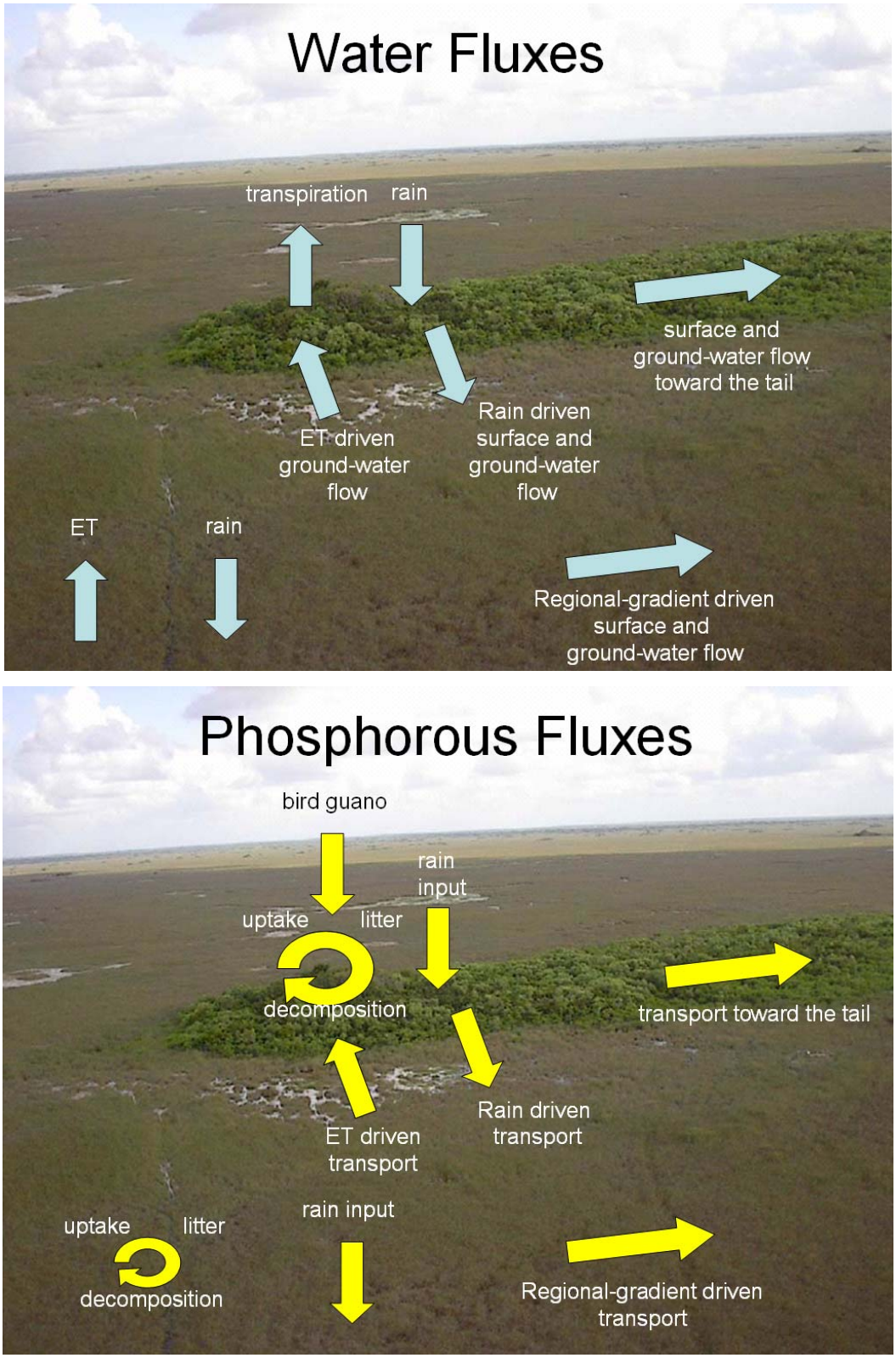

Figure 3. Water and Phosphorus fluxes around tree islands of Shark River Slough. Background photo corresponds to Satinleaf tree island and it was reproduced from Bazante et al. [2004].

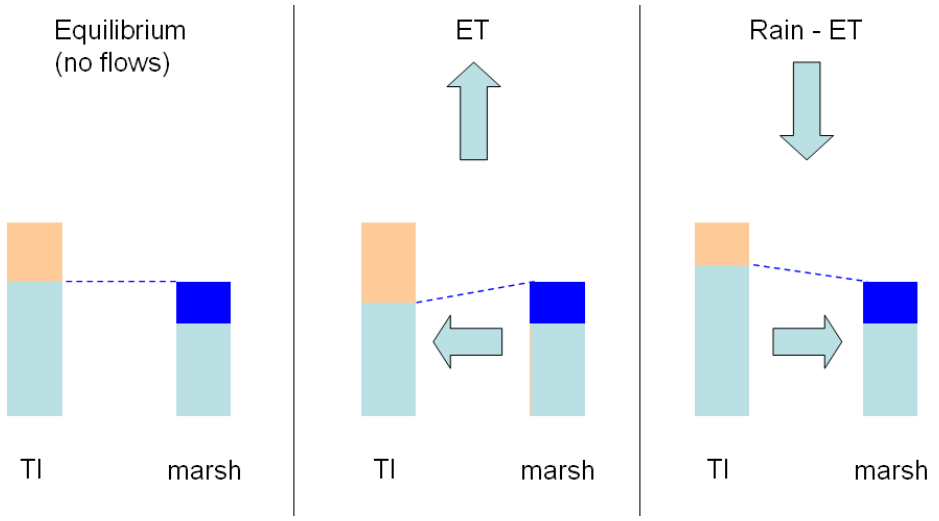

Figure 4. Schematic view of the water fluxes driven by ET and rain around the tree island. See text for details.

In the tree island, there is a similar Phosphorus cycling in the biomass as in marsh areas, probably involving larger Phosphorus amounts. The ET causes advective transport of Phosphorus toward the tree island while rainfall causes advective transport in the opposite direction. The regional gradient flow causes advective transport of Phosphorus toward the tail. Finally, additionally to the Phosphorous input in rainfall, an external source of Phosphorus from animals that visit/inhabit the tree islands areas can be expected.

It is worth emphasizing that surface water flow caused by rainfall (runoff) or by the regional gradient, transports Phosphorus not only in dissolved form, but also as constituent suspended particles. Some researchers believe that the transport of Phosphorus as suspended particles may play a key role in the Phosphorus fluxes around tree islands [Ross, personal communication].

Tree Islands in Shark River Slough have been formed for a period of few thousand of years [Ross et al, 2004]. In this slow evolution process, the vegetation coverage and the soil elevation around the tree island are not expected to change considerably after several years, unless a catastrophic event happens (fire, hurricane or freezing). In view of this, an assumption made in this work is to consider that the distribution of Phosphorus in the tree island remains approximately constant on average over several years. In this state of pseudo-equilibrium, Phosphorus inputs in the head of the island (caused by the ET driven fluxes and by the external input from rain and

external sources such as animal activity) must counterbalance approximately the Phosphorus losses (derived from the fluxes driven by rain and regional gradient).

All the Phosphorus fluxes in the aforementioned balance have a spatial and seasonal variability, and it is interesting to understand how those mechanisms take action in space and in time to result in the Phosphorus distribution that has been observed around the tree islands; in particular, a soil-pore-water Phosphorus concentration in the head that is maintained about one hundred times higher than in the marsh.

1.3 Previous Tree Island Modeling Efforts

Three previous tree island models are introduced in this section. Although those models do not capture all the complexity of the Phosphorus transport in the small scale of a tree island, some of their relations and parameters are useful for the model developed later in this work.

1.3.1 Everglades Landscape Model (ELM)

The *Everglades Landscape Model* (ELM) is a regional scale model designed to improve understanding of the ecology of the greater Everglades landscape. This model integrates, or dynamically combines, the hydrology, water quality, and biology of the mosaic of habitats in the Everglades landscape. It encompasses the greater Everglades region with grid cells of 1 km^2 area [Fitz, 2006].

Table A-1 in Appendix A1.2 shows a list of the biomass related parameters considered in ELM version 2.5 for several habitats that may be found around the tree islands of Shark River Slough. The correspondence of those habitats with the vegetation types defined by Ross et al. [2004] is summarized in Table A-2, Appendix A1.2.

1.3.2 Everglades Landscape Vegetation Model (ELVM)

The *Everglades Landscape Vegetation Model* (ELVM) was developed to study the spatial and temporal interactions among vegetation, water, fire and nutrients. This model was implemented by Wu et al. [2003] in order to study the tree island development and stability in extensive regions of the Everglades. It can simulate an area as large as 10,000 km^2, with a grid cell size of 1 ha, over a period of 100 years, with a time step of one day.

In each cell there are five vegetation community types as follows: tree islands,

Cladium jamaicense (sawgrass), *Typha spp*. (cattail), wet prairies (dominated by *Eleocharis spp*. and *Panicum spp*.), and slough (deeper water areas dominated by water lilies, *Nymphaea spp*. and broadleaf emergent species). Growth and succession within the cell are controlled by a set of forcing functions such as hydroperiod, water depth, nutrients (N and P) and disturbances (fires, hurricanes and freezes). The evolution of the water level is an input from other models.

The equations and parameters in version 2.02 of the ELVM model [Wu, 2004] are described in the Appendix A1.3. The equations in that version slightly differ from the ones reported by Wu et al. [2003]. The Appendix A1.3 also encloses an evaluation of the model for several vegetation types (Tree Island, Sawgrass and Wet prairie) for the case of no stress. The results from this special case are compared with measured values.

1.3.3 Model by Stothoff and Coworkers

A distribution of enhanced evapotranspiration (ET) zone locations superimposed on a regional gradient was recently simulated by Stothoff and co-workers. The results reported in Ross et al. [2006] have shown a nutrient distribution in groundwater in the form of elongated concentration plumes similar to the distribution observed in the fixed tree islands (see Figure 5). Thus, the authors suggested that the Phosphorus transport driven by evapotranspiration and the regional flow is important to explain the nutrients patterning in the Everglades.

The following comments emerge from the simulation by Stothoff and co-workers:

1) The results support the chemo-hydrodynamic hypothesis considering that only the head of the island is needed to obtain the elongated nutrient distribution, regardless of the soil elevation behind the island. In other words, those results suggest that a tree island with just a head would have a distribution of nutrients downstream and after that, the typical distribution of vegetation and the soil elevation in the tail would develop gradually.

2) The simulation assumed that pure water is input from upstream and that the external input of nutrients is uniform over the entire area. Both assumptions are not realistic.

3) The plume distribution is obtained under steady state conditions. However, the water table level has seasonal variations. Thus, the nutrient distribution (plume) may

change during the year, and may be far the steady state conditions.

4) The model only considers the uptake of pure water (not nutrients) in the enhanced evapotranspiration zones, which produces the nutrient accumulation around those zones. However, during transpiration vegetation also takes up the dissolved nutrients and the net effect in the concentration of Phosphorus in soil water depends on the Phosphorus released as litter, the litter transport and its decomposition. Moreover, all those litter related processes may have a seasonal dependence.

5) The rainfall driven flows are not considered in this model. Rainfall may cause groundwater flow from the tree islands to the marsh and, therefore, produce an advective Phosphorus transport contrary to the one driven by ET.

6) The overland flow is not considered in this model. This flow caused from regional gradient and from rainfall runoff may transport dissolved Phosphorus and also Phosphorus constituent suspended particles away from the head of the island.

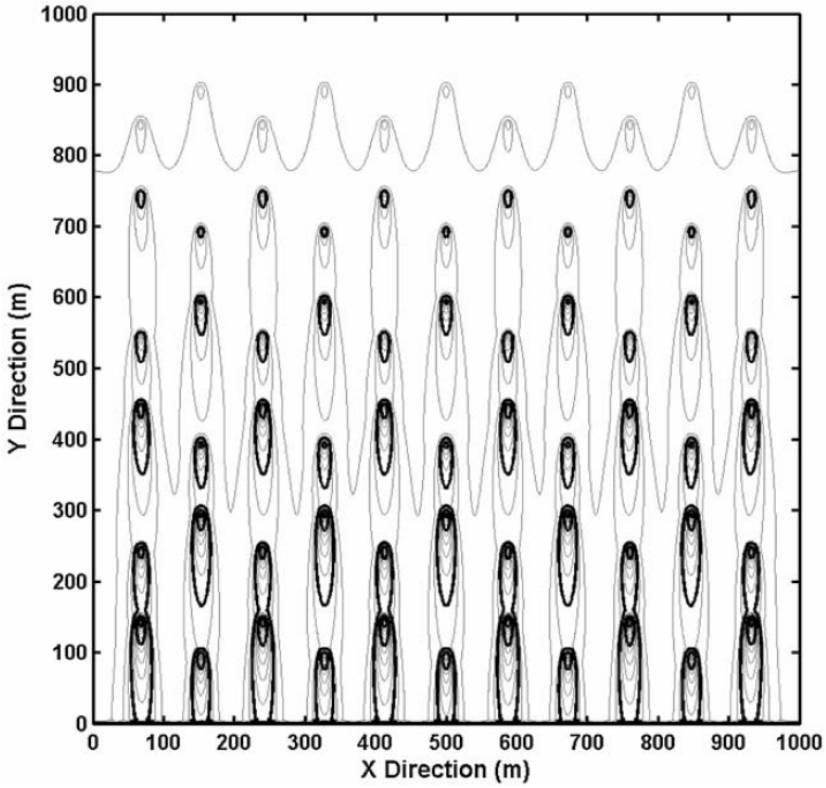

Figure 5. Steady-state concentration (ranging from 0 to 34 mg/m^3) of pore-water Phosphorus. The gray contours are going every 2 mg/m^3 and the black ones every 10 mg/m^3. The ratio of slough concentration to peak evapotranspiration-zone concentration is about 5.5 for downstream zones. Reproduced from Ross et al. [2006].

In summary, the model proposed by Stothoff and co-workers to reproduce a Phosphorus concentration plume around the tree islands does not include important mechanisms of the Phosphorus cycling. Moreover, their model does not consider the temporal variability of the mechanism involved, such as seasonal variations in regional water table and other variables, temporal distribution of rainfall events and diurnal changes in the ET rates.

1.4 Objectives

The limitations of the simple model proposed by Stothoff and co-workers (previously discussed in sub-section 1.3.3) in reproducing the Phosphorus spatial distribution around the tree island, are noticeable after analyzing the complexity of the Phosphorus fluxes around the tree islands. Other previous ecological models like ELM and ELVM are not focused on quantifying the processes of Phosphorus transport in the smaller scale of a tree island.

Previous approaches of finding steady state Phosphorus distributions (by Stothoff and co-workers) or estimating the annual average pools and fluxes from limited field data [Troxler-Gann, 2005] do not account for the temporal variability of the Phosphorus distribution at several time scales, i.e., variations due to seasonal changes in water elevation and other parameters, rainfall events and ET rate changes during the day and the night.

The contribution of this dissertation is to consider the spatial and temporal variability of the different mechanisms involved in the Phosphorus transport in tree islands.

To this end, this dissertation focuses on the development of a process-based high-resolution numerical model to study the spatial and seasonal variability of the Phosphorus mass and fluxes in tree islands of the Everglades, and in particular, around the fixed tree islands located in Shark River Slough. The developed model has been used to address the following specific objectives:

1) Provide a quantitative assessment of the spatial distribution and temporal variations of Phosphorus mass and fluxes around tree islands.

2) Compare the effects of rainfall and ET events on Phosphorus accumulation in the head of the tree island.

3) Quantify the relative importance of dissolved Phosphorus transport versus transport of Phosphorus as suspended particles in overland flow.

4) Explore the potential influence of an external input of Phosphorus, such as animal activity (e.g., bird guano) and other sources on the average Phosphorus levels in the tree island..

5) Infer vegetation changes (like growth or decay) from Phosphorus accumulation or losses in certain areas.

Chapter 2. Model Development

This chapter contains a detailed description of the conceptual model, equations and numerical procedure proposed in this work. The main basis of the model relies on detailed balancing of the Phosphorus fluxes around the tree islands introduced in the section 1.2 of the previous chapter.

2.1 Conceptual Model

Figure 6 summarizes the conceptual model proposed to study the Phosphorus transport in tree islands. It has three vertical layers: a surface water layer, a soil layer and a rock layer. There are water pools in each layer that interact through lateral and vertical flows. For each water pool, there is a dissolved Phosphorus pool that is transported due to advective and diffusive processes. In the groundwater layers, dissolved Phosphorus is interacting with adsorbed Phosphorus onto solid surfaces. Rainfall represents an external input of water and dissolved Phosphorus into the surface water pools while evaporation causes a water output. The live biomass pool takes up water and dissolved Phosphorus from the soil layer pools while transpiring and releasing Phosphorus in the form of litter into the surface water layer pool. Phosphorus in the suspended litter pool can be transported horizontally by convection or diffusion, and also interact with the deposited litter pool due to deposition or erosion processes. Finally, Phosphorus in the deposited litter pool is released as a solution due to decomposition processes.

The conceptual model proposed covers most of the processes involved in the Phosphorus transport in tree islands and improves the spatial and temporal resolution of previous modeling efforts. The transport of Phosphorus in suspended litter and the adsorption in soil and rock layers have been recognized as two important processes in the Phosphorus transport, and their inclusion in this work is a substantial enhancement to the model formulation. The division in soil and rock layers (usually referred to as vadose zone and saturated layer, respectively) is also an improvement regarding previous models that consider only a single layer. This allows consideration of the different processes and physical parameters in each of the two layers.

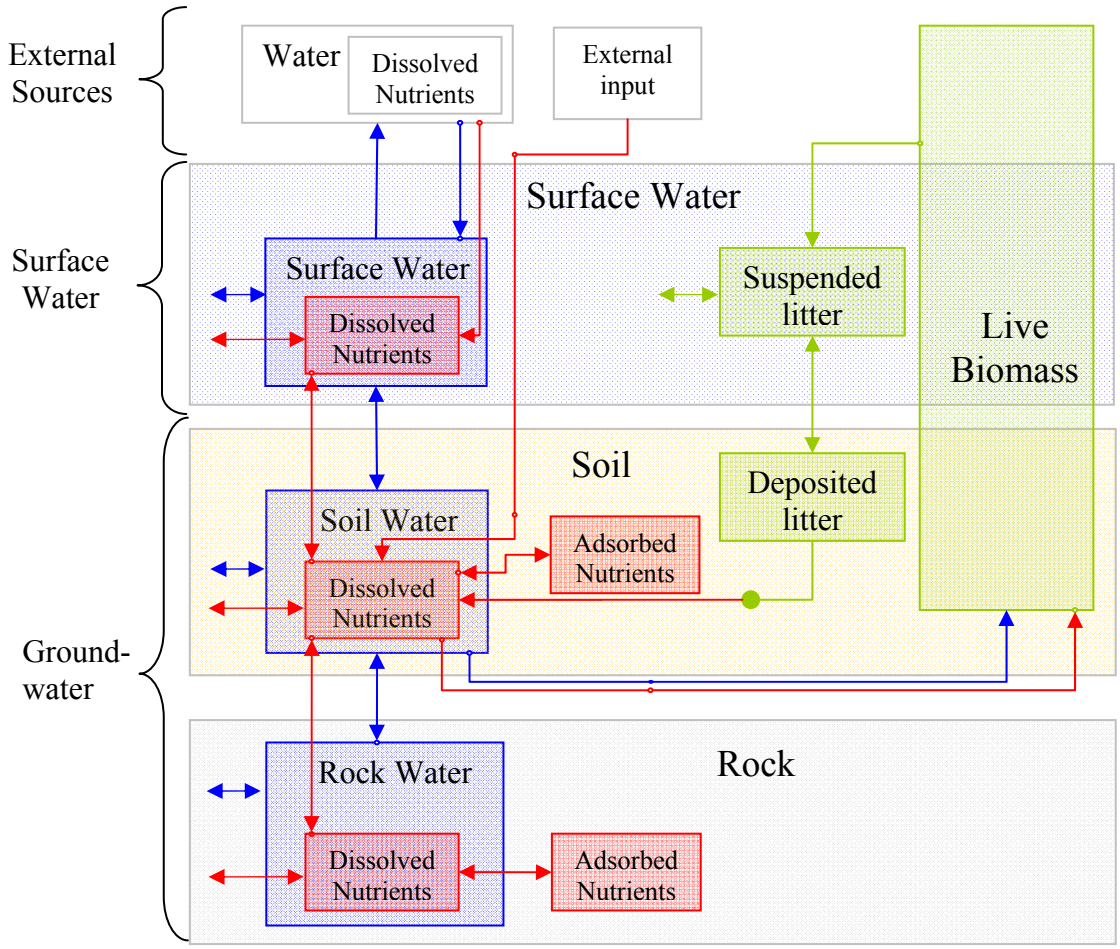

Figure 6. Proposed conceptual model in the vertical column. The word "Nutrients" refers specifically to Phosphorus. Lateral arrows that do not end in a box represent the horizontal transport between neighbor areas.

2.2 Numerical Model Implementation

The water flow and transport of dissolved Phosphorus in the model were implemented at first in a commercially available numerical simulator MODHMS. This model is based on MODFLOW and it integrates overland and groundwater flow, as well as the dissolved species transport [Panday and Huyakorn, 2004], [HydroGeoLogic (HGL) Inc., 2006]. MODHMS can consider unsaturated water flow and the adsorption of species onto solid surfaces. Besides, it allows the use of non-uniform grid spacing, which is an advantage while considering the spatial variability of the parameters around the tree islands. The net external input of dissolved Phosphorus from external sources (e.g., animal activity and other sources), biomass uptake and litter decomposition can be

considered numerically by injecting in each soil cell as a small volume of concentrated water by using the WEL package.

During the course of this investigation, it was determined that the applicability of the solute transport in MODHMS is limited by the fact that MODHMS does not have the capability to consider a negative external input of Phosphorus, i.e., the extraction of water with dissolved species such as that caused by uptake/transpiration by vegetation. Thus, the transport equations for dissolved Phosphorus were coded by using MatLab as the programming tool in order to overcome that limitation. The developed code uses the solution of the water flow problem from MODHMS. It reproduces the same numerical results obtained with MODHMS for the transport problem in approximately the same running time. In the developed code, the dissolved Phosphorus can be removed whenever mass is available, by including an outgoing water flow with dissolved species. Thus, there is in general a desired Phosphorus extraction rate as input and an equal or lower extraction rate from mass availability as output.

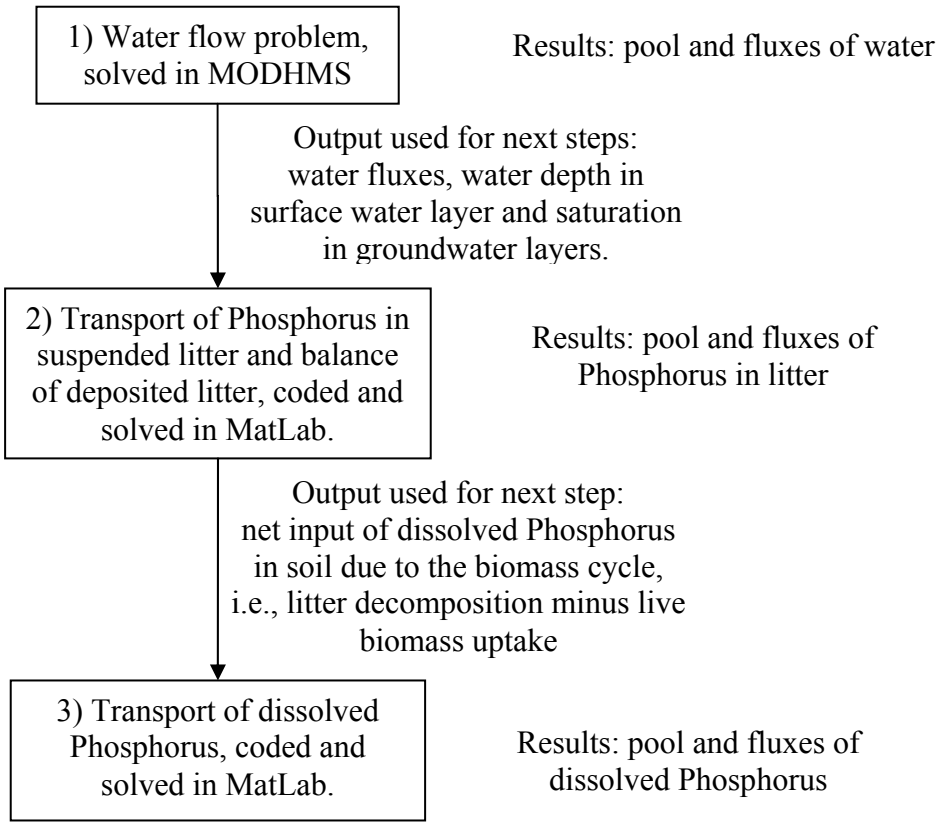

Figure 7. Steps followed in the solution procedure.

In addition to this, MODHMS cannot handle the transport of Phosphorus in suspended litter particles or consider the balance equation of deposited litter. These processes were also added in the MatLab code. The litter balance equations are solved by using the solution of the surface water flow problem from MODHMS. Then the estimated net dissolved Phosphorus input from biomass uptake, litter decomposition and external input is introduced in the transport-of-dissolved-Phosphorus problem. Figure 7 summarizes the model solution procedure.

In the following sections, the balance equations for the transport of dissolved Phosphorus, for the transport of Phosphorus in suspended litter and for the deposited litter are presented as well as the numerical procedure proposed. The equations for the water flow problem and the numerical procedure utilized in MODHMS are reported elsewhere [Panday and Huyakorn, 2004], [HydroGeoLogic (HGL) Inc., 2006]. A discussion about how MODHMS considers the infiltration from the OL layer and the meaning of the leakance coefficient in its approach is presented in Appendix A2.1.

2.2.1 Transport of Dissolved Phosphorus

The equations and the numerical procedure used in MODHMS for the transport of dissolved Phosphorus are described in detail elsewhere [Panday and Huyakorn, 2004], [HydroGeoLogic (HGL) Inc., 2006]. For this work, a simplified version of the balance equation was programmed, corresponding to a single component case, no reaction or decay and no transfer to the inactive phase. Under these assumptions the advection-diffusion equation valid for the groundwater layers is

$$\frac{\partial}{\partial t}(\phi SC)+\vec{\nabla}\cdot\left(\vec{V}C\right)=\vec{\nabla}\cdot\left(D^{*}\vec{\nabla}C\right)-\frac{\partial}{\partial t}\left(\rho_{B}X_{a}\right)+\varepsilon_{c}. \qquad (1)$$

Here C is the concentration of dissolved component (mass per unit volume), ϕ the porosity, S the water saturation, t the time, $\vec{V}$ the macroscopic velocity, D^{*} the effective diffusion coefficient, ρ_{B} the soil bulk density, X_{a} the mass fraction adsorbed on soil and ε_{c} represents the source of mass per unit of volume and time.

The vertically averaged advection-diffusion equation for the overland layer is

$$\frac{\partial}{\partial t}(hC)+\vec{\nabla}\cdot\left(h\vec{V}C\right)=\vec{\nabla}\cdot\left(D^{*}h\vec{\nabla}C\right)+h\varepsilon_{c}. \qquad (2)$$

The discretized version of eq. (1) and (2) in finite differences (finite volume approach) is

$$\frac{G^{m+1}C^{m+1} - G^m C^m}{\Delta t} = (1-f)F^m + fF^{m+1}, \tag{3}$$

for each i, j, k grid cell in the model. Indexes i, j and k runs for x, y and z direction, respectively and *m* is the time step number. *G* is an accumulation factor that satisfies

$$G = \Delta X \Delta Y \Delta Z \begin{cases} 1 & \text{OL layer} \\ \left(\phi S + \rho_B \dfrac{\partial X_a}{\partial C}\right) & \text{GW layers} \end{cases}. \tag{4}$$

$\Delta X \Delta Y$ is the horizontal area and $\Delta Z = h$ the layer depth. The term $\dfrac{\partial X_a}{\partial C}$ is found from the equilibrium adsorption equation (see equation (27) section 3.2.2.5) and it is in general a function of the concentration C.

Parameter f in equation (3) determines the time scheme as explicit ($f = 0$), implicit ($f = 0.5$) or fully implicit ($f = 1$). The fully implicit scheme ($f = 1$) is used to avoid numerical oscillations as it is implemented in MODHMS.

The net incoming mass per unit time, F, contains the contribution of the advective and diffusive transport, and from sources and sinks, i.e.

$$F = F_{conv} + F_{diff} + F_{\varepsilon}, \tag{5}$$

where

$$\begin{aligned} F_{conv} = {} & FRF_{i-1}C_{i-1/2} - FRF\,C_{i+1/2} + \\ & FFF_{j-1}C_{j-1/2} - FFF\,C_{j+1/2} + \\ & FLF_{k-1}C_{k-1/2} - FLF\,C_{k+1/2} \end{aligned} \tag{6}$$

$$\begin{aligned} F_{diff} = {} & \Delta y\left\{\left(D^* h\right)_{i+1/2}\left(\frac{C_{i+1} - C}{x_{i+1} - x}\right) - \left(D^* h\right)_{i-1/2}\left(\frac{C - C_{i-1}}{x - x_{i-1}}\right)\right\} + \\ & \Delta x\left\{\left(Dh\right)_{j+1/2}\left(\frac{C_{j+1} - C}{y_{j+1} - y}\right) - \left(D^* h\right)_{j-1/2}\left(\frac{C - C_{j-1}}{y - y_{j-1}}\right)\right\} + \\ & \Delta x \Delta y\left\{D^*_{k+1/2}\left(\frac{C_{k+1} - C}{z_{k+1} - z}\right) - D^*_{k-1/2}\left(\frac{C - C_{k-1}}{z - z_{k-1}}\right)\right\} \end{aligned} \tag{7}$$

$$F_{\varepsilon} = \begin{cases} F_{rain} & \text{OL layer} \\ F_{animal} + F_{release} - F_{uptake} & \text{GW layers} \end{cases} \tag{8}$$

Here FRF means volumetric flow rate at right face, FFF flow at front face and FLF flow at lower face. All these water flows at cell phases, the OL water depth (h) and GW water saturation (S), are obtained from the MODHMS solution to the water balance equations.

The concentration (C) at cell faces in the advective term (6) is assumed as the upstream value in order to prevent numerical oscillations. An analysis of the numerical diffusion introduced by this scheme is presented in the next section.

In the diffusive term (7), the product of the effective diffusion coefficient (D^*) and the transversal area at the cell faces are computed through the harmonic mean, i.e., the reciprocal of effective diffusion at cell faces equal to the sum of reciprocal values at cell centers. In the effective diffusion coefficient, only the pure diffusive part is considered, which is affected by the tortuosity, i. e.

$$D^* = D\begin{cases} 1 & \text{OL layer} \\ \phi^{4/3} S^{10/3} & \text{GW layer} \end{cases}; \tag{9}$$

where D is the diffusion coefficient in the bulk liquid. Equation (9) neglects dispersion and is rigorously valid in the low velocity limit. However, as discussed in Appendix A2.2, the numerical scheme proposed introduces dispersion.

The source term F_{ε} in (8) has the rain input for the OL layer (F_{rain}) and an external input for the GW layers, which in the soil layer of our conceptual model is the sum of the external input from animal activity and other sources (F_{animal}) and release-by-decomposition input ($F_{release}$) minus the mass uptake by vegetation (F_{uptake}).

The unknown concentrations C^{m+1} are found by solving the system of balance equations (3) by using the iterative Newton-Raphson method. The initial values used for the unknown concentrations are their values at the previous time step. By moving all the terms in equations (3) to the left hand side and expressing them in the matrix form $\vec{H} = \vec{0}$, the Newton-Raphson procedure uses the first order approximation;

$$\vec{H}^{(n+1)} = \vec{H}^{(n)} + \sum_p \frac{\partial H^{(n)}}{\partial C_p}\left(C_p^{(n+1)} - C_p^{(n)}\right) = \vec{H}^{(n)} + \overleftrightarrow{M}\left(\vec{C}^{(n+1)} - \vec{C}^{(n)}\right). \quad (10)$$

Superindexes n and $n+1$ refer to the iteration steps. The values for the unknown concentrations at the next iteration step ($\vec{C}^{(n+1)}$) are found by imposing $\vec{H}^{(n+1)} = \vec{0}$, as

$$\vec{C}^{(n+1)} = \vec{C}^{(n)} - \overleftrightarrow{M}^{-1}\vec{H}^{(n)}. \quad (11)$$

The matrix $\overleftrightarrow{M}$ to be inverted is large and sparse. Thus, several methods available in MatLab to solve the system of equations (11) were tested. The fastest method for this kind of sparse matrix is the generalized minimum residual method (function "*gmres*") with a preconditioner obtained from the LU factorizations (function "*luinc*"). In order to reduce the running time an important step to fine-tune is performed by optimizing the drop tolerance in *luinc* and the tolerance in *gmres*, as well as the limiting maximum number of total iterations in gmres. Further running time reductions are obtained by evaluating analytical expressions for the derivatives $\left(\frac{\partial H^{(n)}}{\partial C_p}\right)$ instead of their numerical derivatives while building the sparse matrix $\overleftrightarrow{M}$ and also by reusing that matrix in subsequent Newton-Raphson iterations.

In case of obtaining negative concentration at cells with negative net input source term F_ε, the absolute value of F_ε is reduced iteratively until the condition of non-negative concentration is reached.

2.2.2 Litter Balance Equations

A balance equation for litter is developed using conservation of mass and consideration of the following processes. The above-ground biomass litter can be suspended and transported by surface water. After some time, part of the suspended litter can be deposited, but if the water velocity is high enough, it can be eroded. In some situations, the litter can be re-suspended even at zero water velocity. The developed vertically averaged model equation to represent the mass balance of suspended litter in the overland layer has the form:

$$\frac{\partial}{\partial t}\left(hC_L\right) + \vec{\nabla}\cdot\left(h\vec{V}C_L\right) = \vec{\nabla}\cdot\left(hD_L^*\vec{\nabla}C_L\right) + \varepsilon_{Lprod} - \varepsilon_{Ldep} + \varepsilon_{Lres} + \varepsilon_{Lero}. \quad (12)$$

Here C_L is the suspended litter concentration, h the water depth, $\vec{V}$ is the horizontal velocity, D_L^* the effective diffusion coefficient, ε_{Lprod} is the above-ground litter production rate (mass per unit area per unit time), ε_{Ldep} the deposition rate, ε_{Lres} the resuspension rate and ε_{Lero} the erosion rate.

Similar balance equations to equation (12) have been reported for suspended particles in the literature [Tsujimoto, 1999], [Wu, et al., 2005], except for the resuspension term introduced here. The sedimentation and erosion processes are very sensitive to the characteristics of the particles (density, size and shape). Usually, the particles are classified as several types and for each particle type a constitutive relation for the net deposition rate ($\varepsilon_{Ldep} - \varepsilon_{Lero}$) is specified and a balance equation like (12) is written. Then every equation is solved independently (in the low concentration limit) and the total sedimentation rate is the sum of all the contributions [Julien, 1995].

On the other hand, the resuspension rate term (ε_{Lres}) is included on (12) in order to take into account other processes that contribute to the resuspension of the particles. In the case of the Everglades, the rewetting of dry areas can resuspend dry litter (with a lower bulk density than water) [Davis, 1994], the production of gas in the peat layer can also produce particle resuspension [Jose Bazante, personal communication], as well as other water movements near the bottom produced by wind waves and water temperature differences, animal activity, etc.

Leaf litter suspended in surface water in the Everglades is modeled as a group of suspended litter particles, with representative dimensions. For the deposition and erosion terms the following simple dependencies are assumed:

$$\varepsilon_{Ldep} = v_S C_L , \tag{13}$$

$$\varepsilon_{Lero} = \frac{C_E}{v_S} V^2 . \tag{14}$$

The deposition rate is assumed proportional to the averaged concentration and to the settling velocity v_S. On the other hand, the erosion rate is considered proportional to the bottom stress, which is proportional to the surface slope in steady state conditions and therefore according to the Manning equation, is proportional to the horizontal velocity

squared. C_E is a particle-dependent parameter in the proportionality factor that has units of concentration. This proportionality assumes that the critical stress necessary to resuspend the litter particles is negligible. A more complex treatment of the erosion deposition terms is offered by Tsujimoto [1999] and Wu, et al. [2005].

The dependence of the net sedimentation rate on the velocity from (13) and (14) is sketched in Figure 8. The maximum deposition rate occurs at zero horizontal velocities. As the horizontal velocity increases, the net sedimentation rate decreases until reaching a null value, where deposition and erosion rates are equal. A further increase in the velocity produce negative net deposition rates, which means a net erosion of particles from the bottom.

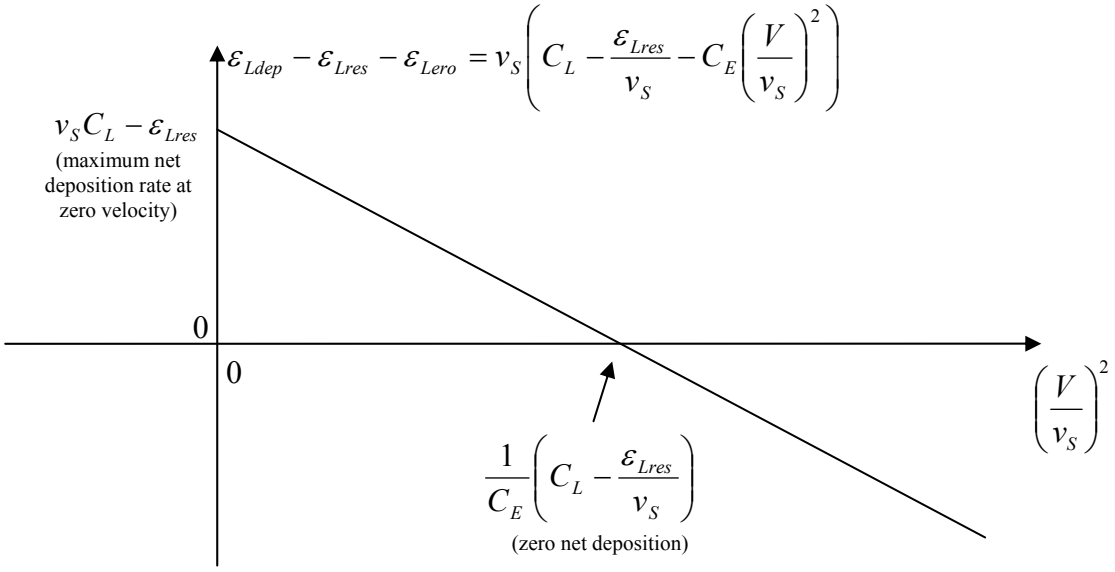

Figure 8. Dependence of the net sedimentation rate on the horizontal velocity according to equations (13) and (14).

The deposited litter amount (L) satisfies the balance equation

$$\frac{\partial L}{\partial t} = -r_{dec} L + \varepsilon_{Ldep} - \varepsilon_{Lres} - \varepsilon_{Lero}, \tag{15}$$

where $r_{dec} L$ is the decomposition rate.

Because the Phosphorus litter content depends on the vegetation type and where it is produced, it is more convenient to write the previous balance equations for the mass of Phosphorus and not for the mass of litter.

Notice that the solutions for the suspended and deposited litter in a steady uniform case are:

$$0 = \varepsilon_{Lprod} - \varepsilon_{Ldep} + \varepsilon_{Lres} + \varepsilon_{Lero} \Rightarrow C_L^{\infty} = \frac{\varepsilon_{Lprod} + \varepsilon_{Lres}}{v_S} + C_E \left(\frac{V}{v_s} \right)^2 , \tag{16}$$

$$0 = -r_{dec} L + \varepsilon_{Ldep} - \varepsilon_{Lres} - \varepsilon_{Lero} \Rightarrow L^{\infty} = \frac{v_S}{r_{dec}} \left(C_L^{\infty} + \frac{\varepsilon_{Lres}}{v_S} - C_E \left(\frac{V}{v_S} \right)^2 \right) = \frac{\varepsilon_{Lprod}}{r_{dec}} . \tag{17}$$

The equilibrium values C_L^{∞} and L^{∞} are used as initial condition and also as boundary conditions in the model developed here.

Due to the similarity between the transport of dissolved Phosphorus and the transport of suspended litter, the same numerical implementation for dissolved Phosphorus was used here. However, in this case, the transport is only in the OL layer, and the horizontal water fluxes from MODHMS (FRF and FFF) are set zero for the GW layers as well as the vertical fluxes (FLF) for all layers. The diffusive transport is limited in a similar way. In the suspended litter transport problem, there is not adsorption, which makes the system of equations linear. In the case of the source terms, $\varepsilon_{Lprod} + \varepsilon_{Lero}$ they have an equivalent treatment as an external input mass rate in the dissolved Phosphorus transport problem. The deposition rate term ε_{Ldep}, however, depends on the concentration C_L and it is included as an equivalent ET uptake rate in the dissolved Phosphorus transport problem.

The deposited litter balance equation (15) is simpler to solve because there are not spatial derivatives. Therefore, once the concentration C_L is determined at the end of the time step Δt, and therefore the net deposition litter rate ($\varepsilon_{Ldep} - \varepsilon_{Lres} - \varepsilon_{Lero}$) is known, the deposited litter mass is computed as

$$L^{m+1} = \frac{L^m + \left(-\frac{r_{dec}}{2} L^m + \varepsilon_{Ldep} - \varepsilon_{Lres} - \varepsilon_{Lero} \right) \Delta t}{1 + \frac{r_{dec}}{2} \Delta t} . \tag{18}$$

Notice that the discrete mass rate due to decomposition (R_{dec}) is computed here from the central derivative on time, i.e.

$$R_{dec} = F_{release} = r_{dec} \frac{L^m + L^{m+1}}{2}. \quad (19)$$

The deposited litter cannot be a negative magnitude. Thus, if it is negative from (18), ε_{Lero} is set to be zero and the computation of ${C_L}^{m+1}$ and L^{m+1} is repeated.

Once the suspended and deposited litter problems are solved, the net input rate of dissolved Phosphorus into the soil due to the biomass is computed as the release rate ($F_{release}$) minus the uptake (F_{uptake}), which in this work is assumed to be equal to the Phosphorus-in-the-above-litter production rate (ε_{Lprod}).

Finally, notice that the litter balance equations can be solved independently from the dissolved Phosphorus transport problem under the assumption that the live biomass uptake (F_{uptake}) is not a function of the dissolved Phosphorus concentration in soil.

2.3 Assumptions and Limitations

It is important to recognize that the proposed model formulation has some assumptions and limitations in describing the Phosphorus transport in the tree islands; these assumptionsare listed below.

1) Litter is not only deposited into the surface water but also below the ground. The litter from the roots (below-ground biomass litter) in the model developed by Wu et al. 2002 represents a Phosphorus flux from the live biomass into the soil layer. By considering only the above-ground biomass litter production and omitting the below-ground biomass one, the model is assuming that the Phosphorus amount in the below-ground biomass litter pool is constant. Thus, the rate of Phosphorus produced in below-ground biomass litter is assumed equal to that released from it by decomposition.

2) The model assumes that the suspended litter does not decompose. In the Everglades, the suspended litter would transit a distance of 650 m (the length of the model domain considered in this study) with a typical sheet flow speed of 1m/s in about 18 hours, if it is not deposited. This is a very short time compared to the typical half time of the decomposition process of several months (see section 3.6.2). Thus, in the Everglades conditions no appreciable decomposition occurs while litter particles are suspended.

3) The conceptual model assumes that the litter decomposes totally, supplying Phosphorus into the solution. However, a more detailed model differentiates between the litter in an early stage of decomposition and the litter in an advanced stage of decomposition, which is commonly referred to as peat or organic soil. They have in general different mass fractions of Phosphorus and different decomposition rates. By considering only one deposited litter pool, the conceptual model assumes that mass fraction and decomposition rates are equal to an average value from early and advanced stages of decomposition.

4) The model does not include the immobilization and mineralization processes in soil. Therefore, it is assuming that those processes do not cause a significant net change in the dissolved Phosphorus pools. However, immobilization and mineralization processes in soils around tree islands may be important according to the field experiments conducted by Davis [1991]. The lack of further studies on tree island soils and the complexity of those soil processes lead us to neglect it in conceptual model. A discussion presented in section 3.6.4 address this limitation.

5) A more complete approach of the Phosphorus transport would include mortality events like hurricanes, freezes and fires [Wu et al. 2002]. In this work, the effects of those disturbances in the Phosphorus mass and fluxes are not considered. Mortality events for the live biomass like hurricanes, freezes and fires in general result in a reduction in the live biomass pool. Freezes cause an additional transformation of live biomass into dead biomass (litter). However, in hurricanes the litter produced might be carried out from the island as a consequence of the strong winds, reducing the total amount of Phosphorus in the pools of the tree island. The fires in general burn an amount of live biomass, litter and organic soil, and the resulting mineralized Phosphorus is easily dissolved by surface or rain water. Usually, the fires affect the *Claudium jamaicense* (sawgrass) areas and do not penetrate in the woody trees and bushes of the tree island, which maintain higher humidity. Thus, the fire may cause an input of Phosphorus in the surface water from the marsh vegetation that could help to maintain a higher accumulation of Phosphorus in the tree islands. In summary, these mortality events may be important in the Phosphorus transport, but their consideration is beyond the scope of this investigation.

6) The effect of the wind drag is neglected in the model. It is known that sustained wind may cause surface water displacements and surface slope changes [Jenter and Duff, 1999]. In fact, the inclusion of the wind drag in the model by Langevin et al. [2005] was found significant to predict coastal salinity in the southern part of the Everglades. Thus, the applicability of this model is limited to situations where the contribution of wind into the water momentum equation is relatively small.

7) The model formulation does not consider explicitly the possible Phosphorus input from enriched groundwater and from dry atmospheric deposition. The input from these two mechanisms was suggested by Wetzel et al. [2005] as more important than the input from other external sources such as animal activity. The input from ET-driven water flows through phosphorite-bearing sediments is to some extent contradictory to the low Phosphorus levels measured in groundwater wells in Shark Slough Valley [Rene Price, personal communication, 2006]. On the other hand, there are no measurements of the dry atmospheric deposition in the tree islands [Wetzel et al., 2005] and how effective the tree island head may be on trapping preferentially the fallout. In the case that these two Phosphorus sources are present in the tree islands in some amount, they would be considered implicitly in the external input rate (see Figure 6) that has likely a higher contribution from other sources, e.g., animal activity.

Besides the assumptions and limitations related to the conceptual model, there are others assumptions introduced during the model implementation, which are listed below.

1) MODHMS uses the Manning Equation as the momentum equation for the OL water flow problem. As discussed later in Appendix 3.4.1, the Forchheimer equation may be more appropriate for the flow through a dense vegetated surface.

2) The dispersion of dissolved and suspended Phosphorus is not explicitly considered in the model formulation. Further discussions, about the dispersion coefficient are presented in the parameterization chapter.

3) The dissolved Phosphorus in groundwater layers is assumed to be in equilibrium with adsorbed Phosphorus onto solid surfaces. A formulation that uses adsorption and desorption rates would consider the time approaching the equilibrium.

4) The suspended particle transport approach considers just one average type of suspended particle and not the entire variety of shapes and densities of the litter

particles, such as branches, dead leaves, small decomposing leaf pieces, and reproductive material.

5) The density reduction in litter after being in aerobic conditions is ignored in the suspended particle transport approach, and therefore so is the higher resuspension after rewetting.

6) The suspended particle transport formulation does not consider the sediment bed transport. It is not clear, however, how much the sediment bed transport contributes to a vegetated surface.

7) Vegetation is assumed to be in equilibrium, i.e., the Phosphorus uptake is assumed equal to the production rate of Phosphorus in the aboveground litter. This assumption is made to reflect an "established" vegetation biomass in the tree island with dynamics varying much slower in time than the hydrologic and nutrient stocks and fluxes. In fact, the litter production measured throughout the year is approximately constant (see discussion in Section 3.6.1), suggesting slowly varying (slower than intra-annual) biomass dynamics.

8) The live biomass uptake is assumed independent of the dissolved Phosphorus concentration in soil. This is likely the case in Everglades when Phosphorus is a limiting nutrient and the active uptake is the dominant process over the passive uptake (see more details in later section 3.7.2).

The analysis of the results from this model must consider the assumptions in the conceptual and numerical model listed above.

Chapter 3. Model Parameterization

In this chapter, the review of the available data in the literature and its preprocessing is presented. This is necessary to establish the model parameters and their typical ranges as well as the forcing variables.

The chapter is divided into sections that include the vertical layer boundaries around the tree islands, the transport properties in the different layers, the water source components, the lateral boundary conditions, the initial conditions, the biomass related parameters, the external fluxes and the description of the base case.

Three different tree islands are considered in the numerical simulations, which correspond to the three islands of Shark River Slough studied intensively by Ross et al. [2004]. They are Satin Leaf (SL), Gumbo Limbo (GL) and Black Hammock (BH).

3.1 Vertical Layer Boundaries and Vegetation Coverage

This section describes the spatial distribution assumed around the tree islands for the top and the bottom elevation of the groundwater layers as well as for the vegetation coverage.

3.1.1 Soil Layer

The top and bottom boundaries of the soil layer correspond to the soil surface and the bedrock elevation, respectively. Ross et al. [2004] surveyed the three tree islands of Shark River Slough by establishing a transect along their major axis, labeled “NS” and three transversal transects labeled “WE1”, “WE2”, and “WE3”. The soil surface elevation, soil depth and vegetation height were measured along those transects at intervals of 5 m or more. The bedrock elevation is obtained by subtracting the soil depth from the soil surface elevation. Also, soil and soil water samples were collected at intervals of 25 to 50 m along the transects during the wet seasons (November) of 2001 and 2002.

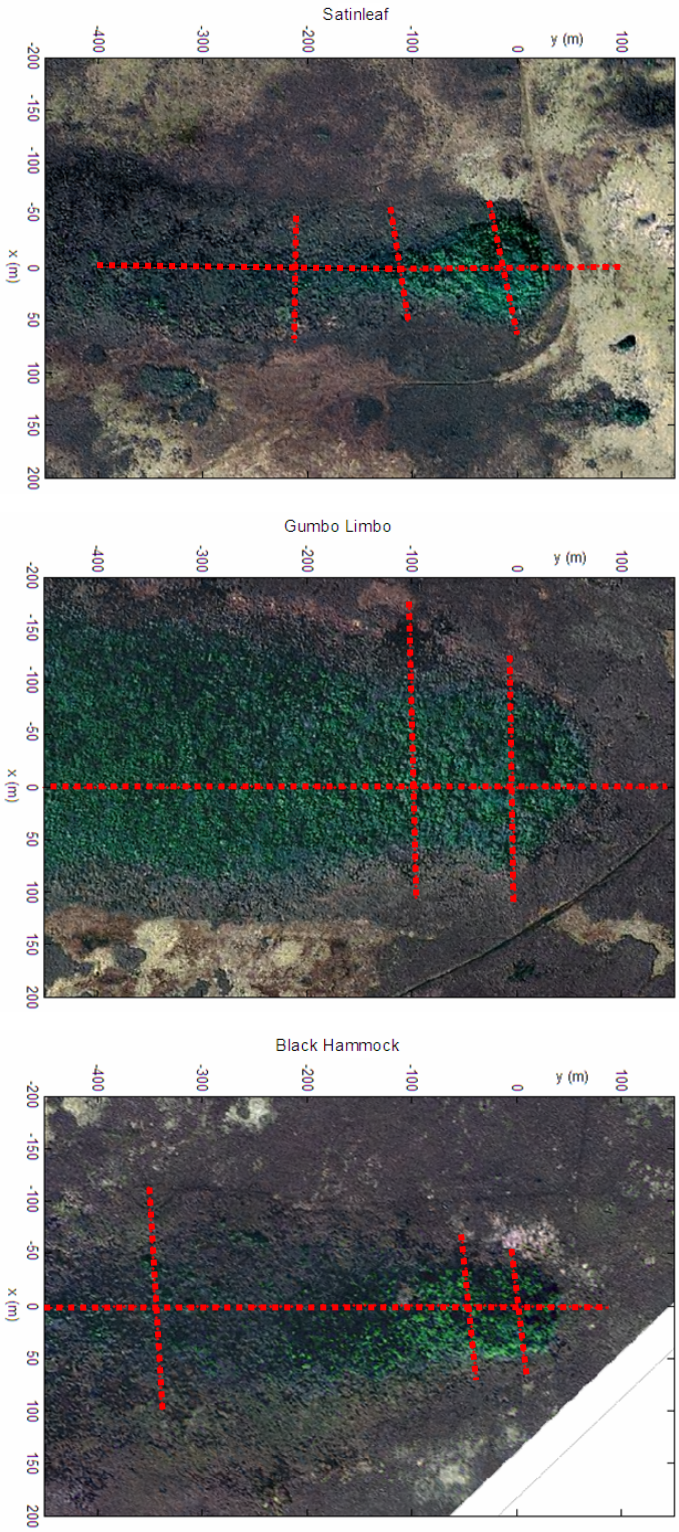

Figure 9. Original transects defined by Ross et al. [2004] superimposed on the tree island images downloaded from Labins webpage (http://data.labins.org/). Original UTM coordinates are rotated and translated according to the parameters shown in Table A-9.

The soil surface elevation and bedrock elevation from the four transects do not contain the spatial variability of those variables. The realistic soil surface elevation map was presented by Ross et al. [2004] in their Figure 6-1 was obtained by interpolation of the transect data after introducing other fictitious points in order to capture the shape of the tree island. This procedure was followed also in this work in order to complete the set of needed maps. Further details of the procedure and some the maps obtained for the three Tree Islands (SL, GL and BH) can be found in Appendix A3.1.

3.1.2 Vegetation Coverage

The vegetation around tree islands has been classified as Hardwood Hammock (HH), Bayhead (BH), Bayhead Swamp (BS), Tall Sawgrass (TS) and Marsh (MA) [Ross et al. 2004]. The Marsh type sometimes is subdivided in three small grassy vegetation types: medium Sawgrass (MS), Sparse Sawgrass (SS) and Spikerush Marsh (SM). The vegetation coverage type maps shown in Figure 10 were obtained from the original maps provided by Pablo Ruiz at SERC, FIU by following the detailed visual surveying and mapping procedure described in Appendix A3.2.

The classification in vegetation types suggested by Mike Ross and co-workers at FIU is based on their field experience and it is difficult to translate into quantitative criteria. Ross et al. [2004] found that those types are not only related to the available species and their height but also to other parameters like soil surface elevation (and therefore hydroperiod length), bedrock elevation, soil properties, soil pore water properties and the canopy openness (see Table 6.6 in [Ross et al. 2004]). In particular, the nutrient (Phosphorus) availability differences are remarkable among different vegetation types, as shown in Table 2. Thus, the vegetation type classification by Mike Ross et al. is equivalent to the concept of habitat introduced in the ELM model [Fitz, 2006].

The vegetation coverage type maps are used to assign the spatial distribution of the vegetation resistance (Manning coefficient), among others parameters in the model.

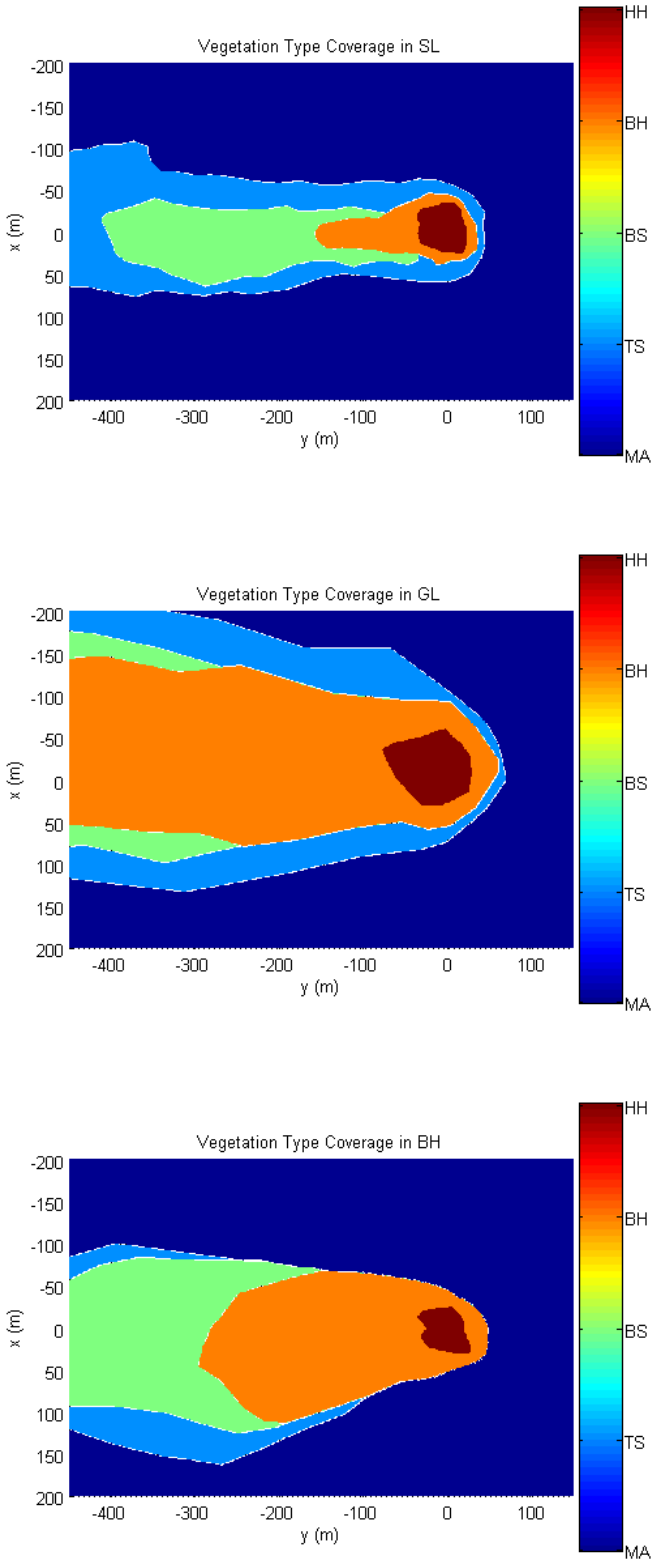

Figure 10. Vegetation coverage type maps in the tree islands of Shark River Slough.

Vegetation Type	Mean water depth (m)	Total Phosphorus in soil		SRP ($\mu g/l = 10^{-6}$ kg/m^3)
		kg P/kg dry %	(kg P /m^3)	
Spikerush marsh (SRM)	0.41	0.0286	0.0572	1.04
Sparse Sawgrass (SS)	0.37	0.0283	0.0566	1.70
Tall Sawgrass (TS)	0.32	0.0342	0.0684	2.00
Bayhead swamp (BS)	0.13	0.155	0.31	3.67
Bayhead (BH)	-0.04	0.125	0.25	5.34
Hardwood hammock (HH)	-0.69	4.60	18.4	111.9

Table 2. Vegetation types in Shark River Slough and some correlated parameters, according to Ross et al. [2006]. The total mass Phosphorus in soil per unit of volume is estimated by assuming a bulk density of 400 kg/m^3 for HH and 200 kg/m^3 otherwise.

3.1.3 Rock Layer

The bottom of the rock layer is considered to be at the limit between the Fort Thompson Formation and the Confining to Semiconfining Unit (CSU), in order to include the complete hydrologic unit called Water Table Aquifer in the model (see Figure A-18 in Appendix A3.3). In the region of the tree islands of Shark River Slough, the top elevation of the CSU is around -15 ft (-4.572 m) NAVD88, as shown in Figure A-17. Thus, the bottom of the rock layer adopted for all the tree islands is -4.572 m NAVD88 ≈ -4.112 m NGVD29 (see conversion in Table A-9). As the maximum bedrock elevation in the tree islands (shown in Figure A-14) is about 2 m NAVD88, it is concluded that the thickness of the bedrock layer considered is less than or equal to 7 m.

3.2 Transport Properties

In this section, the transport properties in the surface water layer, the soil layer and the rock layer of the conceptual model are defined.

3.2.1 Surface Water Layer

3.2.1.1 Horizontal Flow Resistance. Manning Coefficients

There are some attempts in the literature to express the surface flow resistance in the Everglades by using Manning equation, which in a one dimensional case has the form

$$V = \frac{1}{n} h^{\frac{2}{3}} \sqrt{S}\,, \tag{20}$$

where n is the Manning coefficient, h the water depth, V is the absolute value of the vertically averaged velocity, S the surface water slope.

According to a written communication by J. K. Lee, U.S. Geological Survey [1998] as cited by Swain et al. [2004], 14 measurements for *Claudium jamaicense* (sawgrass) gave an average Manning coefficient of 0.43 $s/m^{1/3}$ with a range from 0.23 to 0.60 $s/m^{1/3}$. For *Eleocharis cellulose* (spikerush), four measurements gave an average n of 0.46 $s/m^{1/3}$ with a range from 0.36 to 0.57 $s/m^{1/3}$. For mixed rush/sawgrass, six measurements gave an average Manning coefficient of 0.38 $s/m^{1/3}$ with a range from 0.26 to 0.61 $s/m^{1/3}$. The range of average values for different vegetation types is 0.08 $s/m^{1/3}$. On the other hand, Schaffranek [1999] stated that the preliminary analysis of data from 15 locations in Shark River Slough yielded an average value of the frictional resistance Manning coefficient between 0.42 and 0.44 for sawgrass of sparse to medium density, sparse rushes, mixed rushes and sawgrass, and cattails, whereas an average value of 0.48 was determined for very dense sawgrass. Based on these data, Swain et al. [2004] assigned values of Manning coefficient that vary spatially in the model according to a remotely sensed vegetation coverage map and range from 0.38 to 0.46 $s\ m^{-1/3}$, while in open-water areas they are assigned a nominal value of 0.02 $s\ m^{-1/3}$.

Vegetation Type	Manning Coefficient ($s\ m^{-1/3}$)	Reference
Spikerush marsh (SRM)	0.43	Sawgrass of sparse to medium density, sparse rushes, mixed rushes and sawgrass, and cattails [Schaffranek, 1999]
Sparse sawgrass (SS)		
Tall sawgrass (TS)	0.48	Very dense sawgrass [Schaffranek, 1999]
Bayhead swamp (BS)	0.075	Heavy brush in Flood Plains [Kreith et al., 1999]
Bayhead (BH)	0.05	Light brush in Flood Plains [Kreith et al., 1999]
Hardwood hammock (HH)	0.03	Clean and straight natural channels [Kreith et al., 1999]

Table 3. Manning coefficients assumed by default for the model as a function of the vegetation type coverage.

Plausible values of the Manning coefficients corresponding to each vegetation coverage type around tree islands are listed in Table 3. The values suggested by Schaffranek [1999] are applied to the grassy vegetation types (SRM, SS and TS). In the

head of the islands, however, where the big trees (HH vegetation type) inhibit the presence of small grass or brushes, the resistance is minimum [Bazante et al., 2006] and Manning coefficient was assumed as the value accepted for clean and straight natural channels by Kreith et al. [1999]. For the case of the vegetation types BH and BS, the Manning coefficient is taken from the values reported for light and heavy brushes in flood plains, respectively.

In Appendix A3.4, additional details about the vegetated flow resistance and the applicability of Manning equation are discussed. The Forchheimer Equation was found as a better option than Manning equation to fit the flow through Sawgrass in the indoor flume experiments conducted by Jenter [1996]. On the other hand, MODHMS could only consider the vegetated flow resistance by using a Manning type equation.

In summary, as MODHMS is used to obtain the overland flow in the numerical implementation, Manning equation is used with the coefficients varying according to the vegetation type coverage, as listed in Table 3. Those Manning values assumed initially are later modified during the calibration process.

3.2.1.2 Effective Diffusion Coefficient

The transport of dissolved Phosphorus in water has an advective and a diffusive component. MODHMS allows considering a diffusion coefficient and longitudinal and transversal dispersivity coefficients.

ELM v2.5 assumes a molecular diffusion coefficient for the Phosphorus dissolved in surface water of 8.8×10^{-10} m^2/s, which is close to the value of 0.683 cm^2 /d (7.9×10^{-10} m^2/s) used by Newman and Pietro [2001]. However, the purely diffusive transport (i.e., by molecular diffusion) is only dominant at extremely low flow velocities. An effective diffusion approach has been adopted here to take into account the effects of enhanced diffusive transport (dispersion) caused by flow heterogeneities.

The magnitude of the effective diffusion coefficient for surface water is scale dependent, increasing with the size of the water body [Langevin et al., 2005]. The effective diffusion coefficient is on the order of 1 to 10 m^2/s in open channels, and two orders of magnitude greater in estuaries [Fischer et al., 1979].

On the other hand, the numerical method introduces a numerical diffusion effect in the dissolved Phosphorus concentration. The diffusion coefficient related to this effect

can be estimated by substituting typical grid spacing, time step and OL water speed in equation (87) derived in Appendix A2.2. The value of 2 m^2/s obtained for this coefficient is in the lower part of the range reported in open channels, which is reasonable to expect given the slow-flowing nature of surface water in wetlands such as the Everglades.

In this work, the effective diffusion coefficient is assumed by default to be equal to the numerical diffusion value. It is worth noting that given the typical values of surface water velocity (0.01 m/s), grid spacing (5 m) and effective/numerical diffusion (2 m^2/s) provided in Appendix A.2.2, the value of the numerical Peclét number is Pe ≈ O(0.01), indicating a diffusion-dominated transport regime

3.2.2 Soil Layers

3.2.2.1 Porosity

A broad range of porosity for peat soils in the Everglades has been reported in the literature. Merrit [1996] assumed a porosity of 0.2 for the peat soils. Newman and Pietro [2001] reported a porosity of 0.97 within the surficial 4 cm of Everglades Nutrient Removal (ENR) soil. Harvey [2004] and Newlin et al. [2004] measured a porosity value for peat of 0.93 near the S10C water control structure located on between WCA-2A and WCA-1. However, they use a porosity of 0.98 while modeling the transport of isotopes through peat in WCA-2A. The porosity values near 1 refer likely to the total porosity and not to the open porosity that contributes to the water flow.

Soil name	Depth (in)	Moist bulk Density (g/cm^3)	Saturated hydraulic conductivity (micro m/sec)	Available water capacity (in/in)	Organic Matter (%)	pH
Pahokee muck, depressional	0-46	0.20-1.00	42-141	0.20-0.25	75-90	5.6-7.3
Dania muck, depressional	0-15	0.15-0.35	42-141	0.20-0.30	60-90	5.6-7.3

Table 4. Characteristics of two typical soils in Shark River Slough extracted from the web soil survey (http://websoilsurvey.nrcs.usda.gov/app/WebSoilSurvey.aspx) published by Natural Resources Conservation Service (NRCS), US Department of Agriculture.

The soil database available at web soil survey (http://websoilsurvey.nrcs.usda.gov) does not have soil data exactly in the area of the tree islands. However, it does provide two types of soils to the west of the former L-67 extension levee, and some of their

characteristics are listed in Table 4. That data is in agreement with the mean soil characteristics reported by Ross et al. [2006] and reproduced in Table 5. The available water capacity of the soils in Table 4 (from 20 to 30 %) is the quantity of water that the soil is capable of storing for use by plants. This range is in agreement to the expected open porosity of the soil that contributes to the water flow.

Region	pH	Bulk Density (g/cm^3)	Organic Matter (%)	Carbonate (%)	Total N (%)	Total P (%)
Marsh	7.16	0.20	66.0	13.66	2.81	0.011
Tree Island	6.64	0.26	66.4	8.76	2.37	2.68

Table 5. Characteristics of the soils (top 10 cm) in marsh and three islands of the Shark River Slough reproduced from Table 3 in reference [Ross et al., 2006].

Another estimate of the porosity can be made by using the bulk density (ρ_b) value for the marsh of 0.20 g/cm^3 in Table 5 and the value of 0.40 g/cm^3 reported for the HH soils by Ross et al. [2004]. Bazante et al. [2004] collected the solid particles suspended in surface water in marsh areas and measured a particle density (ρ_p) around 1.5 g/cm^3. Those suspended particles may be thinner than the ones composing the marsh soils, but it is assumed that they have the same composition and, therefore, the same particle density. Bazante et al. [2004] also measured a particle density of 2.1 g/cm^3 for the soil in the head of Gumbo Limbo Tree Island. The porosity (ϕ) is related to those densities by the equation

$$\phi = 1 - \frac{\rho_b}{\rho_p}; \tag{21}$$

which gives porosity values of 0.87 and 0.81 for marsh and HH soils, respectively. Notice however that the bulk density referred to here is not a real field bulk density derived from a volumetric collection but a laboratory measurement in which the soil is lightly tamped into the crucible [Ross, personal communication, 2006]. In the field, the soil in general is more compacted and the soil porosity in the field is likely lower than the one in the laboratory. For example, if the volume of the soil in the field is 0.8 times the volume in the lab, then the porosity values in the field would be 0.83 and 0.76 for marsh and HH soils, respectively.

In this work, it is assumed by default that porosity values are 0.93 and 0.5 for marsh and HH soils, respectively. However, validity range of (0.3, 0.97) is accepted during the calibration process for all vegetation type areas, as shown in Table 27.

3.2.2.2 Hydraulic Conductivity

The hydraulic conductivity of peat soils in the Everglades has been estimated or assumed inside a broad range in the literature. Merrit [1996] assumed a hydraulic conductivity of 10 ft/d (35×10^{-6} m/s) for the peat soils in the region of the Tree Islands. Harvey et al. [2000] estimated the hydraulic conductivity in peat soils from several areas of Taylor Slough in the range 1 to 15×10^{-4} cm/s (1 to 15×10^{-6} m/s). Langevin [2003] assumed a horizontal conductivity of 3 m/d (35×10^{-6} m/s) and a vertical one of 0.3 m/d (3.5×10^{-6} m/s) to represent peat and marl units in the upper part of the Biscayne Aquifer. Harvey, Krupa and Krest [2004] reported a mean average conductivity for the peat soils in WCA-2A of 0.6 m/d (6.9×10^{-6} m/s). Langevin et al. [2005] assumed 1 m thick sediment layer with a vertical hydraulic conductivity value of 0.1 m/d (1.2×10^{-6} m/s).

Troxler [2005] and Troxler et al. [2005] used different hydraulic conductivity values to calculate subsurface water fluxes according to the tree island soil depth and soil type (i.e. island vs. marsh). However, the values are reported incorrectly in units of $cm^{-1}s^{-1}$ and they are not considered here.

Finally, NRCS reports a hydraulic conductivity for the typical organic soils of the area in the range 42 to 141×10^{-6} m/s, as shown in Table 4.

In this work, it is assumed by default a uniform hydraulic conductivity in the peat soils of 10×10^{-6} m/s. However, the validity range of (1, 140) $\times10^{-6}$ m/s is accepted during the calibration process, as shown in Table 27.

3.2.2.3 Unsaturated Flow Parameters

Measurements or estimates of parameters related to the unsaturated flow and the moisture retention in the Everglades soils have not been found in previous reports. However, the soil layer in the head of the considered tree islands is not completely saturated most of the year. MODHMS can consider unsaturated flow via Van Genuchten equations [Panday and Huyakorn, 2004], [HydroGeoLogic (HGL) Inc., 2006]

$$k_{rw} = S_e^{1/2}\left[1-\left(1-S_e^{1/\gamma}\right)^{\gamma}\right]^2,$$
$$S_e = \begin{cases}\left[1+(\alpha h_c)^{\beta}\right]^{-\gamma} & \text{for } \psi < 0 \\ 1 & \text{for } \psi \geq 0\end{cases}; \tag{22}$$

where the involved parameters satisfy

$$S_e = \frac{(S_w - S_{wr})}{(1-S_{wr})},$$
$$\psi = h - z,\ h_c = h_{ap} - \psi,\ \gamma = 1 - \frac{1}{\beta}. \tag{23}$$

Here k_{rw} is the relative permeability, S_w the water saturation, S_{wr} the residual water saturation, S_e the effective water saturation, α, β and γ are empirical parameters. Moreover, ψ is the pressure head, h the water table level, z the vertically upward coordinate, h_c the capillary head and h_{ap} the pressure head in air, which is taken as atmospheric ($h_{ap} = 0$). Notice that the relative permeability and the moisture retention in soil are obtained from the Van Genuchten equations by specifying the parameters α, β and S_{wr}.

The European Soil Database (http://eusoils.jrc.it/ESDB_Archive/ESDBv2/) reports average relative permeability and moisture retention curves for organic soils by using the Mualem-van Genuchten parameters presented in Table 6. The equations in this model are slightly different from the van Genuchten equations (22) and (23), so that [Van Genuchten et al., 1991]:

$$k_{rw} = S_e^{l}\left[1-\left(1-S_e^{1/\gamma}\right)^{\gamma}\right]^2,$$
$$S_e = \begin{cases}\left[1+(\alpha h_c)^{\beta}\right]^{-\gamma} & \text{for } \psi < 0 \\ 1 & \text{for } \psi \geq 0\end{cases}. \tag{24}$$

Here the effective water saturation is defined as

$$S_e = \frac{(S_w - S_{wr})}{(S_{ws} - S_{wr})}. \tag{25}$$

Notice that in the Mualem-van Genuchten model there is a maximum value for water saturation (S_{ws} = 0.766), corresponding to a hydraulic conductivity K_s. However,

in the case of the Everglades organic soils, there is no reason to think that the soil cannot be fully saturated (S_{ws} = 1), as it is assumed implicitly in the van Genuchten equations. As MODHMS do not use the Mualem-Van Genuchten equations, it is suggested in Table 6 a set of van Genuchten parameters that follow approximately the moisture retention curve for the organic soils according to the European Soil Database, as shown in Figure 11. Note that the proposed parameters are chosen to reproduce the point of highest saturation. However, they do not reproduce the permeability curve suggested by the European Soil Database, as shown in the same figure.

Parameter	Mualem-Van Genuchten	Van Genuchten
S_{wr}	0.010	0.010
α (cm^{-1})	0.0130	0.68
β	1.2039	1.14
γ	$1-\frac{1}{\beta}$=0.1694	$1-\frac{1}{\beta}$=0.1228
l	0.4	0.5
S_{ws}	0.766	1
K_s (cm/day) (m/s)	8.0 9.3e-7	86.4 1.0e-5

Table 6. Parameters of the Mualem-van Genuchten model and of the van-Genuchten model used to create Figure 11.

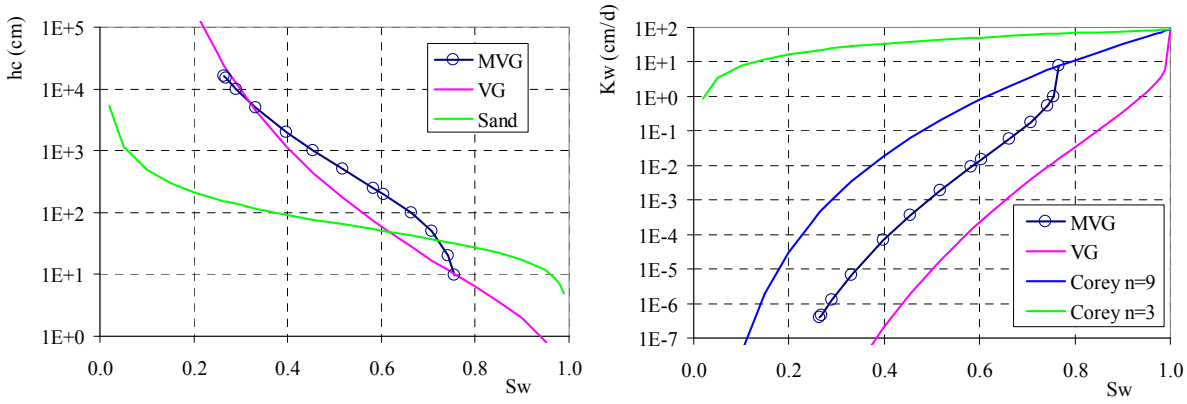

Figure 11. Moisture retention and permeability curves obtained with the Mualem-van Genuchten (MVG) and the van-Genuchten (VG) equations using the parameters in Table 6. The moisture retention curve for sand reported by Hammecker et al. [2004] computed from the Van Genuchten parameters (α = 2.78 m^{-1}, β = 1.917 and S_{wr} = 0.01) is also included. Moreover, two Corey permeability curves obtained by using exponents of 9 and 3 are shown.

On the other hand, MODHMS can also consider a Corey correlation for the relative permeability with the form:

$$k_{rw} = S_e^n , \tag{26}$$

where n is the Corey exponent.

Figure 11 shows that the permeability curve obtained by using a Corey exponent of 9 matches the point of highest saturation of the Mualem-van Genuchten curve. Thus, this Corey curve, as well as the previous proposed Van Genuchten moisture retention curves, reproduces the organic soils data from the European Soil Database for the highest saturation values, which is the common saturation range for the peat soil in the Everglades.

Relative permeability curves with Corey exponents higher than 6 make difficult the MODHMS convergence to the solution [S. Panday, personal communication, 2006]. The steeper the moisture retention and relative permeability curves, the higher the nonlinearity of the equations, which makes the convergence more difficult. For this reason, the moisture retention curve for sand reported by Hammecker et al. [2004], as well as a relative permeability curve obtained with a Corey exponent of 3, were also included in Figure 11.

In summary, the van Genuchten parameters for sandy soils reported by Hammecker et al. [2004] (α = 2.78 m^{-1}, β = 1.917 and S_{wr} = 0.01) for the moisture retention curve, and a Corey exponent of $n = 3$ for the relative permeability correlation, are used by default in order to consider the unsaturated flow in the peat soil layer and at the same time, to assure the convergence of MODHMS. Moreover, a validity range of α = (0.6, 3.0) m^{-1}, β = (1.1, 2.0), and n = (1, 6) is accepted during the calibration process, as shown in Table 27.

3.2.2.4 Effective Diffusion Coefficient

MODHMS allows considering a diffusion coefficient and longitudinal and transversal dispersivity coefficients. In groundwater, the magnitude of the flow velocity is typically a few orders of magnitude less than in surface water. In the numerical scheme, this is counteracted by a much larger time step, resulting in a similar magnitude of the Courant number, i.e., $C_r \approx O(100)$ and therefore a value of the Peclét number $Pe \approx$

$O(0.01)$, indicating a diffusion-dominated transport regime in groundwater (as it was in surface water).

Following the discussion in Section 3.2.1.2, given the existence of a numerical diffusion of the same order of the typical effective diffusion coefficients (for groundwater in this case), the model effective diffusion is assumed by default to be equal to the numerical diffusion value.

3.2.2.5 Equilibrium Adsorption Curve

Adsorbed Phosphorus is assumed to be in equilibrium with the solution, according to an adsorption correlation. This is the case, for example, of the equilibrium adsorption curve for Phosphorus in peat soils reported by Kadlec and Hammer [1988], which satisfies the Freundlich equation

$$x = a\left(\frac{C}{\mathrm{kg/m^3}}\right)^b . \tag{27}$$

Here, x is the adsorbed Phosphorus (kg of adsorbed Phosphorus/ kg of dry soil) and C is the concentration of dissolved Phosphorus. Kadlec and Hammer [1988] stated that parameters $a = 7.55\times10^{-3}$ kg P/kg dry soil and $b = 0.46$ found in laboratory studies for sedge peat soils are typical Freundlich parameters for a wetland. However, it is well known that the equilibrium adsorption curve depends in general on the soil and water composition.

In the case of the soils around the tree islands of Shark River Slough, characteristics like pH, organic matter content, electric conductivity, total nitrogen, total Phosphorus, total carbon and total carbonate, are correlated with the vegetation coverage type as shown in Table 6-6 published by Ross et al. [2004]. This suggests the existence of a Phosphorus equilibrium adsorption curve for each vegetation type.

There are three laboratory studies reported in the literature on the Phosphorus equilibrium adsorption curve for the Everglades soils conducted by Richardson and Vaithiyanathan [1995], Zhou and Li [2001] and Porter and Sanchez [1992]. However, none of those studies analyzed specifically the soil around the tree islands of Shark River Slough. In fact, the soil samples studied by Porter and Sanchez [1992], as well as most of the samples studied by Zhou and Li [2001], are from agricultural areas, which in general

have a different composition. Zhou and Li [2001] also analyzed three soil samples from pinelands and three from wetlands, characterized by pH of 7.6 ± 0.3 and organic carbon content of 7 ± 2.3 %, which are closer to the range of HH soil values (pH of 7.55 ± 0.65 and total carbon content of 15.3 ± 4.7 %) than samples from other soil types around the tree islands (see Table 6-6 by Ross et al. [2004]). Total carbon in general is higher than the organic carbon since the soil has relative high carbonate content (inorganic carbon from the limestone in the soil) [M. Zhou, personal communication, 2006]. On the other hand, Richardson and Vaithiyanathan [1995] studied soils samples from WCA-2A, which are closer to Shark River Slough. For a subset of the samples, the authors reported carbon content of 46 ± 4 % and nitrogen content of 3 ± 0.3 %, which are close to the values in soils for all the vegetation types, except for the more aerobic HH soils (nitrogen content of 1.13 ± 0.39). In this model, an average equilibrium adsorption curve from the wetland soils studied by Zhou and Li [2001] for the HH soil and an average curve from the WCA-2A soils studied by Richardson and Vaithiyanathan [1995] for the other soils around the tree islands are proposed.

In the case of Richardson and Vaithiyanathan [1995], they sampled soils in the WCA-2A along a Phosphorus enrichment gradient and at two depths (0-10 cm and 10-20 cm). The equilibrium adsorption curve was found in each soil sample by introducing replicas into solutions at different concentrations of P (0, 0.01, 0.03, 0.1, 0.2, 1, 10, 50, and 100 mg/l), letting them equilibrate and measuring the equilibrium Phosphorus concentration (EPC). Then the adsorbed mass per unit of mass of soil (X) was computed. Finally, a Freundlich equation was fitted to the data (EPC , X) with the form

$$X = k\left(\frac{EPC}{\text{mg/L}}\right)^{b} - Q\,. \tag{28}$$

The fitted parameter Q was interpreted as is the amount of Phosphorus already adsorbed in the soils, which is related to the concentration EPC_0 at which the original adsorbed phosphate is in equilibrium with the initial solution (there is neither adsorption nor desorption), and was calculated from the above equation for each soil by using $X = 0$.

Notice that even when Richardson and Vaithiyanathan [1995] called equation (28)

as a "modified Freundlich model", it is totally equivalent to the Freundlich equation (27), by realizing that $x = X + Q$ and $a = k\left(\frac{\text{kg/m}^3}{\text{mg/L}}\right)^b = k\left(10^3\right)^b$.

Richardson and Vaithiyanathan [1995] reported the Freundlich parameters (k and b) in their Table 1 for each soil sample, which vary over a wide range. In order to obtain a typical equilibrium adsorption curve equation, the median values of the reported Freundlich parameters $k = 23.5$ mg/kg and $b = 0.81$ were found. The median value of k in equation (28) is equivalent to $a = 6.33\times10^{-3}$ kg/kg in equation (27). The equilibrium adsorption curve with median parameters, reproduce the trend of the reported values of Q and EPC_0, as shown in Figure 12. The points (EPC_0, Q) correspond to the values (x, C) of the soils at the field and capture the variability in concentration (C) and in other soil characteristics. Therefore, the adsorption curve with median parameters can be a good estimate of the average adsorption curve.

In the work of Zhou and Li [2001], pineland and wetland soils were sampled. The equilibrium adsorption curve was found analogously in each soil sample by introducing replicas into solutions at different concentrations of P (0, 0.1, 1, 5, 20, 50, 100, 200, 400, 600, 800, 1000, or 1250 mg/l). From the three curves obtained for wetland soils, the one for the soil sample 18 lie in the center of them and was taken to be representative of that soil type (see Figure 12). The Freundlich parameters in this case are $k = 159$ mg/kg ($a = 3.06\times10^{-3}$ kg/kg) and $b = 0.428$.

According to Table 2, the average SRP is 0.11 mg/l in the soils for the HH vegetation coverage type and $0.001 \le C \le 0.005$ mg/l for the other vegetation types. The range of the original Phosphorus concentrations (EPC_0) of the samples analyzed (see Figure 12) only includes the HH soils. This is also the case of the range of the original solution concentrations in the laboratory method to determine the Freundlich parameters (k and b) on both papers. Therefore, even when the range of non-zero Phosphorus concentrations considered in the work by Richardson and Vaithiyanathan [1995] is lower than in the work by Zhou and Li [2001], it is still higher than the concentrations in most of the soils around the tree islands of Shark River Slough. It can be expected that a fit

from adsorption experiments with $C \leq 0.005$ mg/l would give a more linear adsorption curve ($b \to 1$ in the Freundlich equation).

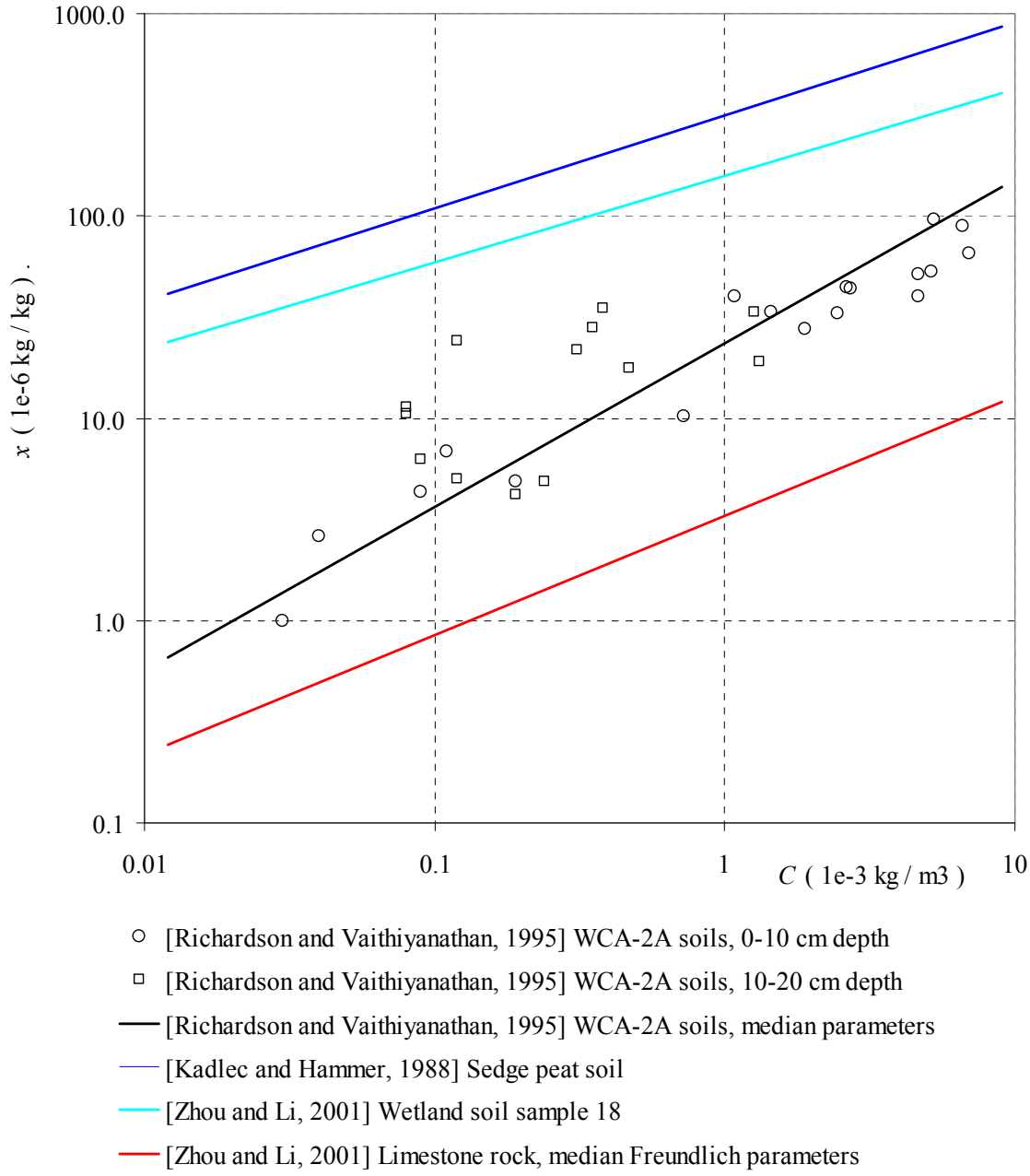

Figure 12. Phosphorus equilibrium adsorption curve. See text for details.

In summary, from the lack of other data in the literature, this work assumes for the soil layers the equilibrium adsorption curve given by the Freundlich equation (27) with the values reported by Zhou and Li [2001] for sample 18 ($a = 3.06\text{e-}3$ kg/kg and $b = 0.428$) in the case of the HH soils, as well as the median values of the parameters

reported by Richardson and Vaithiyanathan [1995] ($a = 6.33\times10^{-3}$ kg/kg and $b = 0.81$) for other soils, which correspond to the cyan and black line in Figure 12, respectively. Notice that those curves predict a higher Phosphorus adsorption in the head of the island than in other soils as hypothesized by Ross et al. [2004].

3.2.2.6 Bulk Density

The bulk density of the soil (ρ_B) is needed to obtain the mass of adsorbed Phosphorus per unit of volume ($\rho_B X$).

Ross et al. [2004] reported an average bulk density of 0.40 g/cm^3 for the HH soils, 0.15 g/cm^3 for BH, and around 0.1 g/cm^3 for BS and Marsh soils. Those values were measured in the lab and they have an error associated with the sample manipulation as discussed in previous section. Moreover, a more recent paper by Ross et al. [2006] reports average bulk density values of 0.20 g/cm^3 for Marsh soils and 0.26 g/cm^3 for Tree Island soils (see Table 5). This is consistent with the average bulk density in the Shark River Slough marsh of 0.220 g/cm^3 reported by Chambers and Pederson [2006].

The reported values of bulk density in other areas of the Everglades also have shown a similar uncertainty. Newman and Pietro [2001] reported an average bulk density in WCA1 soils of 0.289 g/cm^3. However, more recently, Corstanje et al. [2006] estimated values of 0.073 for 0-10 cm soil depth and 0.077 for 10-20 cm soil depth. These lower values are in agreement with the value of 0.068 g/cm^3 reported by DeBusk et al. [1994] for 0-20 cm soil depth in the WCA-2A. Harvey [2004] and Krupa and Krest [2004] found differences among the bulk density values for WCA-2A interior (0.06 g/cm^3) and for WCA-2A near leeves (0.09 g/cm^3) and they hypothesized that it may be a consequence of fine-grained mineral sediments delivered when overbank flooding occurred over the past 30 years.

In summary, from the lack of other data in the literature, this work assumes for the soil layers a bulk density of 400 kg/m^3 in the case of the HH soils and 200 kg/m^3, otherwise.

3.2.3 Rock Layer

3.2.3.1 Porosity

No measured or estimated value of the porosity in the bedrock in Shark River Slough was found in the literature.

Langevin [2001, 2003] assumed a value of 0.2 for limestone rock layers equal to specific yield estimated by Merritt [1996a]. On the other hand, Harvey [2004] and Newlin et al. [2004] used a porosity of 0.3 while modeling the transport of isotopes through the rock layer in WCA-2A.

In this work, a porosity value of 0.20 is assumed by default for the rock layer. However, a validity range of (0.2, 0.35) is accepted during the calibration process, as shown in Table 27.

3.2.3.2 Hydraulic Conductivity

The hydraulic conductivity data reported in the literature for the rock layer cover a wide range.

Fish and Stewart [1991] shown (their Table 5) wells to the north of the tree islands with hydraulic conductivities about 500 ft/day (1.8×10^{-3} m/s) at 11 to 17 ft below the soil surface (Fort Thompson formation). Merrit [1996] assumed a hydraulic conductivity of 500 ft/d (1.8×10^{-3} m/s) for the Fort Thompson Formation in the region of the Tree Islands.

Nemeth et al. [2000] used a hydraulic conductivity of 25000 ft/day (88×10^{-3} m/s) for the Fort Thompson Formation in a region to the east of the Tree Islands.

Langevin [2001, 2003] assumed an horizontal conductivity of 9000 m/d (104×10^{-3} m/s) and a vertical conductivity of 9 m/d (0.104×10^{-3} m/s) and 90 m/d (1.04×10^{-3} m/s), respectively; which are the values used in calibrated flow model by Merritt [1996a] to represent Miami Limestone, Fort Thompson, and permeable zones of the Tamiami Formation.

Langevin et al. [2005] assumed the remaining part of the Biscayne aquifer to be isotropic and homogeneous with vertical and horizontal hydraulic conductivity values of 0.75 m/d (0.0087×10^{-3} m/s) and 5000 m/d (0.58×10^{-3} m/s), respectively.

In this work, a uniform hydraulic conductivity in the rock of 1.8×10^{-3} m/s is

assumed by default. However, a validity range of $(0.1, 100)\times10^{-3}$ m/s is accepted during the calibration process, as shown in Table 27.

3.2.3.3 Unsaturated Flow Parameters

It is expected that most of the time the rock layer remains fully saturated in the marsh, but it may not be totally saturated in the head of the tree island. Due to the lack of data in the literature, the minor change in the saturation in this layer, and the possibility of having some peat soil intrusion in the rock layer, this work assumes the same moisture retention and relative permeability curves as in the soil layer.

3.2.3.4 Effective Diffusion Coefficient

Langevin [2001] assumed a horizontal and vertical dispersivity of 1 m and 0.1 m, respectively to represent Miami Limestone, Fort Thompson, and permeable zones of the Tamiami Formation. However, results from the cross sectional models, which were able to simulate the approximate position of the saltwater interface, suggest that longitudinal dispersivity ranges between 1 and 10 m, and transverse dispersivity ranges from 0.1 to 1 m for the Biscayne aquifer.

In this work, a zero effective diffusion coefficient for this layer is assumed by default due to the uncertainties in the effective diffusion coefficient and the existence of a numerical diffusion introduced by the numerical procedure.

3.2.3.5 Equilibrium Adsorption Curve

In the work of Zhou and Li [2001], the authors measured the adsorption of Phosphorus in soil and limestone rocks from the Everglades. Contrary to the soil samples, the adsorption measurements in rock samples were made by using original solutions with a lower concentration of Phosphorus (0, 0.04, 0.1, 1, 2, 5, 20, 50, 100, 200, or 400 mg/l). The equilibrium adsorption curves were fitted with the Freundlich equation (28) and the fitted parameters were reported in Table 3 of their work. The published curves are plotted in Figure 13 as red dashed lines.

In order to obtain a representative equilibrium adsorption curve for Phosphorus in the limestone bedrock, the median of the Freundlich parameters were obtained ($k = 3.3$ mg/kg and $b = 0.59$, corresponding to $a = 1.94\times10^{-4}$ kg/kg in equation (27)). The curve corresponding to the median parameters is shown in Figure 13 as a solid green line and is

a measure of an average dependence. The proposed curve is also shown in Figure 12, in order to highlight that the adsorbed amount in limestone rock is less than the one in soil samples as stated by Zhou and Li [2001].

Applying the results of Zhou and Li [2001] to estimate the Phosphorus equilibrium adsorption curve in the limestone around tree islands has two problems. As mentioned in the case of the soil samples, here again the Phosphorus concentrations used in the lab measurements contain the typical SRP values of the bedrock in the head of the island (below the HH soil) but they are higher than SRP values around it. On the other hand, the rock samples were ground in the lab to pass through a 2-mm sieve, which may cause an increase in the surface area of the sample exposed.

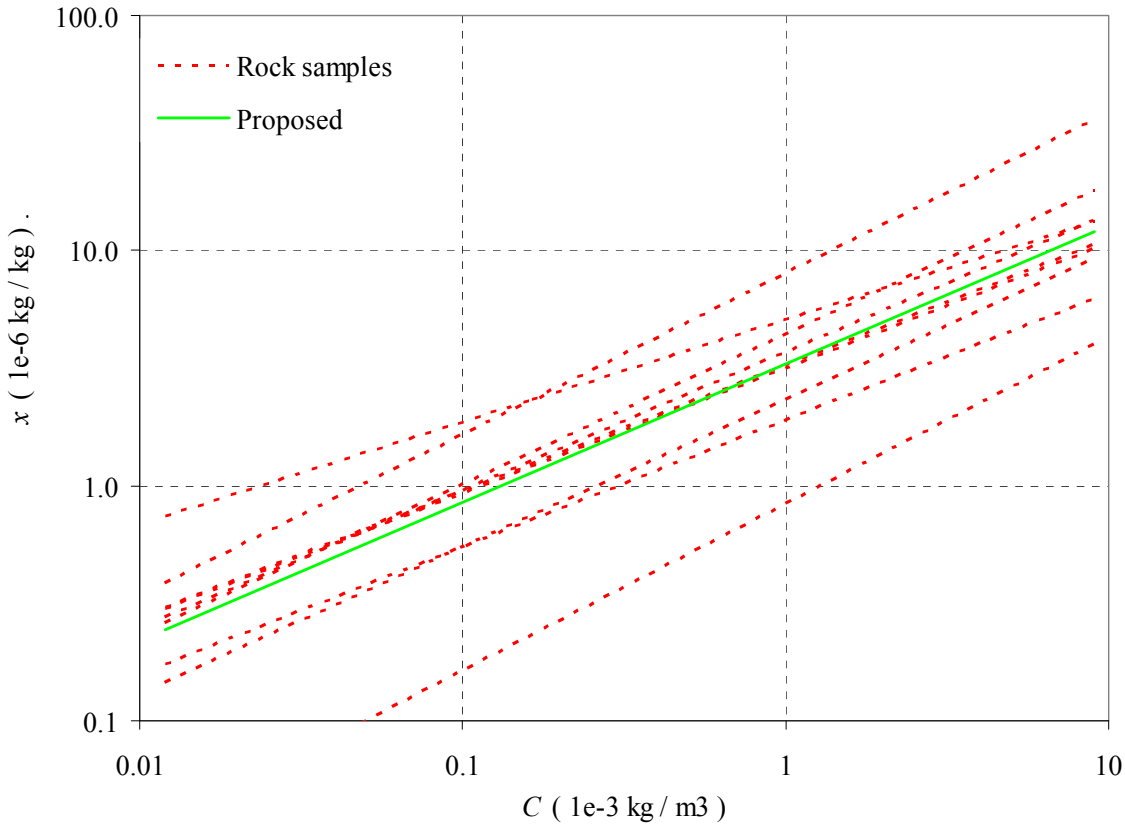

Figure 13. Equilibrium adsorption curve for limestone bedrock. The red dashed lines correspond to the Freundlich equation obtained for nine samples by Zhou and Li [2001]. The green solid line is the proposed equation by using median of the Freundlich parameters.

From the lack of other data in the literature, this work assumes for the rock layer the equilibrium adsorption curve given by the Freundlich equation (27) with the median

values of the parameters reported by Zhou and Li [2001] ($a = 1.94\times10^{-4}$ kg/kg and $b = 0.59$), which corresponds to the green line in Figure 12 and Figure 13.

3.2.3.6 Bulk Density

The bulk density of the limestone bedrock could be estimated by assuming that it is composed only by calcium carbonate (density of 2.83 g/cm^3) with a porosity of 20 %. This gives a bulk density of 2.26 g/cm^3= 2260 kg/m^3.

3.3 Water Sources

The rainfall and evaporation are the sources in the water balance equation for the surface water layer, and the transpiration for the soil layer. On the other hand, the dissolved Phosphorus concentration in all those water fluxes are necessary to estimate the sources in the dissolved-Phosphorus mass balance equation, as well as the additional dissolved Phosphorus input rate in the soil layer due to external sources (e.g., animal activity and other sources) and due to biomass net release. The rainfall and ET related data to be used in the model are presented in this section.

3.3.1 Rainfall

In this section, the existing time series data of rainfall depth rate are processed. The reported values of Phosphorus concentration in rainfall water are presented as well.

3.3.1.1 Rainfall Depth Rates

Daily rainfall rates at each tree island location were found by using available rainfall station data in the area. The daily rainfall depth rates in the three tree islands were interpolated by using an inverse square-distance weighting scheme from data of those stations. This scheme needs rain data from at least one station in the given day. The interpolated daily mean rainfall depth rates are shown in Figure 14, and they cover a period of about 55 years. Further details about the available daily rainfall data and their processing are presented in Appendix A3.5.

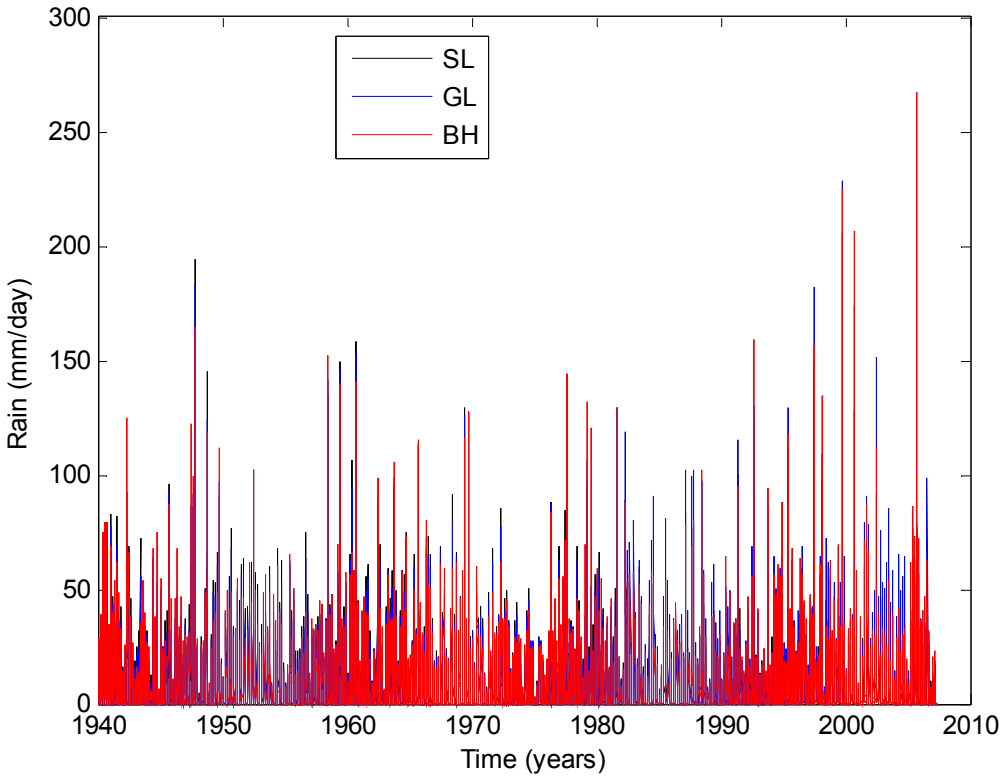

Figure 14. Interpolated daily rainfall depth rates in the tree islands of Shark River Slough.

The mean and median values of the rainfall depth rate for every day of the year since 1940 are also shown in Figure 15, which reveals a remarkable seasonal dependence. The average annual rainfall depths for the tree islands computed from the mean daily values in Figure 15 are shown in Table 7.

Tree Island	Stage (m) NAVD88	Northing slope	Easting slope	Sy	Sx	Total slope	Rainfall depth (m)	ET depth (m)
SL	1.506	3.7e-5	1.8e-5	4.1e-5	0.2e-5	4.1e-5	1.382	1.168
GL	1.424	3.8e-5	1.9e-5	4.2e-5	0.4e-5	4.2e-5	1.399	
BH	1.443	3.9e-5	1.3e-5	3.7e-5	-1.7e-5	4.3e-5	1.420	

Table 7. Mean annual values. Stages obtained from averaging mean daily values in Figure 27. Slopes from the median daily values in Figure 28 and Figure 29 as well as, from the rotated values in Figure 30. Rainfall depths from processing daily values in Figure 14. ET depth from processing the daily values in Figure 22.

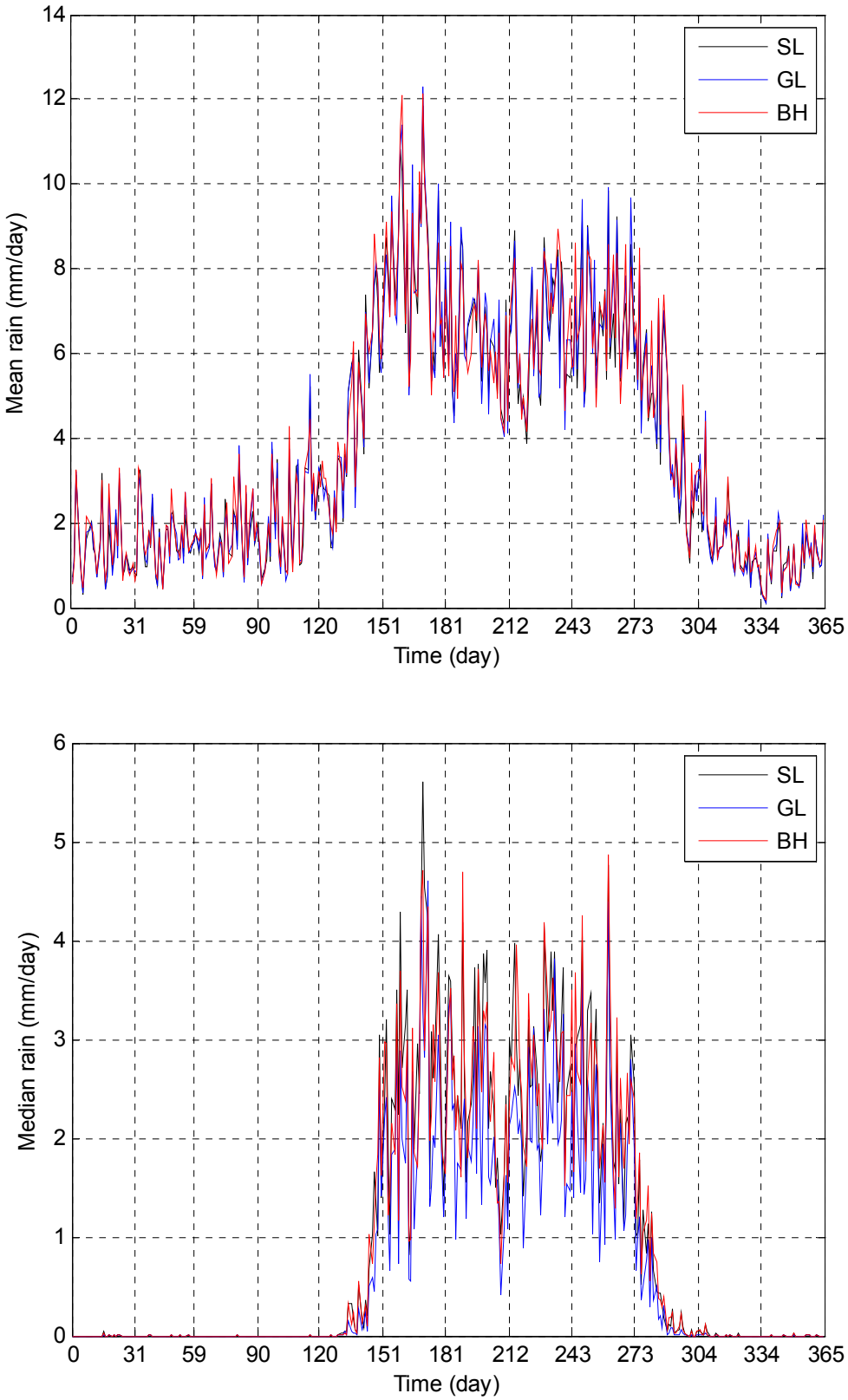

Figure 15. Mean and median daily rainfall depths from interpolated values of Figure 14.

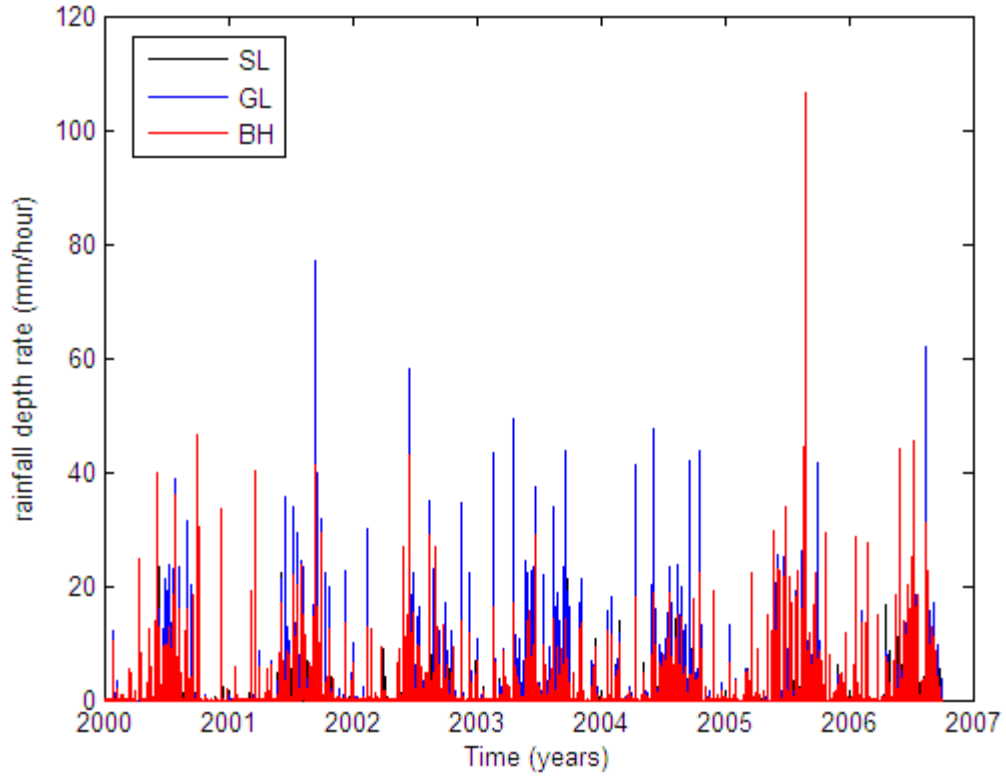

Figure 16. Interpolated hourly rainfall depth rates in the tree islands of Shark River Slough.

Hourly rainfall depth rates at the three tree islands were also obtained from neighbor stations by using an inverse square-distance weighting scheme. Further details about the available hourly rainfall data and their processing are presented in Appendix A3.5. The interpolated daily mean rainfall depth rates are shown in Figure 16 and they cover a period of more than 6 years.

The numerical model could use the daily or hourly rainfall depth rates interpolated at tree islands and presented in Figure 14 or Figure 16, respectively.

3.3.1.2 Phosphorus Concentration in Rainfall

According to McCormick et al. [2002], Phosphorus inputs to the Everglades are derived primarily from atmospheric deposition (rainfall and dry fallout), which is typically low in P. Estimates of annual atmospheric P inputs in South Florida and reconstructions of P accumulation in Everglades soils indicate that historical loading rates were extremely low, probably averaging less than 100 mg/m^2y. Redfield [1998] reported

an average rate of bulk atmospheric P deposition in the Everglades of 30 mg/m^2y, and more recently Redfield [2002] reported a value of 62 mg/m^2y. Assuming a mean rainfall depth rate of 1.4 m/y (see Table 7), the last deposition rate corresponds to a concentration of total Phosphorus in rainfall of 44×10^{-6} kg/m^3. This is consistent with the annual averaged total Phosphorus concentration in rainfall of 29×10^{-6} kg/m^3 reported by Davis [1994] for West Palm Beach and the value of 10.6×10^{-6} kg/m^3 reported by Noe et al. [2001] for South Florida. It is worth noticing that the dissolved Phosphorus concentration must be lower than those values due to the fact that not all the Phosphorus mass in rainfall is dissolved.

Seasonal effect of the atmospheric deposition for the Everglades area has not been reported. However, if a constant concentration is assumed in rainfall, the Phosphorus deposition rate would be higher in the rainy season.

In the case of Hubbard Brook, located at north central New Hampshire, the dissolved Phosphorus input in rainfall is computed in Table 8 from the phosphate and rainfall depth data reported by Likens and Bormann [1995] for four periods of the year. Notice that the rainfall rate is about constant during the year, but the input rate of Phosphorus is about one half from December to February in comparison to the other periods.

	Jun-Sep	Oct-Nov	Dec-Feb	Mar-May	Annual
Months	4	2	3	3	12
Days	122	61	90	92	365
Input rate (g PO_4 / ha)	51.1	20.0	19.1	40.7	130.9
Input rate (g P/ ha)	16.7	6.5	6.2	13.3	42.7
Rainfall depth (cm)	46	22.2	32.2	31.8	132.2
Concentration (10^{-6} kg/m^3)	3.6	2.9	1.9	4.2	3.2
Rainfall depth rate (cm/day)	0.38	0.36	0.36	0.35	0.36
Input rate (10^{-5} g/m^2/day)	1.37	1.07	0.69	1.44	1.17
Input rate (10^{-3} g/m^2/year)	4.99	3.90	2.53	5.27	4.27

Table 8. Data reported by Likens and Bormann [1995] to estimate the Phosphorus input in rainfall.

In this work, it is assumed a Phosphorus concentration in rainfall of 1.5×10^{-6} kg/m^3, which is the typical concentration of soil water in marsh areas (see Table 2). Assuming an annual rainfall depth rate of 1.4 m/year (see Table 7), the dissolved-Phosphorus averaged input rate by rainfall is 2.1 mg/m^2/year. This value is in the order of

the average dissolved Phosphorus input in rainfall of 4.3 mg/m^2/year obtained from Likens and Bormann [1995] data in Table 8. Both values, however, are two orders of magnitude lower than the total Phosphorus input value of 570 mg/m^2/year used by Oliver and Legovic [1988] in their model for Okefenokee Marshland, Georgia.

3.3.2 Evapotranspiration

In this section, the existing time series data of evaporation depth rate are processed and the correlation between evapotranspiration rate and water depth is analyzed. Moreover, the contribution of evaporation and transpiration on the total ET rate is discussed, as well as the Phosphorus uptake during the transpiration (water uptake) process.

3.3.2.1 Evapotranspiration Depth Rates

Measurements of evapotranspiration (ET) rates in Shark River Slough are not as abundant as measurements of rainfall and water stage. In fact, the unique time series data available for that area were taken by German [2000] in the station "Site 7" from 1996 to 2003. The hourly ET rates after gap filling are shown in Figure 17. The details about the station location and the data processing are presented in Appendix A3.6.

Daily ET depth rates can be calculated by adding the hourly depths and are presented in Figure 18. This graph reveals a clearly seasonal dependence of the ET, which is more difficult to see in the hourly depth rates plotted in Figure 17 because of the fluctuation between day and night.

The almost eight years of data of Figure 17 are processed to find the mean and median ET values for a given hour and day of the year. The median is more effective for removing extreme values of ET, as it is seen in Figure 19 and Figure 20. Then, from those median values, a running average in each hour with a 7-days window is performed to obtain the smoother daily oscillations presented in Figure 21. Also, daily averaged ET depth rates are calculated by adding the hourly depths and are plotted in Figure 22. The mean annual ET depth for the tree islands is estimated from those values and it is shown in Table 7.

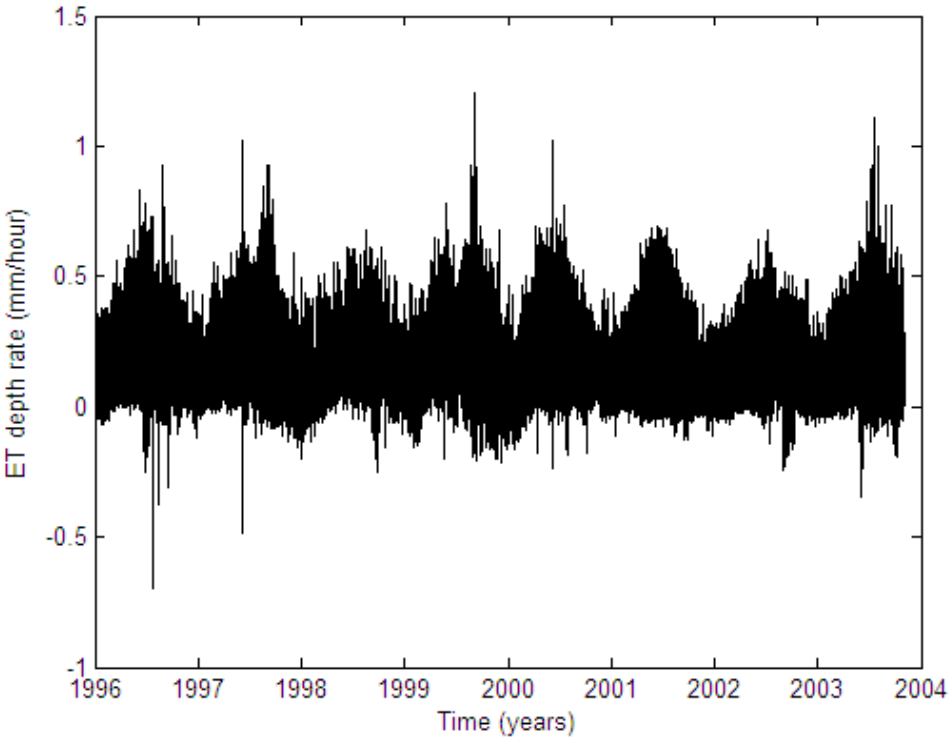

Figure 17. Evapotranspiration hourly rates in station "Site 7" by German [2000] after gap filling.

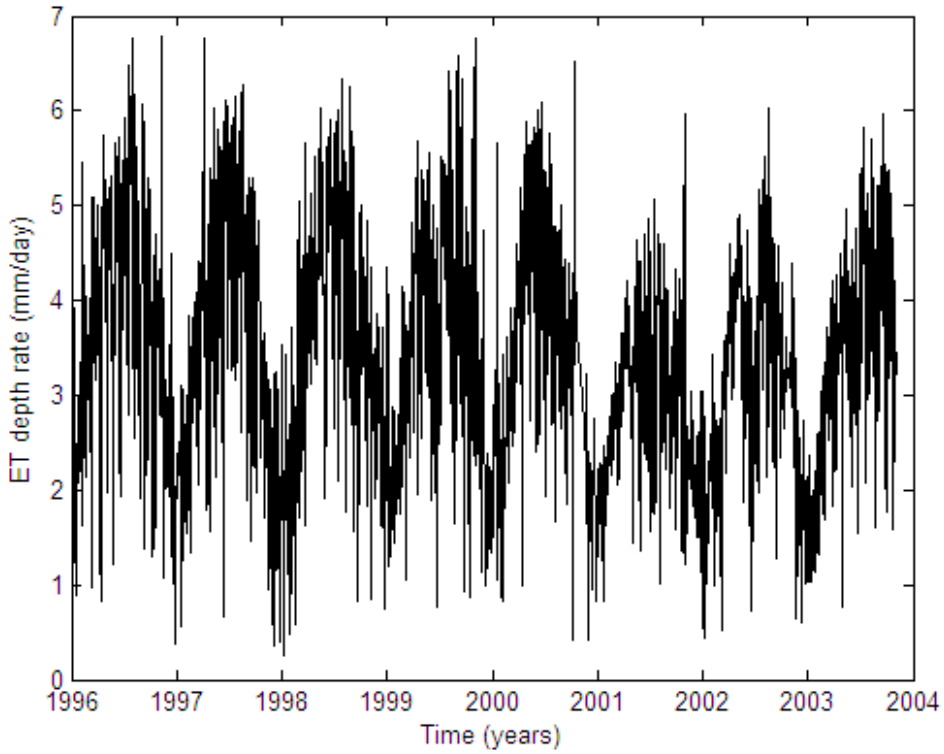

Figure 18. Daily evapotranspiration rates computed from data shown in Figure 17.

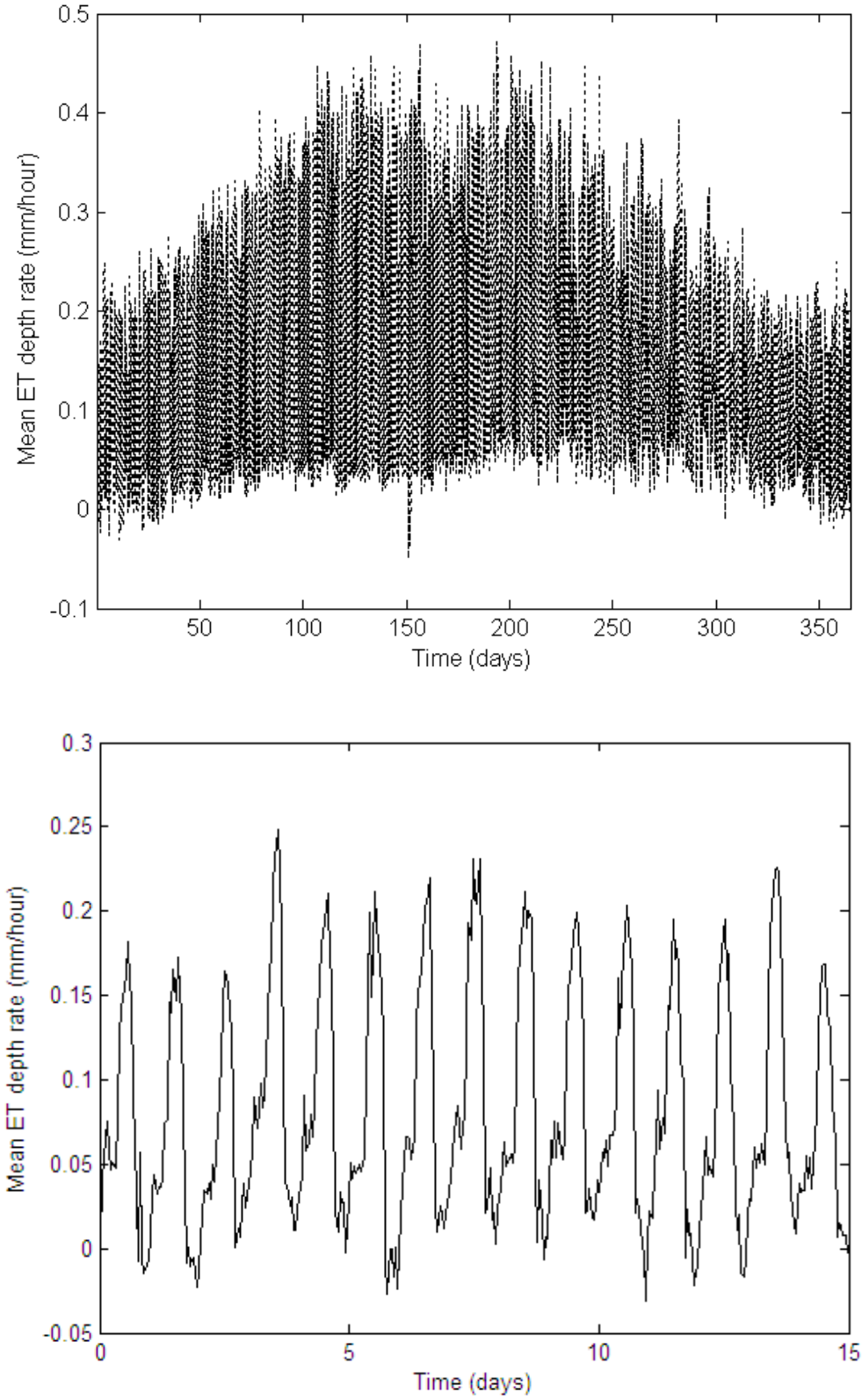

Figure 19. Hourly ET depths from the mean of the almost eight year data shown in Figure 17. The bottom graph shows the first 15 days of the year.

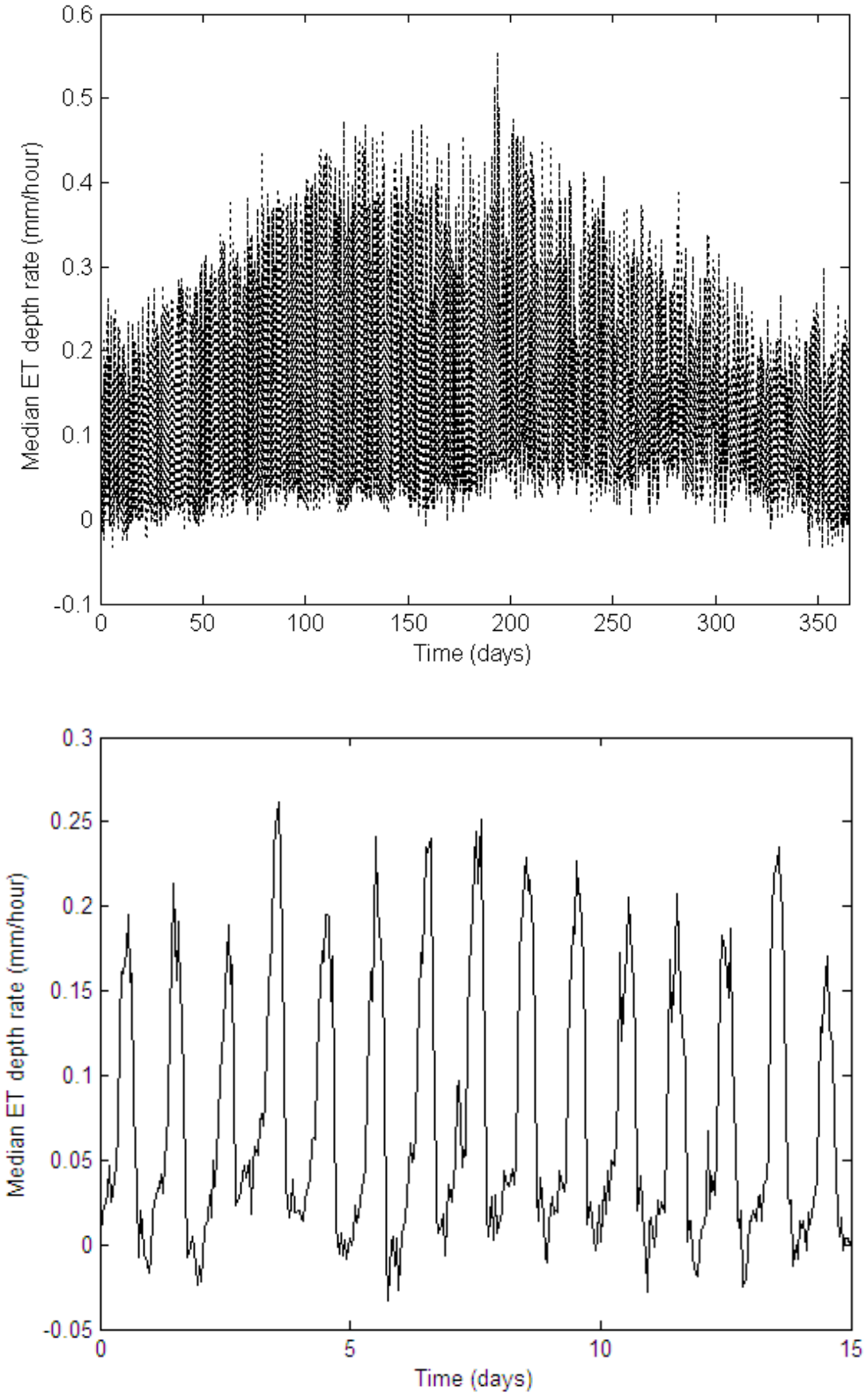

Figure 20. Hourly ET depths from the median of the almost eight year data shown in Figure 17. The bottom graph shows the first 15 days of the year.

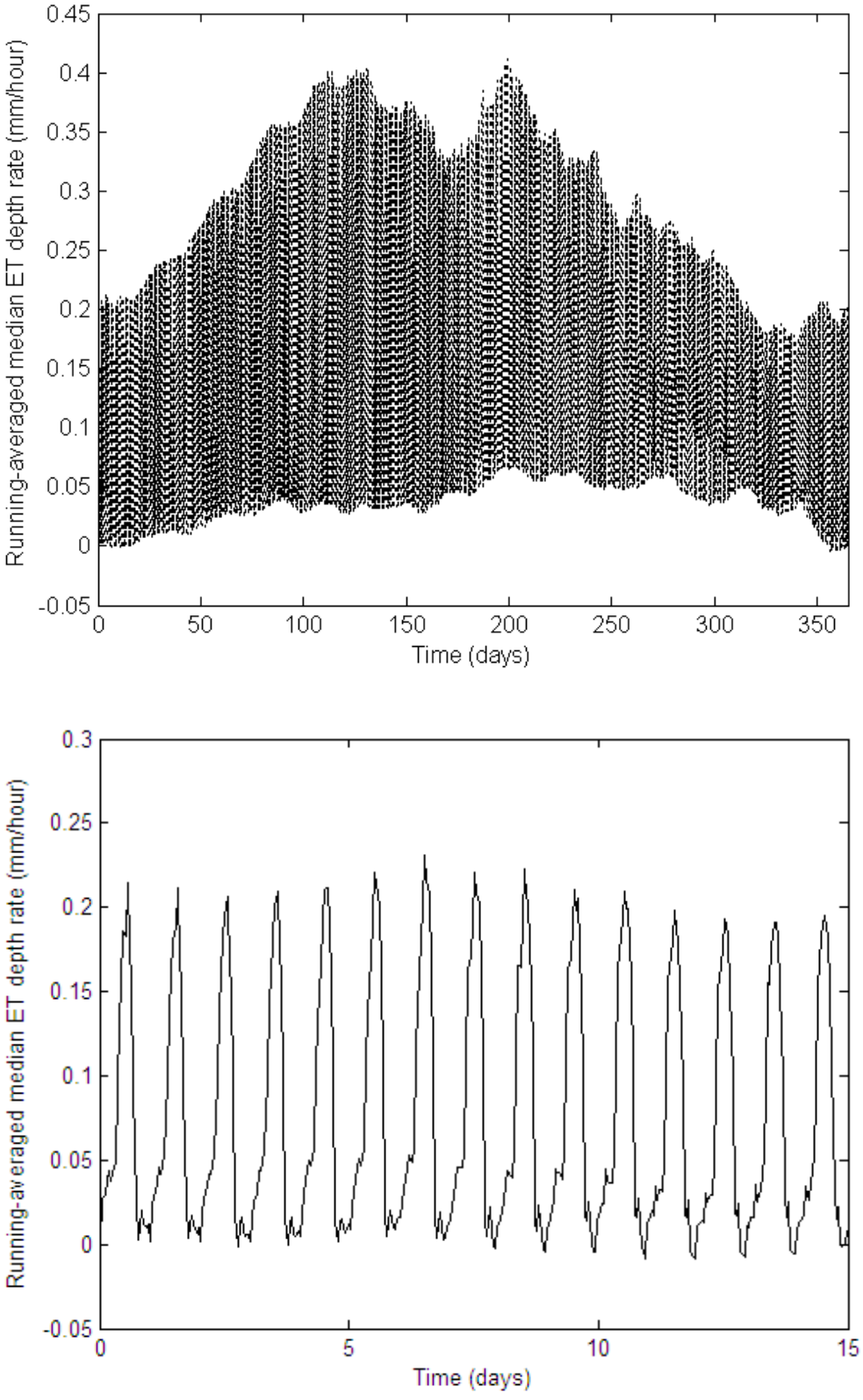

Figure 21. Hourly ET depths from the running average of the values of Figure 20 with a window of 7 days. The bottom graph shows the first 15 days of the year.

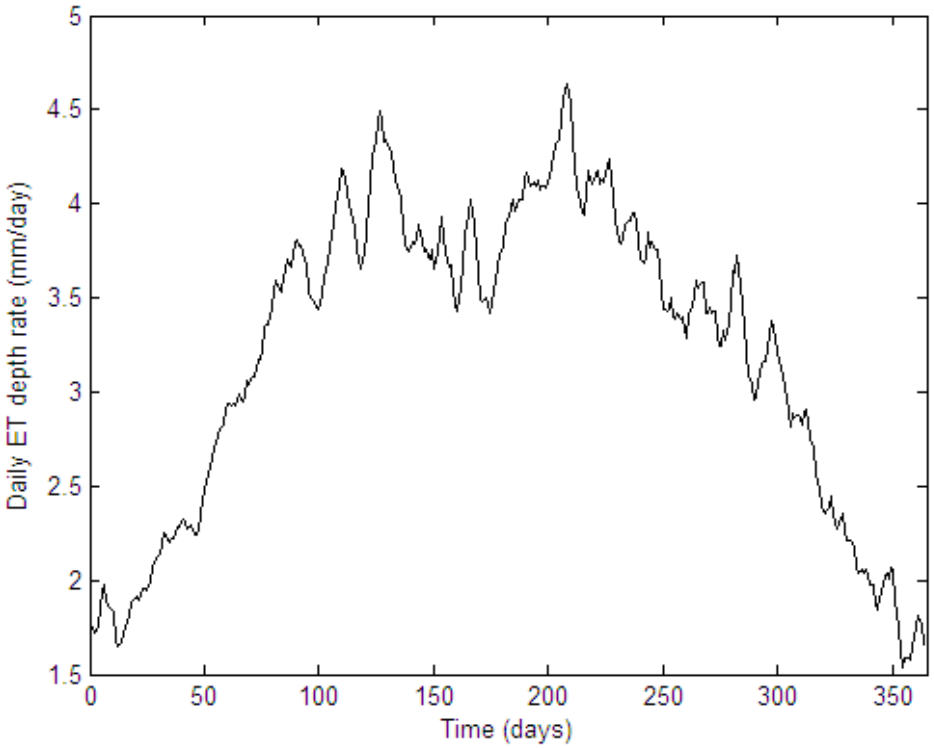

Figure 22. Mean daily ET depths obtained from the hourly values in Figure 21.

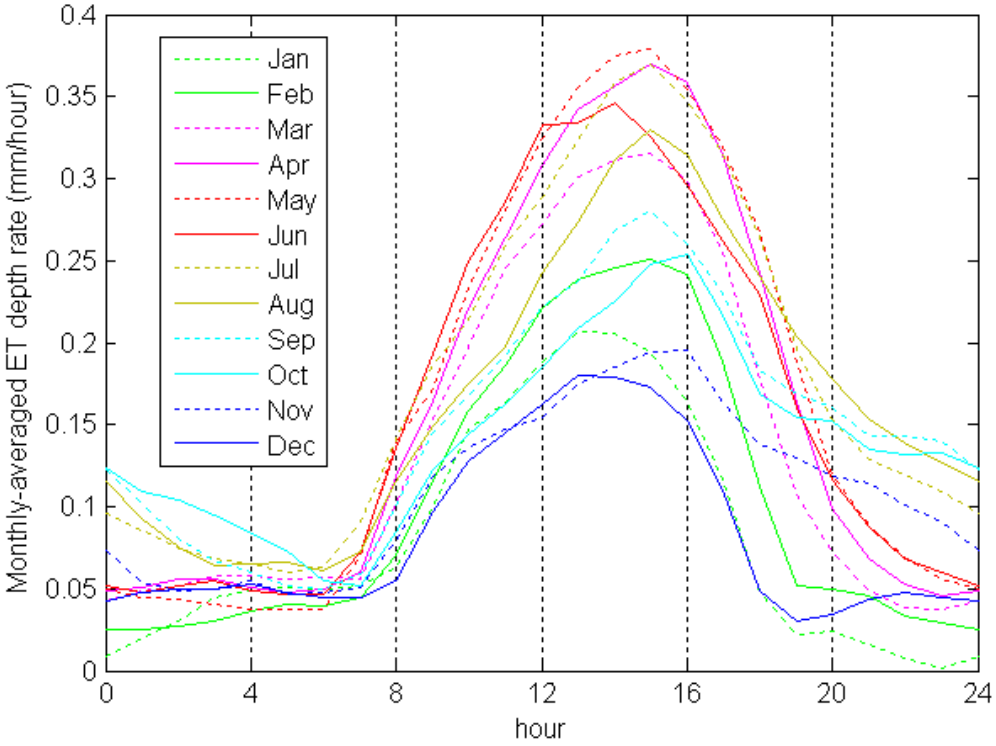

Figure 23. Monthly-averaged hourly ET rates obtained from the median hourly rates in Figure 20.

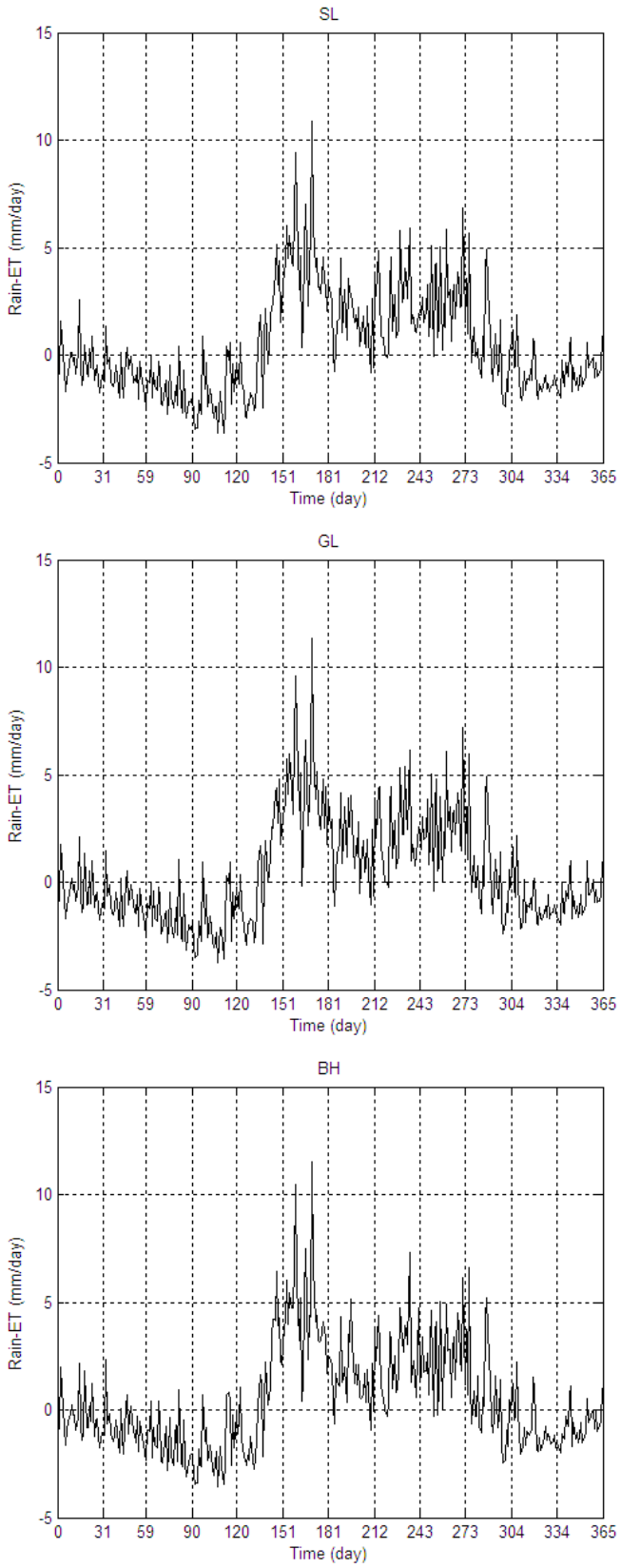

Figure 24. Average net daily recharge (rainfall minus the ET rate) for each tree island.

The numerical model can consider the hourly or daily ET depth rates presented in Figure 17 or Figure 18, respectively. However, in the case that the time period is not covered by those data, the mean hourly or daily ET rates shown in Figure 21 or Figure 22, respectively, is used for the missing data period.

Figure 23 shows the monthly-averaged values from the median hourly rates in Figure 20. This shows how the daily averaged ET depth rate on the different months of the year.

The daily net recharge, which is computed as the rainfall (mean rate in Figure 15) minus the ET rate (Figure 22) is plotted in Figure 24 for each tree island. Notice that even when the annual ET is lower than the annual rainfall depth (see Table 7), there is a dry period (November to April) when there is on average a negative recharge (dry season). A similar recharge graph by using monthly average rates was published by Ross et al. [2006].

3.3.2.2 Evaporation and Transpiration Contribution

The evaporation and the transpiration serve as the conceptual model for the uptake of water from the surface water layer and from the soil (root) layer, respectively. Therefore, it is relevant in our Phosphorus balance model to find the separate contribution of evaporation and transpiration in the ET rates.

A major role of evaporation in the ET rate occurs in open water sites with scarce emergent vegetation, like sites 2 and 3 selected by German [2000]. In contrast, for areas covered by melaleuca trees, the evaporation only occurs from the intercepted rainfall and was estimated between 12 % and 23 % of the total ET rate, with lower contributions during the dry season [Chin, 1998].

It should be mentioned that the ET components may depend on temperature, wind speed, air humidity and water availability in different ways. Moreover, in the case of transpiration, there is also an effect by the sunlight intensity, which is noticeable in the sap flow measurements, when there is a temporarily shadow from a cloud [Stenberg, personal communication, 2006]. Therefore the contribution of evaporation and transpiration to the total ET may vary during the year.

Because of the lack of additional data, the model assumes by default the constant contribution of transpiration and evaporation in the total ET as listed in Table 9. Those

ratios are adjusted in the calibration tests, though.

Vegetation Type	T/ET (%)	E/ET (%)
Marsh (MA)	10	90
Tall sawgrass (TS)	50	50
Bayhead swamp (BS)	65	35
Bayhead (BH)	80	20
Hardwood hammock (HH)	90	10

Table 9. Partition assumed by default in the model for transpiration (T) and evaporation (E) in total evapotranspiration (ET), for the different vegetation types.

3.4 Boundary Conditions

The lateral boundary conditions in the water flow problem are specified as a sequence of constant heads at the boundary cells of the model. In the Phosphorus transport problem, the boundary conditions are specified as a concentration at those boundary cells. The bottom of the rock layer is assumed disconnected, which means zero vertical fluxes of water and dissolved Phosphorus.

The head in the whole column at the lateral boundary is assumed uniform, but the concentration may vary in each layer. The assumption of equal groundwater head as in the surface water is an approximation, because in general there are vertical flows and therefore, head differences between layers. However, this should not have a considerable effect on the flow pattern around the tree island because the boundaries are far from the tree island. On the other hand, even when the head gradient in the surface water layer causes on average a surface water flow in a south-west direction in the Shark River Slough area, there is a groundwater flow to the east coast that should cause a groundwater head gradient in this direction near the coastal ridge [Fennema et al., 1994]. However, the tree islands in this study are not so close to the coastal ridge, and the groundwater head gradient predicted by Fennema et al. [1994] for that area is a minimum, as shown in their Figure 10.12.

The existing time series data of surface water elevation (stage) are processed next. As a result, time series of water table elevation at the center of the islands as well as water table gradients are obtained. They are necessary to obtain the time series of head at all lateral boundary cells on the model.

3.4.1 Surface Water Elevation

The time series of mean daily stages from observation stations around the tree islands were used to obtain the daily mean stages at tree island centers and also the daily mean slope components, which are shown in Figure 25 and Figure 26, respectively. Further details about the station locations, the stage data processing and the interpolation procedure are described in Appendix A3.7.

The mean and median stage values for every day of the year are also shown in Figure 27, which reveals a mean seasonal variation of about 40 cm. The mean and median slope values for every day of the year are also shown in Figure 28 and Figure 29. However, the seasonal variations of the northing and easting slopes are not so clear. In this case, there are fluctuations obtained for the mean slopes in Satinleaf that are removed by using the median values. The mean annual values of stage and slopes for the tree islands are shown in Table 7. Notice that Gumbo Limbo located at the center of Shark River Slough has a lower mean stage, but the mean total slope is about the same for all the tree islands.

The grid in the numerical model is aligned to the NS transect of tree islands defined by Ross et al. [2004], that match approximately their longitudinal axis. Thus, the time series of the slopes in the rotated coordinate system are computed by using the angles in Table A-8. The median slopes in the rotated system after 7 days-window running averaging are shown in Figure 30. Notice that in general the slope oriented along the tree island (Sy) is much bigger than the transversal slope (Sx), as expected. However, in the case of BH, there is a transversal component toward the center of the slough, which has a maximum in the driest period (starting May). This overland flow to the center of the slough has been also noticed from surface water velocity measurements by Solo-Gabriele et al. [personal communication, 2006].

Besides the daily stage data, available hourly data from stations were also processed as described in Appendix A3.7. However, not all stage stations around the tree islands have hourly values reported and the hourly interpolated data has differences associated to the use of more distant stations for Satinleaf. Daily and hourly values are very close for other tree islands.

In summary, this work considers the interpolated daily stages presented in Figure

25 and the slope components in Figure 26, in order to determine the head time series at all the lateral boundary condition cells for the time period needed.

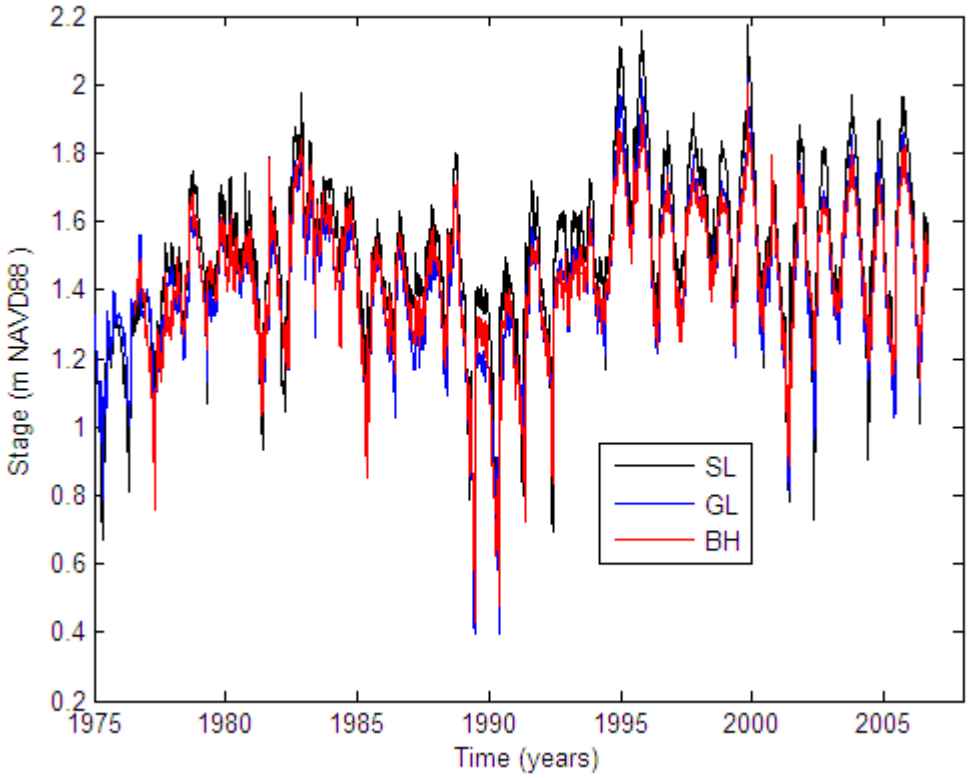

Figure 25. Interpolated daily mean stages in the tree islands of Shark River Slough.

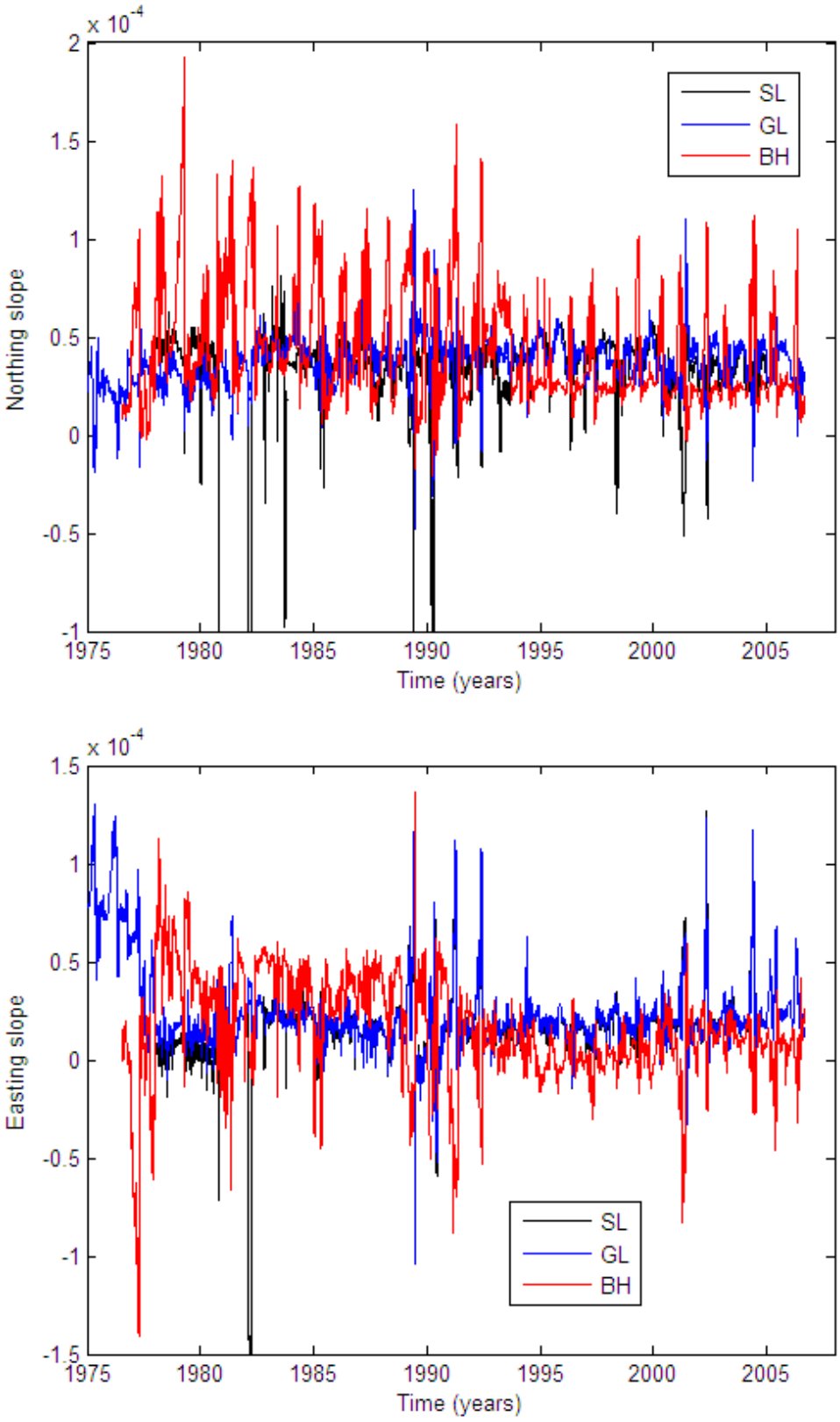

Figure 26. Slopes obtained from the stage interpolation in the tree islands of Shark River Slough.

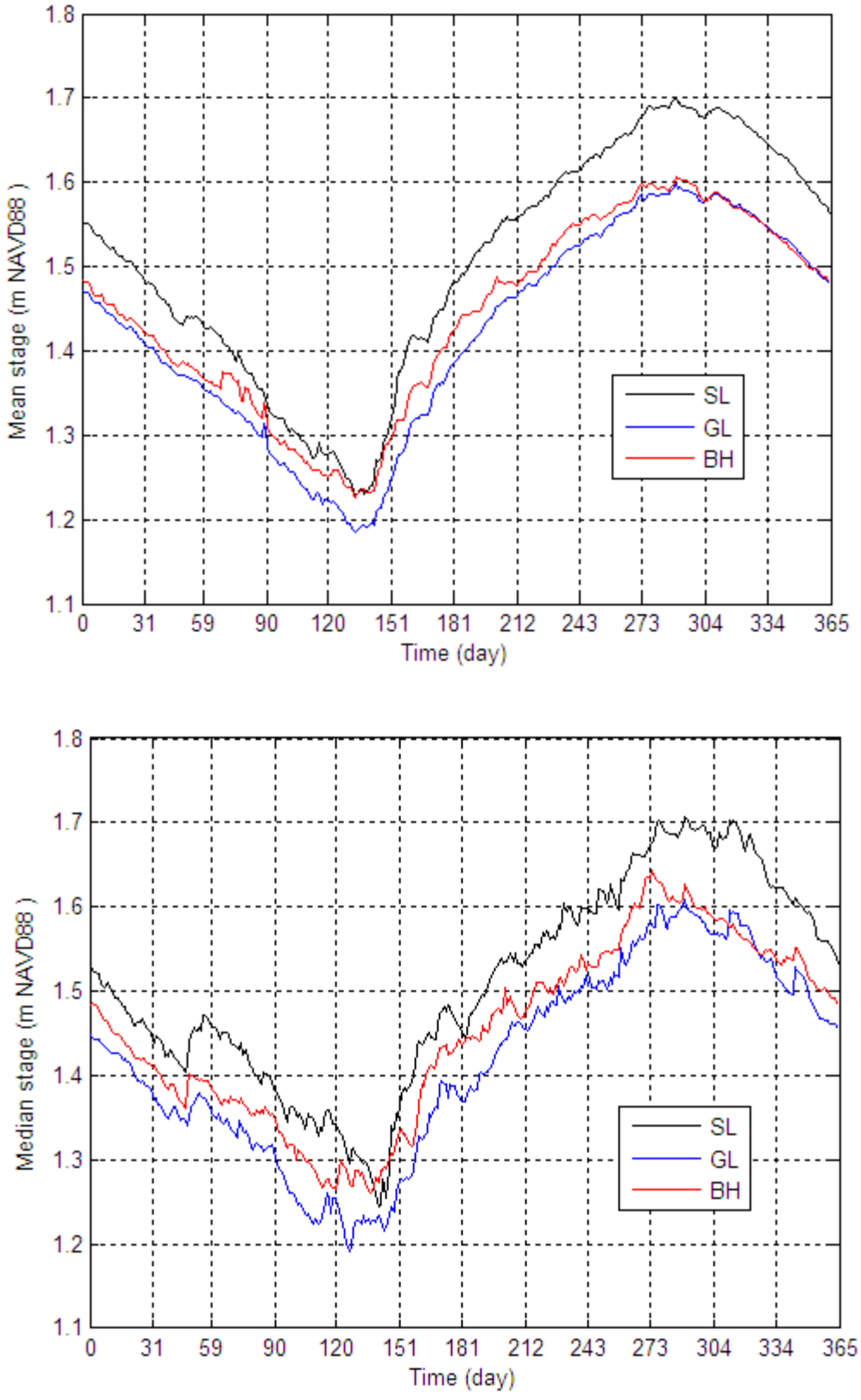

Figure 27. Mean and median daily stages from interpolated values of Figure 25.

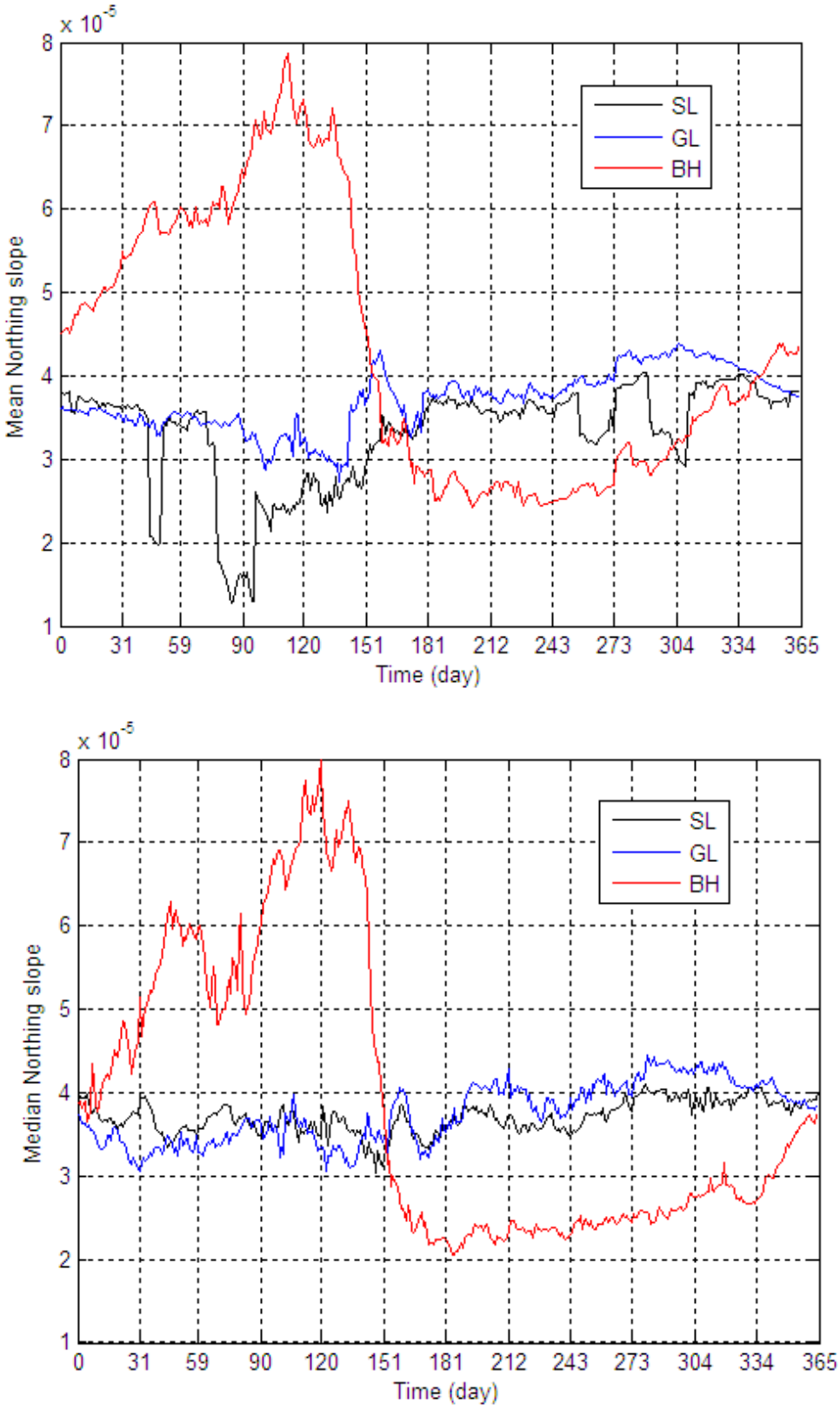

Figure 28. Mean and median daily northing slopes from interpolated values of Figure 26.

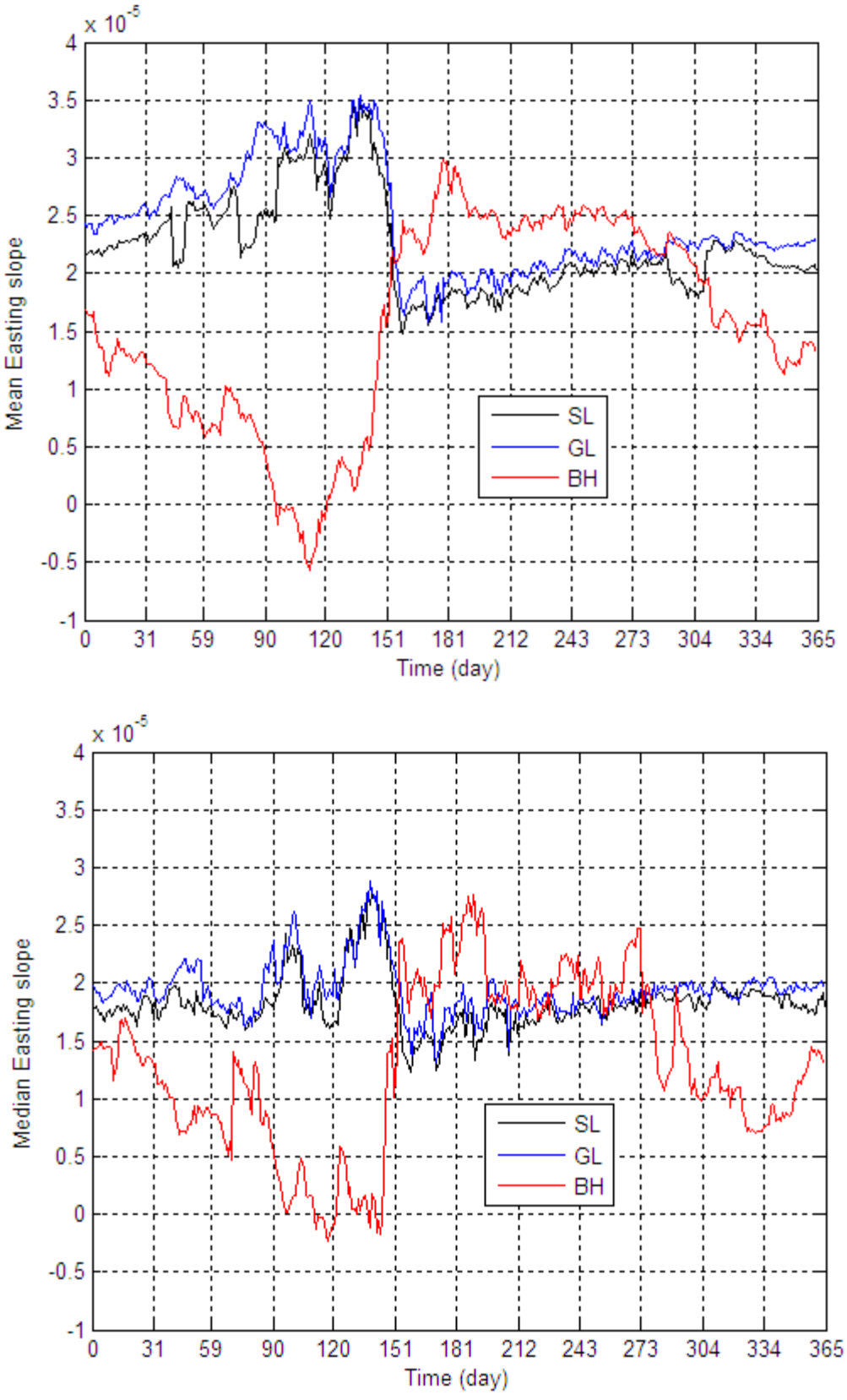

Figure 29. Mean and median daily easting slopes from interpolated values of Figure 26.

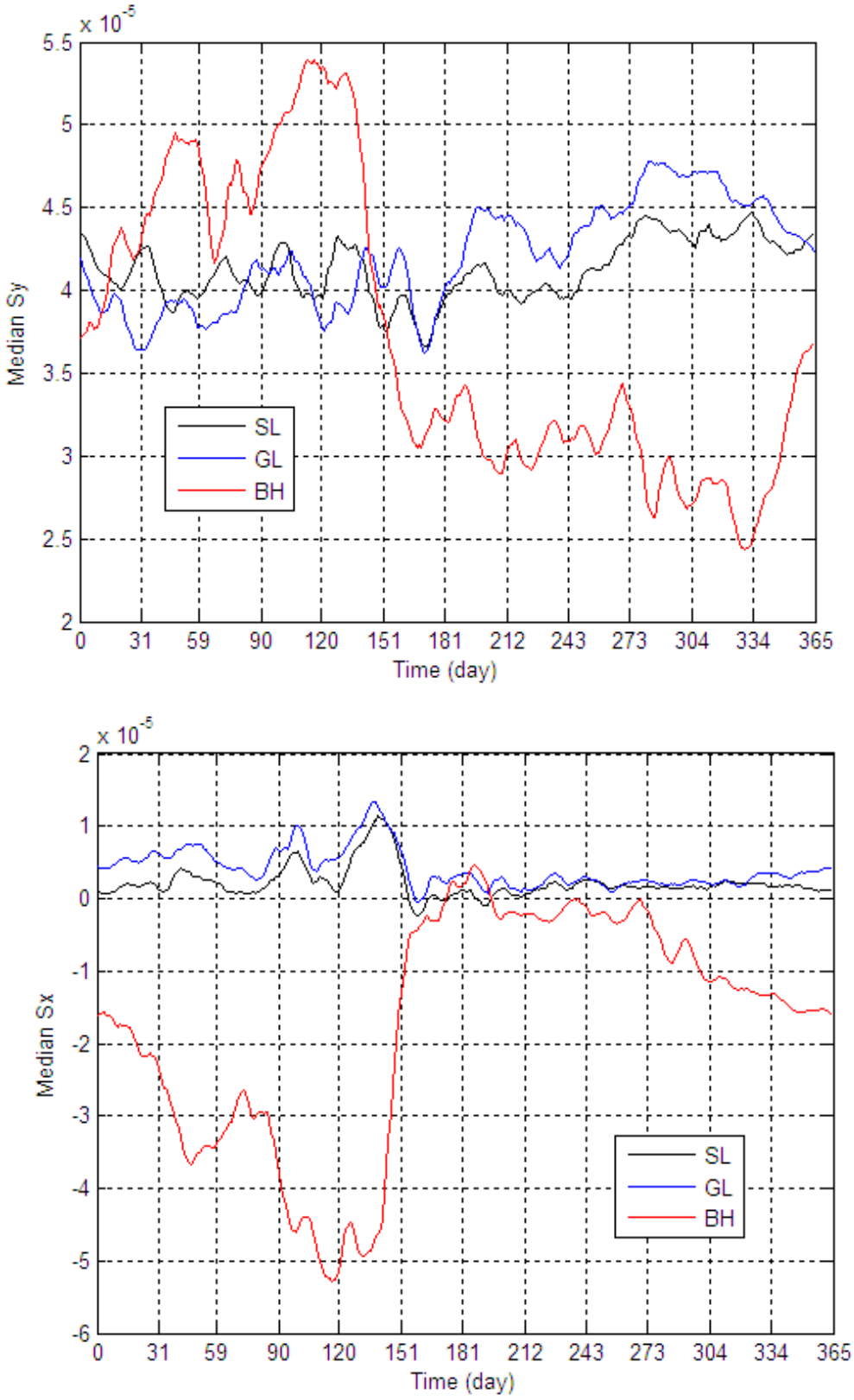

Figure 30. Median slopes in the rotated coordinate system of each tree island, after 7 days-window running averaging.

3.5 Initial Conditions

This section, describes how the initial conditions for water flow and Phosphorus transport are set.

3.5.1 Heads in Different Layers

At the beginning, heads values are assumed linearly interpolated from the values at the boundaries in all the layers. Even when the head differences in the whole model are low, this interpolation procedure may cause erroneous flows. Thus, the model started running several days before in order to remove the effect of this approximation on the results. In other words, a "warming" period is considered so that the model "forgets" the assumed initial condition.

3.5.2 Phosphorus Concentration in Surface Water

The mean total Phosphorus (TP) concentration in surface water was reported by McCormick et al. [2002] as 12 μg/l after analyzing water quality data collected at station P33. Noe et al. [2001] stated that the mean surface-water TP concentrations across the Everglades ranges from 76 to 42 μg/l in Typha and Typha/Cladium mix, which is significantly greater than in Cladium communities (11 μg/l) and unenriched sloughs (10 μg/l). As a consequence of the low supply and availability of P to the ecosystem, water-column TP concentrations in oligotrophic areas average about 10 μg/l. However, no seasonal dependence of this parameter was reported in the literature and a further analysis of the water quality data collected at station P33 is made.

The total Phosphorus and the reactive Phosphorus (orthophosphate or SRP) measured in surface water at station P33 was downloaded from DBHydro. The data cover the period from 1985 to 2006 and has about 220 values of each parameter (a total of 14 to 22 values per month). Both measurements are commonly made over the same water sample.

The monthly median values of both parameters are plotted in Figure 31. The soluble reactive Phosphorus (orthophosphate) is on average below the detection limit (4 μg/l). This result is consistent with the mean SRP values in soil water reported in Table 2 for most of the vegetation types (SRM, SS, TS, and BS). Meanwhile, the total Phosphorus (that also includes the Phosphorus composing the suspended sediments)

clearly shows a seasonal dependence in that figure. A base value of 5 μg/l is obtained on average from August to February of the next year; meanwhile higher values are obtained from March to July. Coincidently, the total Phosphorus peaks (11 μg/l) in May, when the median monthly values for the water surface elevation at station P33 (shown in Figure 32) is minimum. According to Davis [1994], the peak in the Phosphorus concentration in that period may be a consequence of the reflowing of the drying marsh and also a consequence of the fires. In other words, at the beginning of the rainy season rainfall may carry Phosphorus from aboveground water locations (such as the accumulated bird guano, litter and soil decomposition products, etc.). Besides, fires in the marsh, which are more frequent during the dry season, may produce an input of Phosphorus in surface water.

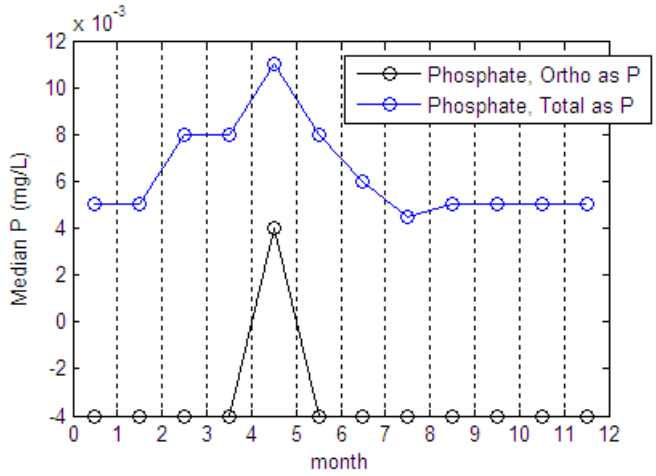

Figure 31. Median monthly values for total and dissolved Phosphorus in surface water at station P33. Negative values indicate that the value is lower than the detection limit (4 μg/l).

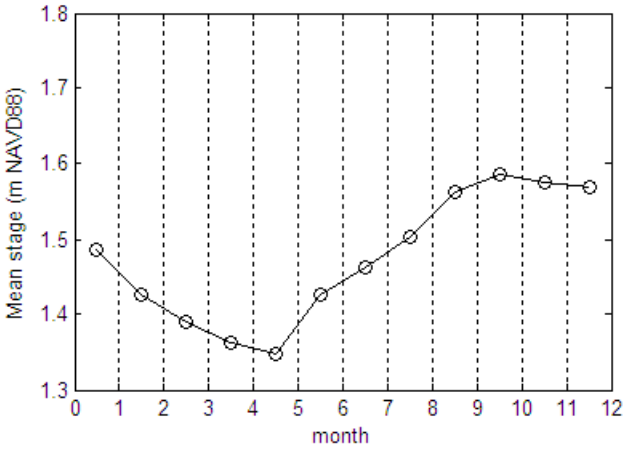

Figure 32. Median monthly values for water surface elevation at station P33 existing at the time when the total Phosphorus was measured.

Notice also that the data processing of total Phosphorus measurements from station P33 by using median to avoid punctual extremely high values, gives lower monthly values than the mean value of 12 μg/l reported by McCormick et al. [2002].

In this work, the initial and boundary concentration of dissolved Phosphorus in surface water (SRP) is assumed as in the soil pore water in the marsh, which from Table 2 is about 1.5 μg/l (1 μg/l $=10^{-6}$ kg/m^3).

3.5.3 Phosphorus Concentration due to Suspended Organic Particles

In the conceptual model, the Phosphorus-in-suspended litter mass is a fraction of the total Phosphorus in the surface water column. From the median total P evolution on station P33 presented in Figure 31 and the typical SRP value in marsh areas (1.5 μg/l), one can state that the median Phosphorus-in-suspended litter must be lower than 3.0 to 9.5 μg/l in marsh areas.

Suspended litter may consist of entire leaves but also fine organic particles, which are the result of partial leaf decomposition. In general, the settling velocity of the particles increases with the particle size, as predicted by Stokes equation for spherical particles. Moreover, bigger litter particles are more likely to be trapped while flowing through the vegetated spaces. Thus, the smaller litter particles are more mobile and they likely have the major contribution on the Phosphorus-in-litter transport.

Direct measurements of the suspended organic particles concentration were performed by Bazante et al. [2004]. They reported in marsh areas around SL and GL tree islands mean concentration of volatile (organic) particles of about 1.1 mg/l in three measures in a period from October 2002 to July 2003. If it is assumed that the Phosphorus content in the marsh litter is 2.7×10^{-4} mg P/mg in Table 14, the Phosphorus-in-suspended organic particles concentration is 0.30 μg P/l, which is a small fraction of the of total water column P in Figure 31.

On the other hand, Noe et al. [2006] reported that in the central part of the WCA3 area suspended particles held on average 37% of total water column P, while the mean total suspended sediment concentration is 0.81 mg/l. Direct sequential chemical extraction of particulate P found 65% of microbial + labile fractions. From the median total P evolution on station P33 presented in Figure 31, this implies that the median

Phosphorus-in-suspend litter concentration is in the range from 1.0 to 2.7 μg P/l, which is about one order of magnitude higher than the value estimated from the measurements by Bazante et al. [2004]. However, this Phosphorus concentration range combined with the mean total suspended sediment concentration and the litter fraction reported give a Phosphorus-in-litter content range of (0.19, 0.51) % kg P/kg, which is about one order of magnitude higher than the marsh value in Table 14 and also higher than the HH litter content. Thus, combining the leaf litter content in Table 14 with the mean total suspended sediment concentration and the litter fraction reported, the Phosphorus-in-suspend litter concentration is 0.14 μg P/l, which is closer to the value estimated from the measurements by Bazante et al. [2004].

The source of the discrepancy between the data of Noe et al. [2006] and Ross et al. [2006] is unknown. The litter enrichment due to microbial activity, as observed previously by Davis [1991] (see Figure 41) is not likely the reason, because Phosphorus content in litter is similar as in soil as shown in Table 14. On the other hand, the adsorption on suspended particles can be estimated by using the Freundlich adsorption equation (27) with the parameters assumed for marsh areas and the typical concentration (1.5 μg/l). The mass fraction adsorbed under these conditions is 1.21×10^{-7} kgP/kg, which is negligible regarding the Phosphorus-in-litter content.

In this work, it is assumed a mean Phosphorus-in-suspended litter concentration in marsh areas of 0.30 μg P/l, which is the value estimated from Bazante et al. [2004] in their measurements in the Shark River Slough.

3.5.3.1 Deposition Rate of Suspended Organic Particles

Leonard et al. [2006] reported the accumulation rated of suspended particles in MA and TS areas around GL Tree Island. The values measured on selected sites and in transects are presented in Figure 33 and Table 10, respectively.

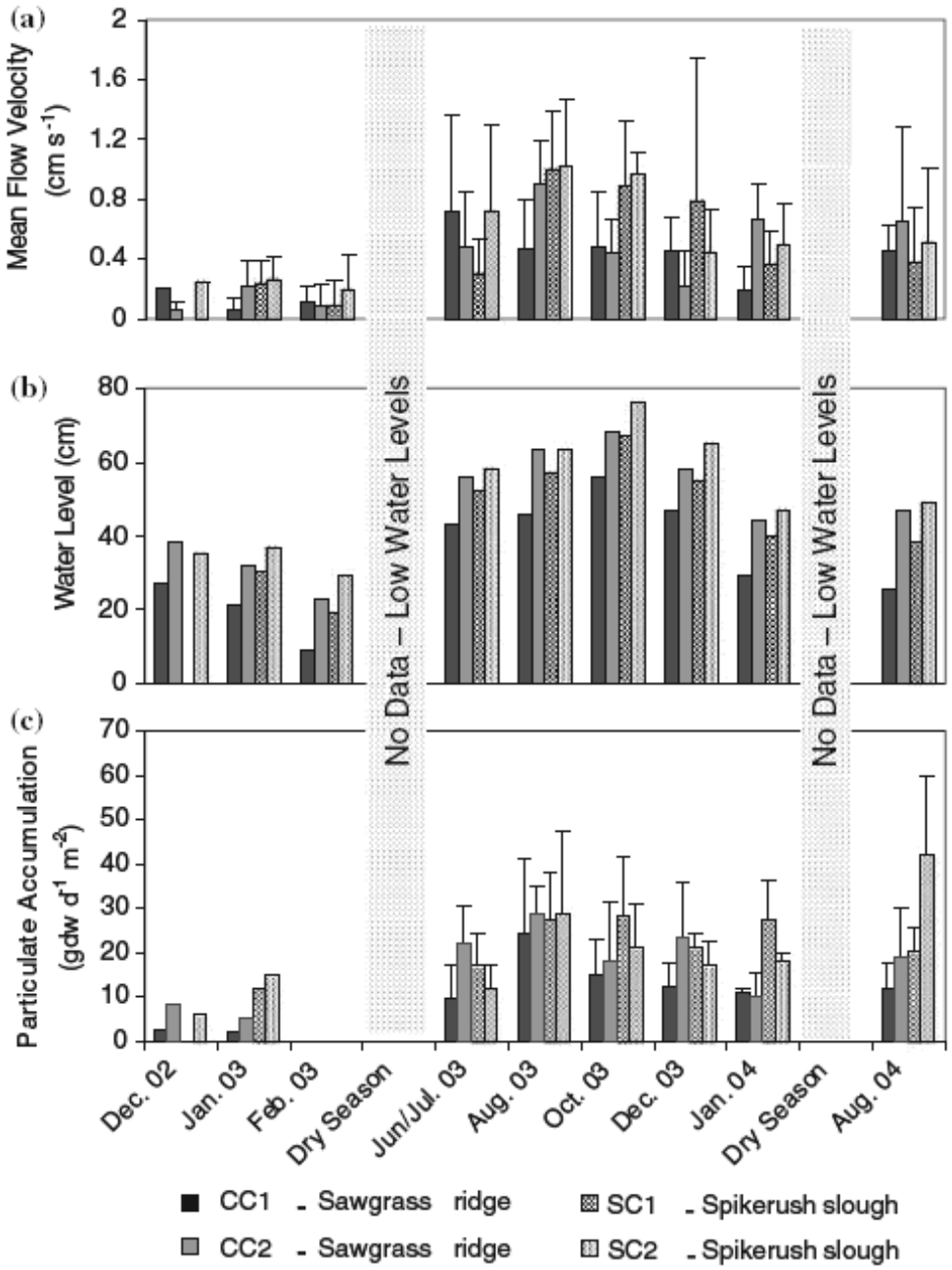

Figure 33. Mean bi-monthly surface velocities (a), water levels (b), and particulate accumulation rates (c) measured at selected sites around Gumbo Limbo tree island. Reproduced from Leonard et at. [2006].

	October 03		December 03		January 04	
V (cm/s)	0.65 ± 0.12	0.93 ± 0.10	0.51 ± 0.08	0.74 ± 0.07	0.15 ± 0.02	0.21 ± 0.02
Particle Acc. (gdw/d/m^2)	44.8 ± 18.3	122.4 ± 17.4	14.7 ± 9.2	31.7 ± 8.8	19.9 ± 6.2	18.6 ± 5.9

Table 10. Surface water velocities and particle accumulation rates at transects around Gumbo Limbo Tree Island, after Leonard et at. [2006].

The graphs in Figure 33 were digitized and the water depth and particulate accumulation rates as a function of the surface velocity are plotted in Figure 34. The particle accumulation values from transects in Table 10 are also included. This plot illustrates that particle accumulation rates increase for higher velocities, which is the expected effect of the erosion. In the next section, the particle accumulation dependency on velocity is used to estimate the erosion parameter.

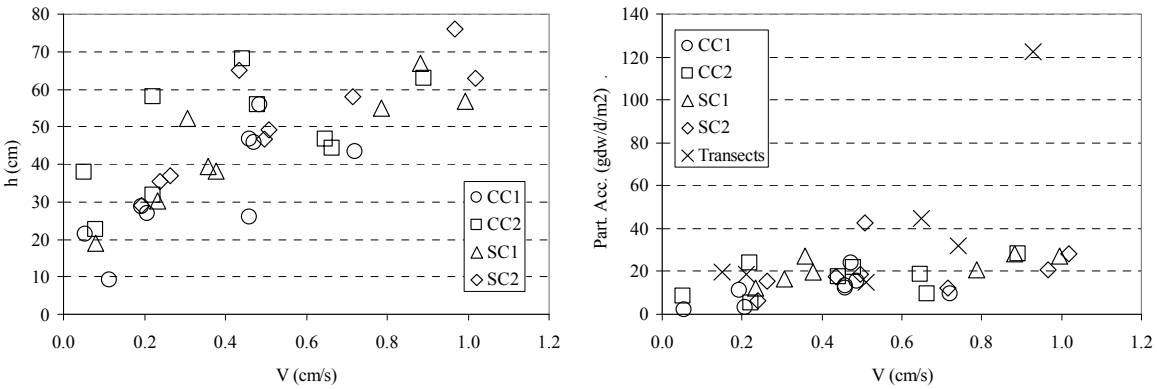

Figure 34. Water depth and particulate accumulation rates as a function of the surface velocity after digitizing graphs in Figure 33 and also including the values in Table 10.

3.5.3.2 Estimation of Deposition, Resuspension and Erosion parameters

The particle accumulation rates in Figure 34 can be transformed to mean deposition rate of Phosphorus ($Rd = v_S C_L$) in marsh areas by using the Phosphorus content in litter of litter 2.7×10^{-4} gP/g in Table 14. If it is assumed that those deposition rates occur at equilibrium concentration, then the velocity dependency is given by equation (16). The fitting of this dependency to the deposition rate data is presented in Figure 35, which gives $\varepsilon_{Lprod} + \varepsilon_{Lres}$ = 0.763 gP/m^2/y = 2.42x10^{-11} kgP/m^2/s and $\frac{C_E}{v_S} = 7.42\text{x}10^{-10}$ kgP.s/m^4. When the value ε_{Lprod} = 0.135 gP/m^2/y = 4.28x10^{-12} kgP/m^2/s (see Table 17) for the Phosphorus-in-litter production rate in marsh areas is used, the estimated resuspension rate is ε_{Lres} = 0.628 gP/m^2/y = 1.99x10^{-11} kgP/m^2/s.

Furthermore, the mean deposition rate from the values in Figure 35 is $Rd = v_S C_L$ = 2.11 gP/m^2/y and mean Phosphorus-in-suspend litter concentration in marsh areas is C_L = 0.30 μgP/l. Assuming that that mean deposition rate occurs at that mean

concentration, the quotient gives a settling velocity of $v_S = 2.23\text{x}10^{-7}$ m/s. With that value, a proportional erosion factor of $C_E = 1.65\text{x}10^{-16}$ kgP/m^3 is obtained.

Because of the lack of other information in the literature, in this work it is assumed that the litter transport parameters $\varepsilon_{Lres} = 1.99\text{x}10^{-11}$ kgP/m^2/s, $v_S = 2.23\text{x}10^{-7}$ m/s and $C_E = 1.65\text{x}10^{-16}$ kgP/m^3 are constant on time and that they are valid not only for marsh but also for all vegetation type areas.

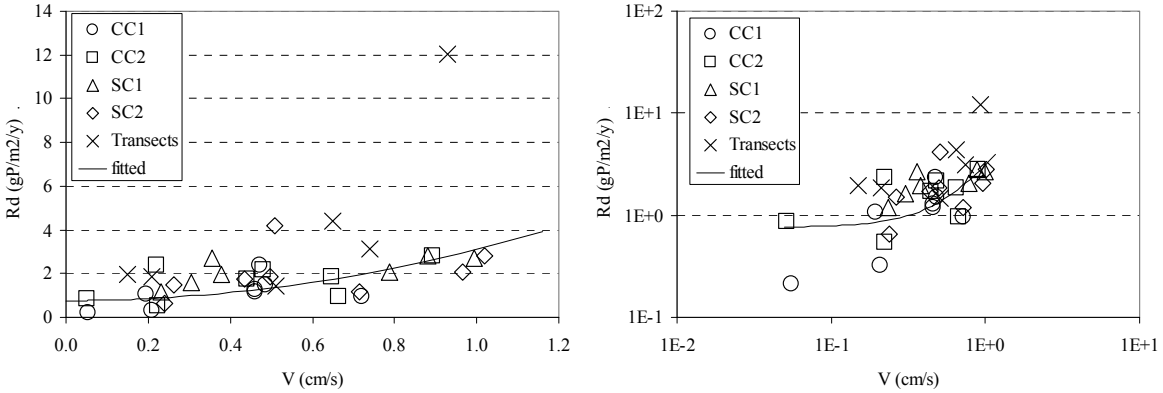

Figure 35. Phosphorus deposition rates estimated from Figure 34 and the result of fitting equation (16) to them.

3.5.4 Phosphorus Concentration in Soil Pore Water

Ross et al. [2004] surveyed the three tree islands at intervals of 25 to 50 m along the transects and collected soil water samples during November 2002. The SRP values measured on those samples are presented in Table 3 of their report and they show a high dispersion even inside the same vegetation type area. The fluctuations in the measurements and the sampling spacing make difficult to construct a map of the dissolved Phosphorus concentration in soil pore water.

In the surveyed data, the soluble reactive Phosphorus (SRP) correspond to the Phosphorus concentration in pore water, meanwhile the total Phosphorus includes the amount composing the organic soil, the amount adsorbed and also the amount dissolved in pore water [K. Jayachandran, personal communication, 2006].

The Phosphorus concentration in soil water is correlated to the vegetation coverage as shown in Figure 1. The values for Phosphorus were digitized and are presented in Table 2.

In this work, an attempt was made to obtain the mean and median values from the transect measurements, grouped according to the vegetation coverage maps in Figure 10, and the results were different to the ones in Table 2. This is understandable due to possible differences in the vegetation coverage type used in this work and the one considered at that time. Also, they included other field measurements in the Shark River Slough area [Ross, personal communication, 2006]. In addition to this, M. Ross and co-workers likely used their field experience to discard some extreme values. So, in this model, it is assumed that initial and boundary conditions are equal to the concentrations in pore soil water shown in Table 2 for the different vegetation types.

3.5.5 Phosphorus Concentration in Rock Pore Water

In case of the bedrock, the same concentration as in the marsh soil is assumed initially, i.e. 1.5 μg/l (10^{-6} kg/m^3), which is close to the SRP values measured in groundwater extracted from shallow wells in the Everglades located far from the canals and far from the coastal line [Rene Price, personal communication, 2006]. However, this is only an initial guess and the Phosphorus concentration in the rock layer around tree islands is obtained during the calibration process.

3.6 Biomass Related Parameters

The section discusses the values assigned in the model for different biomass related parameters such as the litter production rate, litter decomposition rate and biomass Phosphorus content. The Phosphorus content in soil is also presented and the contribution of the soil in the Phosphorus cycling is discussed. This lead to the assumptions made for removing the Phosphorus-in-soil pool from our conceptual model.

3.6.1 Litter Production Rate

Ross et al. [2004] used litter traps on Hardwood Hammock, Bayhead and Bayhead Swamp areas of the three tree islands in the period 2001-2003 to collect the litter. The production rate of total and leaf litter is reproduced in Table 11. In general, the total and leaf litter production rate decreases from HH to BS, meanwhile the percentage of dead leaves increases, as shown in the same table.

The seasonal dependence of litter production rates measured by Ross et al. [2004] cannot be clearly extracted from the data collected, as shown in Figure 36. According to

Pablo Ruiz [personal communication], there are both deciduous and evergreen trees in HH, BH and BS vegetation type areas. Evergreen trees produces about the same litter during the whole year and deciduous trees produces more litter at certain time of the year. However, the timing of flushing changes for different species. For example, *Celtis laevigata* (sugarberry) is a deciduous hammock tree which by December and January is almost, if not completely, leafless. On the other hand, *Bursera simaruba* (gumbo limbo), also a deciduous hammock species, which drops its leaves during spring, usually at the peak of the dry season. Similar patterns are also true for several bayhead and bayhead swamp species like *Salix caroliniana* (willow) and *Annona glabra* (pond apple) which have different leafless periods. Based on this, Pablo Ruiz [personal communication, 2006] concluded that there are likely two periods of deciduous litter fall: one in mid-winter (November-December) for temperate species and the second in mid-spring (April-May) for tropical species.

In addition, there is a litter production component associated to strong winds. Most of the windstorms litter deposits are associated with the tropical hurricane season (June-November) which can defoliate an entire forest. However, a strong winter storm (cold front typically from November to February) can cause also a significant spike on the amount of litter on the forest floor [P. Ruiz, personal communication, 2006].

Parameter	Tree Island	Vegetation type		
		HH	BH	BS
Litter production rate ($kg/m^2/yr$)	SL	1.088	0.740	0.144
	GL	0.779	0.746	0.208
	BH	1.062	0.667	0.183
	Average	0.976	0.718	0.179
Leaf litter production rate ($kg/m^2/yr$)	SL	0.844	0.594	0.126
	GL	0.632	0.638	0.172
	BH	0.831	0.525	0.157
	Average	0.769	0.586	0.152
Dead leaves in litter (%)	SL	77.6	80.3	87.3
	GL	81.2	85.5	82.7
	BH	78.2	78.6	85.7
	Average	79.0	81.5	85.2

Table 11. Parameters related to the litter production in different plant communities of Shark River Slough tree islands. Extracted from Ross et al. [2004].

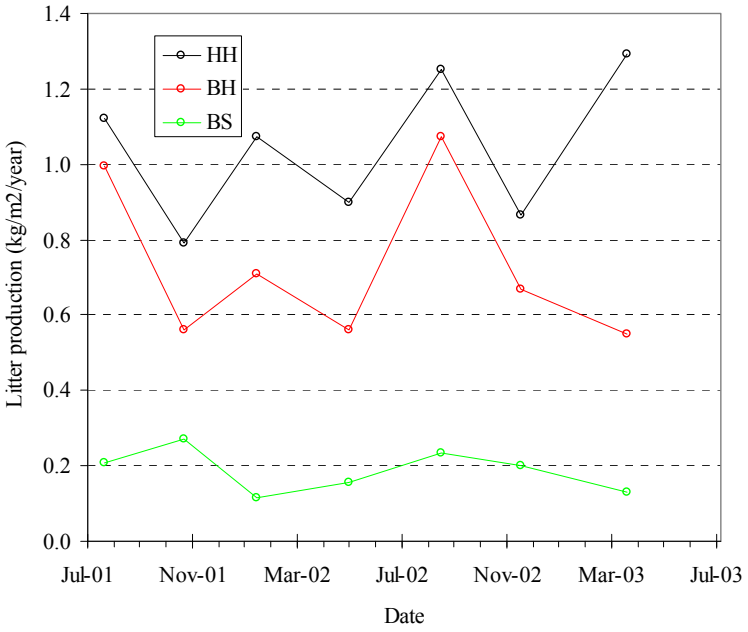

Figure 36. Evolution of the litter production rate at several vegetation types areas reported by Ross et al. [2004].

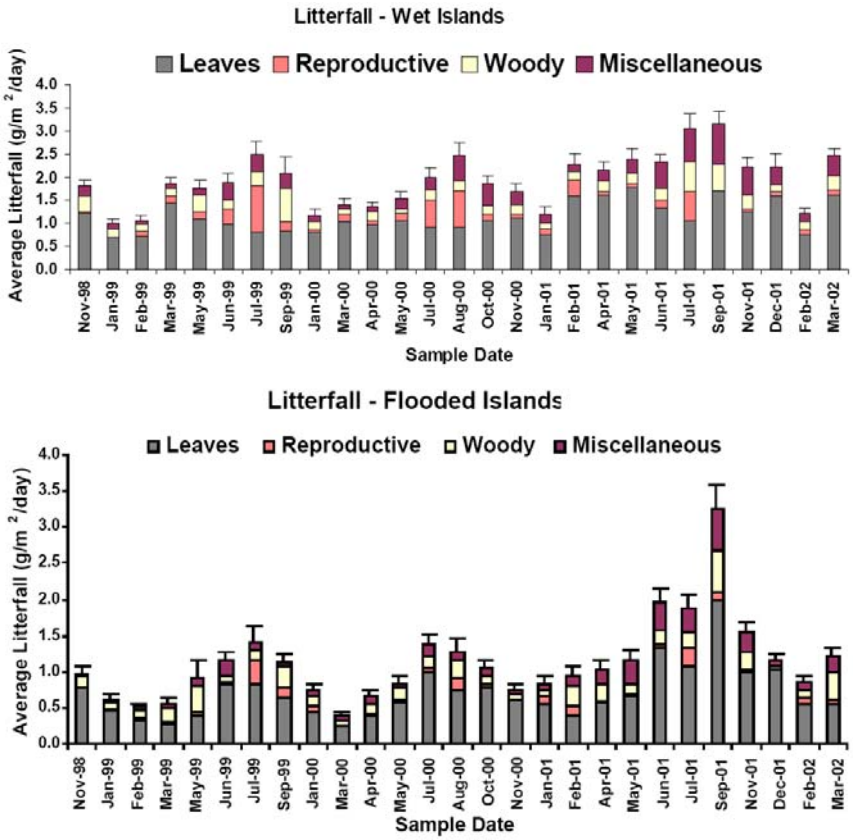

Figure 37. Evolution of the litter production rate on tree islands at WCA3A under short hydroperiod (wet) and long hydroperiod (flooded). Extracted from Sklar et al. [2003].

Figure 37 shows the evolution of the litter production measured by Sklar et al. [2003] on tree islands at WCA3A. The seasonal dependence is more clearly defined in the second graph, corresponding to the longer hydroperiod case. However, notice that a maximum litter fall production around July to September is not consistent with the above comments from Pablo Ruiz and also with the dependence assumed by the Wu's model (see how seasonC from Figure A-4 is considered in equation (57)).

The litter production rates of Hammocks in Florida Key reported by Ross et al. [2003] are shown in Table 12. Those values are close to the BH values on the tree islands. The above-ground biomass estimated by those authors from published correlations is also presented and cover the range from 2.7 to 16.3 kg/m^2.

Table 4. Measures of structure and productivity for 5 vegetation types: Transitional Thorn Woodland (TTW); Pine Rockland Forest (PRF); Low, Medium and High Productivity Hammock (LPH, MPH, and HPH, respectively)

Vegetation Type	Location	Canopy Height (m)	Basal area (m^2 ha^{-1})	Total tree biomass (Mg ha^{-1})	Annual litterfall (Mg ha^{-1})	Annual wood production (Mg ha^{-1})
TTW	K4	4	4.4	4.7	2.9	–
	S4	5	14.4	35.4	4.26	0.38
PRF	B2	12	12.1	47.5	2.76	3.05
	S3	10	21.0	39.6	2.24	3.31
	S5	12	15.2	33.8	2.17	3.32
LPH	S2	5	22.2	45.3	5.73	2.04
	S7	6	24.3	102.0	5.01	1.76
MPH	B3	8	32.5	109.0	7.99	2.96
	L2	8	15.0	27.4	5.61	2.60
	K1	8	27.5	75.7	5.31	2.05
HPH	K5	13	35.8	136.0	7.35	5.02
	K9	10	33.9	120.0	6.85	4.29
	L3	8	39.4	163.0	6.79	3.27

Table 12. Mean litter production in different plant communities of Florida Keys reproduced from [Ross et al., 2003].

In this work, the annual average values presented in Table 11 for the litter production rates and dead live fraction for HH, BH and BS vegetation types are assumed. For TS vegetation type areas, the value of 1.8 kg/m^2/yr reported by Davis [2006] is used. For MA areas, an intermediate value of 0.5 kg/m^2/yr is adopted from the range reported by Ewe et al. [2006]. There is not enough data about the complex seasonal dependence of the litter production rate, and for simplicity, they are assumed constant through the whole year.

3.6.2 Litter Decomposition Rate

Several decomposition studies of sawgrass litter have been done in WCA-2A along the Phosphorus gradient. Davis [1991] found that approximately half of the litter mass remained intact after 2 years in anaerobic conditions, which implies an average decomposition (decay) rate of 0.95×10^{-3} day^{-1}. DeBusk and Reddy [1998] reported that anaerobic decomposition rate for plant litter and peat in WCA-2A is approximately one-third the rate of aerobic decomposition. Debusk and Reddy [2005] found mean decomposition rates in sawgrass litter of 1.7×10^{-3} day^{-1}.

	HH	BH	BS	Average
Black Hammock	28.8 ± 4.0 (6)	38.3 ± 7.6 (6)	54.6 ± 6.5 (5)	39.7
Gumbo Limbo	45.8 ± 5.5 (3)	49.7 ± 17.4 (6)	30.2 ± 9.1 (5)	41.9
Satinleaf	34.3 ± 2.9 (5)	40.7 ± 4.2 (6)	26.4 ± 14.8 (3)	35.4
Average	34.4	42.9	38.7	38.7

Table 13. Relative mass (%) of litter lost after a six-month (January-July 2002) period in Shark River Slough tree islands. The number of observations is given in parenthesis. Extracted from Ross et al. [2002].

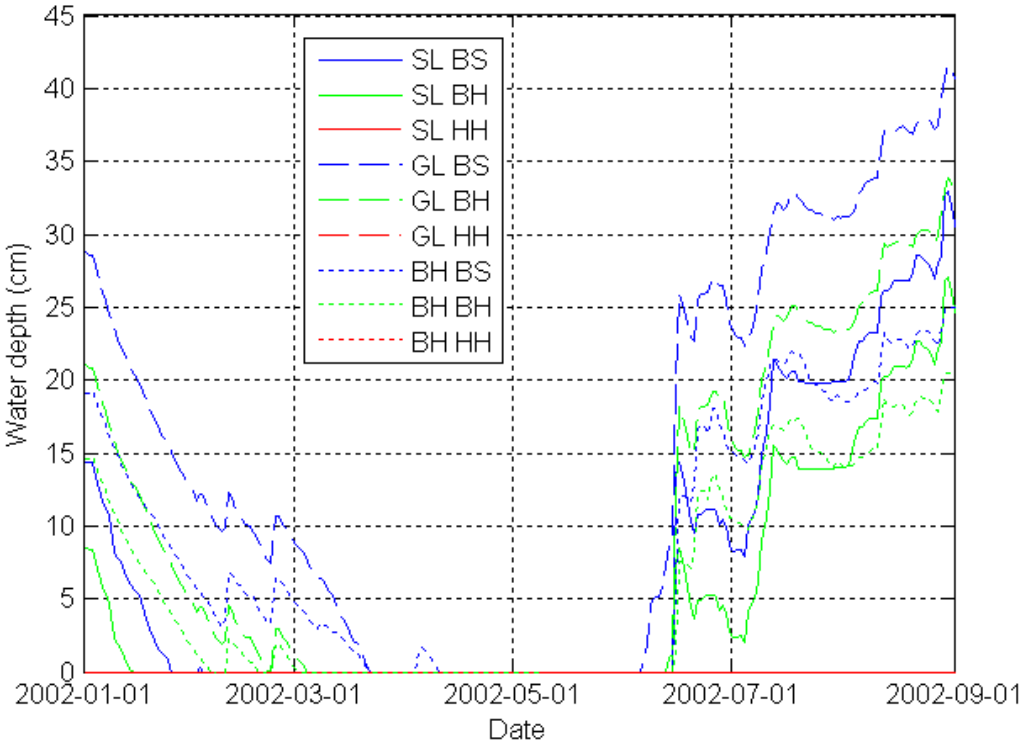

Figure 38. Average water depth in HH, BH and BS areas in different tree islands (SL, GL and BH) for the first part of year 2002.

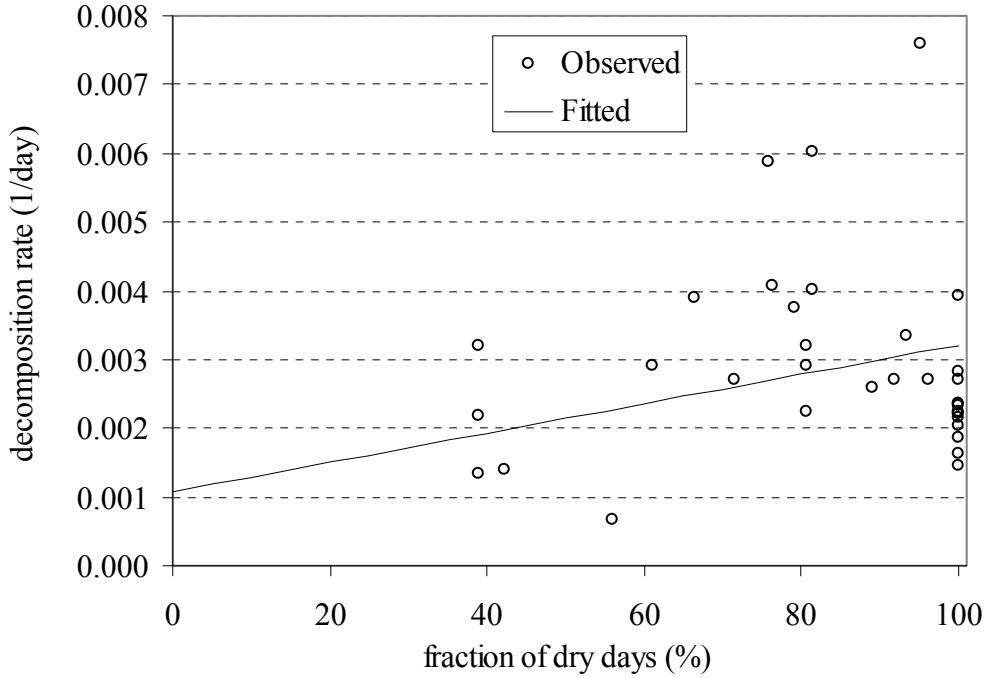

Figure 39. Decomposition rate reported for decomposition bags as a function of the fraction of dry days at bags locations from Ross et al. [2002] data. See text for fitted line details.

Ross et al. [2002] studied the decomposition of senescent or recently fallen leaves in the HH, BH, and BS vegetation type areas in the tree island of Shark River Slough. The relative mass of litter lost after the six-month period reported by the authors, does not show a clear dependence with the vegetation type coverage, as shown in Table 13. The overall average value of 38.7 % of mass lost after a 6 month period corresponds to an average decomposition rate of 2.68×10^{-3} day^{-1}.

The decomposition bags in that case were submitted to different conditions (aerobic or anaerobic) depending on the soil elevation where they occurred. By considering the spatial-averaged soil surface elevation in Table A-33 for the different vegetation types and the mean stage at each tree island, the mean water depth during that period was computed (see Figure 38). However, even inside the same vegetation type area the soil elevation may vary. Therefore, the fraction of dry days was computed at each bag location and the decomposition rate is plotted as a function of them in Figure 39. The data shows a high dispersion and the fitted line was obtained by assuming that the anaerobic decomposition rate (0 % fraction of dry days) is one-third of aerobic one

(100 % fraction of dry days). The best fitted values are 1.07 and 3.21×10^{-3} day^{-1} for the anaerobic and aerobic rates, respectively. Notice that the anaerobic rate value is lower than the one for *Cladium jamicense* (1.7×10^{-3} day^{-1}). About one half of this difference can be explained from the composition of leaves in litter bags (85% according to Table 11) assuming that the other 15 % is not decomposed appreciably after that six month period.

In the Wu et al. model, the annual averaged decomposition rate is assumed as 1.9×10^{-3} day^{-1} for tree island vegetation type and 1.85×10^{-3} day^{-1} for sawgrass and wet prairie (see Table A-3). Moreover, the seasonal dependence adopted for that parameter makes the daily decomposition rate 20% higher in June-July and 20% lower in December-January.

In this work, a litter decomposition rate in anaerobic conditions of 1.0×10^{-3} day^{-1} is assumed for all vegetation types. The decomposition rate in aerobic conditions is assumed as three times the rate of anaerobic decomposition. The seasonal dependence on that parameter is considered only by changing from anaerobic to aerobic decomposition rate when the soil surface becomes dry or from aerobic to anaerobic when it becomes wet.

3.6.3 Live Biomass and Litter Phosphorus Content

The N:P content ratio in leaves of common plant species around the tree islands of Shark River Slough such as *Chrysobalanus icaco*, *Cladium jamaicense* (sawgrass) and *Eleocharis cellulosa* (Spikerush) were reported by Ross et al. [2006]. Besides those Phosphorus content data, other measurements in leaves of *Typha domingensis* and of unknown species in BH and BS areas were available [M. Ross, personal communication, 2006]. All those values are used to compute the weighted average across species presented in Table 14 by making an educated guess of the species abundance in the different vegetation type areas.

Ross et al. also measured the Phosphorus content in dead leaves accumulated in litter traps. The average of all those measurements for each vegetation type is also presented in Table 14.

On the other hand, the soils around the three islands are mostly organic, composed of decomposing litter. Ross et al. [2006] reported an average of 66% of organic matter for those soils (see Table 5). Therefore, the total Phosphorus in soil

reported by Ross et al. [2006] in Table 2 is a measure of the Phosphorus content on decomposing litter and it is also included in Table 14.

The model by Wu et al. assumes that the Phosphorus is contained equally in live biomass (below and above) and in litter, according to the mass fractions presented in Table A-3 for their vegetation types and reproduced in Table 14. The value for the tree island type is very low compared to the ones reported by Ross et al. This is reasonable because mass fraction of Phosphorus in leaves is much higher than in trunks, which contains the higher amount of above-ground biomass. See for example in Table A-5 that the leaf biomass predicted by the Wu et al. model for the tree island vegetation under no stresses is about 1.6 % of the total biomass.

Vegetation type	HH	BH	BS	TS	MA
Leaves (Ross et al. data)	0.130	0.063	0.038	0.029	0.027
Leaf litter (Ross et al. data)	0.213	0.086	0.072	---	---
Soil [Ross et al., 2006]	---	0.125	0.155	0.034	0.028
Total biomass (Wu et al. Model)	0.030			0.027	0.069
Photosynthetic biomass (ELM model)	0.034				
Non-photosynthetic biomass (ELM model)	0.048				

Table 14. Phosphorus content (% kg P/ kg dry mass) in leaves and leaf litter in different vegetation type areas [Ross et al., unpublished results]. They are also included the values reported for the soil and the ones assumed in other models.

The Everglades Landscape Model (ELM) assumes the same Phosphorus content for all the vegetation types around the tree islands, as shown in Table A-1. Surprisingly, this model assigns a higher content of Phosphorus to the non-photosynthetic biomass than to the photosynthetic one, as shown in Table 14. According to the Phosphorus content reported by Ross et al., the photosynthetic biomass values assumed by ELM are more representative of BS, TS and MA vegetation types.

Davis [1991] reported the mean annual Phosphorus content in *Cladium jamaicense* (sawgrass) leaves along the Phosphorus gradient in WCA-2A, which is reproduced in Figure 40. The SRP in surface water around the tree islands of Shark River Slough is about 1.5 μg/l, where according to graph correspond to a mass fraction of P in leaves equal to or lower than 0.02 %. This is in concordance with the M. Ross et al. results in Table 14.

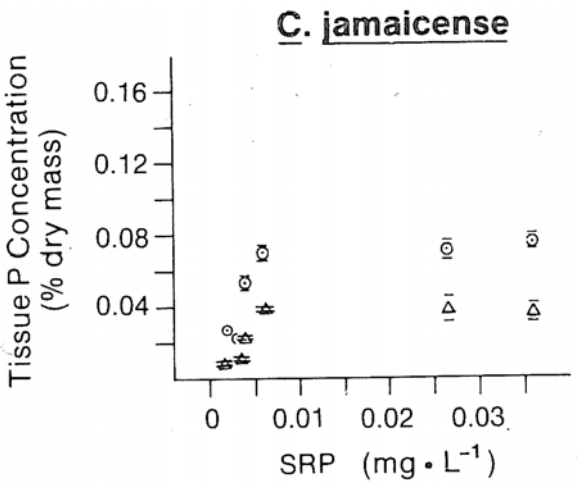

Figure 40. Tissue P concentrations in living (circles) and dead (triangles) leaves in relation to mean annual SRP in surface water at WCA-2A. Values represent the annual mean plus/minus standard error. Reproduced from Davis [1991].

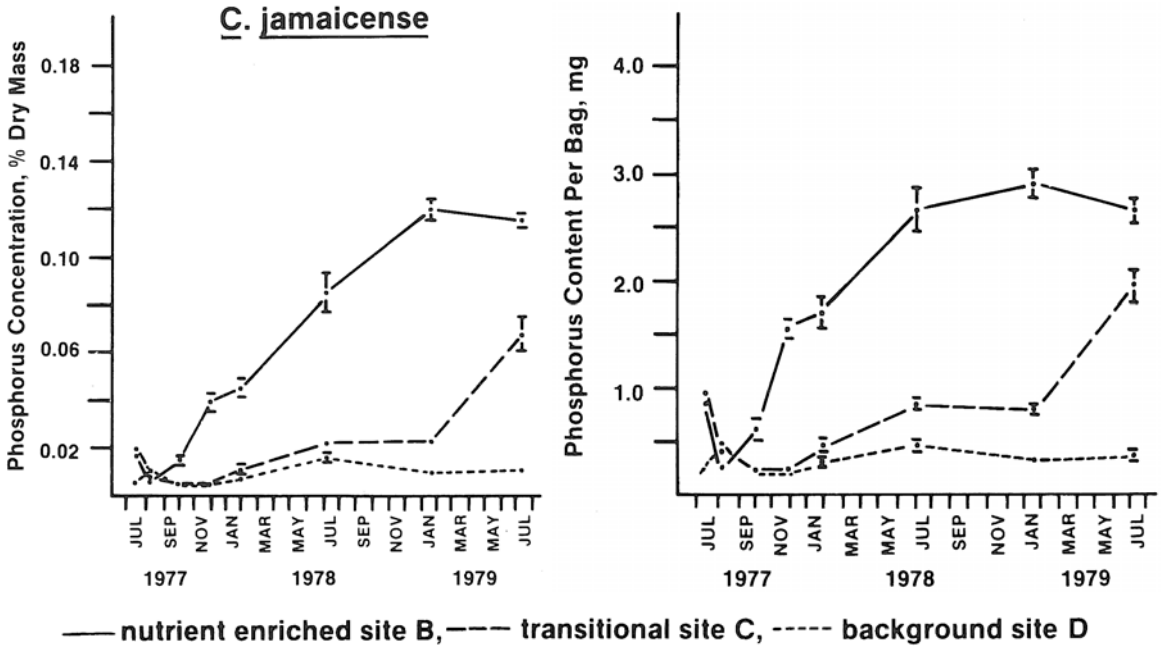

Figure 41. Results of a field decomposition experiment of sawgrass litter in three different P conditions (enriched, transitional and background or oligotrophic) during 2 years. Reproduced from Davis [1991].

In the region of Figure 40 where the Phosphorus content in leaves reaches a plateau, the P content in dead leaves is about one half of the one in live leaves. It is known that plants reabsorb part of the Phosphorus composing the leaves before dispose them. In fact, the ability of *Cladium jamaicense* (sawgrass) to retain P within the plant helps it to survive in extremely low-P environments [Richardson et al., 1999]. For this

reason, it is striking that the Phosphorus content measured by M. Ross et al. in leaves is lower than in leaf litter. It is plausible that the leaf lying on litter traps could be contaminated from animal activity (bird guano, etc). Another possible explanation is that the relative Phosphorus content increases as the litter decomposes [D. DeAngelis, personal communication, 2006]. However, Davis [1991] found that the Phosphorus content in litter at the oligotrophic site (that best corresponds to the Shark River Slough area) changed little over time, as shown in Figure 41.

In this model, it is assumed that the Phosphorus content on leaves (first row in Table 14) corresponds to the Phosphorus content in litter and it is also assumed that the litter fraction has the same relative content during the whole decomposition process.

3.6.4 Phosphorus in Soil

The total Phosphorus content in soil reported by Ross et al. [2006] for each vegetation type is presented in Table 2 and includes the amount constituent in the organic and inorganic soil, the amount adsorbed on soil particles, and the amount dissolved in pore water.

In Table 15, the total Phosphorus content in soil is compared to the content of Phosphorus in litter assumed from Table 14 and to the fractions corresponding to the dissolved and adsorbed amounts, which are estimated from the typical Phosphorus concentration in pore water from Table 2. The parameters involved on this calculation are also in Table 15.

From that table, the mass of dissolved Phosphorus is about three orders of magnitude lower than the mass of adsorbed Phosphorus, which is also three orders of magnitude lower than the total mass in soil. Thus, the mass of constituent Phosphorus in soil (organic and inorganic) is approximately equal to the total Phosphorus values measured in soil samples by Ross et al. [2006].

On the other hand, the mass fraction of constituent Phosphorus in soil and the one in litter from leaves match approximately those for the MA and TS vegetation types. This suggests that the soil is mainly formed by leaf litter, in this case grassy vegetation, and that during the decomposition the Phosphorus content fraction remains relatively constant. Besides, the Phosphorus content in soil in Table 15 is 35.4, 1.8 and 3.5 times higher than in leaves for HH, BH and BS, respectively. This result is apparently contradictory to the

fact that those vegetation types (HH, BH and BS) are composed by trees and bushes the Phosphorus content in leaves is expected to be higher than in the decomposing litter because of the fraction of woody litter with a lower Phosphorus content and also for the lower decomposition rate that the woody litter has compared to the leaf litter.

Parameter	Vegetation type				
	HH	BH	BS	TS	MA
In leaves and litter: first row in Table 14 P mass/ total dry mass (10^{-3})	1.30	0.63	0.38	0.29	0.27
In soil: from Table 2 total P mass/ total dry mass (10^{-3})	46.0	1.25	1.55	0.342	0.285
bulk density: total dry mass/ total volume (kg/m^3)	400	200	200	200	200
total P mass / total volume (kg/m^3)	18.4	0.25	0.31	0.068	0.057
In pore water: from Table 2 dissolved P mass/water volume (10^{-6} kg/m^3)	111.9	5.34	3.67	2	1.5
porosity: from Table 28 pore volume/total volume	0.68	0.37	0.37	0.37	0.37
saturation assumed: water volume/porous volume	1	1	1	1	1
dissolved P mass/total volume (10^{-6} kg/m^3)	76.1	1.98	1.36	0.74	0.56
dissolved P mass/ total dry mass (10^{-9})	190	9.9	6.8	3.7	2.8
equilibrium adsorption curve parameter a (10^{-3} kg P/ kg dry)	3.06	6.33	6.33	6.33	6.33
equilibrium adsorption curve parameter b	0.428	0.81	0.81	0.81	0.81
adsorbed P mass/total dry mass (10^{-6})	62.3	0.34	0.25	0.15	0.12

Table 15. Parameters involved in the estimation of the Phosphorus mass in soil layer cells for different vegetation type areas.

Ross et al. [2004] stated that the accumulation of Phosphorus in soil may be a consequence of the decomposition process. Because carbon and nitrogen are cycled into the gaseous phase and Phosphorus is not, then an accumulation of Phosphorus is expected if it is not dissolved in pore water. Those authors also found in the HH soil that Phosphorus is correlated to the presence of Calcium and that the HH soil has a pH higher than neutral, as shown in Table 16. Thus, Ross et al. [2004] concluded that Phosphorus

could be building up in HH areas as calcium phosphate under alkaline conditions and that further studies of the Phosphorus cycling in soil are necessary.

Vegetation type	pH	Organic Matter (%)	Total P (%)	Total C (%)	Total CO_3 (%)	C:P (molar ratio)
HH	7.7	26.9	5.38	16.5	11.3	7.89
BH	6.6	67.7	0.97	37.2	6.8	99.0
BS	6.1	76.5	0.22	45.3	8.4	531
MA	6.7	69.3	0.08	41.7	9.1	1343

Table 16. Soil parameters obtained by averaging the data for the three tree islands reported by Ross et al. [2004].

The mineralization and immobilization processes of Phosphorus in soil are sketched in Figure 42 [Brady and Weil, 2007]. Mineralization occurs when Phosphorus goes from organic to inorganic forms and immobilization from inorganic to organic, passing through soluble phosphate form. Organic forms include P in live soil organism biomass, in dead biomass, and in humus. The inorganic forms at high pH are Ca-P minerals and at low pH, Fe-P and Al-P minerals. The solubility of all those minerals is very low and, therefore, the inorganic forms are also referred to as insoluble fixed P.

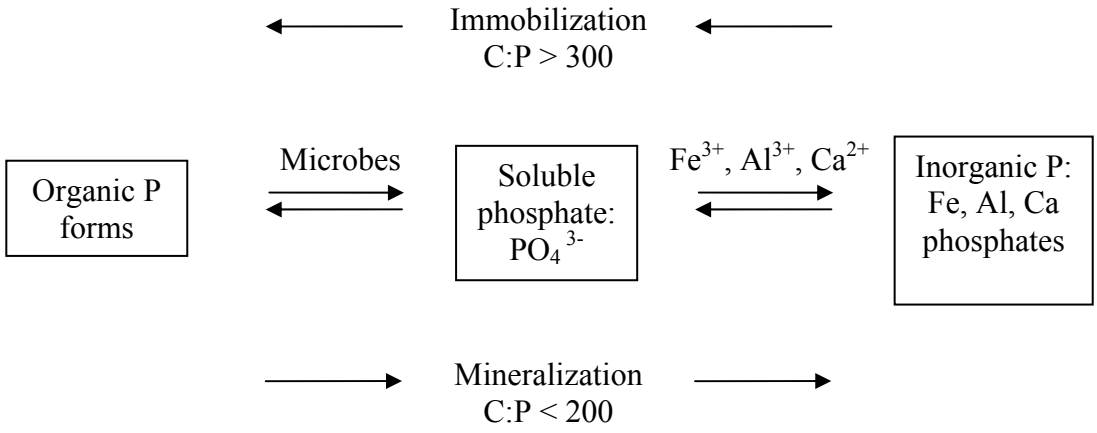

Figure 42. Immobilization and mineralization processes of Phosphorus in soil. Adapted from Brady and Weil [2007].

According to Brady and Weil [2007], the net immobilization of soluble Phosphorus is most likely if C:P molar ratio is greater than 300, and the mineralization if C:P molar ratio is lower than 200. Thus, the molar ratio computed in Table 16 from total C and P weight fraction suggest that in HH and BH areas there is net mineralization, while net immobilization occurs in BS, TS and MA areas. The pH values in HH and BH

areas also suggest that in HH are forming Ca-P minerals and in BH Fe-P and Al-P minerals.

On the other hand, Davis [1991] reported decomposition experiments where the Phosphorus content increased inside the bags filled with *Cladium jamaicense* (sawgrass) litter (see Figure 41). Those cases correspond to enriched areas, where Phosphorus content in vegetation and soil is higher than in oligotrophic areas that correspond to MA areas around the tree islands. The explanation for that is that the higher microbial activity [Davis, 1994] is not only decomposing the litter but also capturing Phosphorus from pore water. Thus, microbes in BS and TS areas that contribute to litter decomposition and create a net immobilization, might be also capturing some Phosphorus from water.

The complexity of the Phosphorus cycling in soil and the lack of further studies on tree island soils led me to remove it from the conceptual model. Thus, instead of considering the decomposing litter producing peat and soluble Phosphorus and the decomposing peat producing soluble Phosphorus, the conceptual model just considers the litter producing soluble Phosphorus directly. This assumption is rigorously true if the decomposition rate in litter is equal to the decomposition rate of the peat soil. Moreover, by removing the soil pool from the conceptual model the net contribution of the immobilization and mineralization processes is being neglected.

3.7 External Phosphorus Fluxes

According to the conceptual diagram in Figure 6, there are three fluxes of dissolved Phosphorus related to the pore soil water that need to be added as external fluxes in the model. They are an input due to external sources (e.g., animal activity and other sources), an output due to vegetation uptake and one input due to litter decomposition. This section describes how their magnitudes are estimated.

The net external input of Phosphorus from all those sources could be implemented in MODHMS by using a well in each soil layer cell. The water flow rate (Q) is very small compared to other water fluxes (rainfall and evapotranspiration). However, the concentration (C) is very high in order to reproduce the desired mass rate per unit area (R). If the area of the cell is A, the concentration is computed as

$$C = \frac{RA}{Q}. \tag{29}$$

The WEL package, however, is limited to injecting dissolved Phosphorus. In case of extraction (Q<0) that package extracts pure water (C=0). This problem is solved by implementing the transport part of the problem in a separate code (developed in MatLab).

3.7.1 Phosphorus Input from Animal Activity

There are wading birds and other animals that hunt in marsh areas and return to the tree islands for eating their prey, for resting and/or nesting. This activity represents a net Phosphorus transport from marsh areas to the tree island.

It is not easy to estimate the net input of Phosphorus in different areas of the tree islands caused by the activity of birds and other animals. Frederick and Powell [1994] estimated the input of Phosphorus from a current colony of wading birds in the Everglades as 0.9 g/m^2/yr (0.25×10^{-5} kg/m^2/day). However, in historical colony sites this could have been as high as 120 g/m^2/yr (33×10^{-5} kg/m^2/day). Oliver and Legovic [1988] accepted in their model for Okefenokee Marshland, Georgia, an input of Phosphorus by wading birds of 4.6 g P/m^2/year (1.3×10^{-5} kg/m^2/day).

In this model, a constant input rate from external sources (e.g., animal activity and other sources) through the year is assumed. This rate is a fitting parameter in the model with the expectation to obtain parameters in the range reported in the literature in the areas with trees and bushes corresponding to HH, BH and BS vegetation types. As the Phosphorus is extracted from the marsh, it is expected also to obtain a negative Phosphorus input rate in marsh areas inside the model domain.

3.7.2 Phosphorus Uptake by Vegetation

The Phosphorus uptake is divided into passive and active uptake. Passive uptake is a consequence of the water transpired at the concentration in pore water. However, the passive uptake of phosphate ions is curtailed by the slow movements of these ions on the root surfaces [Brady and Weil, 2007]. The active uptake is related to active processes in the roots that capture Phosphorus from pore water, so that the Phosphorus mass uptake per water volume transpired may be higher than pore water concentration when the Phosphorus is limited. In the case of phosphate ions, they move to plant roots through

symbiosis with mycorrhizal fungi [Brady and Weil, 2007].

Thus, passive uptake rate could be easily estimated from the transpiration rate and the concentration of Phosphorus in pore water. In the MODHMS setup, the passive uptake (with no impediments for the movements of the ions on root surface) could be considered by setting ETFRAC=1 in the EVT input file. The total uptake rate, however, is linked to the net primary production rate of the plant and to the content of Phosphorus in the biomass, as stated in equation (63) of Wu's model. If vegetation is in equilibrium, the annual net primary production is equal to the annual litter production.

Vegetation type	Leaf litter production rate ($kg/m^2/y$)	Leaf P mass fraction (10^{-3})	P uptake rate ($kg/m^2/y$)	Leaf litter anaerobic decomposition rate (10^{-3} d^{-1})
HH	0.769	0.130	1.000	1.07
BH	0.586	0.063	0.369	
BS	0.152	0.038	0.058	
TS	1.800	0.029	0.522	1.7
MA	0.500	0.027	0.135	

Table 17. Parameters related to Phosphorus fluxes between biomass and soil cells in the model.

In the model the Phosphorus uptake is computed (assuming that the vegetation is in equilibrium) from the leaf litter production rate from Table 11 and the leaf P mass fraction in Table 14. The uptake rates obtained for each vegetation type area are presented in Table 17. Those rates are not the total P uptake by vegetation in reality. Consequently, it is being assumed that the Phosphorus uptake allocated in woody biomass and in roots is in equilibrium with the release by the corresponding litter decomposition.

3.7.3 Phosphorus Release by Decomposing Litter

In general, the produced litter is decomposed, contributing to increase the dissolved Phosphorus and Phosphorus in organic soil (peat). In this work however, it is assumed that the litter can be decomposed completely, releasing all the Phosphorus into the solution. Moreover, it is assumed that the Phosphorus content in litter per unit of dry mass remain constant during the whole decomposition process. All those assumptions justify the use of equation (66) from Wu's model to find the Phosphorus release rate. In this model, the litter decomposition rate in aerobic conditions is assumed three times the

anaerobic rate (shown in Table 17), which introduces a spatial variability on the decomposition process and also a seasonal dependence.

3.8 Base Case Models

The numerical model for each Tree Island needs to define a horizontal grid. An optimum numerical grid would consider the highest spacing (to reduce the computational time) that captures the spatial variations (to keep the discretization error low enough). MODHMS is able to consider a non-uniform grid spacing that can be used to have higher cell width in the marsh areas far from the islands, where the spatial variations are lower. Thus, non-uniform horizontal grids were defined for each Tree Island following the procedure described in Appendix A8.3.1.

The default parameters specified in previous sections were used to create the base case MODHMS model for each Tree Island. ViewHMS is the preprocessor that helps to create the input files for MODHMS. The parameters introduced in ViewHMS for the base case are tabulated in Appendix A3.8.2.

The preprocessor ViewHMS were used in the first tests to create the input files. However, in later tests the MODHMS input files were created manually or by using MatLab functions created for that purpose. The variables necessary for the different packages or input files are detailed in Appendix A3.8.3. Also their values for the base case (called default values) are given.

3.9 Assumptions and Limitations

The parameterization of the model developed in this work is limited by the information available in the literature. Thus, it introduces the following assumptions and limitations in addition to the ones made previously in the conceptual model and in the numerical model implementation.

1) The soil surface and bedrock maps may have errors associated to the interpolation and extrapolation procedure in areas far from the transect points. In particular, uncertainties in the topography may produce differences in the OL flow pattern.

2) The vegetation type map has errors due the way the map was created. Moreover, it cannot be exact because the vegetation is dynamic and it may change

from one year to another. In addition, the classification in 5 vegetation types neglects the variability inside the classes. All these uncertainties affect the parameters related to the vegetation types like the vegetation resistance, which may also produce differences in the OL flow pattern.

3) Assuming that the no-flow bottom of the rock layer is the bottom of the Water Table Aquifer neglects the interaction with deeper GW zones.

4) Considering smooth bottom and top rock layer boundaries, and uniform hydrodynamic properties (like porosity and conductivity) may be inappropriate due to the presence of openings in the rock layer created by slow carbonate rock dissolution.

5) Seasonal dependence of the Phosphorus uptake, litter production rate, and Phosphorus input from external sources (e.g., animal activity and other sources) is neglected in the model.

6) The above-ground litter is considered as leaf litter. The other components of the above-ground litter (woody and reproductive) have the same treatment as the root litter, i.e., it is assumed that Phosphorus uptake allocated in those fractions is in equilibrium to with the Phosphorus release.

The default values assumed for some of the parameters in the model are improved during the calibration process conducted in next section.

Chapter 4. Model Calibration

In this chapter, three different calibration steps are documented, in the following order.

1) The overland flow resistance parameters (Manning coefficient) were adjusted in order to fit the surface water velocities measurements by Bazante et al. [2004].

2) The groundwater flow parameter (conductivities, porosities, etc.) were adjusted in order to fit the water table data measured by Ross et al. [2004] in tree island wells.

3) The initial dissolved Phosphorus concentration and the external Phosphorus input were adjusted to fit the averaged Phosphorus concentration in soil measured by Ross et al. [2006].

4.1 Surface Water Parameters Calibration

In this section, the overland flow resistance parameters (Manning coefficient) were adjusted in order to fit the surface water velocities measurements by Bazante et al. [2004].

4.1.1 Available Data

The existing surface water velocities around the tree islands were measured by using Acoustical Doppler Velocity meters (ADV) [Bazante et al., 2004, 2006]. The velocities were continuously recorded during several months in stations located next to the tree islands and also along transects at specific times. In the case of Gumbo Limbo Tree Island, water stage measurements were also taken continuously using a pressure water level data logger. The station and transect locations are shown in Figure 43. The coordinates of the stations are presented in Table 18. The transects labeled as SL2, GL1, GL2 and GL3 are part of the original transects established by Ross et al. [2004] (see Figure 9). Unfortunately, the points of the transect GL3 are out of the area considered in the model. Bazante et al. [2004, 2006] defined the new transect GL0 passing immediately upstream of GL and some of those points are included in the modeled area (see Figure 43).

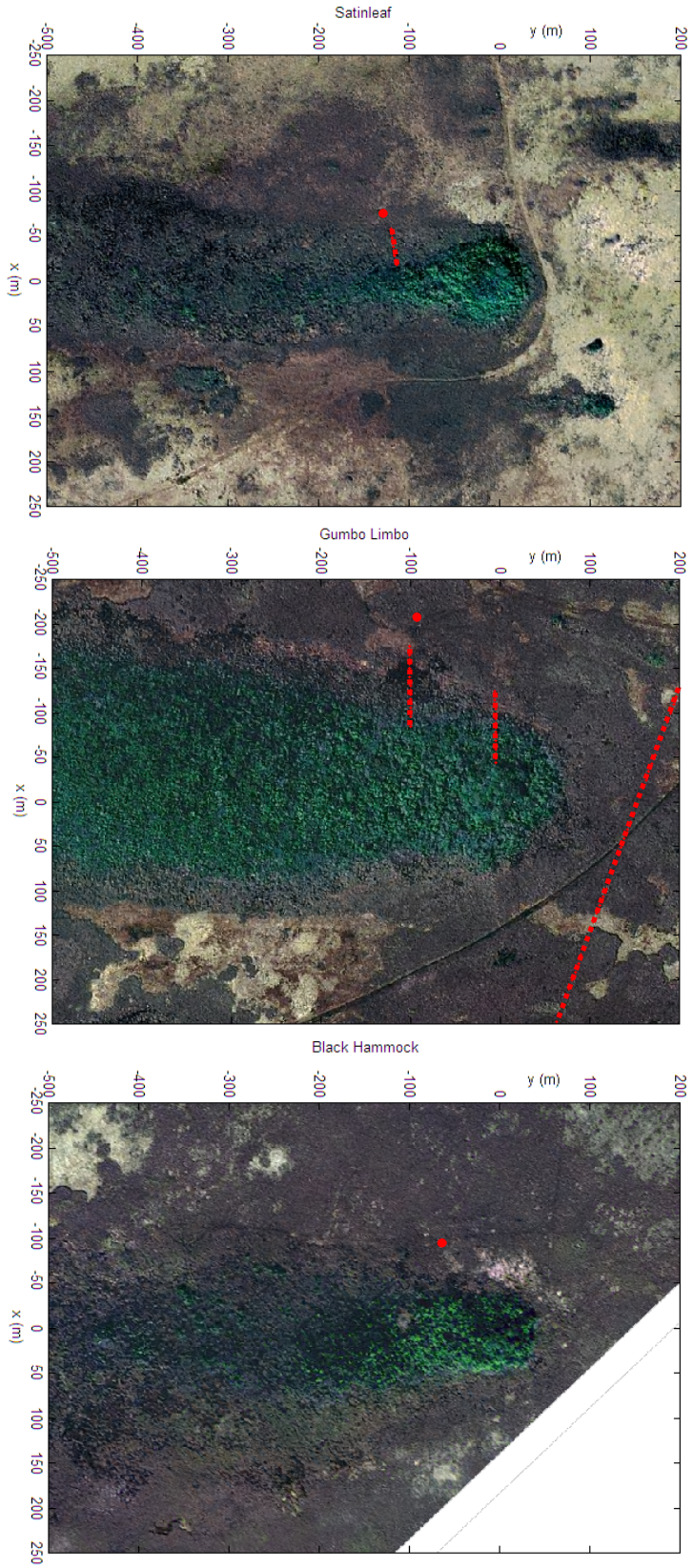

Figure 43. Station and transect locations where Bazante et al. conducted velocity measurements. Stations are marked with red disks and transect points with dashed red lines.

	UTM (WGS84).		Model coordinates		Corresponding model cell	
Tree island	Easting (m)	Northing (m)	x (m)	y (m)	x (m)	y (m)
SL	524380.33	2837949.05	-75.3	-128.6	-80, -70	-130, -125
GL	525801.62	2834791.97	-206.5	-93.3	-200, -190	-95, -90
BH	531175.82	2832651.44	-95.0	-63.8	-100, -90	-65, -60

Table 18. Coordinates of the stations for the surface water velocity measurements and corresponding cell in the model.

	MA	TS	BS	BH	HH
GL0	20	0	0	0	0
GL1	3	3	0	7	4
GL2	5	11	0	9	0
GL3	0	0	0	0	0
SL2	1	5	2	0	0
Stations	3	0	0	0	0

Table 19. Number of points used by Bazante et al. and located inside the model area, according to the vegetation coverage assumed in the model.

The transect points located inside the model correspond to cells with different vegetation coverage, as shown in Table 19, while the three station locations correspond to cells covered by marsh (MA).

Some preprocessing was conducted on the raw field data delivered by Bazante and co-workers [2004]. The stage measurements at GL station were usually taken every 15 minutes and were converted to daily values by finding the median value. Then they are transformed to water depth by assuming a soil surface elevation of 1.06 m in NAVD 88 at that location. All velocity measurements (in stations and transects) were transformed to absolute horizontal velocity by using only the x and y velocity components. The z velocity component is omitted because its contribution to the horizontal velocity is small and the ADV measurements of that component are usually affected due to particle settling [Bazante et al., 2004]. In the case of velocity measurements from stations (taken usually every 15 minutes), possible outliers were discarded by imposing standard deviations less than 1 cm/s and signal strength between 40 and 70 counts [J. Bazante, personal communication, 2006]. After that, daily velocity values are obtained from the median of the remaining values. In addition, other periods of data were omitted due to the presence of Utricularia tangled on probe [Bazante et al., 2004].

4.1.2 Model Setup

In order to cover the period for all transect and continuous measurements, the MODHMS models was set up by using daily data from August 1st, 2002 to July 1st, 2004. The daily values of rainfall rates, stage and slopes were previously presented in Figure 14, Figure 25 and Figure 26, respectively. They are reproduced here for the time period covered in Figure 44 and Figure 45. As previously, the numerical model aligns the tree islands along the NS transect defined by Ross et al. [2004] and the slopes need to be rotated by using the angles in Table A-8. The rotated slopes for the simulation period are also shown in Figure 46.

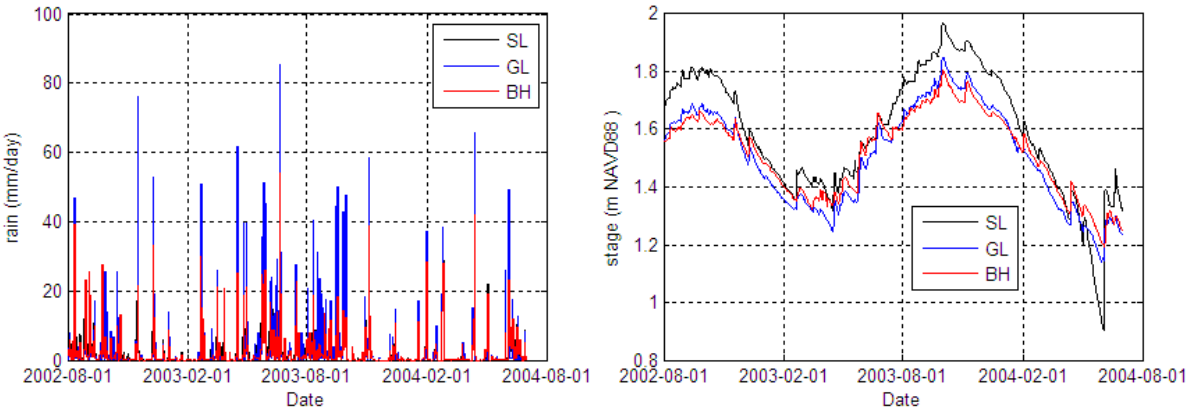

Figure 44. Interpolated daily rainfall depth rates and mean stages in the tree islands of Shark River Slough in the period where surface water velocity measurements are tested.

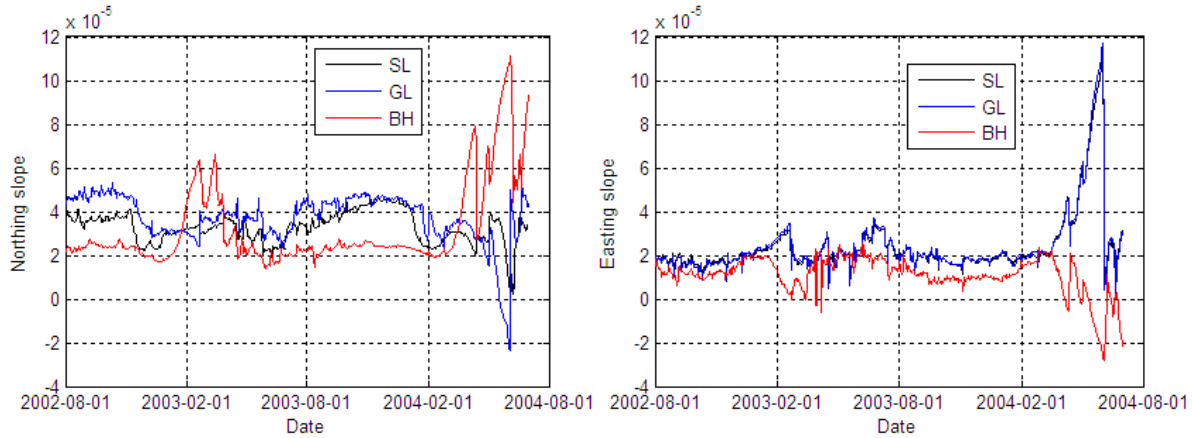

Figure 45. Slopes obtained from interpolated stages in the tree islands of Shark River Slough in the period where surface water velocity measurements are tested.

In the case of the daily ET rates, there were no sets of field measurements that extended over the whole time period considered (see Figure 18). Thus, daily averaged ET

rates were assumed, where field data was not available, as shown in Figure 47. Averaged values have less noise, but it follows the average seasonal trend as can be seen on the first period in that figure. On the other hand, a minor effect of the ET rates on the overland velocities is expected.

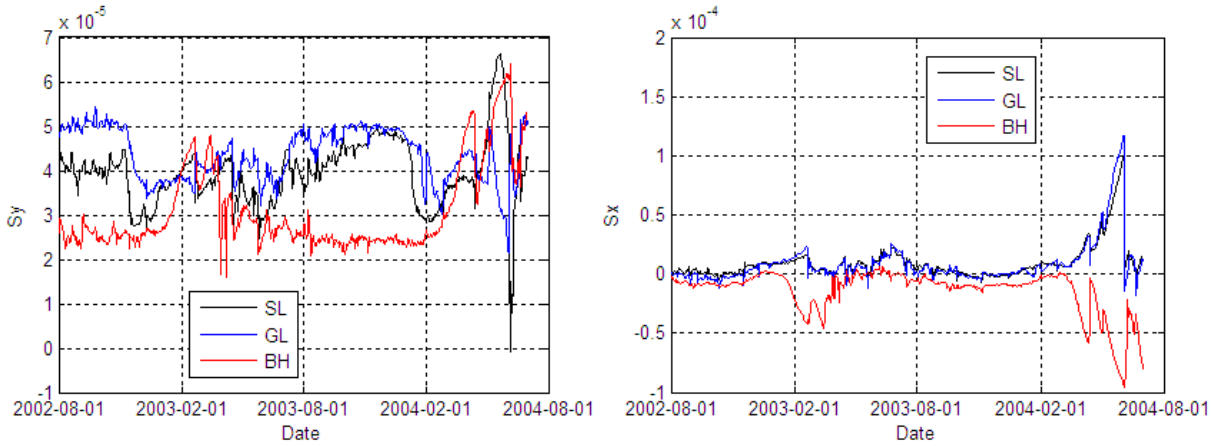

Figure 46. Slopes from Figure 45 now in the rotated coordinate system of each tree island.

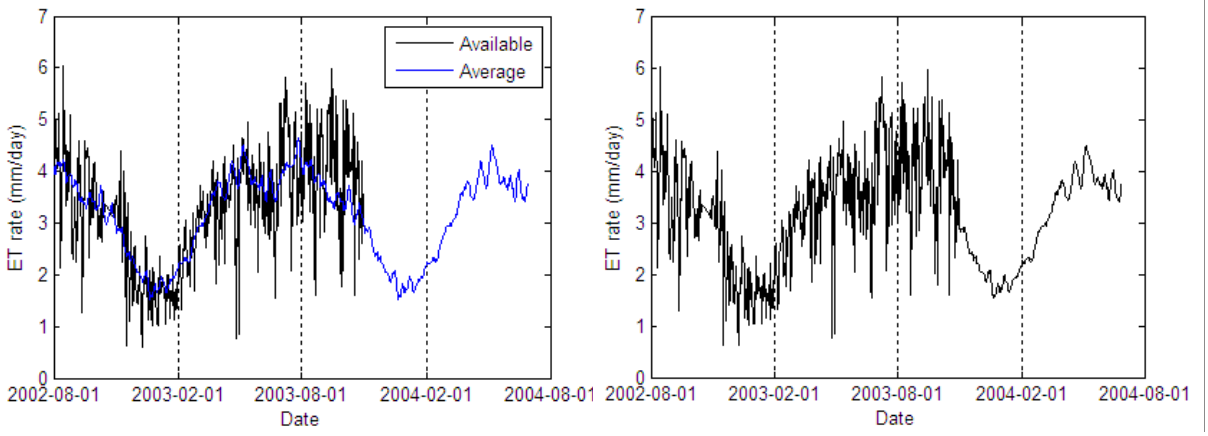

Figure 47. ET daily rates. In the first graph, the available measured and the averaged rates. In the second graph, the composite curve assumed by substituting the missing measured rates with the averaged ones.

All other parameters of the model were assumed according to the base case described previously.

4.1.3 Results for the Base Case

Model results by using the Manning coefficients for the base case are compared to the continuous measurements from stations in Figure 48. The water depth in GL tree island is reproduced pretty well by the model except in the driest days (end of May,

2004). This match between the water depth measured by Bazante et al. and the one obtained from the model is a validation for the water elevation interpolated from neighbor stations.

The velocity values predicted by the model are presented in Figure 48 and they are smoother than the values recorded by Bazante et al. [2004]. One possible reason is that the slope obtained by interpolation from neighboring stage stations contains some spatial averaging. Another probable cause is that there is a temporal averaging when using daily averaged values of slope and rainfall rates.

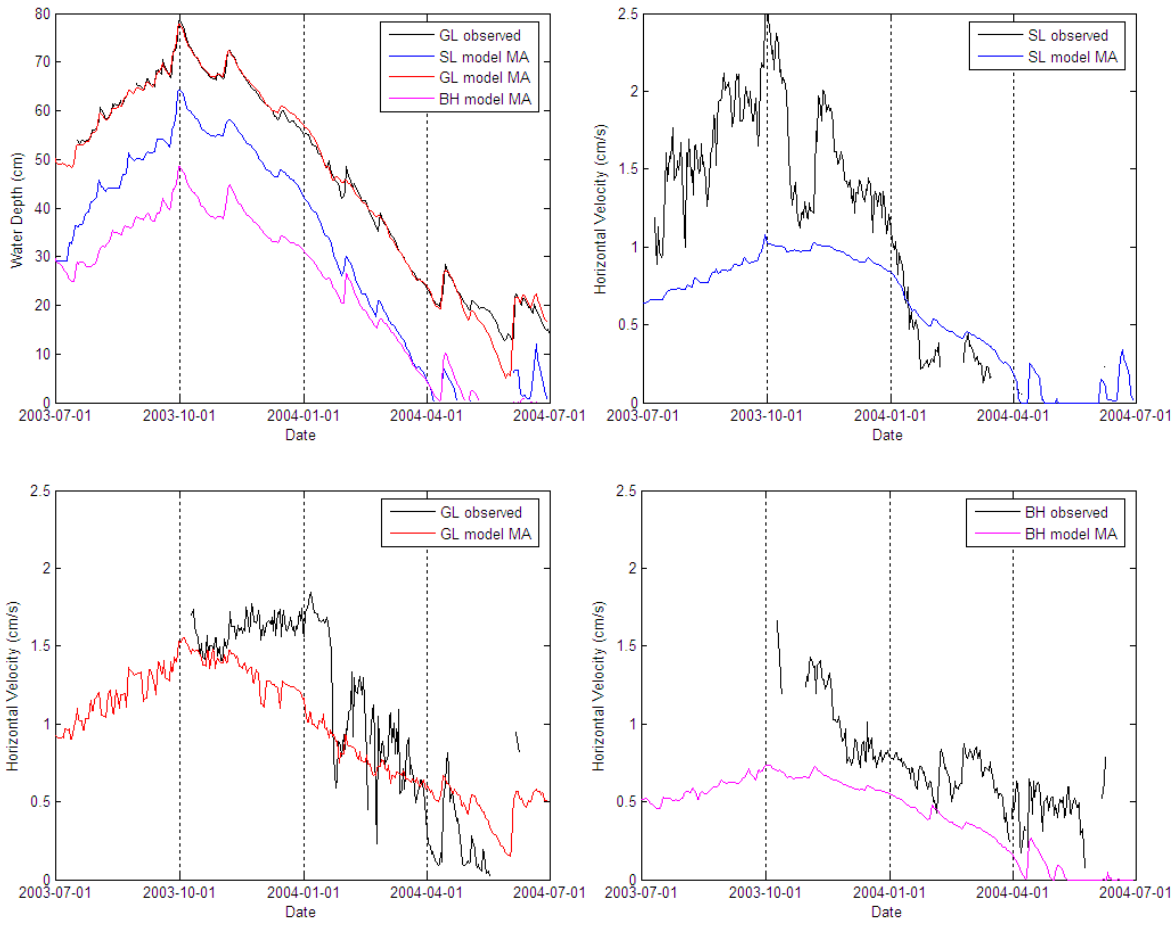

Figure 48. Model results of water depth and overland horizontal velocity (speed) for the base case compared to the continuous measurements from stations. The estimated Manning coefficient is also included in s $m^{-1/3}$.

On the other hand, the model underpredicts in general the velocity values for the periods with higher water depth, particularly for SL. This can be confirmed by considering the median value of the differences between model and field velocities,

which is presented in Table 20. This suggests that the model deviation in SL may be a consequence of uncertainties in slope estimation, because GL and BH are very close to stations NP-203 and P33, respectively, while SL is not so close to any stage station (see Figure A-34).

Another potential explanation for the differences in SL is the effect of the observation tower trail on the surface water slopes of the area. The simulation of the water flow in the area reported by Stothoff [2004], for example, assumed that the trail has a higher elevation than the surrounding marsh. However, the trail has pipes that communicate the surface water on both sides and there is also a canal running in the north-south direction [J. Bazante, personal communication, 2006]. In the Eden project, water stages similar to those in this work were obtained by neglecting the trail effect and conducting the interpolation between station stages. [L. Pearlstine, personal communication, 2006].

It should also be mentioned that the measured speed at a point (microscopic speed) is different in general from the averaged speed in the model, which is averaged vertically and also horizontally in the cell dimensions. Local vegetation distribution and distance from the bottom affect the microscopic speed.

The detailed results for the base case at transect points are shown in Figure A-44. The differences between observation and model results are summarized in Figure 49. In general, water depth is predicted with no systematic deviations with an error range of 10 cm, which is reasonable considering the fluctuations in the soil surface elevation covered by vegetation around three islands. The absolute velocity values, however, are clearly overpredicted by the model for the vegetation types around the head (BS, BH and HH). This is also concluded from the median value of the differences between model and field velocities, presented in Table 20, as well as from the median value of the absolute differences in Table 21. This overprediction in the velocity values means that the assumed values of Manning coefficient are too low for cells with those vegetation types. In other words, it is concluded that the Manning coefficients assumed in the base case must be adjusted for all vegetation type areas.

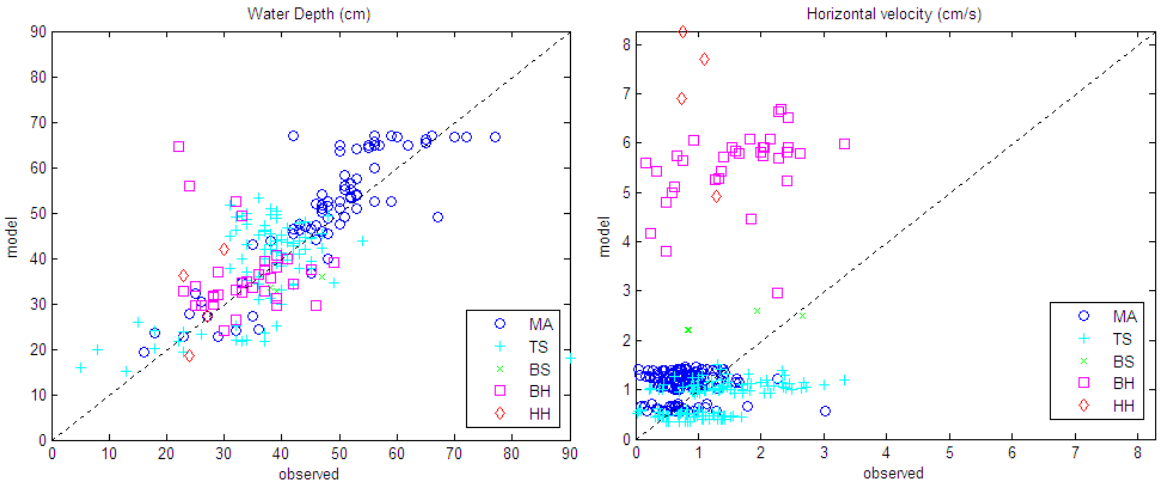

Figure 49. Comparison between all the measurements and their corresponding model results for the base case, according to the vegetation type assumed.

The procedure sketched in Figure 50 was implemented in order to find the Manning coefficient required to fit the velocities observed in the field. First the Manning coefficient assumed are used by the model to give values of surface slope, water depth and speed at each cell. Then the model slope is substituted in Manning equation (20), together with the observed values of depth and speed in order to estimate the Manning coefficient that would match the field observations. In the cases where observed values of water depth are not available, water depth values from the model are used. After that, the estimated Manning coefficients are compared to the assumed ones as shown in Figure A-43 and Figure A-45. Notice that the axis in those figures for Manning coefficients goes up to 1, even when the predicted values are higher in a few cases. Finally, the median values of the estimated coefficients for each vegetation type (also shown in those figures and in Table 22) are compared to the assumed ones, in order to propose new values in the next iteration.

From the continuous measurements, the regional slope used for SL model may have errors, so in Figure A-46 some of the plots of Figure A-45 are reproduced, but only considering GL transect points.

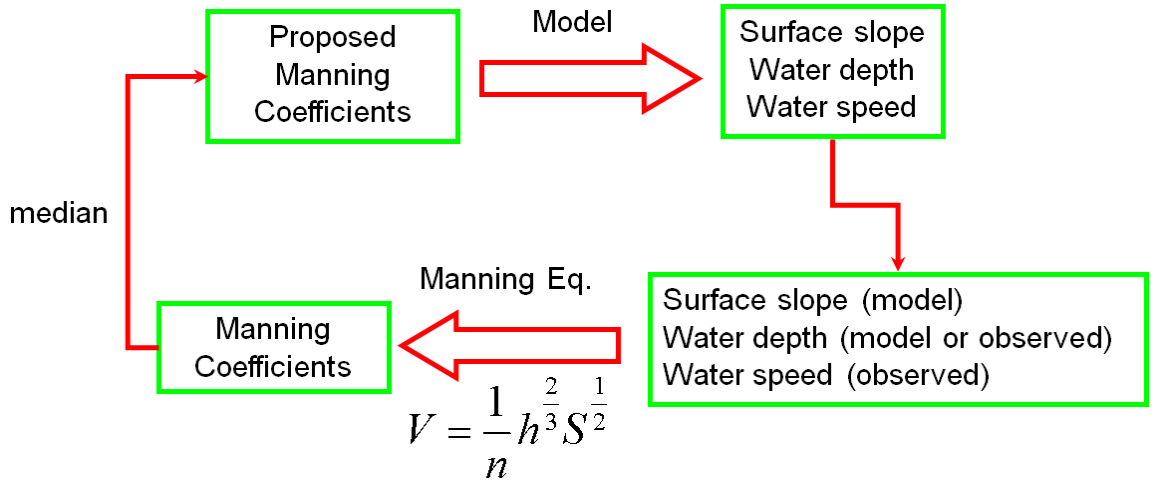

Figure 50. Procedure for fitting Manning coefficient in each vegetation type area.

4.1.4 Results Adjusting the Manning Coefficients

Table 22 suggests that Manning coefficients for vegetation types BS, BH and HH are in the range from 0.16 to 0.21. Thus, a case (M1) with a Manning coefficient value of 0.2 for those vegetation types was defined, the OLF input files were modified and the MODHMS models were run again. Summarized results for case M1 and further cases are presented in Table 20, Table 21 and Table 22.

In case M1, the models predict the velocity better for the vegetation types BS, BH and HH. However, the median values of the estimated Manning coefficients for transects in Table 22 suggest that the assumed values for MA and HH are higher, and the value for TS lower. Notice that the BS and HH types have only 4 points each and the estimated coefficients have more uncertainty than in other types with more data points. On the other hand, the median values of the estimated Manning coefficients for stations in Table 22 suggest that the assumed value for MA is lower.

As the vegetation resistance in the marsh areas is visibly heterogeneous, it appears that in the process of finding the best averaged Manning coefficient for that vegetation coverage, the differences between the model-predicted velocity and the field measurements in 29 different transect points located in the marsh (see Table 19) should receive more weight regarding the differences on the three station points. Thus, even when there are a greater number of measurements on the stations than in transect points (about 6 to 1 according to Table 20), a total deviation (last column in Table 20 and Table

21) and an overall Manning coefficient for the marsh (last column in Table 22) are defined by assuming the same weight for all the transect as for all the station deviations.

	VT	MA	TS	BS	BH	HH		TI	SL	GL	BH	MA
Transect values	All	136	125	4	34	4		Station values	240	225	214	
	GL	126	82	0					0			
Base Case	All	0.38	**-0.33**	**1.01**	**4.03**	**6.39**		Base case	-0.49	-0.13	-0.32	**0.03**
	GL	0.39	-0.21	---					---			0.08
Case M1	All	0.28	**-0.39**	**-0.23**	**0.12**	**0.76**		Case M1	-0.45	-0.23	-0.29	**-0.02**
	GL	0.31	-0.36	---					---			0.03
Case M2	All	0.30	**-0.11**	**-0.16**	**0.12**	**0.53**		Case M2	-0.44	-0.23	-0.29	**-0.01**
	GL	0.32	-0.04	---					---			0.03
Case M3	All	0.28	**0.06**	**-0.28**	**0.04**	**0.34**		Case M3	-0.46	-0.26	-0.29	**-0.03**
	GL	0.30	0.11	---					---			0.01
Case M4	All	0.29	**-0.05**	**-0.16**	**0.22**	**0.28**		Case M4	-0.47	-0.26	-0.29	**-0.03**
	GL	0.31	0.03	---					---			0.02

Table 20. Median values of the difference between model and field velocities in cm/s. Transect points are divided according to vegetation type (VT) and also in two cases: all the transects and only GL transects. Station points are divided according to the tree island (TI).

	VT	MA	TS	BS	BH	HH		TI	SL	GL	BH	MA
Transect values	All	136	125	4	34	4		Station values	240	225	214	
	GL	126	82	0					0			
Base Case	All	0.41	**0.47**	**1.01**	**4.03**	**6.39**		Base case	0.49	0.30	0.32	**0.40**
	GL	0.44	0.35	---					---			0.38
Case M1	All	0.34	**0.44**	**0.49**	**0.44**	**0.76**		Case M1	0.45	0.33	0.29	**0.35**
	GL	0.36	0.46	---					---			0.34
Case M2	All	0.35	**0.33**	**0.50**	**0.46**	**0.53**		Case M2	0.44	0.33	0.29	**0.35**
	GL	0.36	0.40	---					---			0.34
Case M3	All	0.33	**0.35**	**0.51**	**0.52**	**0.44**		Case M3	0.46	0.35	0.29	**0.35**
	GL	0.35	0.42	---					---			0.34
Case M4	All	0.33	**0.32**	**0.50**	**0.46**	**0.38**		Case M4	0.47	0.34	0.29	**0.35**
	GL	0.34	0.39	---					---			0.33

Table 21. Similar to Table 20 but showing the median values of the absolute difference between model and field velocities in cm/s.

	VT	MA	TS	BS	BH	HH		TI	SL	GL	BH	MA
Transect values	All	136	125	4	34	4		Station values	239	225	214	
	GL	126	82	0					0			
Base Case	P	**0.43**	**0.48**	**0.08**	**0.05**	**0.03**		P	**0.43**			
	All	0.63	0.32	0.16	0.16	0.21		E	0.27	0.38	0.24	0.46
	GL	0.65	0.37	---					---			0.48
Case M1	P	**0.43**	**0.48**	**0.20**	**0.20**	**0.20**		P	**0.43**			
	All	0.55	0.30	0.21	0.21	0.31		E	0.28	0.35	0.27	0.43
	GL	0.60	0.30	---					---			0.46
Case M2	P	**0.43**	**0.35**	**0.20**	**0.20**	**0.25**		P	**0.43**			
	All	0.57	0.29	0.23	0.21	0.33		E	0.29	0.36	0.27	0.44
	GL	0.60	0.30	---					---			0.46
Case M3	P	**0.44**	**0.30**	**0.23**	**0.21**	**0.30**		P	**0.44**			
	All	0.59	0.30	0.24	0.21	0.34		E	0.29	0.36	0.27	0.45
	GL	0.61	0.30	---					---			0.46
Case M4	P	**0.44**	**0.33**	**0.20**	**0.19**	**0.33**		P	**0.44**			
	All	0.58	0.29	0.23	0.21	0.36		E	0.29	0.36	0.27	0.44
	GL	0.60	0.30	---					---			0.46

Table 22. Manning coefficient proposed (P) and the median value estimated (E) from the model in s $m^{-1/3}$. Transect points are divided according to vegetation type (VT) and also in two cases: all the transects and only GL transects. Station points are divided according to the tree island (TI).

From the results for case M1, a case M2 is defined by changing the Manning coefficients for TS and HH to 0.35 and 0.25, respectively. After that, the median velocity differences in Table 20 for the new case M2 produced a lower result relative to the previous cases. However, according to the predicted coefficients in Table 22, one could still try to change them slightly, and a case M3 was thus defined.

The median velocity differences for case M3, shown in Table 20, are lower relative to the previous cases. Therefore, Manning coefficients in case M3 produce the best fitting so far. However, the median of the absolute velocity differences in Table 21 does not have a minimum in case M3. Therefore, another case M4 was defined, to try to find lower median values in Table 21. The process of trying to minimize the velocity deviations is stopped after that and the Manning coefficients for case M4 are considered as the ones that best fit the velocity data of Bazante et al. [2004]. More detailed results for case M4 are shown in Figure 51 and Figure 52, as well as in figures on Appendix A4.1.2. The water depth in case M4 does not change appreciably relative to the base case results, and those graphs were not repeated in Figure 51 for this case.

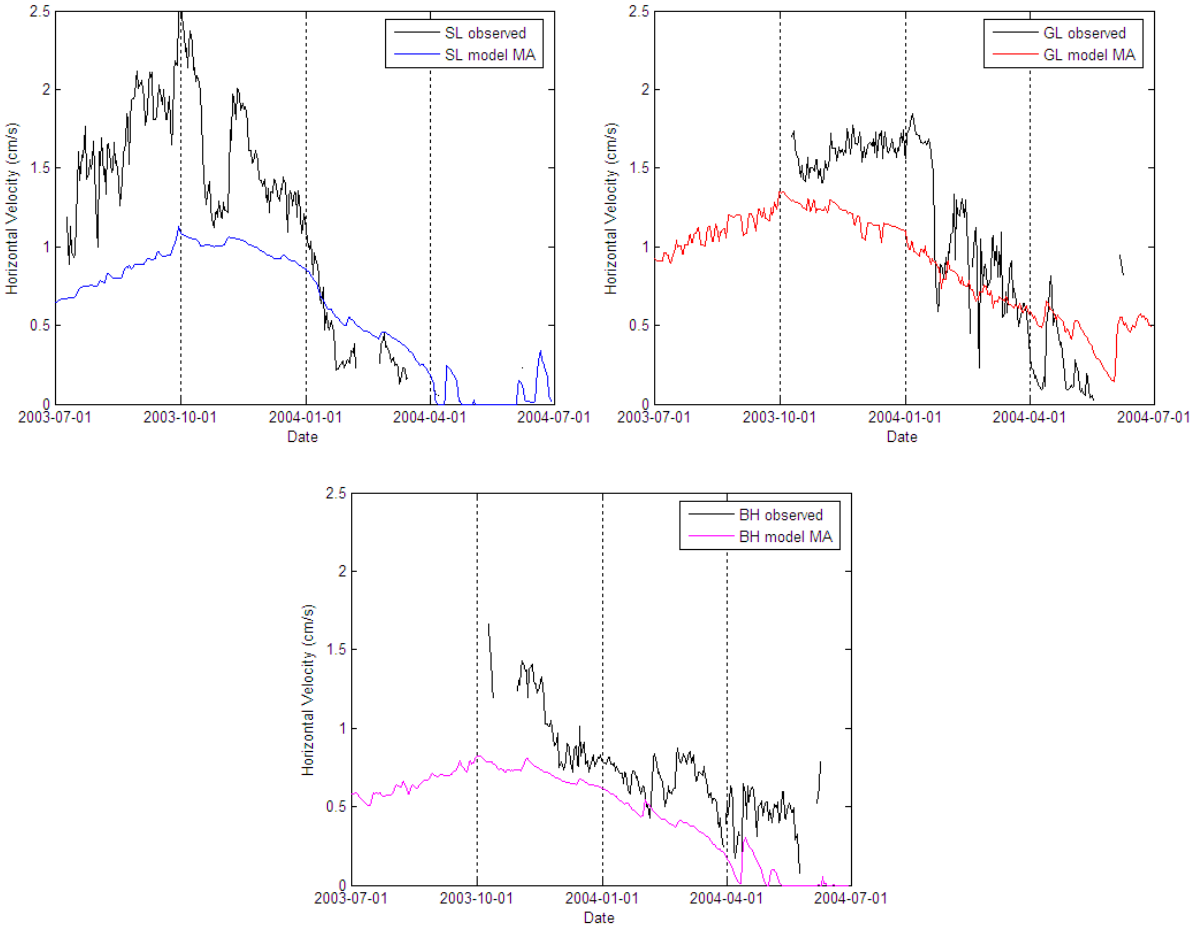

Figure 51. Model results of overland horizontal velocity for the case M4 compared to the continuous measurements from stations. They are comparable to the base case results presented in Figure 48.

In summary, a set of Manning coefficients (case M4 in Table 22) has been obtained that best reproduces the overland velocity data measured by Bazante et al. [2004]. For vegetation types BS and HH, there were only four measurements and the fitted coefficients have a larger uncertainty. In the case of the marsh, a trade off was needed in such a way that the accepted Manning coefficient in general underpredicts the velocity measurements from stations (see Figure 51) and overpredicts the measurements at transect points (see Figure A-49 and Figure A-50).

It should be mentioned that the good matching between the field and model velocities is striking because those velocities represent different scales [J. Bazante and H. Solo-Gabriele, personal communication, 2006]. The ADV measures the average velocity in a sphere of a few centimeters diameter, so that it changes with the relative position of

the submerged stems and leaves and with the height where the sensor is located relative to the bottom. The model velocities, however, are vertical averaged values, which are also averaged over the horizontal area of the model cell. Recall that the smallest cell of the model is 5m x 5m and the biggest 20 m x 20 m. Thus, it is reasonable that the model reproduces velocities only in an averaged sense and it is not able to replicate the all the spatial variability of the measured velocities at transect point locations as shown in Figure 52.

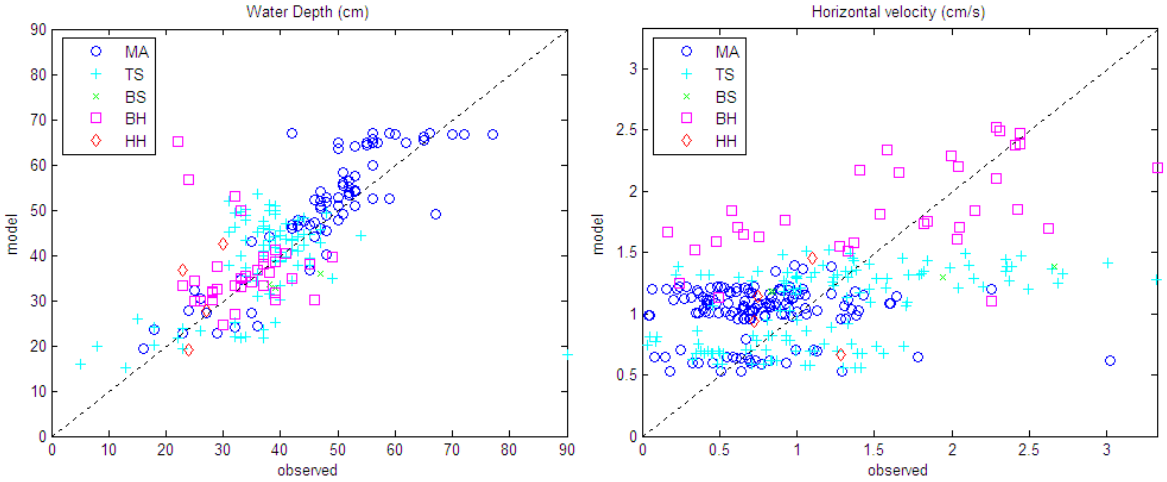

Figure 52. Comparison between all the measurements and their corresponding model results for the case M4, according to the vegetation type assumed. They are comparable to the base case results in Figure 49.

In Appendix A4.1.3, sensitivity tests on case M4 were conducted by changing the stage stations used to obtain the regional slope at SL. As result, there are only small variations among the predicted values at the continuous station, which is an evidence of the robustness of the interpolation method and the accuracy of stage time series data used. Moreover, it supports the hypothesis that the observation tower trail has only a minor effect on the regional surface water slope of the area.

The Manning equation validity around the tree islands is discussed in Appendix A4.1.4. The field velocity data by Bazante et al. [2004] seem to follows a Manning type dependency on water depth at least in marsh areas. However, from the analysis of the flume data reported by Jenter [1996] in Appendix A3.4.1, a Forchheimer type dependence might be more appropriate for TS areas around the tree islands.

4.2 Ground-water Parameters Calibration

In this section, the groundwater flow parameter (conductivities, porosities, etc.) were adjusted in order to fit the water table data measured by Ross et al. [2004] in tree island wells.

4.2.1 Available Data

Measurements on the daily fluctuations of the water table level in several wells located at different sites of the tree islands were reported by Ross et al. [2004]. The locations of the wells were specified by P. Ruiz [personal communication, 2006] and the corresponding coordinates are presented in Table 23 and in Figure 53. Notice that in the case of Gumbo Limbo Tree Island, the BH well is the only one inside the modeled area.

Tree Island	Well name, vegetation type area	UTM (WGS84)		Model coordinates		Model cell index		Offset (cm)
		Easting (m)	Northing (m)	x (m)	y (m)	x	y	
SL	HH	524494	2838024	-0.2	-15.0	21	71	-0.5
	BH	524448	2837936	-7.9	-114.0	20	52	-1.1
	BS	524403	2837849	-15.1	-211.7	18	34	-3.3
	MA	524489	2837721	114.3	-295.6	37	22	-2.4
GL	BH	525996	2834708	5.2	-99.2	39	67	1.3
	BS	525758	2834125	0.5	-728.9	---	---	12.1
	MA	525421	2834226	-349.9	-760.1	---	---	8.5
BH	BH	531260	2832596	4.2	-46.0	24	76	-10.7
	BS	531034	2832364	0.2	-369.9	24	14	-9.2
	MA	530965	2832455	-112.5	-351.4	5	17	-10.0

Table 23. Location of the wells and their fitted offset for the measured water table elevation data (see text for details).

The water table elevation data at tree island wells obtained from D. Reed, at FIU are presented in Figure 54 and Figure A-59. The daily stage data interpolated from neighbor stations at the tree islands heads (presented previously in Figure 25) are also included in those graphs.

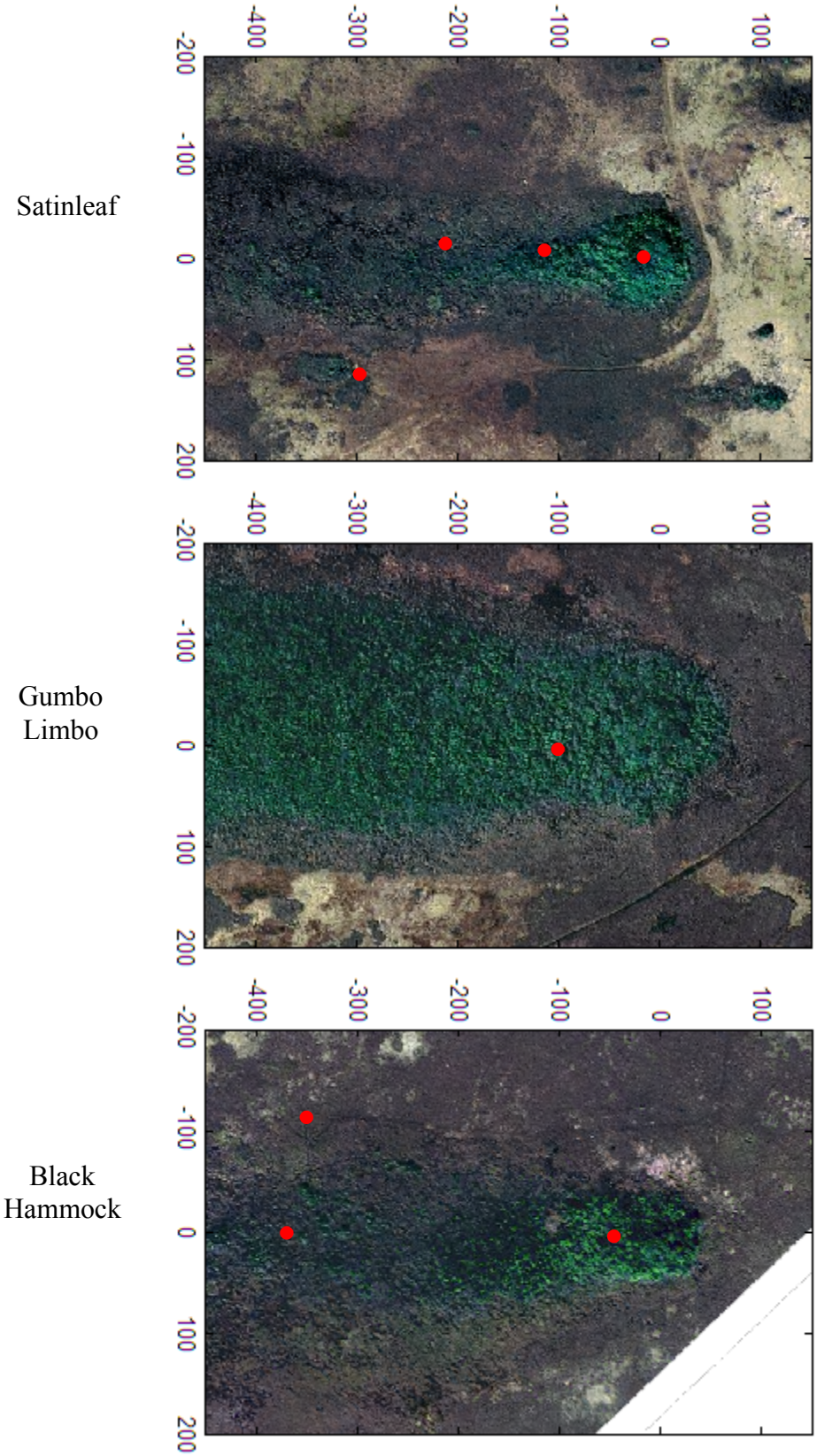

Figure 53. Position of the groundwater wells shown as red disks for Satinleaf, Gumbo Limbo and Black Hammock tree islands, from above to below.

Figure 54. Available water table elevation data at Satinleaf wells for year 2002, compared to the interpolated stage from neighbor stations.

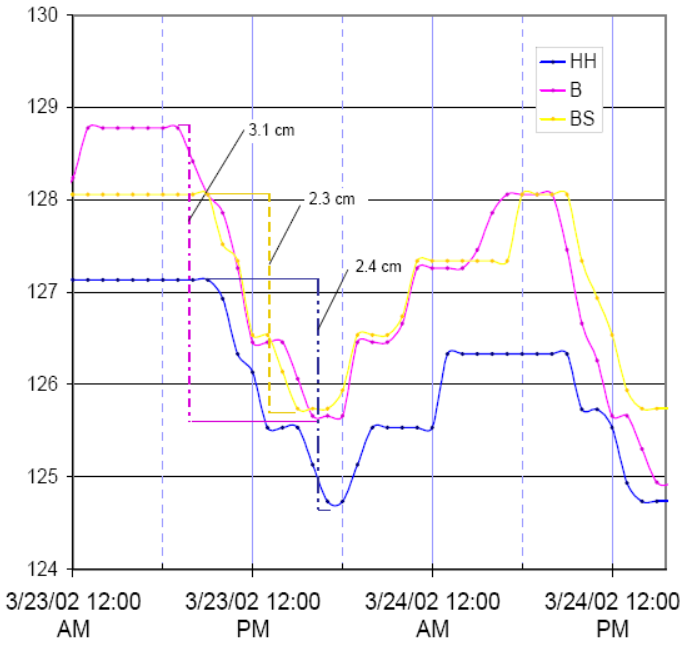

Figure 55. Water table oscillations in Satinleaf tree island, extracted from Ross et al. [2004].

On a daily scale, when there is no rainfall, the water table drops during the day and recovers during the night, as shown in the zoomed-in graph of Figure 55. The stepwise shape of the curves is a consequence of the setup used to measure the water depth by Ross et al. [2004]. The digital capture of the voltage signal from the piezoresistor in a number of channels gives discrete values of stage separated about 0.8 cm, which is the step size observed in Figure 55 [D. Reed, personal communication, 2006]. As the span (voltage range) cannot be reduced for long term measurements, the way to measure with better resolution would be to have an AD converter with a higher number of channels.

Notice also in Figure 55 that the absolute water elevation measured is shifted among different wells, which may be associated either with real water table differences or with errors in the measurement procedure.

Each well consisted of a two-inch screened PVC pipe, driven to the bedrock and capped at the base in order to prevent groundwater intrusion [Ross et. al., 2004]. In the dry season, the low hydraulic conductivity of the soil and the rock may cause the head differences among wells to remain over time. However, when there is water above the soil surface, the measured water table elevation in the well must be close to water elevation above the surface, which differs according to the water surface slope. Recall that the mean regional slope of 4e-5 in Table 7 means a vertical difference of about 0.4 cm every 100 m. Thus, it is expected that the measured water table elevation change as a function of the distance among wells at about that slope when they are inundated.

The differences caused by the water surface slope are small compared to the observed differences in Figure 54 and Figure A-59 during the wet season. Thus, there may be errors in the measurement procedure.

The water elevation is calculated from the voltage measured by adding the elevation of the piezoresistor (water elevation at zero voltage) and the voltage multiplied by a conversion factor. Errors in the piezoresistor elevation can be easily corrected by adding an offset to the water table levels at each well. Regarding the conversion factor, Ross et al. [2004] reported that the sensors were sensitive to water temperature (about 3 cm every 10 ^{o}C at 50 cm depth), but the corresponding correction was not made. Therefore, a correction to the piezoresistor signal was made in order to match the well

elevations with the stage elevations when the water levels are higher.

The procedure followed to correct the water table data is described in Appendix A4.2.2. The fitted offset values are in the range of ± 10 cm and they are presented in the last column in Table 23. No significant effect of the water temperature was found.

4.2.2 Model Setup

In order to reproduce the water table elevation data with the model, the measurements (taken commonly every 15 minutes) are reduced to hourly time series. Then, MODHMS input files were setup for each tree island by using hourly stress periods. Consequently, the heads from the model at the end of each stress period at the soil cells with wells are comparable to the water table elevation hourly data. The model coordinates of the cells with wells are specified in Table 23.

The period covered by the hourly measurements and the one considered in the model for each tree island are presented in Table 24. Notice that the simulation starts about 15 days before the first measurement in order to avoid effects of the assumed initial conditions.

TI	Measurements		Model	
	Start	End	start	End
SL	01/24/02 16:00	11/12/03 03:00	01/09/02 0:00	11/13/03 0:00
GL	04/16/03 13:00	11/06/03 23:00	04/01/03 0:00	11/07/03 0:00
BH	04/07/03 12:00	11/05/03 23:00	03/23/03 0:00	11/06/03 0:00

Table 24. Period covered by the water table measurements at wells and by the model. In the case of GL tree island only the BH well measurements are considered.

For those periods, the model considers daily averaged data for stages and slopes, (shown in Figure 25 and Figure 26). The northern and eastern slopes are rotated to the coordinate system of the model by using the angles in Table A-8. As discussed before, the daily averaged values of stage and slopes are slightly different from the hourly values (see Figure A-35, Figure A-36 and Figure A-37), which are interpolated from a lower number of neighbor stations.

In the case of the rainfall and ET rates, the model considers in next section the hourly rates presented in Figure 16 and Figure 17, respectively. There were no field ET measurements by the end of year 2003 and hourly averaged ET rates were assumed as shown in Figure A-60.

All other parameters of the model were assumed according to the base case described before, except for the Manning coefficients, which were fitted in the previous calibration procedure (case M4).

4.2.3 Results for the Best Fitted Manning Coefficients

The base case model with the modified Manning coefficients (previous case M4) was run for the time periods in Table 24 by using hourly stress periods (case K0 in Table 25). The obtained water table level and the soil water saturation for the wells inside the modeled area are shown in Figure A-62. The comparison between the heads from the model and the measured ones are also shown in Figure A-65, Figure A-66 and Figure A-67. A magnified view of those graphs for the driest months of the year (April and May) are presented from Figure 56 and Figure 57. In those figures, the head from field measurements are corrected by an offset, which is shown in the plot label. Moreover, the remaining difference between model and measured head is labeled as “head difference”.

The offset for each well data is obtained by imposing the condition that the median of the head differences is zero. Then, a head error for each well (labeled as error 1) is estimated as the median of the absolute differences regarding the median. Another estimation of the error is obtained as the square root of the mean of those squared differences (error 2). It is clear that the first median-based estimator is less sensitive to spikes in those differences than the second one. The number of points (head differences), the offset and the two estimators of the head error are shown for each well in Table 26. Moreover, an overall head error (E) is computed from the head error (E_k) and number of points (n_k) for each well k by using the formula

$$E = \sqrt{\frac{\sum n_k E_k^2}{\sum n_k}} . \qquad (30)$$

The values obtained for the overall head error 1 and error 2 are presented in Table 25.

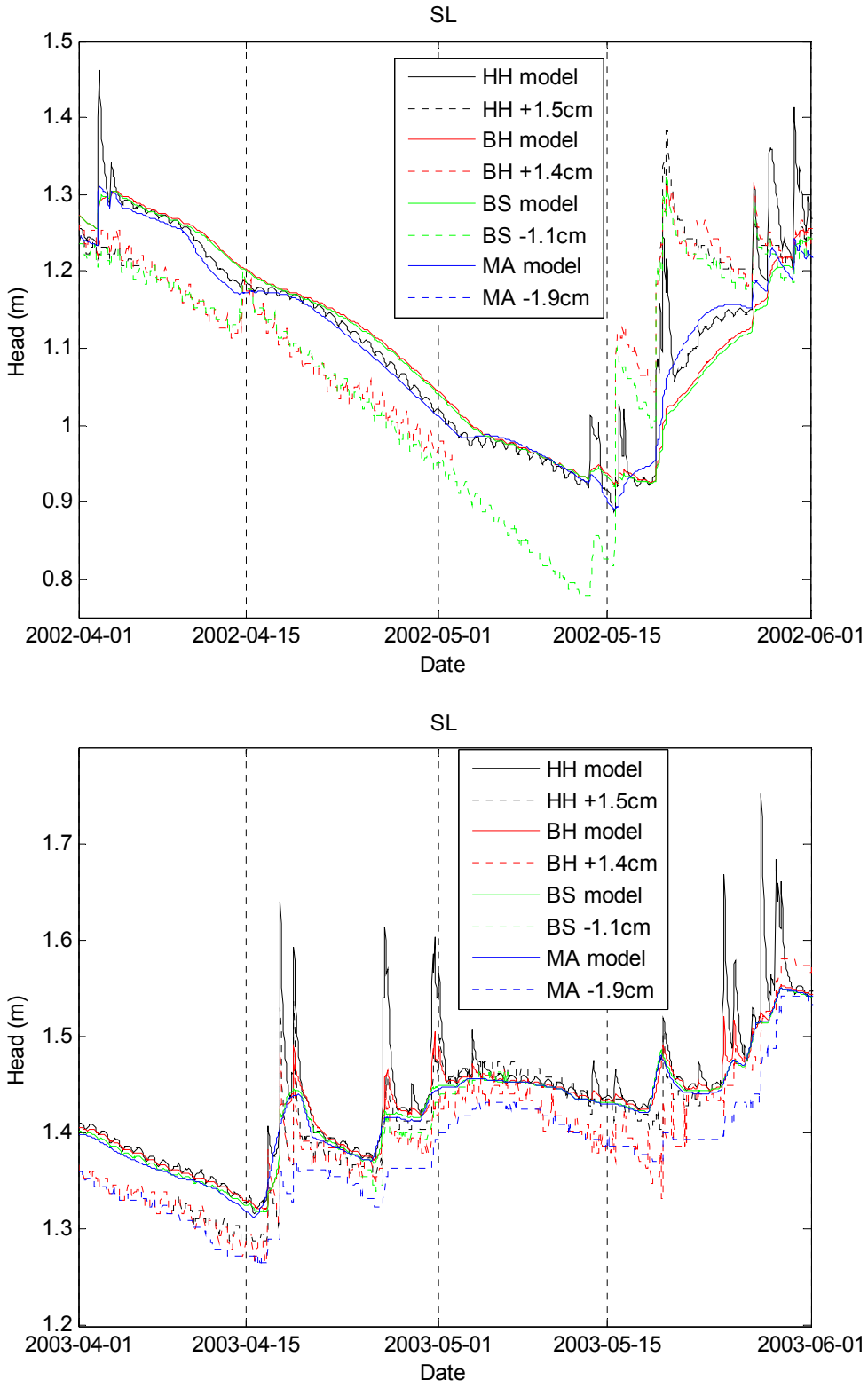

Figure 56. Comparison between the water table levels obtained from the model and from the field measurements in SL wells for the case K0 during the driest period of 2002 and 2003. These are magnified views of Figure A-65.

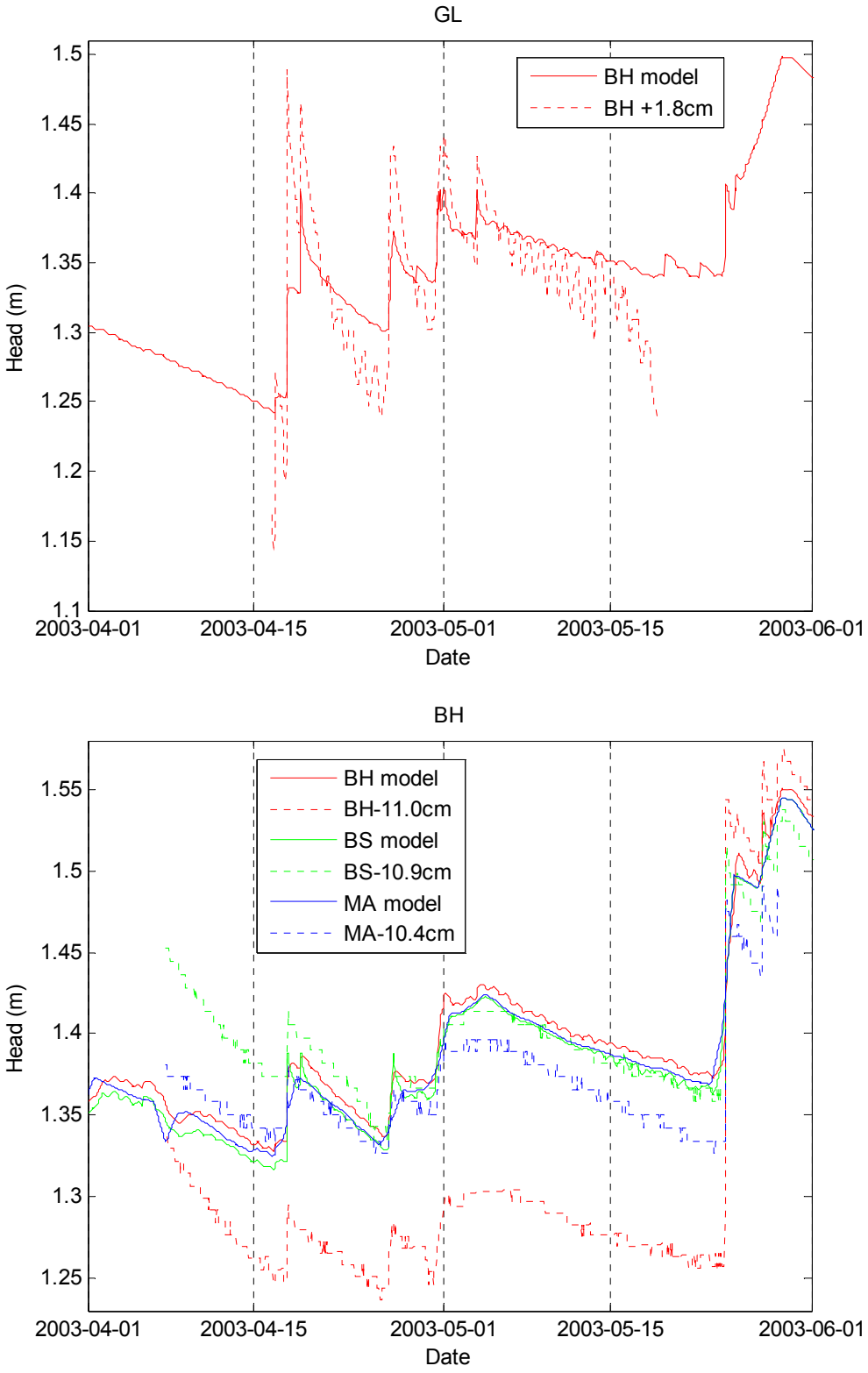

Figure 57. Comparison between the water table levels obtained from the model and from the field measurements in GL and BH wells for the case K0 during the driest period of 2003. These are magnified views of Figure A-66 and Figure A-67.

Case	stress period	f_L	Overall head error (cm)			
			error 1	error 2	error 3	error 4
K0	hourly	$\sim 10^4$	2.445	4.374	---	---
K1	two per 24 hours	$\sim 10^4$	2.480	4.445	0.521	1.677
K2	two per 24 hours	10	2.480	4.394	0.526	1.649

Table 25. Stress period and leakage coefficient corresponding to the first cases tested, trying to reproduce the water table elevation data from wells, and their corresponding overall error estimators.

Case	TI: / Well:	SL HH	SL BH	SL BS	SL MA	GL BH	BH BH	BH BS	BH MA
K0	Offset (cm):	1.50	1.42	-1.07	-1.89	1.78	-10.95	-10.90	-10.41
	Head error 1 (cm):	2.41	2.74	2.88	3.09	1.10	0.85	0.94	0.86
	Head error 2 (cm):	4.46	4.56	5.20	3.56	2.24	5.18	3.38	1.83
	Points:	8701	10804	10890	6759	3117	4980	1391	3231
K1	Offset (cm):	1.66	1.44	-1.07	-1.85	1.77	-10.96	-10.94	-10.41
	Head error 1 (cm):	2.49	2.82	2.91	3.08	1.10	0.79	0.85	0.86
	Head error 2 (cm):	4.67	4.63	5.26	3.59	2.26	5.21	3.26	1.78
	Points:	726	900	909	563	260	415	116	269
	Head error 3 (cm):	0.59	0.63	0.55	0.40	0.48	0.37	0.33	0.28
	Head error 4 (cm):	2.57	1.55	1.60	0.96	1.66	1.40	1.17	0.92
	Points:	716	891	900	562	256	413	115	265
K2	Offset (cm):	1.60	1.44	-1.08	-1.85	1.77	-10.97	-10.99	-10.41
	Head error 1 (cm):	2.50	2.83	2.90	3.08	1.10	0.77	0.92	0.86
	Head error 2 (cm):	4.59	4.59	5.19	3.59	2.24	5.14	3.29	1.78
	Points:	726	900	909	563	260	415	116	269
	Head error 3 (cm):	0.61	0.63	0.55	0.40	0.50	0.38	0.34	0.28
	Head error 4 (cm):	2.53	1.55	1.59	0.96	1.70	1.27	0.76	0.91
	Points:	716	891	900	562	256	413	115	265

Table 26. Result summary of the first cases tested to reproduce the water table elevation data.

It is clear that the model results for the case K0 show some discrepancies with the measured well data, which are detailed below.

1) The minimum water level measured at SL wells in the very dry period of 2002 (April and May) is not reproduced by the model (as shown in Figure A-65 and Figure 56). At that period the reported water table levels are different from the model prediction. Something similar occurs for the heads at the BH well in the BH tree island shown in Figure 57. The groundwater parameters (such as conductivity and porosity) can be adjusted to fit the measured water levels. However, it should be mentioned that the uncertainty of the head imposed as boundary condition (which is obtained by interpolating the stage of neighbor stations) may be higher in the driest

period, when the groundwater flow does not equilibrate the local head differences as quickly as the overland water flow does.

2) In general the model does not reproduce the observed amplitude of the water table oscillations detailed previously in Figure 55. The only case where the model reproduces the amplitude in the range of the observed ones is for the HH well in SL Tree Island (see Figure 56). Even when there may be errors in the ET maximum rates used by the model, it is likely an effect of the assumed groundwater parameters (like conductivity and porosity) and of the ET partition coefficients specified in Table 9.

3) The model response to rainfall events differs in general from the observed response. In the plots, where the head differences are presented, a positive spike means that the model overpredicts the head during and after a rainfall event and a negative means an underprediction. In general, positive and negative spikes are observed, which may be a consequence of the local variability of the rainfall rate that cannot be captured by interpolating from neighboring stations. However, in the case of the HH well in SL Tree Island, the model overpredicts the water table elevation during most rainfall events (as shown in Figure A-65 and Figure 56). Notice that the model for the case K0 assumes a very high leakance from the OLF layer, which may produce a higher infiltration rate than expected during rainfall events. Moreover, other groundwater parameters assumed (such as conductivity and porosity) may need improvements.

In summary, the preliminary model results suggest the need to adjust of some of the model parameters like the porosity and conductivity of the GW layers, the OL layer leakance and the ET partition coefficients in order to match the seasonal, daily and rainfall-driven fluctuations of the water table.

4.2.4 A More Efficient Model

About 2 days were needed to run the case K0 for Satinleaf on a desktop computer with a Dell Pentium 4 (3.0 GHz) processor and about one day for Gumbo Limbo and for Black Hammock tree island MODHMS models. Four days to complete all tree island runs may be time prohibiting considering the numerous runs required for calibrating the GW parameters. Therefore, additional effort was conducted in order to decrease the running time of the models.

An attractive approach could be the increasing of the stress period length in such a way that some details at the hourly scale may be lost, but the daily water table oscillations are approximately preserved. Thus, two stress periods that represent the daytime and the nighttime were built into 24 hour period in order to capture approximately the maximum and minimum ET rate periods, respectively.

From the monthly averaged ET curves in Figure 23, the period with higher rates is found between 10AM and 6PM. Note that those times in Figure 55 correspond approximately to the moments where the water table level start to decrease (at about 9AM) and to increase (at about 6PM). Therefore, the stress periods suggested for the new case K1 go from 10AM to 6PM (8 hour period) and from 6PM to 10AM of the next day (16 hour period). For both periods the hourly ET rates are averaged (see Figure A-70) as well as the hourly rain depth rates.

The number of time steps needed by MODHMS to complete each stress period as a function of model time for the cases K0 and K1 is shown on Figure 58. Notice that MODHMS needs more than one time step to meet the convergence criterion mostly during the dry season where the saturation is lower than one in a bigger number of the soil cells. At that time, there are higher non-linearity effects due to the moisture retention and relative permeability curves. On the other hand, even when the stress period length is increased 8 and 16 times in case K1, the number of time steps per stress period do not more than double. Thus, the considerable reduction in the total number of time steps produces a decrease in the execution time of about one order of magnitude. Further execution-time reduction is obtained by computing the starting time step (parameter DELT in ATO file) by using the number of time steps from the previous run. With these improvements the total execution time for all the three tree islands in case K2 presented in the next section was less than two hours.

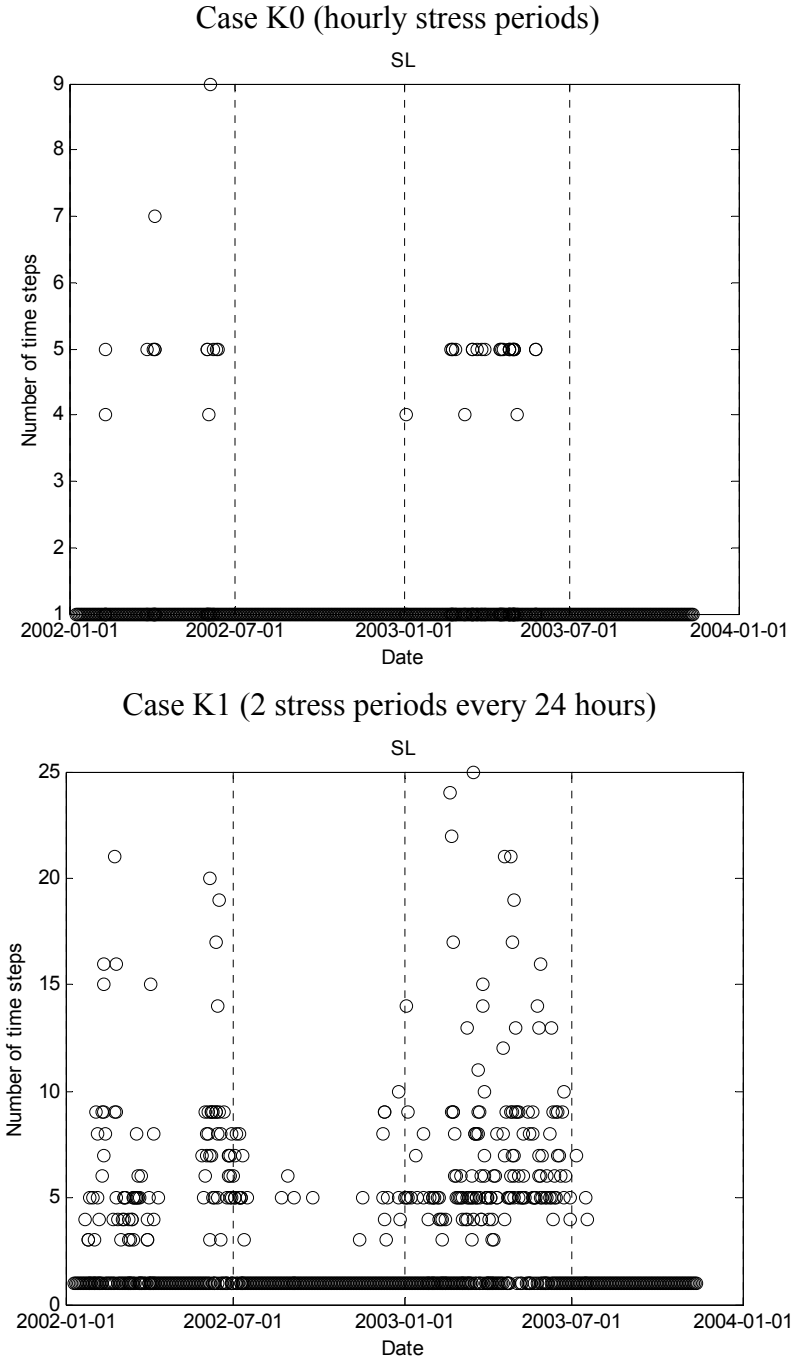

Figure 58. Number of time steps needed by MODHMS to complete each stress period as a function of time for the cases K0 and K1 in SL tree island. Plots for other tree islands in Figure A-77.

At the same time, the results for the case K1 do not differ considerably when comparing the figures presented in Appendix A4.2.4 with the corresponding ones for case K0. Of course, the fact that the average rainfall and ET in two stress periods per day, introduces some loss of detail on an hourly basis scale, for example, in the height decrease of most of the rainfall spikes. Additionally, the number of points available to compare model and measurement data are lower in case K1 (two points per day), which might affect the comparison between model and measurements. Fortunately, the water table elevations at 10AM and 6PM are very close to the maximum and minimum points of the water table oscillations, respectively, and the water table oscillations are still captured in the K1 case. In favor of the K1 case, notice also that despite the different number of points compared in cases K0 and K1, the overall error in Table 25 remains about the same.

Other estimates of the error (labeled as 3 and 4) were introduced in Table 25 and Table 26 in order to evaluate more specifically the ability of the model to reproduce the daily oscillations of the water table. In those cases, the offset is assumed to be variable with time and it is estimated at every time stress period end (10AM or 6PM) by matching the observed and modeled water table at previous times (6PM or 10AM, respectively). It can be inferred that the difference between the model and the experimental data corrected with a variable offset is a better measure of how well the daily oscillations are reproduced.

4.2.5 Test Changing OL Leakage

In cases K0 and K1, the leakage coefficient was chosen about four orders of magnitude higher than the one predicted by using the conductivity and the depth of the soil layer (equation (72) in Appendix A2.1), so that the infiltration is much faster from OL to soil than from soil to rock. As discussed in the previous section, this may cause that the model to overpredict the water table peak during a rain event, by favoring infiltration over the runoff process.

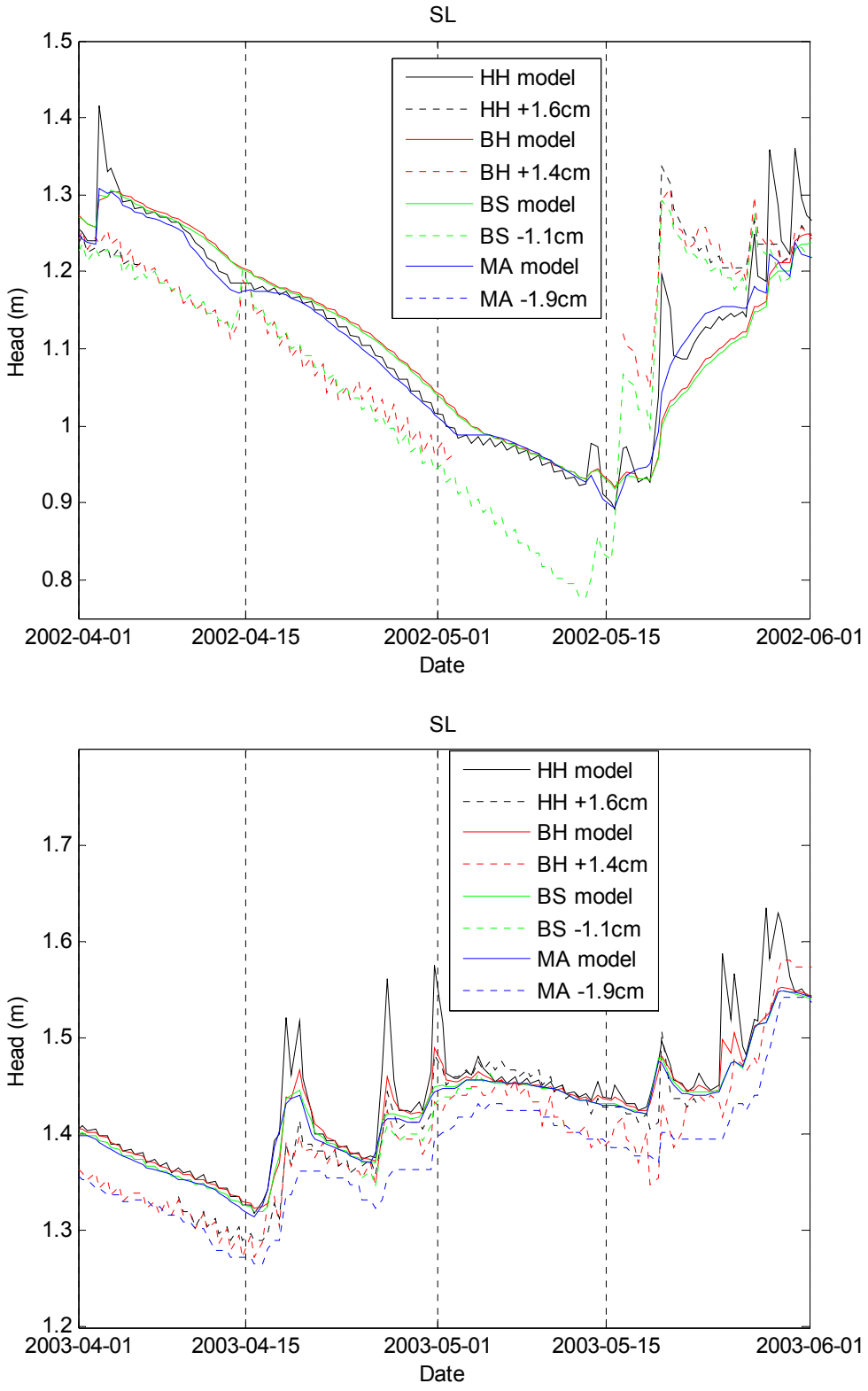

Figure 59. Comparison of the water table level obtained through the model and from field measurements in SL wells for the case K2. It is comparable to Figure 56 for case K0.

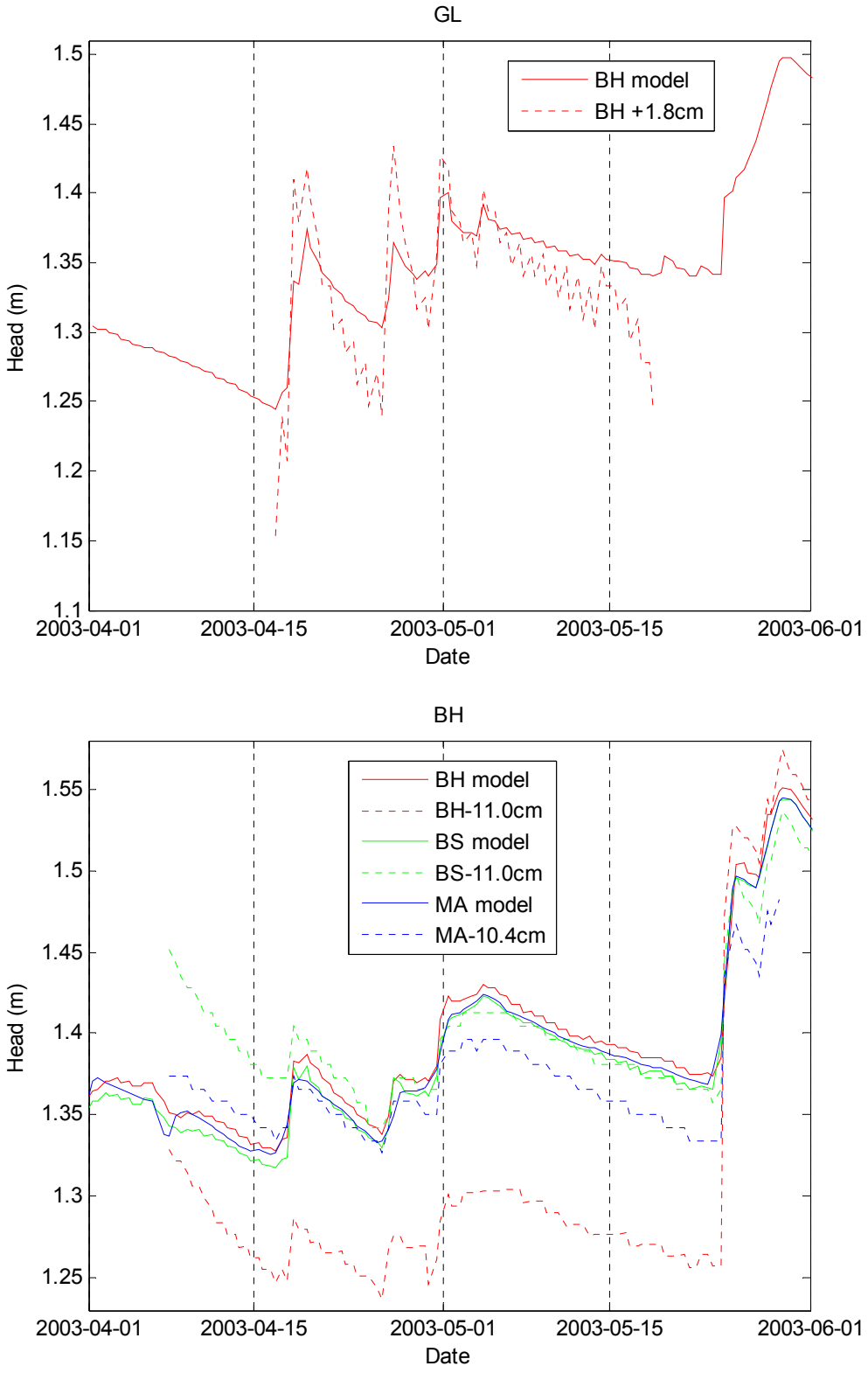

Figure 60. Comparison of the water table level obtained through the model and from field measurements in GL and BH wells for the case K2. It is comparable to Figure 57 for case K0.

Then, a new case K2 was defined with a leakage coefficient for each OL cell by using $f_L = 10$ in equation (79). The overall head errors and head error obtained for different wells are presented in Table 25 and Table 26, respectively. The modeled and measured head for different tree islands are plotted in Figure 59 and Figure 60 around the end of the dry season. The difference between the modeled and measured head for this case in wells at SL Tree Island is also plotted in Figure A-78, which is comparable to Figure A-76 for the case K1. In those graphs, it can be stated that most of the spike amplitudes associated to rainfall events for the HH well decreased slightly for the K2 case as expected. Notice also that the improvement in the prediction of the heads during the rainfall events is captured in the estimation error 2 but not in error 1, which is less sensitive to the extreme differences.

It is probable that the decrease in the leakage needs to be combined with a change on the soil hydraulic conductivity in order to obtain a further decrease in the head error. For this reason, the next section presents a procedure for adjusting several parameters at the same time.

4.2.6 Adjusting Several Parameters

The model parameters that could influence the head errors are listed in Table 27. The leakage coefficient introduced in previous section might improve the prediction of the model during rainfall events. The soil and rock hydraulic conductivities also influence the flow response of the system from head gradients caused by rainfall events, diurnal ET rates and boundary condition variations. Soil and rock porosity determine the water accumulation capability in those layers. The soil porosity is differentiated for HH soils and the other peat soils, as discussed previously.

The effective conductivity in the case of unsaturated flow is influenced by the relative permeability coefficient, which is determined by the Corey exponent and the residual saturation. The saturation, however, remains far from the residual saturation in tree island soils (see for example Figure A-62), and the VANSR parameter is not adjusted. The water accumulation capability in the unsaturated flow is determined by the moisture retention curve, which depends on the Van Genuchten parameters.

The ET partition between transpiration and evaporation also must be adjusted to match the measured well data, and it is different for each vegetation type.

The values of all those fitting parameters, as used in case K2, are listed in Table 27. Also an uncertainty range for the parameters is specified from the different values reported in the literature. For the ET partition coefficient, the ratio of the transpiration (T) to total ET (T/ET) is constrained to a monotonic variation through the different vegetation types. This means that in the model MA would transpire less than or equal than TS, TS less than or equal than BS, and so on, as expected.

Parameter	Vegetation type	case K2	Validity range assumed	Variation added	case K6	case K24	case K38	case K51	Case K59
Leakance coefficient f_L on (79)	All	10	(1, 10^4)	0.1 f_L	11	12.1	13.31	14.64	16.10
Soil conductivity HY, VHY (10^{-5} m/s)	All	1.0	(0.1, 14)	0.1 HY	1.1	1.21	1.33	1.46	1.61
Rock conductivity HY, VHY (10^{-3} m/s)	All	1.8	(0.1, 100)	0.1 HY	1.98	2.18	2.40	2.64	2.90
Soil porosity SF2	HH	0.50	(0.3,0.97)	0.01	0.51	0.52	0.53	0.54	0.54
	Others	0.93	(0.3,0.97)	0.01	0.93	0.92	0.91	0.90	0.90
Rock porosity SF2	All	0.20	(0.2,0.35)	0.01	0.20	0.20	0.20	0.20	0.20
VANAL (1/m)	All	2.78	(0.6, 3.0)	0.01	2.78	2.77	2.76	2.75	2.75
VANBT	All	1.917	(1.1, 2.0)	0.01	1.917	1.907	1.897	1.887	1.887
BROOK	All	3	(1, 6)	0.1	3	2.9	2.8	2.7	2.7
T/ET (%)	HH	90	(---,100)	1	90	90	90	90	90
	BH	80	(---,---)	1	80	80	80	80	80
	BS	65	(---,---)	1	65	65	65	65	65
	TS	50	(---,---)	1	50	50	50	50	50
	MA	10	(0,---)	1	10	10	10	10	10
Overall head error 1 (cm)	---	2.480	---	---	2.467	2.459	2.449	2.432	2.421
Overall head error 2 (cm)	---	4.394	---	---	4.348	4.287	4.231	4.181	4.149
Overall head error 3 (cm)	---	0.526	---	---	0.524	0.520	0.515	0.514	0.513
Overall head error 4 (cm)	---	1.649	---	---	1.625	1.593	1.564	1.539	1.526

Table 27. Parameters adjusted while fitting water table well data up to case K59.

During the fitting process, each fitting parameter is changed at a time according to the variation or step listed in Table 27. A positive error variation (error increases) suggests that the parameter needs to be changed in the other direction. Thus, a simple

procedure was applied to find the parameter combination that minimizes the error as sketched in Figure 61.

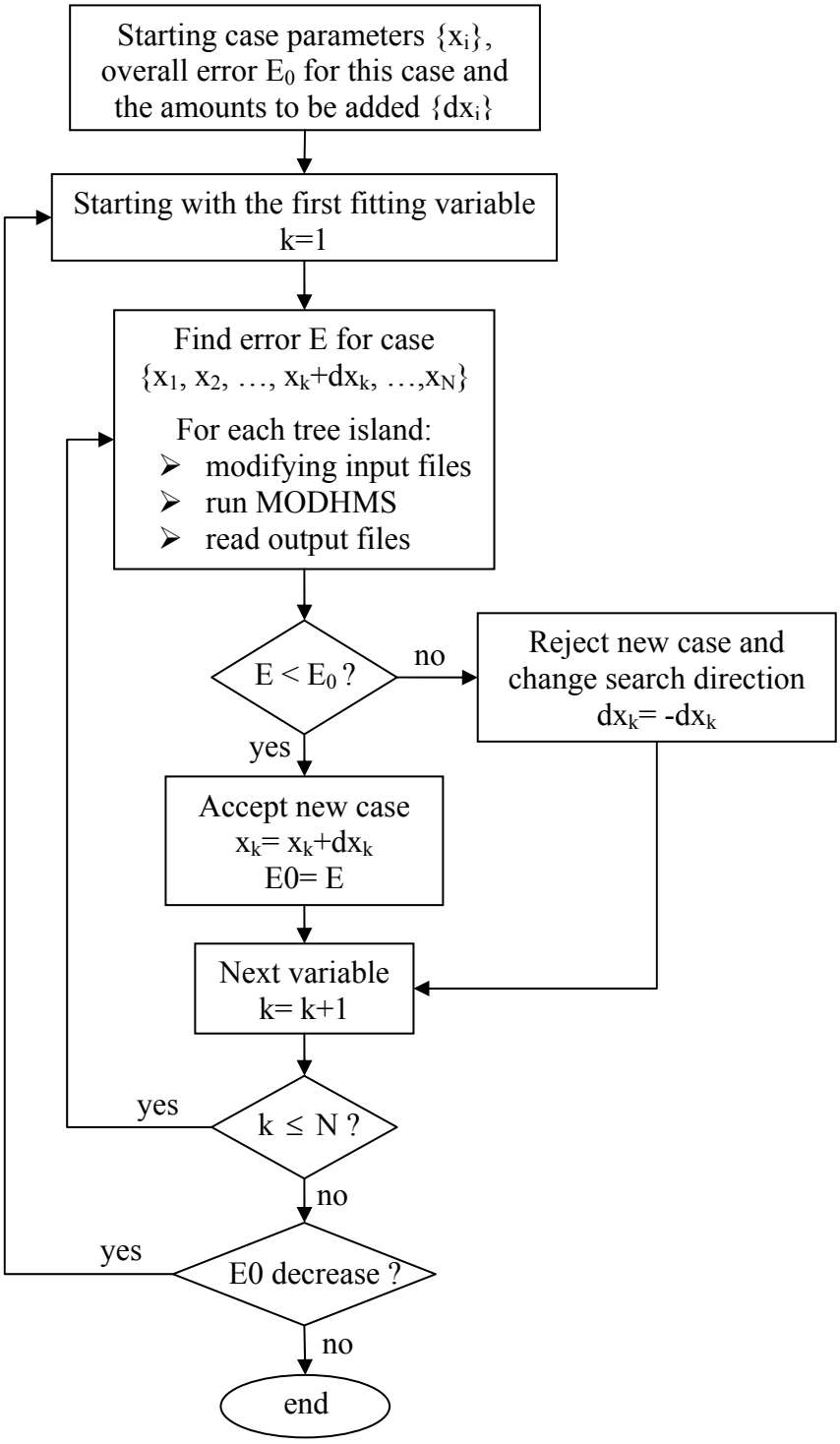

Figure 61. Proposing procedure for finding parameters that minimize the error.

The iterative procedure is conducted by a shell program coded for this purpose. In each iteration, the input files are modified (BCF, OLF or EVT files according to the modified parameter) and MODHMS is executed. After this is done for the three tree islands, the output files are processed to obtain the overall error and to accept or reject the parameter variation proposed.

A faster PC was used in this case and the determination of one overall error (by running MODHMS for the three TI cases) takes about one hour and ten minutes. This PC has four processors, which allows running up to four minimizing procedures at the same time in about the same time. The overall error 2 was selected at the beginning as the target for the minimization procedure in order to capture the response to rainfall events as well.

Some of the accepted cases following the minimum-searching procedure in Figure 61 are shown also in Table 27. The variation in most of the parameters causes a decreasing not only in the overall error 2 but also in other error estimators. Notice also that the rock porosity does not have any effect on the error, which is reasonable from the fact that the rock cells in the model remain fully saturated. In the case of the transpiration contribution on ET, MODHMS input files have been created, with errors for those cases, and the procedure was stopped after the case K59 to fix this problem.

The fitting procedure followed after case 59 is detailed in Appendix A4.2.6. In this stage, the procedure in Figure 61 was improved by reducing the step (dx_k) if variable (x_k) oscillates without producing an error decreasing. Once a local minimum was reached the objective function (overall error type) was changed and the minimum-searching procedure continued.

The parameters for the cases that give the minimum of the four overall errors are listed in Table 28. It is clear from the evolution of the different overall errors shown in Figure A-80, that the set of parameters that minimized overall errors from 1 to 3 are closer together in general than the one that minimized overall error 4. Recall that error estimator 2 and 4 are influenced by error peaks associated to rainfall events, contrary to error 1 and 3. On the other hand, errors 3 and 4 are computed from a variable offset in order to be more sensitive to the daily oscillations. Thus, the set of parameters that minimized overall error 4 is not considered further.

Parameter	Veg. type	case K2	K1095	K728	K2206	K3233
Leakance coefficient f_L on (79)	All	10	33.60	36.35	37.33	28.37
Soil conductivity HY, VHY (10^{-5} m/s)	All	1.0	1.54	1.03	1.31	0.898
Rock conductivity HY, VHY (10^{-3} m/s)	All	1.80	2.00	3.19	2.47	15.7
Soil porosity SF2	HH	0.50	0.71	0.97	0.68	0.79
	Others	0.93	0.37	0.36	0.37	0.58
Rock porosity SF2	All	0.20	0.20	0.20	0.20	0.20
VANAL (1/m)	All	2.78	2.49	2.49	2.49	2.69
VANBT	All	1.917	1.400	1.396	1.400	1.608
BROOK	All	3	1.1	1.0	1.0	1.0
T/ET	HH	0.90	0.99	1.00	1.00	1.00
	BH	0.80	0.99	1.00	1.00	1.00
	BS	0.65	0.80	0.83	0.80	0.80
	TS	0.50	0.79	0.81	0.80	0.73
	MA	0.10	0.22	0.24	0.22	0.33
Overall head error 1 (cm)	---	2.480	**2.205**	2.229	2.218	2.272
Overall head error 2 (cm)	---	4.394	3.739	**3.713**	3.726	3.786
Overall head error 3 (cm)	---	0.526	0.468	0.470	**0.462**	0.501
Overall head error 4 (cm)	---	1.649	1.547	1.534	1.541	**1.422**

Table 28. Parameters for cases with lowest error compared to the starting case K2.

From the other three sets of parameters, the one that minimized error 3 also gave the second minimum values for overall errors 1 and 2 as shown in Table 28. So, the case K2206 that minimized error 3 is accepted as the best set of parameters for reproducing the water table data.

The heads obtained in case K2206 are presented in Figure 62 and Figure 63 (see also the corresponding head differences from Figure A-82 to Figure A-84), which can be compared to the ones shown previously for cases K1 and K2. In those magnified graphs for the driest months, the daily head oscillations from case K2206 are higher and closer to the observed ones for the three tree islands. The new fitted case also reproduces better the rainfall peaks in SL and GL tree islands on the driest period.

Notice also in Table 28 that the soil porosity for other soils decreased significantly during the calibration process from its initial value of 0.93 to values lower than 0.6, which is closer to the expected value for the “open” porosity and the specific yield. This verifies to some extent the calibration procedure, and it is an indication of the robustness of the model and the data used.

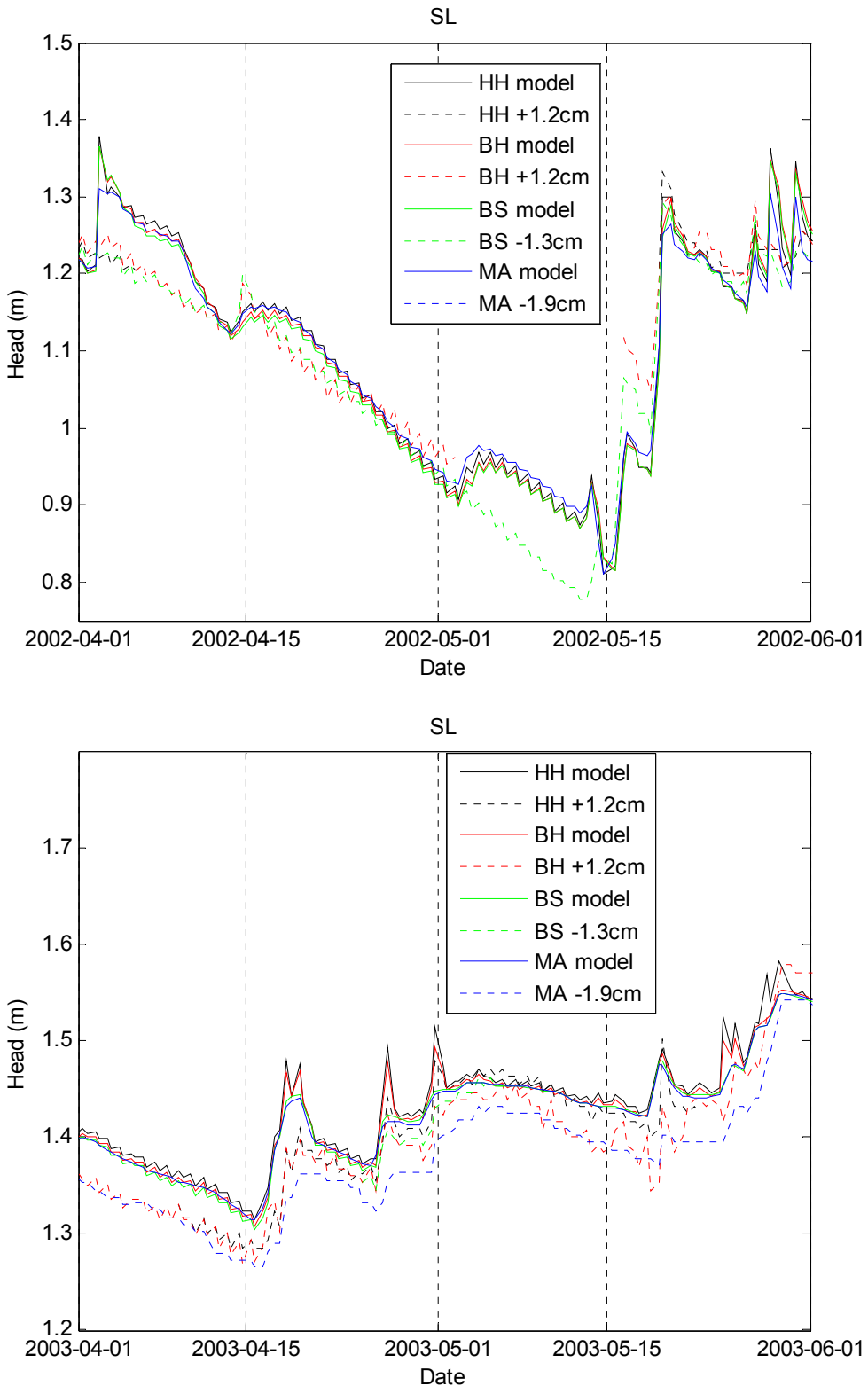

Figure 62. Comparison between the water table level from the model and from the field measurements in SL wells for case K2206. It is comparable to Figure 59 for case K2.

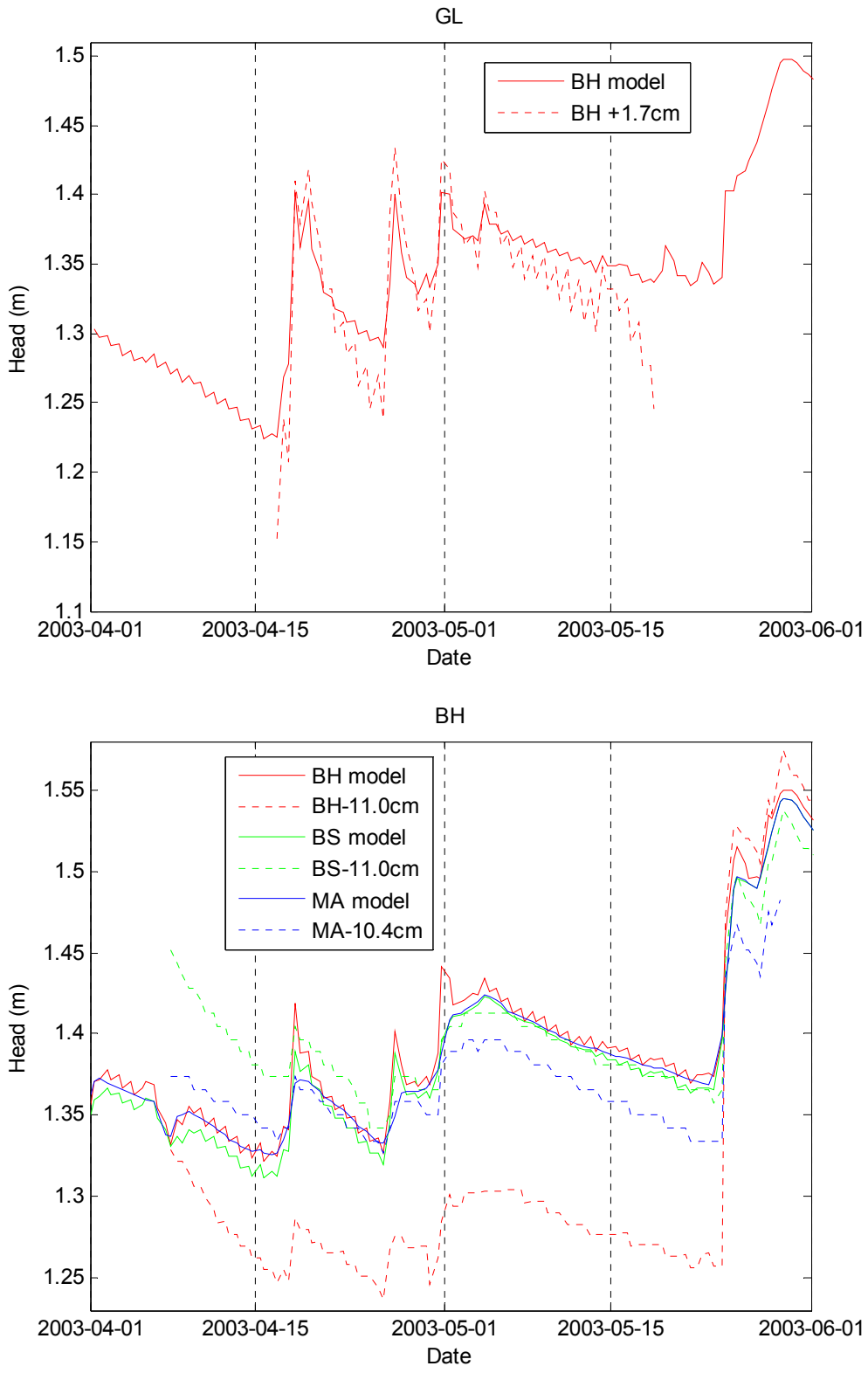

Figure 63. Comparison between the water table level from the model and from the field measurements in GL and BH wells for case K2206. It is comparable to Figure 60 for case K2.

In summary, the procedure to adjust the parameters in this work started minimizing one objective function by using constant parameter steps and ended using several objective functions to escape from local minima and variable parameter steps. It may seem attractive to use the response to several variables at the same time to determine the numerical derivatives of the objective function at that point and to approach the error minimum. This steepest descent approach is used for example by PEST (http://www.sspa.com/pest/) and it is particularly useful when parallelization is possible. In this work, the use the response of all the variable changes to make the next guess of the set of parameters was tried without success. The noise observed in variable derivatives (see Figure A-79), when the error changes are about zero, may likely cause that approach to fail.

Finally, a closer look at the graphs with the measured water table level shows that the daily oscillations in some wells do not start when the head decreases below the soil surface or do not stop when the head increases above the soil surface. On the other hand, the rock and soil surface elevation assumed at the well cells are averaged cell values obtained by interpolation from transect values. Thus, the head errors may be affected by the error in those assumed elevations. The details of the soil and bedrock surface elevations fitting at well grid cells are presented in Appendix A4.2.7. In general, error type 3 does not decrease appreciably by changing the soil and rock layer elevation at well cells, which may indicate that the predicted water table level at the well is influenced by the surrounding cells to some extent and not only by the assumed cell elevations where the well is located.

4.3 Transport Parameters Calibration

In this section, the external Phosphorus input and the initial dissolved Phosphorus concentration in the rock layer were adjusted to fit the averaged Phosphorus concentration in soil measured by Ross et al. [2006].

4.3.1 Available Data

The averaged dissolved Phosphorus concentration in soil pore water is presented in Table 2 for the different vegetation types mapped in Figure 10. Those values were

found by using transect data collected in tree islands on November 2002 and they can be used to obtain the external Phosphorus input at each vegetation type area.

4.3.2 Model Setup

The model uses the hydrodynamic parameters of the best fitted case so far (K4100) and the transport parameters specified for the base case. A 10 year simulation period from November 15, 1992 to November 15, 2002 is considered due to the availability of daily stage data during this period without appreciable gaps. The daily stages used by the model for that period are shown in Figure A-91 and the corresponding slopes in Figure A-92 and Figure A-93.

The available ET data does not extend for the whole period and hourly averaged values for each day of the year are considered for the periods with missing data, as shown in Figure A-94. Besides, it is important to consider the ET rate daily oscillation in the advective fluxes of Phosphorus, so that two stress periods per 24 hours are considered as in the previous section. They are from 10AM to 6PM (8 hour period) and from 6PM to 10AM of the next day (16 hour period). The rainfall and ET rates averaged on those stress periods for the whole ten year period are plotted in Figure A-95.

4.3.3 Calibration Procedure

The calibration procedure is intended to find an external Phosphorus input value that reproduces the averaged concentration of Phosphorus dissolved in soil water (SRP) for each vegetation type observed in the field (Table 2) at the end of this ten year period. Moreover, the initial concentration of dissolved Phosphorus in pore water is not known and it is also adjusted while the external Phosphorus input is fitted.

Initially, the concentrations for each vegetation type in Table 2 are assumed uniformly in the soil layer cells, as shown in Figure 64. For the rock layer and the OL layer, the concentration in Marsh soil water (1.5 μg/l) is also assumed. A null value for the Phosphorus input from external sources is assumed as a starting point. After simulating the ten-year period, the model gives the new concentration map for the soil layer, from which the averaged values for each vegetation type are computed. Those values are in general different to the ones in Table 2 and a factor is computed to multiply the final soil cell concentration values for each vegetation type and meet that condition.

The value of the resulting concentration is limited to the range defined by the averaged values of the neighbor vegetation types in Table 2. At the same time, the Phosphorus input for the different vegetation types is calculated trying to prevent those variations in Phosphorus concentration for the next iteration. The external Phosphorus input is considered in MODHMS as a high-concentrated water inflow at soil layer cells, depending on their horizontal area (WEL file). Iteration stops when there are no appreciable changes in the Phosphorus input from external sources and in the initial concentrations.

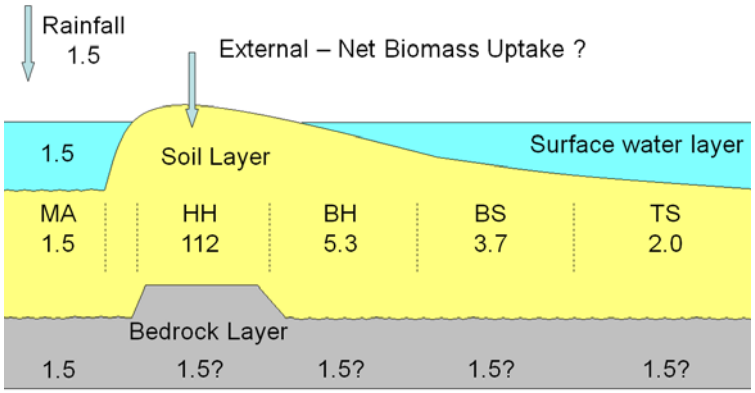

Figure 64. Schematic representation of the spatial distribution of the Phosphorus concentration in the model along the longitudinal tree island axis. The values presented are in mg/l= 10^{-6} kg/m^3.

The iterative procedure is implemented as a shell in MatLab. In every iteration, the input files are modified (initial concentration arrays in BTN and OLF files, as well as the injected concentration in WEL files), MODHMS is executed and the output files are processed to propose new maps of initial concentrations and new values external input rates for each vegetation type.

The calibration has been conducted progressively in three steps, which correspond to the next three sections. In the first step, the fitting procedure was conducted by running the MODHMS inside a shell to solve the dissolved Phosphorus transport problem. In this case, a simpler model was assumed by neglecting the biomass contribution to the Phosphorus cycling. In the second step, MODHMS was replaced by the developed code in MatLab to solve the dissolved Phosphorus transport problem. This allowed validation of the developed code and to find a better estimation of the external input rates for all vegetation type areas. In the third step, the biomass contribution is considered by solving

also the balance equations for Phosphorus in suspended and in deposited litter. The model results from this step by considering all the components of the conceptual model are the final results from this work and they are utilized in Chapter 5 to make a quantitative assessment of the spatial distribution and temporal variations of Phosphorus mass and fluxes around tree islands, as well as the other main objectives listed on section 1.4.

4.3.4 Using MODHMS for the Dissolved Phosphorus Transport

MODHMS was used initially to find the external Phosphorus input in a simple case that only includes the transport of dissolved Phosphorus. In this case, it was assumed that the vegetation uptake is balanced by the Phosphorus released by litter decomposition at each location at every time. In the conceptual model of Figure 6, this corresponds to removing the Phosphorus pools in live biomass, suspended litter and deposited litter, as well as their related Phosphorus fluxes. In the MODHMS setup, no uptake due to transpiration is imposed by setting ETFRAC=0 in the EVT input file.

4.3.4.1 Hydrodynamic Module Results

Under the conditions specified in the model setup, MODHMS solves the water flow problem at each time step before solving the transport of dissolved Phosphorus. However, the water flow problem does not depend on the setup of the transport of Phosphorus and its solution is exactly the same for every 10-year simulation period during the fitting procedure for the external Phosphorus input.

The mean overland water depth and soil layer saturation obtained for each vegetation type area and each tree island are presented in Figure A-96 and Figure A-97. The OL water depth and the saturation in the HH soil layer show an oscillatory seasonal dependency that has a minimum value at the end of the dry season (end of May) and a maximum at the end of wet season (end of September). For other vegetation type areas, the minimum soil saturation occurs at the same time but the curve is flatter (close to 1) during the wet season.

4.3.4.2 Dissolved Phosphorus Transport Module Results

The evolution of the mean concentration in water for each vegetation type area during the 10 years modeled, assuming no external input (Nin=0), is shown in Figure 65 for the soil and rock layers in the case of Satinleaf Tree Island. Notice, the model at the

first iteration predicts a visible decrease in the soil pore water concentration on the HH vegetation type, which must be equilibrated by introducing an external mass input rate (Nin>0) that can be attributed to an external source such as animal activity and other sources. On the other hand, the concentration in the rock layer for the HH vegetation increases, which means that the initial concentration assumed was too low.

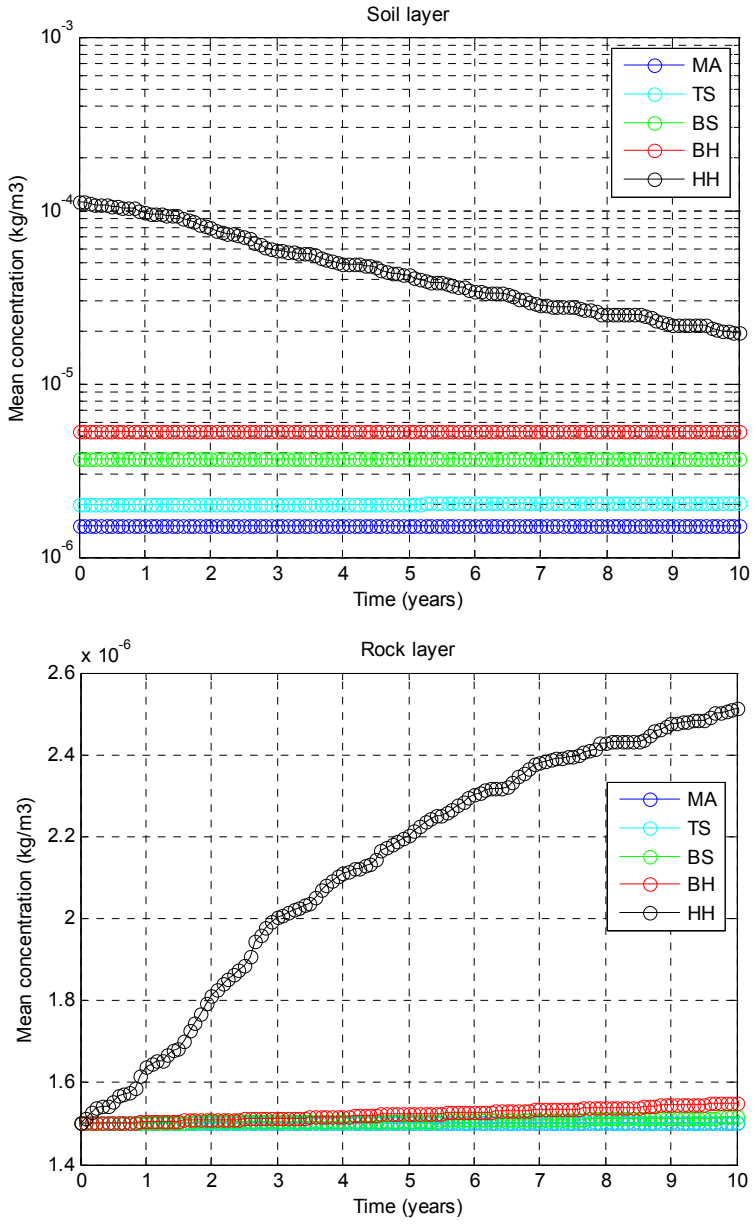

Figure 65. Evolution of the mean concentration in water for each vegetation type area (assuming no external input in the soil) in the case of Satinleaf Tree Island.

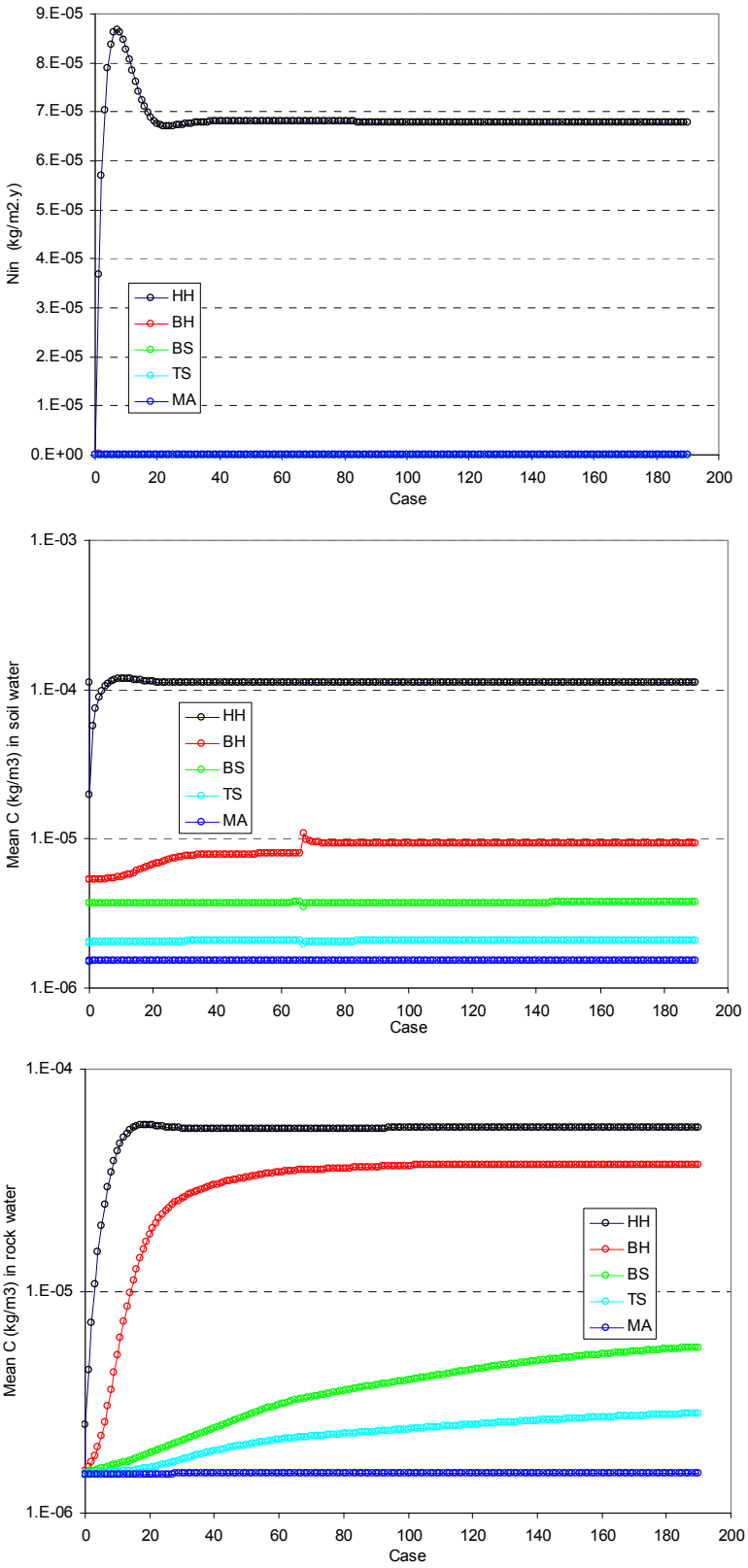

Figure 66. Evolution of the fitted input rate (Nin) and mean concentrations in soil and rock during the iterative procedure for SL Tree Island.

The results of the iterative procedure for estimating Nin and the initial concentrations are plotted in Figure 66 for SL as well as in Figure A-98 and Figure A-99 for other three tree islands. The Phosphorus input mass rate for keeping the concentration of 111.9×10^{-6} kg/m^3 in the HH soil water reach a plateau at about 6.8×10^{-5}, 2.4×10^{-5} and 5.2×10^{-5} kg/m^2/y for SL, GL and BH, respectively. The differences obtained for the external input mass rates for the different tree islands is an expected consequence of different time series of rainfall and head boundary conditions considered, as well as of different vegetation coverage type and layer elevations.

In the case of vegetation types other than HH, the iterative procedure predicts a negative mass input rate, which is not possible to consider in MODHMS. As mentioned before in the model implementation section, the WEL package considers the concentration of dissolved species only if there is fluid injection, and not if there is fluid extraction [HydroGeoLogic (HGL) Inc., 2006].

The initial concentration along the longitudinal transect of each tree island, proposed in the last case run, is shown in Figure A-101. Notice that the concentration profile in soil and rock layers is displaced in the direction of the flow. This explains why the Phosphorus transported from HH into BH soil layer cells suggests a negative Nin for the BH area.

4.3.4.3 Representation of Pools and Fluxes

The balance of water volume and Phosphorus mass obtained from MODHMS is sketched for each tree island in Figure 67 and Figure 68, respectively. For each layer and each vegetation type, there is a pool representing the stock of water and Phosphorus at the end of the 10 year simulation. The differences in the pool amount per unit area among tree islands are understandable due to differences in the average layer thickness. The ten-year average fluxes going out or into the pools are also displayed. The volume or mass conservation imposes the condition that the sum of all the incoming fluxes should be equal to the increase in the stock of the pool (accumulation rate), which is also presented below the volume or mass in each pool. The water volume and the Phosphorus mass conservation conditions are satisfied very well by MODHMS, as shown in those diagrams.

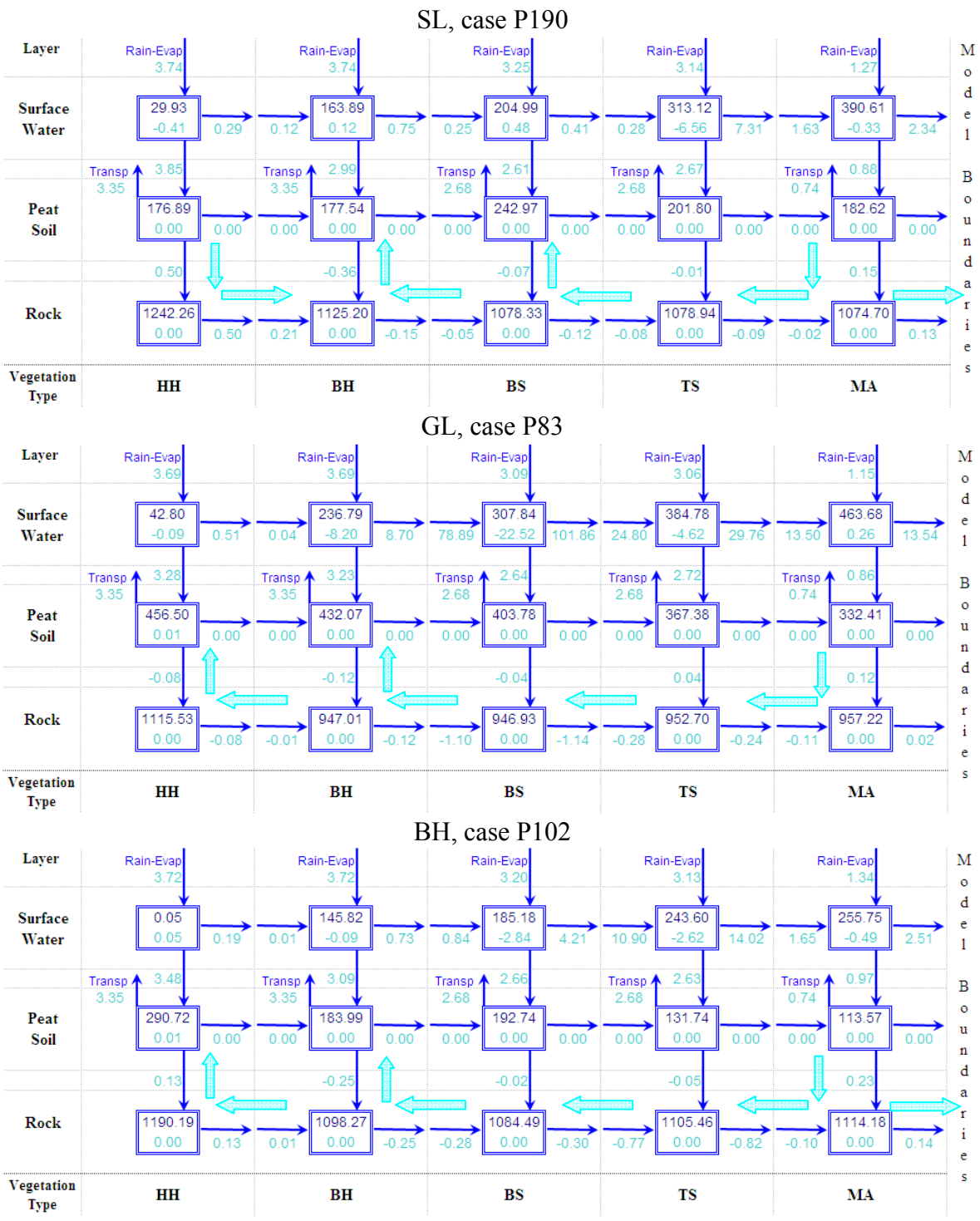

Figure 67. Pools and fluxes of water volume in the model after a 10 year simulation for each tree island. Pool volume values for each layer and vegetation type are presented in dark blue and correspond to the end of the simulation. They are normalized by unit horizontal area (mm). Volume flux values presented in cyan correspond to the average over the ten years, and they are also normalized by unit horizontal area (mm/day). This diagram is valid for all the 10 years simulation in this chapter while varying the transport related parameters.

SL, case P190

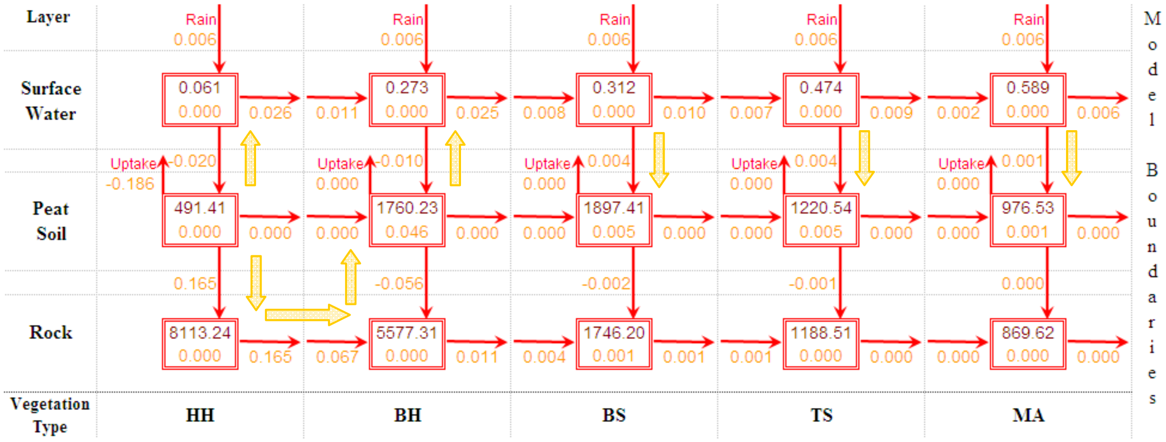

GL, case P83

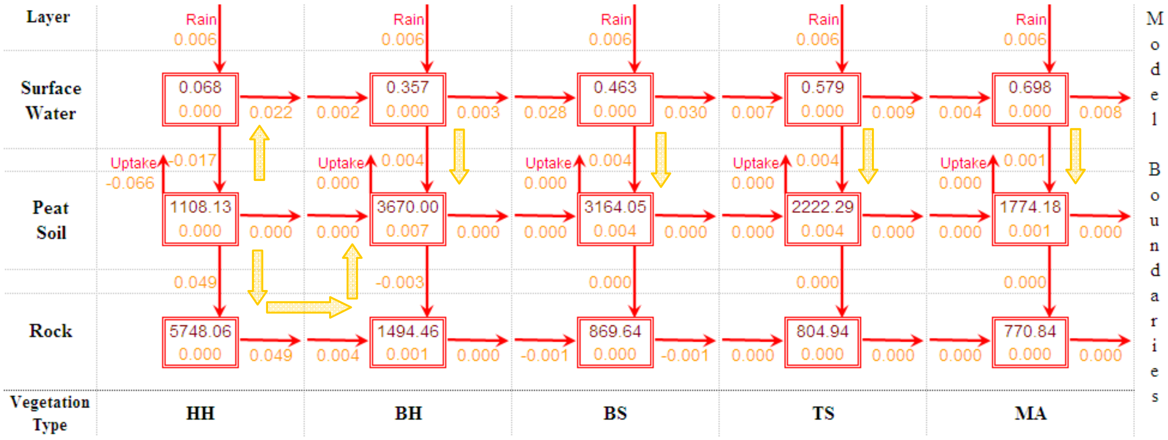

BH, case P102

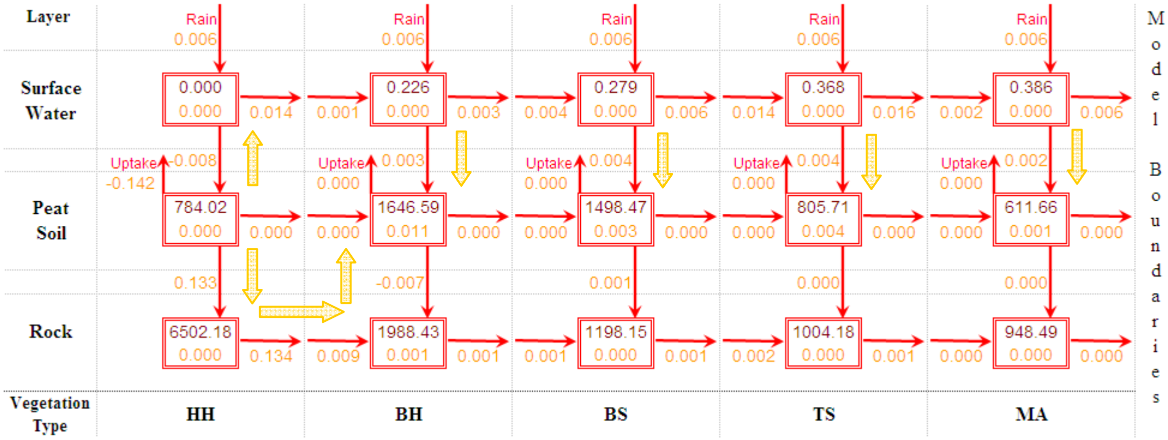

Figure 68. Pools and fluxes of dissolved and adsorbed Phosphorus mass in the model after a 10 year simulation for each tree island. Pool mass values for each layer and vegetation type are presented in dark red correspond to the end of the simulation. They are normalized by unit horizontal area (mg/m^2). Mass flux values presented in pink correspond to the average over the 10 years, and they are also normalized by unit horizontal area (mg/m^2/day).

Seasonal fluxes in different directions might be canceling each other approximately in a ten-year average. Notice for example in the water balance that the infiltration on average is about the transpiration rate, which may be far from what happens during the wet or the dry season.

Horizontal water fluxes in the soil layer are negligible due to the very low conductivity of the peat soil. Thus, in order to compensate for head differences in soil layer, water moves vertically in the soil layer and horizontally in the surface water layer or in the rock layer. Cyan wide arrows are added in Figure 67 to show the flow in the rock layer. Notice that for all tree islands water infiltrates on average from soil to rock in MA areas and comes out from rock to soil layer on the BH regions. In the HH region, water emerges on average from rock to soil for GL and BH tree islands but infiltrates in SL Tree Island. Notice however, the absolute values of those rock layer fluxes are much smaller than the transpiration rates, which are compensated mostly by water coming from the OL layer.

The advective transport of dissolved Phosphorus is affected by the water flows and by the concentration in each pool at each time. The wide orange arrows are added in Figure 68 to show the most important Phosphorus fluxes from this simpler MODHMS model. The infiltration due to the transpiration causes a net advective transport of Phosphorus from the overland layer into the soil for BS, TS and MA areas. However, in the HH area there is a net transport from the soil to the overland layer (soil pool losses). In the BH area the vertical transport depends on the tree island. Moreover, there is an important amount of Phosphorus moving from the soil to the rock in the HH area, then moving laterally at the rock layer and finally emerging in the BH area to the soil layer. In summary, those processes are compensated by a positive external input (representing a negative net uptake) in the HH area and by negative input in other areas that cannot be considered in MODHMS.

4.3.5 Using the Developed Code for Dissolved Phosphorus Transport

In this section, the dissolved Phosphorus transport equation (1) was solved by using the new code developed in MatLab as described in Chapter 2, in order to consider the extraction of the dissolved components (negative external input rates), which is not possible in MODHMS.

4.3.5.1 Testing the Developed Code

The code developed in MatLab to solve alternatively the transport of dissolved Phosphorus was applied to the previous cases P190, P83 and P102 for SL, GL and BH, respectively; already solved with MODHMS.

The evolution of the dissolved mass obtained for each vegetation type and layer of SL and their relative deviation regarding the MODHMS results are presented in Figure 69. The average deviation is computed by adding the absolute dissolved mass differences of the cells in the same vegetation type and layer, and then by dividing the result by the horizontal area covered. The relative deviation in Figure 69 is then obtained by dividing the average deviation by the dissolved mass value. From this figure, it can be concluded that the developed numerical MatLab code reproduces MODHMS results adequately.

Regarding the computational efficiency, the running time for the last MODHMS 10-year-period solutions is 2.6, 7.2 and 5.1 hours for SL, GL and BH tree islands, respectively. Conversely, the running time of the developed numerical procedure in those cases is 1.05, 1.65 and 1.47 hours, respectively. As stated before, this difference is reasonable because MODHMS solves the water and the Phosphorus transport problems, whereas the developed code solves only the Phosphorus transport equation, while using the water flow field already determined from MODHMS. Thus, the developed code is about three times faster and it is more convenient for making a high number of runs during the calibration of the external input rates.

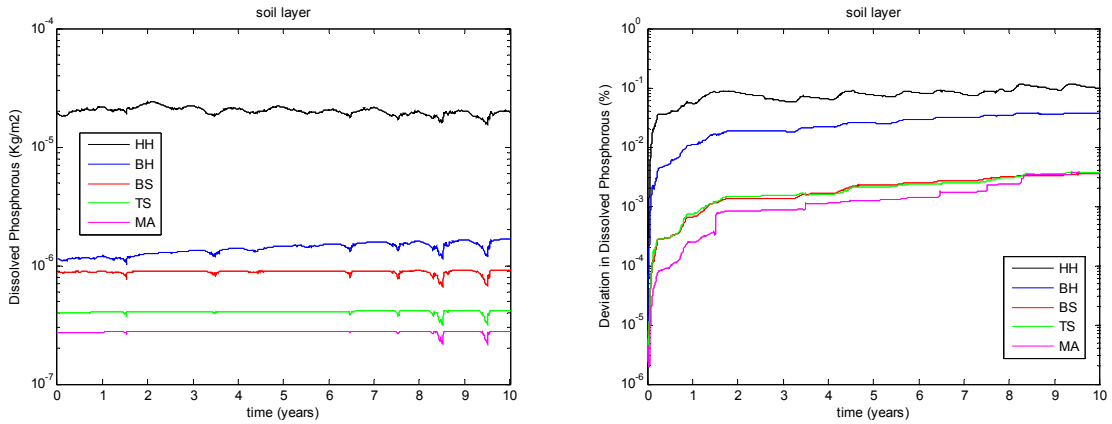

Figure 69. On the left hand side, the 10-year evolution of the mass of dissolved Phosphorus in soil layer, in different vegetation type areas of SL tree island, obtained from the MatLab code. On the right hand side, the deviations regarding the previous MODHMS results. Similar graphs for other layers are shown in Figure A-102.

4.3.5.2 Considering a Diffusion Coefficient

The numerical diffusion introduced in the model was found to be of the same order of the effective diffusion-dispersion coefficients reported in the literature, as discussed before in section 3.2.1.2. For this reason and due to the uncertainties in the effective coefficient from the literature, the effective diffusion-dispersion coefficient was neglected in the model by default. However, as shown in Appendix A2.2, the numerical diffusion vanishes if the water is at rest (zero velocity), which is in disagreement with the diffusion from thermal molecular movements, from thermal convective flows, from animal disturbances, etc. Thus, including a diffusion coefficient in the model may be relevant after observing the fluctuations in the concentration profile shown previously in Figure A-101. Therefore, the molecular diffusion coefficient for the dissolved Phosphorus (7.9×10^{-10} m^2/s) was included in the model to assess its effect on the results.

The concentration profiles obtained in Figure 70 for each layer after including the diffusion coefficient are similar to those in Figure A-101 obtained without considering it. Only some differences in the OL concentrations around the HH area are observed, but these do not introduce significant changes in the mass balance because those cells are dry or almost dry. Nevertheless, the molecular diffusion coefficient was included in further model simulations in order to have diffusion in zero or almost zero velocity situations.

4.3.5.3 Considering Negative External Input Rates

MODHMS does not allow consideration of negative values of Nin, as mentioned before. In this section, the developed numerical procedure is used in order to find iteratively the negative or positive values of Nin in order to maintain the dissolved Phosphorus concentration in soil after 10 years. This case is referred to as Case L0 from now on.

The adjusted Nin values reach a plateau after a few iterations (see Figure A-103). The HH values are close to the previous ones reached (see Figure 66, Figure A-98 and Figure A-99), when no negative values were considered. On the other hand, the negative Nin values for the other areas are close to the ones proposed on the first iteration.

The concentration profiles (presented in Figure A-104) are also similar to those in Figure 70 obtained without considering negative Nin values.

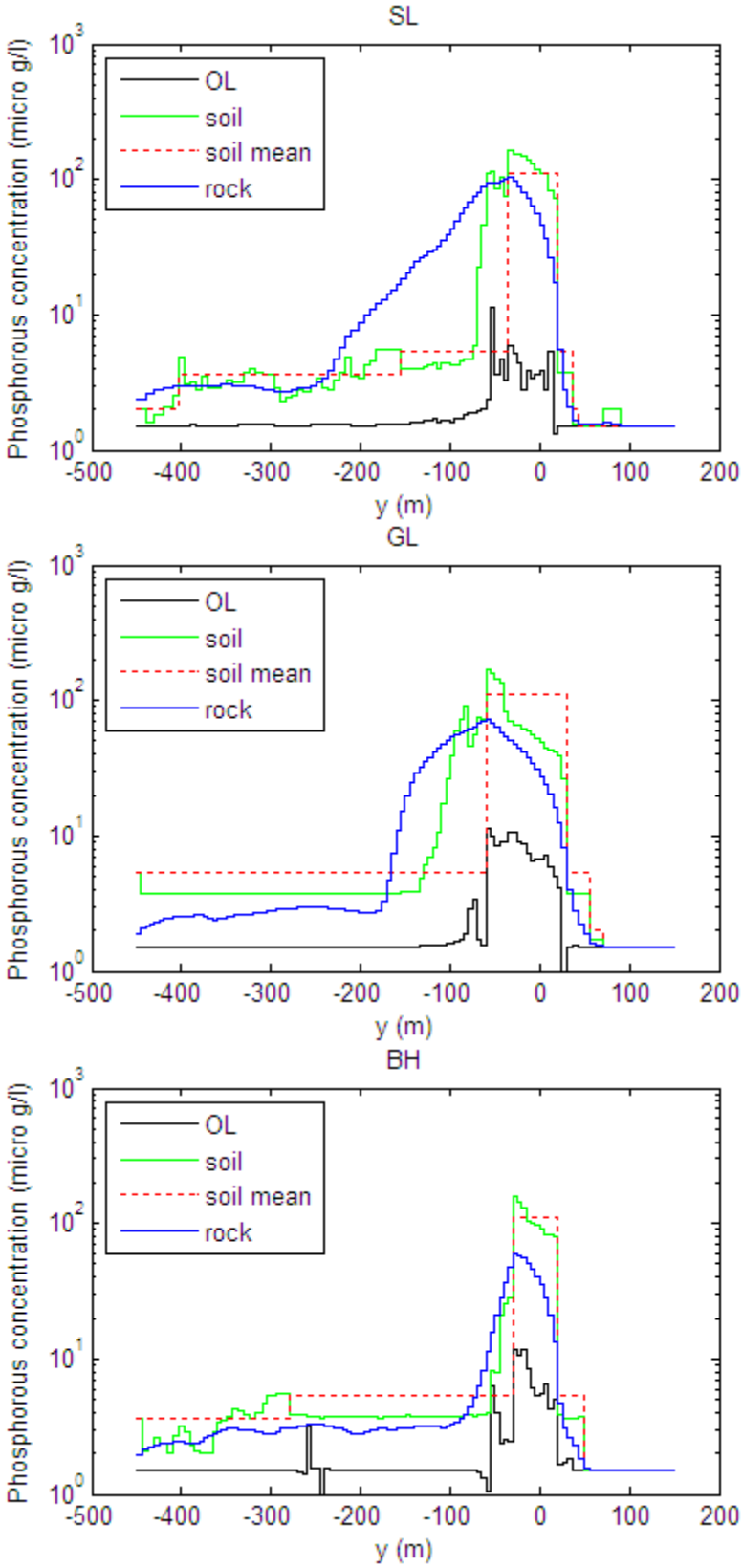

Figure 70. Initial concentration along the tree island axes obtained from the last case run by including the diffusion coefficient 7.9×10^{-10} m^2/s.

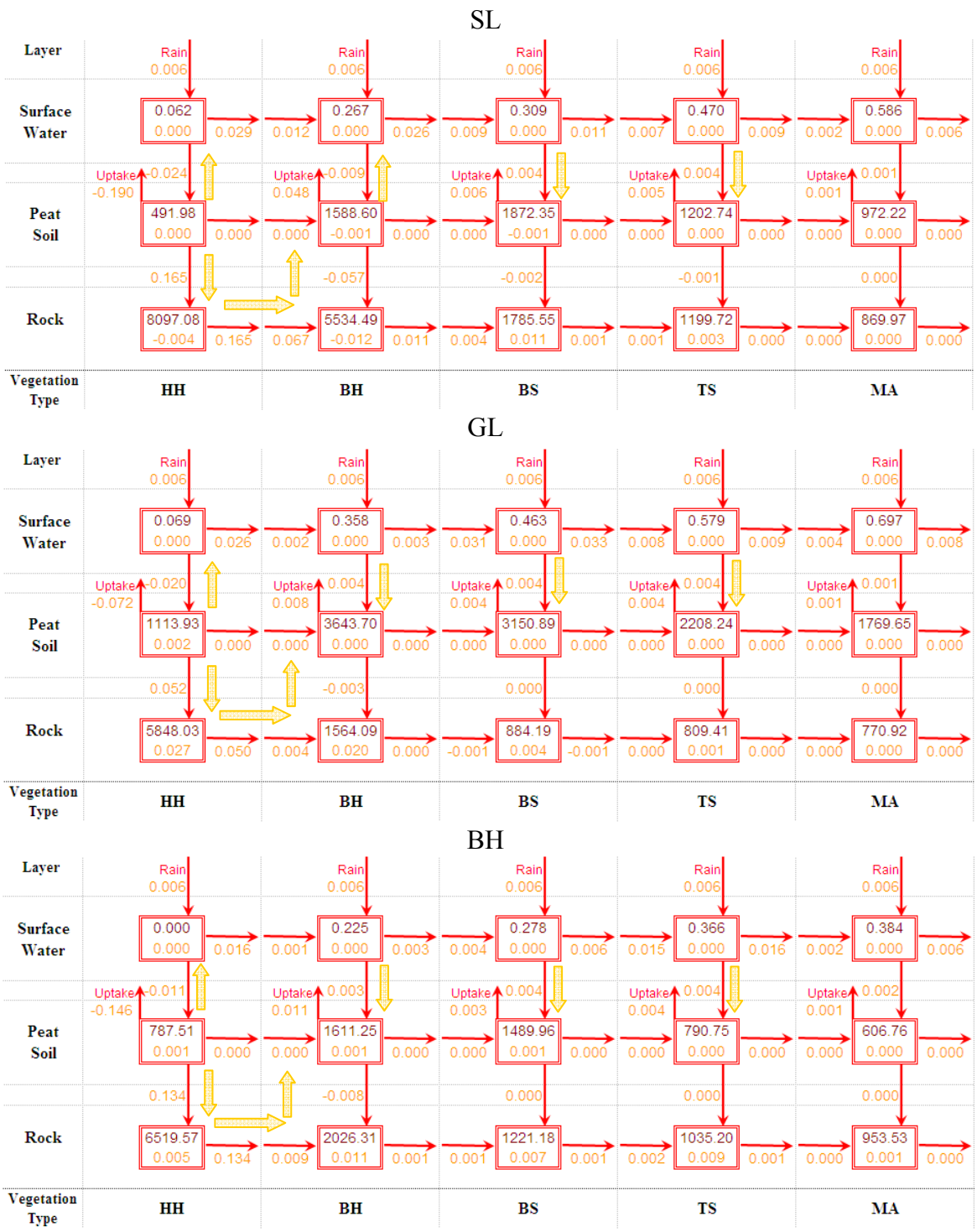

Figure 71. Pools and fluxes of dissolved and adsorbed Phosphorus mass in the model after a 10 year simulation for each tree island for case L0. Pools amounts are in mgP/m2 and fluxes in mgP/m2/day units.

The Phosphorus pools and fluxes in this case are shown in Figure 71, which can be compared to the ones in Figure 68. Now, the net uptake rate (which is in those cases just the opposite of Nin) is positive for vegetation type areas from BH to MA. Nin rate is mostly used to make almost zero the Phosphorus change in soil pools on these areas after 10 years, but the value of the other fluxes does not change significantly.

Chapter 5. Results and Discussion

The results of the developed model obtained by solving the full set of Phosphorus balance equations are presented and discussed in this chapter. At the end, the results are summarized and further discussed in correspondence to the main objectives stated on section 1.4.

5.1 Solving the Full Set of Equations

In previous sections, only the transport of dissolved Phosphorus was being considered in the model by assuming that the vegetation uptake is balanced by the Phosphorus released by litter decomposition at each location and at every time. In this section, the mass balance equations (12) and (15) are also solved for suspended and deposited litter, respectively. In this case, the total input rate into the dissolved Phosphorus pool in soil is given by equation (8), i.e., it is the sum of the input from external sources (Nin, which is still assumed constant on time and uniform inside the different vegetation type areas) and the net Phosphorus release rate from biomass (which is equal to Phosphorus released by decomposition minus the uptake from live biomass and varies spatially and temporally according to the solution of the litter balance equations). The model results from this section are the final results from this work and they are utilized next to make a quantitative assessment of the spatial distribution and temporal variations of Phosphorus mass and fluxes around tree islands, as well as the other main objectives listed on section 1.4.

5.1.1 Net Phosphorus Release Rate from Biomass

As stated in the model implementation section 2.2, the fact that the Phosphorus uptake by biomass is assumed independent of the concentration of dissolved Phosphorus in soil, allows decoupling the problems and solving first the Phosphorus-in-litter balance equations. Once those equations are solved and the net Phosphorus release by biomass (release from litter decomposition minus live biomass uptake) is known, the dissolved Phosphorus transport problem is solved.

In the parameterization chapter, some constant and uniform parameters (ε_{Lres} = 1.99x10^{-11} kgP/m^2/s, v_S = 2.23x10^{-7} m/s and C_E = 1.65x10^{-16} kgP/m^3) were proposed for the erosion and deposition processes while solving the litter balance equations (12) and (15). Besides, the Phosphorus-in-litter production rate (ε_{Lprod}), which is assumed equal to the Phosphorus uptake by biomass, is considered constant on time but variable with the different vegetation types according to Table 17. Moreover, the litter decomposition rate (r_{dec}) has an anaerobic value (1×10^{-3} day^{-1}) and an aerobic one (3×10^{-3} day^{-1}), which are applied if water is ponded or not, respectively. This introduces a seasonal dependence on the decomposition rate.

The equilibrium values for the litter related variables C_L^{∞} and L^{∞} (given by (16) and (17), respectively) were used as initial conditions. However, this is only an approximation because the surface water velocity V and the decomposition rate r_{dec} change with time, and the litter variables may be far from their steady state. This may affect particularly the deposited litter amount because the characteristic time of the decomposition ($1/r_{dec}$) is on the order of the seasonal oscillation period. Therefore, the 10-years period was run once by using the equilibrium values as initial conditions and then the final values found for C_L and L were used as new initial conditions and the 10-year run was repeated.

The Phosphorus-in-litter pools obtained at the end of the simulation period are shown in Figure 72, with the 10-year averaged fluxes as well. From this diagram, the Phosphorus mass change in the suspended and deposited pools is almost negligible after 10 years, which is a validation for the initial condition chosen.

In all the vegetation types areas the Phosphorus-in-litter deposition rate is in average higher than the sum of resuspension and erosion rates. This represents a positive average net influx from the suspended litter into the deposited litter pool, which is almost equal to the dissolved Phosphorus release rate due to the decomposition process.

A positive horizontal flux of Phosphorus in suspended litter in all the vegetation type areas is observed in the direction from the tree island head to the model boundaries. However, the incoming and outgoing fluxes at each vegetation type area are different in

general, which causes the Phosphorus-in-litter production (equal to vegetation uptake) to be different, in general, from the Phosphorus mass rate released by litter decomposition. Thus, the averaged net dissolved Phosphorus release rate from biomass $\left\langle R_{dec} - \varepsilon_{Lprod} \right\rangle$ is positive for BS and MA areas and negative for the other ones (HH, BH and TS) as shown in Table 29. In other words, the transport of suspended litter removes, on average, Phosphorus from HH, BH and TS areas and it brings Phosphorus into BS and MA areas.

Vegetation type	Tree Island	Nin (L0) ($mg/m^2/y$)	$\left\langle R_{dec} - \varepsilon_{Lprod} \right\rangle$ ($mg/m^2/y$)	Nin (L0) - $\left\langle R_{dec} - \varepsilon_{Lprod} \right\rangle$ ($mg/m^2/y$)	Nin (L1) ($mg/m^2/y$)
HH	SL	69.2	-153	222	216
	GL	26.5	-234	261	283
	BH	53.3	-92.7	146	139
BH	SL	-17.6	-140	122	124
	GL	-2.85	-170	167	165
	BH	-4.12	-146	142	143
BS	SL	-2.04	59.4	-61.4	-61.6
	GL	-1.29	86.6	-87.8	-88.1
	BH	-1.14	64.3	-65.5	-65.6
TS	SL	-1.71	-321	319	319
	GL	-1.42	-345	343	343
	BH	-1.56	-321	320	320
MA	SL	-0.42	3.99	-4.42	-4.41
	GL	-0.41	2.01	-2.42	-2.41
	BH	-0.52	5.58	-6.09	-6.05

Table 29. Comparison of Phosphorus external input rate (Nin) for L0 and L1 cases.

The result of the litter transport in the scale of the tree island model domain is a net Phosphorus-in-suspended litter lost, as confirmed by the positive horizontal flux from MA to the boundary condition cells for all the tree islands in Figure 72.

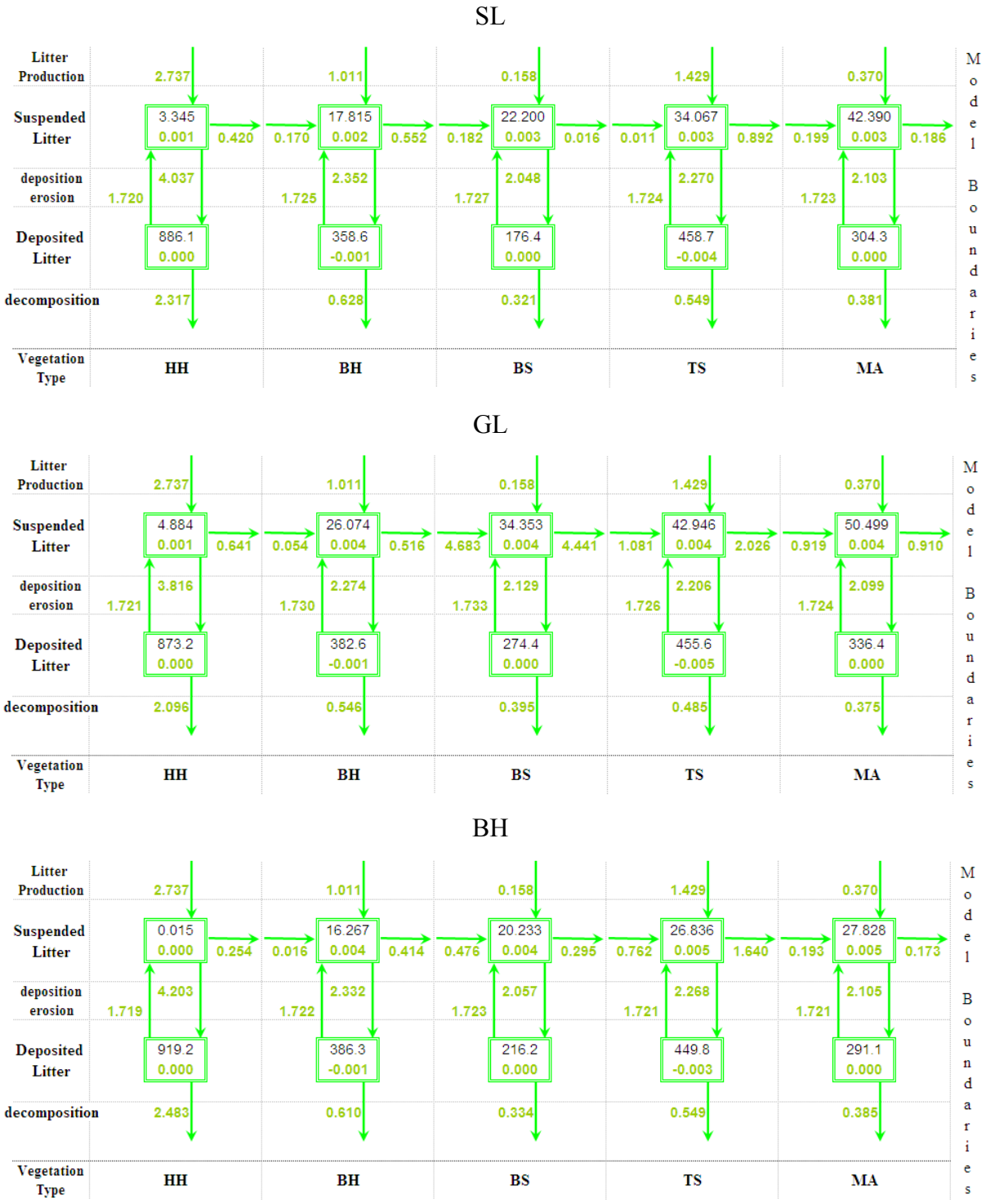

Figure 72. Pools and fluxes of Phosphorus mass in the biomass part of the model after a 10 year simulation for each tree island for case L1. Pools amounts are in mgP/m^2 and fluxes in mgP/m^2/day units. In the model, the Phosphorus-in-litter production is assumed equal to the vegetation uptake.

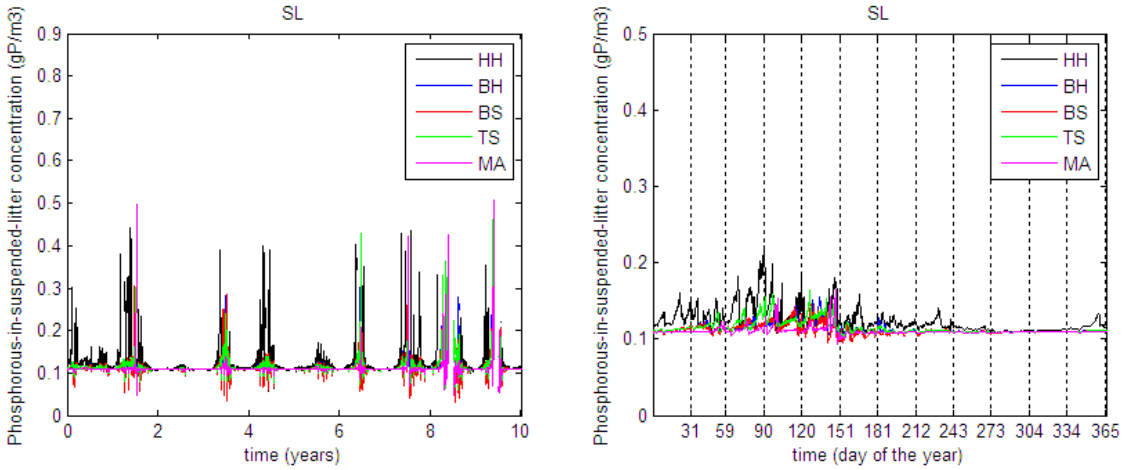

Figure 73. On the left hand side, the evolution of the Phosphorus-in-suspended litter concentration (C_L) averaged for each vegetation type area in case L1. On the right hand side, those values are averaged for each day of the year. See plots for other tree islands in Figure A-105.

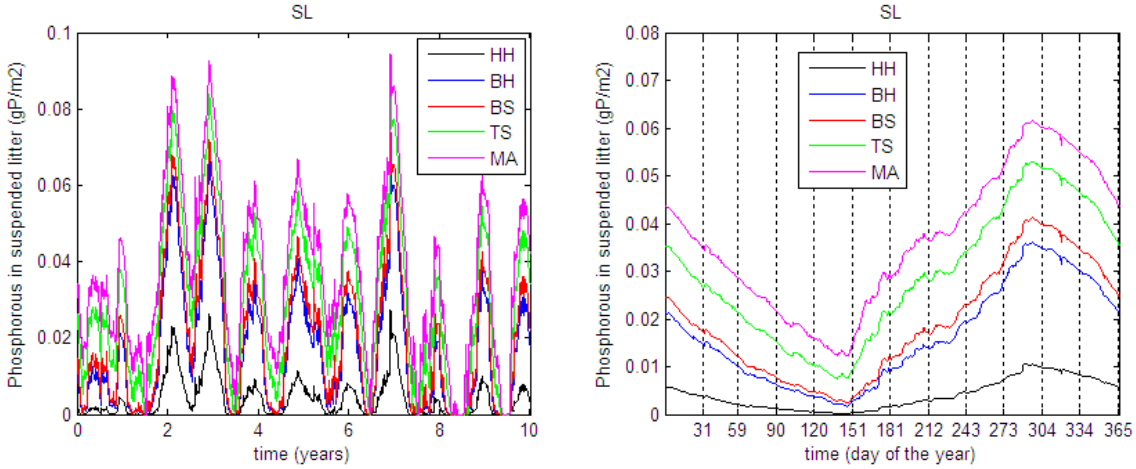

Figure 74. On the left hand side, the evolution of the mass per unit area ($C_L h$) of Phosphorus in suspended litter averaged for each vegetation type area in case L1. On the right hand side, those values are averaged for each day of the year. See plots for other tree islands in Figure A-106.

The evolution predicted by the model for the suspended Phosphorus amounts is shown on Figure 73 and Figure 74. The averaged value computed for each day of the year is also presented in those figures, in order to illustrate better the seasonal dependence. From those graphs, the Phosphorus mass in suspended litter per unit area has a minimum value at the end of the dry season (end of May) and a maximum at the end of wet season (end of September), which is similar to the seasonal dependence of the water

depth shown in Figure A-96. The Phosphorus-in-suspended litter concentration (C_L), however, has maximum values during the dry season. In addition, the Phosphorus-in-suspended litter mass per unit area has a noticeable spatial distribution. It increases monotonically away from the head of the island, i.e., from HH to MA areas.

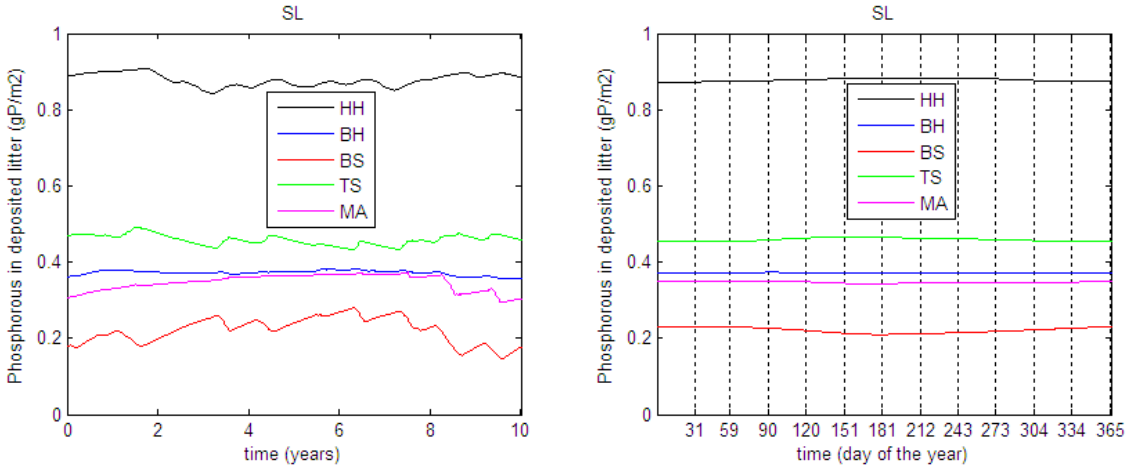

Figure 75. On the left hand side, the evolution of the Phosphorus-in-deposited litter (L) averaged for each vegetation type area in case L1. On the right hand side, those values are averaged for each day of the year. See plots for other tree islands in Figure A-107

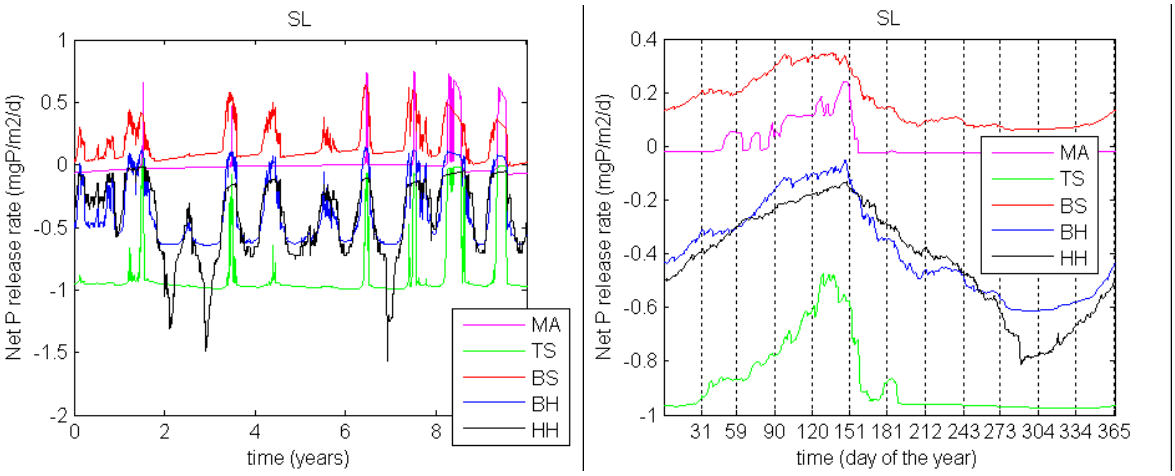

Figure 76. On the left hand side, the evolution of the net release rate of Phosphorus (R_{dec} - ε_{Lprod}) averaged for each vegetation type area in case L1. On the right hand side, those values are averaged for each day of the year. See plots for other tree islands in Figure A-108.

The evolution and the seasonally averaged dependence of the Phosphorus-in-deposited litter (L) is shown in Figure 75. This variable has a temporal dependence

without a clear seasonal dependence. The spatial dependence is remarkable and similar for all tree islands. The HH area has the highest L amounts followed by TS, BH, MA and BS ones. The reason why the Phosphorus-in-deposited litter in BS area is the lowest, close to the one in MA areas can be understood from Figure 72. The amount of Phosphorus-in-litter produced in BS and MA areas is lower than in other vegetation type areas. Even when in BS and MA areas there is a net sequestration of Phosphorus-in-suspended litter (because the horizontal incoming flux is in average higher that the outgoing one), the net result is a lower mass of Phosphorus-in-deposited litter per unit area.

The evolution of the net release of Phosphorus from biomass (R_{dec} - ε_{Lprod}) is presented in Figure 76. In this case, there are abrupt temporal changes due to the decomposition rate change from anaerobic to aerobic conditions or vice versa. However, there are also smooth changes at the same decomposition rate due to the changes in the mass in the deposited litter pool. The seasonal dependence shown also in that figure reveals, on average, an increase in the net release rate during the dry season compared with the wet season, which is expected from the dependence of the decomposition rate. Regarding the spatial distribution of the net release rate, BS area has the highest positive value followed by MA. Then, HH and BH are at about the same level and after them the TS area corresponding to the lowest net release rate.

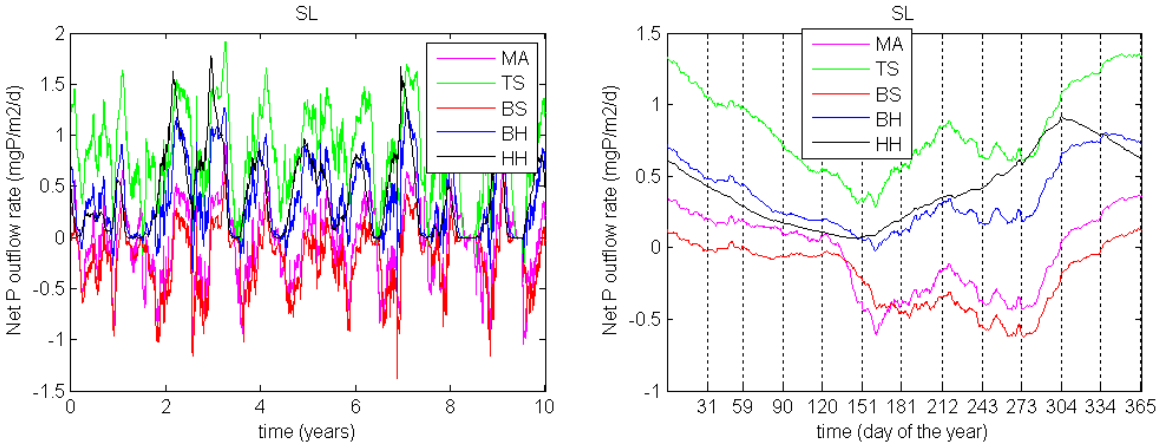

Figure 77. On the left hand side, the evolution of the net outflow rate of Phosphorus averaged for each vegetation type area in case L1. On the right hand side, those values are averaged for each day of the year. In both cases, a running average with a 30-days window was performed. See plots for other tree islands in Figure A-109.

The evolution of the net outflow of Phosphorus in suspended litter from the different vegetation type areas is presented in Figure 77. In this case, the daily fluctuation was considerable and a running average was performed. Notice that the net outflow rates for all vegetation type areas are closer to zero at the end of the dry season, as expected from the lower water levels and the lower suspended litter transport. The net Phosphorus outflow from HH, BH and TS areas is positive through the whole year, which represents sustained Phosphorus losses as suspended litter from those areas. The maximum losses from the head of the island (HH vegetation type) are around the end of the wet season (end of October). In other vegetation type areas the maximum losses occurs around December. In the case of the BS and MA vegetation types, there is a negative outflow rate during the wet season (specifically from mid May to November), which represent a period of phosphorous accumulation in deposited liter at those areas.

5.1.2 Estimation of External Input Rate

Once the net release rate of Phosphorus from biomass is obtained for each stress period, the external input rate (Nin) is fitted as previously for each vegetation type area trying to recover the average concentration of dissolved Phosphorus in soil pore water after the ten year period. The initial guess for Nin is found by subtracting the averaged net release $\left\langle R_{dec} - \varepsilon_{Lprod} \right\rangle$ to the Nin value fitted for case L0, as shown on Table 29. A few iterations were necessary to reach a plateau in the adjusted Nin values as shown in Figure A-110. The fitted Nin values for this case (labeled as L1) are close to the initial guess but different from the Nin estimated for case L0 without considering the biomass cycle processes, as shown on Table 29.

The concentration profiles presented in Figure 78 are not as smooth as the ones in Figure A-104 obtained without considering the biomass cycle processes. In this case, the Phosphorus-in-suspended litter transport causes, in general, different net Phosphorus-in-litter deposition in different cells. This is reflected as a higher spatial variability also in the dissolved Phosphorus released into the soil layer from deposited litter decomposition. The spots with higher dissolved Phosphorus input rates in soil pore water would have higher concentration. In some areas, the higher concentration in soil is correlated to a higher concentration in the rock cells located below, as shown in the profiles on Figure

78. This result is in correspondence with the high statistical dispersion in the SRP values in pore soil water surveyed by [Ross et al., 2004] at the tree islands, even inside the same vegetation type areas.

The dissolved and adsorbed Phosphorus pools at the end and the averaged fluxes in this case are shown in Figure 79. Notice that the picture here does not differ considerably from previous cases in Figure 68 and Figure 71. The infiltration due to the transpiration causes a net advective transport of Phosphorus from the overland layer into the soil for BS, TS and MA areas. However, in the HH area there is a net transport from the soil to the overland layer (soil pool losses) and in BH area it depends on the tree island. Moreover, there is an important amount of Phosphorus moving from the soil to the rock in the HH area, then moving laterally at the rock layer and finally emerging in the BH area to the soil layer.

Other kinds of pools and fluxes diagrams is presented are Appendix A5.1.3 for each vegetation type area at each tree island. Most of the information in those diagrams has been previously presented in Figure 67, Figure 72 and Figure 79. The main difference is that those diagrams look similar to the conceptual model diagram in Figure 6 for each vegetation type area, which makes them easier to understand. Similar diagrams for the whole tree island area are also included in Appendix A5.1. Those diagrams show a lateral outgoing mass flux of dissolved Phosphorus in the OL layer that is a fraction of the mass input rate from rainfall. The numerical results indicate that dissolved Phosphorus losses are very low compared to the Phosphorus losses as suspended litter. These losses are balanced by the calculated total Phosphorus input from an external source. Therefore, the model results suggest that tree islands lose Phosphorus on average mostly as suspended litter and that this amount must be compensated by an external input that may be a result of animal activity (e.g., bird guano, etc), net biomass uptake by a dynamically varying vegetation, and in-soil mineralization.

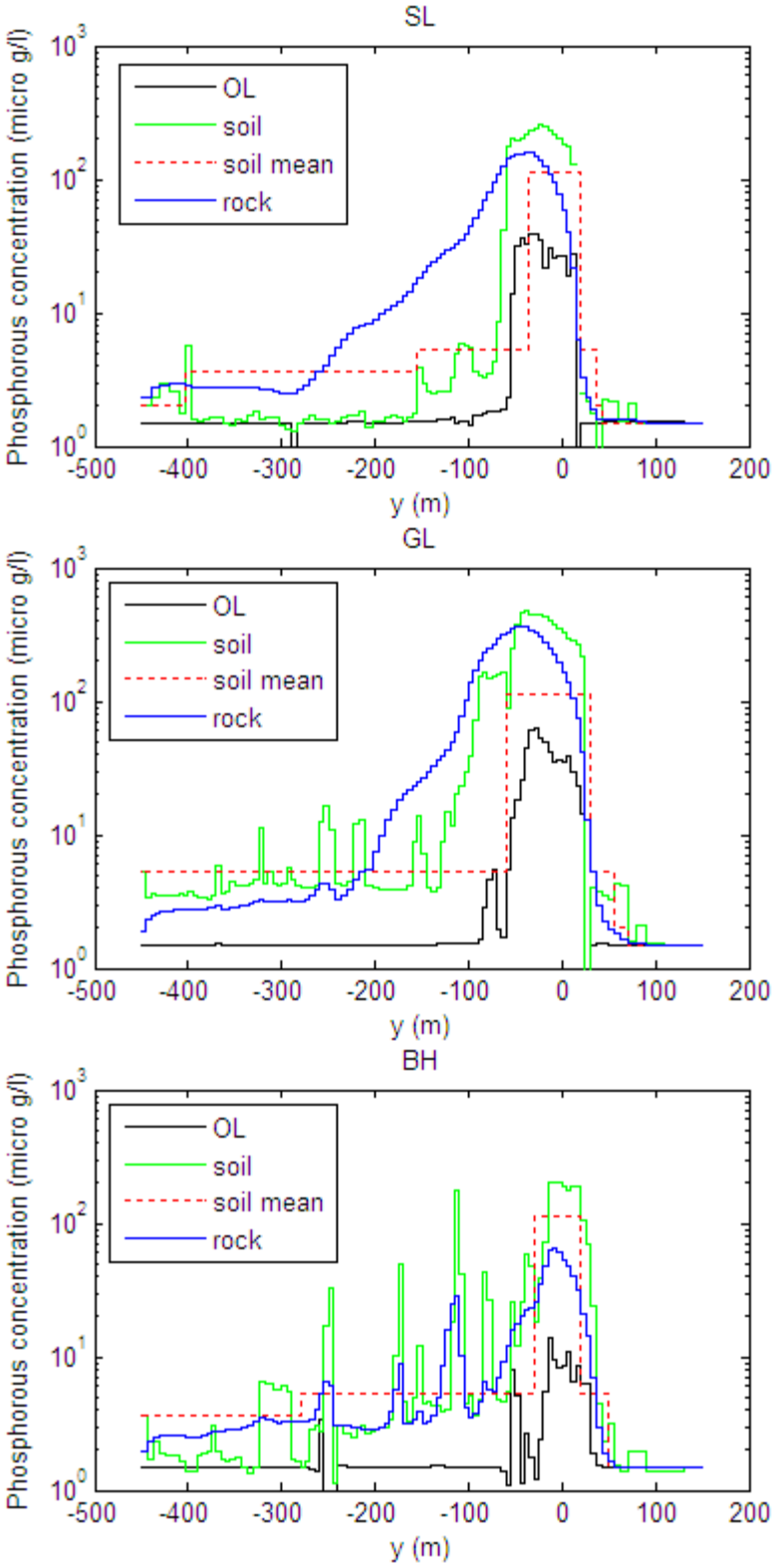

Figure 78. Initial concentration along the tree island axes obtained from the last run for case L1.

SL

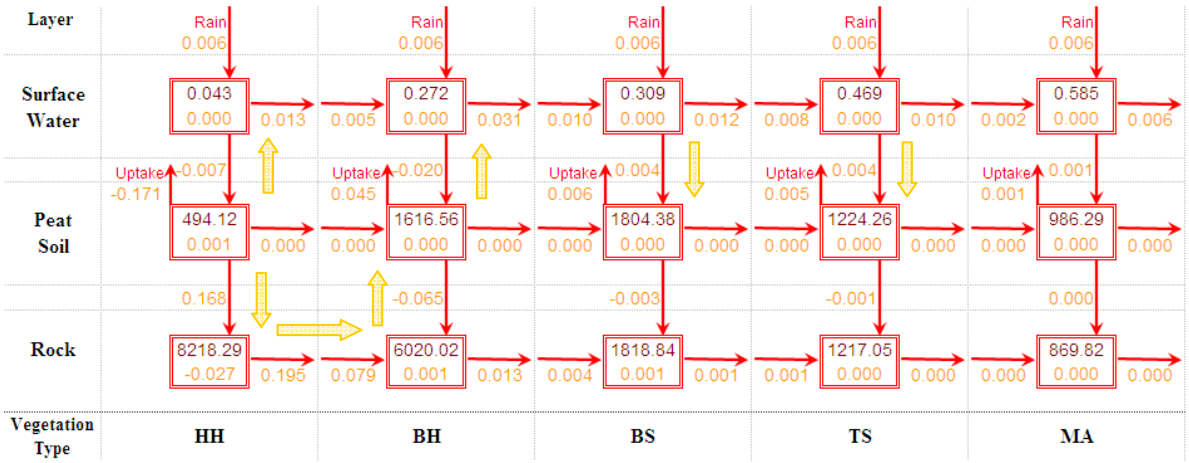

GL

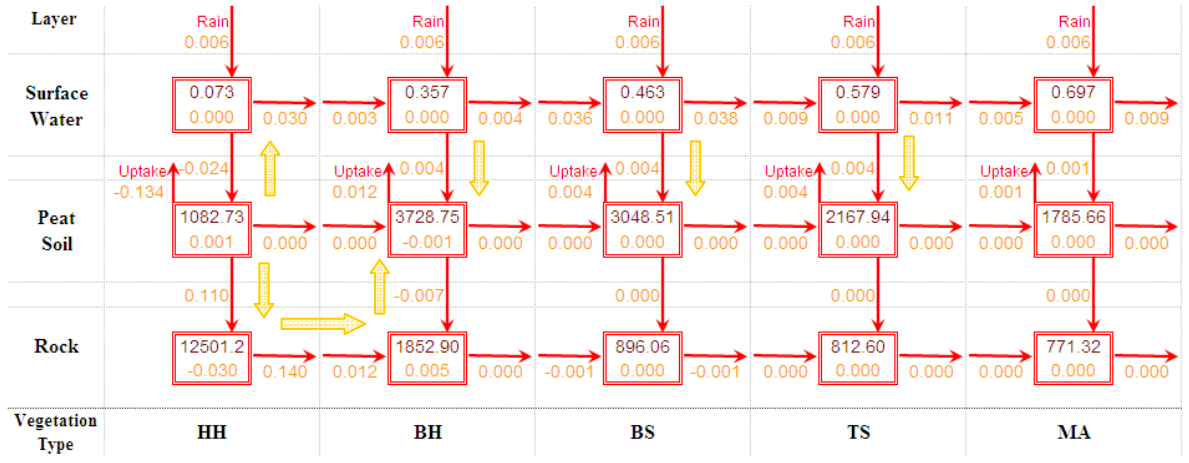

BH

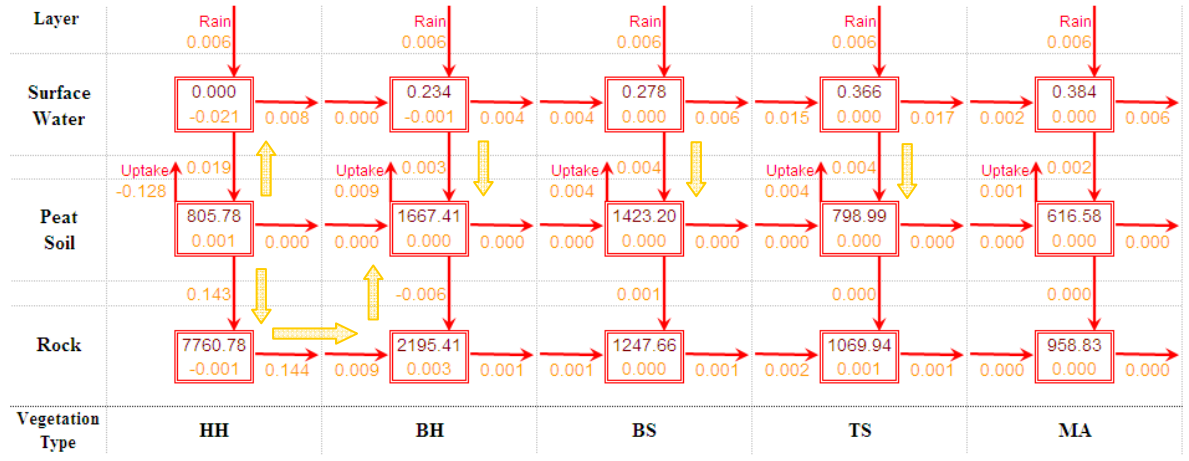

Figure 79. Pools and fluxes of dissolved and adsorbed Phosphorus mass in the model after a 10 year simulation for each tree island for case L1. Pools amounts are in units of mgP/m^2 and fluxes in mgP/m^2/day.

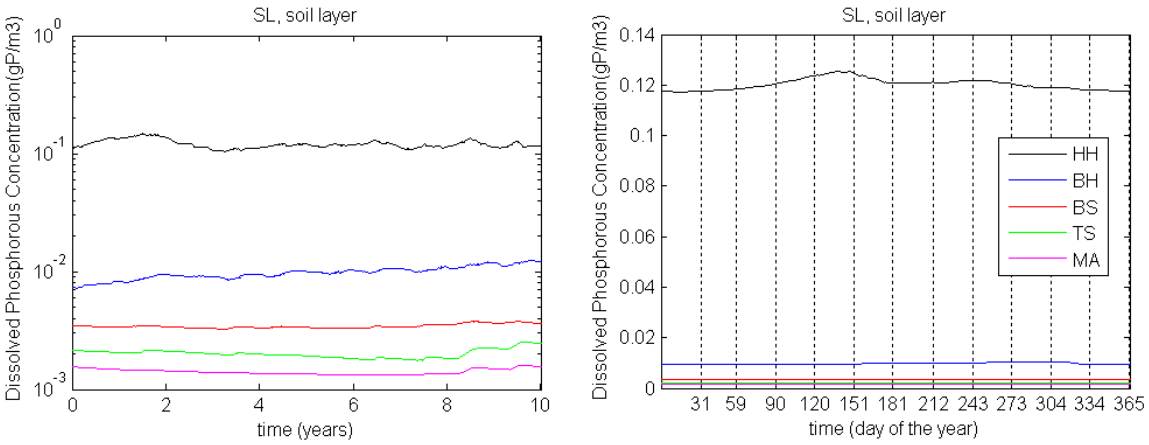

Figure 80. On the left hand side, the evolution of the dissolved Phosphorus concentration (C) in soil layer averaged for each vegetation type area in case L1. On the right hand side, those values are averaged for each day of the year. See plots for other tree islands in Figure A-111.

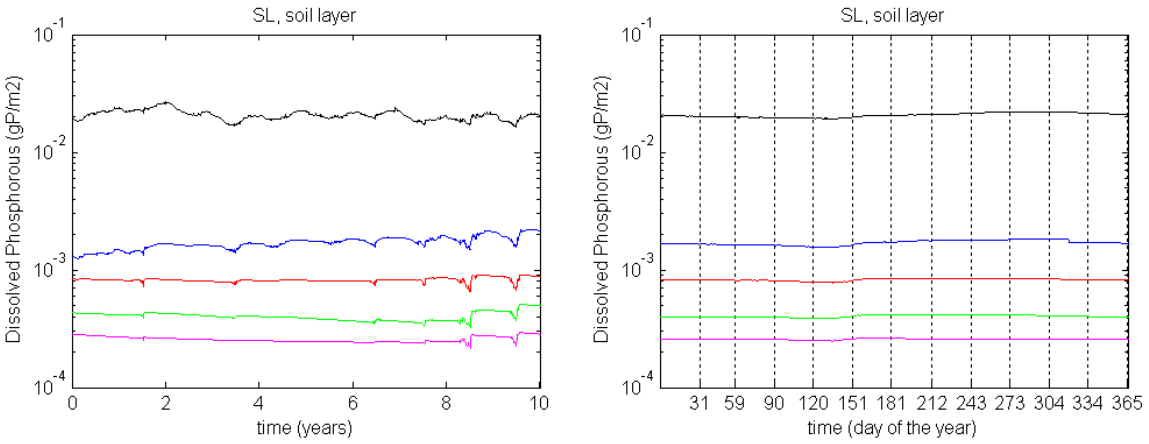

Figure 81. On the left hand side, the evolution of the mass of dissolved Phosphorus per unit area (Ch) in soil layer averaged for each vegetation type area in case L1. On the right hand side, those values are averaged for each day of the year. See plots for other tree islands in Figure A-112.

Pools and fluxes diagrams of Appendix A5.1.3 divide the pool of dissolved and adsorbed Phosphorus of Figure 79 in the two components. Notice that the adsorbed Phosphorus mass in soil and rock is much higher than the mass dissolved in pore water.

The evolution of the dissolved Phosphorus concentration in soil water as well as its average seasonal dependence is shown on Figure 80. Notice that the average concentration in each vegetation type area remains about constant during the whole 10-year time period modeled and that it does not show remarkable seasonal changes. A

similar result is obtained for the mass of dissolved Phosphorus per unit area presented in Figure 81 and for the dissolved Phosphorus concentration in rock water layer in Figure 82. The high mass of adsorbed Phosphorus onto soil and rock surface is acting as a buffer that keeps the dissolved Phosphorus concentration in pore water about constant. Finally, the dissolved Phosphorus concentration in surface water shows a higher variability during the dry season, as shown in Figure 83.

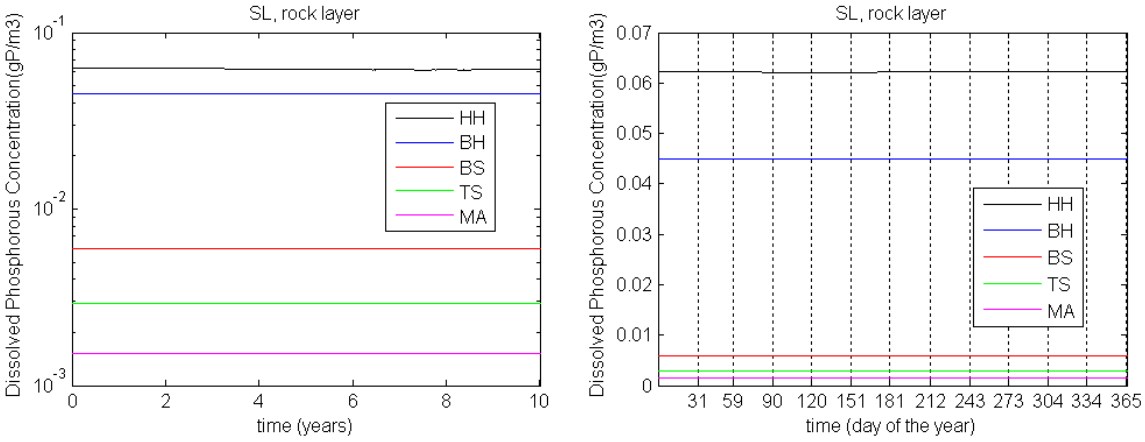

Figure 82. On the left hand side, the evolution of the dissolved Phosphorus concentration (C) in rock layer averaged for each vegetation type area in case L1. On the right hand side, those values are averaged for each day of the year. See plots for other tree islands in Figure A-113.

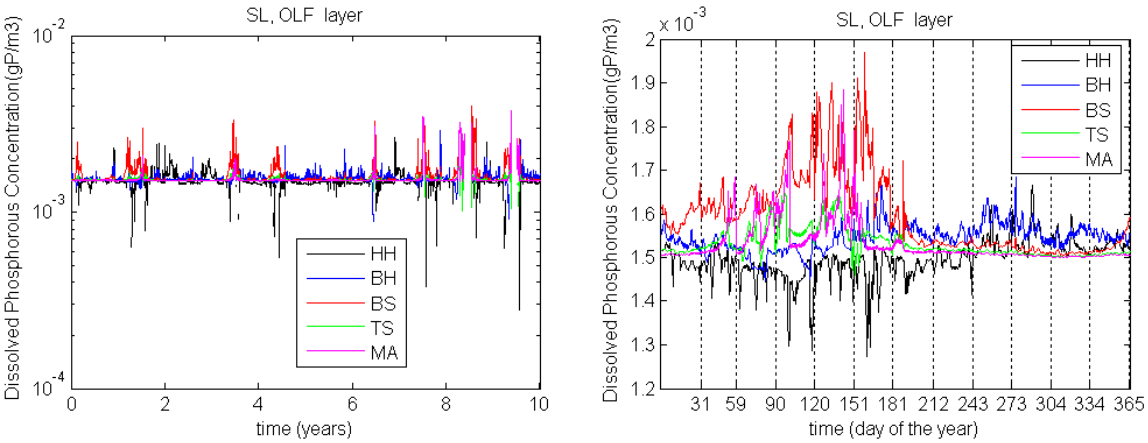

Figure 83. On the left hand side, the evolution of the dissolved Phosphorus concentration (C) in OL layer averaged for each vegetation type area in case L1. On the right hand side, those values are averaged for each day of the year. See plots for other tree islands in Figure A-114.

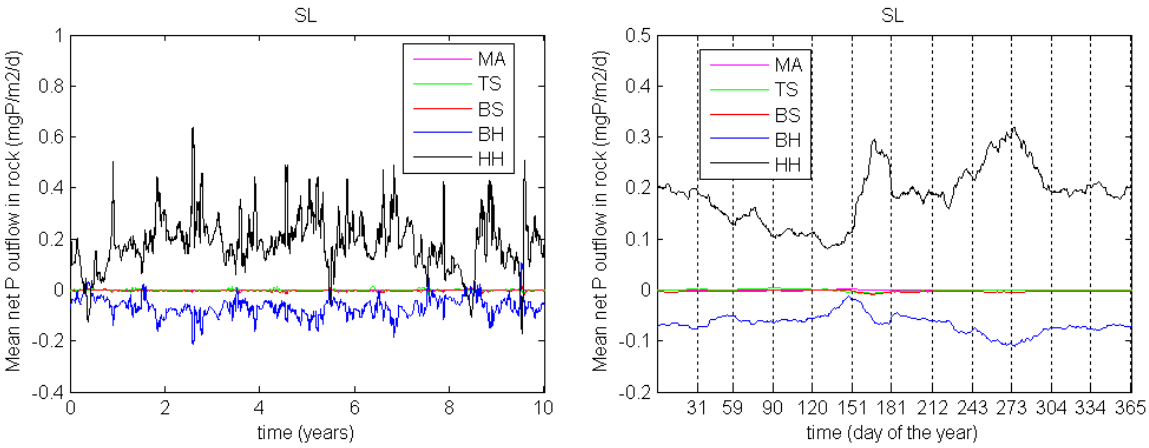

Figure 84. On the left hand side, the evolution of the net dissolved Phosphorus outflow in the rock layer averaged for each vegetation type area in case L1. On the right hand side, those values are averaged for each day of the year. In both cases, a running average with a 15-days window was performed. See plots for other tree islands in Figure A-115.

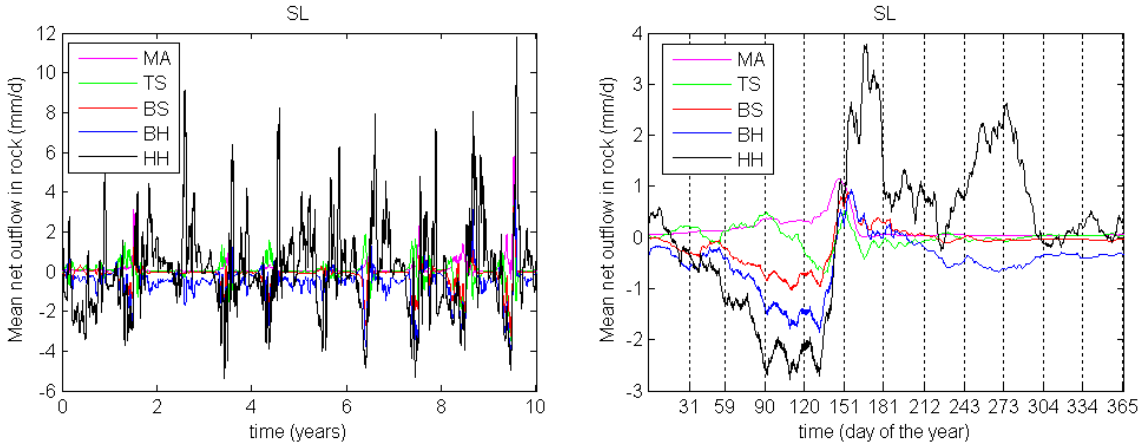

Figure 85. On the left hand side, the evolution of the net water outflow in the rock layer averaged for each vegetation type area in case L1. On the right hand side, those values are averaged for each day of the year. In both cases, a running average with a 15-days window was performed. See plots for other tree islands in Figure A-116.

The evolution of the dissolved Phosphorus net outflow rate in rock water as well as its average seasonal dependence is shown on Figure 84. Notice that it is positive in general for HH and negative for BH, representing a net sustained mass flow through the rock layer from HH into BH area. The difference between the two absolute magnitudes is because the mass flows are divided by the area at each vegetation type, which are different. The outflow spikes through the rock layer are related to heavy-rainfall-driven water outflow events, as seen in Figure 85. However, it may be striking to notice that there is a consistent positive P mass outflow from HH area late in the dry season when

the water outflow is mostly negative, i.e., when the ET-driven water fluxes rule. This net "diffusive" effect is expected from the alternating advective flow between the HH area with higher concentration and the surrounding BH area. Even when the alternating water flow balances out, the advective mass transport from higher concentration area prevails.

5.1.3 Rainfall and ET Driven Fluxes

Several plots in the period containing two different raining events at SL tree islands are shown in Figure 86 and Figure 87. The net recharge rate was computed as the rainfall minus total ET rate (i.e., sum of evaporation and transpiration rates) and it is very similar for different vegetation areas at the same tree island as shown in those graphs. As the rainfall depth rate is assumed uniformly distributed, the small differences in the net recharge for different areas are caused by slight differences in the total evaporation depth rates. This is in correspondence with the small differences in the 10-year averaged net recharge rate for different areas that can be computed from the pools and fluxes representation on Figure 67. Notice also in Figure 86 and Figure 87 that the rainfall rate peak superimposes the ET oscillatory pattern, which has higher rates during the day and lower at night.

The horizontal volumetric and mass flow from HH areas is also shown in Figure 86 and Figure 87. Note that water from rainfall flows away from HH area mainly through the rock layer, which may be comparable to the flow through the OL layer (runoff). However, as the surface water has a low dissolved Phosphorus concentration, the transport of dissolved Phosphorus occurs primarily through the rock layer. This loss of dissolved Phosphorus in HH area during rainfall events causes a decrease in the Phosphorus pool in soil (dissolved and adsorbed), as shown in the accumulation rate for the HH area also plotted in those figures. When there is no rain, the ET driven water flow toward the HH area cannot avoid a positive Phosphorus mass outflow (loss) from it. However, a positive accumulation rate in HH soils in absence of rain is observed in those figures because of the external Phosphorus input.

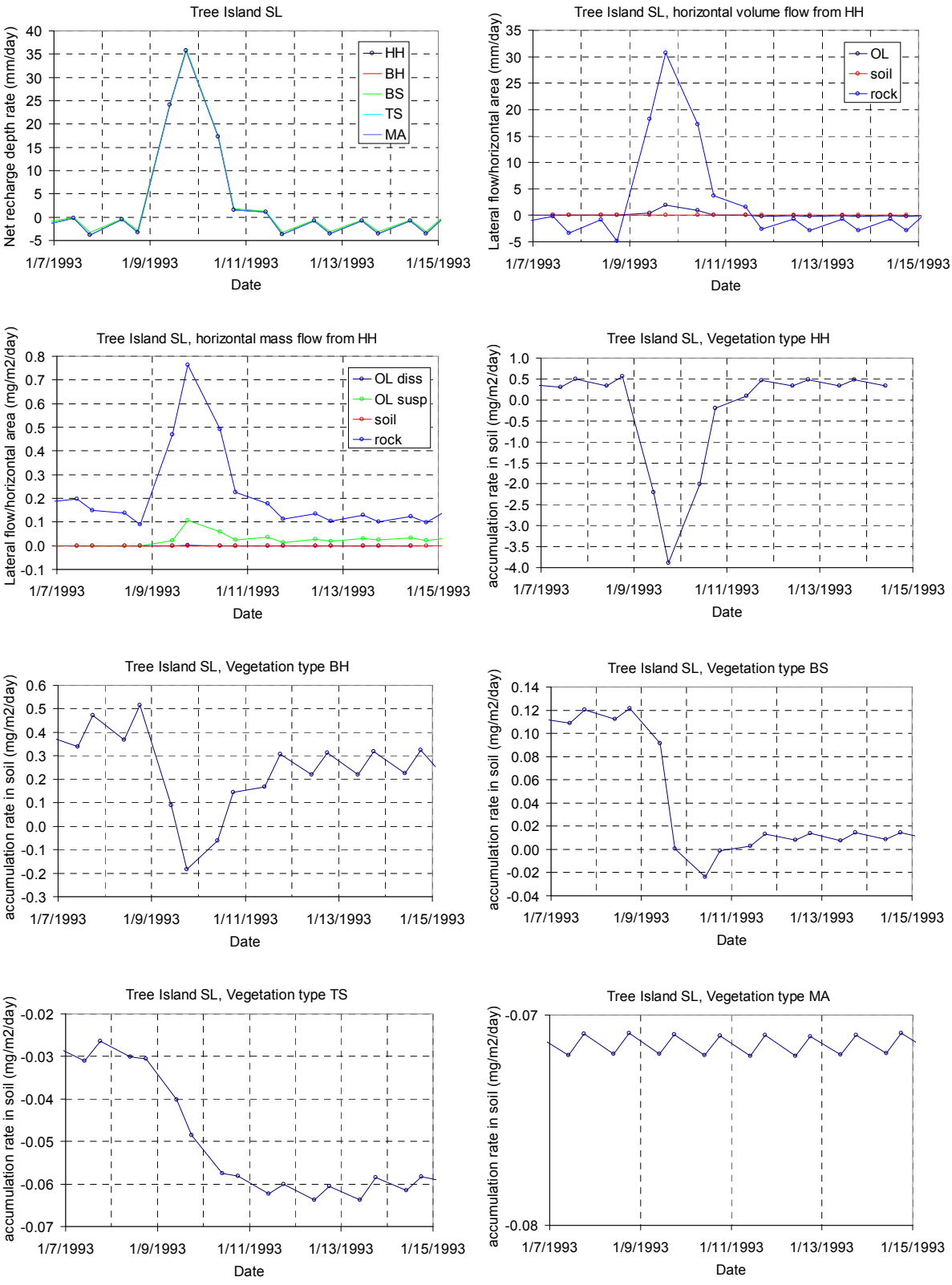

Figure 86. Several plots showing the evolution of the variables at SL Tree Island around the rainfall event occurred on Jan 9, 1993. See text for details.

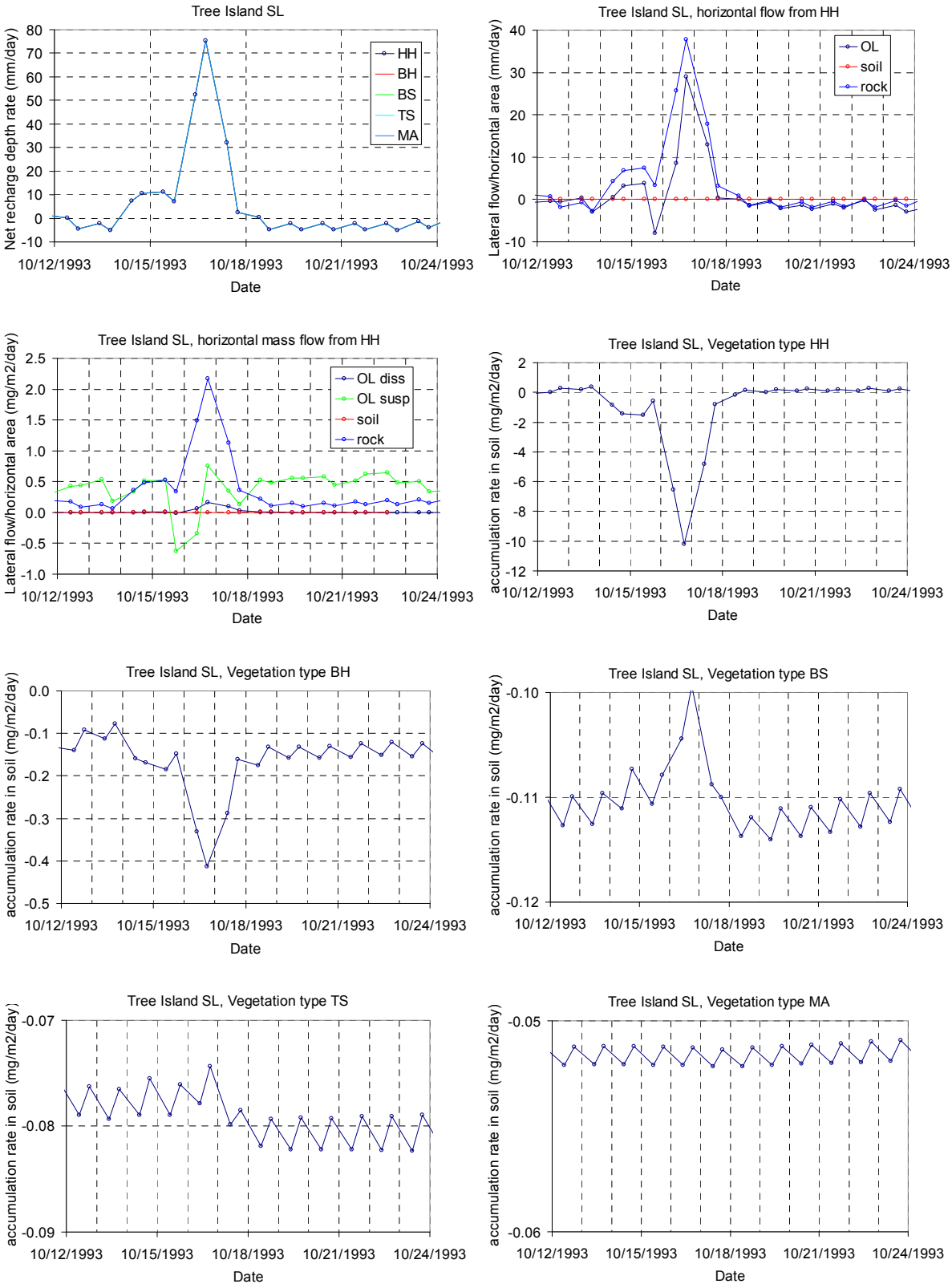

Figure 87. Several plots showing the evolution of the variables at SL Tree Island around the rainfall event occurred on Oct 16, 1993. See text for details.

These results are in correspondence with the expected rainfall and ET driven fluxes from the head of the island sketched in Figure 3 and Figure 4 of the introductory chapter. However, the inability of the ET-driven Phosphorous transport to concentrate Phosphorous in the head of the island, before and after the two rainfall events studied (in October and January), is contrary to the important role of ET in Phosphorus accumulation hypothesed by other authors in the literature.

On the other hand, the effect of the rainfall event on the Phosphorus accumulation rate in soil decreases from HH to MA areas, as shown in the accumulation rate plots in Figure 86 and Figure 87. In BH areas a decrease of the accumulation rate is observed during the rainfall, in form of broad peak with similar shape. Moreover, in the BH, BS and TS areas there may be stepwise changes in the accumulation rates associated to the water level change after the rain. In the MA area, the accumulation rate seems not to be affected by the rainfall events.

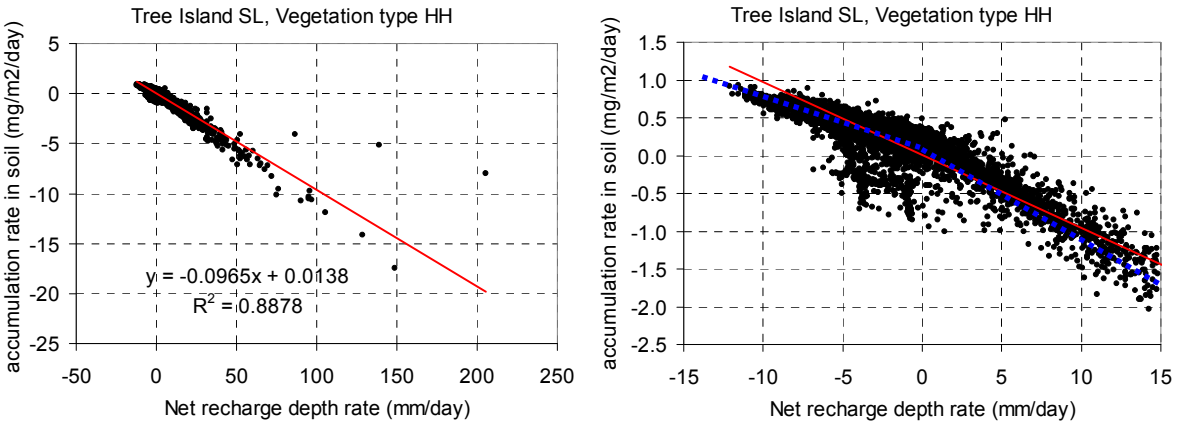

Figure 88. Negative correlation between the accumulation rates of dissolved and adsorbed Phosphorus in soil layer at HH areas and the net recharge rate (rainfall - total ET rate). See plots for other tree islands in Figure A-137.

The plots related to the same rainfall events for the case of GL and BH tree islands are presented in Figure A-135 and Figure A-136. Here again, it is observed that rainfall driven Phosphorus transport through the rock layer produces losses of Phosphorus in HH soils and a positive accumulation of Phosphorus in soil in absence of rainfall. In fact, there is a clear negative correlation between the net recharge (rainfall minus ET) rate and the Phosphorus accumulation rate in soil, which is shown in Figure 88 by using the whole 10-year period of data resulting from the model. The net result of

these rainfall and ET driven processes is a net loss of Phosphorus in HH soils, as sketched before on Figure 79.

Finally, the Phosphorus-in-suspended litter fluxes from HH to BH areas during the two rainfall events were also included from Figure 86 and Figure 87. The rainfall events may increase these OL fluxes in the case of runoff or a consequent increase in the water levels. In those graphs, the rainfall driven peaks corresponding to the lateral transport of dissolved Phosphorus through the rock layer were always higher than the Phosphorus-in-suspended litter transport peaks. Nevertheless, there is in average an important positive transport of Phosphorus-in-suspended litter from HH to BH areas. According to Figure 72 and Figure 79, the net Phosphorus losses from HH areas due to suspended litter transport averaged in a 10-year frame are from 1.5 to 4 times higher than the net losses from dissolved Phosphorus transport through the rock layer.

5.2 Results for Research Objectives

In this section, the model results are further discussed in correspondence with the five main objectives (or research questions) listed in section 1.4.

5.2.1 Spatial and Temporal Variations of Phosphorus Mass and Fluxes

The spatial and temporal variations of the Phosphorus mass and fluxes around the tree islands, as predicted by the model, are presented in this section by considering the spatial distribution in three temporal scales: annual, seasonal and daily. This analysis is the first main objective listed in section 1.4 and it was used to later address the other four objectives.

5.2.1.1 Annual Scale

The annual averaged fluxes of Phosphorus-in-suspended litter were sketched in Figure 72. The net horizontal transport of suspended litter removes in average Phosphorus from HH, BH and TS areas and it brings Phosphorus into BS and MA areas. There is also a positive flux of Phosphorus-in-suspended litter from MA areas to the model boundary. On the other hand, the Phosphorus-in-suspended litter mass per unit area increases monotonically away from the head of the island, i.e., from HH to MA areas.

In Figure 72, the Phosphorus-in-deposited litter in HH area has the highest amounts followed by TS, BH, MA and BS ones. The lowest amounts in BS and MA are consequence of the low amount of Phosphorus-in-litter produced in those areas, that are not compensated by the by the horizontal net inflow of Phosphorus-in-suspended litter.

As result from the litter transport and decomposition process, the net release of Phosphorus from biomass shown in Table 29 has the highest positive value in BS area followed by MA. Then, HH and BH are at about the same level and after them the TS area corresponding to the lowest net release rate.

The annual averaged fluxes of dissolved Phosphorus were sketched in Figure 79. The infiltration due to the transpiration causes a net advective transport of Phosphorus from the overland layer into the soil for BS, TS and MA areas. However, in the HH area there is a net transport from the soil to the overland layer (soil pool losses) and in the BH area it depends on the tree island. Moreover, there is an important amount of dissolved

Phosphorus moving from the soil to the rock in the HH area, then moving laterally at the rock layer and finally emerging in the BH area to the soil layer. The annual Phosphorus losses in HH areas from this transport, however, are from 1.5 to 4 times lower than the losses due to suspended litter transport.

In Figure 79, the amount of dissolved and adsorbed Phosphorus mass is a maximum in BH areas of the soil layer and in HH areas of the rock layer, decreasing monotonically toward the MA area. According to the figures of Appendix A5.1, the mass of adsorbed Phosphorus is much higher than the dissolved Phosphorus mass in pore water.

The external input rate predicted by the model to keep the average dissolved-Phosphorus concentration in soil pore water is positive in HH, BH and TS areas and negative in BS and MA areas, as shown in Table 29. According to this table, this is mainly caused by the transport of suspended litter.

In the pools and fluxes diagrams for the whole tree island presented in Appendix A5.1, there is a lateral outgoing mass flux of dissolved Phosphorus in the OL layer that is a fraction of the mass input rate from rainfall. The dissolved Phosphorus losses, however, are very low compared to the Phosphorus losses as suspended litter, which are very close to the total Phosphorus input from external sources. Therefore, the model suggests that on average tree islands lose Phosphorus mostly as suspended litter and that this amount must be compensated by an external input.

The concentration profiles presented in Figure 78 show spots with higher concentration which are favored by the suspended litter transport and subsequent release by decomposition. In some areas, the higher Phosphorus concentration in soil is correlated to a higher concentration in the rock cells located below. This result is in correspondence with the high statistical dispersion in the SRP values in pore soil water surveyed by [Ross et al., 2004] at the tree islands, even inside the same vegetation type areas.

5.2.1.2 Seasonal Scale

According to Figure 73 and Figure 74, the Phosphorus-in-suspended litter mass per unit area has a minimum value at the end of the dry season (end of May) and a maximum at the end of wet season (end of September), which is similar to the seasonal

dependence of the water depth shown in Figure A-96. The Phosphorus-in-suspended litter concentration, however, has maximum values during the dry season.

The Phosphorus-in-suspended-litter transport causes sustained losses through the year at HH, BH and TS areas; meanwhile it causes a period of Phosphorus accumulation at BS and MA areas during the wet season. Figure 77 shows that the maximum Phosphorus loss rate at all vegetation type areas occurs in the period from the end of October to the beginning of January.

The Phosphorus-in-deposited litter plots in Figure 75 show a temporal dependence without a clear seasonal dependence.

The net release of Phosphorus from biomass plotted in Figure 76 reveals in average an increase during the dry season compared with the wet season, which is expected from the seasonal dependence of the decomposition rate.

The dissolved Phosphorus concentration in soil and rock water does not show remarkable seasonal dependence, as shown in Figure 80 and Figure 82, respectively. A similar result is obtained for the mass of dissolved and adsorbed Phosphorus per unit area presented in Figure 81. The high mass of adsorbed Phosphorus onto soil and rock surface is acting as a buffer that keeps the dissolved Phosphorus concentration in pore water about constant. On the other hand, the dissolved Phosphorus concentration in surface water shows a higher temporal variability during the dry season as shown in Figure 83.

The dissolved Phosphorus transport causes in average a sustained net Phosphorus mass outflow through the rock layer from the HH into the BH area, as shown in Figure 84. This Phosphorus outflow is higher during the rainy season, as expected from the rainfall-driven advective flows. However, it may be striking to notice that there is a positive Phosphorus mass outflow from HH area late in the dry season when the ET driven water fluxes rule, as shown in Figure 85. This net “diffusive” effect is expected from the alternating advective flow between the HH area with higher concentration and the surrounding BH area.

5.2.1.3 Daily Scale

On the daily scale, the soil surface changes from dry to wet or from wet to dry may cause abrupt changes in the decomposition rate from aerobic to anaerobic conditions or vice versa, respectively. Those changes in the decomposition rates affect the net

release of Phosphorus from biomass as shown in Figure 76. Moreover, frequent wet-dry changes during the dry season produce the high temporal variability in dissolved Phosphorus concentration in surface water observed in Figure 83.

Nevertheless, the most important daily-scale changes in the Phosphorus mass and fluxes around tree islands are related to the rainfall events and to the daily oscillations in the ET rates. In section 5.1.3, several variables were plotted from Figure 86 and Figure 87 during two rainfall events. The water from rainfall flows away from HH area mainly through the rock layer, which may be comparable to the flow through the OL layer (runoff). However, as the surface water has a low dissolved Phosphorus concentration, the transport of dissolved Phosphorus occurs primarily through the rock layer. This loss of dissolved Phosphorus in the HH area during rainfall events causes a decrease in the Phosphorus pool in soil (dissolved and adsorbed). When there is no rain, the ET driven water flow toward the HH area cannot avoid a positive Phosphorus mass outflow (loss) from it. However, a positive accumulation rate in HH soils in absence of rain is observed in those graphs because of the external Phosphorus input. In fact, there is a clear negative correlation between the net recharge (rainfall minus ET) rate and the Phosphorus accumulation rate in soil, which is shown in Figure 88.

These results are in correspondence with the expected rainfall and ET driven fluxes from the head of the island sketched in Figure 3 and Figure 4 of the introductory chapter. However, the inability of the ET-driven Phosphorous transport to concentrate Phosphorous in the head of the island, before and after the two rainfall events studied, is contrary to the important role of ET in Phosphorus accumulation hypothesed by other authors in the literature.

On the other hand, the effect of the rainfall event on the Phosphorus accumulation rate in soil decreases from HH to MA areas. In the MA areas, the accumulation rate seems not to be affected by the rainfall events. The net result of these rainfall and ET driven processes is a net annual loss of Phosphorus in HH soils as sketched on Figure 79.

The Phosphorus-in-suspended litter fluxes from HH to BH areas during the two rainfall events were also included from Figure 86 and Figure 87. In those graphs, the rainfall driven peaks corresponding to the lateral transport of dissolved Phosphorus through the rock layer were always higher than the Phosphorus-in-suspended litter

transport peaks. Nevertheless, in annual average, the transport of Phosphorus-in-suspended litter from HH to BH areas is higher than the dissolved Phosphorus transport.

5.2.2 Effect of Rainfall and ET on Phosphorus Accumulation

As discussed in section 5.1.3, the dissolved and adsorbed Phosphorus mass in HH soils decrease during rainfall events mainly through advective outgoing fluxes through the rock layer. When there is no rain, the ET driven water flow toward the HH area cannot avoid a positive Phosphorus mass outflow from it. A positive accumulation rate in HH soils in absence of rain is observed because of the external Phosphorus input. In fact, there is a negative correlation between the net recharge rate and the Phosphorus accumulation rate in HH soils. The net result of these rainfall and ET driven processes is an annual net loss of Phosphorus in HH soils.

These results in a daily scale are in agreement with the seasonal dependence of the dissolved Phosphorus transport through the rock layer from HH into BH area discussed in section 5.1.2. This Phosphorus outflow is higher during the rainy season, as expected from the rainfall-driven advective flows. However, there is also a positive Phosphorus mass outflow from HH area late in the dry season when the ET driven water fluxes rule. As result, a sustained net Phosphorus mass outflow (loss) is obtained through the whole year. The rainfall events may increase the OL outgoing fluxes of Phosphorus in suspended litter in the case of runoff or a consequent increase in the water levels. In the two rainfall events analyzed in section 5.1.3, they were observed OL outgoing fluxes of Phosphorus in suspended litter. However, the rainfall driven peaks corresponding to the outgoing transport of dissolved Phosphorus through the rock layer were always higher than the Phosphorus-in-suspended litter transport peaks.

In summary, the model predicts a negative effect of the rainfall events on Phosphorus accumulation in the head of the tree islands due to outward dissolved transport in the rock layer. These rain-driven Phosphorous losses in addition to the losses caused by the suspended litter transport need to be compensated by an external input. The possible positive effect of the ET driven water flows on Phosphorous accumulation was found not as relevant as hypothesed by other authors in the literature. The ET driven water flows through the rock layer do not prevent a sustained net Phosphorus mass outflow (loss) during the whole year.

5.2.3 Importance of Suspended and Dissolved Phosphorus Transport

On average, there is an important positive transport of Phosphorus-in-suspended litter from HH to BH areas. In fact, the average annual net Phosphorus losses from HH areas due to suspended litter transport are from 1.5 to 4 times higher than the net losses from dissolved Phosphorus transport through the rock layer, which is the net result of the rainfall and ET driven fluxes.

In other vegetation type areas the transport of Phosphorus-in-suspended litter is the most important process. The differences in the horizontal incoming and outgoing fluxes determine almost completely the input from external sources necessary to keep the average dissolved Phosphorus concentration in soil.

In the scale of the whole tree island model, the dissolved Phosphorus losses are found to be very low compared to the Phosphorus losses as suspended litter; these losses are balanced by the calculated external Phosphorus input on the whole model area. Therefore, the model results suggest that tree islands lose Phosphorus on average mostly as suspended litter and that this amount must be compensated by an external input that may be a result of animal activity input (e.g., bird guano, etc), net biomass uptake by a dynamically varying vegetation, and in-soil mineralization.

In summary, the model predicts that the Phosphorus-in-suspended litter transport is more relevant in general for the tree island than the dissolved-Phosphorus transport, even when the contribution of the dissolved-Phosphorus transport cannot be neglected in the tree island head.

5.2.4 Importance of External Input in Tree Island Preservation

In section 5.2.2, it was concluded from the model results that ET driven fluxes were not able to compensate the dissolved Phosphorus losses in soil at the tree island head caused by rainfall events. Moreover, in section 5.2.3 the model results suggested that the Phosphorus-in-litter transport cause the most important Phosphorus losses or buildups in the different vegetation type areas that can be only equilibrated from an external Phosphorus input. On the scale of the whole tree island, there are Phosphorus losses as suspended litter that need to be compensated from a net Phosphorus input from an external source, such as animal activity. This finding supports the hypothesis that tree

island preservation is dependent on the preservation of the wading birds and other wild life forms in the Everglades.

5.2.5 Phosphorus-Driven Vegetation Changes

The input rates necessary to compensate Phosphorus losses in HH and BH areas in the range from 0.1 to 0.3 $g/m^2/y$ (see Table 29) are reasonable regarding the value of 0.9 $g/m^2/y$ estimated for a colony of wading birds in the Everglades by Frederick and Powell [1994]. However, it is unlikely that the animal activity could generate an input rate of 0.3 $g/m^2/y$ in TS areas or cause a negative input rate in BS areas. These unexpected results may be a consequence of considering the vegetation pool in equilibrium. In the case of biomass growth or death, the Phosphorus mass in the live biomass pool changes and the model assumption of Phosphorus uptake being equal to the Phosphorus-in-litter produced may no longer be applicable.

Sawgrass die-off events have been observed while comparing aerial photos of the same areas around the tree islands [Jose Bazante, personal communication]. The hypothesis that has been proposed is that these events may be a consequence of longer hydroperiod causing water stress (by extended period of flooding) to the sawgrass. The model however, is suggesting another hypothesis to explain the observed sawgrass die-off. If in tall sawgrass areas the Phosphorus is being lost due to the transport of suspended litter, then the tall sawgrass would become eventually nutrient stressed. The Phosphorus removal rate is higher in wet periods than in drier ones as shown on the seasonal dependence on Figure 76, which may explain a correlation to extended hydroperiod. Therefore, the vegetation in TS areas would eventually die due to lack of Phosphorus, and it would be succeeded by a lower density MA vegetation type.

On the other hand, the transport of suspended litter in MA areas of the model causes a net Phosphorus deposition, as shown in Table 29, and these areas may become favorable for the sparse sawgrass to growth and become a TS vegetation type. Next, the TS area would exist until is nutrient stressed and so on, as sketched in Figure 89.

The study about the validity of the hypotheses concerning the cyclic succession of TS and MA vegetation types around the tree islands, based on their effect of removal or accumulation of Phosphorus in soil, is an attractive project to extend this study in a future work. It should be mentioned however, that an accurate field estimate of the average

Phosphorus levels in soil in the different tree island areas would require an intensive sampling due to the high spatial variability of point measurements of Phosphorus content in soil and in pore water, as revealed in the surveyed data collected by the Ross et al. [2004].

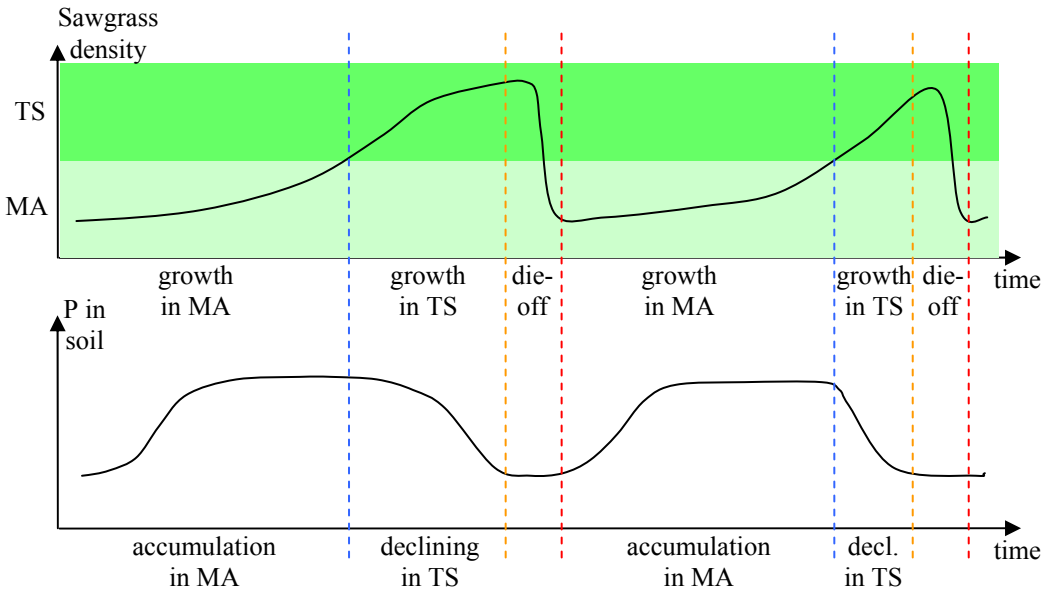

Figure 89. Probable evolution of Sawgrass density and Phosphorus concentration in soil pore water during a cyclic succession of TS and MA vegetation types around tree islands.

Chapter 6. Conclusions and Recommendations

This chapter contains a summary of the model development and the main results, as well as the recommendations for future work.

6.1 Model Development Summary

In this work a conceptual and numerical model is proposed and developed to study the temporal and spatial variations of the Phosphorus mass and fluxes around the tree islands of Shark River Slough in the Everglades.

The conceptual model considers the advective and diffusive transport of dissolved Phosphorus, adsorption into soil, input from rainfall and external sources (e.g., animal activity and other sources), and the Phosphorus cycling in biomass that includes uptake, release as litter, transport as suspended litter and release from the decomposition of the deposited litter. The water flow and transport of dissolved Phosphorus in the numerical model are implemented originally by using MODHMS. However, the transport equations for dissolved Phosphorus were also programmed using a finite volume scheme (coded in MatLab) in order to overcome the limitation that the WEL package of MODHMS has in not considering extraction of dissolved species. The developed code reproduces the MODHMS results adequately. In addition, the Phosphorus mass balance equations in suspended litter particles and in deposited litter are implemented in the same code in order to consider the biomass contribution to the Phosphorus cycling.

The parameterization of the model was based primarily on the data collected by Ross and co-workers in the three islands of Shark River Slough. The time series for rainfall and stage were taken mainly from SFWMD database, as well as water quality data. ET data was obtained from measurements conducted by German [2000]. The values of other parameters of the model were obtained from the literature at Shark River Slough, other areas of the Everglades or even other sites.

The assumptions and limitations introduced in the development of the conceptual model, the numerical implementation and the parameterization were clearly stated. The calibration of the model was conducted in the three stages described next.

The Manning coefficients for each vegetation type area of the model were calibrated from surface water velocity data collected by Bazante and co-workers. The developed calibration procedure computes the Manning coefficient from field velocities, field water depths and local slopes from the model. The median values of the estimated Manning coefficients for each vegetation type are used in each iteration to propose new coefficients in the model for the next step. The velocity from the calibrated model reproduces on average the field measurements, which is reasonable considering that those velocities represent different scales.

The calibration of several groundwater flow parameters was conducted from water table data collected at wells by Ross and co-workers. The adjusted parameters are the leakage, the conductivity and porosity at soil and rock layers, the unsaturated flow parameters and the transpiration contribution into the total ET rate. They all have a validity range defined from the literature that bounds their variation during the calibration process. The change of the stress periods from one hour long to twice a day was necessary to decrease the running time and make possible the high number of different runs during the calibration process. Four objective functions (overall errors) were defined from the deviations between the observed and the modeled data, which have different sensitivity to extreme values and to daily oscillations. Once the objective function is chosen, a simple minimizing procedure is followed in order to find the set of parameters that produces a local minimum in the overall error. For this purpose, a shell was coded in order to modify the input files, run the MODHMS executable, read the output files and obtain the overall errors. The objective function and the starting point were changed in order to avoid getting stuck in local minima and try to reach the global minimum for each overall error. At the end, a similar procedure to adjust the top and bottom elevation of the soil layer at observation-well cells was carried out. After the calibration process, the prediction of the seasonal oscillations, the rainfall peaks and the diurnal oscillations in the water table was improved.

The transport part of the model was calibrated by fitting the external Phosphorus input rate from external sources as well as the initial Phosphorus concentration. The calibration procedure imposed that the averaged concentration in the soil layer for each vegetation type area at the beginning and the end of a ten-year period must be equal to

the averaged values measured in the field. The calibration has been conducted progressively in three steps. In the first step, the fitting procedure was conducted by running the MODHMS inside a shell to solve the dissolved Phosphorus transport problem. In this case, a simpler model was assumed by neglecting the biomass contribution to the Phosphorus transport. MODHMS was unable to find the negative values for the external input of Phosphorus for some vegetation type areas. In the second step, MODHMS was replaced by the developed code in MatLab to solve the dissolved Phosphorus transport problem. This allowed validation of the developed code and determination of the external input rates for all vegetation type areas. In the third step, the biomass contribution to the Phosphorus mass and fluxes is considered by solving the balance equation for Phosphorus in suspended and in deposited litter.

The model results were presented in several ways. The spatial dependence of the water volume and Phosphorus mass was represented in form of boxes (pools) for every vegetation type area and vertical layer. The annual averaged fluxes between the different pools were also displayed. Moreover, the seasonal dependence was presented in plots with average values for each day of the year for every vegetation type area and vertical layer. Graphs showing the temporal evolution of the variables and the profile of the variables along the longitudinal axes of the tree islands were also produced.

6.2 Main Results

The main results from the developed model are related to the five specific objectives for this study that were listed in introductory section 1.4 and addressed later from the model results in Chapter 5.

1) A quantitative assessment of the spatial distribution and temporal variations of Phosphorus mass and fluxes around tree islands was obtained, which was used to address the other objectives. The spatial distribution of mass and fluxes was found for the different vegetation types (HH, BH, BS, TS and MA) in the different vertical layers (OL, soil and rock) of the model. The temporal variations of Phosphorus mass and fluxes were analyzed in an annually averaged, a seasonally averaged and a daily scale. Such detailed assessment of the Phosphorus mass and fluxes in the tree islands has not been estimated (from previous models) or measured before and it is relevant for any future study related to the nutrients in the tree islands of the Everglades.

2) The negative effect of the rainfall events on Phosphorus accumulation in the head of the tree island were confirmed by the model results. However, the possible positive effect of the ET driven water flows on Phosphorous accumulation was found not as relevant as hypothesed by other authors in the literature. The dissolved and adsorbed Phosphorus mass in HH soils decreased during rainfall events mainly through advective outgoing fluxes through the rock layer. When there is no rain, the ET driven water flow toward the HH area cannot avoid a positive Phosphorus mass outflow (loss) from it. A positive accumulation rate in HH soils in absence of rain is observed because of the external Phosphorus input. This is translated into a clear negative correlation between the net recharge (rainfall minus ET) rate and the Phosphorus accumulation rate in HH soils. OL outgoing fluxes of Phosphorus in suspended litter from HH were also observed during rainfall events, but the rainfall driven peaks corresponding to the outgoing transport of dissolved Phosphorus through the rock layer were always higher than the Phosphorus-in-suspended litter transport peaks. The rain-driven Phosphorous losses in addition to the losses caused by the suspended litter transport need to be compensated by an external input. The ET driven water flows through the rock layer do not prevent a sustained net Phosphorus mass outflow (loss) during the whole year.

3) The transport of dissolved Phosphorus around tree islands is found in general to be less relevant than the transport of Phosphorus constituent suspended (litter) particles in overland flow. The average annual net Phosphorus losses from HH areas due to suspended litter transport are from 1.5 to 4 times higher than the net losses from dissolved Phosphorus transport through the rock layer, which is the net result of the rainfall and ET driven fluxes. In other vegetation type areas the differences in the horizontal incoming and outgoing fluxes determine almost completely the input from external sources (e.g., animal activity and other sources) necessary to keep the average dissolved Phosphorus concentration in soil. On the scale of the whole tree island, the dissolved Phosphorus losses are very low compared to the Phosphorus losses as suspended litter, which is very close to the total Phosphorus input from external sources. In summary, the model predicts that the Phosphorus-in-suspended litter transport is more relevant in general for the tree island than the dissolved-

Phosphorus transport, even when the contribution of the dissolved-Phosphorus transport cannot be neglected in the tree island head.

4) The model results indicate that an external input of Phosphorus from an external source (e.g., animal activity and other sources) is needed to preserve the average Phosphorus levels in the tree island. According to the model, ET driven fluxes are not able to compensate the dissolved Phosphorus losses in soil at the tree island head caused by rainfall events and by the Phosphorus-in-litter transport. In the scale of the whole tree island, there are Phosphorus losses as suspended litter that needs to be compensated from a net external input of Phosphorus. This is an important result from the model because it supports the hypothesis that tree island preservation may depend on the preservation of the wading birds and other wildlife forms in the Everglades.

5) Vegetation changes are inferred from Phosphorus accumulation or losses in certain areas. The input rates to compensate Phosphorus gain or losses in BS, TS and MA areas could not be justified by animal activity. Therefore, Phosphorus mass may be accumulating in BS and MA areas and decaying in TS areas, which may cause the growth and reduction of the vegetation, respectively.

6.3 Future Work

The quantitative assessment of the spatial distribution and temporal variations of Phosphorus mass and fluxes around tree islands is a complex problem and it was necessary to make assumptions in order to simplify that problem so that an adequate numerical solution was possible with the developed computational methods and data, in the timeframe of this PhD thesis. Thus, additional work may be focused in further exploring some of the limitations in the model formulation, its implementation and parameterization. The proposed improvements are listed below.

1) The soil surface elevation and the vegetation coverage could be better mapped around the tree islands when new data becomes available in order to obtain a better assessment of the OL flow pattern. The classification of the vegetation in more than 5 types may help the more precise determination of the vegetation resistance among other vegetation related parameters. There are ongoing efforts about using image analysis of aerial pictures to obtain a more detailed vegetation mapping around the

three islands [Jose Bazante, personal communication]. Moreover, a vegetation dynamic module could be coupled to the model in order to obtain the vegetation coverage changes on time and also to relate the vegetation resistance not only to the vegetation type but also to the above-ground biomass amount at every model cell.

2) Manning's equation (used as the momentum equation for the OL water flow problem) could be replaced by a more appropriate equation (like the Forchheimer equation) at higher density vegetated areas like TS. The wind stress could be also included in the momentum equation for a better prediction of the surface water movement in days of sustained wind.

3) The existence of openings in the limestone rock layer originated by slow carbonate rock dissolution is well known in the Everglades. This could be represented in the model by defining the rock layer boundaries accordingly and by assigning non-uniform hydrodynamic and transport properties. A survey to obtain such a detailed representation of the rock layer around the tree islands may be necessary in the future, but in a shorter term, some sensitivity test with the model could be performed by introducing some spatial variability in those properties. Moreover, the soil and rock layers in the model could be further subdivided and other deeper GW layers included in order to have a better representation of the porous media flow and transport.

4) The dispersion coefficient of dissolved and suspended Phosphorus AD equation could be explicitly considered in the model formulation. The velocity dependence of the dispersion coefficient could be assumed linear with a dispersivity that depends in general on the vegetation coverage and the model cell dimensions. Ideally, the dispersivity could be found by fitting the model to results from field tracer tests performed around tree islands of the Everglades.

5) The suspended particle transport approach could consider several (soil and litter) particle types with a variety of shapes and densities. Moreover, the density litter reduction after being in aerobic conditions can be considered in the suspended particle transport approach and, therefore, a higher resuspension after rewetting [Wade et al., 1980]. The suspended particle transport formulation could consider also the sediment bed transport. Due to the importance of the Phosphorus-in-suspended litter transport revealed in this work, any improvement in this module may result in

better estimations of the Phosphorus buildup or loss rates in different areas of the tree island and consequently, in a more exact prediction of the external input rate needed from animal activity and other sources, and of the Phosphorus-driven vegetation changes.

6) The inclusion of other components of the above-ground litter (rather than the leaf litter), the belowground litter and the organic soil pools, as well as the immobilization and mineralization processes in soil could give a more complete quantitative picture of the Phosphorus mass and fluxes. In particular, the effect of soil processes that produce Phosphorus sequestration (as measured by Davis [1991]) might be contained within the external input rates calculated by the developed model.

7) The amount of Phosphorus in live vegetation was assumed to be in equilibrium in the model, i.e., the Phosphorus uptake by vegetation is assumed equal to the Phosphorus-in-the-above-litter production rate. The predicted seasonal variations in the Phosphorus cycling could be improved by including the seasonal changes in the amount of Phosphorus in the live biomass pool (i.e., variations in the Phosphorus uptake and release in litter) in the model. The temporal variability of the live biomass pool could also consider mortality events like hurricanes, freezes and fires. Ideally, a vegetation dynamic module can be coupled to the model developed in this work to obtain not only the temporal variations of Phosphorus in the live biomass pool as a function of the forcing variables (temperature and water depth) and mortality events, but also to reproduce possible vegetation changes driven by the spatial redistribution of Phosphorus in soil.

8) The seasonal variability of the external Phosphorus input from animal activity could be introduced in the model based on the different behavior of the wading birds and other animals during the dry and wet season, the nesting period, etc.

9) The possibility of Phosphorus input from the other sources suggested by Wetzel et al. [2005] (i.e., Phosphorus-bearing sediments and dry atmospheric deposition) must be quantified from field measurements. The developed model predicted high pore-water Phosphorus concentration and adsorbed mass in the rock layer beneath the tree island head due to the advective exchange with the peat soil layer. Therefore, it may be difficult to distinguish any Phosphorus amount carried by

groundwater from pre-existing Phosphorus-bearing sediments.

Further improvements could also be done in the parameterization of the model. The model uses a considerable number of parameters that could be reevaluated when new data becomes available. In some cases, the temporal and spatial dependency of the parameters was ignored due to the lack of data in the literature. Sensitivity tests would also be helpful to evaluate the effect of the uncertainty in the parameters in model results.

Despite all the above improvements proposed for the model, the developed model can be used as predicting tool for the tree islands of Shark River Slough studied here. The model could be run for hypothetical future conditions and answer important questions for conservation and restoration efforts in the Everglades and similar wetlands. For example, the question of what would be the Phosphorus distribution around the tree islands in case of a change in forcing parameters such as the seasonal dependence of the water elevation (hydroperiod length), the Phosphorus content in incoming surface water and the population of wading birds (external input rate from animal activity).

Finally, the hypothesis about possible Phosphorus-driven sawgrass die-off and cyclic succession between TS and MA vegetation types around the tree islands inferred from model results would motivate other researchers to extend this numerical study and also to perform specific field measurements in future works. As mentioned above, the model performance could be improved as new data becomes available for parameterization and calibration. Moreover, the approach would be enhanced by including the above recommendations, especially the ones in points 5, 6 and 7. Regarding the field measurements, Phosphorus concentration in soil pore water and vegetation density could be surveyed at the same area initially covered by sawgrass at different times for a few years in order to detect possible correlation between the Phosphorus concentration and the vegetation density changes. It is anticipated that an accurate field estimate of the average Phosphorus concentration in soil would require an intensive sampling due to the high spatial variability observed in point measurements by Ross et al. [2004].

References

Ahn, H., 2003. H. *Rainfall Frequency Analysis in the ENP Area*, draft report.

Bazante, J., G. Jacobi, and H. Solo-Gabriele, 2004. *Documenting the Importance of Water Flow to Everglades Landscape Structure, and Sediment Transport in Everglades National Park,* Draft Report.

Bazante J., G. Jacobi, H. M. Solo-Gabriele, D. Reed, S. Mitchell-Bruker, D. L. Childers, L. Leonard, M. Ross, 2006. *Hydrologic Measurements and Implications for Tree Island Formation within Everglades National Park*, Journal of Hydrology **329**, 606– 619.

Brady, N. and R. Weil, 2007. *The Nature and Properties of Soils*, Pearson International Edition, 14th Edition, 992 pages.

Carter, V., H. A. Ruhl, N. B. Rybicki, J. T. Reel, and P. T. Gammon, 1999. *Vegetative Resistance to Flow in South Florida: Summary of Vegetation Sampling at Sites NESRS3 and P33, Shark River Slough, April, 1996.* U.S. Geological Survey Open-File Report 99-187.

Carter, V., J. T. Reel, N. B. Rybicki, H. A. Ruhl, P. T. Gammon, and J. K. Lee, 1999. *Vegetative Resistance to Flow in South Florida: Summary of Vegetation Sampling At Sites NESRS3 and P33, Shark River Slough, November, 1996*. U.S. Geological Survey Open-File Report 99-218.

Chambers, R. M. and K. A. Pederson, 2006. *Variation in Soil Phosphorus, Sulfur, and Iron Pools among South Florida Wetlands*. Hydrobiologia **569**, 63-70.

Chin, D., 1998. *Evapotranspiration of Melaleuca Forest in South Florida*, Journal of Hydrologic Engineering **3**(2), 131-139.

Corstanje, R., S. Grunwald, K. R. Reddy, T. Z. Osborne, and S. Newman, 2006. *Assessment of the Spatial Distribution of Soil Properties in a Northern Everglades Marsh*, Journal of Environmental Quality **35**, 938-949.

Davis S. M., 1991. *Growth, Decomposition, and Nutrient Retention of Cladium Jamaicense Crantz and Typha Domingensis Pers. in the Florida Everglades*. Aquatic Botany **40**, 203–224.

Davis S. M., 1994. *Phosphorus Inputs and Vegetation Sensitivity in the Everglades.* In: Everglades: *The Ecosystem and Its Restoration* (Eds S.M. Davis and J.C. Ogden), pp. 357–378. St. Lucie Press, Delray Beach.

Davis, S. E., D. L. Childers and G. B. Noe, 2006. *The Contribution of Leaching to the Rapid Release of Nutrients and Carbon in the Early Decay of Wetland Vegetation*. Hydrobiologia 569, 87-97.

DeBusk W. F. and Reddy K. R., 1998. *Turnover of Detrital Organic Carbon in a Nutrient-Impacted Everglades Marsh*. Soil Science Society American Journal 62, 1460–1468.

DeBusk, W. F., K. R. Reddy, M. S. Koch, and Y. Wang, 1994. *Spatial Distribution of Soil Nutrients in a Northern Everglades Marsh: Water Conservation Area 2A*, Soil Science Society American Journal **58**, 543-552.

Debusk, W. F., K. R. Reddy, 2005. *Litter Decomposition and Nutrient Dynamics in a Phosphorus Enriched Everglades Marsh*, Biogeochemistry **75**, 217–240.

Ewe, S. M. L., E. E. Gaiser, D. L. Childers, D. Iwaniec, V. H. Rivera-Monroy, R. R. Twilley, 2006. *Spatial and Temporal Patterns of Aboveground Net Primary Productivity (ANPP) along Two Freshwater-Estuarine Transects in the Florida Coastal Everglades*. Hydrobiologia **569**, 459–474.

Fennema R. J., C. J. Neidrauer, R. A. Johnson, T. K. MacVicar, and W. A. Perkins, 1994. *A Computer Model to Simulate Natural Everglades Hydrology*. In: Davis SM, and Ogden JC, editors. *Everglades: The Ecosystem and Its Restoration*. Delray Beach (FL): St. Lucie Press, p 249–90.

Fish, J. E., 1988. Hydrogeology, *Aquifer Characteristics, and Ground-Water Flow of the Surficial Aquifer System, Broward County, Florida*. U.S. Geological Survey Water-Resources Investigations Report 87-4034, 92 p.

Fish, J. E., and M. T. Stewart, 1991. *Hydrogeology of the Surficial Aquifer System, Dade County, Florida*. U.S. Geological Survey Water-Resources Investigations Report 90-4108, 50 p.

Fischer, H. B., J. E. List, R. C. Y. Koh, et al., 1979. *Mixing in Inland and Coastal Waters*, 263. Academic Press, New York (pp. 126–127).

Fitz, H. C. and F. H. Sklar. 1999. *Ecosystem Analysis of Phosphorus Impacts and Altered Hydrology in the Everglades : A Landscape Modeling Approach*, pp. 585-620 In: Reddy, K.R., G.A. O'Connor, and C.L. Schelske, (Editors). Phosphorus Biogeochemistry in Subtropical Ecosystems. Lewis Publishers, Boca Raton, FL, USA.

Fitz, H. C. 2006. *Documentation of the Everglades Landscape Modeling ELM v2.5*, SFWMD.

Frederick, P. C. and V. G. N. Powell, 1994. *Nutrient Transport by Wading Birds in The Everglades.* In: Everglades: The Ecosystem and Its Restoration (Eds S.M. Davis and J.C. Ogden), pp. 571–584. St. Lucie Press, Delray Beach.

German, E. R., 2000. *Regional Evaluation of Evapotranspiration in the Everglades,* USGS Water-Resources Investigations Report 00–4217.

Hammecker, C., L. Barbiero, P. Boivin, J. L. Maeght and E. H. B. Diaw, 2004. *A Geometrical Pore Model for Estimating the Microscopical Pore Geometry of Soil with Infiltration Measurements*. Transport in Porous Media **54**, 193–219.

Hamill, T. M. and S. J. Colucci, 1998. *Evaluation of Eta-RSM Ensemble Probabilistic Precipitation Forecasts*. Monthly Weather Review **126**, 711–724.

Harvey, J. W., J. M. Jackson, R. H. Mooney, J. Choi, 2000. *Interactions Between Groundwater and Surface Water in Taylor Slough and Vicinity, Everglades National Park, South Florida: Study Methods and Appendixes.* US Geological Survey Open-File Report 00-483, 67 pp.

Harvey, J. W., S. L. Krupa, J. M. Krest, 2004. *Ground Water Recharge and Discharge in the Central Everglades*, Ground Water **42** (7), 1090–1102.

Harvey, J. W., J. T. Newlin, J. M. Krest, J. Choi1, E. A. Nemeth, and S. L. Krupa, 2004. *Surface-Water and Ground-Water Interactions in the Central Everglades, Florida*. USGS Scientific Investigations Report 2004–5069, 88 p.

HydroGeoLogic (HGL) Inc., 2006. *MODHMS (Version 3.0) – A MODFLOW-based Hydrologic Modeling System.* Documentation and User's Guide, HydroGeoLogic Inc., Reston, Virginia.

Hodnett, M. G., L. Pimentel da Silva, H. R. da Rocha, and R. Cruz Senna, 1995. *Seasonal Soil Water Storage Changes Beneath Central Amazonian Rainforest and Pasture*, Journal of Hydrology **170**, 233–254.

Jenter, H., *Vegetation Affects Water Movement in the Florida Everglades*, USGS, Fact Sheet 147-96, United States Geological Survey, Reston, VA, 1996.

Jenter, H. L., and Duff, M. P., 1999, *Locally-Forced Wind Effects on Waters with Emergent Vegetation*. Third International Symposium on Ecohydraulics, 9 p.

Julien, P. Y., 1995. *Erosion and Sedimentation*, Cambridge University Press.

Kadlec, R. H. and D. E. Hammer, 1988. *Modeling Nutrient Behavior in Wetlands*, Ecological Modelling **40**, 37-66.

Kadlec, R. H., 1990. *Overland Flow in Wetlands: Vegetation Resistance*, Journal of Hydraulic Engineering, ASCE **116** (5), 691–706.

Kreith, F., S. A. Berger, et. al., 1999. *Fluid Mechanics, Mechanical Engineering Handbook*, Ed. Frank Kreith, Boca Raton: CRC Press LLC.

Laio, F., A. Porporato, L. Ridolfi, I. Rodriguez-Iturbe, 2001. *Plants in Water-Controlled Ecosystems: Active Role in Hydrologic Processes and Response to Water Stress. II. Probabilistic Soil Moisture Dynamics*. Advances in Water Resources **24**, 707-723.

Langevin, C. D. 2001. *Simulation of Ground-Water Discharge to Biscayne Bay, Southeastern Florida*. U.S. Geological Survey Water-Resources Investigations Report 00–4251.

Langevin, C. D., 2003. *Simulation of Submarine Ground Water Discharge to a Marine Estuary: Biscayne Bay, Florida*. Ground Water **41** (6), 758–771.

Langevin, C., Swain, E., and Wolfert, M., 2005. *Simulation of Integrated Surface-Water/Ground-Water Flow and Salinity for a Coastal Wetland and Adjacent Estuary*. Journal of Hydrology **314**, 212–234.

Lapidus, L., G. F. Pinder, 1982. *Numerical Solution of Partial Differential Equations in Science and Engineering,* Wiley New York.

Lee, J. K., L. C. Roig, H. L. Jenter, H. M. Visser, 2004 *Drag Coefficients for Modeling Flow through Emergent Vegetation in the Florida Everglades*, Ecological Engineering **22**, 237–248.

Leonard, L., A. Croft, D. Childers, S. Mitchell-Bruker, H. Solo-Gabriele and M. Ross, 2006. *Characteristics of Surface-Water Flows in the Ridge and Slough Landscape of Everglades National Park: Implications for Particulate Transport*, Hydrobiologia **569**, 5–22.

McCormick P. V., S. Newman, S. Miao, D. E. Gawlik, D. Marley, K. R. Reddy and T. D. Fontaine, 2002. *Effects of Anthropogenic Phosphorus Inputs on the Everglades.* In: The Everglades Hydroscape (Eds K. Porter and J. Porter), pp. 83–126. St Lucie Press, Boca Raton.

Merritt, M. L. 1996a. *Simulation of the Water Table Altitude in the Biscayne Aquifer, Southern Dade County, Florida, Water Years 1945–89*. U.S Geological Survey Water-Supply Paper 2458.

Merritt, M. L. 1996b, *Numerical Simulation of a Plume of Brackish Water in the Biscayne Aquifer Originating from a Flowing Artesian Well, Dade County*, Florida. U.S. Geological Survey Water-Supply Paper 2464.

Miao, S. L. and F. H. Sklar, 1998. *Biomass and Nutrient Allocation of Sawgrass and Cattail along a Nutrient Gradient in the Florida Everglades*, Wetlands Ecology and Management **5**, 245–263.

Nemeth, M. S., W. M. Wilcox, H. M. Solo-Gabriele, 2000. *Methods for Quantifying Ground-Water Seepage Beneath Levee 31N, Miami-Dade County, Florida*, US Geological Survey Water-Resources Investigations Report, 00-4066, 80 p.

Nepf, H. M., E. W. Koch, 1999. *Vertical Secondary Flows in Submersed Plant-Like Arrays*, Limnology and Oceanography **44** (4), 1072–1080.

Newman, S., J. B. Grace, J. W. Koebel, 1996. *Effects of Nutrients and Hydroperiod on Typha, Cladium, and Eleocharis: Implications for Everglades Restoration*, Ecological Applications **6** (3), 774-783.

Newman, S. and K. Pietro, 2001. *Phosphorus Storage and Release in Response to Flooding: Implications for Everglades Stormwater Treatment Areas*, Ecological Engineering **18**, 23–38.

Noe, G. B., D. L. Childers, and R. D. Jones. 2001. *Phosphorus Biogeochemistry and the Impact of Phosphorus Enrichment: Why Is the Everglades so Unique?* Ecosystems **4**, 603–624.

Noe G., J. Harvey, R. Schaffranek, J. Saiers, and L. Larsen, 2006. *Spatiotemporal Variation in the Characteristics of Suspended Particles in the Everglades: Implications for the Ridge and Slough Landscape*, GEER conference, June 2006.

Oliver, J. D. and T. Legovic, 1988. *Okefenokee Marshland Before, During and after Nutrient Enrichment by a Bird Rookery*, Ecological Modelling **43**, 195-223.

Panday, S., P. S. Huyakorn, 2004. *A Fully Coupled Physically-Based Spatially-Distributed Model for Evaluating Surface/Subsurface Flow*, Advances in Water Resources **27**, 361–382.

Porter, P. S. and C. A. Sanchez, 1992. *The Effect of Soil Properties on Phosphorus Adsorption by Everglades Histosols*. Soil Science **154**, 387–398.

Redfield, G., 1998. *Quantifying Atmospheric Deposition of Phosphorus: A Conceptual Model and Literature Review for Environmental Management*. SFWMD.

Redfield, G. W., 2002. *Atmospheric Deposition of Phosphorus to the Everglades: Concepts, Constraints, and Published Deposition Rates for Ecosystem Management*. The Scientific World Journal **2**, 1843–1873.

Reese, R.S., and Cunningham, K.J., 2000, *Hydrogeology of the Gray Limestone Aquifer in Southern Florida*, U.S. Geological Survey Water-Resources Investigations Report 99-4213, 244 p.

Richardson, C. J. and P. Vaithiyanathan. 1995. *Phosphorus Sorption Characteristics of Everglades Soils along a Eutrophication Gradient*. Soil Science Society of America Journal **59**, 1782-1788.

Richardson et al. 1999. *Nutrient Effects on Stand Structure, Resorption Efficiency, and Secondary Compounds in Everglades Sawgrass*, Ecology **80** (7), 2182-2192.

Ross M. S. et al., 2002. *Everglades National Park Tree Islands: Interactions of Vegetation, Hydrology and Soils*. Annual Report of 2001-2002.

Ross, M. S., C. L. Coultas and Y. P. Hsieh, 2003. *Soil-Productivity Relationships and Organic Matter Turnover in Dry Tropical Forests of the Florida Keys*, Plant and Soil **253**, 479–492.

Ross, M. S., D. T. Jones et al., 2004. *Tree Islands in the Shark River Slough Landscape: Interactions of Vegetation, Hydrology and Soils*. Final Report from SERC, FIU.

Ross, M. S., P. L. Ruiz, K. Jayachandran, C. L. Coultas and J. P. Sah, 2004. *Nutrient Relationships in the "Ridge-and-Slough" Vegetation Mosaic of the Southern Everglades, Florida, USA*. IAVS presentation.

Ross M. S., S. Mitchell-Bruker, J. P. Sah, S. Stothoff, P. L. Ruiz, D. L. Reed, K. Jayachandran and C. L. Coultas, 2006. *Interaction of Hydrology and Nutrient Limitation in the Ridge and Slough Landscape of the Southern Everglades*. Hydrobiologia **569**, 37–59.

Rybicki, N. B., J. T. Reel, H. A. Ruhl, P. T. Gammon, V. Carter, J. K. Lee, 1999. *Biomass and Vegetative Characteristics of Sawgrass Grown in a Tilting Flume as Part of a Study of Vegetative Resistance to Flow*, USGS Open-File Report 99-230, United States Geological Survey, Reston, VA.

Schaffranek, R. W., 1999, *Hydrologic Studies in Support of South Florida Ecosystem Restoration*, Proceedings 26th Annual ASCE Water Resources Planning and Management Division Conference, 8 p.

Sklar, F. H., H. C. Fitz, Y. Wu, R. Van Zee, C. McVoy, 2001. *The Design of Ecological Landscape Models for Everglades Restoration*. Ecological Economics **37,** 379–401.

Sklar, F. H. and A. van der Valk, 2002. *Tree Islands of the Everglades : an Overview. In Tree Islands of the Everglades.* Pages 1 – 18 in F. H. Sklar F. H. and A. van der Valk, editors. *Tree Islands of the Everglades*. Kluwer Academic Publishers, Boston, MA, USA.

Sklar, F. H. et al. 2003. *Hydrologic Needs. Effects of Hydrology on the Everglades Protection Area*, Chapter 6 in 2003 Everglades Consolidated Report.

Sobczak, R., 2007. *New Web-Based Approach for Summarizing Watershed Conditions in the South Florida Water Management District*. Presentation held at Special Symposium on Water Quality Issues in South Florida, Annual Science Meeting of the SFC CESU, FIU. Related webpage: www.fgcu.edu/bcw/hcu.htm

SFWMD 1998. *Natural System Model* Version 4.5 http://www.sfwmd.gov/org/pld/hsm/models/nsm/

Stothoff, S. A., 2004. *Progress Report on Interaction between Field and Modeling* ENP-PR-2003-01, Stothoff Environmental Modeling, Winston-Salem, NC.

Stothoff, S. A., 2004. *Progress Report on Model Calibration*, ENP-PR-2003-02, Stothoff Environmental Modeling, Winston-Salem, NC.

Troxler-Gann, T. G., 2005. *Ecosystem Responses to Hydrologic Change and Mechanisms of Nitrogen Sequestration in Seasonally Flooded Tree Islands of The Southern Everglades*. PhD Thesis, FIU.

Troxler-Gann, T. G., D. L. Childers, D. N. Rondeau; 2005. *Ecosystem Structure, Nutrient Dynamics, and Hydrologic Relationships in Tree Islands of the Southern Everglades, Florida, USA.* Forest Ecology and management **214**, 11-27.

Tsujimoto, T. 1999. *Fluvial Processes in Streams with Vegetation*, Journal of Hydraulic Research **37**, 789– 803.

USGS, 2003. *Gazetteer of GPS Positioned Gage Sites in the Everglades National Park and Big Cypress National Preserve*, Established by USGS/NMD 2000-2003, First Edition.

Van Genuchten, M. Th., F. J. Leij and S. R. Yates. 1991. *The RETC Code for Quantifying the Hydraulic Functions of Unsaturated Soils.* EPA/600/2-91/065. 93 pp.

Wade, D., J. Ewel, R. Hofstetter, 1980. *Fire in South Florida Ecosystems*, Forest Service General Technical Report SE-I7, US Department of Agriculture.

Wetzel, P. R., A. G van der Valk, S. Newman, D. E. Gawlik, T. Troxler-Gann, C. A. Coronado-Molina, D. L. Childers, and F. H. Sklar, 2005. *Maintaining Tree Islands in the Florida Everglades: Nutrient Redistribution is the Key*. Frontiers in Ecology and the Environment **3** (7), 370–376.

Wetzel, P. R., 2002. *Analysis of Tree Island Vegetation Communities*. In: F. H. Sklar, A. Van Der Valk (Eds.), Tree Islands of the Everglades, first ed. Kluwer Academic Publishers, Dordrecht, Chapter 12, pp. 357-390.

Wu, Y., *ELVM Program Code,* version 2.02, November 10, 2004.

Wu, Y., K. Rutchey, W. Guan, L. Vilchek, F. H. Sklar, 2003. *Spatial Simulations of Tree Islands for Everglades Restoration*. In: F. H. Sklar, A. Van Der Valk (Eds.), Tree Islands of the Everglades, first ed. Kluwer Academic Publishers, Chapter 16, pp. 469-498.

Wu, W., F. D. Shields, S. J. Bennett, S. S. Y. Wang, 2005. *A Depth-Averaged Two-Dimensional Model for Flow, Sediment Transport, and Bed Topography in Curved Channels with Riparian Vegetation*, Water Resources Research **41**, W03015.

Appendix 1. Addendum for Chapter 1

A1.1 Types of Tree Islands. Additional figures

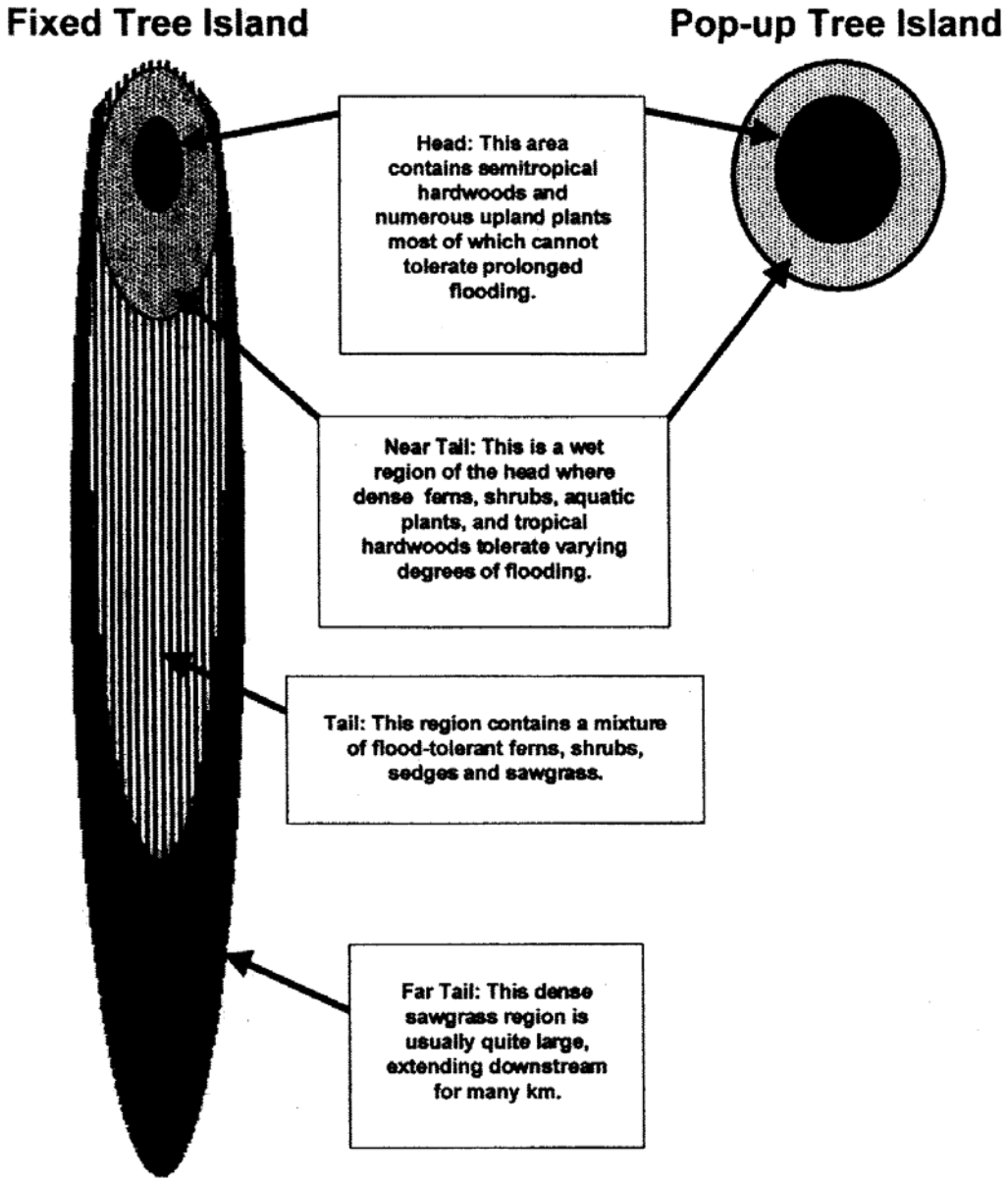

Figure A-1. General anatomy of the two most dominant tree island types in the Everglades. Reproduced from Sklar and van der Valk [2002].

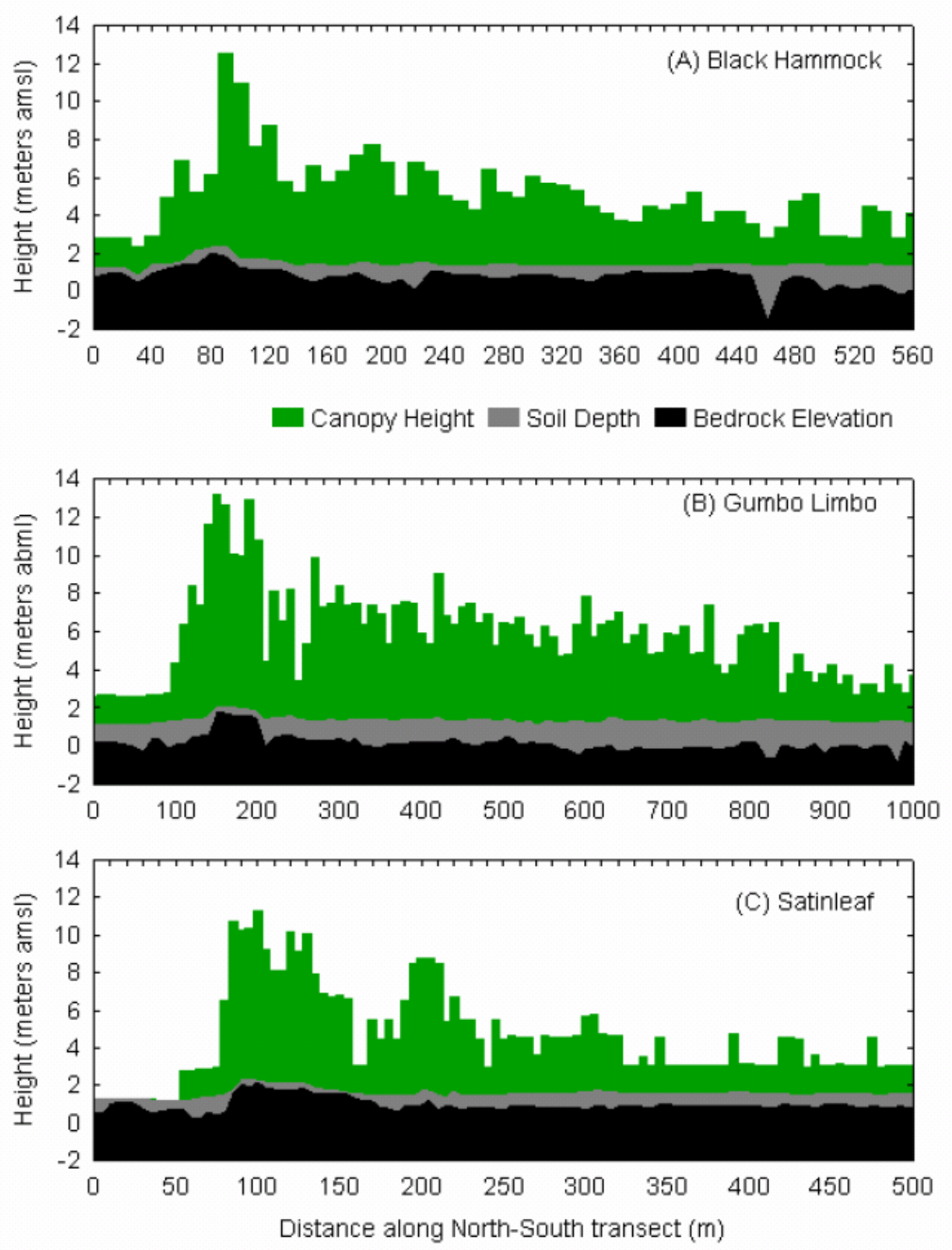

Figure A-2. Canopy height, soil elevation and bedrock elevation along the long axis of three tree islands. Reproduced from Ross et al. [2004].

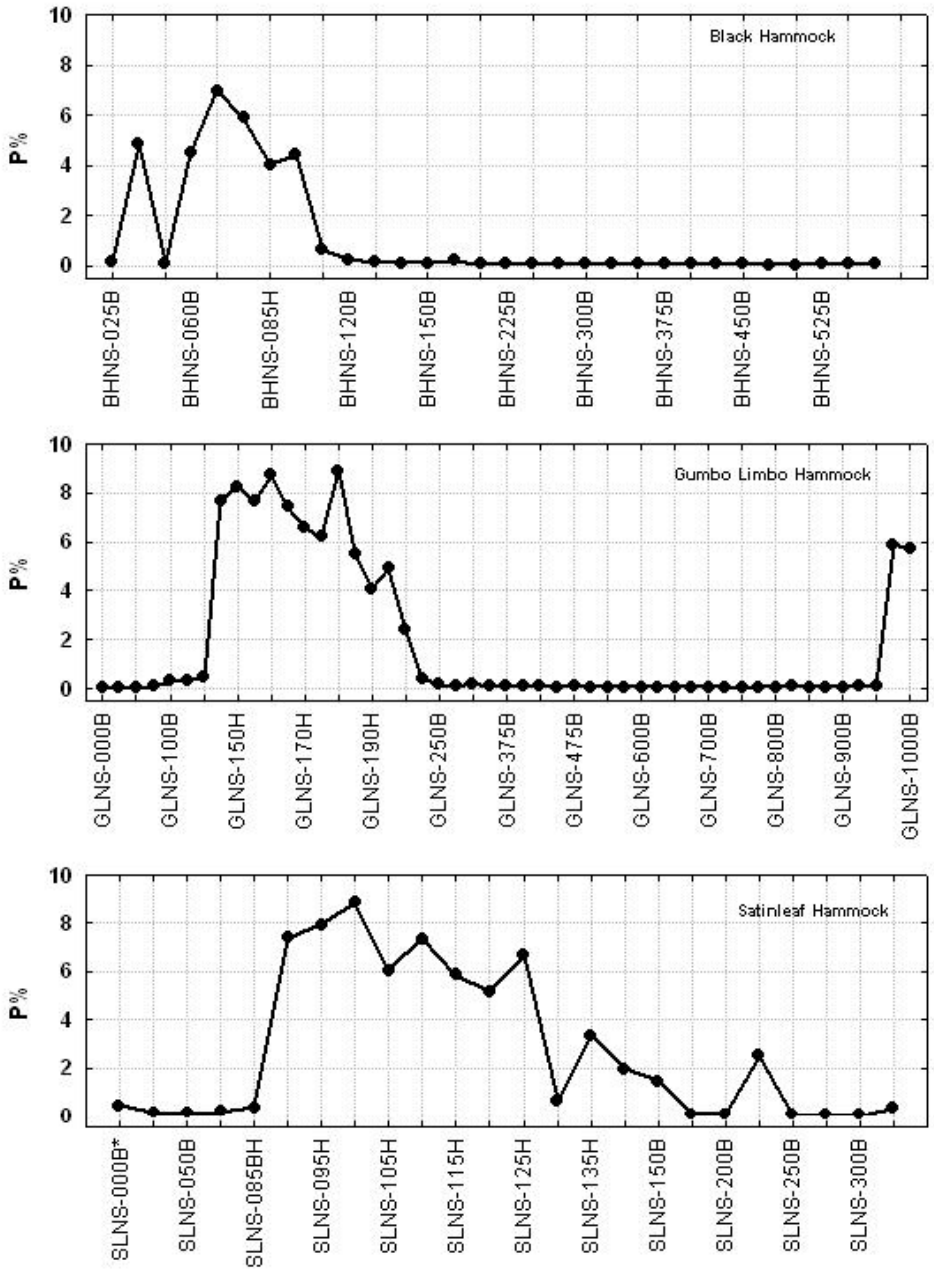

Figure A-3. Total Phosphorus in soil (%) along North-South transects in the three tree islands. Reproduced from Ross et al. [2004].

A1.2 ELM Parameters and Habitat Descriptions

Parameter name	unit	Definition	Habitat			
			Sawgrass RS Pristine	Sawgrass RS Degraded	Wet Prairie	Mixed Hardwood Forest
HP_PHBIO_MAX	kgC/ m^2	Maximum attainable (observed) biomass density of photosynthetic tissue.	1.5	1.3	0.85	0.8
HP_NPHBIO_MAX	kgC/ m^2	Maximum attainable (observed) biomass density of nonphotosynthetic tissue.	0.87	0.87	0.7	3.25
HP_MAC_MAXHT	m	Maximum observed/attainable height of mature plant community (associated with a unit plant density at maturity).	2.5	2.5	2	3.7
HP_NPHBIO_ROOTDEPTH	m	Depth of roots below the sediment/soil zone for the community.	0.65	0.65	0.65	1.5
HP_MAC_MAXROUGH	d/ $m^{1/3}$	The maximum Manning n roughness associated with present vegetation when fully inundated by water.	3	3	2	2
HP_MAC_MINROUGH	d/ $m^{1/3}$	The minimum Manning roughness coefficient for minimal/no vegetation.	0.2	0.3	0.1	0.2
HP_MAC_MAXLAI	1	Maximum observed/attainable Leaf Area Index for a mature community (= area of leaves/area of ground).	3	3	3	3.5
HP_MAC_KSP	mgP/ L	Half saturation coefficient of Phosphorus for the nutrient uptake kinetics of macrophytes.	0.45	0.45	0.5	0.5
HP_PHBIO_RCNPP	1/d	Maximum observed/attainable specific rate of net primary production.	0.03	0.03	0.03	0.03
HP_PHBIO_RCMORT	1/d	Baseline specific rate of photobiomass mortality.	0.002	0.002	0.002	0.002
HP_MAC_WAT_TOLER	m	Depth of pounded surface water above which plant growth becomes restricted. Used in growth control function.	0.8	0.8	0.4	0.1
HP_PHBIO_IC_CTOOM	gC/ gOM	Initial ratio of organic carbon to total organic material in photobiomass (ash free dry weight).	0.48	0.48	0.48	0.48
HP_NPHBIO_IC_CTOOM	gC/ gOM	Initial ratio of organic carbon to total organic material in nonphotobiomass (ash free dry weight).	0.48	0.48	0.48	0.48
HP_PHBIO_IC_PC	gP/ gC	Initial Phosphorus to carbon ratio in photobiomass (ash free dry weight).	0.0007	0.0007	0.0007	0.0007
HP_NPHBIO_IC_PC	gP/ gC	Initial Phosphorus to carbon ratio in nonphotobiomass (ash free dry weight).	0.001	0.001	0.001	0.0005
HP_MAC_TRANSLOC_RC	1/d	Simple, bi-directional baseline translocation rate between non-photo and photo biomass.	0.005	0.005	0.005	0.005

Table A-1. Biomass related parameters considered in ELM version 2.5 for several habitats that may be found around the tree islands of Shark River Slough.

ELM Habitat	ELM Description	Corresponding Vegetation Type
Sawgrass RS Pristine	Area dominated by *Cladium jamaicense* (sawgrass). System dominated by dense growth of Sawgrass to the exclusion of almost all other species. This system is adapted to occasional fires when the surface of ~~the~~ soil is moist so that only the accumulated dead grass is burned off and continual inundation is almost required.	TS
Sawgrass RS Degraded		MA
Wet Prairie	Area with mixture of grasses and sedges. Grassy systems adapted to seasonal inundation and dry periods with fire. Water levels are generally only a few inches in the wet season and fires occur annually to triannually. Dominant species are *Eleocharis cellulosa* (Spikerush), *Rhynochospora tracyi* (bulrushes) and various other sedges and grasses.	MA
Mixed Hardwood Forest	Area dominated by hardwoods representative of tree islands. Duplication of Cypress, with different water tolerances. Aggregation of three forest types, each one characterized by a diverse mixture of broadleaf species, moderate soil nutrient levels and high leaf area index.	BH,BS

Table A-2. Approximate correspondence among some habitats defined in ELM version 2.5 and the vegetation types at tree islands as defined by Ross et al. [2004].

A1.3 ELVM Model

This section describes the equations and parameters in version 2.02 of the ELVM model [Wu, 2004]. The equations in that version slightly differ from the ones reported by Wu et al. [2003]. Moreover, an evaluation of this model for several vegetation types (Tree Island, Sawgrass and Wet prairie) for the case of no stress is conducted. The results from this special case are compared with measured values.

A1.3.1 ELVM Equations

The growth module in the code from 2004 (version 2.02) is based on the equations:

$$\frac{dB_a}{dt} = NPP \cdot \text{aboveC} - L_a - T_{ab}\,; \tag{31}$$

$$\frac{dB_b}{dt} = NPP \cdot \text{belowC} - L_b + T_{ab}\,; \tag{32}$$

where B_a and B_b are the biomass above and below the ground, respectively. NPP is the net primary production rate, L_a and L_b the litter production rates and T_{ab} is a transference rate term. Thus, the total biomass is

$$B = B_a + B_b\,. \tag{33}$$

The parameters that determines the distribution (or allocation) of the net primary production rate (NPP) satisfy that

$$\text{aboveC} + \text{belowC} = 1\,, \tag{34}$$

$$\frac{1}{1 + \dfrac{2-f}{\text{balance}} 1.0238 \cdot \exp\left(-0.00047 \dfrac{\text{kg}}{\text{mg}} \cdot \text{soilTotalP} \right)} = \begin{cases} \text{belowC} & \text{if } NPP \geq 0 \\ \text{aboveC} & \text{if } NPP < 0 \end{cases}. \tag{35}$$

Notice that the case $NPP < 0$ occurs rarely. This relation (35) takes into account the influence of the total soil Phosphorus (TSP in mg/kg) and also the balance between the amount of biomass above and below the surface, as

$$\text{balance} = \frac{B_a}{B_b} \frac{1}{\text{aboveBelowRate}}\,;\ \text{aboveBelowRate} = \frac{B_{a\max}}{B_{b\max}}\,. \tag{36}$$

Moreover, for tree islands, the influence of the water depth is considered in

$$f = \text{WaterDepthC} = \begin{cases} \text{submergeC} & \text{waterDepth} \geq \text{treeSubmergeC} \\ [\text{Linear relation}] & 0 < \text{waterDepth} < \text{treeSubmergeC} \\ 1 & \text{waterDepth} \leq 0 \end{cases} \tag{37}$$

where treeSubmergeC = 60cm. Meanwhile, for other vegetation types,

$$f = \text{WaterDepthC} = \begin{cases} \text{submergeC} & \text{waterDepth} \geq \text{vegHeight} \\ [\text{Linear relation}] & 0 < \text{waterDepth} < \text{vegHeight} \\ 1 & \text{waterDepth} \leq 0 \end{cases} \tag{38}$$

The net primary production rate (NPP) is the gross primary production rate (GPP) minus the respiration rate (RR), i.e.,

$$NPP = GPP - RR\,; \tag{39}$$

where

$$RR = B \cdot \text{respiRateA} \cdot \exp\left(-\,\text{respiRateB} \cdot B\right); \tag{40}$$

$$GPP = \text{gppRate} \cdot \text{leafBiom} \cdot \text{minLimit}\,. \tag{41}$$

The relative growth rate (gppRate) and the leaf biomass (LB) are estimated from the Leaf Area Index (LAI) as

$$\text{gppRate} = \text{gppRateA} \cdot \exp\left(-\,\text{gppRateB} \cdot \text{LAI}^2\right); \tag{42}$$

$$\text{leafBiom} = \text{laiBiomC} \cdot \text{LAI}\,. \tag{43}$$

The Leaf Area Index changes (ΔLAI) are computed from the above-ground biomass changes (ΔB_a) as

$$\Delta\text{LAI} = \begin{cases} \Delta B_a\, \text{treeLAIA} \cdot \exp\left[-\,\text{treeLAIB}\dfrac{B_a}{\text{laiBiomasC}}\right] & \text{Tree Island} \\ \dfrac{\Delta B_a}{\text{laiBiomasC}} & \text{otherwise} \end{cases}. \tag{44}$$

where treeLAIA= 0.15351 $(\text{kg/m}^2)^{-1}$ and treeLAIB= 0.0527.

Integrating relation (44) by considering $\text{LAI} = 0$ when $B_a = 0$, it gives

$$\text{LAI} = \begin{cases} \text{treeLAIA} \cdot \dfrac{\text{laiBiomasC}}{\text{treeLAIB}}\left[1 - \exp\left[-\,\text{treeLAIB}\dfrac{B_a}{\text{laiBiomasC}}\right]\right] & \text{Tree Island} \\ \dfrac{B_a}{\text{laiBiomasC}} & \text{otherwise} \end{cases}. \tag{45}$$

An asymptotic relation from (45) is

$$\mathrm{LAI} \xrightarrow[Ba\to 0]{} \mathrm{treeLAIA}\cdot B_a \text{, for Tree Island.} \tag{46}$$

The LAI relations (45) and (46) are plotted in Figure A-4 for the case of Tree Island vegetation type and compared with the relation (45) for the Sawgrass type.

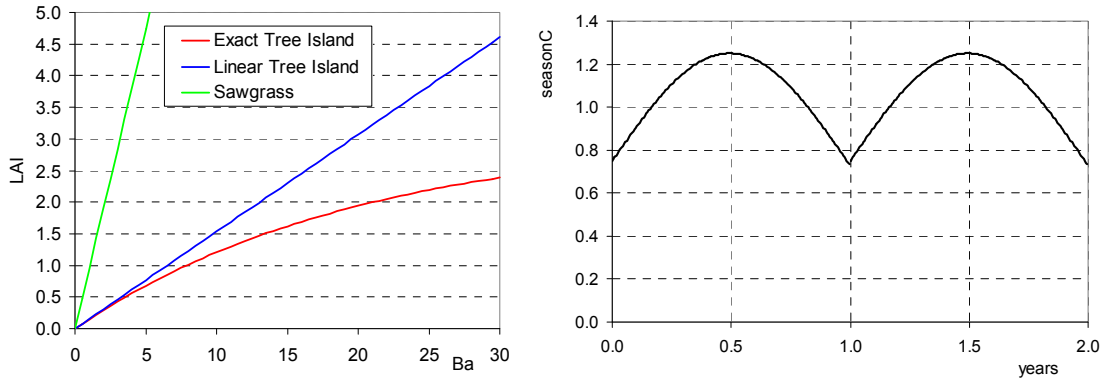

Figure A-4. Left: relation between LAI and B_a according to (45) and (46). Right: coefficient seasonC through a year according to (48).

The parameter that bound the gross primary production rate is

$$\mathrm{minLimit} = (1+\mathrm{growthRate})\cdot \mathrm{seasonC}\cdot \mathrm{waterDepthC}\cdot \mathrm{fireC}\cdot \mathrm{salC}\cdot \mathrm{NPC}\,. \tag{47}$$

The seasonal growth coefficient (seasonC) is given by

$$\mathrm{seasonC} = \frac{1}{2}\sin\left(\frac{iday}{2} * \frac{\pi}{180}\right) + 0.75\,,\ iday = 0,1,...,364\,. \tag{48}$$

Figure A-4 evidences the jump in the derivative of seasonC at the end of the year. The post fire effect coefficient is

$$\mathrm{fireC} = \begin{cases} 3 - \mathrm{daysPostburn}/\mathrm{postburnC} & \text{if } \mathrm{daysPostburn} < \mathrm{postburnC} \\ 1 & \text{otherwise} \end{cases}. \tag{49}$$

Notice that this factor jumps from 2 to 1 at $\mathrm{daysPostburn} = \mathrm{postburnC}$.

The effect of the salinity is

$$\mathrm{salC} = \begin{cases} 1 - \dfrac{\mathrm{salinity}}{\mathrm{salinityC}} & \mathrm{salinity} \le \mathrm{salinityC} \\ 0 & \text{otherwise} \end{cases}. \tag{50}$$

The effect of nutrients on the photosynthesis process is considered in

$$\mathrm{growthRate} = \max(\mathrm{waterTNC}, \mathrm{soilTNC}, \mathrm{waterTPC}, \mathrm{soilTPC}), \tag{51}$$

where

$$\mathrm{waterTNC} = 1 - \exp(-\mathrm{waterTNA}\cdot \mathrm{waterTotalN}), \tag{52}$$

$$\text{soilTNC} = 1 - \exp\left(-\,\text{soilTNA} \cdot \text{soilTotalN}\right), \tag{53}$$

$$\text{waterTPC} = \begin{cases} \dfrac{1}{1 + \text{waterTPA} \cdot \exp\left(-\,\text{waterTPB} \cdot \text{waterTotalP}\right)} & \text{treeIsland and Cattail} \\ \text{waterTPA} \cdot \log\left(\text{waterTPB} \cdot \text{waterTotalP}\right) & \text{otherwise} \end{cases} \tag{54}$$

$$\text{soilTPC} = \begin{cases} \dfrac{1}{1 + \text{soilTPA} \cdot \exp\left(-\,\text{soilTPB} \cdot \text{soilTotalP}\right)} & \text{treeIsland and Cattail} \\ \text{soilTPA} \cdot \log\left(\text{soilTPB} \cdot \text{soilTotalP}\right) & \text{otherwise} \end{cases} \tag{55}$$

Notice that the logarithmic dependencies in (54) and (55) do not offer the right asymptotic behavior as the nutrient concentration tends to infinity. Moreover, when the nutrient concentration tends to zero, the factor $\left(1 + \text{growthRate}\right)$ must tend to zero, which and this behavior is well reproduced from the above relations.

The Nitrogen to Phosphorus ratio effect is included in

$$\text{NPC} = \begin{cases} \dfrac{\text{NPRatioC}}{\text{NPR}} & \text{NPR} > \text{NPRatioC} \\ 1 & \text{otherwise} \end{cases}, \text{NPR} = \max\left(\frac{\text{waterTotalN}}{\text{waterTotalP}}, \frac{\text{soilTotalN}}{\text{soilTotalP}}\right). \tag{56}$$

where NPRatioC= 16.

The litter production rate (LR) for above and below-ground biomass is, respectively,

$$\begin{aligned} LR_a &= \frac{\text{litterAC}}{\text{seasonC}} B_a, \ \text{litterAC} = \text{litterA}\left(0.5 + \frac{B_a}{B_{a\max}}\right); \\ LR_b &= \frac{\text{litterBC}}{\text{seasonC}} B_b, \ \text{litterBC} = \text{litterB}\left(0.5 + \frac{B_b}{B_{b\max}}\right). \end{aligned} \tag{57}$$

Figure A-5 shows the litter production rates for Tree Island and Sawgrass when no seasonal effects are considered (seasonC=1). From that figure and parameter $B_{a\max}$ on Table 4, the Tree Island vegetation type has an above-biomass litter production rate $L_a = 2.3\,\text{kg/m}^2\text{/year}$, when vegetation is well developed $\left(B_a = B_{a\max}\right)$. This value is around twice the average value of about 1 kg/m^2/year reported by Ross et al. [2004]. See further discussions in section 3.6.1.

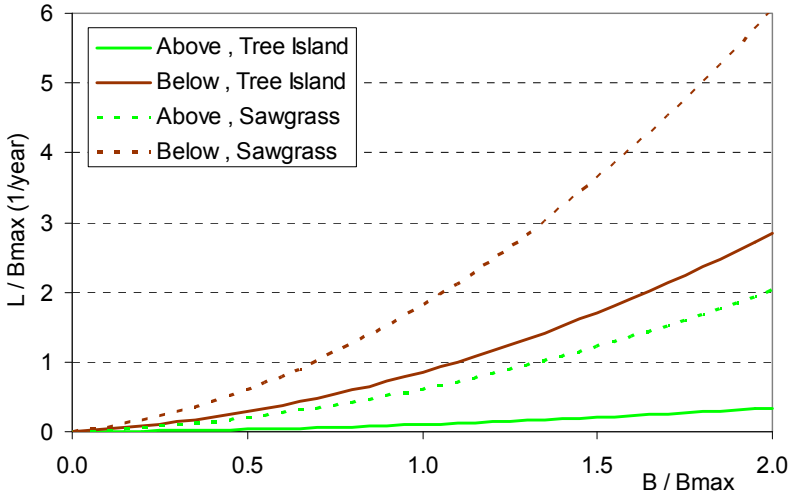

Figure A-5. Litter production rates according to equation (57).

The transference term in equations (31) and (32) is based on the mass transfer that occurs from the leaves to the roots in winter and from the roots to the leaves in summer.

$$T_{ab} = \begin{cases} B_a \cdot \text{winterA} & iday < 60 \text{ and } iday > 330 \\ -B_b \cdot \text{springA} & 90 < iday < 120 \\ 0 & \text{otherwise} \end{cases} . \tag{58}$$

Here winterA= 0.000167 d^{-1} and springA= 0.000334 d^{-1}.

The vegetation height (H_V) changes is computed from the NPP located above as

$$\Delta H_V = NPP \cdot \text{aboveC} \cdot \text{fireC} \cdot \text{seasonC} \cdot \text{heightA} \cdot \exp\left[-\text{heightB} \cdot H_V\right]. \tag{59}$$

The balance equation for the total litter (L) is

$$\frac{dL}{dt} = LR_a + LR_b - LDR, \tag{60}$$

where LDR is the litter decomposition rate given by

$$LDR = \text{decomposeC} \cdot \text{seasonC} \cdot L. \tag{61}$$

This is a very simplistic approach because the decomposition rate is different for example, if the litter is submerged or not in water.

The uptake rates of Nitrogen (NUR) and Phosphorus (PUR) are estimated from the net primary production rate as

$$NUR = \text{NperKg} \cdot NPP, \tag{62}$$

$$PUR = \text{PperKg} \cdot NPP \cdot CP, \tag{63}$$

Parameters	Vegetation Type				
	Tree Island	Saw-grass	Cattail	Slough	Wet prairie
maxAboveBiomass $B_{a\max}$ (kg/m^2)	22.526	1.546	1.912	0.336	0.567
maxBelowBiomass $B_{b\max}$ (kg/m^2)	6.674	1.214	1.356	0.197	0.336
aboveBelowRate	3.3762	1.2735	1.41	1.7056	1.6875
maxLAI	10	8	9	3	6
maxHeight (cm)	2000	350	420	120	160
SEHeight (cm)	500	87.5	105	30	40
maxAge (year)	400	18	18	2	36
optimalDensity (ind./m^2)	0.4	2.99	2.39	2.55	12.18
meanWaterDepth (cm)	-60	0	20	80	50
waterDepthA (10^{-5}) (water depth coefficient for water effect)	-2.15	-8.44	-4.15	-0.8	-1.8
submergeC (effect of submerge on growth and expansion)	0.5	0.7	0.9	1	0.95
laic (10^{-3}) (initial LAI)	27.4	6	9	4	5
vegHeightC (cm) (initial vegetation height)	25	10	15	5	5
aboveBiomassC (10^{-2} kg/m^2) (initial)	4.0	1.32	2.64	0.98	1.02
belowBiomassC (10^{-2} kg/m^2) (initial)	3.0	0.75	1.37	0.12	0.56
waterTPA, soilTPA (10^{-1})	276.10	1.443	607.81	2.4526	1.0099
waterTPB (10^{-2} (10^{-6} kg P/m^3)$^{-1}$)	2.894	16.658	4.122	4.337	35.22
soilTPB (10^{-3} (kg P/kg dry wt)$^{-1}$)	4.633	26.67	6.6	6.94	56.39
laiBiomC (10^{-1} kg/m^2) (LAI to Biomass converting factor)	1.055	1.9325	2.1244	1.12	1.233
NperKg (10^{-3} kg of N / kg of dry wt.)	5.6	5.4	5.8	7.6	7.2
PperKg (10^{-4} kg of P / kg of dry wt.)	3	2.7	3.6	7.2	6.9
NperKg/PperKg (N:P ratio)	18.7	20.0	16.1	10.6	10.4
dryPeriodC (days) (dry period for vegetation succeed)	256	168	120	84	102
wetPeriodC (days) (wet period for vegetation succeed)	109	197	245	281	263
optimalExpanRate (10^{-3})	8.4	4.74	18.84	2.4	3.8
salinityC (ppm)	30	20	15	30	30
respiRateA (10^{-3} d^{-1})	2.484	8.43	9.61	5.76	4.99
respiRateB (10^{-3} (kg/m^2)$^{-1}$)	7.642	80.85	68.28	84.09	47.1
gppRateA (10^{-2} d^{-1})	7.98	7.58	7.845	7.74	7.254
gppRateB (10^{-2})	0.916	3.68	3.07	23.29	5.32
litterA (10^{-4} d^{-1})	1.86	11.1	20.4	10.6	14.6
litterB (10^{-3} d^{-1})	1.56	3.31	6.11	2.75	4.12
postBurnC (days)	180	120	90	30	60
salinityC (ppm)	30	20	15	30	30
waterTNA (10^{-1})	3.238	3.534	4.301	2.980	2.7703
soilTNA (10^{-2})	4.398	4.796	5.838	4.045	3.760
heightA (cm.m^2/kg)	1887.86	2263.98	2196.84	3571.43	2821.91
heightB (10^{-2} cm^{-1})	0.56	2.31	1.93	8.75	5.49
decomposeC (10^{-3} d^{-1})	1.9	1.85	1.85	1.85	1.85

Table A-3. Parameters in the ELVM depending on the vegetation type. Extracted from the C code [Wu, 2004].

The coefficient in equation (63) of Phosphorus is

$$CP = \begin{cases} \text{PperKgA} \cdot \left(1 - \exp\left(-\text{PperKgB} \cdot \text{waterTotalP}\right)\right) & \text{cattail} \\ 1 & \text{otherwise} \end{cases}. \tag{64}$$

Here, PperKgA = 3.3 and PperKgB = 0.02303 $(10^{-6}\ \text{kg/m}^3)^{-1}$.

On the other hand, the return rates of Nitrogen (NRR) and Phosphorus (PRR) are estimated from the litter decomposition rate as

$$NRR = \text{NperKg} \cdot LDR, \tag{65}$$

$$PRR = \text{PperKg} \cdot LDR \cdot CP. \tag{66}$$

The values for the vegetation-type dependent parameters assumed by Wu [2004] are listed in Table 4.

A1.3.2 ELVM Special Case: No Stress

Under no water stress and if 1.0238*exp(-0.00047*TPsoil)) remains close to one, the parameter belowC for the most common case (NPP>0) in (35), reduces to

$$\text{belowC} = \frac{\text{balance}}{\text{balance} + 1} = \frac{B_a}{B_a + B_b \text{aboveBelowRate}}. \tag{67}$$

Notice that if the ratio between the above and below-ground biomass is the aboveBelowRate, then balance=1 and belowC=1/2. This means that in this case the NPP is distributed equally between the above and below-ground biomass. In other cases, this factor allocates more biomass where there is a deficit. An alternative relation to (67) might be

$$\text{belowC} = \frac{\text{balance}}{\text{balance} \cdot \text{aboveBelowRate} + 1} = \frac{B_a}{B_a + B_b} \frac{1}{\text{aboveBelowRate}}. \tag{68}$$

The advantage of a relation like (68) is that aboveBelowRate would be the rate B_a / B_b at equilibrium.

Under ideal conditions for vegetation (no water and nutrient stress, no salinity, no fire, etc), equation (47) reduces to

$$\text{minLimit} = 2 \cdot \text{seasonC}. \tag{69}$$

The differential equations (31) and (32), by using relations (33), (39)-(43), (45), (48), (57), (67), (69) and parameters in Table A-3 were coded in MatLab as part of this work and solved for vegetation types Tree Island Sawgrass, and Wet prairie. The initial

condition for the biomass was 0.01% of $B_{a\max}$ and $B_{b\max}$. The results for a period of 5 years are presented in Figure A-6, Figure A-7 and Figure A-8. The annual mean and the range of the parameters of the model after the year 10 are also shown in Table A-4. The results obtained however show some inconsistencies, which are discussed next.

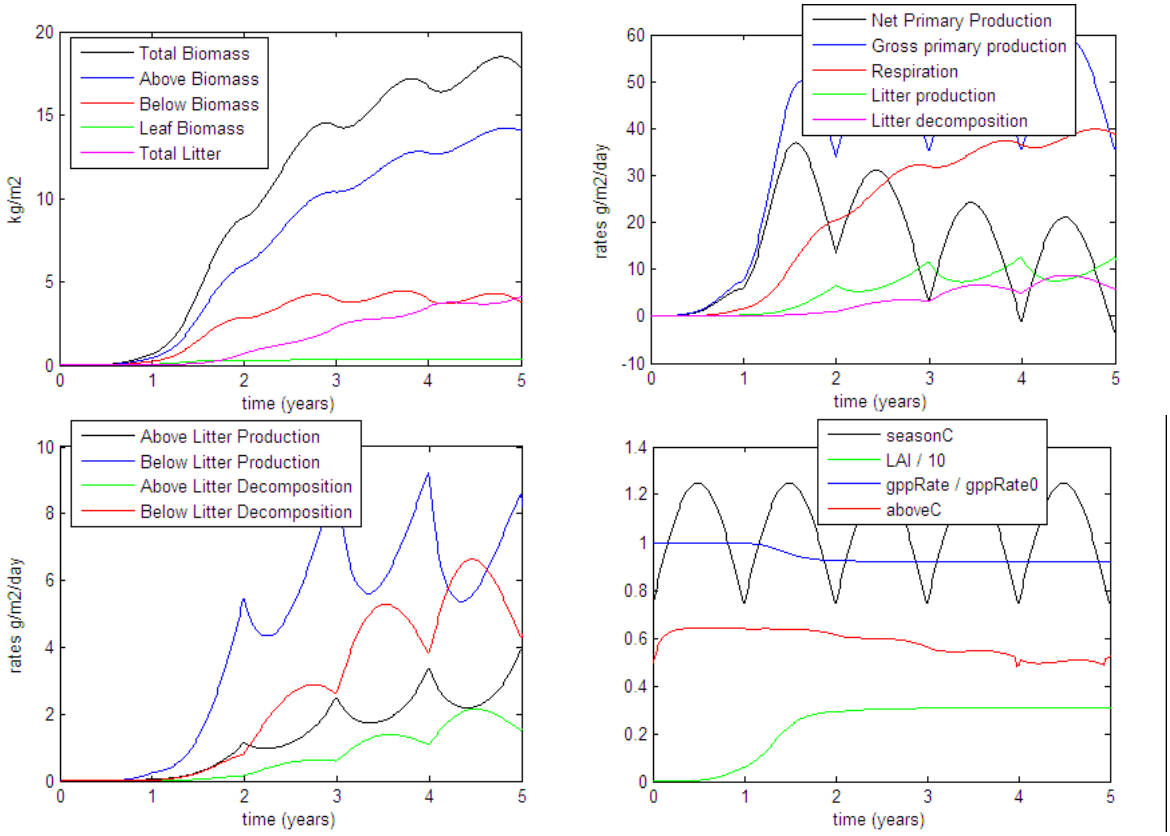

Figure A-6. Results obtained from solving the Wu model for the vegetation type "Tree Island" in an ideal case (vegetation under no stresses).

In the case of tree island vegetation, it is unlikely that the average below-ground biomass slightly decreases with time after the fourth year, while the average above-ground biomass systematically increases (see Figure A-6). On the other hand, in the case of sawgrass, the increase in biomass of 1.5 kg/m^2 in a period of half year (see Figure A-7) is too high compared with the increase of 0.5 kg/m^2 in a year observed by Newman et al. [1996].

One parameter that is well measured in the tree islands is the litter production of the above-ground biomass. According to Table 11, for the Hardwood Hammock the average litter production is about 1 kg/m^2/yr= 2.8 g/m^2/day. However, the above-ground litter production rate predicted from the Wu et al. model for the tree island vegetation

oscillates around 3.5 g/m^2/day (see Table A-5).

In the case of sawgrass, it is striking that according to the Wu et al. model (see Figure A-7), the sawgrass produce around 2.5 g/m^2/day= 0.91 kg/m^2/yr and wet prairie 2.32 g/m^2/day= 0.85 kg/m^2/yr of above-ground litter, which is about the Hardwood Hammock litter production. Ewe et al. [2006] reported lower values for the above NPP rates for sawgrass and marsh areas in the Everglades between 0.36 and 0.61 kg/m^2/yr, and if the vegetation is in equilibrium (no net growing or dying), it is equal to the above-ground litter production rate. Those above NPP rates however, are lower that the range from 0.80 to 2.03 kg/m^2/yr reported by Davis [1989], according to Ewe et al. [2006]. A more recent work published by Davis [2006], he uses an annual litter production rate of 1.8 kg/m^2/yr for sawgrass.

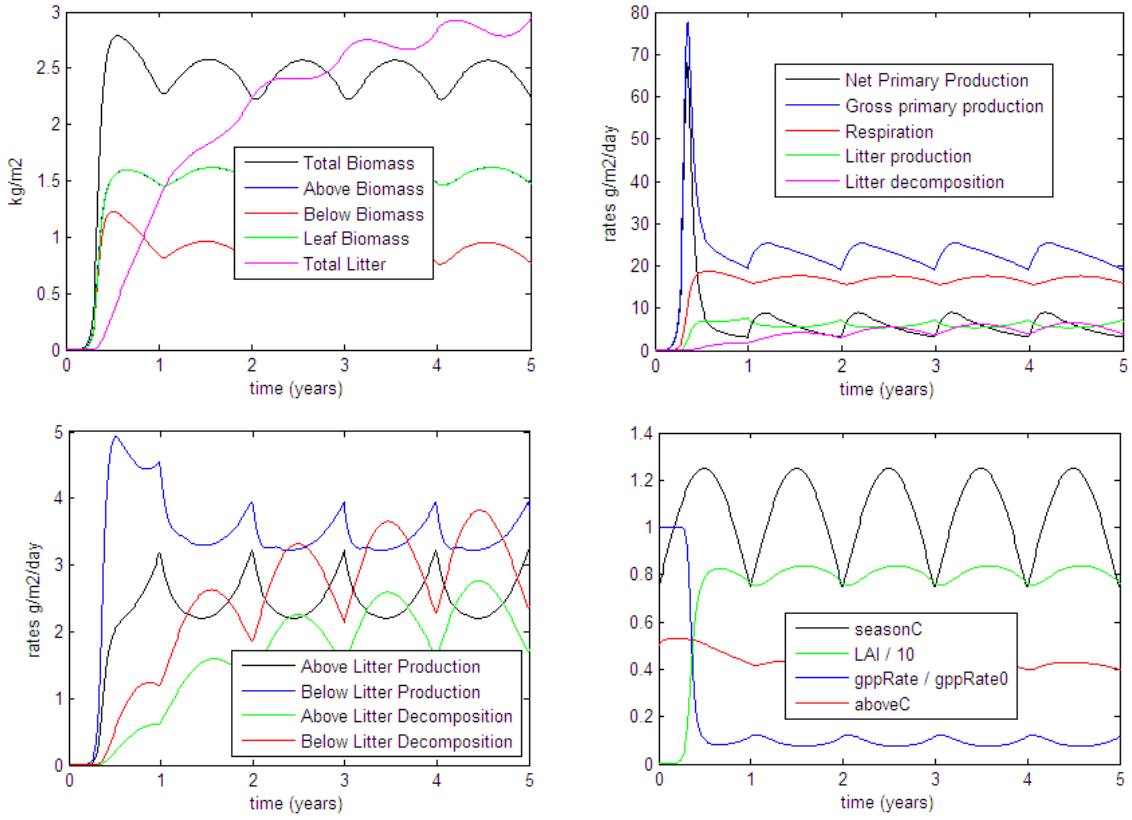

Figure A-7. Results obtained from solving the Wu model for the vegetation type called "Sawgrass" in an ideal case (vegetation under no stresses).

Notice that the net primary production (NPP) rate reaches negative values for the tree island case and not for sawgrass and wet prairie. As shown in Figure A-6, the respiration rate remains about constant meanwhile the gross primary production rate

oscillates and reaches values below the first one. It is unlikely that daily NPP rate becomes negative in the reality [D. DeAngelis, personal communication] but in any case, negative values of NPP cannot be used in equation (63) for estimating the daily Phosphorus uptake, which is positive during the whole year.

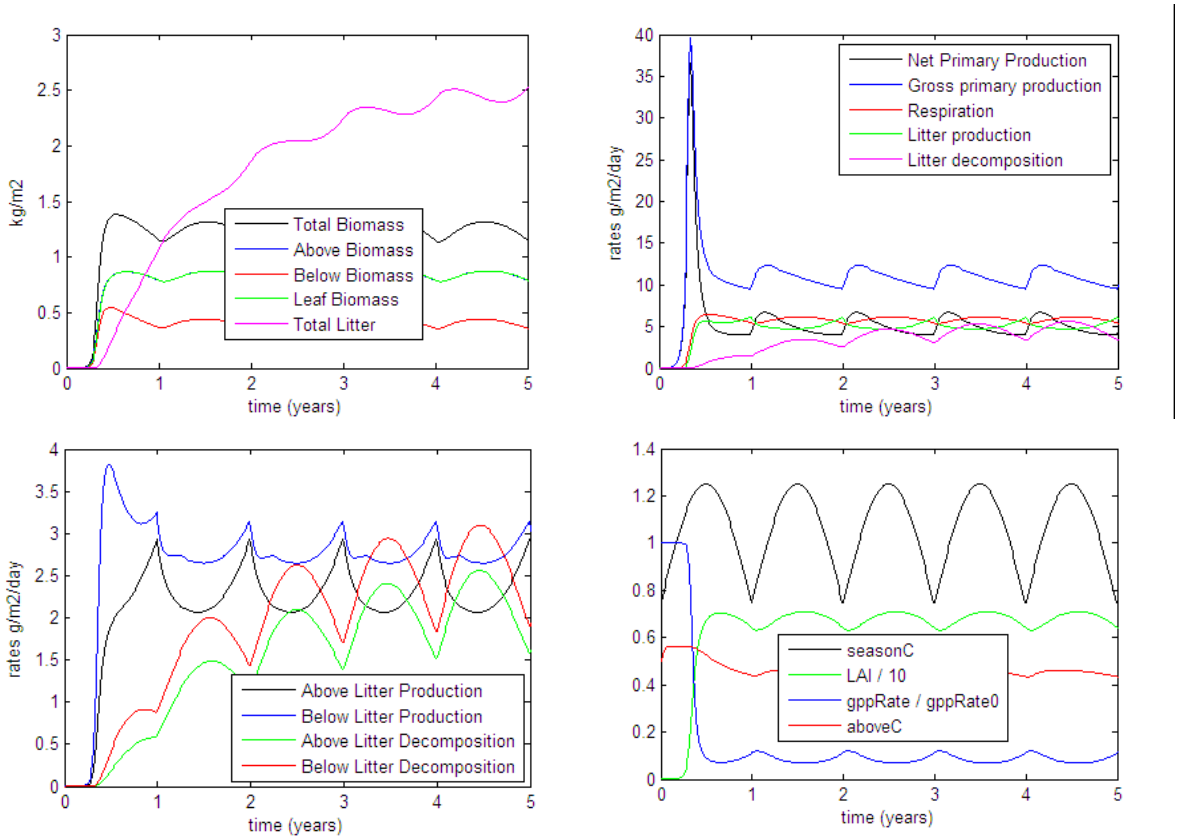

Figure A-8. Results obtained from solving the Wu model for the vegetation type called "Wet prairie" in an ideal case (vegetation under no stresses).

Table A-4 shows a comparison between the mean above-ground biomass and above-ground litter from the model with the field sampling conducted by Carter et al. [1999] on two times of the year 1996 in Shark River Slough. The above-ground biomass of sawgrass and wet prairie (corresponding to sparse vegetation) is overpredicted by the model. The above-ground litter from the model cannot be compared directly to the Carter et al. results, because the last ones are only the standing died biomass and do not account for the fallen biomass. However, it can be seen that the above-ground litter fluctuations from the model are much smaller than the standing died biomass fluctuations. So, the model is likely underpredicting the seasonal fluctuations on sawgrass and wet-prairie litter.

	Vegetation class	Above-ground Biomass (kg/m2)	Above-ground Litter (kg/m2)	La/Ba
Wu Model	tree island	16.04	1.68	0.10
	sawgrass	1.56	1.27	0.81
	wet prairie	0.84	1.17	1.40
Carter et. al. OFR 99-187, April 1996.	Sparse sawgrass	0.12	0.22	1.75
	Medium sawgrass	0.27	0.51	1.86
	Dense sawgrass	0.46	0.80	1.73
	Very dense sawgrass	1.15	2.05	1.77
	Sparse rush	0.00	0.06	24.62
	Sparse Mixed Sg/R	0.07	0.28	3.80
	Medium Mixed Sg/R	0.18	0.56	3.11
	Dense Mixed Sg/R	0.19	1.18	6.06
Carter et. al. OFR 99-218, Nov. 1996. (only sawgrass counted)	Medium sawgrass	0.28	0.22	0.79
	Dense sawgrass	0.52	0.36	0.68
	Very dense sawgrass	1.14	0.50	0.44

Table A-4. Comparison of above-ground biomass and above-ground litter from different sources.

In summary, the results from the Wu Model in the limit case of no stress showed appreciable deviations from the observed data. The overpredicted production rates may be a consequence that the measurements are conducted on vegetation under stress. In a future work, the Wu's model could be set up for the existing stress conditions (water levels, nutrient amounts, etc) in order to better check its validity. Moreover, other unrealistic results (like the decreasing of the below-ground biomass and the negative *NPP* for tree islands vegetation types) could be fixed by changing model equations and parameters.

Wu et al. Vegetation type	Tree Island			Sawgrass			Wet prairie		
Corresponding Ross et. al. Vegetation type	HH, BH, BS			TS			MA		
	mean	min	max	mean	min	max	mean	min	max
Total Biomass (kg/m^2)	19.46	18.74	20.15	2.44	2.22	2.57	1.25	1.14	1.32
Above-ground biomass (kg/m^2)	16.04	15.71	16.36	1.56	1.46	1.62	0.84	0.78	0.87
Below-ground biomass (kg/m^2)	3.42	3.03	3.79	0.88	0.76	0.95	0.41	0.36	0.44
Leaf Biomass (kg/m^2)	0.32	0.32	0.32	1.56	1.46	1.62	0.84	0.78	0.87
Total Litter (kg/m^2)	4.33	4.13	4.55	2.99	2.89	3.10	2.58	2.50	2.67
Above-ground Litter (kg/m^2)	1.68	1.61	1.76	1.27	1.22	1.32	1.17	1.13	1.22
Below-ground Litter (kg/m^2)	2.64	2.51	2.80	1.73	1.68	1.78	1.41	1.36	1.45
Net Primary Prod. ($g/m^2/d$)	8.61	-6.66	17.53	5.85	3.24	8.98	5.06	4.05	6.73
Gross Primary Prod. ($g/m^2/d$)	50.26	34.75	59.30	22.71	19.06	25.38	10.93	9.49	12.35
Respiration ($g/m^2/d$)	41.65	40.34	42.90	16.86	15.66	17.61	5.87	5.37	6.17
Total Litter prod. ($g/m^2/d$)	8.72	7.05	11.91	5.91	5.43	7.23	5.09	4.72	6.14
Above-ground Litter prod. ($g/m^2/d$)	3.50	2.89	4.93	2.50	2.20	3.26	2.32	2.06	2.97
Below-ground Litter prod. ($g/m^2/d$)	5.21	4.06	6.97	3.40	3.22	3.97	2.77	2.65	3.17
Total Litter decomp. ($g/m^2/d$)	8.69	6.13	10.17	5.86	4.10	6.90	5.05	3.53	5.95
Above-ground Litter decomp. ($g/m^2/d$)	3.39	2.39	3.99	2.48	1.74	2.92	2.30	1.61	2.71
Below-ground Litter decomp. ($g/m^2/d$)	5.30	3.74	6.18	3.38	2.37	3.98	2.75	1.92	3.25
seasonC	1.06	0.73	1.25	1.06	0.73	1.25	1.06	0.73	1.25
LAI	3.07	3.07	3.07	8.05	7.56	8.38	6.79	6.32	7.09
gppRate/gppRate0	0.92	0.92	0.92	0.093	0.076	0.122	0.087	0.069	0.120
aboveC	0.45	0.39	0.60	0.418	0.398	0.429	0.452	0.434	0.462
Hv (cm)	1019	1014	1024	278	276	279	134	133	135

Table A-5. Results obtained from solving the Wu model for the vegetation types Tree island and Sawgrass in an ideal case (vegetation under no stresses), between year 10 and 11.

Appendix 2. Addendum for Chapter 2

A2.1 Infiltration from OL Layer

It is useful to explain how the MODHMS considers the infiltration at the bottom of the OL layer by using the leakage. MODHMS is based on MODFLOW, which in its earlier versions only considered groundwater saturated flow. The head value characteristic for each cell is usually assigned to the cell center and the velocities or flows to the cell faces. In the upper cell, however, where there may be a recharge from rainfall, MODFLOW assumed that the head is located at the top of the cell. Thus, the infiltration rate would take into account the flow resistance of the whole upper layer depth.

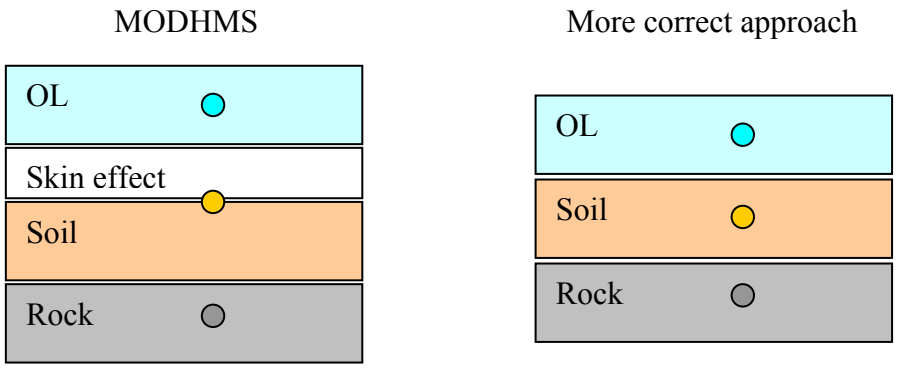

Figure A-9. Schematic view of the vertical position of the head in the model according to MODHMS compared to a more correct approach.

In MODHMS, the heads are located for the GW cells as in MODFLOW, and when they added the OL layer, they introduced a leakage coefficient to represent a skin effect on the soil surface and prevent instantaneous infiltration from OL layer to the soil (see left side in Figure A-9). Therefore, from the OL head (H_{OL}), the soil head (H_{Soil}), and the leakage coefficient (L) the vertical infiltration velocity is given by

$$V_{OL->Soil} = L\left(H_{OL} - H_{Soil}\right). \tag{70}$$

By using an alternative approach, where all the heads are in the cell center (as in the right side in Figure A-9), the vertical infiltration velocity can be found by using the hydraulic conductivity of the saturated soil (Kh_{Soil}), the relative permeability coefficient of the soil (Kr_{Soil}), the soil cell depth (d_{Soil}) and the head difference as

$$V_{OL->Soil} = Kh_{Soil} Kr_{Soil} \frac{\left(H_{OL} - H_{Soil}\right)}{\frac{d_{Soil}}{2}}. \tag{71}$$

By imposing the condition that the head differences as well as the infiltration velocities must be the same in equations (70) and (71), the leakage coefficient is found as

$$L = \frac{Kh_{Soil} Kr_{Soil}}{\frac{d_{Soil}}{2}}. \tag{72}$$

On the other hand, the infiltration from the soil layer into the rock layer according to MODHMS approach would be

$$V_{Soil->Rock} = \frac{1}{\frac{d_{Soil}}{Kh_{Soil} Kr_{Soil}} + \frac{\frac{d_{Rock}}{2}}{Kh_{Rock} Kr_{Rock}}} \left(H_{Soil} - H_{Rock}\right), \tag{73}$$

and for the alternative approach

$$V_{Soil->Rock} = \frac{1}{\frac{\frac{d_{Soil}}{2}}{Kh_{Soil} Kr_{Soil}} + \frac{\frac{d_{Rock}}{2}}{Kh_{Rock} Kr_{Rock}}} \left(H_{Soil} - H_{Rock}\right). \tag{74}$$

In a case where there are no lateral flows, and no saturation changes, the infiltration velocity from volume conservation is

$$V_{OL->Rock} = V_{OL->Soil} = V_{Soil->Rock.} \cdot \tag{75}$$

From MODHMS equations (70) and (73);

$$V_{OL->Rock} = \frac{1}{\frac{1}{L} + \frac{d_{Soil}}{Kh_{Soil} Kr_{Soil}} + \frac{\frac{d_{Rock}}{2}}{Kh_{Rock} Kr_{Rock}}} \left(H_{OL} - H_{Rock}\right). \tag{76}$$

Meanwhile, from alternative model equations (71) and (74), relation (75) implies

$$V_{OL->Rock} = \frac{1}{\frac{d_{Soil}}{Kh_{Soil} Kr_{Soil}} + \frac{\frac{d_{Rock}}{2}}{Kh_{Rock} Kr_{Rock}}} \left(H_{OL} - H_{Rock}\right). \tag{77}$$

Thus, by imposing the condition that vertical infiltration velocity in this particular 1D case must be the same on both models, it results in

$$\frac{1}{L} \to 0, \tag{78}$$

which means no skin effect and it is contradictory to relation (72).

One can alternatively consider that H_{Soil} is different on both approaches, which implies that (72) is not valid and from (78) that $H_{OL} = H_{Soil}$ in the MODHMS approach. However, different head in the soil would cause different saturation for the unsaturated flow (according to the moisture retention curve) and therefore different relative permeability curves.

In summary, there is no way to choose the leakage coefficient that would make equivalent both approaches schematized in Figure A-9.

From all this analysis, a leakage coefficient between the conditions (72) and (78) could be defined by introducing a factor f_L in the saturated version of (72). This is

$$L = f_L \frac{Kh_{Soil}}{\frac{d_{Soil}}{2}}. \tag{79}$$

When $f_L \to 1$, the saturated version of (72) is recovered and when $f_L \to \infty$ the condition of no skin effect (78) is satisfied.

A2.2 Numerical Diffusion and Stability

In this section the numerical diffusion and stability analysis of the numerical scheme to solve the advection-diffusion equation is presented as described by Lapidus and Pinder [1982].

The advection-diffusion equation (1) in case of 1D uniform flow ($\vec{V} = V\,\hat{x}$, $V > 0$) with no diffusion, no external sources and no adsorption, reduces to

$$\frac{\partial C}{\partial t} + V\frac{\partial C}{\partial x} = 0 \text{ or } C_t + VC_x = 0, \tag{80}$$

in a shorter notation. In an implicit scheme on time and an upstream weighting on space, the equation (80) is discretized as:

$$C^{n+1} - C = -C_r\left(C^{n+1} - C^{n+1}_{j-1}\right), \text{ with} \tag{81}$$

$$C_r = V\frac{\Delta t}{\Delta x}. \tag{82}$$

Here index n and j represent the time and space steps, respectively, and C_r is the Courant number. Expanding in Taylor series around (n, j) until second order derivatives,

$$C^{n+1} = C + C_t \Delta t + \frac{1}{2} C_{tt} \Delta t^2 ,$$
$$C_{j-1}^{n+1} = C + C_t \Delta t - C_x \Delta x - C_{tx} \Delta t \Delta x + \frac{1}{2}\left(C_{tt} \Delta t^2 + C_{xx} \Delta x^2\right). \quad (83)$$

Then substituting (81) in (83) and rearranging

$$C_t + V C_x = \frac{1}{2}\left(-2V C_{tx} \Delta t + V C_{xx} \Delta x - C_{tt} \Delta t\right). \quad (84)$$

On the other hand, the second derivatives can be related by using the differential equation (80) as:

$$C_{tx} = \left(C_t\right)_x = \left(-V C_x\right)_x = -V C_{xx} ,$$
$$C_{tt} = \left(-V C_x\right)_t = -V C_{tx} = V^2 C_{xx} . \quad (85)$$

Thus,

$$C_t + V C_x = \left(\frac{1}{2}(1 + C_r)\Delta x V\right) C_{xx} . \quad (86)$$

Therefore, this scheme introduces a numerical diffusion characterized by the diffusion coefficient

$$D = \frac{1}{2}(1 + C_r)\Delta x V . \quad (87)$$

The numerical diffusion could be reduced if the grid spacing and the time step are smaller so that the term $(1 + C_r)\Delta x$ is diminished. However, the minimum cell width is limited by the condition of having a reasonable running time of the numerical procedure. On the other hand, as $V > 0$ in (87), the numerical diffusion cannot be eliminated completely.

It is worth noticing that the diffusion coefficient on (87) is along the flow direction. Thus, for the grid cells that are not oriented in the direction of the flow, numerical diffusion would occur in both directions.

In summary, it is expected the presence of numerical diffusion in the transport of dissolved Phosphorus and of Phosphorus in suspended particles. The order of the numerical diffusion coefficient can be estimated for the OL layer from (87) by using the typical values $\Delta x = 5\text{m}$, $\Delta t = 0.5$ day= 42300 sec and $V = 0.01\text{m/s}$ in the OL layer. In this

case, the Courant number is $C_r = 84.6$ and the equivalent diffusion coefficient for the numerical diffusion is $D = 2.2$ m^2/s. In GW layers, the velocity is lower and from (87), the numerical diffusion coefficient is therefore lower.

The Von Neumann method [Lapidus and Pinder, 1982] can be used to check the stability of the solution. Let us assume a concentration function with the form:

$$C(x,t) = A(t)\exp(ikx). \tag{88}$$

Thus, the values that appeared on the discretized equation (81) are

$$C = A^n \exp(ikj\Delta x),\ C^{n+1} = A^{n+1}\exp(ikj\Delta x) \text{ and } C_{j-1}^{n+1} = A^{n+1}\exp(ik(j-1)\Delta x); \tag{89}$$

and substituting

$$A^{n+1} - A^n = -C_r A^{n+1}(1-\exp(-ik\Delta x)). \tag{90}$$

This allow to obtain the amplification factor as

$$\left|\frac{A^{n+1}}{A^n}\right| = \frac{1}{|1+C_r(1-\exp(-ik\Delta x))|} = \frac{1}{\sqrt{1+2C_r(1+C_r)(1-\cos(k\Delta x))}} \le 1 \text{ for } C_r \ge 0. \tag{91}$$

Therefore, an error introduced in the numerical solution would not grow and the solution is unconditionally stable.

A2.2.1 Test for a simple case

A simple model was build in order to observe how the numerical diffusion in the transport module affect the movement of a "spot" with high concentration in the overland flow layer.

The model has square grid cell of 10-m size, and a horizontal extension of 600 m in y direction and 400 m in x direction. The ground surface is flat with a slope of 1e-4 in y direction. The model has only one groundwater layer. Model parameters assumed for the overland and the groundwater layer are presented in Table A-6 and Table A-7, respectively.

The initial condition head was assumed flat and tilted as the model surface so that the water depth has a uniform value of 20 cm. Boundary conditions are a constant head in upstream, downstream ends, and no flow in x direction. Initial head values at boundary cells are keep constant during the whole simulation period. External sources of water in the model (such as rainfall or ET) are not considered. The initial concentration map is shown in Figure A-10.

OL Flow Properties	OLF Layer
Initial Head. IH (m)	BOTOL+ 0.2
Bottom Elevation. BOTOL (m)	flat tilted according to y slope
Manning Coefficient. X_FRICTN= Y_FRICTN ($s/m^{1/3}$)	0.2
Bottom Leakage Coefficient. BOTTOM LEAKAGE (s^{-1})	1.0
Height of Rill Storage. RILLSH (m)	0
Height of obstructions. OBSTRH (m)	0
Longitudinal dispersivity. LDISPOL (m)	0
Transversal dispersivity. TDISPOL (m)	0
Vertical dispersivity. VTDISPOL (m)	0
Soil partition coefficient. KDOL (Adsorption)	0
Freundlich Isotherm Ex. ETAOL	0
Degradation Rate. ALAMOL1	0
Degradation Rate O. ALAMOL2	0
Initial concentration. SCONCOL (kg/m^3)	500e-6 in selected cell, 1e-6 otherwise.

Table A-6. OL flow properties for the simple model as introduced in ViewHMS.

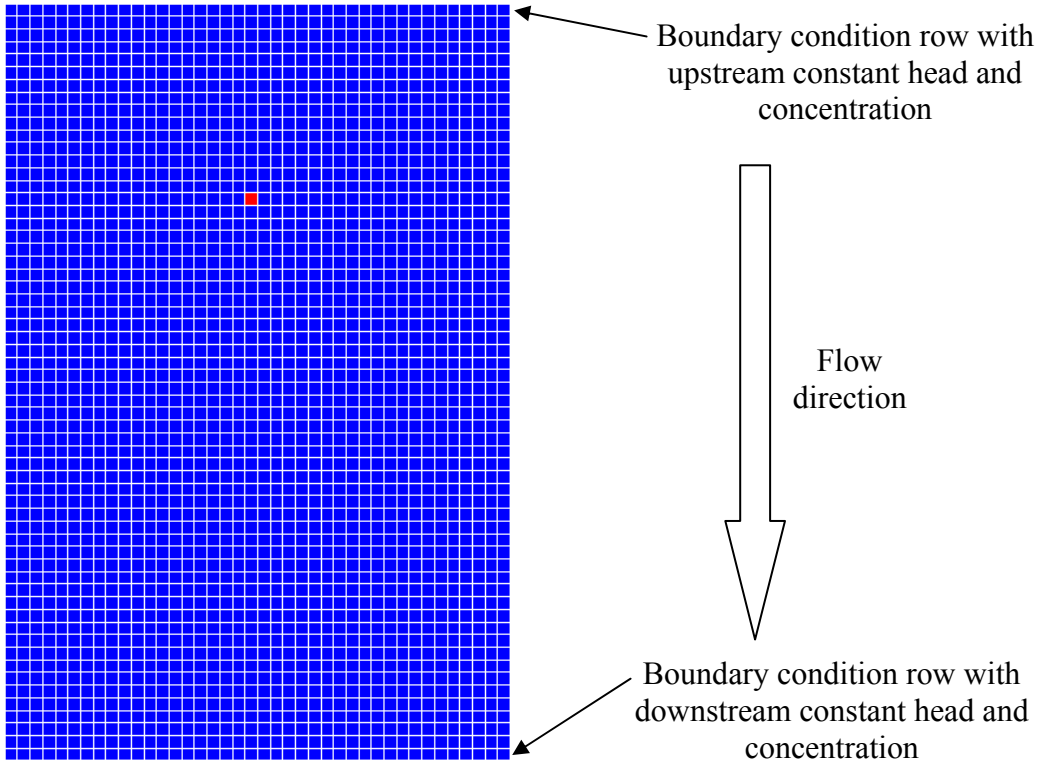

Figure A-10. Initial concentration map. Red color corresponds to 500e-6 kg/m^3 and blue color to 1e-6 kg/m^3. Flow is from above to below.

MODHMS in this simple model solves the flow and the transport in the overland and in the groundwater layer. However, the groundwater layer conductivity was selected

very low so that the movement of the high-concentration spot in the overland layer would be not influenced by groundwater layer. In this simple model setup, the overland flow water speed is constant and uniform with a value of 1.71 cm/s according to Manning equation (20), which matches the MODHMS results of the water flow module.

GW Properties	Layer 1
Primary storage coefficient. SF1	0
Transmissivity. TRAN.	---
Hydraulic conductivity. HY (m/s)	1 e-5
Vertical hydraulic conductivity. VHY (m/s) used when IVHYC=1	1 e-5
Bottom elevation. BOT (m)	TOP -1
Vertical hydraulic conductivity divided by thickness. VCONT (1/s). Not used when IVHYC=1	---
Secondary storage coefficient. SF2= drainable porosity or specific yield	0.3
Top elevation. TOP (m)	BOTOL
Wetting Threshold. WETDRY.	---
Van Genuchten parameter alpha. VANAL (1/m).	3
Van Genuchten parameter beta. VANBT	2
Residual saturation. VANSR	0.01
Brooks-Corey Exponent. BROOK	3
Initial Head. IH (m)	IH from OL
Longitudinal dispersivity. LDISP (m)	0
Transversal dispersivity. TDISP (m)	0
Vertical transverse dispersivity. VTDISP (m)	0
Vertical longitudinal dispersivity. VLDISP (m)	0
Effective porosity. PHI	SF2(soil)
Bulk density. RHOB (kg/m^3)	200
NAPL Saturation. SNAPL	0
Soil partition coefficient (Adsorption) KD (m^3/kg)	3.0e-3
Freundlich Isotherm exponent. ETA	0.4
Degradation Rate. ALAM1	0
Degradation Rate on soil. ALAM2	0
Degradation Rate for inactive phase. ALAM3	0
Degradation Rate for NAPL phase. ALAM4	0
Initial concentration. SCONC ($kg/m^3 = 10^6$ □g/l)	500e-6 in selected cell, 1e-6 otherwise.

Table A-7. Two dimensional properties for the simple model as introduced in ViewHMS.

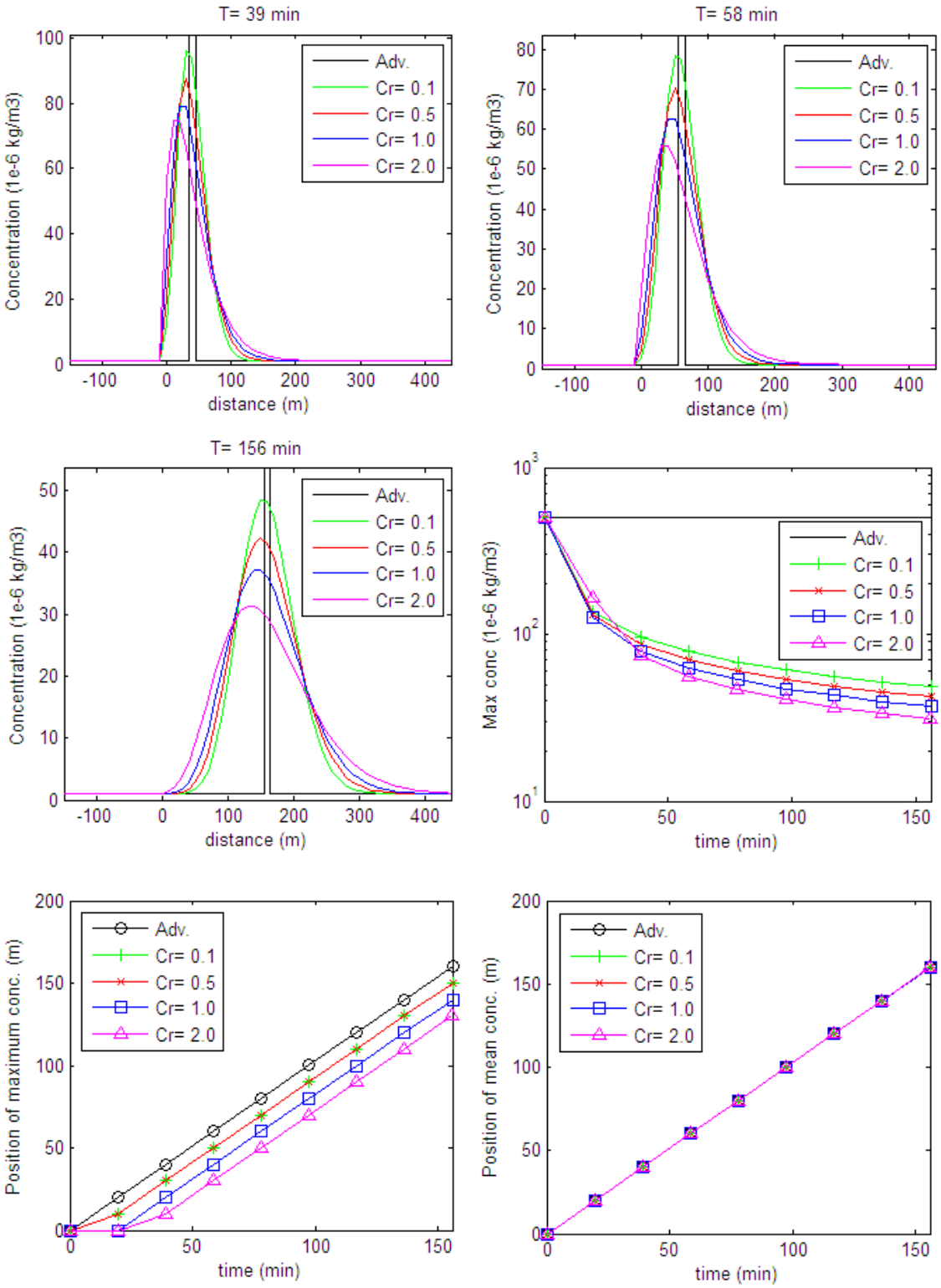

Figure A-11. Some results of the transport module for several Courant numbers. Label "Adv." stands for the results in a pure advection case.

Four different model runs were conducted by using different time steps, so that the Courant number (82) has the values of 0.1, 0.5, 1 and 2. Some results from those runs are compared with the theoretical results of a pure advection transport in Figure A-11.

In all cases, the spot of high concentration move in y-direction showing a widening (or dispersion) in that direction. The position of the maximum and the mean concentration moves at about the same water speed, as expected. The longitudinal dispersion introduced by the numerical scheme is higher for higher Courant numbers as predicted in equation (87), and it does not tend to zero as C_r approaches zero.

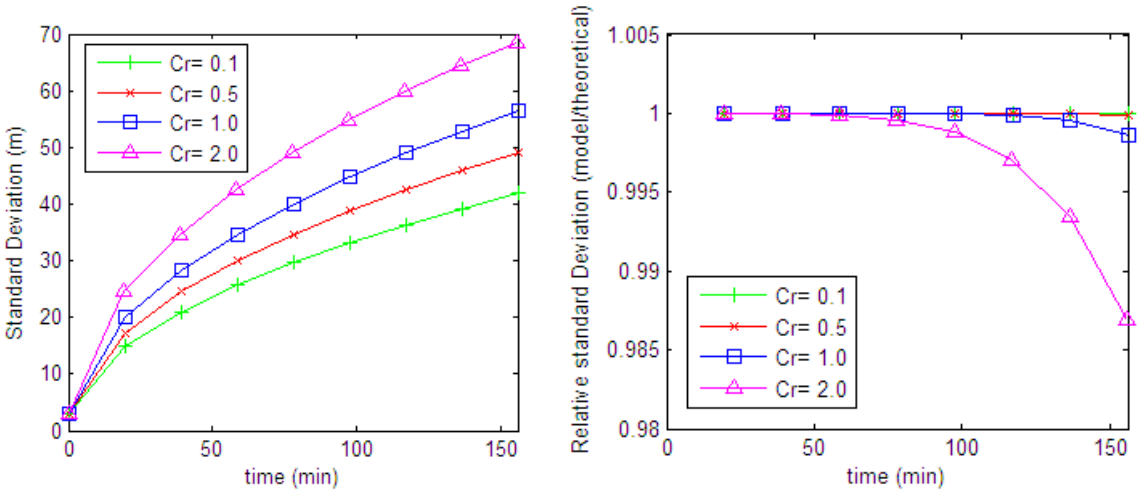

Figure A-12. Standard deviations of the concentration profiles obtained for several Courant numbers. The "theoretical" standard deviation is obtained by substituting (87) in (92).

If the spot of high concentration is submitted to a pure diffusive process in one dimension with a diffusion coefficient *D*, the plume obtained is a Gaussian function with deviation

$$\sigma = \sqrt{2Dt}\,. \tag{92}$$

The plumes obtained in the simple model are not Gaussian, principally at the beginning. However, the standard deviations computed from the concentration profiles match the values obtained by substituting the numerical diffusion coefficient (87) in the Gaussian plume deviation equation (92), as shown on Figure A-12.

Appendix 3. Addendum for Chapter 3

A3.1 Vertical Boundaries of the Soil Layer. Other Details.

The transect points shown in Figure 9 were superimposed on aerial photos of the tree islands by using Autodesk Land Desktop 2005. The photos, which are from year 2004, have a one-meter resolution and were downloaded as SID format from the Labbins webpage (data.labins.org). On that webpage, there are also images available from year 1999, but the tree islands details are more clearly defined in those from 2004. One problem is that the coordinates of the transect data are in the UTM-WGS84 system (also called NAD83 and CSRS98); while the images are georeferenced in the UTM-NAD83 system (Florida East). By using a free software (http://franson.com/coordtrans/) to convert geographic coordinates, the offset between the two coordinate system was found and the world file of the image (*.sdw) was modified in order to reference the 2004 images in the coordinate system of the transect data (WGS84).

Points are created from the vertex of the polylines and they are saved in an ASCII file. The processing of this data was programmed in MatLab, where the points of the original transect and fictitious points are loaded. The coordinate of the points are rotated in order to direct the NS transect toward the y-axis and translated by setting the origin on the point in the transect where the vegetation elevation peaks (see Table A-8). After that, a triangle-based linear interpolation is conducted to obtain the elevation values on a one-meter-spaced grid. Finally, the difference between soil and the bedrock elevation is forced to be higher or equal than a minimum depth of 10 cm. In the grid points where the estimated soil depth is less than the minimum value, that value is assumed and new elevations are computed around the mean value of those two. According to the surfaces that are obtained, the fictitious points are modified and the procedure is repeated. The original and fictitious points as well as the interpolated surfaces for soil and bedrock elevation are shown in Figure A-13 and Figure A-14, respectively. The spatial distribution obtained for the soil depth is also shown in Figure A-15.

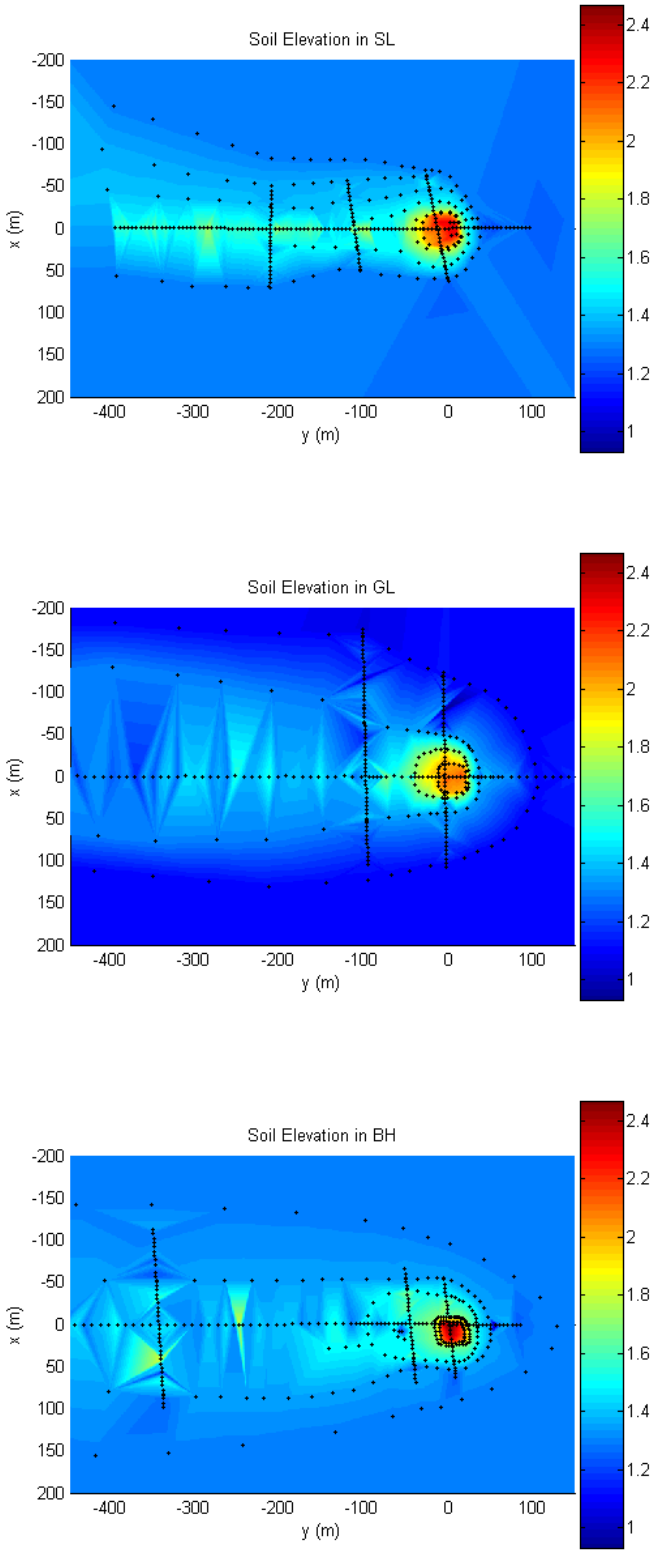

Figure A-13. Interpolated soil surface elevations in the tree islands of Shark River Slough.

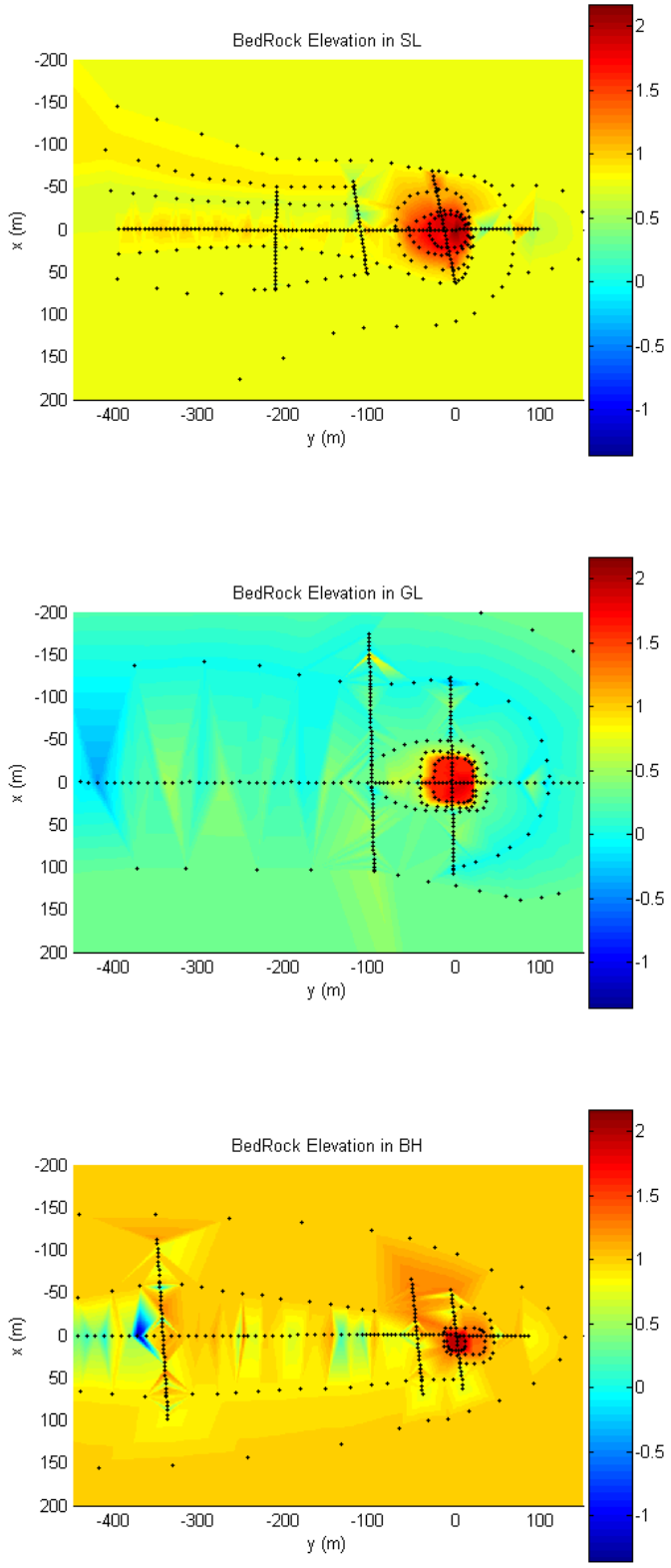

Figure A-14. Interpolated bedrock elevations in the tree islands of Shark River Slough.

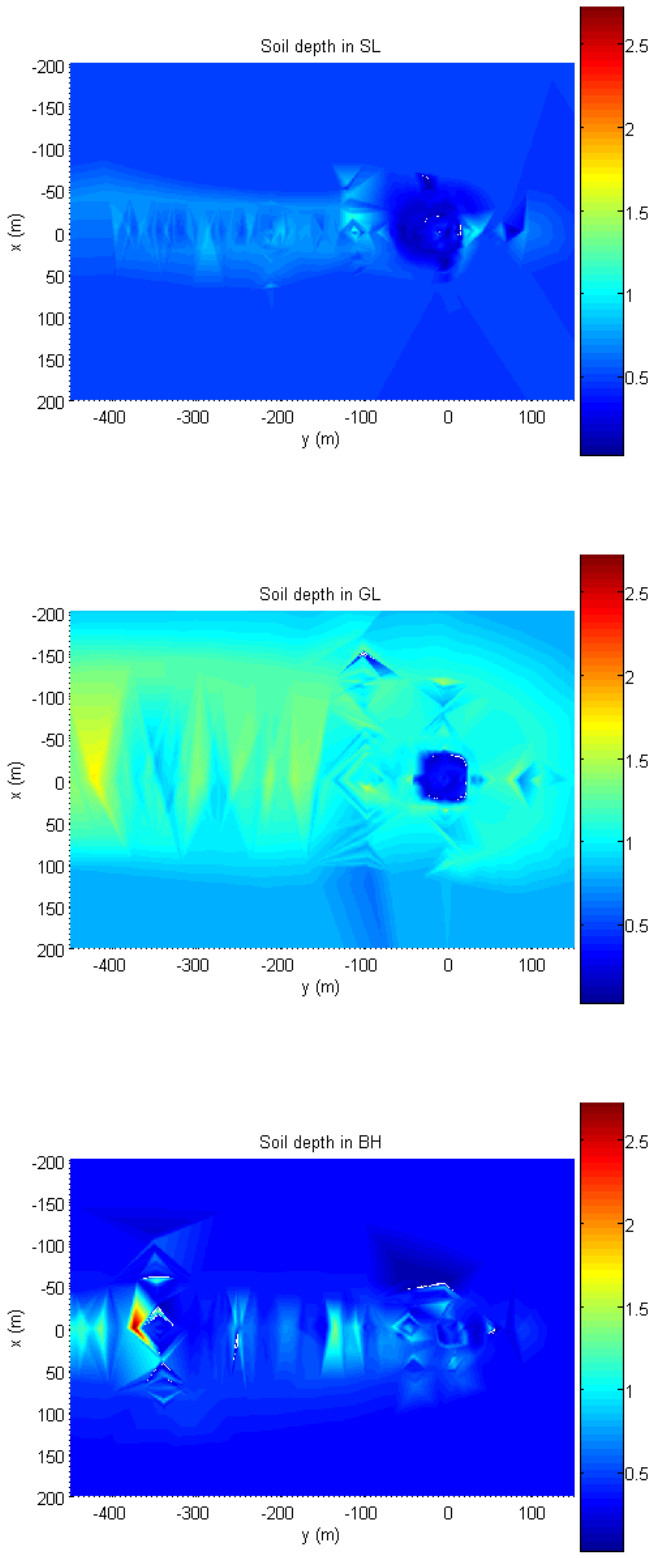

Figure A-15. Soil depth obtained from interpolated soil surface and bedrock elevations in the tree islands of Shark River Slough.

Tree Island	NS Transect angle (degrees)	Origin (0,0)	
		Easting (m)	Northing (m)
Satinleaf (SL)	66.8599	524500.1	2838037.8
Gumbo Limbo (GL)	68.2200	526028.0	2834802.0
Black Hammock (BH)	46.4573	531288.7	2832632.2

Table A-8. Parameters used to transform the coordinates. The NS transect angle is measured from East counter clockwise and the UTM coordinates of the new origins are in the system adopted (WGS84).

A3.2 Vegetation Coverage. Other Details

Maps of the vegetation coverage of the three islands were provided by Pablo Ruiz at SERC, FIU as shape files. The shape files were imported in Land Desktop and each boundary line was converted into two polylines. A vegetation type index along the polylines was assigned from zero to four in the order MA, TS, BS, BH and HH. Then the vertices of the polylines were saved to a file and a triangle-based linear interpolation was made in MatLab. The obtained vegetation coverage type maps are shown in Figure 10.

It should be mentioned that the vegetation coverage of the Tall Sawgrass (TS) around the tree island changes with time because of events like fire and die-off, and it is replaced by other smaller grassy types contained in the Marsh classification [Pablo Ruiz, personal communication]. This makes it difficult to compare the vegetation coverage maps with other information that shows shift over time such as the aerial images from 1999 or 2004, the surveyed transect data of soil elevation and vegetation height, as well as the properties of soil from 2001 and soil water from 2002. Despite the differences found in that information, it was assumed that the vegetation coverage maps provided by Pablo Ruiz from their field experience were correct. Just a minor correction in the original maps was needed in the head of Gumbo Limbo where the area covered by BH and TS overlap, and the TS coverage was redraw according to the 2004 aerial image and the vegetation height from the transect data.

The vegetation height was also interpolated from the transect data collected by [Ross et al. 2004] by using the same procedure described above for the soil surface and bedrock elevation. The resulting vegetation height maps are shown in Figure A-16.

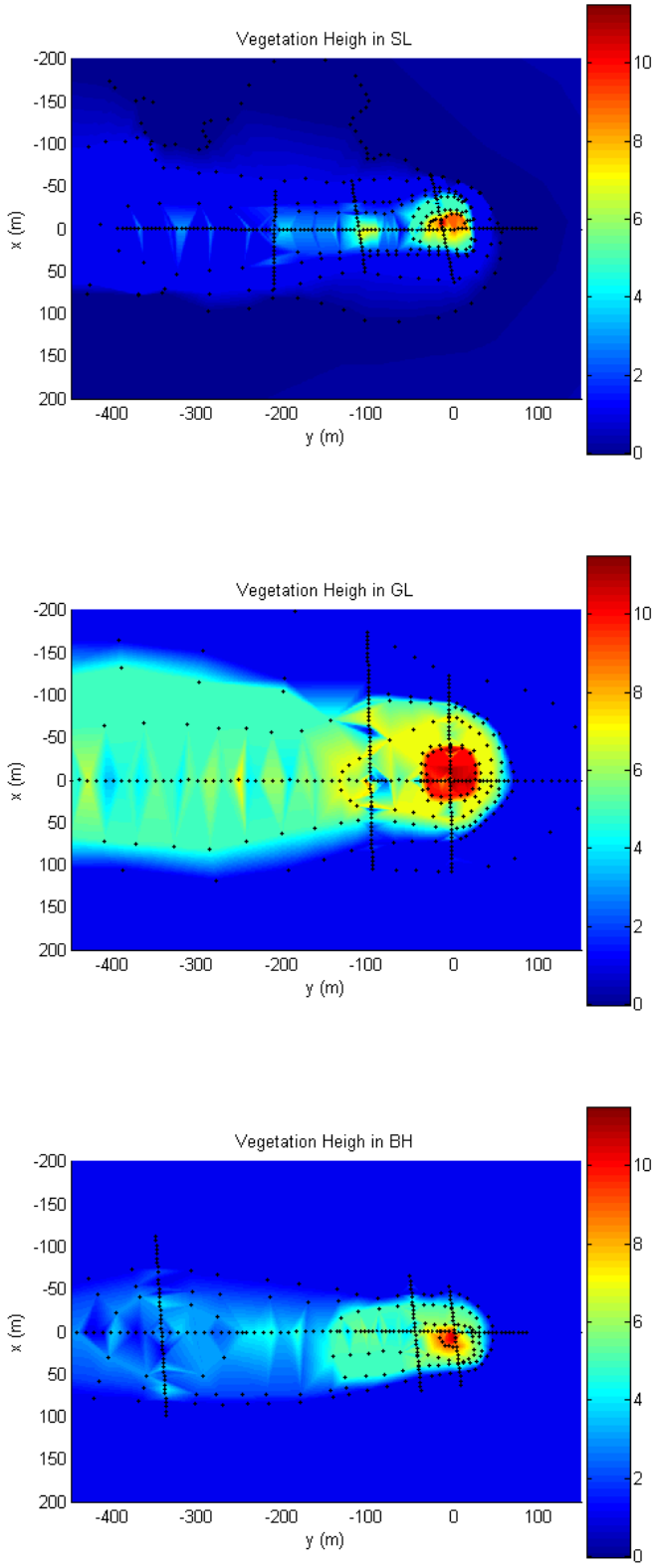

Figure A-16. Interpolated vegetation height in the tree islands of Shark River Slough.

A3.3 Bottom of the Rock Layer. Additional Figures and Tables

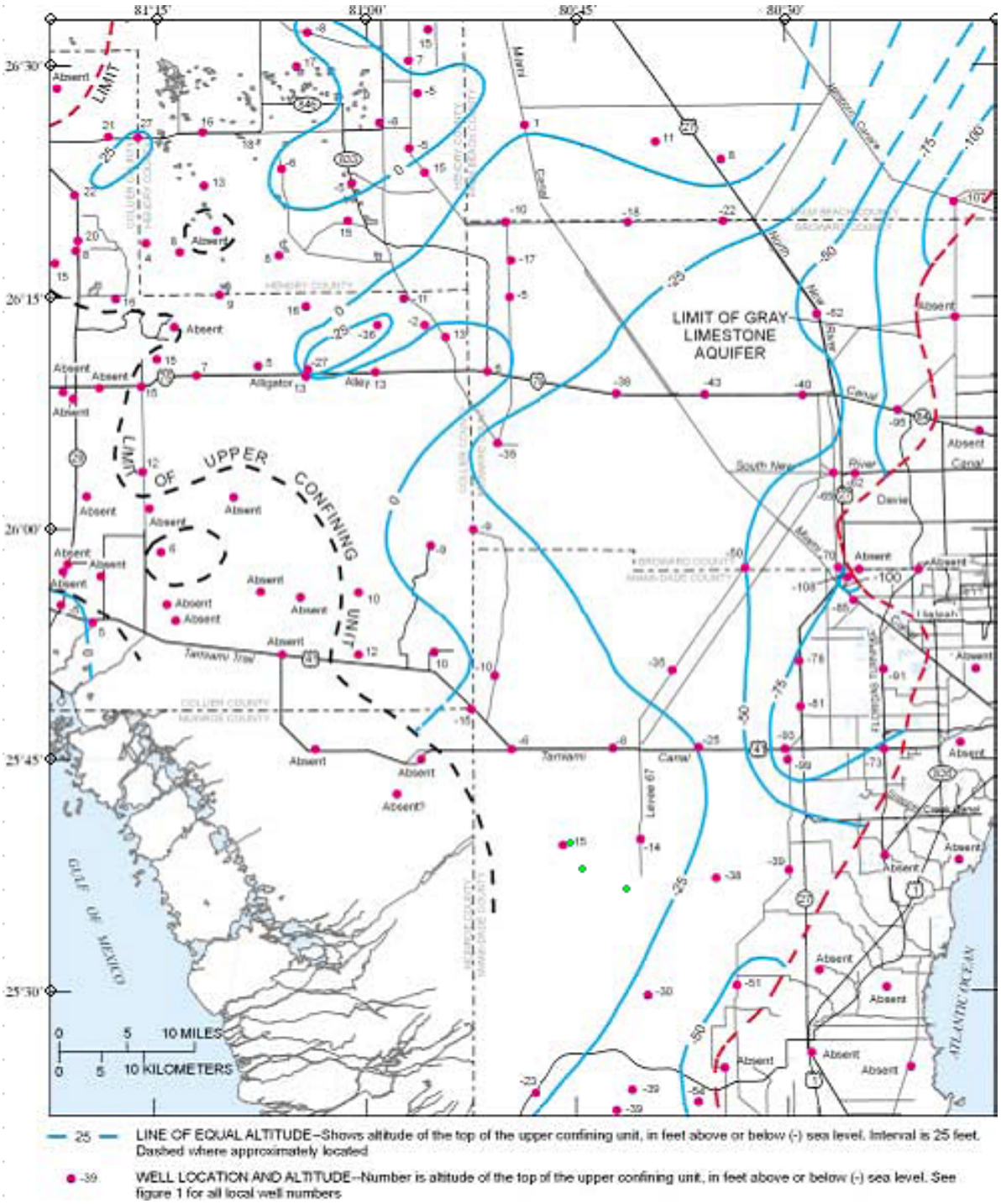

Figure A-17. Top of the Upper Confining Unit reproduced from Reese and Cunningham [2000] in ft NAVD88. Tree islands of Shark River Slough are superimposed as green circles. Red point with value -15 close to Satinleaf Tree Island corresponds to well G-3308 at Observation Tower.

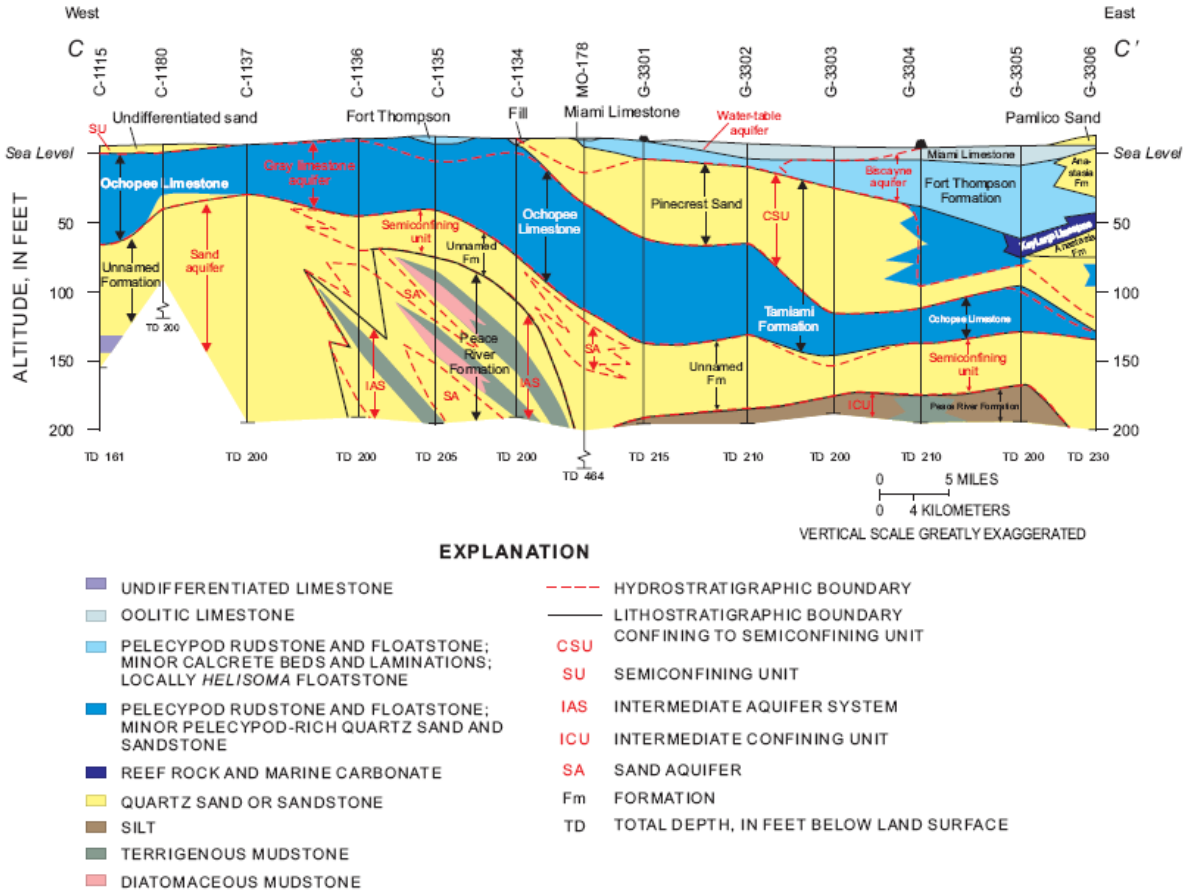

Figure A-18. Hydrogeologic section reproduced from Reese and Cunningham [2000]. Tree islands of Shark River Slough are located south of wells G-3301 and G-3302.

Tree Island	Latitude	Longitude	NAVD88-NGVD29 (m)
Satin Leaf (SL)	25.659779	-80.756168	-0.458
Gumbo Limbo (GL)	25.630758	-80.741066	-0.459
Black Hammock (BH)	25.610798	-80.688563	-0.461

Table A-9. Geographical coordinates in degrees of the tree islands of Shark River Slough, studied by Mike Ross and co-workers at FIU. The datum shift was found using VERTCON (www.ngs.noaa.gov/cgi-bin/VERTCON/vert_con.prl).

A3.4 Horizontal Flow Resistance. Other details

In this section, additional details about the vegetated flow resistance and the applicability of the Manning equation are discussed. In the first part, the Forchheimer

Equation is introduced as an option to fit the flow through Sawgrass in indoor flume experiments. Then the capability of MODHMS to consider vegetated flows is discussed.

A3.4.1 Forchheimer Equation

The Manning equation has been developed for turbulent flow through open water channels, where the resistance to the flow is caused by the surface roughness at the bottom and the sides of the channel. However, in the flow through vegetation the resistance to the flow introduced by steams, branches and leaves along the vertical direction might be important and Manning equation might not be valid.

On several occasions over a 30-month period in 1995 through 1997, USGS researchers measured slope, velocity, and water depth in a 61-m tilting flume with tightly fitted pans of sawgrass emplaced. Unfortunately, the only flow data available is after 13 months of growth, presented by USGS [Jenter, 1996] as shown in Figure A-19. This indoor flume data reveals that the Manning coefficient is not only a function of the vegetation coverage but also of the water depth and the slope in such conditions. The Manning coefficients decrease and reach a plateau as the water surface slope (or velocity) increases. The increase in the Manning coefficients as a function of the water depth might be associated to an increase in the vegetation density as shown in the vertical distribution of averaged total biomass in Figure A-19.

Following the procedure of Stothoff [2004], the 41 points in the Manning coefficient graph in Figure A-19 were digitized and the data were presented in Figure A-20 in the form of mean velocity vs. surface slope. Only 7 points with the lowest velocity, where the experimental determination of the slope has the highest error, were excluded. Surprisingly, the mean water velocity through the tested sawgrass depends only on the surface slope and not appreciably on the water depth, as postulated by Manning equation. This explains the fact that the computed Manning coefficients in Figure A-19 varies with water depth.

Manning equation was satisfactorily tested for open water channels, where the bottom drag produces the flow resistance [Kadlec, 1990]. However, in the literature on flow through an array of vertical cylinders has documented that the influence of the bottom surface on the flow is appreciable only at low water depths. If the water depth is much higher than the stem spacing, then the flow resistance depends only on the

vegetation drag, as shown for example in the vertical velocity profiles reported by Nepf and Koch [1999]. In this work it is believed that in the flume data by Jenter [1996] two factors are combined to give a velocity that is independent from the water depth. First, the near uniform biomass distribution above 20 cm shown in Figure A-19 could cause that the vegetation drag to be almost uniform above this height. Second, the maximum average stem spacing of 5.3 cm computed from the Rybicki et al. [1999] data for the 0-20 cm interval is much less than the 20 cm, which presumes a vegetation drag dominance, even for the minimum water depth tested of 0.5 ft = 15 cm.

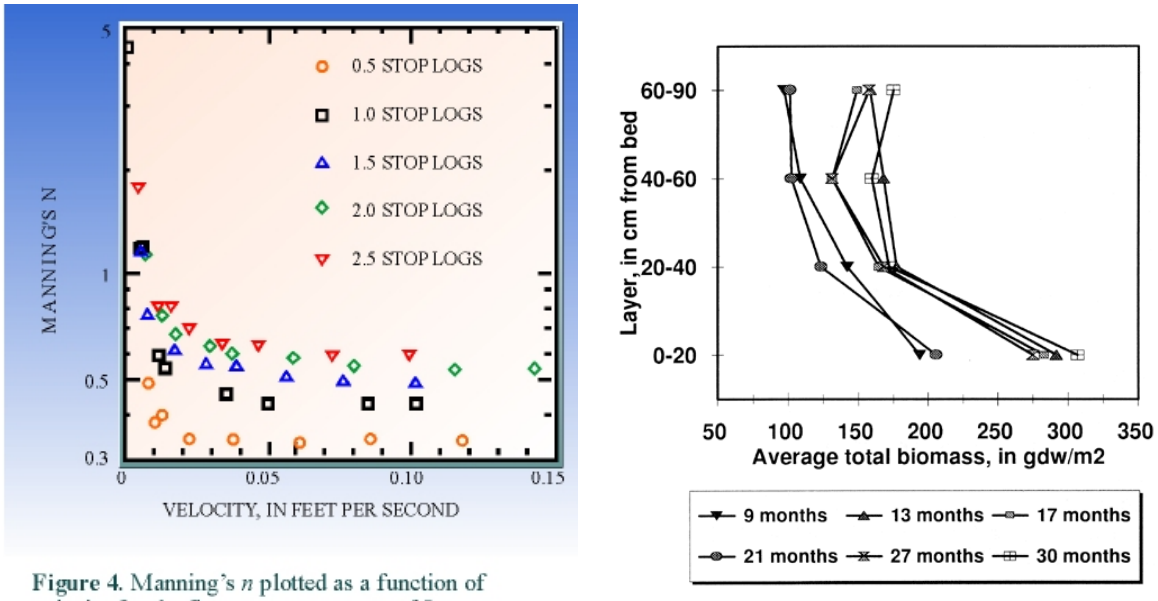

Figure A-19. Manning coefficients for 13-months-old sawgrass reported by Jenter [1996] and the corresponding vertical distribution of averaged total biomass reproduced from Rybicki et al. [1999].

The velocity dependence obtained in Figure A-20 can be reproduced by the Forchheimer equation,

$$V\left(1+C_H\frac{V}{K_H}\right)=-K_H S\,, \tag{93}$$

with the coefficients $K_H = 335\,\text{m/s}$ and $C_H = 1.31\cdot 10^5$. The Forchheimer equation (93) reduces at low velocities ($C_H\frac{V}{K_H} << 1$) to the well-known Darcy equation for porous media flow

$$V = -K_H S\,. \tag{94}$$

Meanwhile, in the high velocity limit ($C_H \frac{V}{K_H} >> 1$), the Forchheimer equation transforms into

$$V = -\frac{K_H}{\sqrt{C_H}}\sqrt{S}\,, \tag{95}$$

which has the same functional dependence with the slope as Manning equation (20) that is associated to a well developed turbulent flow [Kadlec, 1990].

The fitting of the asymptotic limits of the Forchheimer equation, i.e. equations (94) and (95), are also shown in Figure A-20. The high velocity limit equation (95) with the coefficient $K_H / \sqrt{C_H} =$ 0.925 m/s shows a better match, which is consistent with the fact that the Forchheimer coefficients fitted from (93) gives a range of $1.2 < C_H \frac{V}{K_H} < 25$ for the velocity data. Note also that the equation (95) is equivalent to Manning equation (20) for a fixed water depth (stop logs) and the deviations of the equation (95) fitting from the flume data in Figure A-20 are reflecting in Figure A-19 as a dependence of the Manning coefficient on the slope (or velocity).

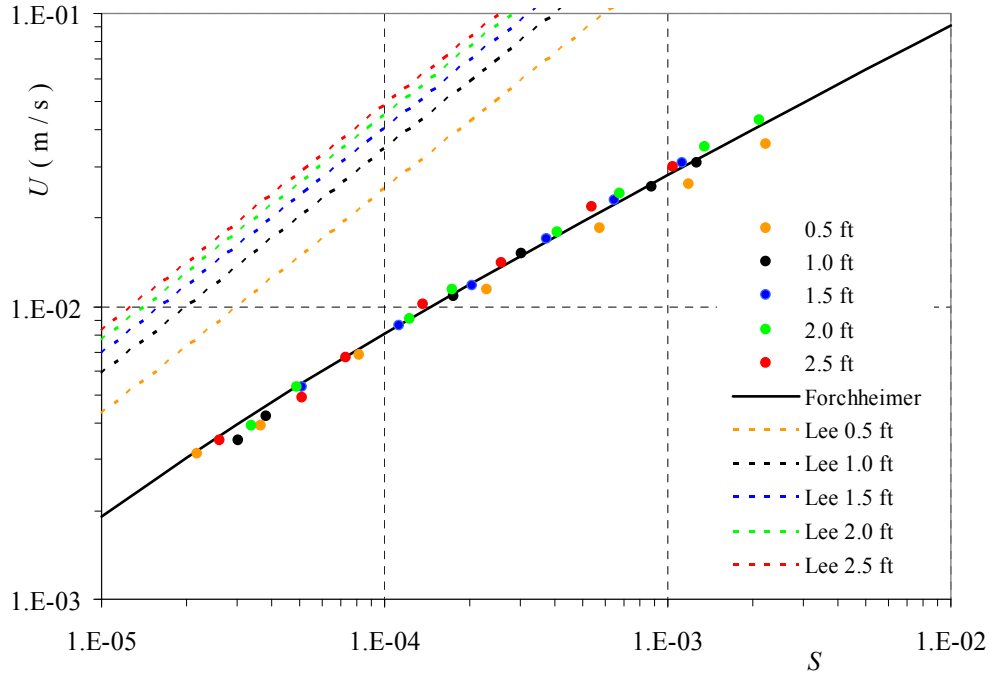

Figure A-20. Indoor flume data for sawgrass from Jenter [1996] fitted by a Forchheimer correlation and its asymptotic limits (dotted lines). Each symbol represents the mean water depth (h) in feet.

A3.4.2 MODHMS Capabilities

The software MODHMS has the option to choose the overland flow velocity correlations among the Manning, the Chezy and the Darcy-Weisbach equations. The last two relations have a similar functional dependence with the form $V \propto \sqrt{hS}$. Therefore, they cannot be applied rigorously to the case of the flow through sawgrass presented in Figure A-20, where the velocity is independent of the water depth.

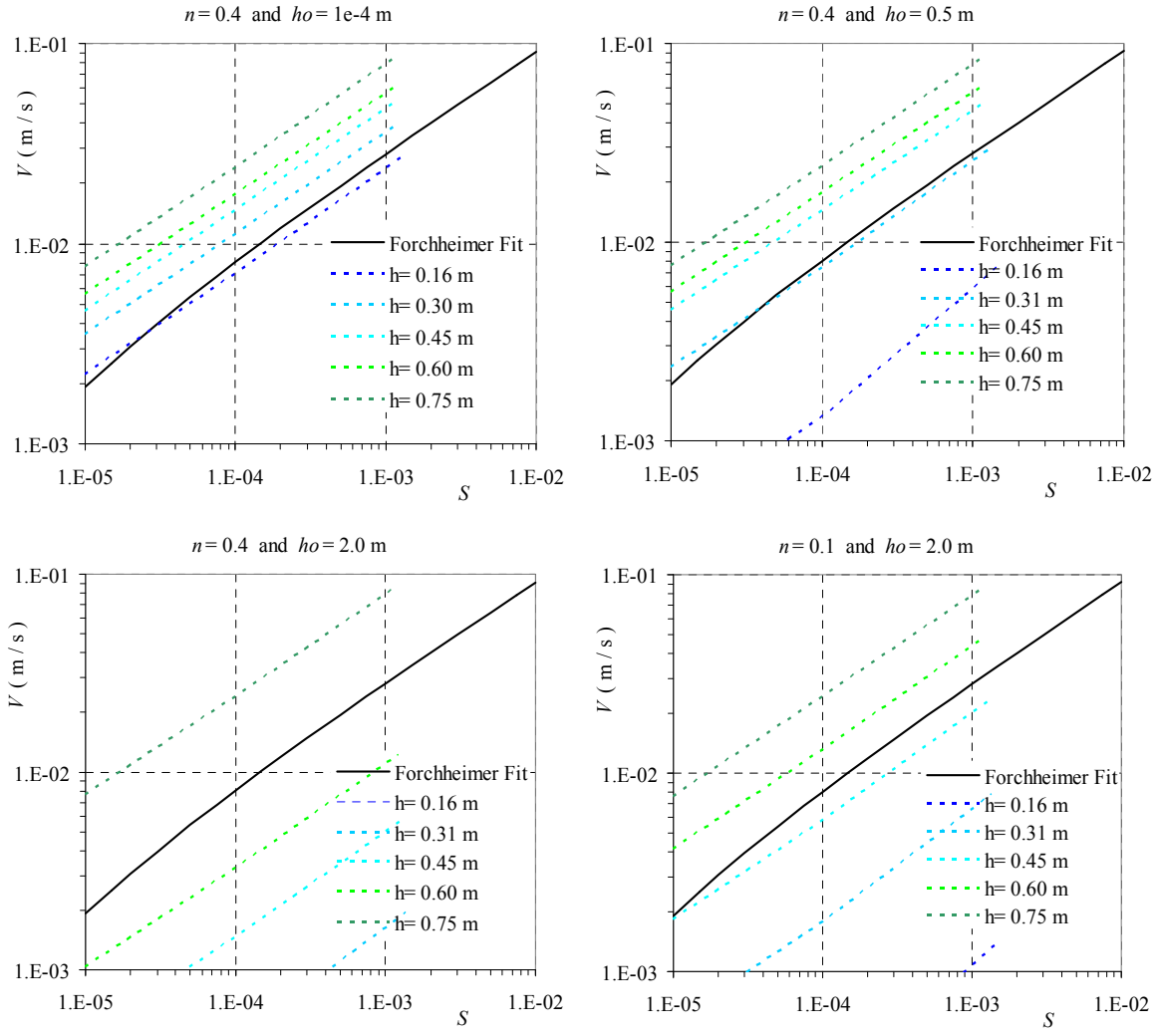

Figure A-21. Comparison of the velocity correlation implemented in MODHMS (dotted lines) for several values Manning coefficients (n) and obstruction heights (ho). The Forchheimer fit shown in Figure A-20 is also included.

The MODHMS also has the option to consider the flow through obstacles (like vegetation, buildings, etc) by defining the rill storage height and the obstruction height (ho) [HydroGeoLogic (HGL) Inc., 2006]. The rill storage is the amount of storage that

must be filled by water before any lateral overland flow can occur and in this model it is assumed negligible. On the other hand, the obstruction height is the height below which the flow is reduced because of the obstructions. MODHMS multiplies the conductance term by a factor from zero to one as the height goes from zero to *ho* .

In order to see the changes that the obstruction height introduces to the overland flow rate, a simple model recreating a flume experiment was implemented in MODHMS. The model has a groundwater layer with negligible conductivity and an overland flow layer where Manning equation rules. The horizontal grid has one column and three rows, i.e., only three cells oriented in the *y* direction. Constant head conditions are applied in the two boundary cells in order to reproduce approximately the desired water depth and slope, and the overland flow rate in the center cell is given by MODHMS after waiting enough time to reach a steady state (one week). Thus, each MODHMS run for a fixed value of Manning coefficient and obstruction height, has a sequence of water depth values from about 0.15 to 0.75 m in intervals 0.15 m, and for each stage the sequence of slopes 10^{-3}, 10^{-4} and 10^{-5}. The results obtained for several combinations of *n* and *ho* are presented in Figure A-21 and Figure A-22.

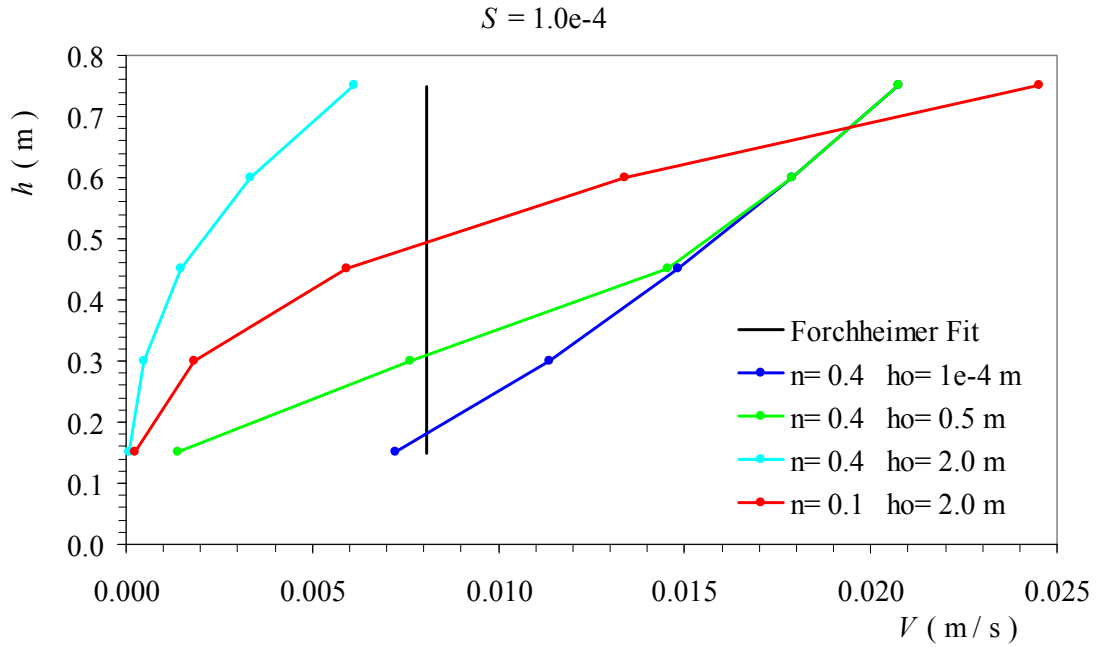

Figure A-22. Vertical dependence of the velocity in the cases shown in Figure A-21 for the slope of 1e-4. Notice that here the mean velocity is plotted, and they are different from the vertical profiles of the microscopic velocity measured for example by Nepf and Koch [1999].

It is clear from Figure A-21, that the variation of the velocity with the water depth is higher when *ho* is not negligible. In other words, Manning equation corrected by the obstruction height is more sensitive on the water depth than the original equation. This effect is contrary to the results for sawgrass reported by Jenter [1996], where the velocity was nearly independent on the water depth. The vertical dependence of the velocity showed in Figure A-22 can help to understand why. The velocity in the case with $n = 0.4$ and $ho = 0.5\,\text{m}$ is equal to the one with *ho* negligible when the water depth is greater than *ho*. This means that if the water depth is higher than the obstruction height the velocity is the same as if there were not obstacles, which is an inaccuracy in the conceptualization of the obstruction height in MODHMS.

In summary, MODHMS could only consider the vegetated flow resistance by using a Manning type equation.

A3.5. Rainfall Data Processing

Daily rainfall data are available for the 33 stations listed in Table A-10, which are located less than 23 km around the tree islands Satin Leaf (SL), Gumbo Limbo (GL) and Black Hammock (BH). The geographical coordinates of the tree islands and the stations are shown in Table A-9 and Table A-11, respectively. The location of tree islands and stations are shown in the map of Figure A-23.

Most of the time series rainfall data were downloaded from the South Florida Water Management District's electronic database, DBHydro (www.sfwmd.gov/org/ema/dbhydro/). These data contain daily average depth rates originally in inches from the US agencies Everglades National Park (ENP), United States Geological Survey (USGS) and South Florida Water Management District (SFWMD) and the data base key is specified in Table A-10. Sometimes in the DBHYDRO data, accumulated rainfall values for more than one day are reported, instead of the daily rainfall. These were eliminated from the series. Several time series labeled here as EDEN were also supplied by Roy Sonenshein at Eden project (http://sofia.usgs.gov/eden/). A few series were also obtained from data collected by Ahn [2003] (labeled as ENP). The period covered by the date and the mean number of valid points every 365 days are also presented in Table A-10. The number of available rainfall station data per day is

presented in Figure A-24.

There are in general differences between the station geographical coordinates reported by DBHYDRO and the ones reported by EDEN project that may be important while interpolating the station data for the tree island locations. It has been assumed here (see Table A-11) that the station coordinates have less error when reported in the Gazetteer by [USGS, 2003], followed next by the EDEN project and lastly DBHYDRO. In the case of station G-620, which is important to the stage interpolation in SL Tree Island, it is located at the Observation Tower [Roy Sonenshein, personal communication].

Station	DBKEY	start	end	valid values / 365 days
84095	PT257 PT258 PT259	6/1/1990	12/28/2001	240.7
88780	PT393 PT394 PT395	7/2/1948	10/26/2001	283.5
3AS3W3	M6888	5/9/2000	2/16/2007	349.5
BCA20	PT551	6/13/2002	3/7/2007	338.8
BCNPA9	TB034	3/8/2006	3/8/2007	365.0
CHEKIKA_EV	16709	10/21/1993	5/13/2005	310.7
G-1502	6029	4/27/1984	1/31/1991	355.7
HOMES.ES	06211 07480	1/1/1914	9/30/1988	345.1
	6268	1/1/1942	7/31/1991	317.0
NESRS1 (SR1)	H6057 EDEN	11/1/1985	9/30/2006	262.2
NP-201	785 6044 EDEN	10/1/1974	9/29/2006	255.8
NP-202	G6149 EDEN	2/4/1993	9/28/2006	333.7
NP-203	6040 EDEN	2/13/1982	9/29/2006	315.3
NP-205	793 G6147 EDEN	5/28/1975	9/29/2006	166.2
NP-206	743 G6155 EDEN	5/15/1975	8/24/2006	233.4
NP-311	H1994 ENP	9/28/1985	12/31/2002	362.8
NP-A13	H1975 EDEN	9/25/1996	9/29/2006	364.4
NP-CR2	H2438	6/7/1996	12/31/1999	347.6
NP-FMB	H2005 ENP	1/1/1949	12/31/2002	363.9
NP-IFS	HB872	1/1/1914	12/31/1999	325
NP-N10	H1974	9/15/1994	11/30/1998	340.1
NP-OT3	H6055	3/19/1993	12/31/1999	359
NP-P33	G6152	11/6/1993	9/29/2006	321.1
NP-P34	6036 ENP	12/1/1983	12/31/2002	342.8
NP-P35	H1999 ENP	2/11/1982	12/31/2002	326
NP-P36	6038 EDEN	10/15/1983	9/29/2006	333.7
NP-RG1	H6056 EDEN	9/14/1996	9/29/2006	321.1
ROCKDALE	7082	8/29/1985	5/25/1990	314.8
S12D	5959 6055 LS269	1/1/1962	4/2/2007	291.3
S174	16584	1/8/1991	3/9/2007	346.0
S331	16662	1/8/1991	4/6/2007	347.5
S338	16661	10/21/1993	4/6/2007	337.5
TAMITR40	6166	1/6/1941	11/30/1998	352.3

Table A-10. Stations with daily rainfall data around the tree islands.

Station	Lat (DDMMSS)	Lon (DDMMSS)	Coordinate source	distance (km)
84095	253004	-803300	DBHYDRO	18.5
88780	254539	-804927	DBHYDRO	13.1
3AS3W3	255111	-804608	DBHYDRO	21.4
BCA20	254223	-805605	EDEN	18.7
BCNPA9	254201	-803759	DBHYDRO	20.4
CHEKIKA	254201	-803759	DBHYDRO	11.4
HOMES.ES	253031	-802959	DBHYDRO	22.1
G-1502	253657	-803502	DBHYDRO	10.5
G-620	253921	-804600	R. Sonenshein	1.1
L67E.S	253736	-804020	DBHYDRO	2.4
L67EX.E	254101	-804021	DBHYDRO	8.2
L67EX.W	254101	-804023	DBHYDRO	8.2
SR1	254130	-803806	[USGS, 2003]	10.4
SR2	254311	-803326	[USGS, 2003]	17.9
SR4	253825	-803910	[USGS, 2003]	4.9
SR5	253755	-803942	[USGS, 2003]	3.6
NP-201	254300	-804310	EDEN	7.3
NP-202	253943	-804231	EDEN	4.7
NP-203	253722	-804419	EDEN	0.9
NP-204	253213	-804705	DBHYDRO	11.3
NP-205	254119	-805052	EDEN	9.7
NP-206	253239	-804019	EDEN	7.6
NP-311	252651	-803734	DBHYDRO	19.1
NP-A13	252950	-804245	EDEN	12.8
NP-CR2	252955	-803718	EDEN	14.1
NP-FMB	254532	-804941	DBHYDRO	13.1
NP-IFS	253035	-802959	DBHYDRO	22
NP-N10	252743	-803618	DBHYDRO	18.5
NP-OT3	253448	-805753	DBHYDRO	22.7
NP-P33	253653	-804209	[USGS, 2003]	1.5
NP-P34	253631	-805628	[USGS, 2003]	19.4
NP-P35	252739	-805153	[USGS, 2003]	22.5
NP-P36	253142	-804744	[USGS, 2003]	12.6
NP-RG1	253453	-803628	EDEN	8.7
NP-RG2	253233	-803621	EDEN	11.2
ROCKDALE	252551	-803447	DBHYDRO	22.7
TMC	253650	-805220	EDEN	12.7
S12D	254544	-804054	EDEN	13.6
S174	252901	-803348	DBHYDRO	18.9
S331	253639	-803035	DBHYDRO	18.0
S338	253938	-802849	DBHYDRO	21.6
TAMITR40	254537	-804929	DBHYDRO	13.1

Table A-11. Station coordinates and minimum distance to the tree islands.

Figure A-23. Google Earth view of the three islands of Shark River Slough and rainfall stations listed in Table A-10.

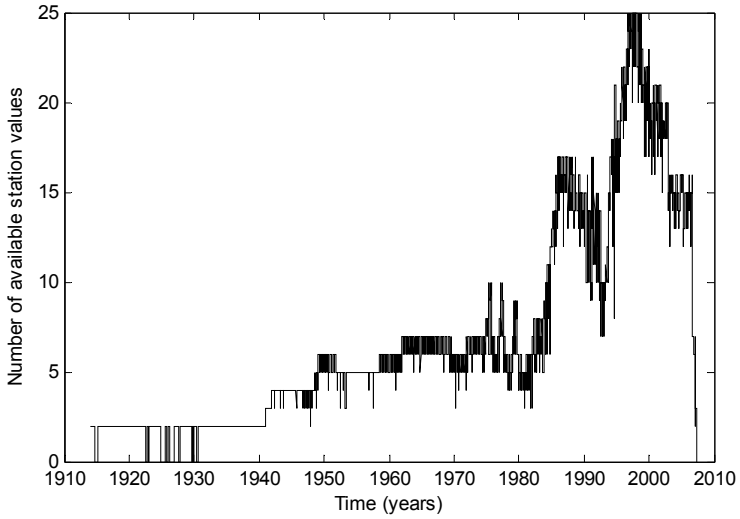

Figure A-24. Number of available data points per day at rainfall stations.

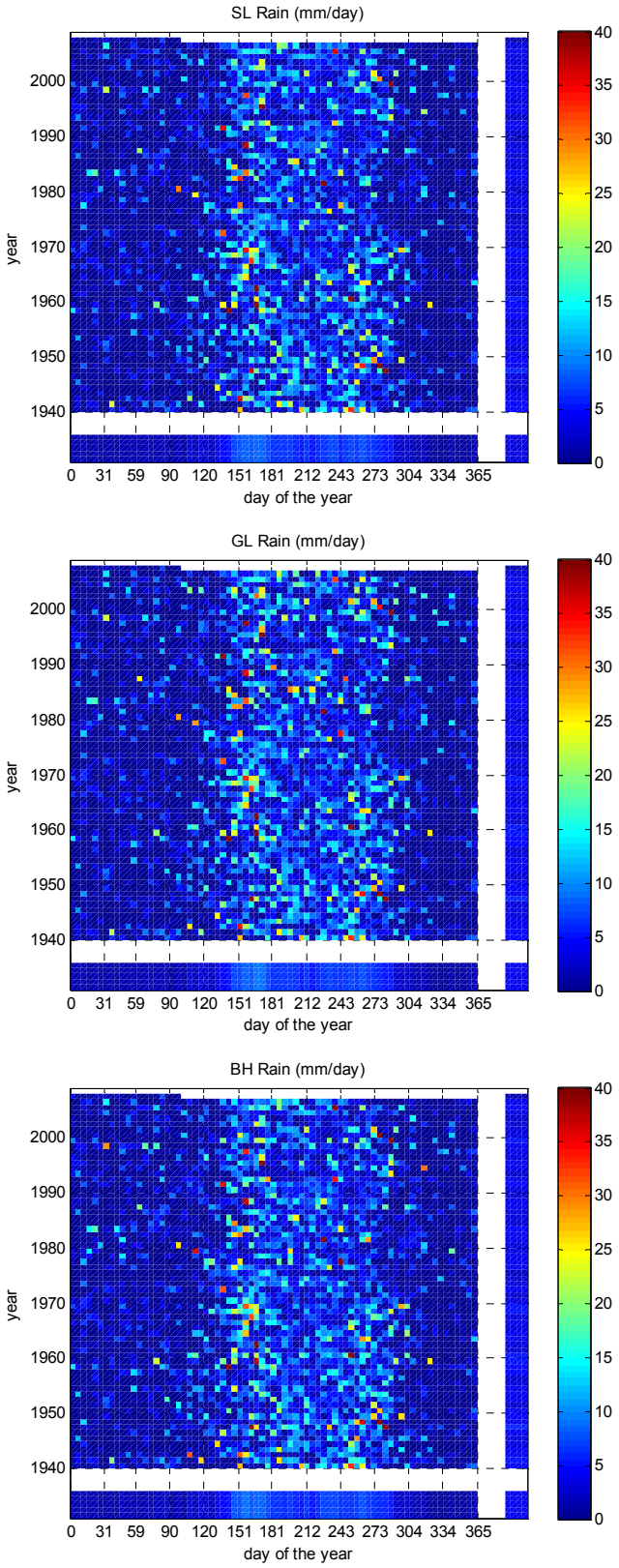

Figure A-25. Calendar representation for the interpolated daily rainfall depth rates (five days averaged) in the tree islands of Shark River Slough.

Another graphical representation of the interpolated rainfall rates shown in Figure 14 is presented in Figure A-25, for each tree island. The original idea of making such calendar graphs of the hydrologic and climatic time series data were taken from Sobczak [2007]. Our representation, however, also shows the day-of-the-year and the annual averages. The calendars in Figure A-25 contain rates averaged over five days, which smooth the daily peaks in Figure A-25, but improve the color visualization of the seasonal trends. The white spots represent missing data and the divisions in the x axis are located at the beginning of each month.

Besides the daily data from stations downloaded from DBHydro, Roy Sonenshein at Everglades National Park provided nine time series of hourly rainfall data for stations located around the tree islands of Shark River Slough (see Figure A-26). The date range covered for those stations is presented in Table A-12. The data have some missing values and the number of valid values for each station after that processing is also listed in that table.

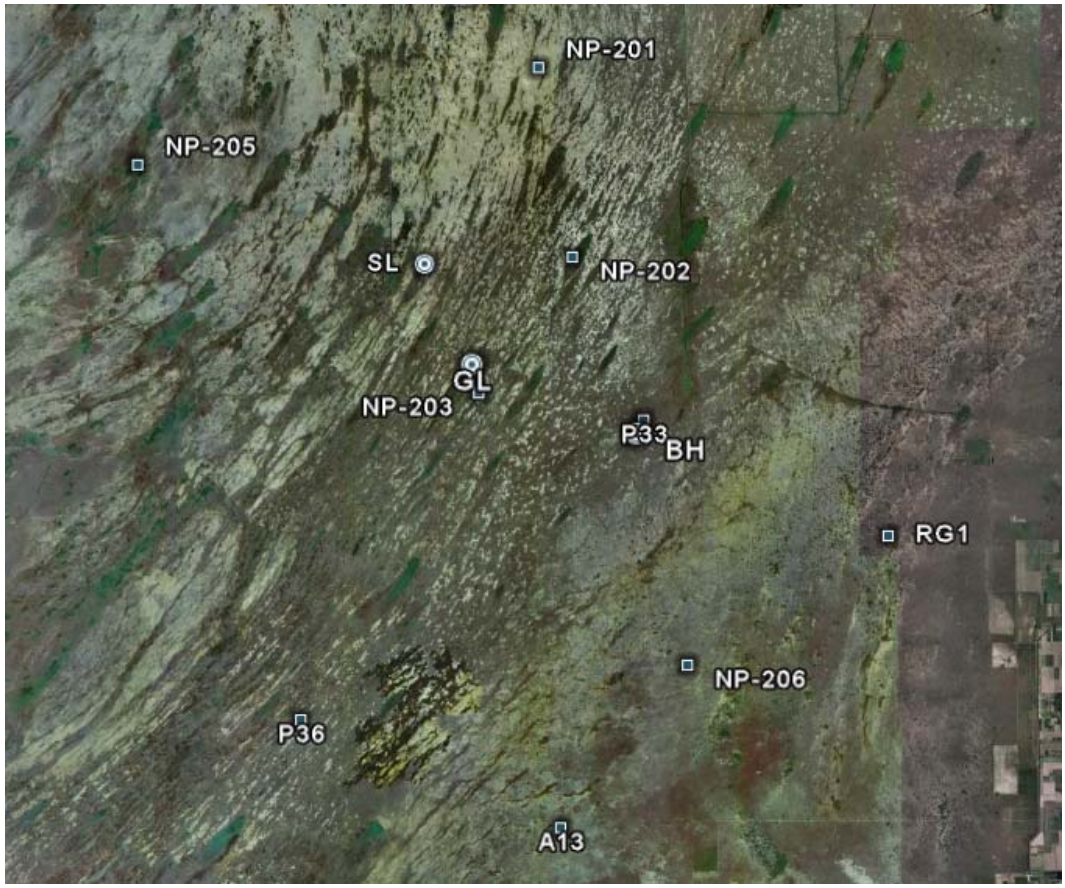

Figure A-26. Google Earth view of the three islands of Shark River Slough and rainfall stations listed in Table A-12.

station	start	end	number valid values / 365 days
A13	1/1/2000	9/30/2006	359.0
NP-201	1/1/2000	9/30/2006	353.7
NP-202	1/1/2000	9/30/2006	346.6
NP-203	1/1/2000	9/30/2006	349.0
NP-205	1/1/2000	9/30/2006	359.5
NP-206	1/1/2000	8/25/2006	322.2
P33	1/1/2000	9/30/2006	310.2
P36	1/1/2000	9/30/2006	364.5
RG1	1/5/2000	9/30/2006	364.0

Table A-12. Location of stations in Shark River Slough with hourly rainfall data.

A3.6 Evapotranspiration Data Processing

Data from station "Site 7" up to year 2000 are available from Sofia (http://sofia.usgs.gov/exchange/german/germanet.html), but the updated data were facilitated by Roy Sonenshein from USGS (ftp://ftpext.usgs.gov/pub/er/fl/miami/et/Everglades_Et_Data_Final.zip). Station "Site 7" is located between Gumbo Limbo and Black Hammock tree islands (see Figure A-23), in a zone with sparse sawgrass of 5 ft tall, which never gets dry. The hourly ET depths computed by German [2000] are presented in Figure A-27. The negative ET values measured mostly during the night are justified because of the occurrence of the water vapor condensation. However, isolated spikes in Figure A-27 may be consequence of errors. When hourly ET values are missing, then the interpolation values from neighboring days was performed. The maximum gap was at the end of year 2000 where there are 32 days without data.

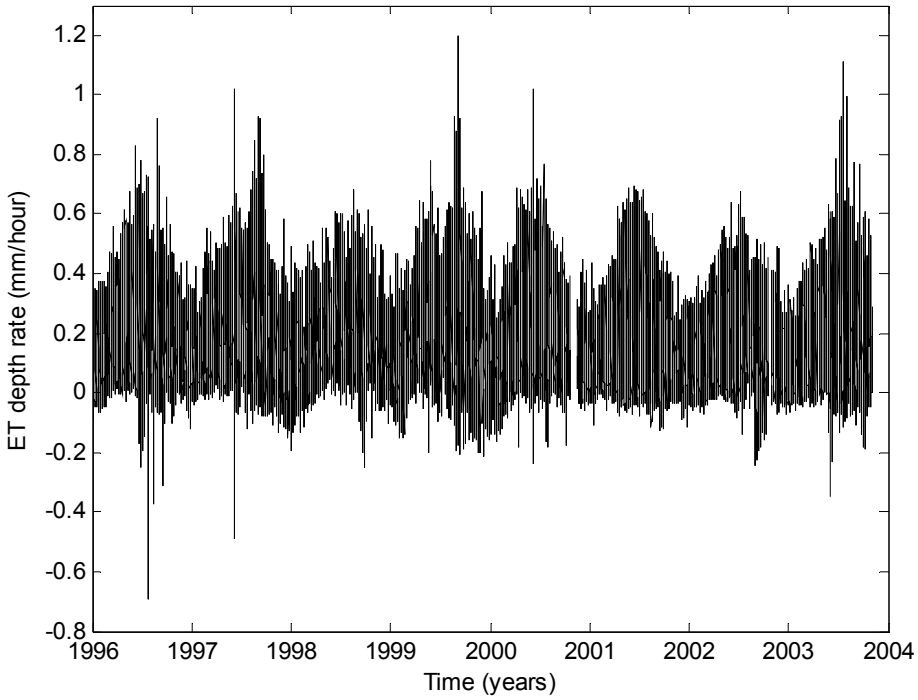

Figure A-27. Evapotranspiration hourly rates determined by German [2000] on Site 7 of Figure A-23 and downloaded from USGS web site.

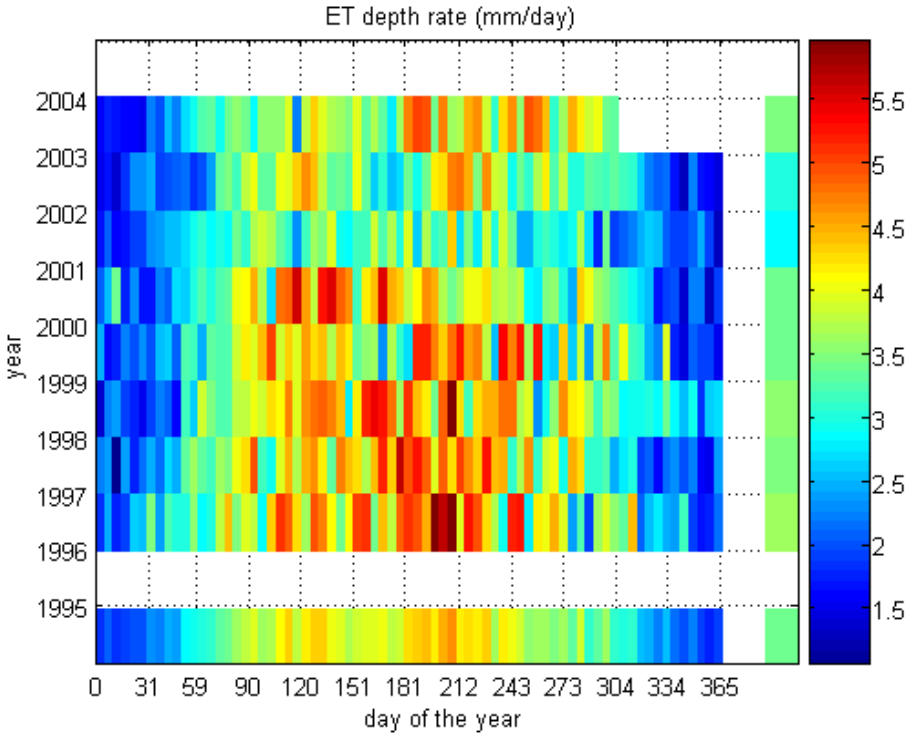

Figure A-28. Calendar representation of the daily evapotranspiration rates on Figure 17. This representation has five-day averaged rates.

A3.6.1 Correlation between Evapotranspiration Rate and Water Depth

ET rate depends on the characteristics in each site, particularly on the soil surface elevation and the vegetation type coverage. A strong correlation between the annual ET rate and the median water depth was found by German [2000] as reproduced in Figure A-29. This represents a linear variation of about 15 inches in annual ET depth for each 2.6 ft of water depth. Taking the Site 7 point (h, ET) and that slope, the linear correlation is written as

$$ET = \frac{15 inches}{2.6 ft}(h - 1.46 ft) + 51.24 inches . \quad (96)$$

This dependence implies that at higher water depth more liquid water is vaporized, which is expected when the water level is below the soil surface. When the water level is above the surface, the correlation (96) may be related to the vertical distribution of dead plant debris [German, 2000].

The ET rate depends on the evaporative fraction, which is the fraction of the available energy (sum of net radiation, soil heat flux, and change in heat storage in water and soil) that is used to transform liquid water in vapor (latent heat). According to German [2000] the mean evaporative fraction at the open water sites (sites 2 and 3) was more than 80 %, and at the vegetated sites ranged from 62 to 79 %. This difference indicates that a higher portion of solar energy is used not in latent heat but in convective heat transfer at vegetated sites.

The nine sites in Figure A-29 are located in the freshwater, non-forested parts of the Everglades, and do not include tree islands as noticed by German [2000]. Therefore, the relation (96) as well as the ET data processed from Site 7 should be rigorously applied only to the areas surrounding the tree islands excluding the areas covered by the vegetation types HH, BH and BHS. From the lack of ET data in those areas, it is assumed that the ET data processed from Site 7 and the relation (96) is also valid there. This assumption may be justified from the fact that in other locations of the world the ET rates of grasses and trees are similar during the rainy season, when plants are not water stressed [Hodnett, 1995].

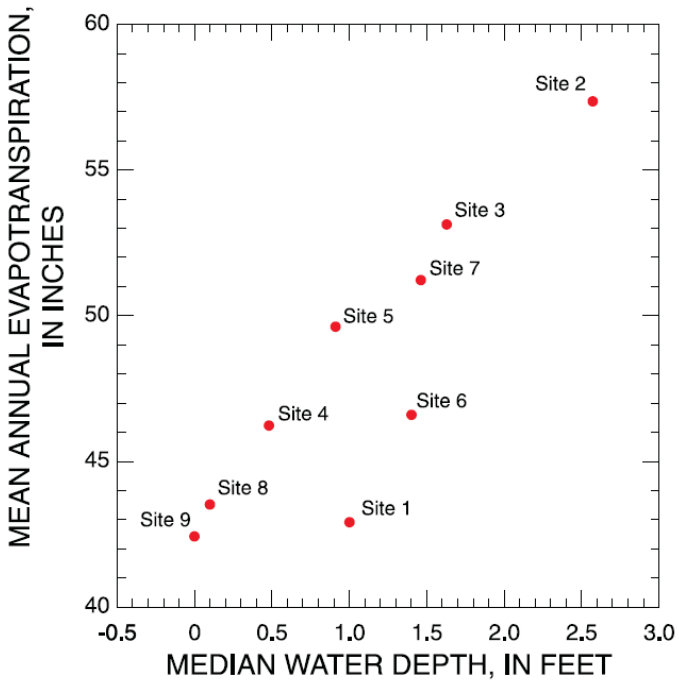

Figure A-29. Correlation between the mean annual ET rate and the median water depth for two year period 1996-1997, extracted from German [2000].

In summary, the numerical model assumes by default a spatially uniform distribution of ET rates shown in Figure 22. Nevertheless, the correlation (96) could be used in a sensitivity test to correct proportionally the daily ET data for the soil surface elevation in each numerical cell.

A3.7 Stage Data Processing

Mean daily values of stage are reported for the twenty one stations listed in Table A-13, which are located around the tree islands of Shark River Slough. Most of those time series were available from DBHydro and two of them only from the Eden project. The location of those stations is presented in Figure A-30 and their geographical coordinates are listed in Table A-11.

The surface water stage in the tree islands detailed in Table A-9 was interpolated by using a triangle-based linear scheme from the time series stage data of stations summarized in Table A-13. The interpolated daily mean stages are shown in Figure 25 for each tree island.

On the other hand, the spatial gradient of the stage (slope) is also obtained. For that, the stage was also interpolated in a point located 10^{-4} degrees to the north and

another one located 10^{-4} degrees to the east, at every tree island. In the geographical region of the tree islands those displacements are equivalent to 36.30 ft to the north and 32.95 ft to the east, respectively. The slopes are just the quotient between the stage difference and the displacement between points.

During the stage interpolation, the elevation data was in the reference system NGVD29. However, by using the vertical conversion from NGVD29 to NAVD88 reported in EDEN files at stations NP-201, RG1 and TMC, the slope differences found between the two coordinate reference systems is -2.1×10^{-8} toward the north and -3.8×10^{-7} toward the east, which are negligible regarding the common water surface slopes in the Shark River Slough. This result indicates that the results from the model are similar by using any of those coordinate reference systems.

After the regional slopes are determined, the interpolated elevations at tree islands are converted to the system NAVD88. The estimated daily mean slopes are shown in Figure 26. Another graphical representation of the interpolated stage and slopes is presented in Figure A-31, Figure A-32 and Figure A-33, for each tree island.

Besides the daily stage data from stations, Roy Sonenshein at the Eden project provided fifteen time series of hourly stage data of stations located around the tree islands of Shark River Slough (see Figure A-34). The data have some repeated values and others that do not match the exact hour. Thus, interpolation at every hour was conducted when there is at least a stage measured value at one hour of difference or closer. The number of valid values for each station after that processing is also listed in Table A-14

The comparison between hourly and daily interpolated stages is shown in Figure A-35 and the one between the slopes is also shown in Figure A-36 and Figure A-37. Notice that the larger deviations are observed for the SL stage and slopes, as well as for the GL slopes. The reason for those differences is that the station G-620 has daily data but not hourly data. Thus, the triangular-based linear interpolation uses different stations when G-620 is missing and deviations in the interpolated stages and slopes are expected. This fact, however, does not affect considerably the stage interpolated at GL because the station NP-203 is very close to that tree island.

In summary, the usage of daily interpolated stage and slopes in the SL case is recommended instead of the hourly ones, which have more error due to the absence of

hourly data from station G-620.

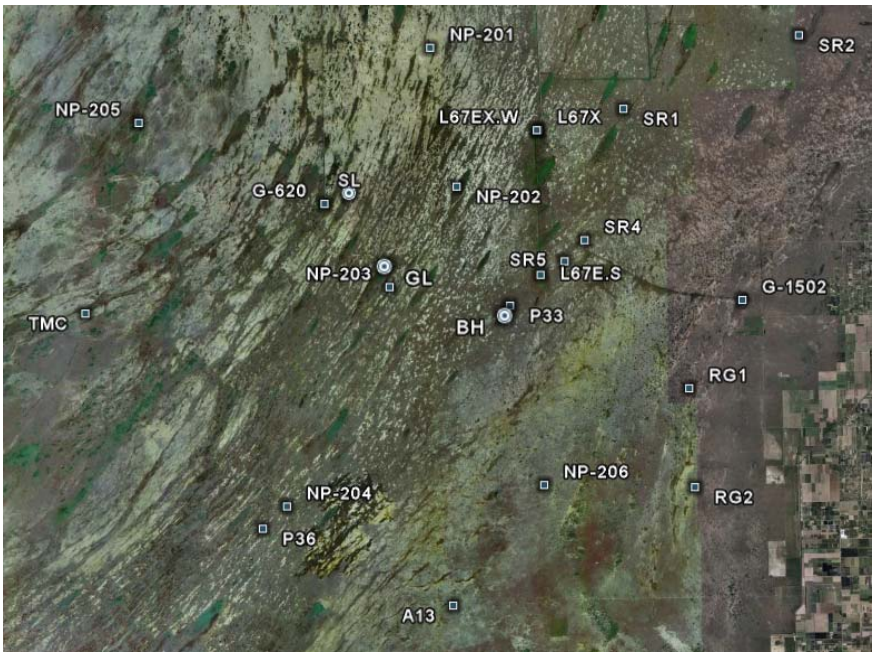

Figure A-30. Google Earth view of the three islands of Shark River Slough and stage stations listed in Table A-13.

Station	DBKEY	start	end	valid values / 365 days
G-1502	P0939	1/1/1978	12/31/2004	365.0
G-620	1079 P0793	8/10/1956	12/31/2004	201.9
L67E.S	P0814	1/1/1978	12/10/1990	365.0
L67EX.E	6545	1/11/1984	2/19/2007	348.7
L67EX.W	5697	9/14/1983	2/19/2007	350.3
SR1	1140	7/23/1976	2/28/2007	338.9
SR2	EDEN	10/1/1999	9/30/2005	353.2
SR4	6544	7/24/1985	2/28/2007	317.0
SR5	6543	7/24/1985	2/28/2007	328.6
A13	EDEN	1/1/2000	9/30/2005	365.0
NP-201	6719	10/1/1974	9/1/2006	311.4
NP-202	6720	1/1/1975	9/1/2006	345.0
NP-203	G6154	10/1/1973	9/1/2006	329.2
NP-204	765	2/17/1974	10/9/1980	365.0
NP-205	G6146	10/1/1974	9/1/2006	359.5
NP-206	6721	10/1/1974	9/1/2006	341.3
P33	6717	10/1/1952	9/1/2006	357.6
P36	6718	2/1/1968	9/1/2006	355.9
RG1	H6066	9/14/1996	9/1/2006	334.7
RG2	H6067	11/21/1996	9/1/2006	362.1
TMC	H6069	3/30/1996	9/30/2005	355.0

Table A-13. Details about stations used for interpolating daily stage data on tree islands.

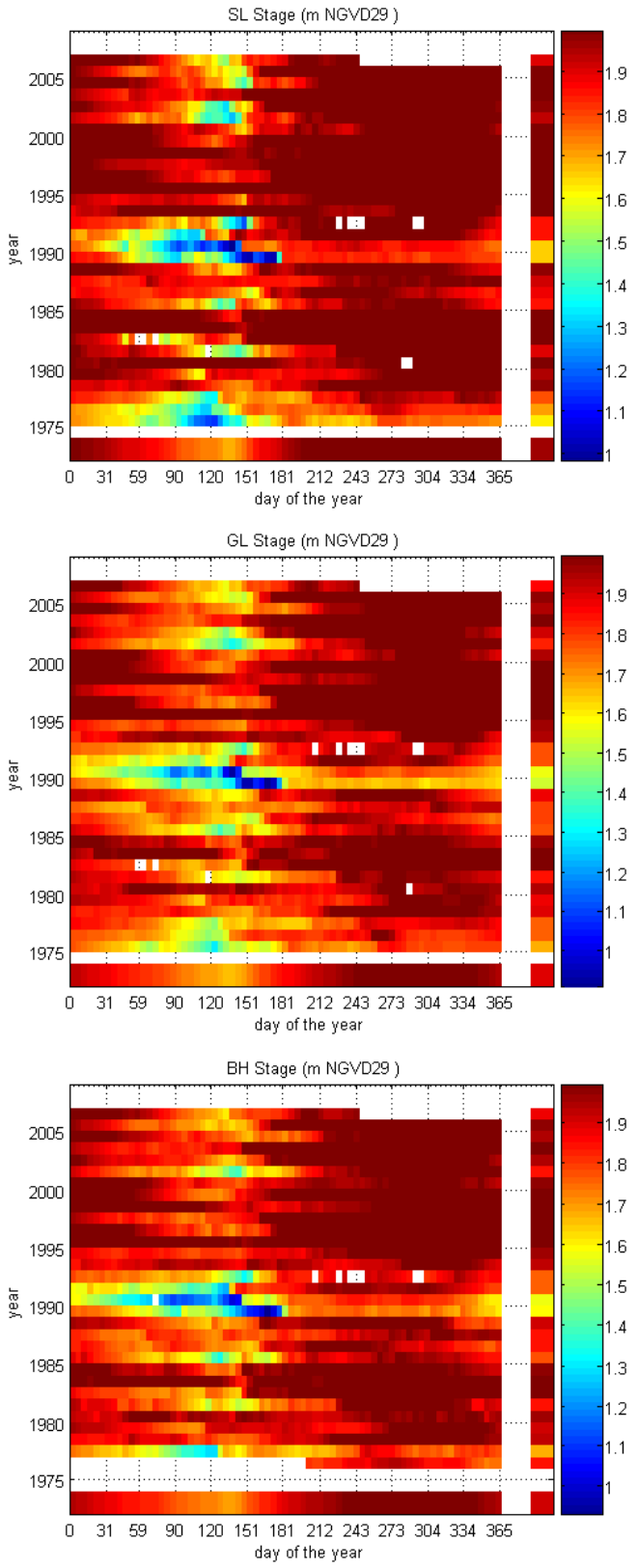

Figure A-31. Calendar representation for the interpolated daily mean stages (five days averaged) in the tree islands of Shark River Slough.

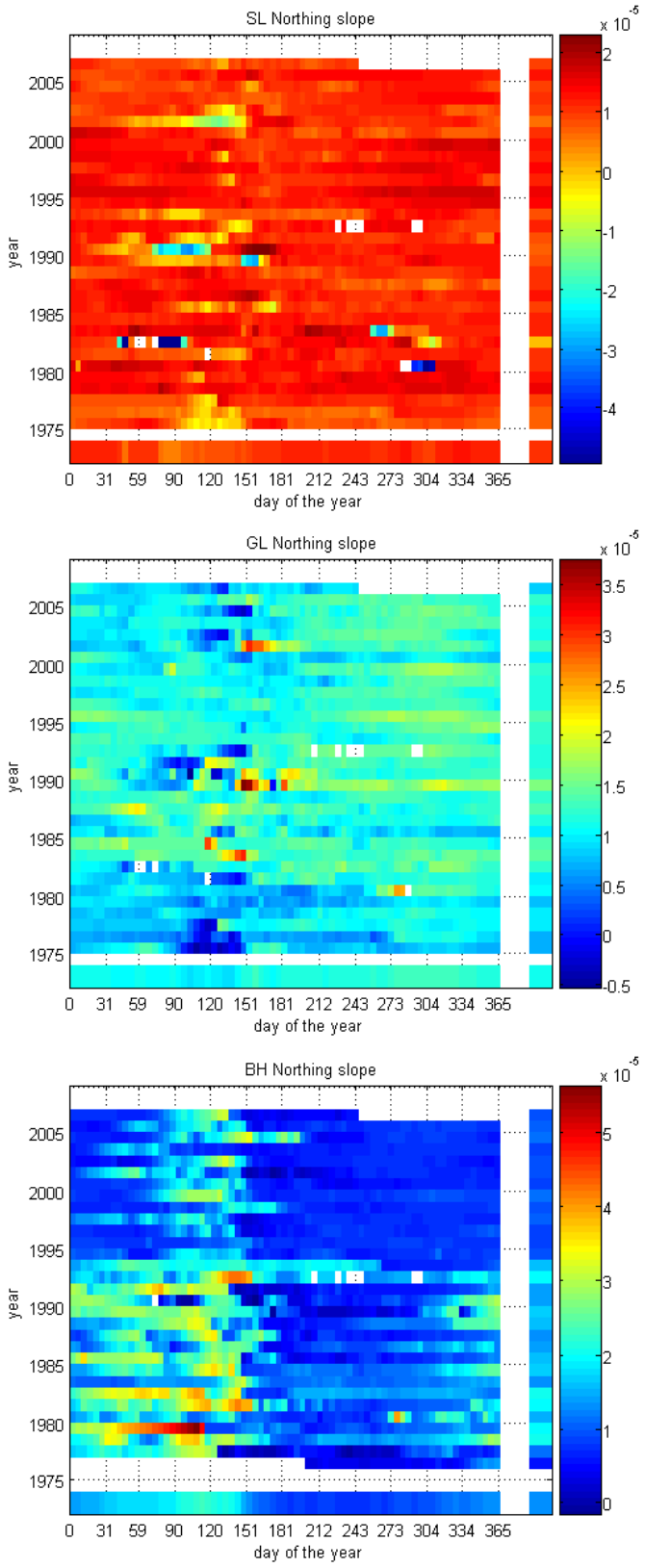

Figure A-32. Calendar representation for the northing slope (five days averaged) obtained from the stage interpolation in the tree islands of Shark River Slough.

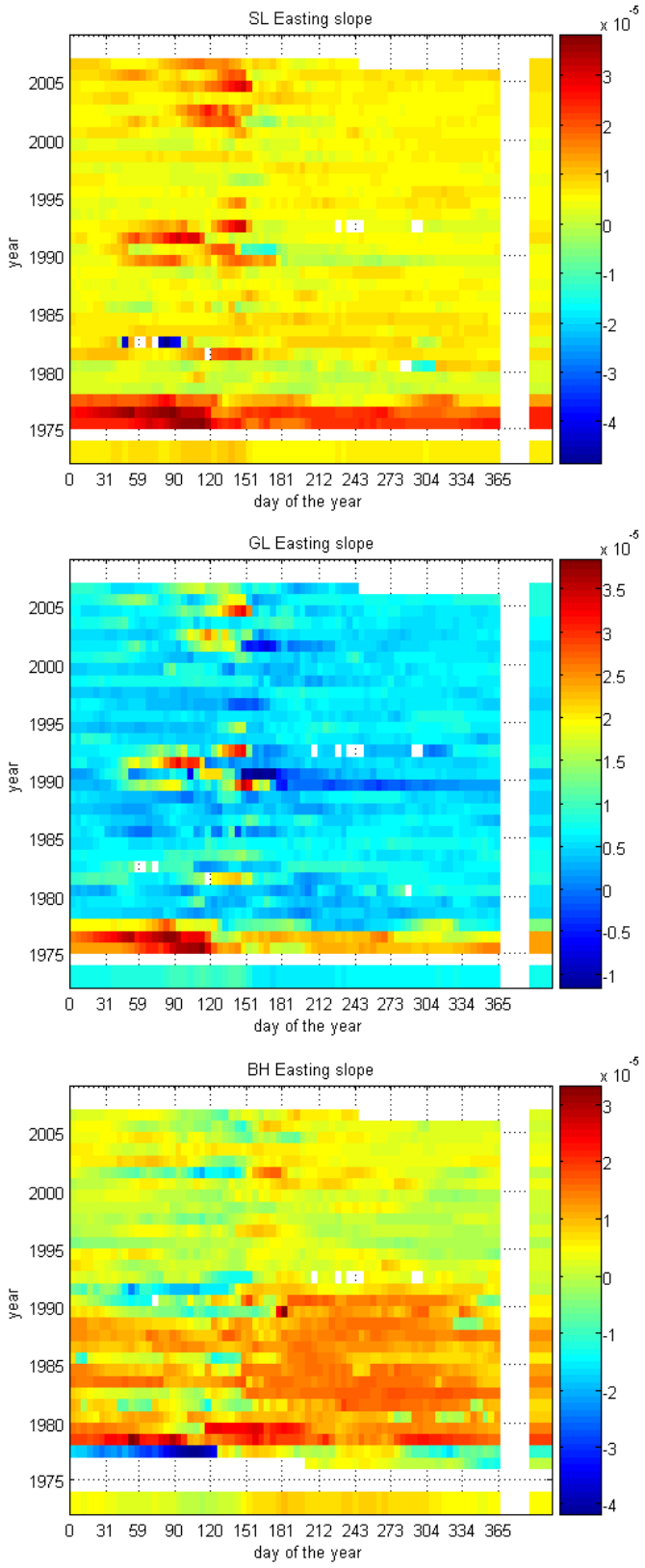

Figure A-33. Calendar representation for the easting slope (five days averaged) obtained from the stage interpolation in the tree islands of Shark River Slough.

station	start	end	number valid values / 365 days
A13	1/1/2000	10/1/2005	365.0
SR1	10/1/1999	10/1/2005	364.3
SR2	10/1/1999	10/1/2005	353.8
SR4	10/1/1999	10/1/2005	344.9
SR5	10/1/1999	10/1/2005	357.4
NP201	1/1/2000	10/1/2005	365.0
NP202	1/1/2000	10/1/2005	364.9
NP203	1/1/2000	10/1/2005	364.8
NP205	1/1/2000	7/5/2005	365.0
NP206	1/1/2000	10/1/2005	364.9
P33	1/1/2000	10/1/2005	365.0
P36	1/1/2000	10/1/2005	364.9
RG1	1/1/2000	10/1/2005	365.0
RG2	1/1/2000	10/1/2005	365.0
TMC	1/1/2000	10/1/2005	364.5

Table A-14. Location of stations in Shark River Slough with hourly stage data and period covered, from Eden project.

Figure A-34. Google Earth view of the three islands of Shark River Slough and stage stations listed in Table A-14.

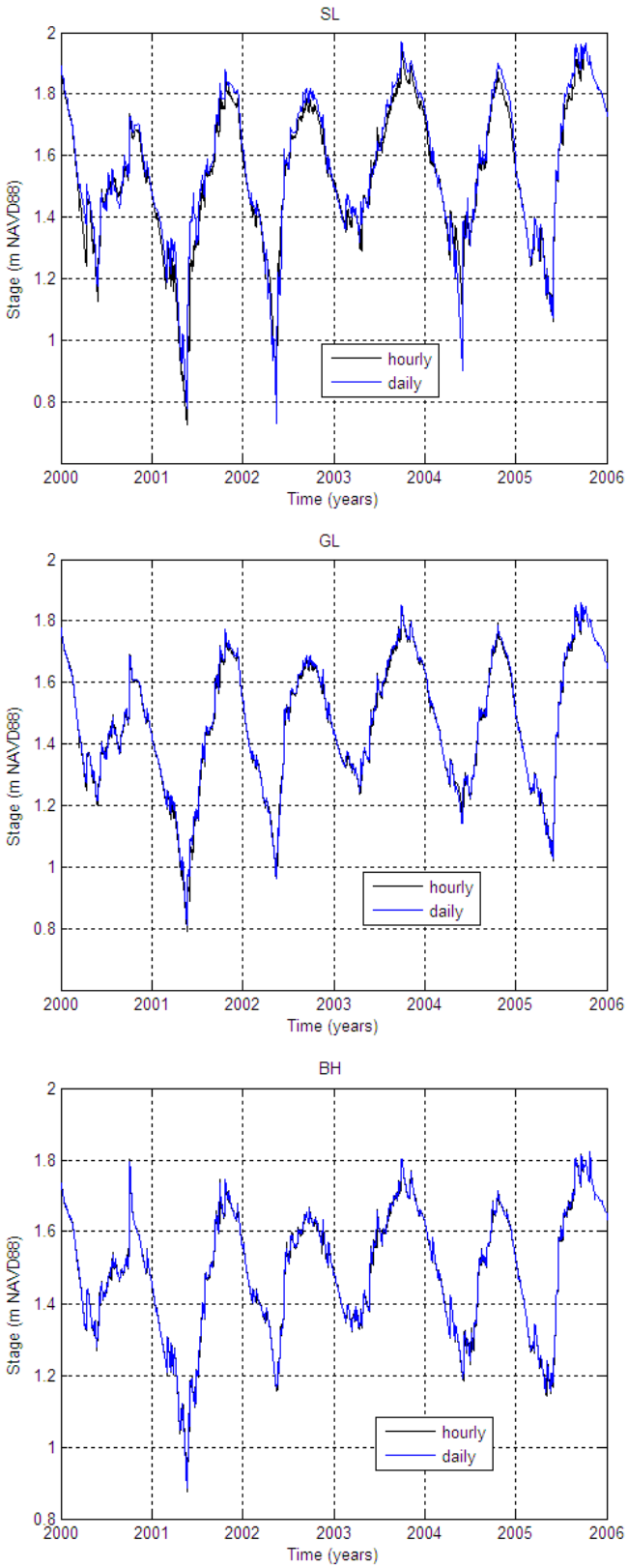

Figure A-35. Interpolated hourly stages in the tree islands of Shark River Slough compared to the daily ones from Figure 25.

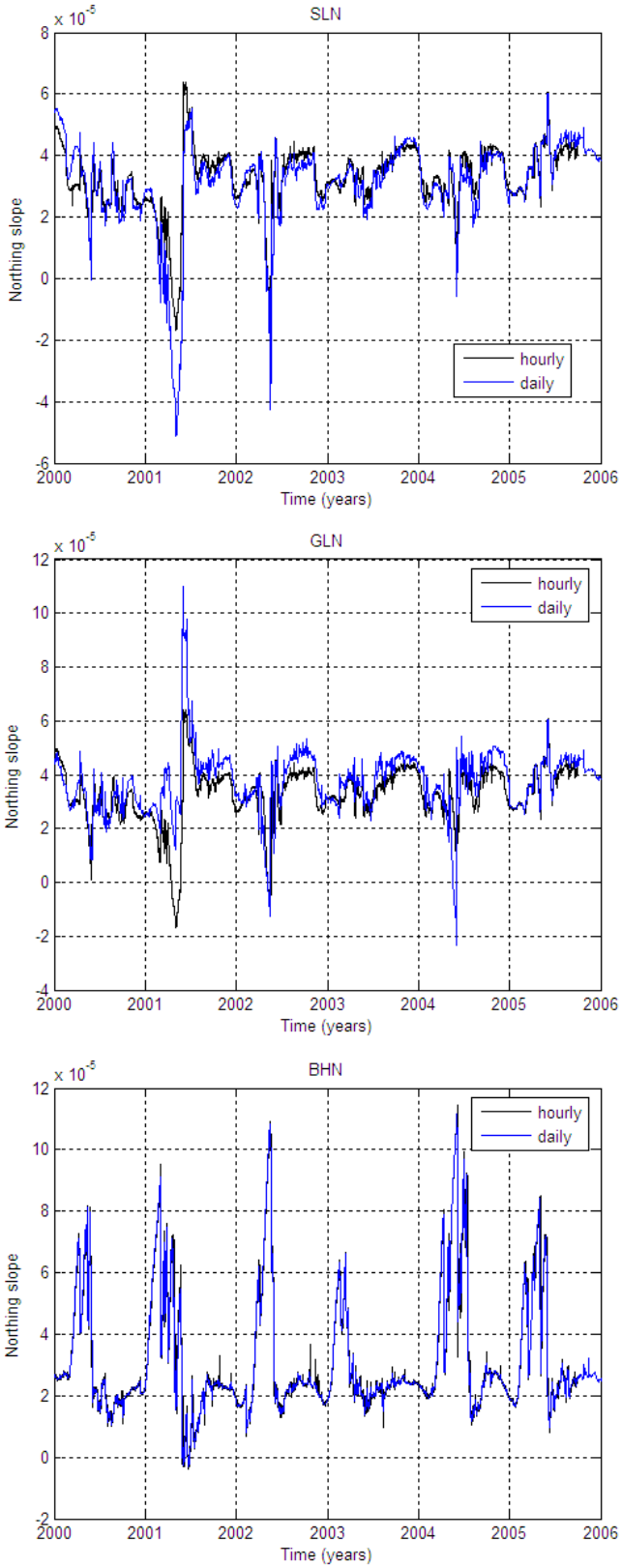

Figure A-36. Hourly northing slopes obtained from the stage interpolation in the tree islands of Shark River Slough, compared to the daily ones from Figure 26.

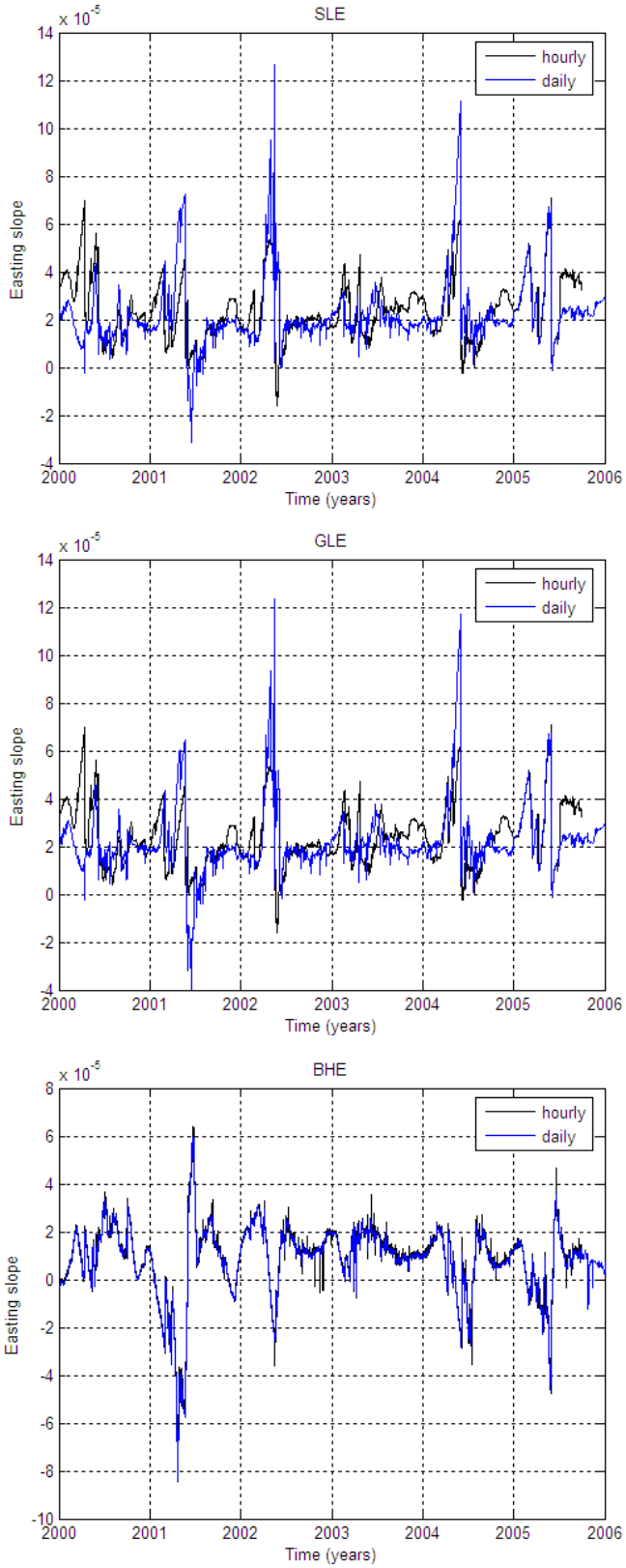

Figure A-37. Hourly easting slopes obtained from the stage interpolation in the tree islands of Shark River Slough, compared to the daily ones from Figure 26.

A3.8 Base Case MODHMS Models. Other Details

This section describes the procedure to determine the horizontal grid spacing as well as the parameters introduced in MODHMS for the base case.

A3.8.1 Grid Selection Procedure

The procedure to find the grid spacing was made in MatLab by dividing the model domain (originally composed by 1 m x 1 m cells) in cells of 20 m wide. Inside each cell, the maximum spatial variation of the vegetation type, soil surface and the bedrock elevation are computed in each direction x and y. The maximum value is found to normalize the computed spatial variations and a number of subdivisions are found in each interval in order to minimize them. Subdivisions are limited to 4, which correspond to a minimum cell width of 5 m. The interpolation of the vegetation type in the non-uniform grid is based on a nearest neighbor scheme, but for the soil surface and the bedrock elevation it is based on a linear triangular one.

A vegetation type map of Satinleaf obtained with a uniform grid and the one with the proposed non-uniform grid are compared in Figure A-38, showing that even when the total number of cells is about the same, the non-uniform grid captures the tree island details better. The soil surface and the bedrock elevation interpolated on the non-uniform grid are also shown in Figure A-39. The vegetation type map as well as soil surface and the bedrock elevation maps of Black Hammock and Gumbo Limbo are also interpolated to their non-uniform grid in Figure A-40, Figure A-41 and Figure A-42.

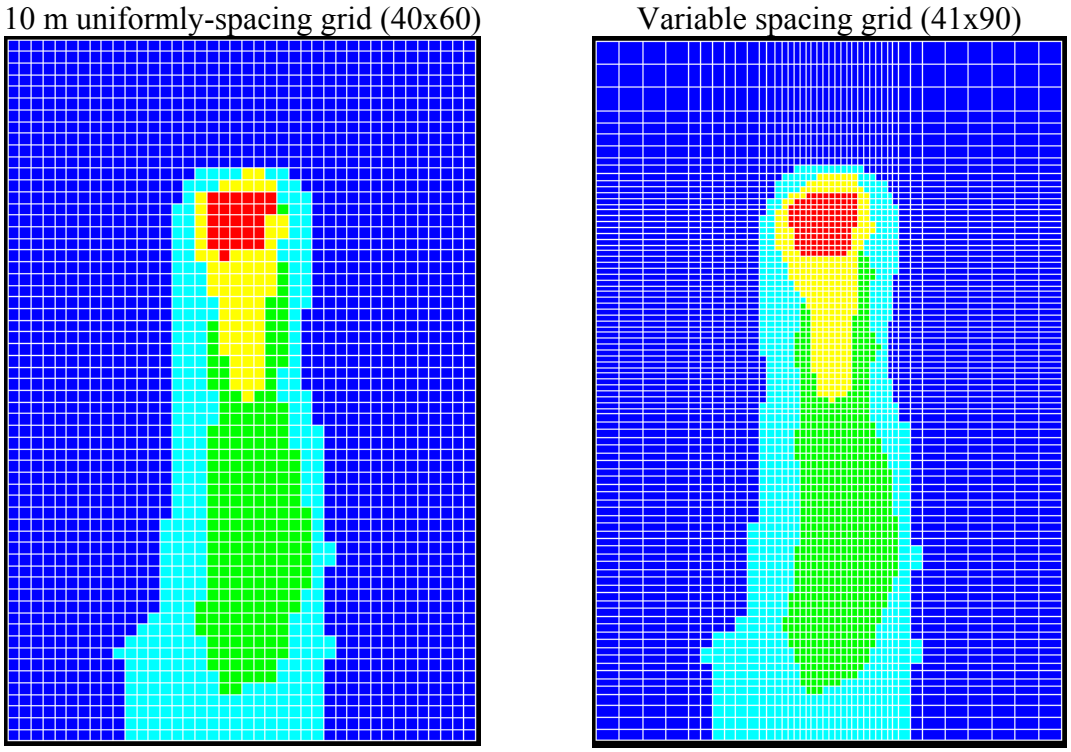

Figure A-38. ViewHMS view of the interpolated vegetation type map of Satinleaf Tree Island shown in Figure 10 in two different grids.

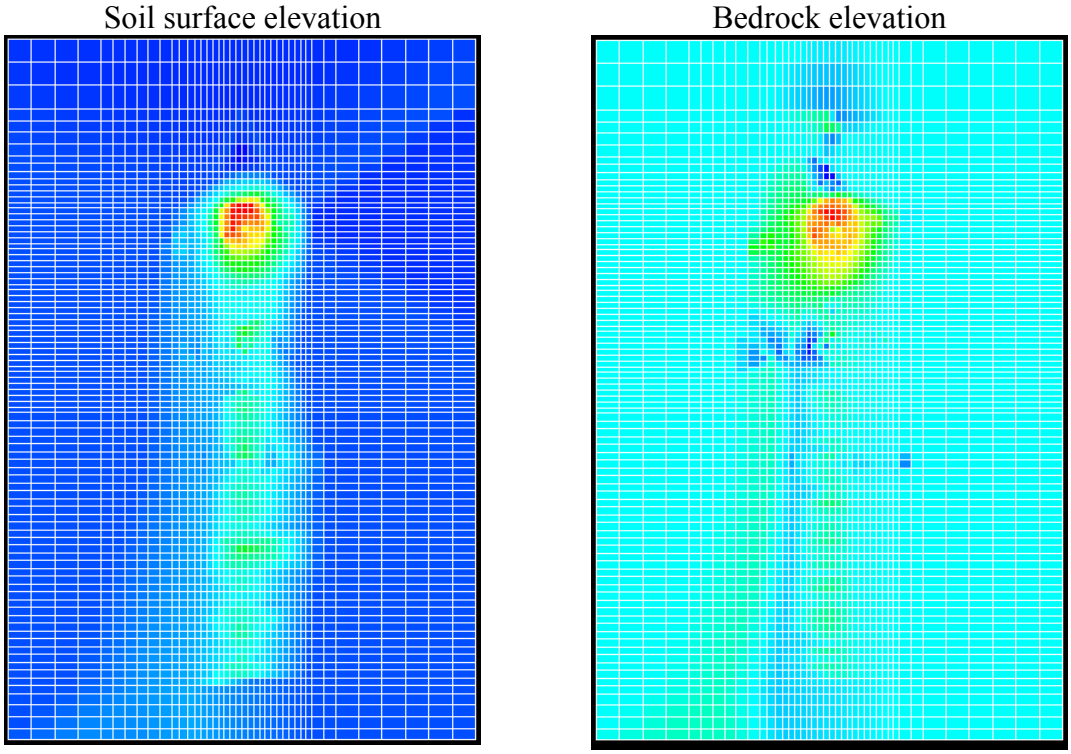

Figure A-39. ViewHMS view of the soil surface elevation and bedrock elevation in Satinleaf tree Island as interpolated in the variable spacing grid (41x90).

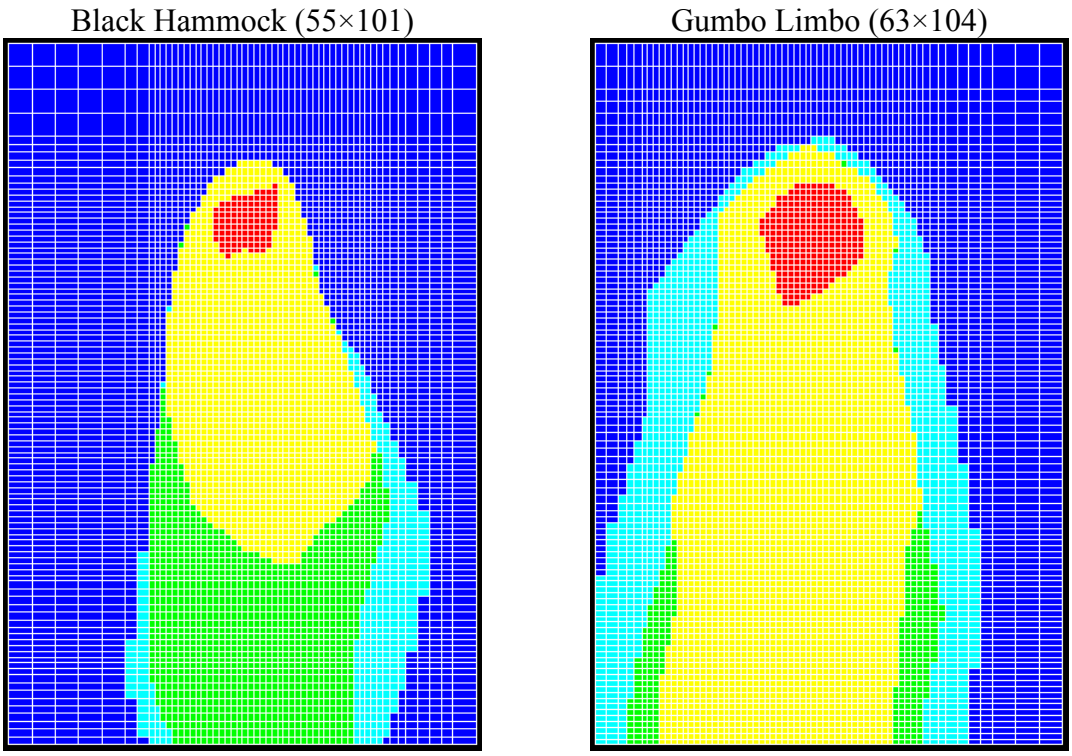

Figure A-40. ViewHMS view of the interpolated vegetation type map of Black Hammock and Gumbo Limbo Tree Islands shown in Figure 10 in variable spacing grids.

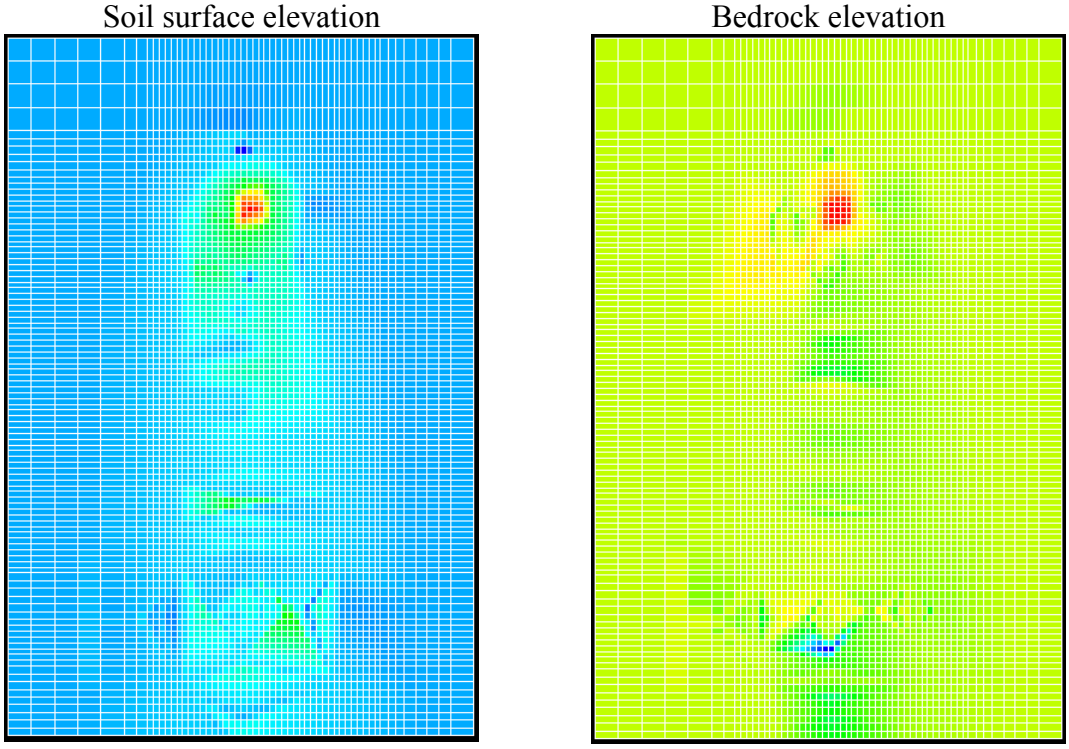

Figure A-41. ViewHMS view of the soil surface elevation and bedrock elevation in Black Hammock tree Island as interpolated in the variable spacing grid (55×101).

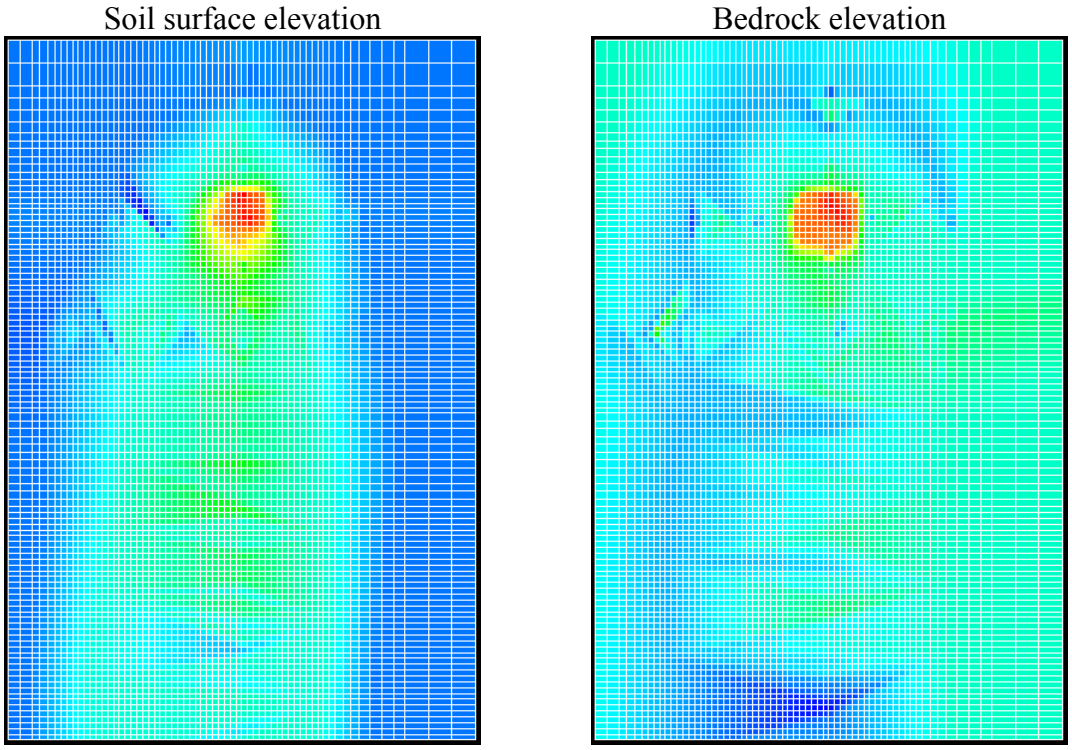

Figure A-42. ViewHMS view of the soil surface elevation and bedrock elevation in Gumbo Limbo tree Island as interpolated in the variable spacing grid (63×104).

A3.8.2 Variables in ViewHMS

OL Flow Properties	OLF Layer
Initial Head. IH	Linear interpolation from mean stage in Figure 27 and median averaged slopes in Figure 30
Bottom Elevation. BOT (m)	Figure A-39, Figure A-41, Figure A-42
Manning Coefficient. X_FRICTN= Y_FRICTN ($s/m^{1/3}$)	From Table 3, according to vegetation type in Figure A-38 or Figure A-40
Bottom Leakage Coefficient. BOTTOM LEAKAGE (s^{-1})	1.0
Height of Rill Storage. RILLSH (m)	0.001
Height of obstructions. OBSTRH (m)	0
Longitudinal dispersivity. LDISPOL (m)	0
Transversal dispersivity. TDISPOL (m)	0
Vertical dispersivity. VTDISPOL (m)	0
Soil partition coefficient. KDOL (Adsorption)	0
Freundlich Isotherm Ex. ETAOL	0
Degradation Rate. ALAMOL1	0
Degradation Rate O. ALAMOL2	0
Initial conc. SCONCOL (kg/m^3)	1.5e-6

Table A-15. OL flow properties for the base case as introduced in ViewHMS.

GW Properties	Layer 1 (soil)	Layer 2 (rock)
Primary storage coefficient. SF1	0	0
Transmissivity. TRAN.	---	---
Hydraulic conductivity. HY (m/s)	1 e-5	1.8 e-3
Vertical hydraulic conductivity. VHY (m/s) used when IVHYC=1	1 e-5	1.8 e-3
Bottom elevation. BOT (m)	Figure A-39 Figure A-41 Figure A-42	-4.572
Vertical hydraulic conductivity divided by thickness. VCONT (1/s). Not used when IVHYC=1	---	---
Secondary storage coefficient. SF2= drainable porosity or specific yield	0.50 for HH 0.93 Otherwise	0.2
Top elevation. TOP (m)	Figure A-39 Figure A-41 Figure A-42	Figure A-39 Figure A-41 Figure A-42
Wetting Threshold. WETDRY.	---	---
Van Genuchten parameter alpha. VANAL (1/m).	2.78	2.78
Van Genuchten parameter beta. VANBT	1.917	1.917
Residual saturation. VANSR	0.01	0.01
Brooks-Corey Exponent. BROOK	3	3
Initial Head. IH (m)	IH from OLF	IH from OLF
Longitudinal dispersivity. LDISP (m)	0	0
Transversal dispersivity. TDISP (m)	0	0
Vertical transverse dispersivity. VTDISP (m)	0	0
Vertical longitudinal dispersivity. VLDISP (m)	0	0
Effective porosity. PHI	SF2(soil)	SF2(rock)
Bulk density. RHOB (kg/m^3)	400 for HH 200 otherwise	2260
NAPL Saturation. SNAPL	0	0
Soil partition coefficient (Adsorption) KD (m^3/kg)	6.33e-3 for HH 3.06e-3 otherwise	1.94e-4
Freundlich Isotherm exponent. ETA	0.81 for HH 0.428 otherwise	0.59
Degradation Rate. ALAM1	0	0
Degradation Rate on soil. ALAM2	0	0
Degradation Rate for inactive phase. ALAM3	0	0
Degradation Rate for NAPL phase. ALAM4	0	0
Initial concentration. SCONC ($kg/m^3 = 10^6$ □g/l)	From Table 2, according to vegetation type in Figure A-38	1.5e-6

Table A-16. GW properties for the base case as introduced in ViewHMS.

2D Properties	Value
ET Surface Elevation. EVT_SURF (m)	TOP(soil)
ET Extinction Depth. EVT_EXDP (m)	TOP(soil)-BOT(rock)
The zone value of each node EVT_IZNETS2	1
Recharge. RECH (m/s)	4.1e-8
Tabulated zonal recharge values. IZNRCH	1
Recharge Concentration. RSF_CONC (kg/m^3)	1.5e-6

Table A-17. 2D properties for the base case as introduced in ViewHMS.

A3.8.3 Variables in MODHMS Input Files

All parameters in MODHMS input files are specified in international system of units (also called MKS).

Variable	Default Value	Comments for ATO file (ATO4 package):
IHEDFM	0	Code for the format in which heads are printed (10G11.4).
IDDNFM	0	Code for the format in which drawdowns are printed (10G11.4).
IHEDUN	88	Unit number to which heads are written.
IDDNUN	95	Unit number to which drawdowns are written.
ICONFM	0	Code for the format in which concentrations are to be printed (10G11.4).
ICONUN	89	Unit number to which concentrations of each species are to be Written.
INCODE	0	Head/drawdown outputs in all layers are treated the same way.
IHDDFL	1	Head and drawdowns (or saturations) are printed or saved according to the specified flags for each layer.
IBUDFL	-1	0: Overall volumetric budget will not be printed -1: Overall volumetric budget will be printed every time step.
ICBCFL	1	Cell-by cell flow terms are printed or recorded on disk depending on specified flags.
ICONFL	1	Concentrations are printed or saved according to the specified flags.
ICONBD	-1	0: Transport budget is not printed. -1: Transport budget is printed every time step.
ICCCFL	1	Transport mass-flux-terms are printed or recorded on disk depending on specified flags.
DELT	86400	First time step size of the stress period (one hour).
TMIN	1e-4	Minimum value of time step size allowed in the stress period (one millisecond).
TMAX	86400	Maximum value of time step size allowed in the stress period (24 hours).
TSMULT	1e10	Time step multiplier. Trying to reach the stress period end.
TSDIV	1.5	Reduction factor of time step size.
NPRTS	0	Number of print times specified.
NPSTP	0	Overall volumetric budget, heads/drawdowns, and cell-by-cell

Variable	Default Value	Comments for ATO file (ATO4 package):
		flow terms will be printed or saved at every time step of the stress period according to the specified flags.
TMVEC	(…)	1-D array containing NPRTS number of print time values at which printing or saving of volumetric budget, heads/drawdowns, or cell-by-cell flow terms is desired in a particular stress period.
Hdpr	0	Head is not printed.
Ddpr	0	Drawdown is not printed.
Hdsv	1	Head is saved.
Ddsv	1	Drawdown is saved.
Conpr	0	Concentration is not printed.
Consv	1	Concentration is saved.

Table A-18. Properties for the base case as introduced in ATO file.

Variable	Default Value	Comments for BAS file:
NLAY	2	Number of model GW layers: layer 1 (soil) and layer 2 (rock).
NROW	90 (SL) 104 (GL) 101 (BH)	Number of model rows.
NCOL	41 (SL) 63 (GL) 55 (BH)	Number of model columns.
NPER	366	Number of stress periods in the simulation.
ITMUNI	1	Time unit of model data = seconds
ITRAN	1	The simulation is for both flow and transport.
IUNIT		Table of input units
1	11	Block-Centered Flow (BCF4) Package
2	12	Well (WEL) Package
3	0	Drain (DRN) Package
4	0	River (RIV) Package
5	22	Evapotranspiration (EVT) Package
6	0	Transient Leakage Package (TLK)
7	0	General-Head-Boundary (GHB) Package
8	16	Recharge-Seepage Face Boundary (RSF4) Package
9	0	Strongly Implicit Procedure (SIP) Package
10	0	Direct Solver Package (DE4)
11	0	Slice Successive Over-Relaxation (SSOR) Package
12	0	Output Control (OC) Package
13	17	Preconditioned Conjugate Gradient (PCG4) Package
14	0	Streamflow-Routing (STR) Package
15	0	Preconditioned Conjugate Gradient (PCG2) Package
16	0	Horizontal-Flow Barrier (HFB) Package
17	23	Basic Transport (BTN1) Package
18	0	Lake (LAK2) Package

Variable	Default Value	Comments for BAS file:
19	0	Interbed-Storage (IBS) Package
20	0	Time-Variant Specified-Head (CHD) Package
21	0	Fractured-Well (FWL4) Package
22	18	Adaptive Time-Stepping and Output Control (ATO4) Package
23	0	Prescribed-Concentration Boundary (PCN1) Package
24	26	Specified-head Concentration Boundary (HCN1) Package
25	19	Overland Flow Package (OLF)
26	0	Channel Flow Package (CHF)
27	0	Analytical Infiltration Package (PRL)
28	21	Observation Node Package (OBS)
29	0	General Finite Differences (GFD)
30	25	Flow and Head (time-varying) Boundary Package (FHB)
31	0	Interception of Precipitation and Evapotranspiration Package
32	0	(IPT)
33	0	Reactive Transport Package (RCT)
34	0	Saltchem Module (SLC)
35	0	Link - AMG Package (LMG)
36	0	Preconditioned Conjugate Gradient 5 Package (PCG5)
37	0	Reservoir Package (RES)
38	0	Multi-Node Fracture Well Package (FWL5)
39	0	Steam-Flow Routing Package (SFR1)
40	0	Lake 3 Package (LAK3)
41	0	Gage Package (GAGE)
		Evapotranspiration Segments Package (ETS1)
IAPART	1	The arrays BUFF and RHS occupy different space.
ISTRT	1	Starting heads are saved and stored in array STRT.
IBOUND	(…)	Boundary arrays for all GW layers. Constant head at upper and lower rows (-1) and otherwise active cell (+1).
HNOFLO	-999	Value of head to be assigned to all inactive cells (IBOUND = 0).
SHEAD	(…)	Head arrays at start of the simulation for all GW layers. By default assumed equal to the OLF cell.
PERLEN	84600	Length of a stress period in seconds (366 days).
NSTP	1	Number of time steps in a stress period. Not used because they are determined for the ATO4 package.
TSMULT	1.0	Multiplier for the length of successive time steps. Not used because they are determined for the ATO4 package.

Table A-19. Properties for the base case as introduced in BAS file.

Variable	Default Value	Comments for BCF file:
ISS	0	Simulation is transient.
IBCFCB	98	>0: Unit number in which cell-by-cell flow terms will be recorded. 0: cell-by-cell flow terms will not be printed or recorded.

Variable	Default Value	Comments for BCF file:
HDRY	-1000	Head assigned to cells that are converted to dry during a simulation.
IWDFLG	1	Wetting capability is active.
WETFCT	0.1	Factor included in the calculation of the head that is initially established at a cell when it is converted from dry to wet.
IWETIT	1	Cell wetting is attempted each iteration.
IHDWET	1	Equation (3b) of McDonald et al. (1991) is used to calculate the initial head at cells that become wet: h = BOT + WETFCT (THRESH).
IAXIS	0	The simulation is not axi-symmetric.
IREALSL	2	0: Pseudo-soil relations are used to define the water-table. 1: Van Genuchten functions are used for retention and relative permeability characteristics of the unsaturated layers and water flow is simulated. 2: van Genuchten function is used to characterize moisture retention, and Brooks-Corey function is used for relative permeability characteristics of the unsaturated layers and water flow is simulated. 5: Tabular input of moisture retention and relative permeability curves is used to characterize unsaturated layers and flows of water is simulated.
ICNTRL	0	0: upstream weighting of the relative permeability term. 1: midpoint weighting.
IVHYC	1	Vertical hydraulic conductivities are read. Leakances are computed from vertical conductivity of each layer as per a volume weighted harmonic mean.
IANIXY	0	Horizontal anisotropy is uniform within each layer as in the original MODFLOW formulation.
ICURVL	0	A rectangular grid is used, as in the original MODFLOW.
IOLDHDR	1	The old MODFLOW style headers are used for cell by cell flow term output in the binary file.
LAYCON	43	Layer-type index array.
TRPY	1	Isotropic conditions for hydraulic conductivity.
DELR	(…)	1D array for the cell width along rows. By default 5, 6.6, 10 or 20.
DELC	(…)	1D array for the cell width along columns. By default 5, 6.6, 10 or 20.
SF1	0	Primary storage coefficient for all GW layers.
HY	(…)	Hydraulic conductivity along grid rows for all GW layers. Default values: 1e-5 for layer 1 (soil) and 1.8e-3 for layer 2 (rock).
VHY	(…)	Vertical hydraulic conductivity of each cell for all GW layers. Default values: 1e-5 for layer 1 (soil) and 1.8e-3 for layer 2 (rock).

Variable	Default Value	Comments for BCF file:
BOT	(…)	Elevation of the aquifer bottom for all GW layers. Default values are plotted in Figure A-39 for layer 1 (soil). For layer 2 (rock) it is -4.572 m.
SF2	(…)	Secondary storage coefficient (drainable porosity or specific yield) for all GW layers. Default values: 0.50 for HH vegetation type and 0.93 otherwise for layer 1 (soil) and 0.20 for layer 2 (rock).
TOP	(…)	Elevation of the aquifer top for all GW layers. Default values are plotted in Figure A-39.
VANAL	2.78	Van Genuchten parameter alpha (1/m).
VANBT	1.917	Van Genuchten parameter beta (exponent).
VANSR	0.01	Irreducible water saturation in Van Genuchten equations.
BROOK	3	The Brooks-Corey exponent for computing relative permeability of unsaturated soil.

Table A-20. Properties for the base case as introduced in BCF file.

Variable	Default Value	Comments for BTN file:
LINR	2	Retardation is nonlinear.
IDCYTP	1	The degradation is only species dependent.
ILAMWS	1	The rate of degradation is same in all phases including soil.
IACLVL	0	Fully upstream weighting scheme.
NSPECI	1	Only one species is considered in the transport simulation.
ICHAIN	0	Transformation of one species to another is not allowed.
IDISP	3	Longitudinal, transverse, vertical transverse and vertical longitudinal dispersivity data are read.
IEQPART	0	Transport occurs in active phase only.
NDENS	0	Number of components whose density effects are to be included for flow.
CNOFLO	-999	The value of concentration to be assigned to all inactive cells.
CCLOSE	1e-13	The concentration change criterion for convergence in the case of nonlinear iterations.
MXITERC	50	The maximum number of outer iterations in the case of nonlinear iterations.
NNOTCV	3	The maximum number of time-step cuts allowed in solving transport equations before aborting the simulation.
THETRD	1.0	Fully implicit scheme is used.
IBCFCC	84	Flag and unit number on which storage and decay terms for all phases are saved if requested.
ICROSS	0	The cross-dispersion terms are neglected.
LDISP	0	Longitudinal dispersivity in GW layers (m).
TDISP	0	Transverse dispersivity in GW layers (m).
VTDISP	0	Vertical transverse dispersivity in GW layers (m).

Variable	Default Value	Comments for BTN file:
VLDISP	0	Vertical longitudinal dispersivity in GW layers (m).
PHI	SF2	Effective porosity array in GW layers (m).
RHOB	(…)	Bulk density of soil (kg/m^3). Default values for layer 1 are 400 for HH vegetation type and 200 otherwise. For layer 2 it is 2260.
DIFF	0.0	Diffusion coefficient (m^2/s).
KD	(…)	Soil partition coefficient (m^3/kg). Default values for layer 1 are 6.33e-3 for HH vegetation type and 3.06e-3 otherwise. For layer 2 it is 1.94e-4.
ETA	(…)	Freundlich exponent. Default values for layer 1 are 0.81 for HH vegetation type and 0.428 otherwise. For layer 2 it is 0.59.
ALAM1	0	Rate of contaminant degradation (1/s).
SCONC	(...)	Concentration at start of the simulation in GW layers (kg/m^3 = 10^6 □g/l). Default values for layer 1 are taken from Table 2, according to vegetation type in Figure A-38. For layer 2 it is 1.5e-6 initially.

Table A-21. Properties for the base case as introduced in BTN file.

Variable	Default Value	Comments for ETS file:
(…)	(…)	Array for time-series of maximum ET rates: TSTART TEND TMULT ETMAX(1) … ETMAX(5) TSTART: Starting time (s). TEND: Ending time (s). TMULT: Multiplying factor. Equal to 1.0 by default. ETMAX: ET maximum rate (m/s). By default the time series contain the average daily rates presented in Figure 22 and extended periodically for 10 years. Each daily value is multiplied by the factors in Table 9 to obtain the five transpiration rates corresponding to each vegetation type coverage.

Table A-22. Properties for the base case as introduced in ETS file.

Variable	Default Value	Comments for EVT file:
NEVTOP	1	ET parameters for cells in the top grid layer.
IEVTCB	92	>0: Unit number on which cell-by-cell flow terms will be recorded. 0: cell-by-cell flow terms will not be printed or recorded.
MXZETS2	5	0: Maximum ET flux (EVTR) is read as per stress periods. n: A separate file is used to read time-series of maximum ET flux (EVTR), and n is the total number of ET zones used in the simulation.
IFRACET	1	Water and mass uptake by plants.

Variable	Default Value	Comments for EVT file:
IEVTCC	90	>0: Unit number on which the cell-by-cell ET mass flux terms. 0: cell-by-cell mass flux terms for ET will not be recorded.
ETFRAC	0.0	Root uptake factor. 0 implies that only water is taken up. 1 implies that the water is taken up at the current concentration.
INSURF	1	An array containing the ET surface elevation will be read.
INEVTR	1	An array containing the maximum ET rate will be read.
INEXDP	1	An array containing the extinction depth (EXDP) will be read.
INIEVT	1	Layer indicator (IEVT) read flag. Not used.
SURF	TOP(1)	The elevation of the ET surface. By default is the top of the soil layer.
EVTR	---	Maximum ET rate (m/s). Substituted by time series values during simulation. When MXZETS2=0. Not entered by default.
IZNETS2	(…)	The zone value of each node, for zonal input of the ET time series. When MXZETS2>0 and INEVTR ≠ 0. By default it is in the range (1, 5), corresponding to the vegetation coverage type in each node.
EXDP	1000	ET extinction depth (m).

Table A-23. Properties for the base case as introduced in EVT file.

Variable	Default Value	Comments for FHB file:
NBDTIM	3651	Number of times at which flow and head will be specified for all selected cells. Daily values during ten years by default.
NGWFLW	0	Number of groundwater cells at which flows will be specified.
NGWHED	516 (SL) 616 (BH) 660 (GL)	Number of groundwater cells at which head will be specified.
IFHBSS	1	Values of flow, head, and auxiliary variables will be interpolated in the same way that values are computed for transient simulations.
IFHBCB	0	Cell-by-cell flow terms will not be recorded.
NFHBX1	0	Number of auxiliary variables whose values will be computed for each time step for each specified-flow cell.
NFHBX2	0	Number of auxiliary variables whose values will be computed for each time step for each specified-head cell.
NOLFLW	0	Number of overland cells at which flows will be specified.
NOLHED	258 (SL) 308 (BH) 330 (GL)	Number of overland cells at which heads will be specified.
NCHFLW	0	Number of channel cells at which flows will be specified.
NCHHED	0	Number of channel cells at which heads will be specified.
ITHTFHB	0	0: The adaptive time-stepping is independent of tabular time inputs for FHB. 1: Time steps are adapted to honor the tabular time value

Variable	Default Value	Comments for FHB file:
		entries of the FHB input.
IFHBCC	0	Cell-by-cell mass flux terms will not be recorded.
IFHBUN	25	Unit number on which data lists will be read.
CNSTM	1.0	Constant multiplier for data list BDTIM.
IFHBPT	1	Data list read at the beginning of the simulation will be printed.
BDTIM	(…)	Time array (s) at which values of specified head will be read.
(…)	(…)	Array for GW layers: Layer Row Column IAUX SBHED(NBDTIM) Layer: layer index of specified-head cell. Row: row index of specified-head cell. Column: column index of specified-head cell. IAUX=-1: concentration is read from HCN file. SBHED: array containing NBDTIM values of the head for each specified-head cell.
(…)	(…)	Array for OLF layer: Row Column IAUX SBHED(NOLHED)

Table A-24. Properties for the base case as introduced in FHB file.

Variable	Default Value	Comments for HCN file:
IHCNCCGW	0	Mass-flux-terms of species in GW will not be printed or recorded
IHCNCCOL	0	Mass-flux-terms of species in OL will not be printed or recorded
IHCNCCCH	0	Mass-flux-terms of species in CH will not be printed or recorded
IHCNCC	0	Unit number on which contaminant mass flux terms of each species at all the specified-head cells will be recorded.
ITMPGW	516 (SL) 616 (BH) 660 (GL)	Number specified-head boundary cells in the current stress period in GW layers.
ITMPOL	258 (SL) 308 (BH) 330 (GL)	Number specified-head boundary cells in OLF layer.
ITMPCH	0	Number specified-head boundary cells in channels.
(…)	(…)	Array over the specified-head boundary cells: Layer Row Column Conc 0 Layer: the layer number. Row: the row number. Column: the column number. Conc: the concentration. Default value: For soil layer are taken from Table 2, according to vegetation type in Figure A-38. For rock layer 1.5e-6.

Variable	Default Value	Comments for HCN file:
(…)	(…)	Array for OLF layer: Row Column Conc 0 Conc: the concentration. Default value: 1.5e-6 ViewHMS does not create or read this array.

Table A-25. Properties for the base case as introduced in HCN file.

Variable	Default Value	Comments for OLF file:
MXOLPLD	0	Maximum number of point loads for 2-d overland flow system in the simulation.
MXZDGO	0	Maximum number of zero-depth gradient and critical depth boundary conditions.
ICHCOL	93	>0: Unit number for saving cell-by-cell budgets and fluxes. 0: no saving.
ICHCOLC	94	>0: Unit number for saving cell-by-cell budgets and mass fluxes from contaminant transport simulation. 0: no saving.
IOLEVP	1	0: evaporation from OLF nodes is not simulated. 1: evaporation from OLF nodes exists in the simulation.
IRFTYPO	0	Manning equation is used to determine frictional resistance.
GRAVT	9.8	Gravitational acceleration (m/s^2). Not used.
VISCKIN	1e-6	Kinematic viscosity of water (m^2/s). Not used.
ISCHEME	0	0: The head of a dry overland flow cell is allowed to fall below its land surface elevation. Infiltration from land surface is always at the capacity of its saturated leakance. 1: Do not allow OLF node heads to fall below land surface. OLF leakance term varies from zero to one over the Rill Storage Height.
IVPAROL	0	Material properties (friction, rill storage, and storage obstruction) 0: are constant 1: vary with stress periods and are input at every stress period.
IMPGOL	0	0: Gradient term of equations is treated semi-implicitly for Newton-Raphson linearization. 1: this term is treated fully implicitly for Newton-Raphson linearization.
IOBKROL	1	0: The conductance term is not adjusted over the obstruction storage height. 1: It is to be adjusted.
KRSILOL	1	0: Flow depths are computed from the elevation of the

Variable	Default Value	Comments for OLF file:
		respective nodes. 1: Flow depths are computed from the sill elevation between the two nodes for which flow is computed.
INITIAL HEAD	(…)	Initial head array for OLF. Default values are obtained from a linear interpolation from mean stage in Figure 27 and median averaged slopes in Figure 30.
BOTTOM ELEVATION	(…)	Bottom elevation array for OLF. Default values are plotted in Figure A-39.
X_FRICTN	(…)	Manning coefficient array for OLF in x-direction. Default values are taken from Table 3, according to vegetation type in Figure A-38.
Y_FRICTN	X_FRICTN	Manning coefficient array for OLF in y-direction.
BOTTOM LEAKAGE	1.0	Leakance array for considering a skin effect at the soil surface. A high value implies a high connectivity between the upper soil layer and the OL layer, which implies that the heads remains about the same.
RILLSH	0.001	Rill storage height on land surface (m).
OBSTRH	0	Obstruction storage height (m).
IBOUNDOL	(...)	Boundary arrays for OLF layer. Constant head at upper and lower rows (-1) and otherwise active cell (+1).
LDISPOL	0	Longitudinal dispersivity of the overland surface (m).
TDISPOL	0	Transverse dispersivity of the overland surface (m).
VDISPOL	0	Longitudinal dispersivity between overland surface and subsurface domains (m).
KDOL	0	The partition coefficient between water and soil sediments of the overland surface.
ETAOL	0	Freundlich exponent.
SCONCOL	1.5e-6	Concentration of water in the overland surface domain at start of the simulation (kg/m^3).
ITMP	0	Number of values of point stresses for OLF, NOLPLD=ITMP.
ITMPEVP	1	0: Evaporation array for this stress period is not required as input in OLF. 1: Evaporation array for this stress period is required as input in OLF.
ITMPZDGO	0	No zero-depth gradient and critical depth boundaries for this stress period.
ITMPSCHEME	0	Coupling.
EVAPORATION RATE	(…)	Evaporation rate array for this stress period. By default array is obtained from the average daily rates presented in Figure 22 and extended periodically. Each daily value is multiplied by the factors in Table 9 to obtain the five evaporation rates corresponding to each vegetation type coverage.

Variable	Default Value	Comments for OLF file:

Table A-26. Properties for the base case as introduced in OLF file.

Variable	Default Value	Comments for PCG file (PCG4 by default or PCG5 package):
MXITER	80	Maximum number of outer iterations.
ITERI	60	Maximum number of inner iterations.
INEWT	1	Newton-Raphson linearization is performed.
BFACT	0.3	Factor by which backtracking is performed if residual reduction criterion is not met.
RESRED	1E10	Increases in residual are allowed by the prescribed factor to allow the Newton algorithm to move easily out of local minima.
IDMPBOT	0	Index for using aquifer geometry to dampen head oscillations between iterations. 1: The dampening is applied. 0: The dampening is not applied.
HCLOSE	1.0e-5	Head change criterion for convergence.
MUTPCG	1	0: no printing from the solver is suppressed. 1: the solver iteration summary is suppressed. 2: the solver iteration summary, as well as convergence behavior at each iteration, is suppressed.
MNORTH	7	Maximum number of orthogonalizations allowed for the Orthomin solver to solve the transport matrix equation.
RCLOSE (PCG4)	1.0e-15	Relative closure criterion for convergence. Convergence is achieved when either RCLOSE or HCLOSE values have been met by the respective changes at any inner iteration.
LEVELS (PCG5)	1	Level of ILU factorization.
IACCELS (PCG5)	1	ORTHOMIN acceleration method.
NATURL (PCG5)	2	A red/black reduced system is used.
ISTOR1 (PCG5)	20	Factor controlling the amount of storage allocated in the workspace array used by the package to store pointers needed in the factorize and solve phases.
ISTOR2 (PCG5)	19	Factor controlling the amount of storage allocated in the workspace array used by the package to store pointers needed in the factorize and solve phases.

Table A-27. Properties for the base case as introduced in PCG file.

Variable	Default Value	Comments for RCH file:
NRCHOP	1	1: Recharge is only to the top grid layer. 2: Vertical distribution of recharge is specified in array IRCH.
IRCHCB	97	Unit number on which cell-by-cell flow terms will be recorded
IUNCNF	0	The specified recharge (RECH) is applied always like in a

		confined case.
MXSEEP	0	Maximum number of seepage boundary cells active at one time.
MXZRCH	0	0: MODFLOW's input structure for recharge is used with variations only at stress periods. n: Recharge varies as a time series, and n is the total number of recharge zones used in the simulation.
IPNDPOR	0	0: Pounding porosity is not read and the full cell area is assumed to be pounded. 1: An array of pounding porosity is read. The pounding porosity is the fraction of the total cell area that is wetted by lakes/ponds, and is used to determine the total pounded storage, if pounding occurs.
INRECH	1	An array of recharge rates, (RECH) is read.
INIRCH	0	When NRCHOP = 2, an array of layer numbers (IRCH) is read.
INPNDEL	0	When IUNCNF > 0, an array of pounding elevations (PNDEL) is read.
INSEEP	0	Number of seepage face boundaries during the current stress period.
INCONC	1	Concentration array is read.
RECH	(…)	The recharge depth rate array (m/s). By default, the array is assumed uniform and is obtained from the average daily rates presented in Figure 15 and extended periodically
IZNRCH	---	Integer array identifying the zone value of each node. Not included.
CONC	1.5e-6	Concentration in the recharge (kg/m^3).

Table A-28. Properties for the base case as introduced in RCH file.

Variable	Default Value	Comments for WEL file:
MXWELL	(NROW-2)* (NCOL-2)	The maximum number of wells used at any time.
IWELCB	85	>0: unit number on which cell-by-cell flow terms will be recorded whenever ICBCFL =0: Cell-by-cell flow terms will not be printed or recorded.
IWELCC	86	>0: unit number on which mass-flux-terms of species at well cells will be recorded whenever ICCCFL =0: Mass-flux-terms of species will not be printed or recorded.
ITMP	MXWELL	Number of wells active during the current stress period.
(…)	(…)	Array for well rates: Layer, Row, Column, Q, Conc

Table A-29. Properties for the base case as introduced in WEL file.

Appendix 4. Addendum for Chapter 4

A4.1 Surface Water Parameters Calibration

In this section, additional details about the Manning coefficient calibration from surface water velocity measurements are described.

A4.1.1 Results for the Base Case. Additional Figures

The following graphs show detailed results for the base case.

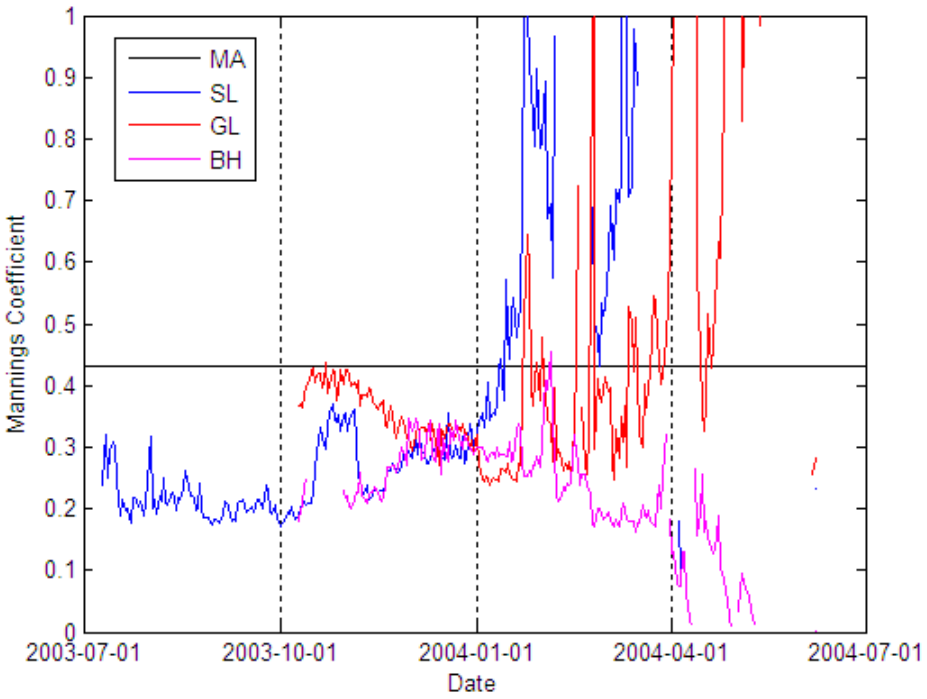

Figure A-43. Manning coefficients estimated by using equation (20) from observed or simulated station data presented in Figure 48 and model slope from the base case.

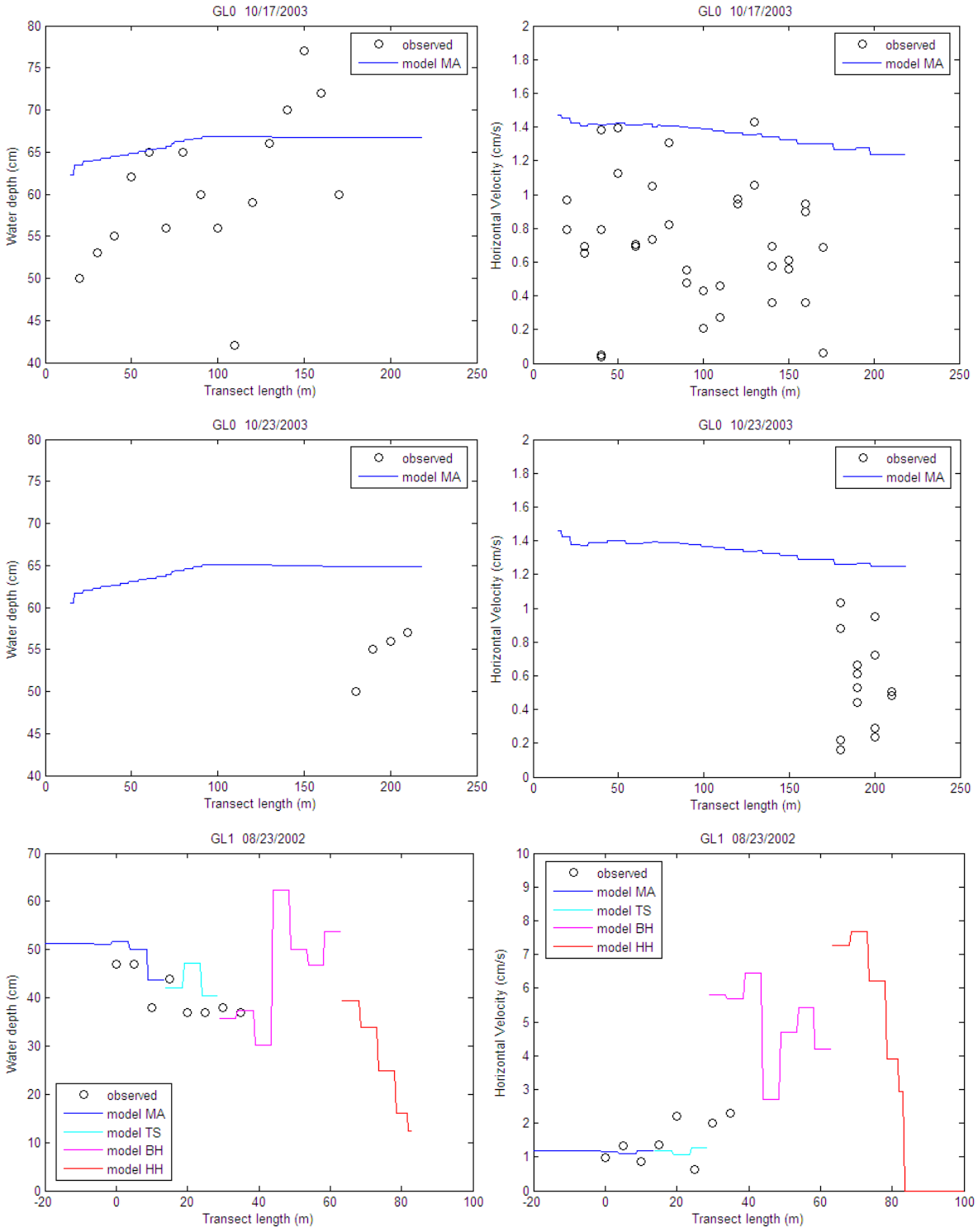

Figure A-44. Model results from the base case and the measurements at transect locations.

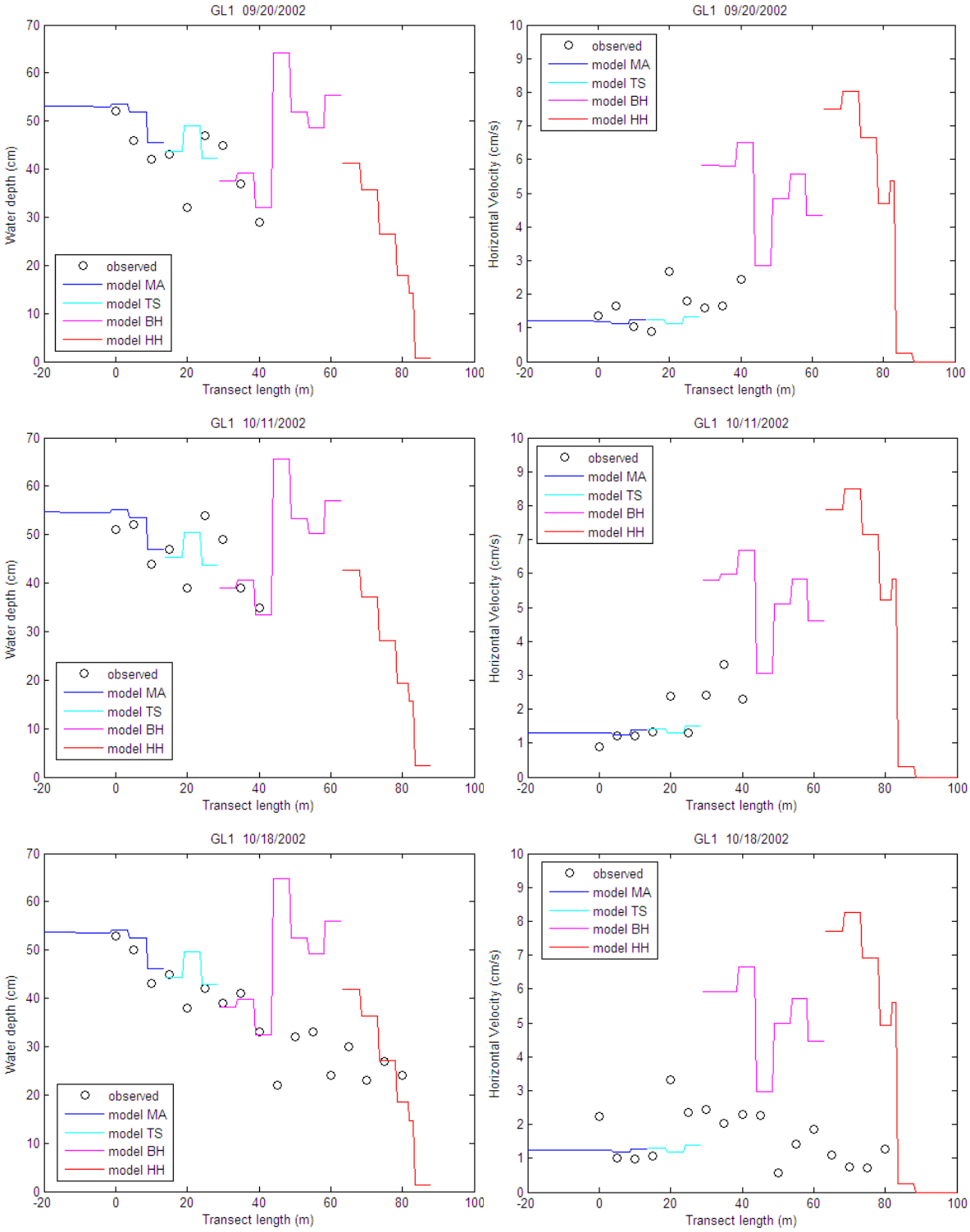

Figure A-44. Model results from the base case and the measurements at transect locations. Continuation.

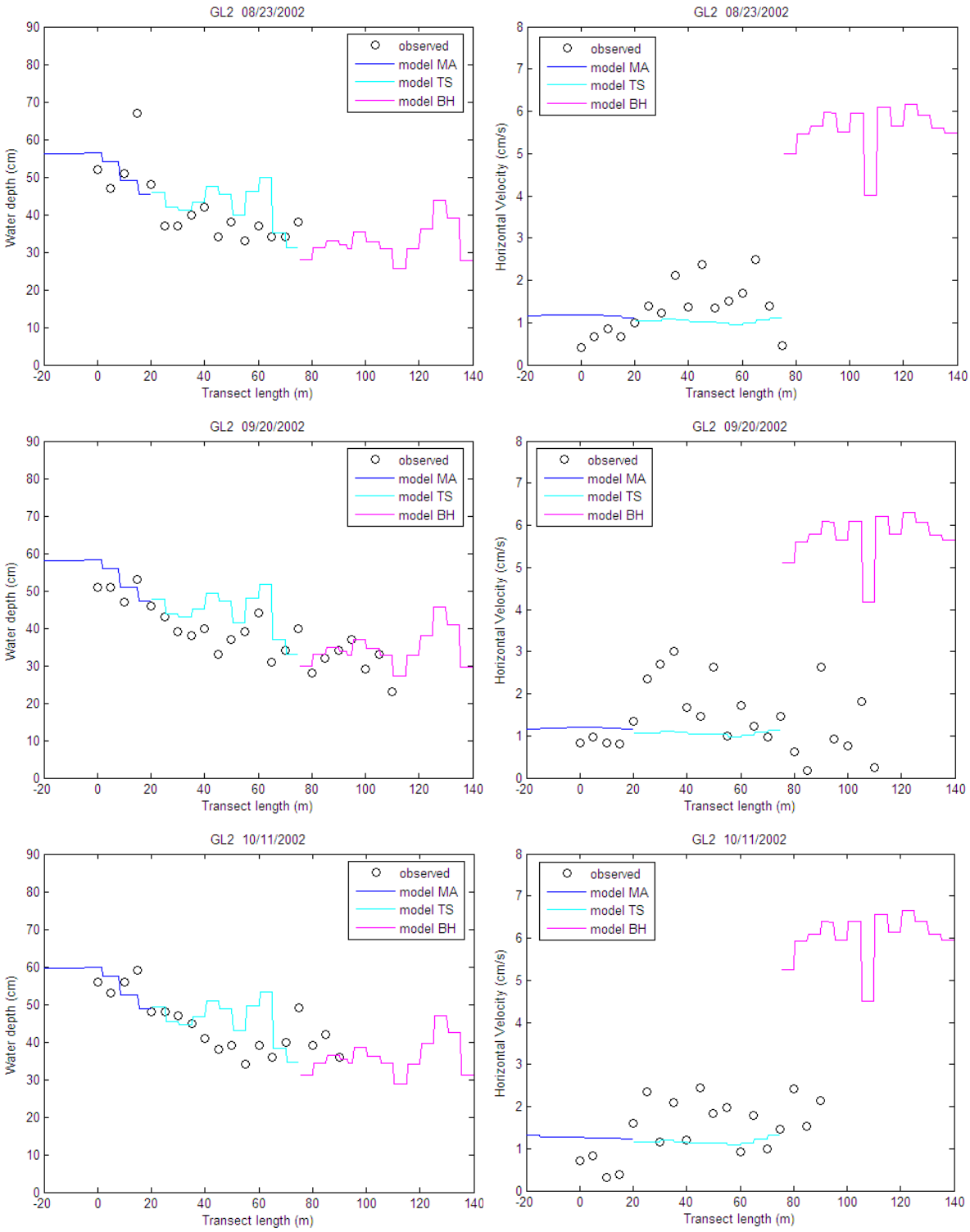

Figure A-44. Model results from the base case and the measurements at transect locations. Continuation.

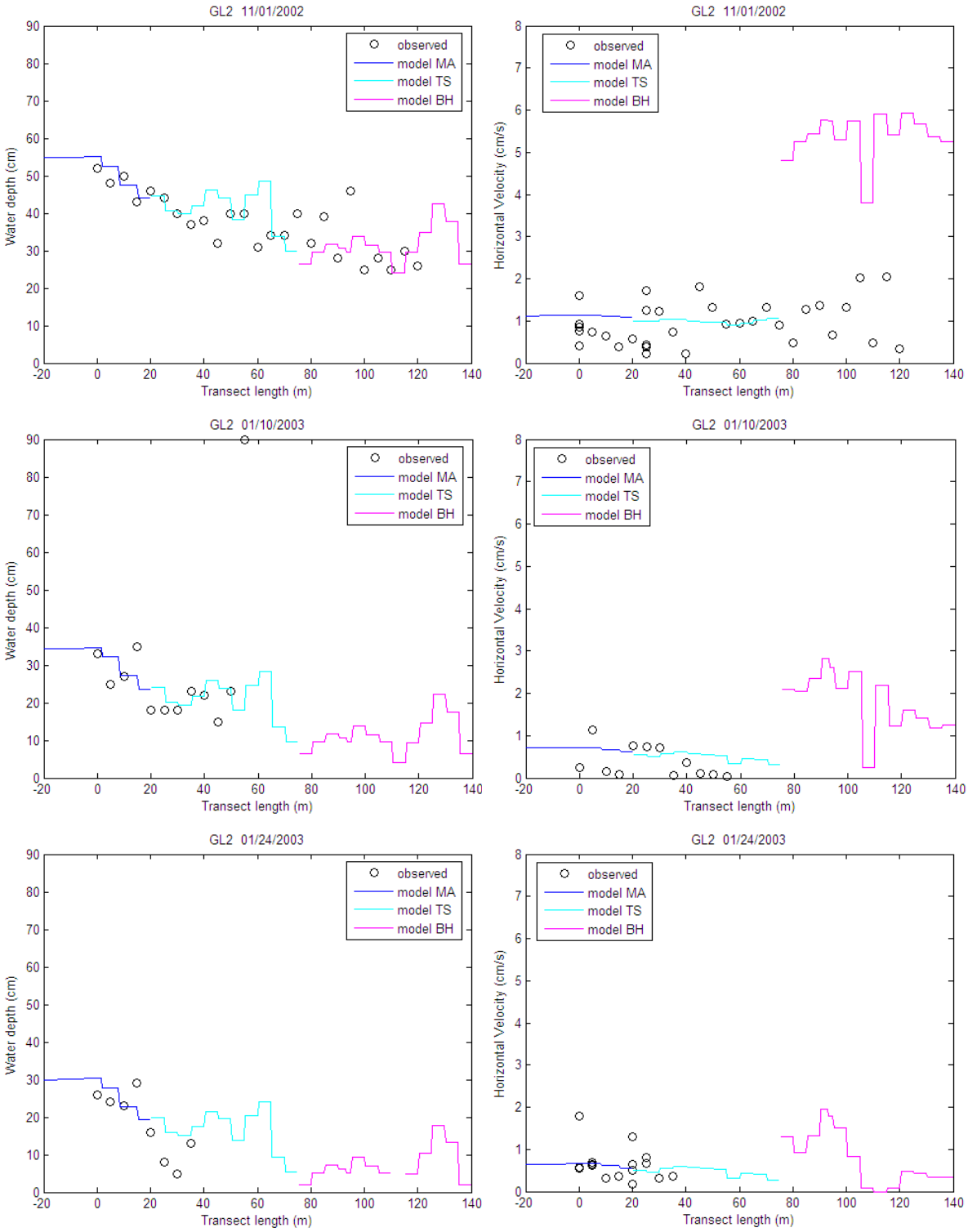

Figure A-44. Model results from the base case and the measurements at transect locations. Continuation.

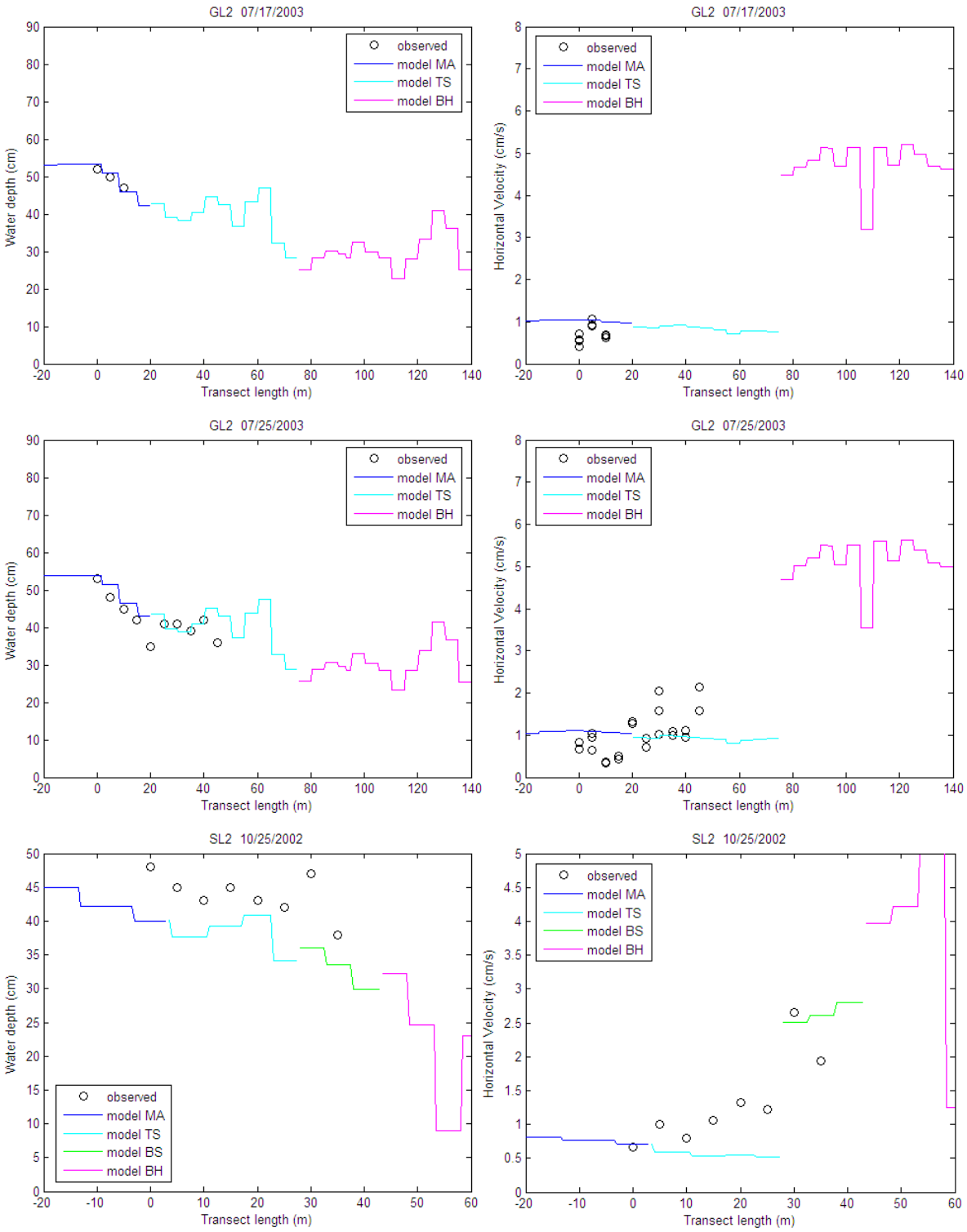

Figure A-44. Model results from the base case and the measurements at transect locations. Continuation.

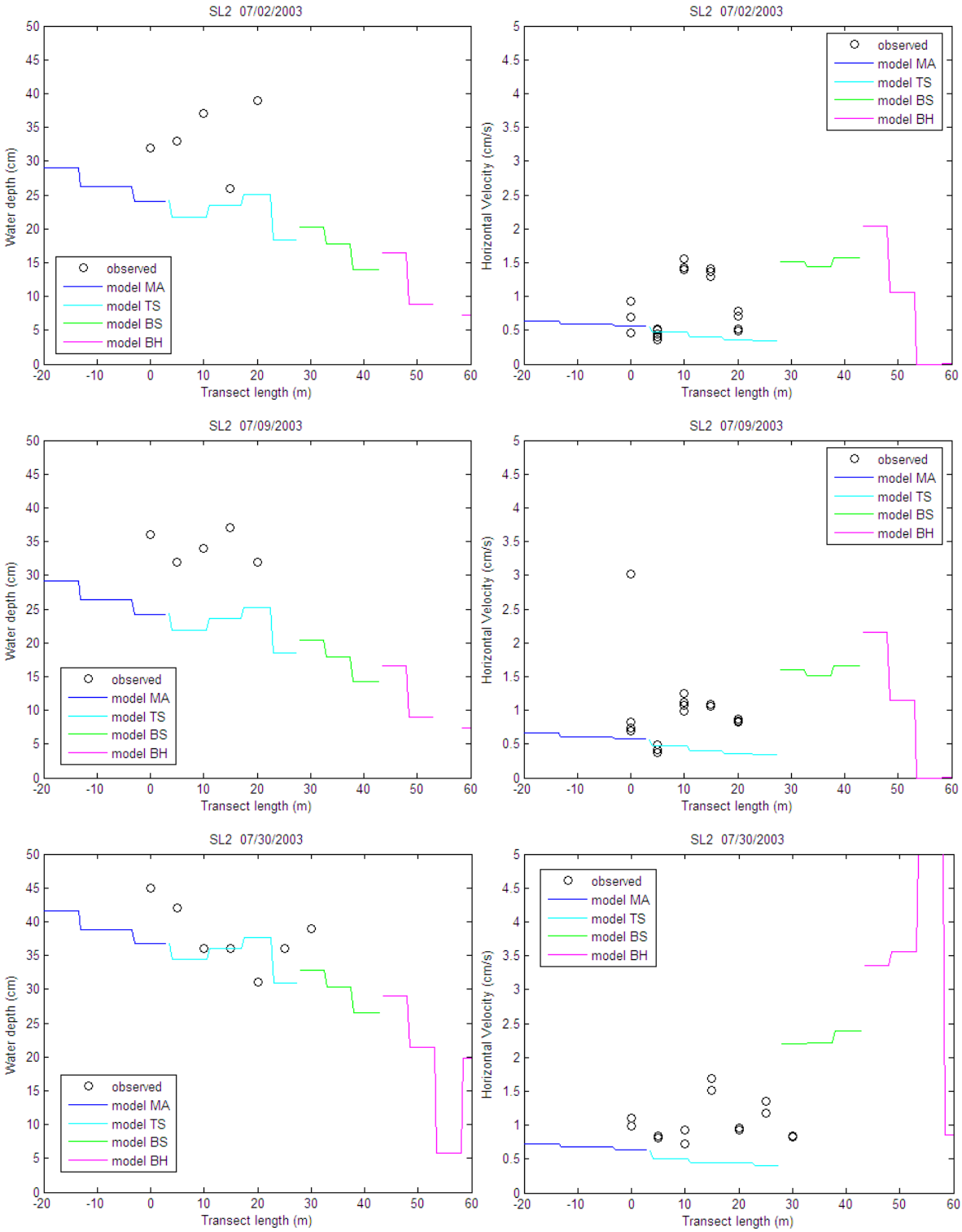

Figure A-44. Model results from the base case and the measurements at transect locations. Continuation.

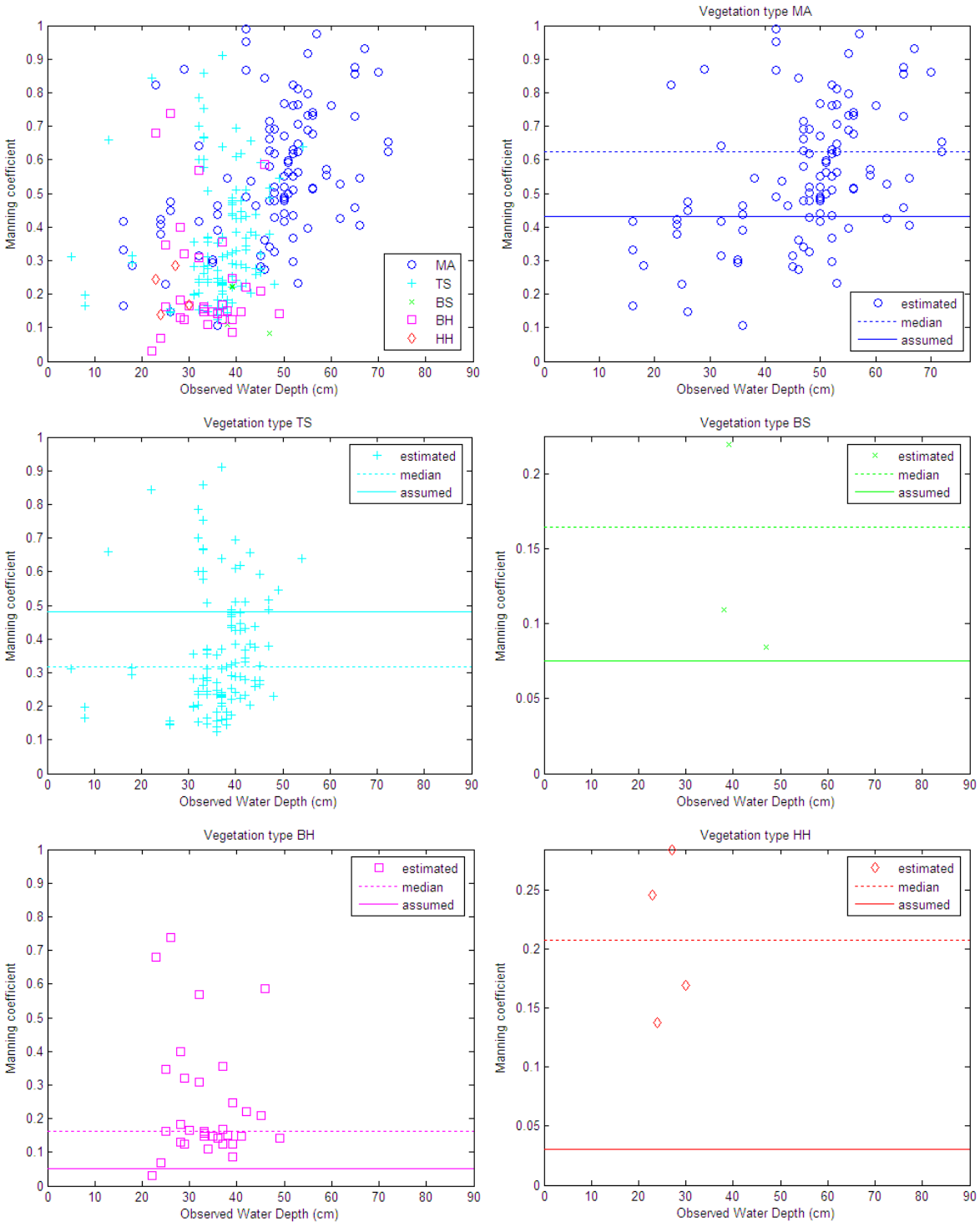

Figure A-45. Manning coefficients estimated by using equation (20) from observed transect data and model slope. They are compared with the value assumed in the model for each vegetation type in the base case (Table 22).

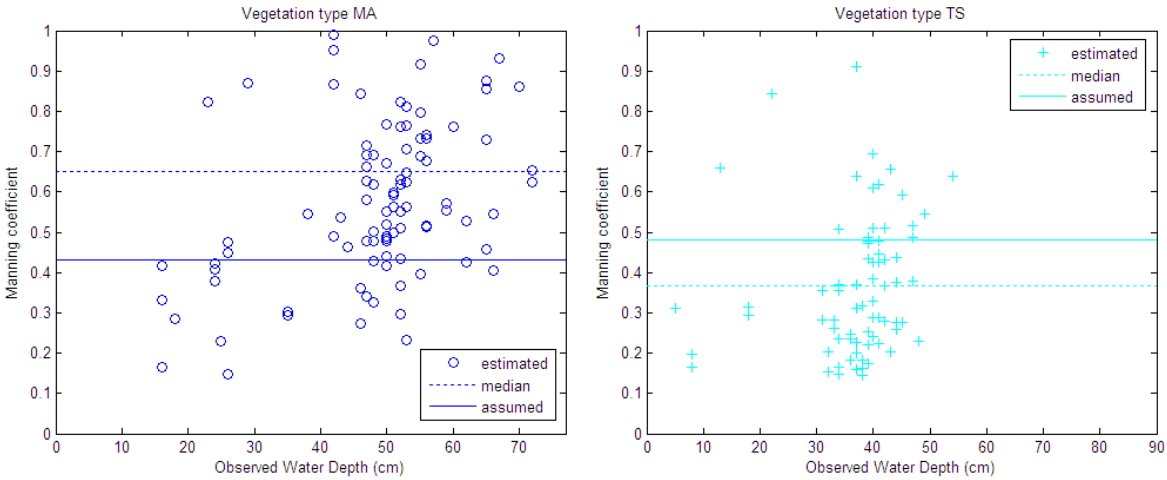

Figure A-46. Similar to Figure A-45, but only considering data from GL tree island.

A4.1.2 Results Adjusting the Manning Coefficients. Additional Figures

The following graphs show detailed results for the case M4.

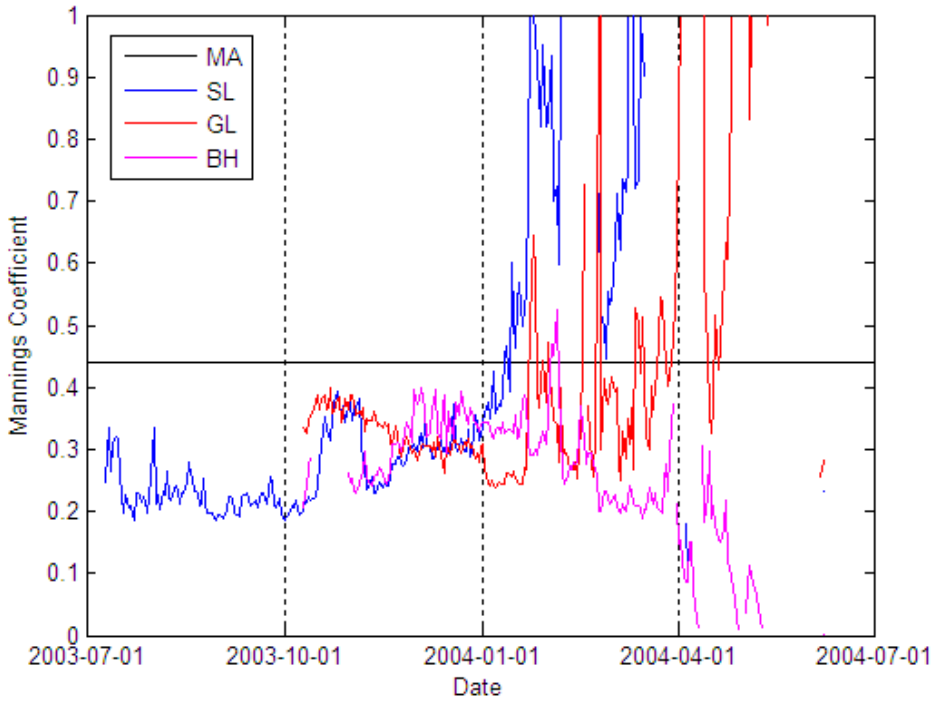

Figure A-47. Manning coefficients estimated by using equation (20) from observed or simulated station data presented in Figure 48 and model slope from the case M4.

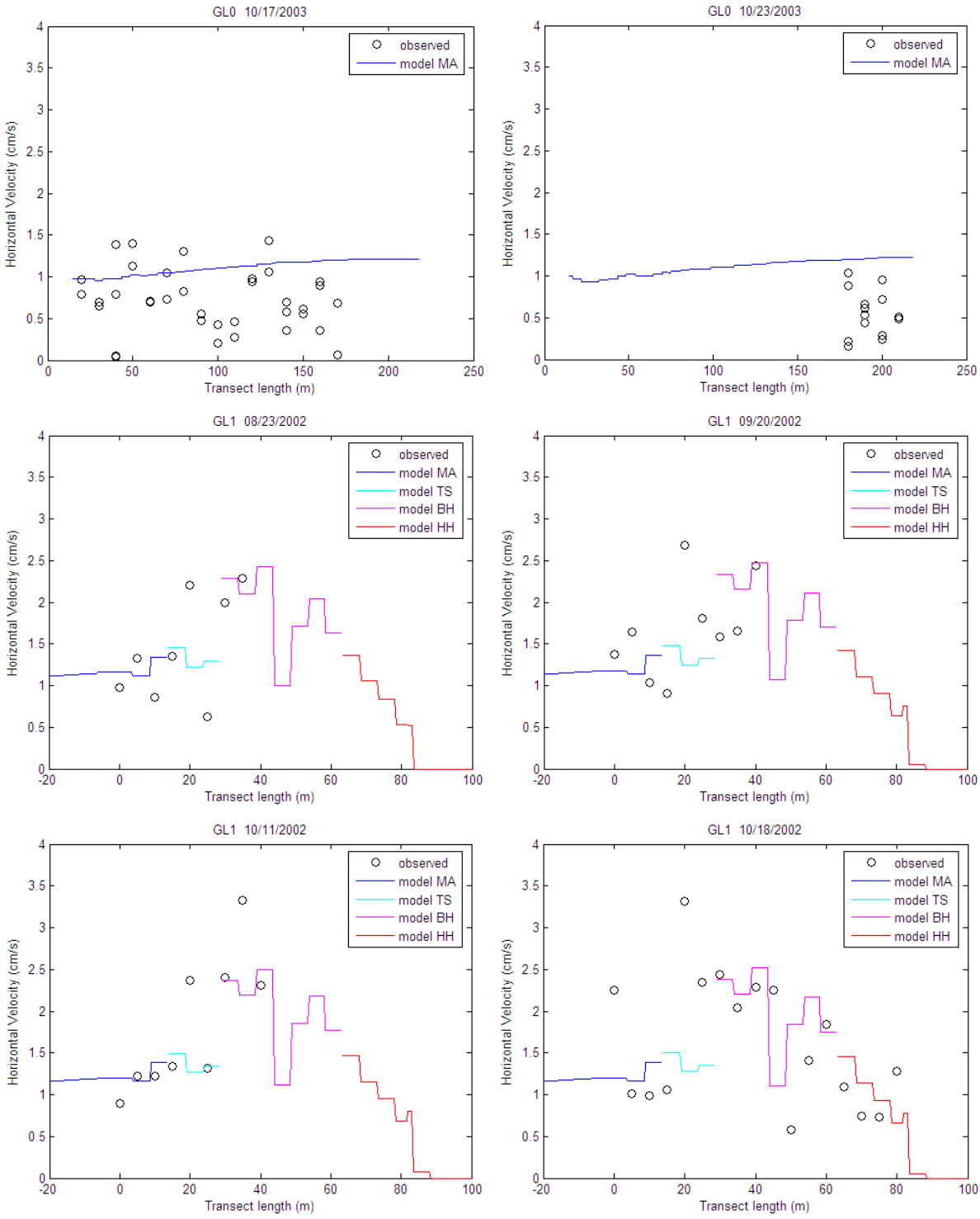

Figure A-48. Model results for the case M4 compared to the measurements at transect locations. They are comparable to the base case results in Figure A-44.

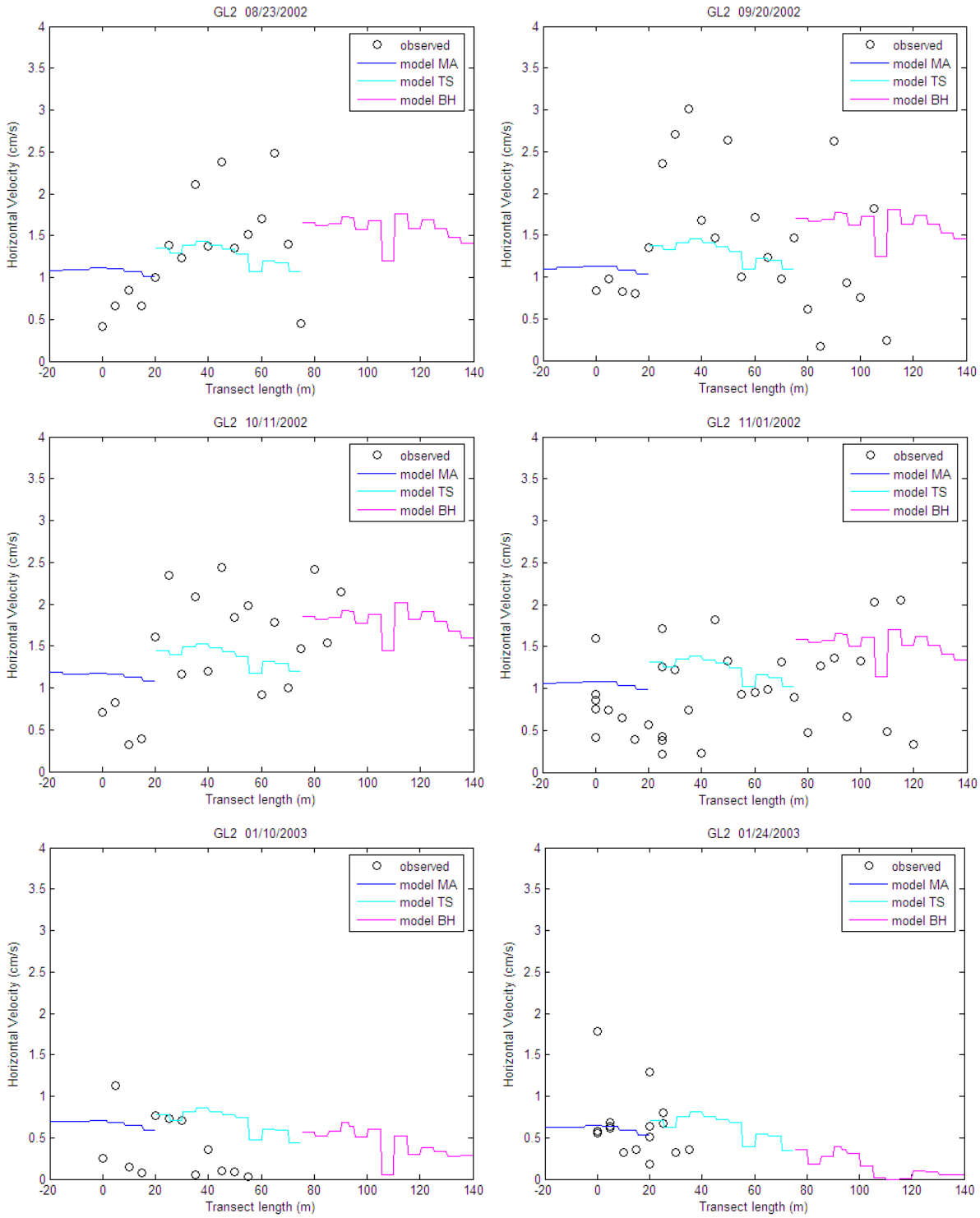

Figure A-48. Model results for the case M4 compared to the measurements at transect locations. They are comparable to the base case results in Figure A-44. Continuation.

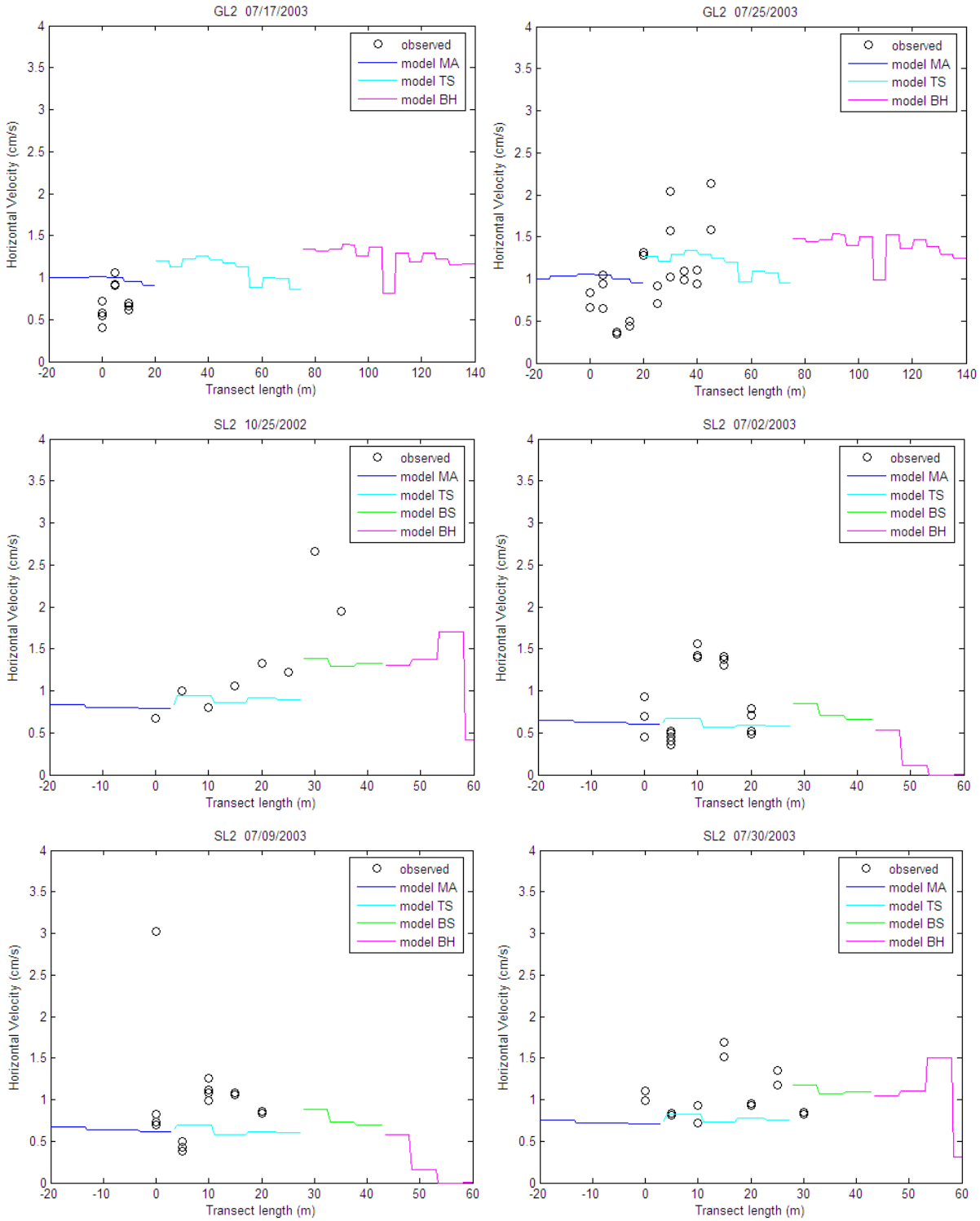

Figure A-48. Model results for the case M4 compared to the measurements at transect locations. They are comparable to the base case results in Figure A-44. Continuation.

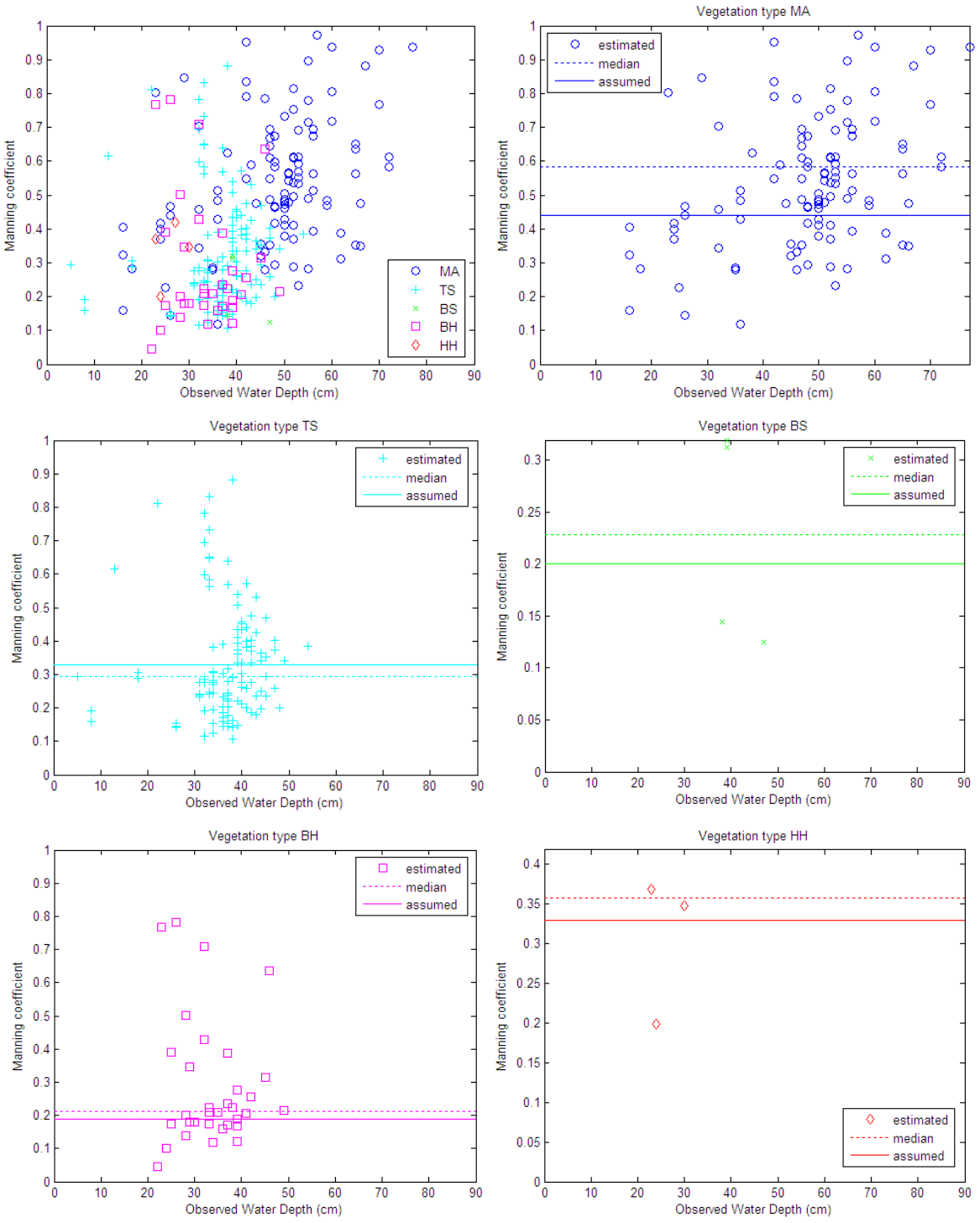

Figure A-49. Manning coefficients estimated by using equation (20) from observed data and model slope. They are compared with the value assumed in the model for each vegetation type in the case M4 (Table 22). They can be compared to the base case in Figure A-45.

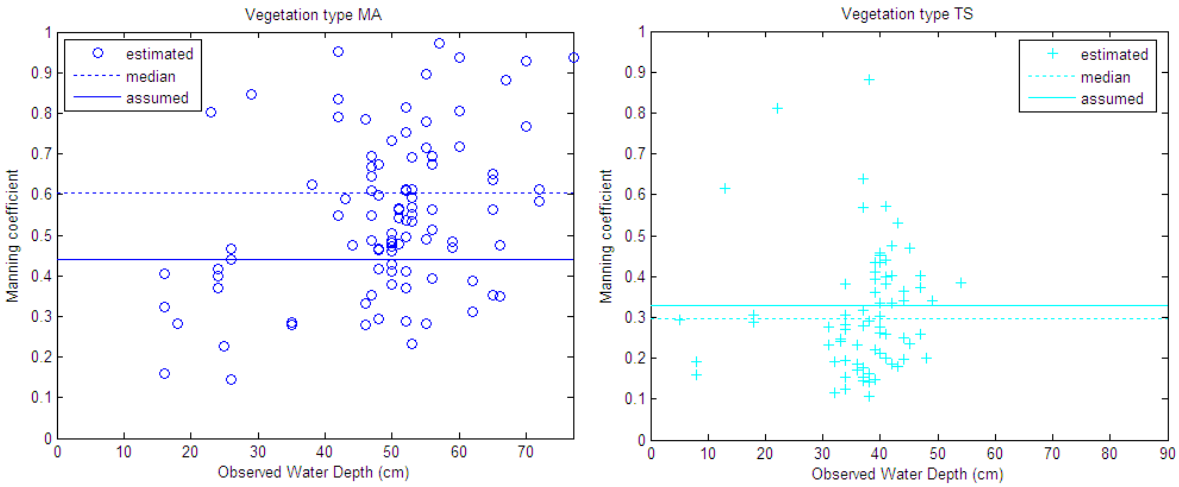

Figure A-50. Manning coefficients estimated from eq. (20) from observed data and model slope. They are compared to the value assumed in the model for each vegetation type in the case M4 (Table 22). They can be compared to the base case in Figure A-46.

A comparison between the regional slope (that is used to set the boundary conditions in the model) and the slopes found by the model at the station and transect point locations are shown in Figure A-51. The local slope shows significant differences regarding the regional slope (particularly in the transect point locations) likely due to the topography and vegetation resistance distributions around tree islands. It is relevant to point out that the estimation of Manning coefficient from the field measured water depth and velocity using the regional slope (and not the local slope as it was done here) would contain errors associated to this fact.

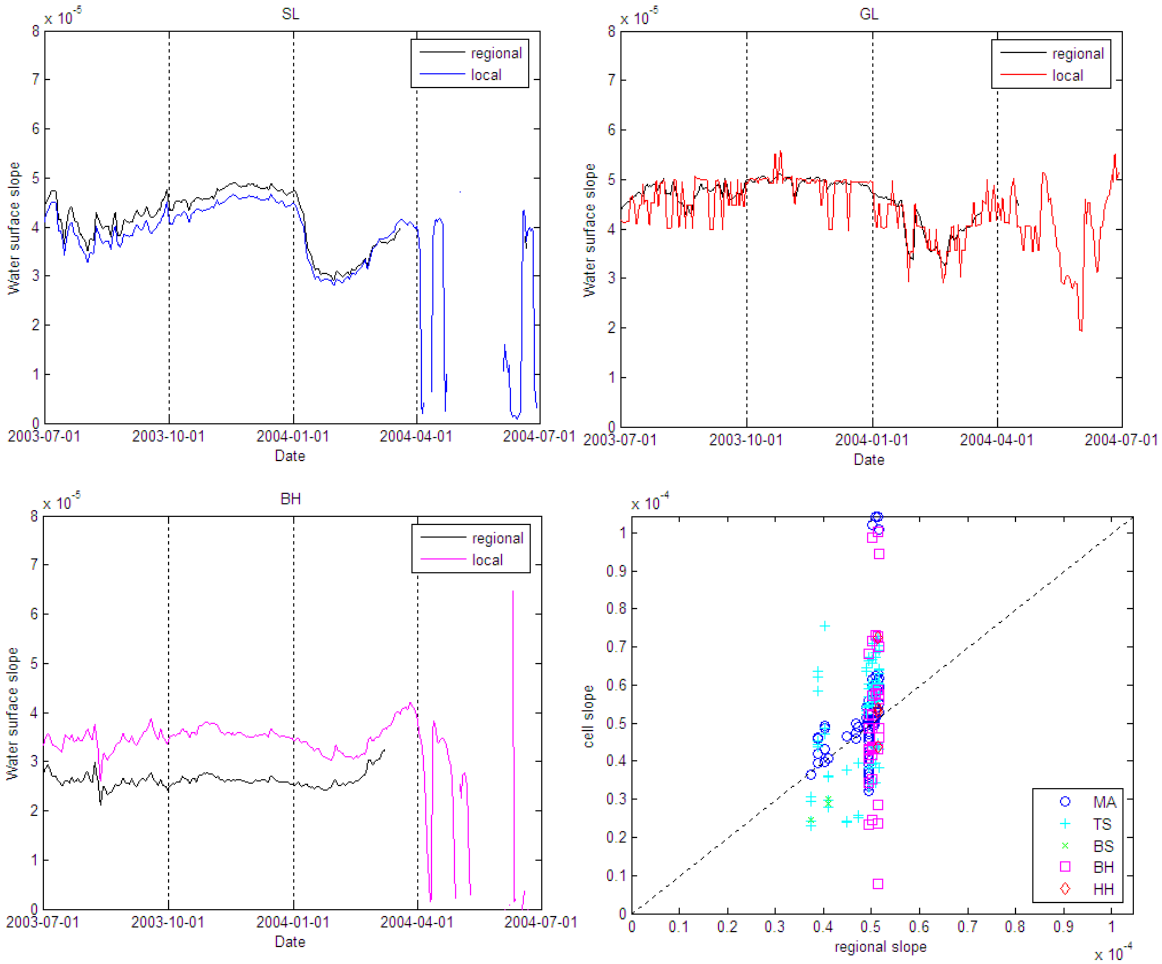

Figure A-51. Comparison among the regional slopes that are used to set the constant head boundary condition in the model and the slopes at the station and transect cells for case M4.

A4.1.3 Results Changing SL Slope

As the surface water slope estimated for SL may have errors because of the presence of the observation tower trail, in this section different ways to estimate the slope are considered. A map with the stations around SL Tree Island is shown on Figure A-52. The current interpolation method uses a triangle that contains SL with vertices NP-201, NP-202 and G-620 to find the stage and the slope at SL. However, one could try the slopes obtained from other triangles as described in Table A-30.

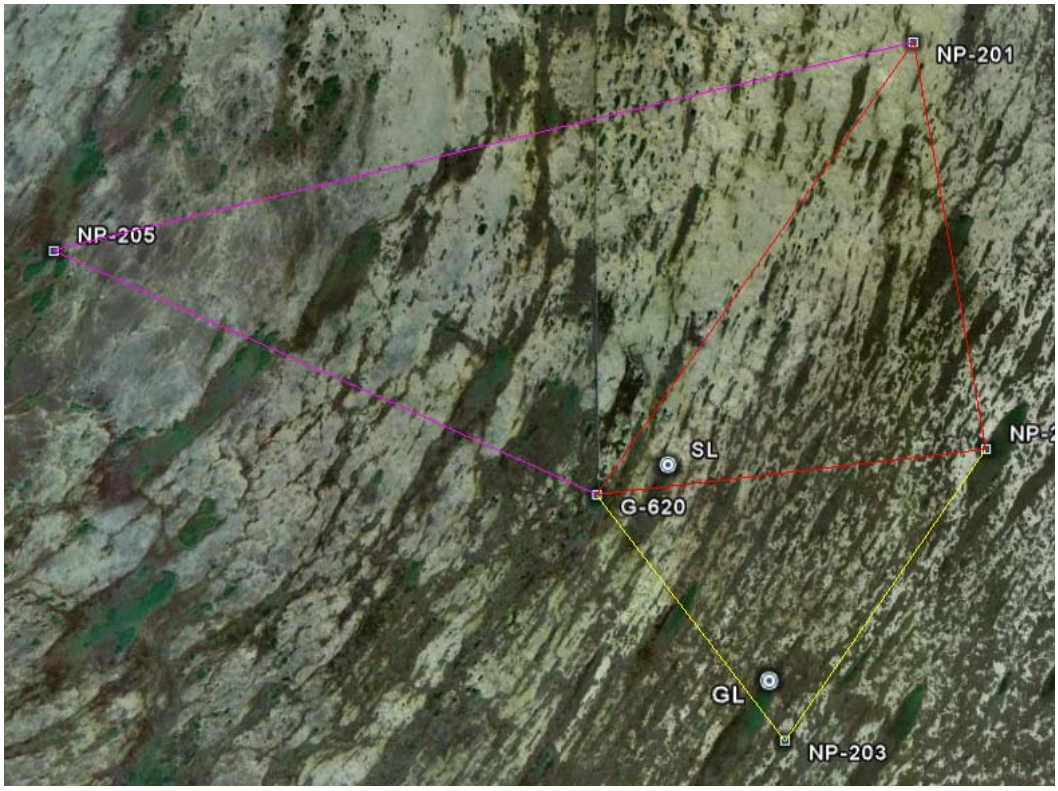

Figure A-52. Google Earth view of the sites where the stages are interpolated to find the slope.

Case	Stations forming vertices of triangle
S12	NP-201, NP-202,G-620
S15	NP-201, NP-205, G-620
S23	NP-202, NP-203, G-620

Table A-30. Stations used to obtain the slope at SL for different cases.

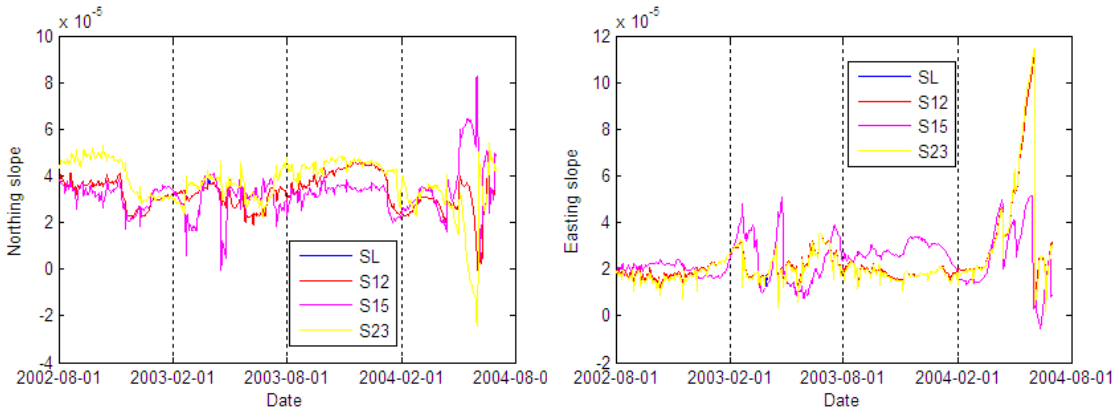

Figure A-53. Slopes obtained from different stations close to SL tree island.

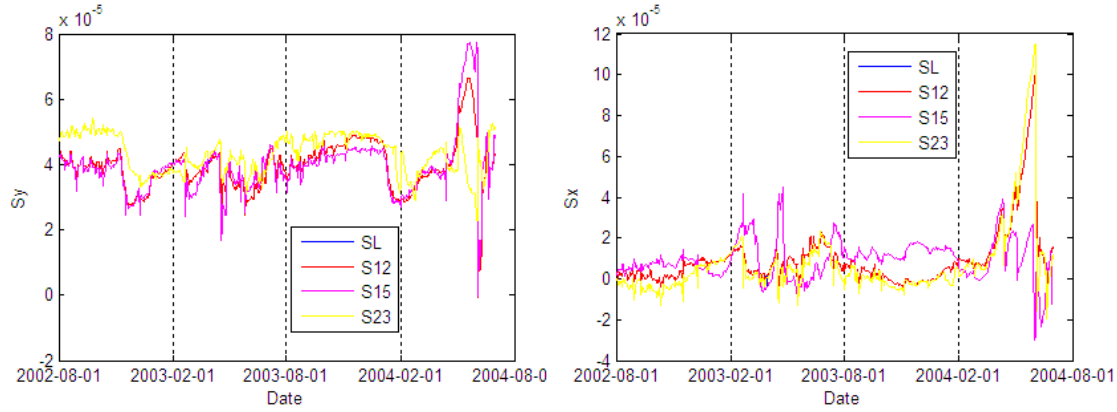

Figure A-54. Slopes from Figure A-53 now in the rotated coordinate system of SL tree island.

The slopes obtained from the previous interpolation method and from the stations listed in Table A-30 are shown in Figure A-53 and Figure A-54. There is a perfect match between the previous estimated slope and the one in the case S12, as expected.

The slopes for the tree cases listed Table A-30 were used to modify case M4 from section 4.1.4 by creating new input boundary condition files (FHB). The results for the different slopes are shown in Figure A-55. The different slopes do not introduce appreciable changes in the water depth, as they are so low and it is considered the same mean water stage in the area. In the case of the predicted surface water velocity, there are only small variations among the predicted values, which is an evidence of the robustness of the interpolation method and the accuracy of stage time series data used. The fact that the use of the stage at stations located several kilometers toward the west (NP-205), the north (NP-201), the east (NP-202) or the south (NP203) to determine the slope at Satinleaf does not produce too different results, support the hypothesis that the

observation tower trail has only a minor effect on the regional surface water slope of the area. The reason why in Figure A-55 the model underpredicts the velocities at Satinleaf station when the water level is higher may be explained from differences between the average vegetation resistance considered by the model at the simulation cell and the resistance just at the station point. There may be deviations also due to the lack of validity of Manning equation.

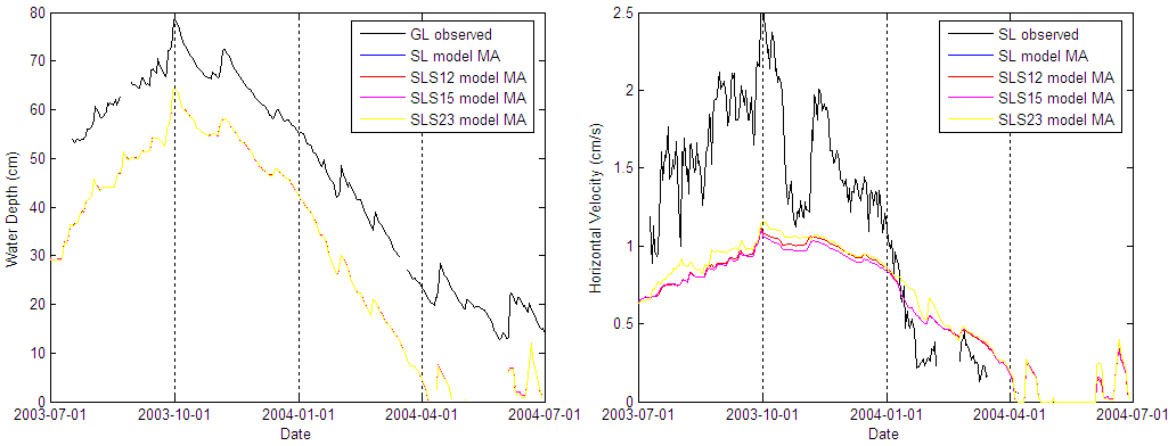

Figure A-55. Model results of water depth and overland horizontal velocity in SL for different slopes compared to the continuous measurements from stations.

A4.1.4 Manning Equation Validity

There is an apparent similarity between the dependence of the Manning coefficient on velocity from the model in Figure A-56 and the one reported by Jenter [1996] in Figure A-19.

Figure A-57 shows the dependence of measured velocity on the slope estimated from the model, as with the flume data in Figure A-20. However, in this case the correlation between the velocity and the slope is not so clear. The slopes around tree islands are in a narrow range compared to the range of the two orders of magnitude reached in the flume experiments. Moreover, for the same slope, there may be variations in the vegetation resistance that may produce deviations, particularly in the transect points in Figure A-57.

In addition to this, the field velocity is correlated to the water depth as shown in Figure A-58, particularly at the stations located in marsh areas. This seems to be in agreement with a Manning type equation (at least for marsh areas) and in contradiction to

the Forchheimer one followed by the Jenter [1996] data in Figure A-20. Likely, a Manning type equation would rule in the less dense vegetated areas and a Forchheimer type in the more dense ones (like TS), with a transition zone. Curiously, in a more recent paper by Lee et al. [2004] about those experiments, those authors include also field measurements and they proposed a new velocity correlation, which depends on water depth and does not fit the original data of Jenter [1996].

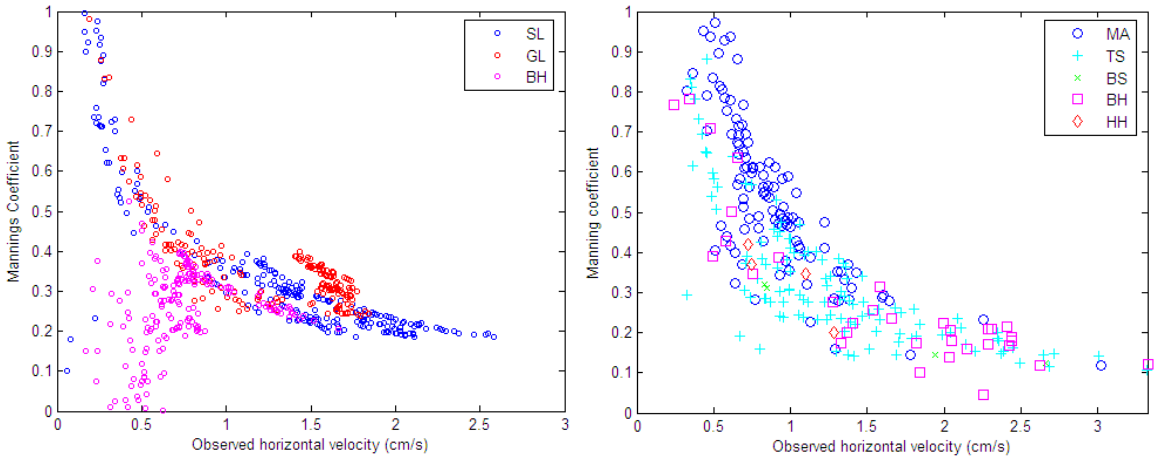

Figure A-56. Estimated Manning coefficients in stations and transects as a function of the measured velocity for case M4.

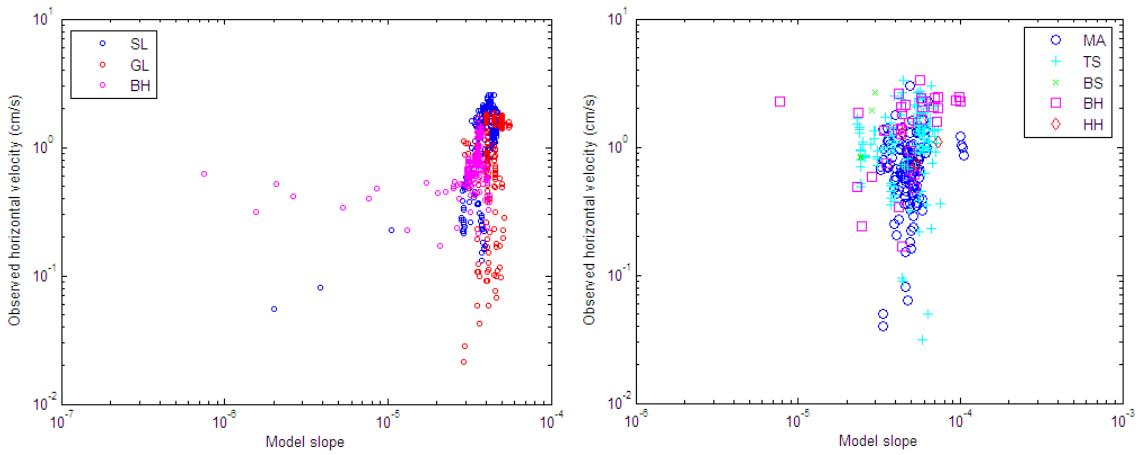

Figure A-57. Measured velocity in stations and transects as a function of the slopes estimated by the model for case M4.

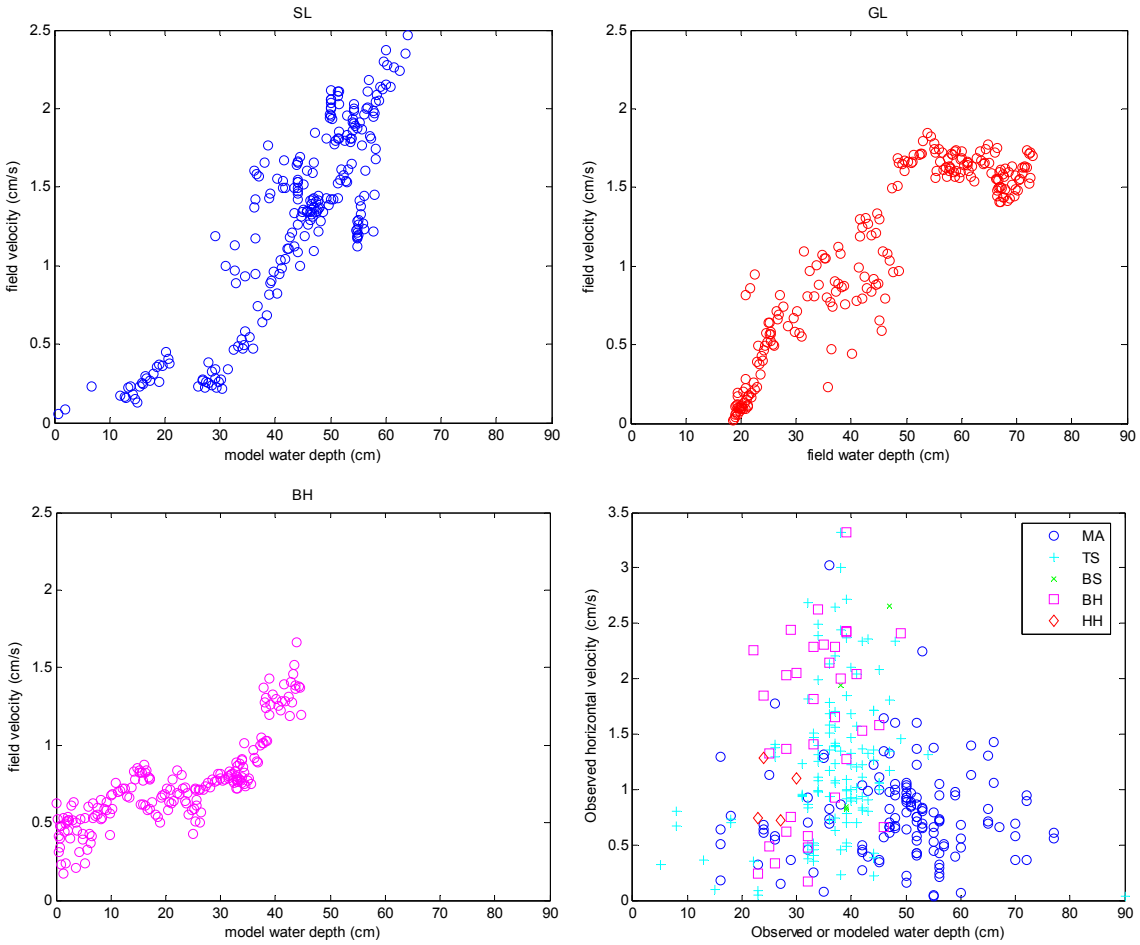

Figure A-58. Measured velocity in stations and transects as a function of the water depth observed or modeled for case M4.

A4.2 Ground-water Parameter Calibration

In this section, additional details about the ground-water parameters calibration from water table measurements are described.

A4.2.1 Available Data and Model Setup. Additional Figures

The additional figures to section 4.3.2 are presented below.

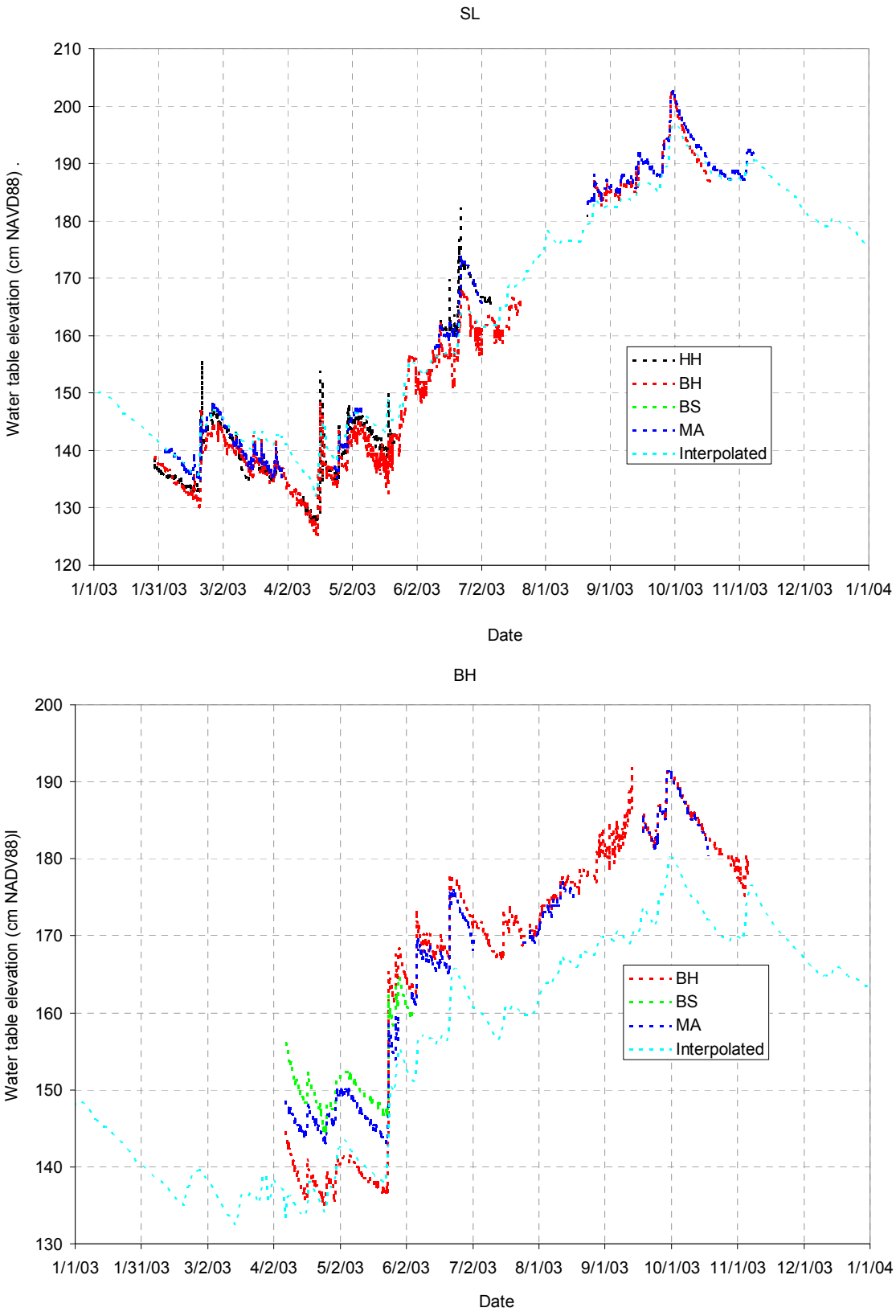

Figure A-59. Available water table elevation data at tree island wells for year 2003, compared to the interpolated stage from neighbor stations.

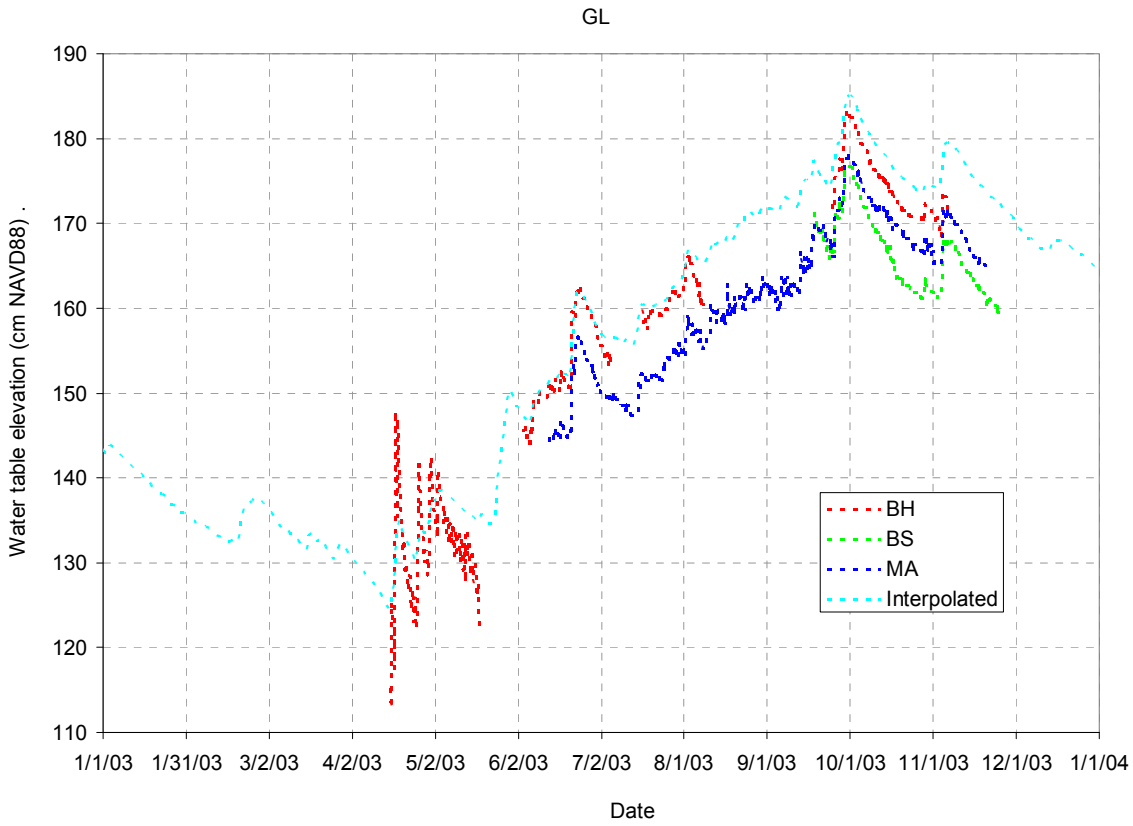

Figure A-59. Available water table elevation data at tree island wells for year 2003, compared to the interpolated stage from neighbor stations. Continuation.

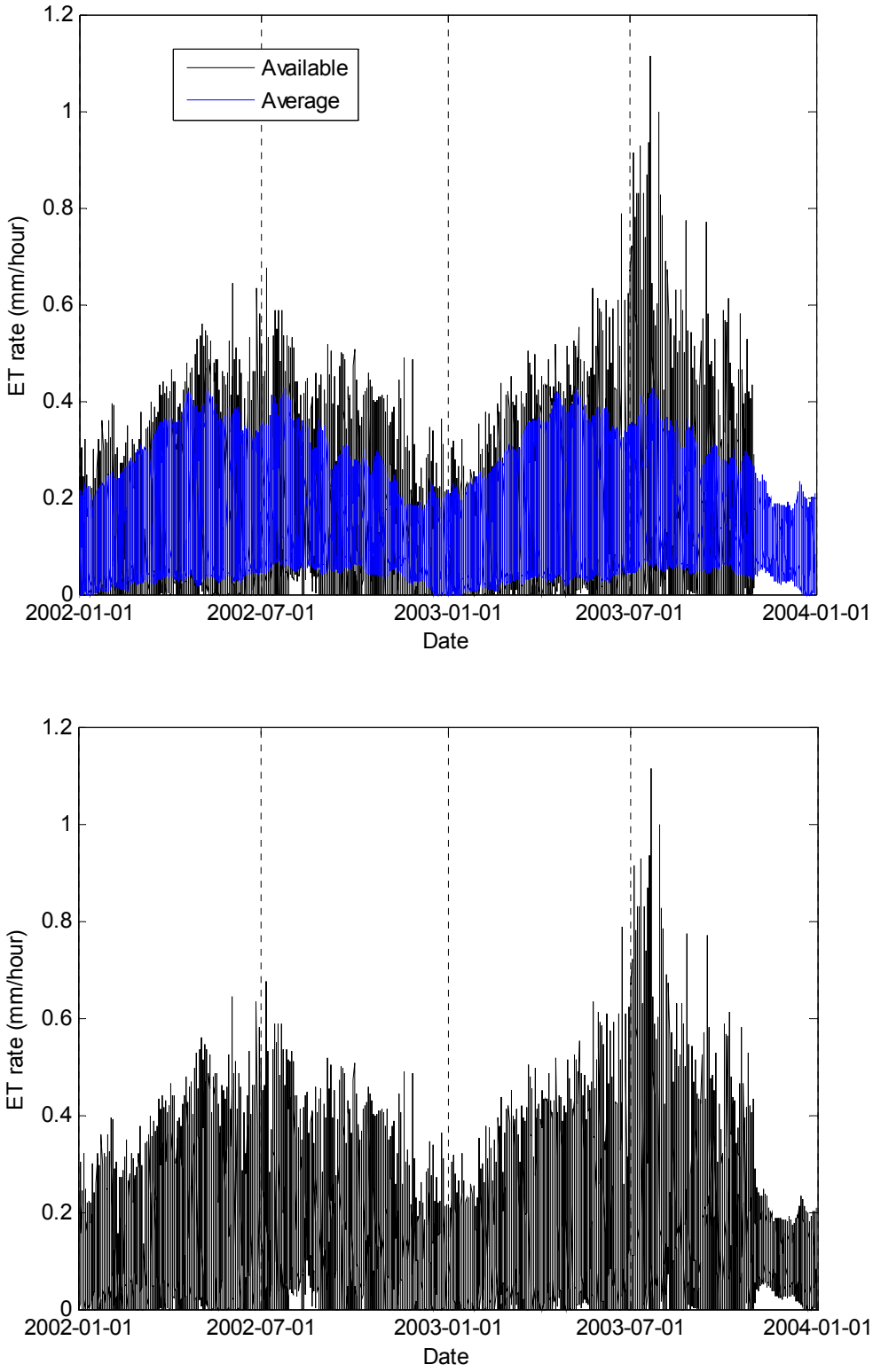

Figure A-60. ET hourly rates for years 2002 and 2003. Above, the available measured rates and the averaged ones. In the second graph, the composite curve assumed by substituting the missing measured rates with the averaged ones (gap filling).

A4.2.2 Correction of the Measured Water Table Elevations

The corrected water table elevation (H_c) was computed by using the measured value (H), the elevation of the piezoresistor (H_p), an offset value (H_0) and a temperature correction factor (α), which was estimated in the lab as -0.3 cm/^{o}C [Ross et al., 2004], and T is the water temperature.

$$H_c = \left(H - H_p\right)\left(1 + \alpha\left(T - 20^0 C\right)\right) + H_p + H_0 . \quad (97)$$

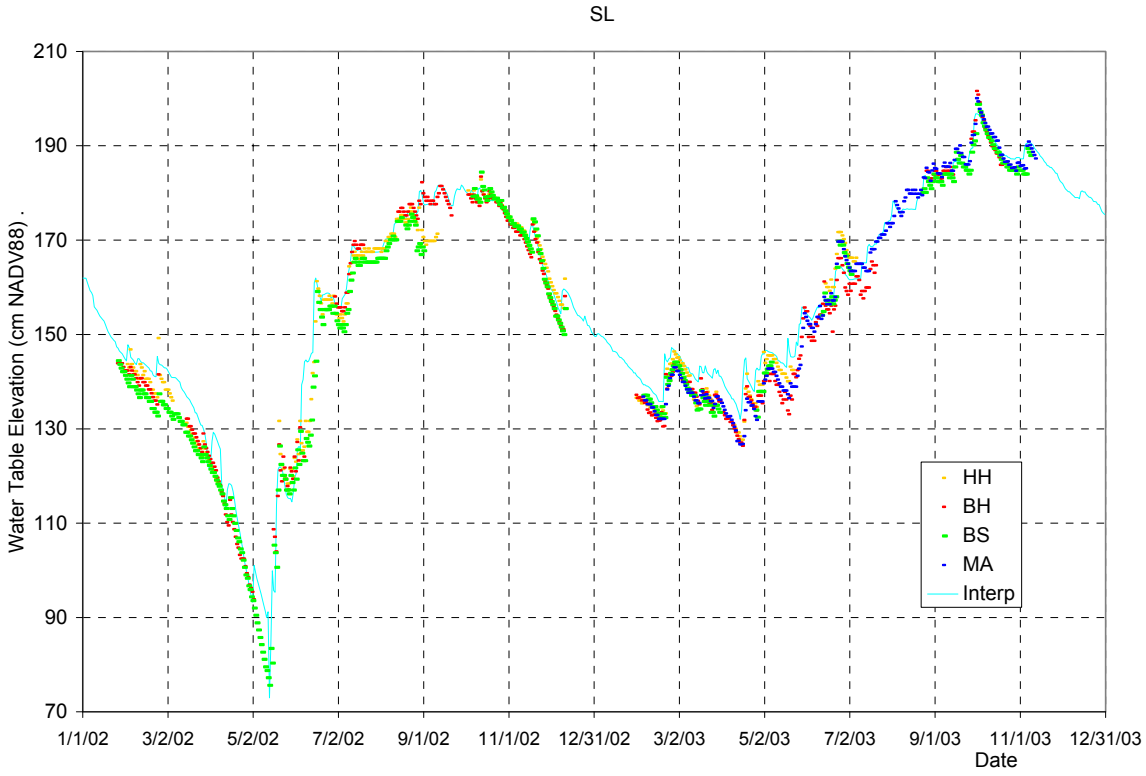

Figure A-61. Corrected water table elevation measured at 6 AM in tree island wells compared to the interpolated stage.

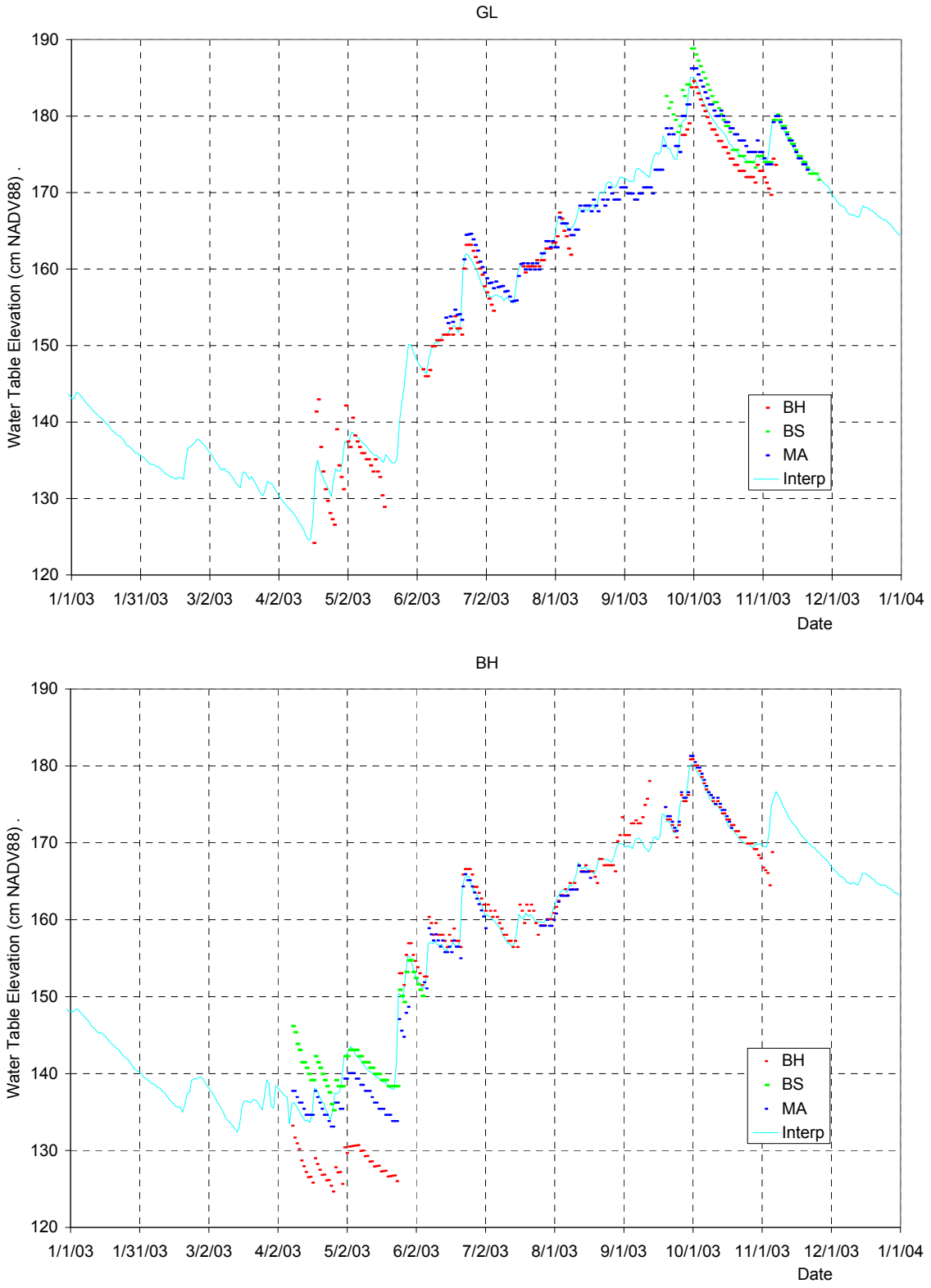

Figure A-61. Corrected water table elevation measured at 6 AM in tree island wells compared to the interpolated stage. Continuation.

The water temperature in wells is assumed equal to the data measured at the bottom of the surface water by German [2000]. The elevation of the piezoresistors is known and was changed occasionally. Thus, parameters α and H_0 were fitted in the following way. A daily water table elevation data was constructed by taking well measurements at 6AM. At that time, the water table elevation is partially recovered from diurnal transpiration during previous daytime (as shown in Figure 55) and it is assumed that the elevation among wells should match at least during the period with high water table elevation values. Then, for the days where the interpolated well stage data is not less than 30 cm from its maximum value for each tree island, the difference between the 6AM well values and the daily interpolated well stage data is computed. The fitting of a different offset H_0 for each well and a common factor α requires that the average of the median values of the absolute differences is a minimum.

Surprisingly, the fitted value of α obtained from this procedure was negligible (in the order of 10^{-7}), which means that the field measurements in the period with highest water elevation are not correlated to the temperature data reported by German. The obtained offset values H_0 are presented in the last column in Table 23. Notice that they are in the range of ± 10 cm. The matching between the water table elevation data and the interpolated stage improves by adding the fitted offset, as shown in Figure A-61.

A4.2.3 Results for the Best Fitted Manning Coefficients. Additional Figures

Additional plots of water table level and soil saturation obtained for the case K0 are presented below.

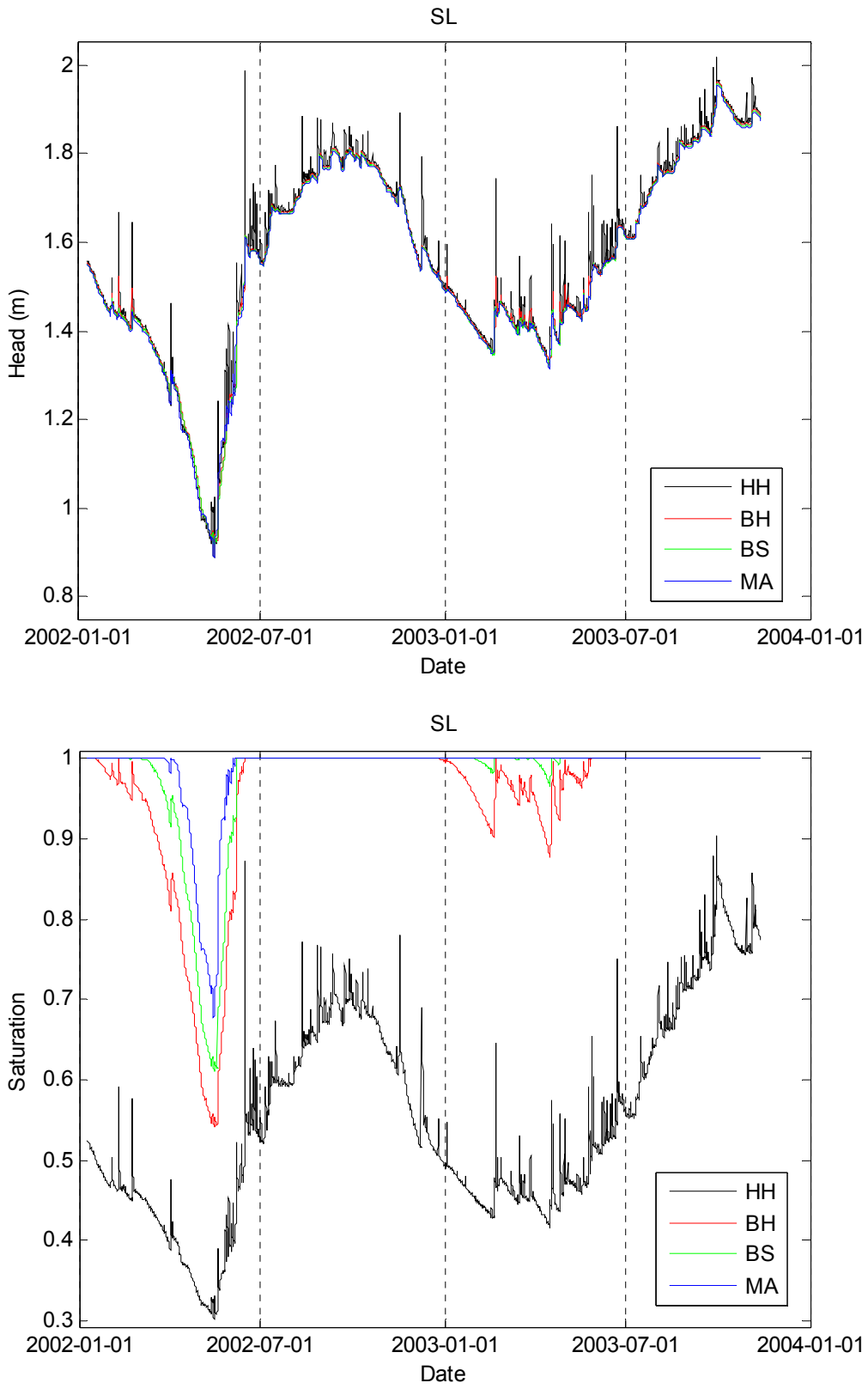

Figure A-62. Water table level and soil saturation obtained from the model for Satinleaf wells for the case K0.

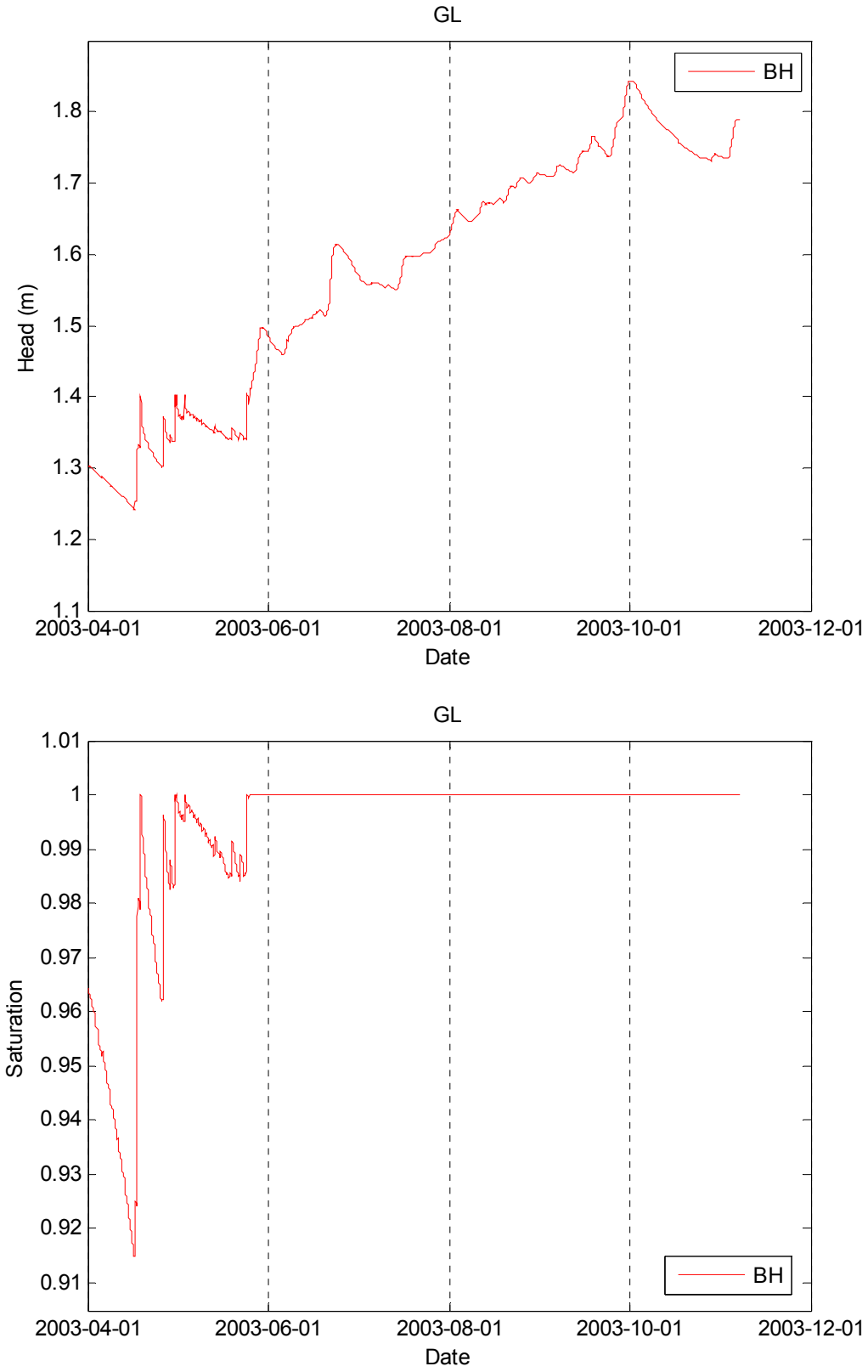

Figure A-63. Water table level and soil saturation obtained from the model for Gumbo Limbo wells for the case K0.

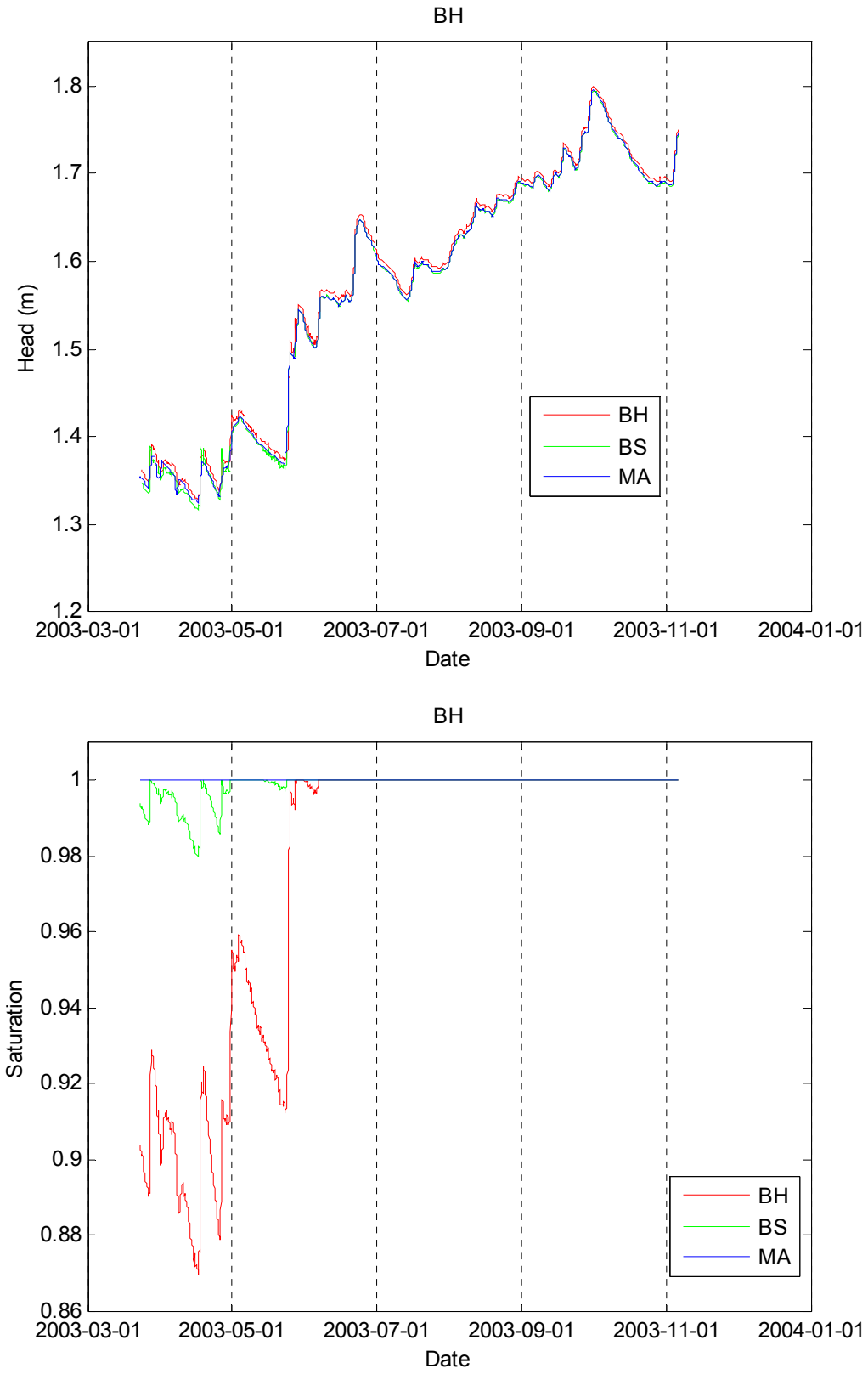

Figure A-64. Water table level and soil saturation obtained from the model for Black Hammock wells for the case K0.

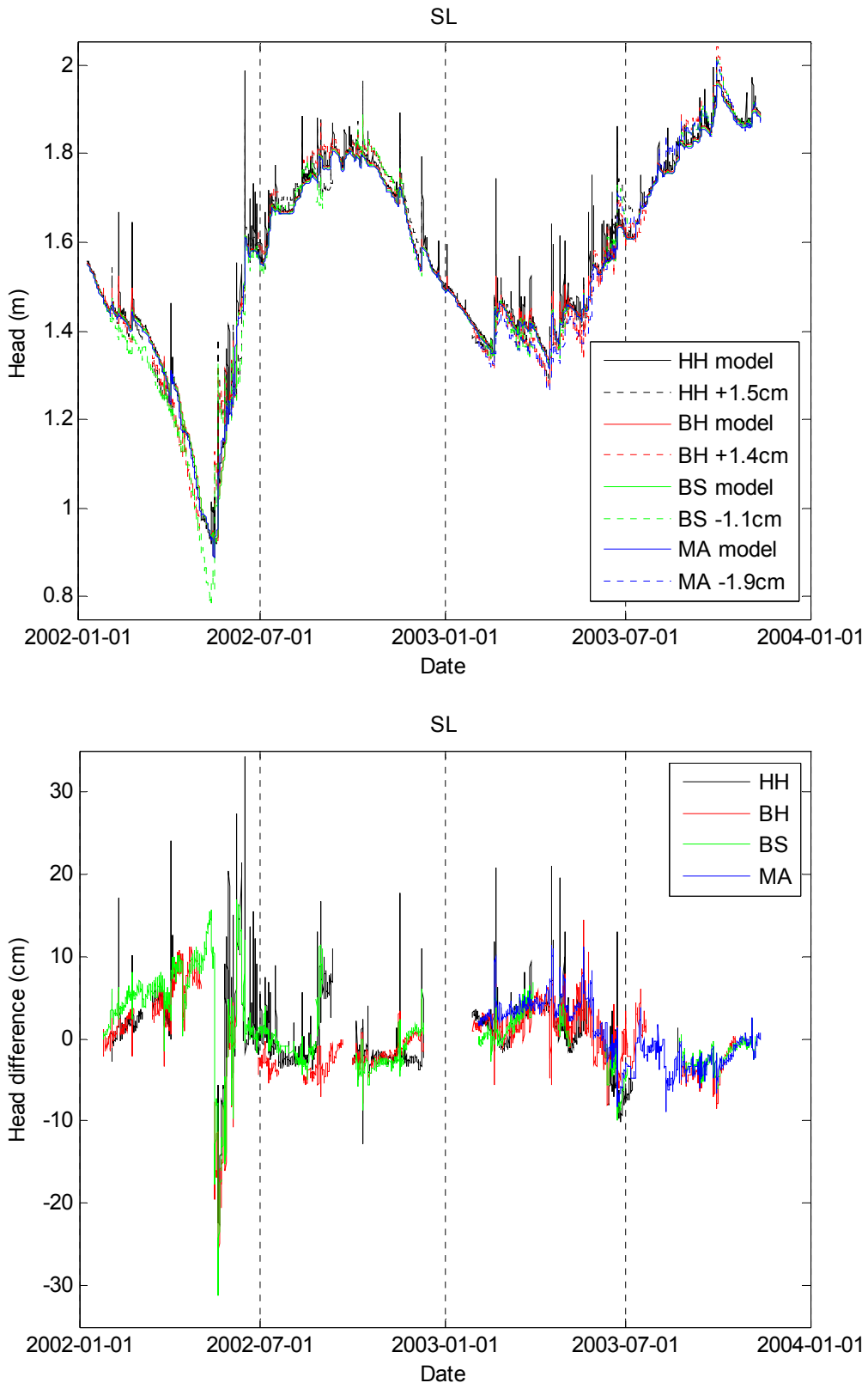

Figure A-65. Comparison between the water table levels obtained from the model and from the field measurements in SL wells for the case K0.

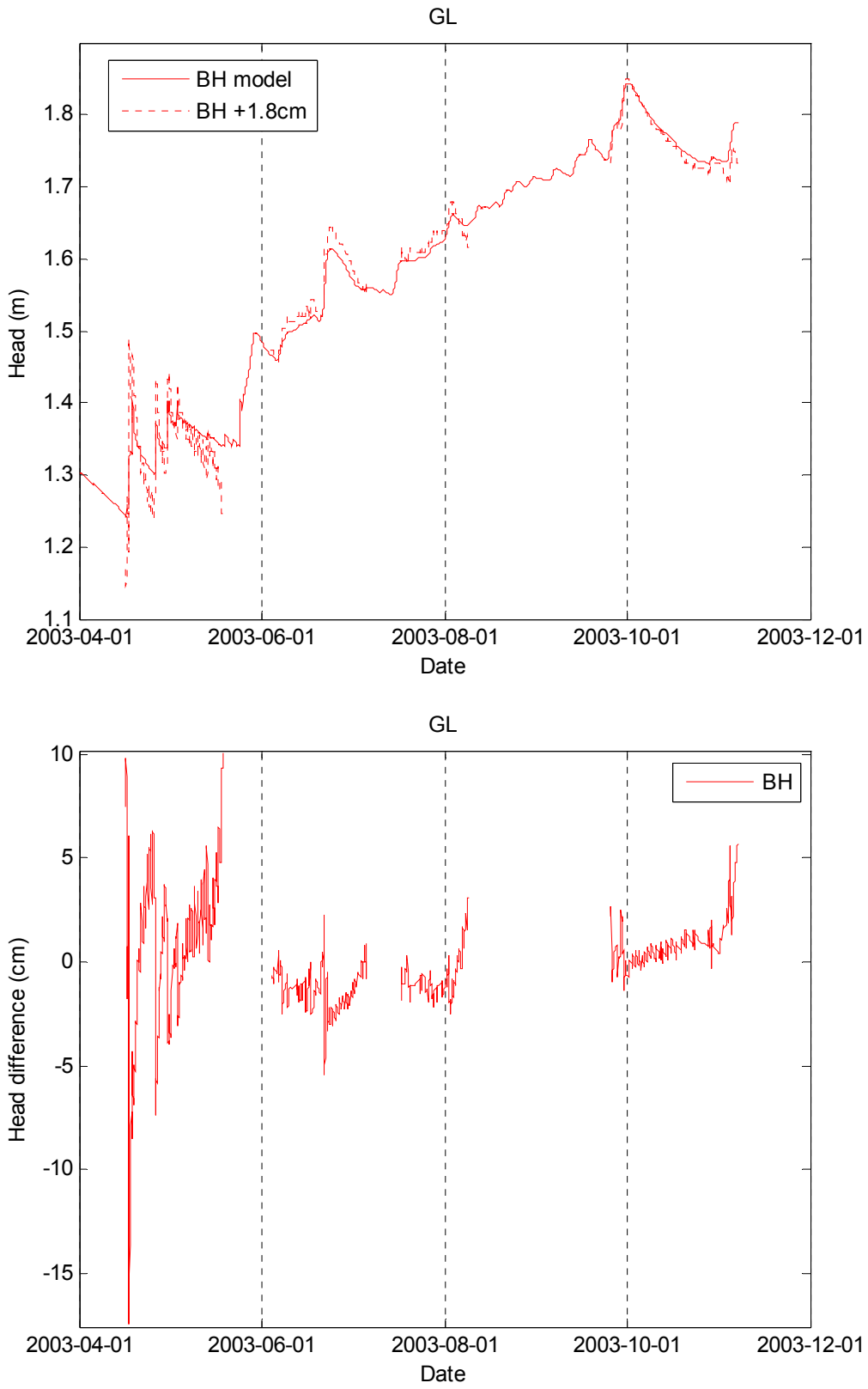

Figure A-66. Comparison between the water table levels obtained from the model and from the field measurements in GL wells for the case K0.

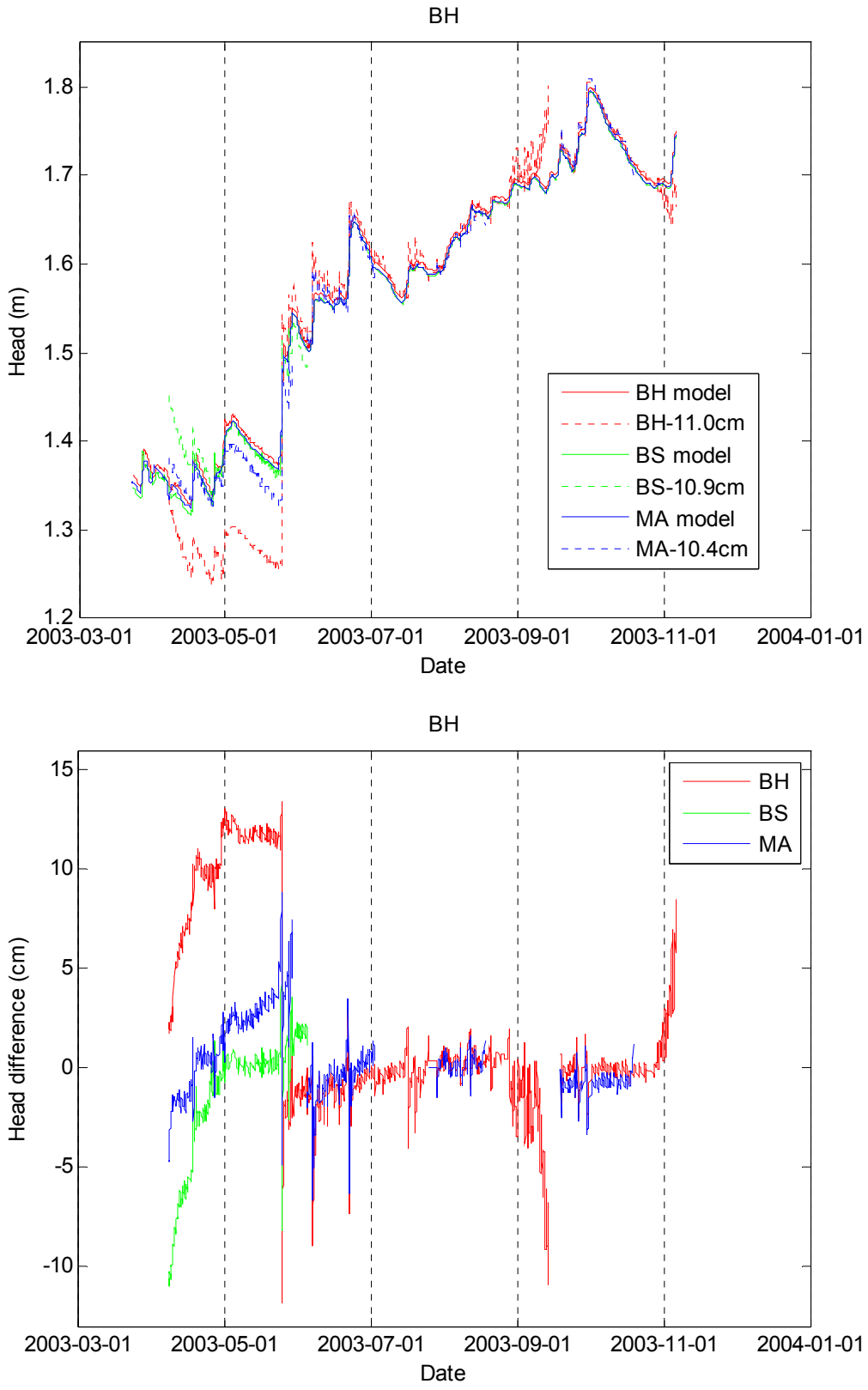

Figure A-67. Comparison between the water table levels obtained from the model and from the field measurements in BH wells for the case K0.

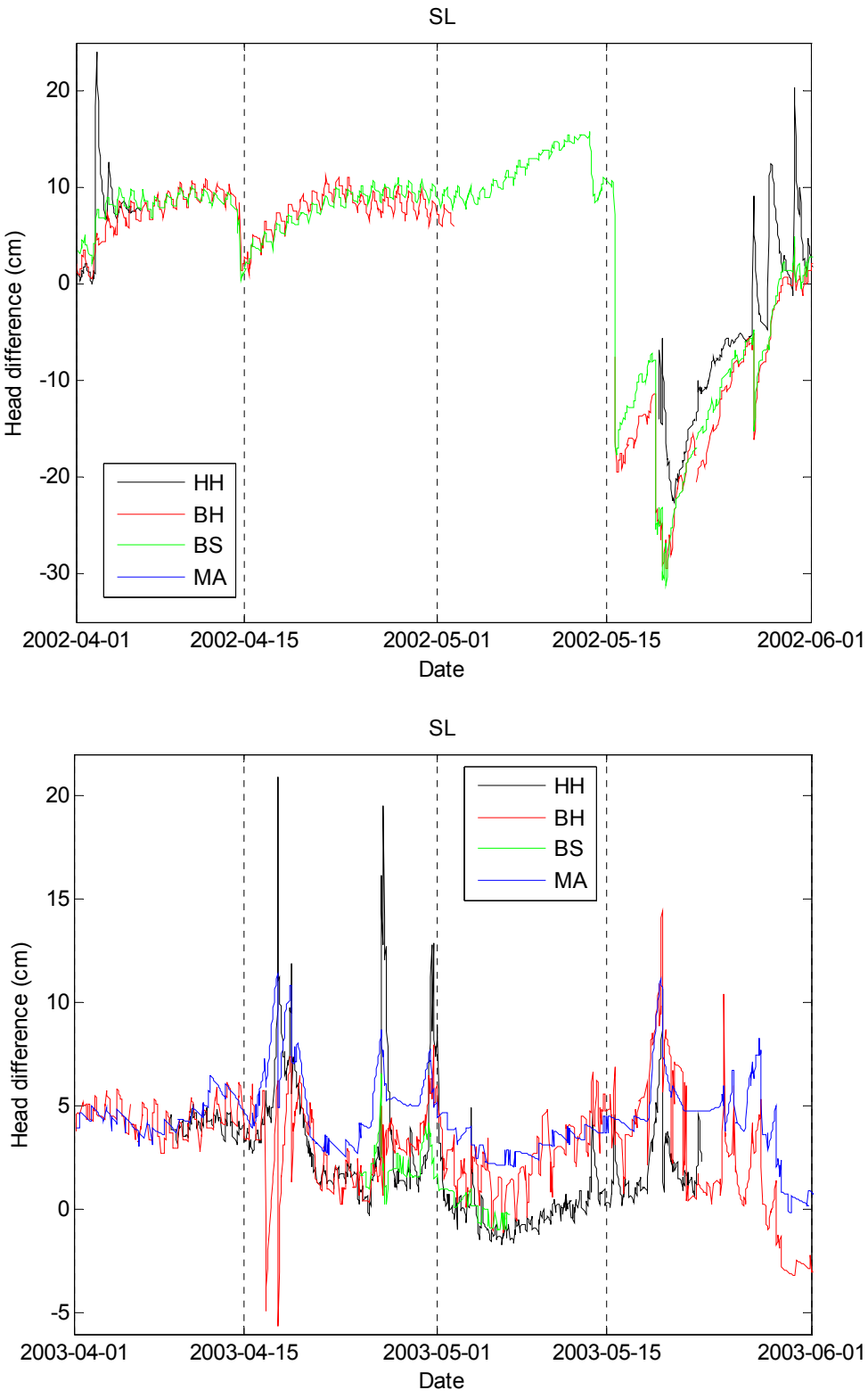

Figure A-68. Difference between the water table levels obtained from the model and from the field measurements in SL wells for the case K0 during the driest period of 2002 and 2003. These are magnified views of Figure A-65.

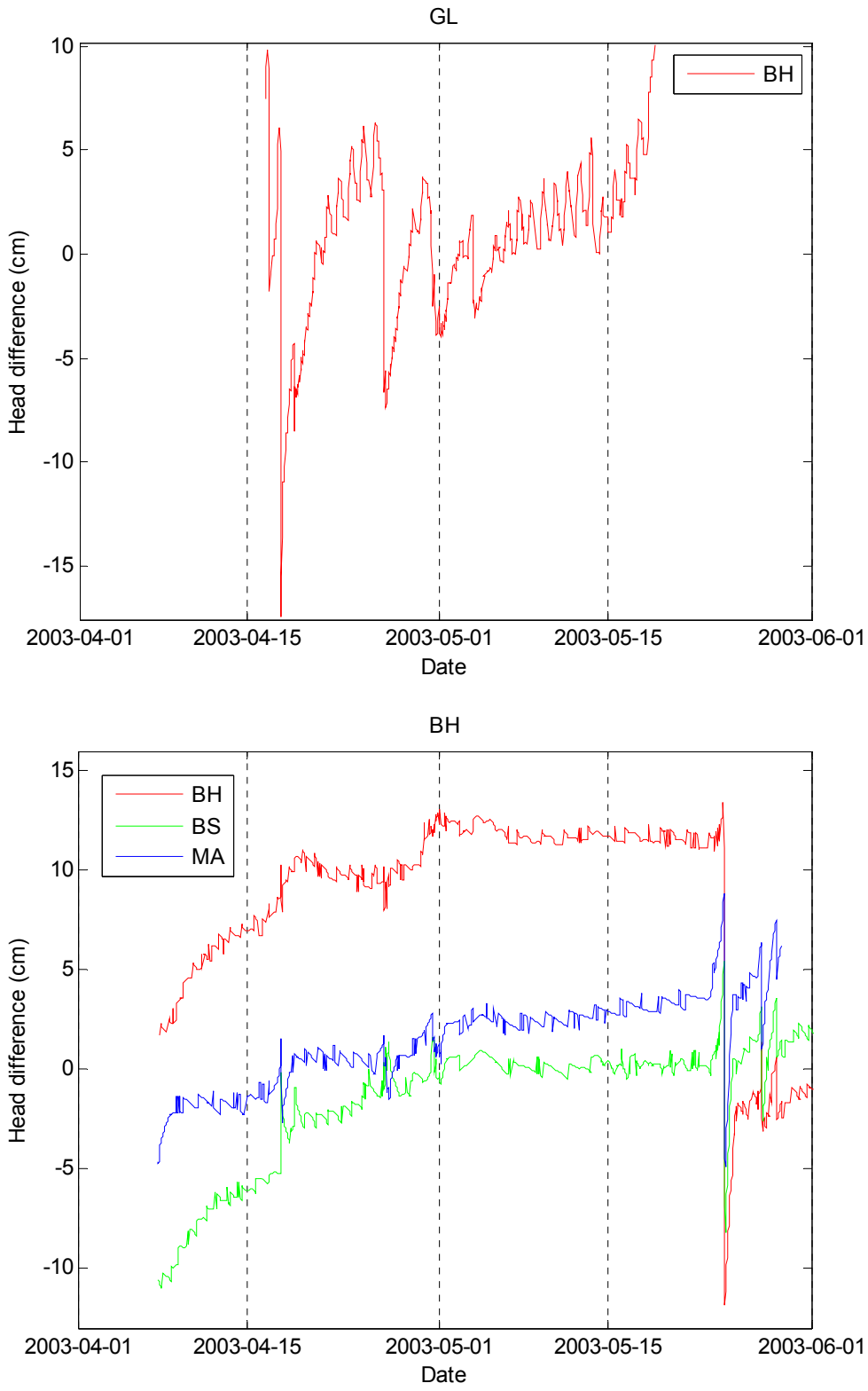

Figure A-69. Difference between the water table levels obtained from the model and from the field measurements in GL and BH wells for the case K0 during the driest period of 2003. These are magnified views of Figure A-66 and Figure A-67.

A4.2.4 A More Efficient Model. Additional Figures

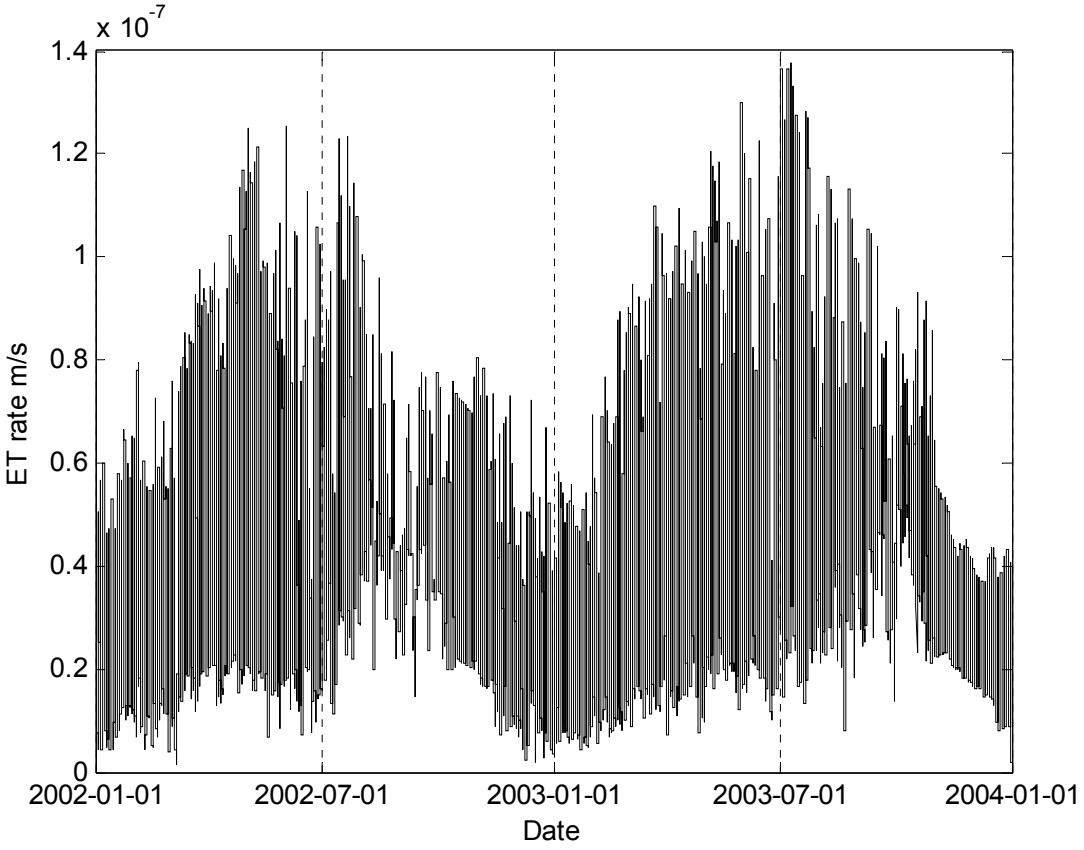

Figure A-70. ET rates corresponding to the case with two stress periods per day, obtained from the hourly rates in Figure A-60.

The results for the case K1 do not differ considerably when comparing Figure A-71, Figure A-72 and Figure A-73 with the corresponding ones for case K0 (Figure A-65). This can be also stated by comparing the head differences for case K1 in Figure A-74, Figure A-75 and Figure A-76 with their corresponding graphs for case K0 from Figure A-65 to Figure A-69.

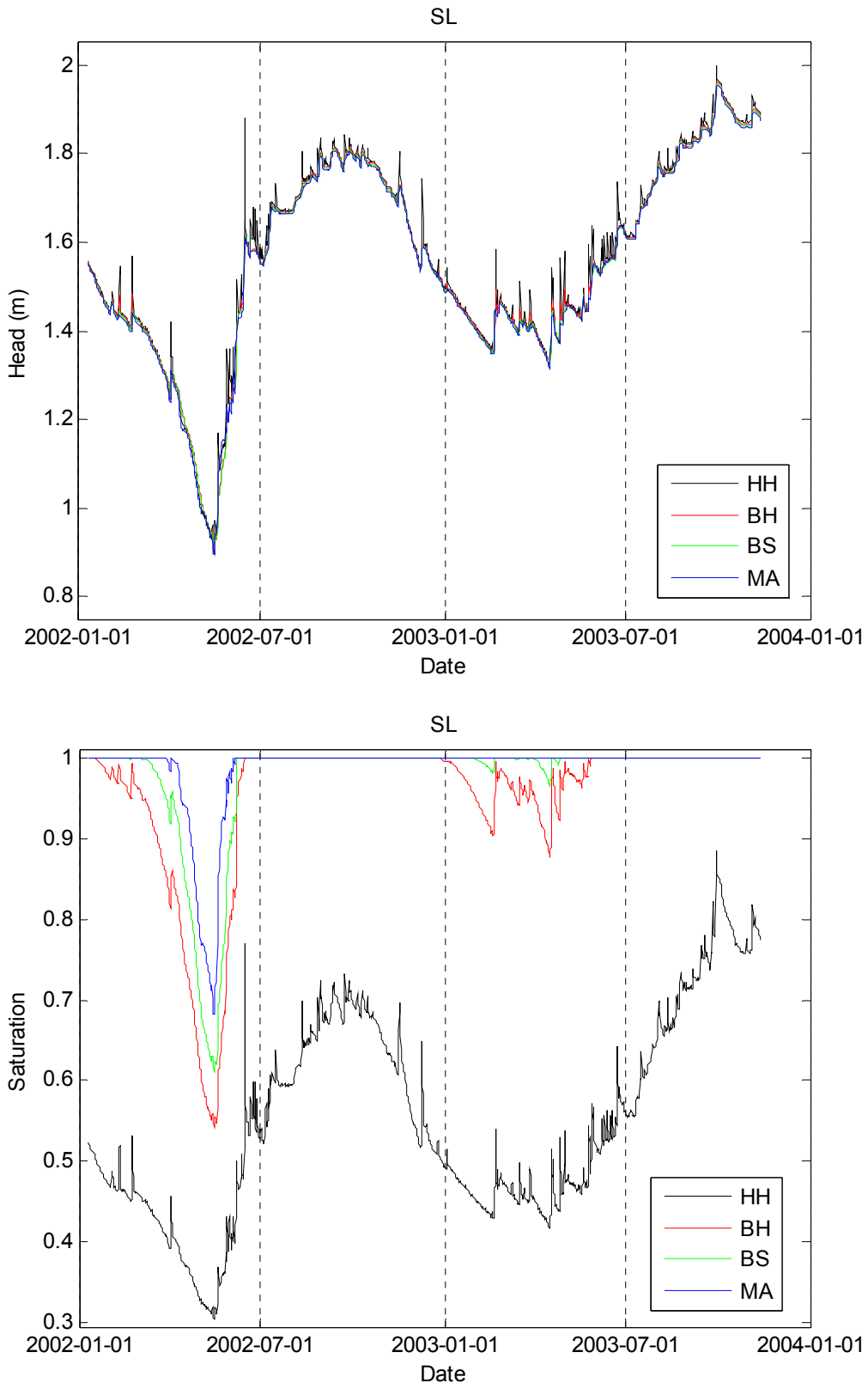

Figure A-71. Water table level and soil saturation obtained from the model for Satinleaf wells for the case K1. It is comparable to Figure A-62 for case K0.

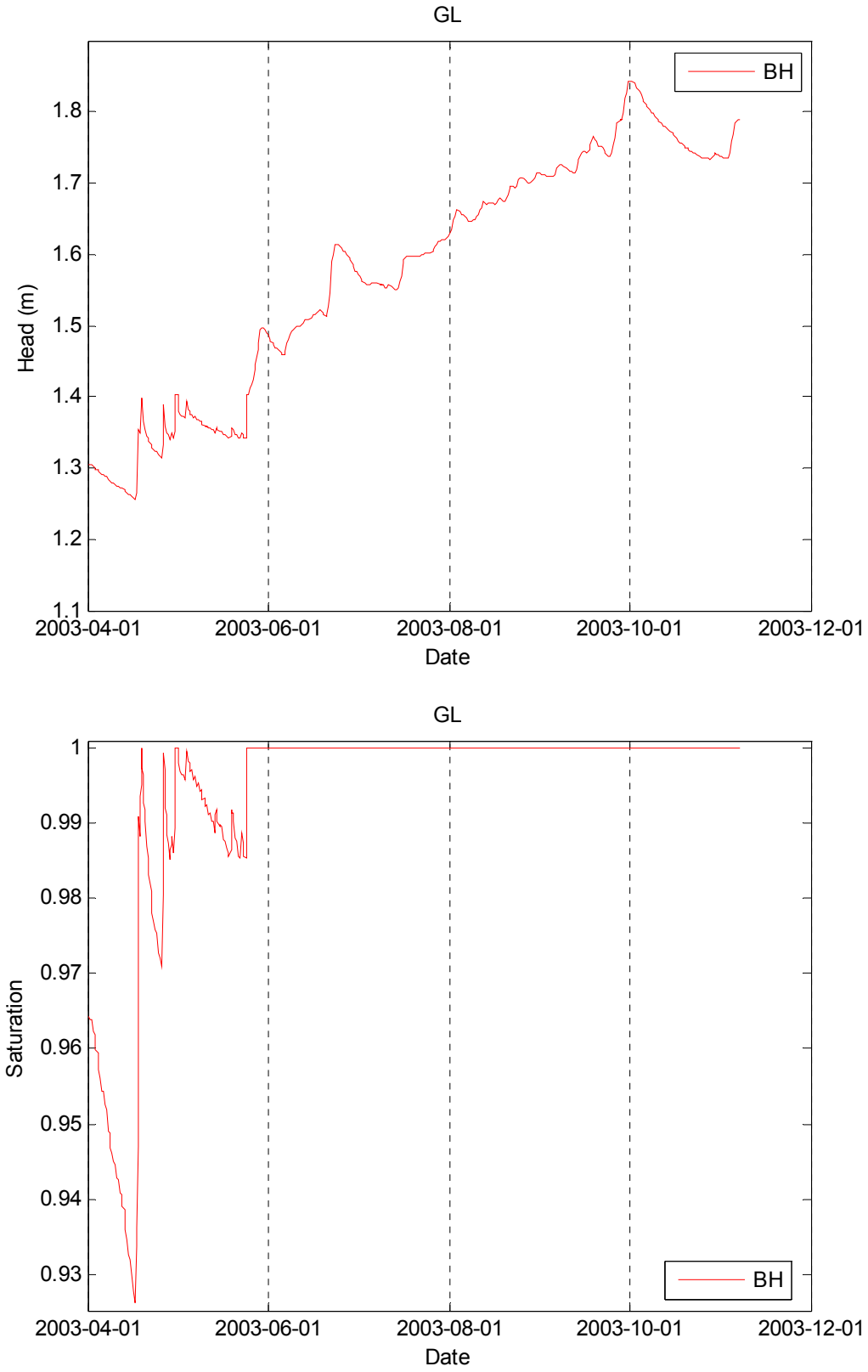

Figure A-72. Water table level and soil saturation obtained from the model for Gumbo Limbo wells for the case K1. It is comparable to Figure A-63 for case K0.

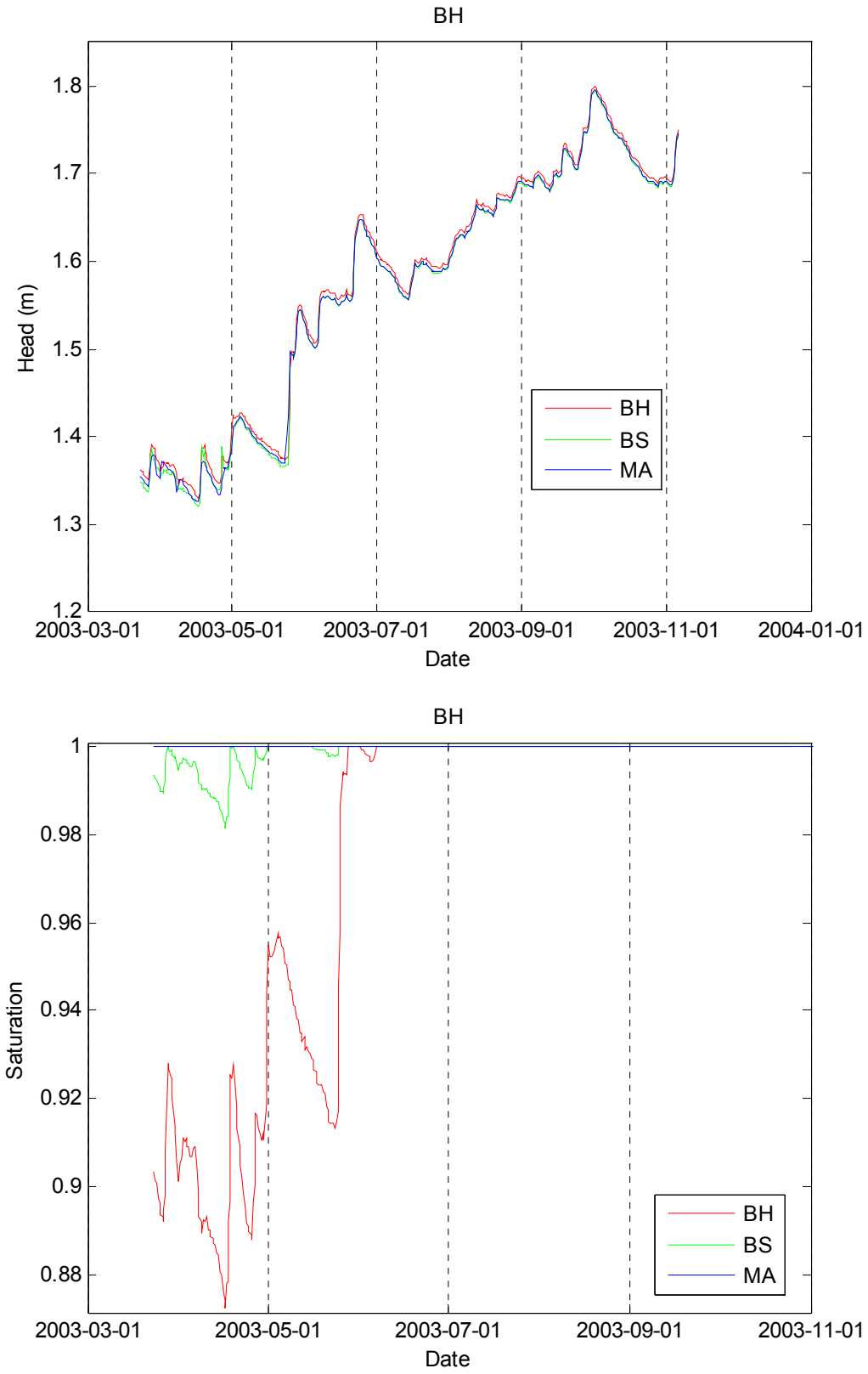

Figure A-73. Water table level and soil saturation obtained from the model for Black Hammock wells for the case K1. It is comparable to Figure A-64 for case K0.

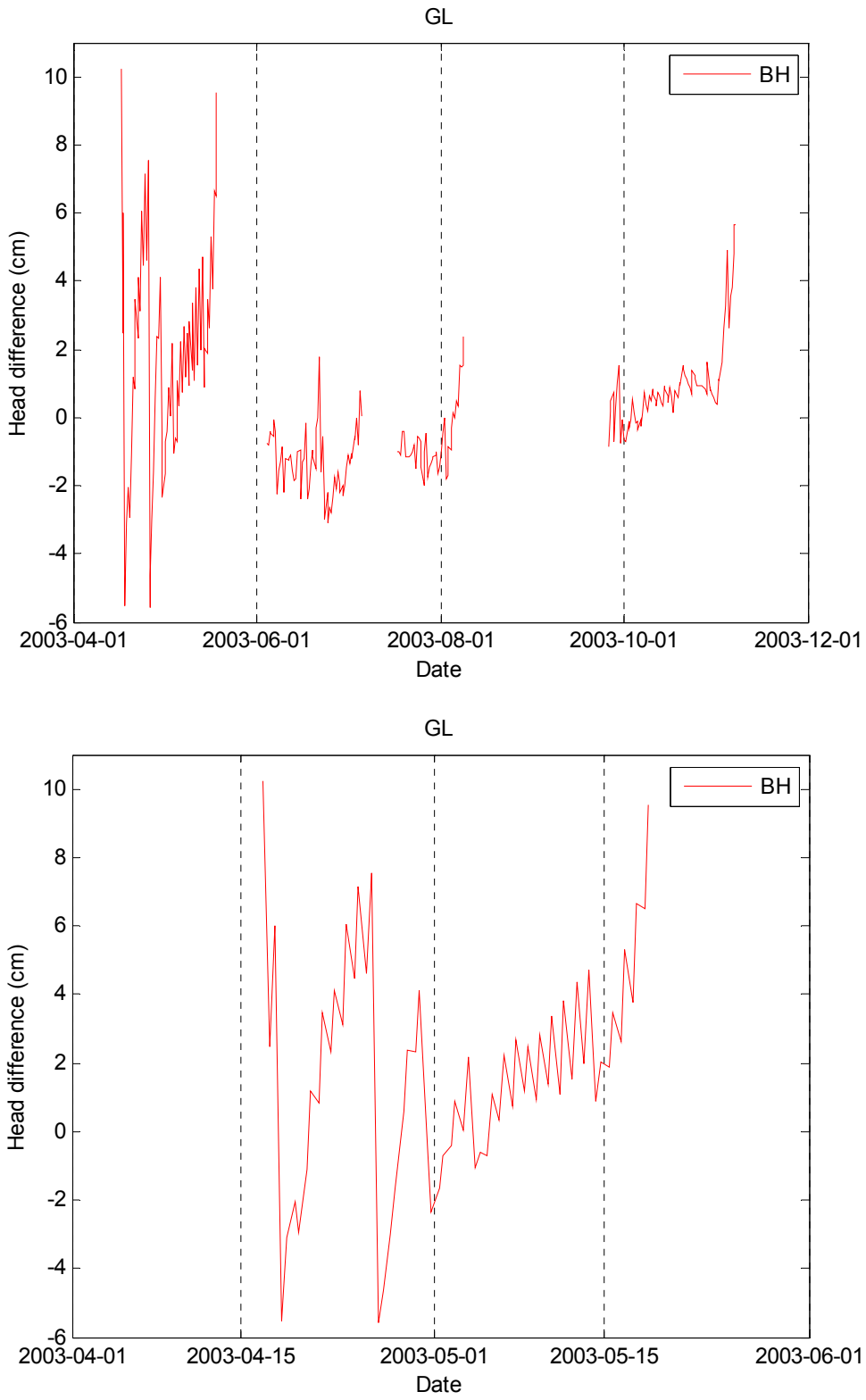

Figure A-74. Difference between the water table levels obtained from the model and from the field measurements in GL wells for the case K1. It is comparable to Figure A-66 and Figure A-69 for case K0.

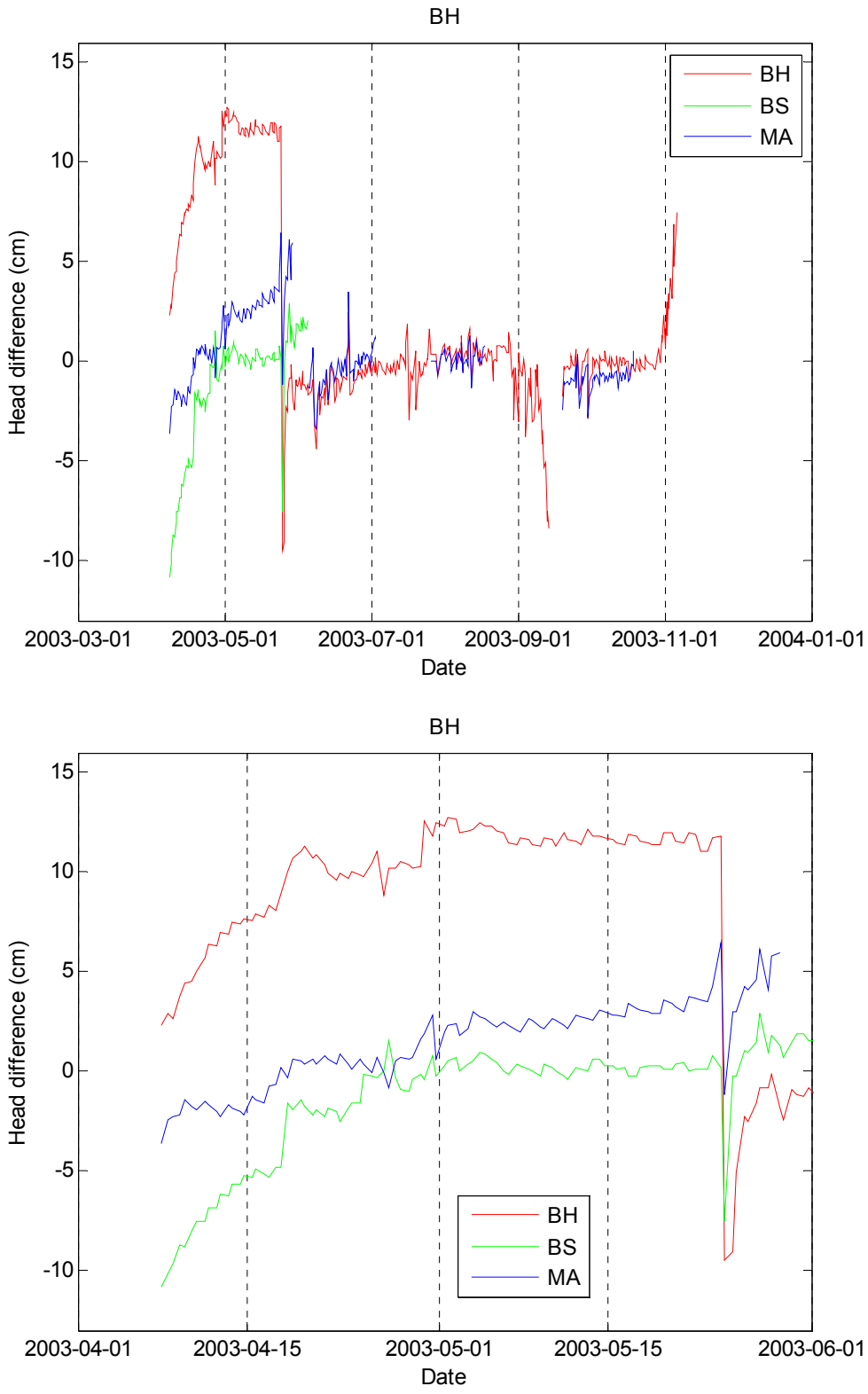

Figure A-75. Difference between the water table levels obtained from the model and from the field measurements in BH wells for the case K1. It is comparable to Figure A-67 and Figure A-69 for case K0.

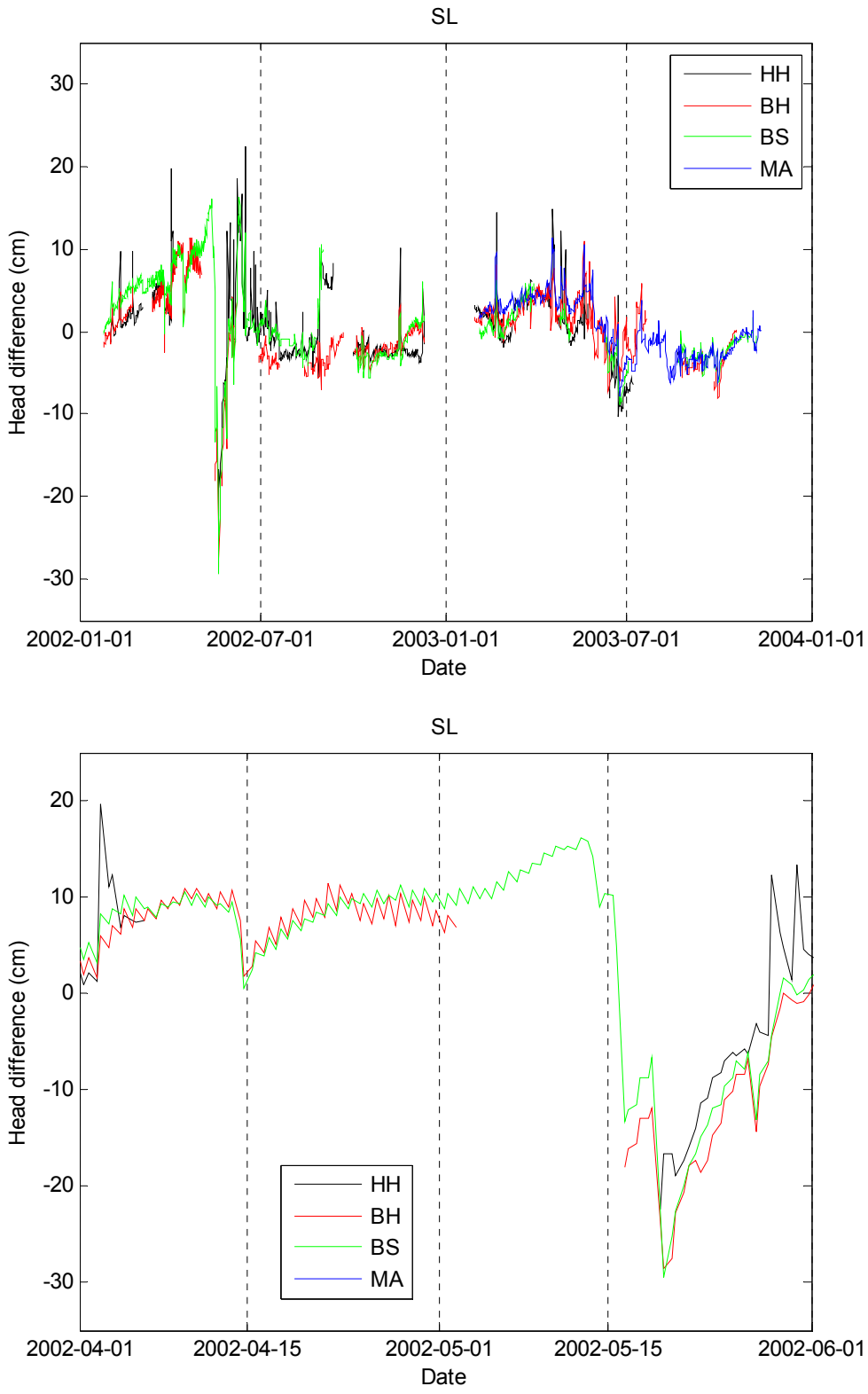

Figure A-76. Difference between the water table levels obtained from the model and from the field measurements in SL wells for the case K1. It is comparable to Figure A-65 and Figure A-68 for case K0.

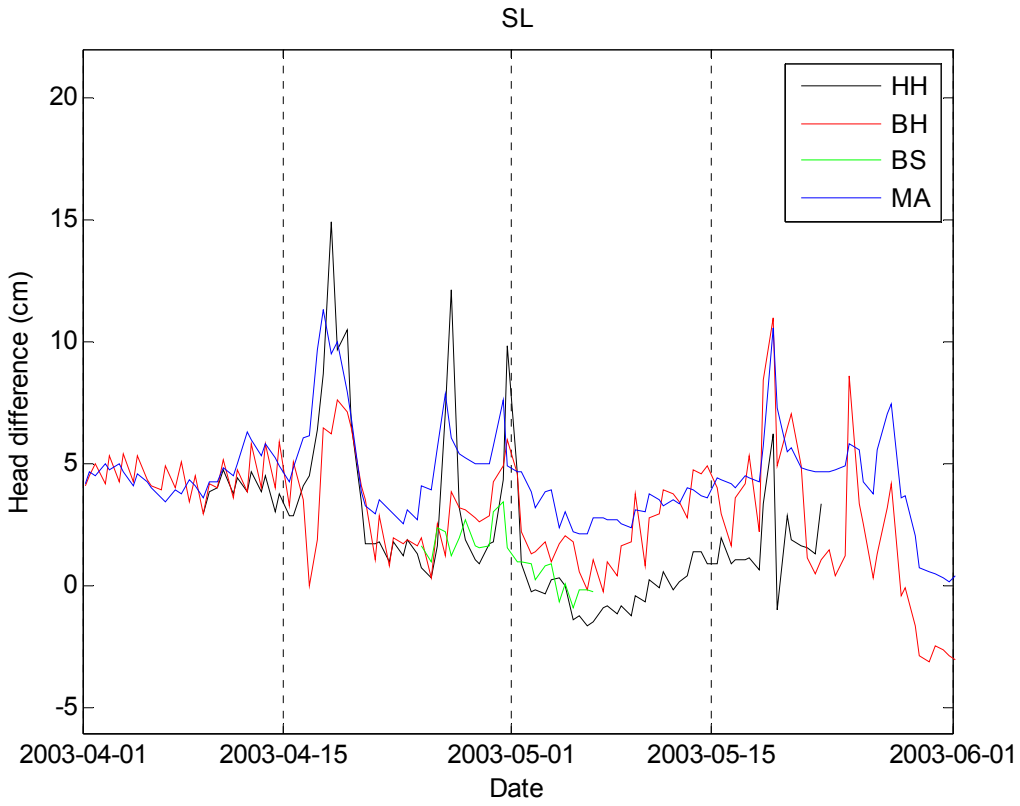

Figure A-76. Difference between the water table levels obtained from the model and from the field measurements in SL wells for the case K1. It is comparable to Figure A-65 and Figure A-68 for case K0. Continuation.

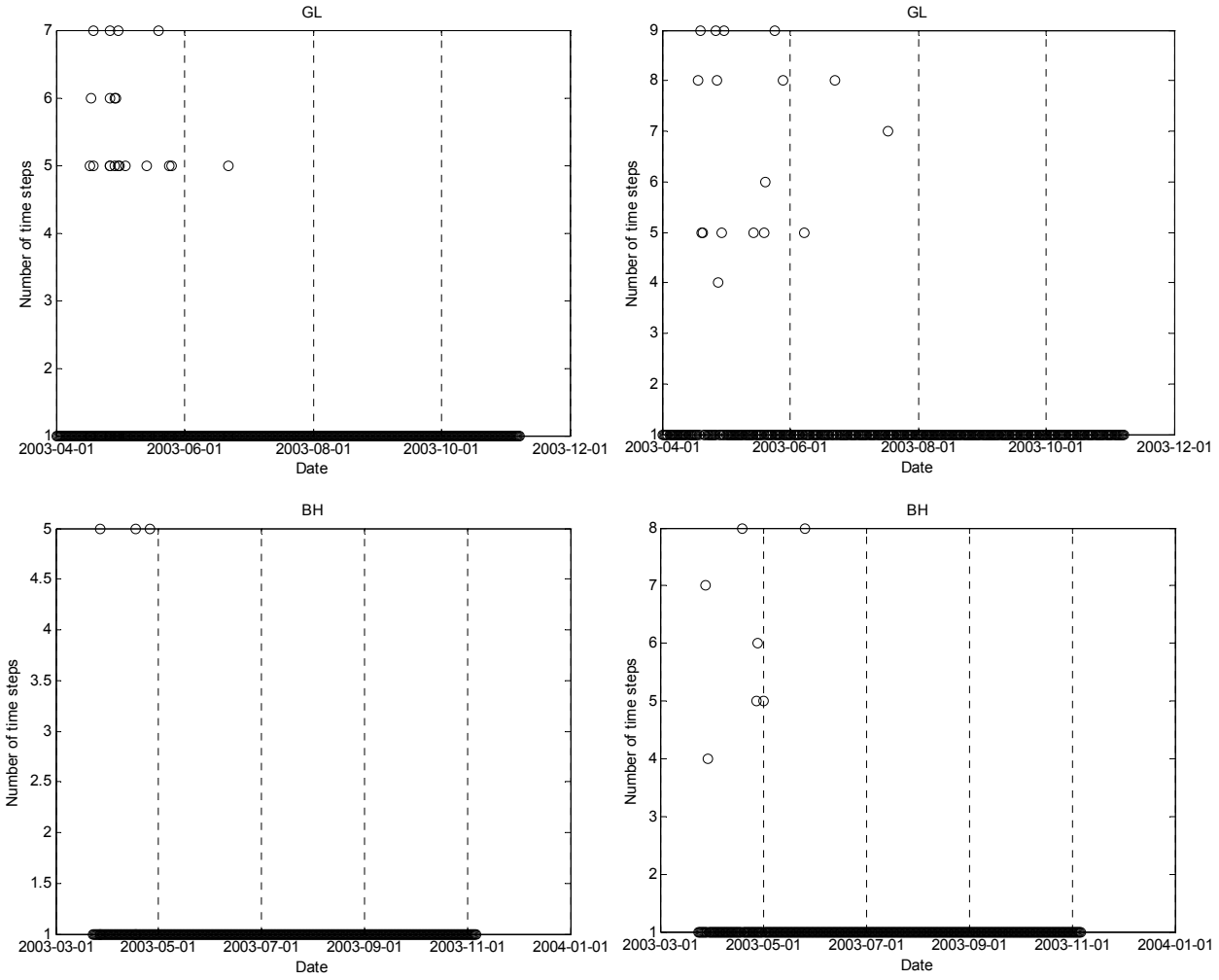

Figure A-77. Number of time steps needed by MODHMS to complete each stress period as a function of time for the cases K0 and K1, in GL and BH tree islands.

A4.2.5 Test Changing OL Leakage. Additional Figures

This section contains additional figures obtained from the model for case K2.

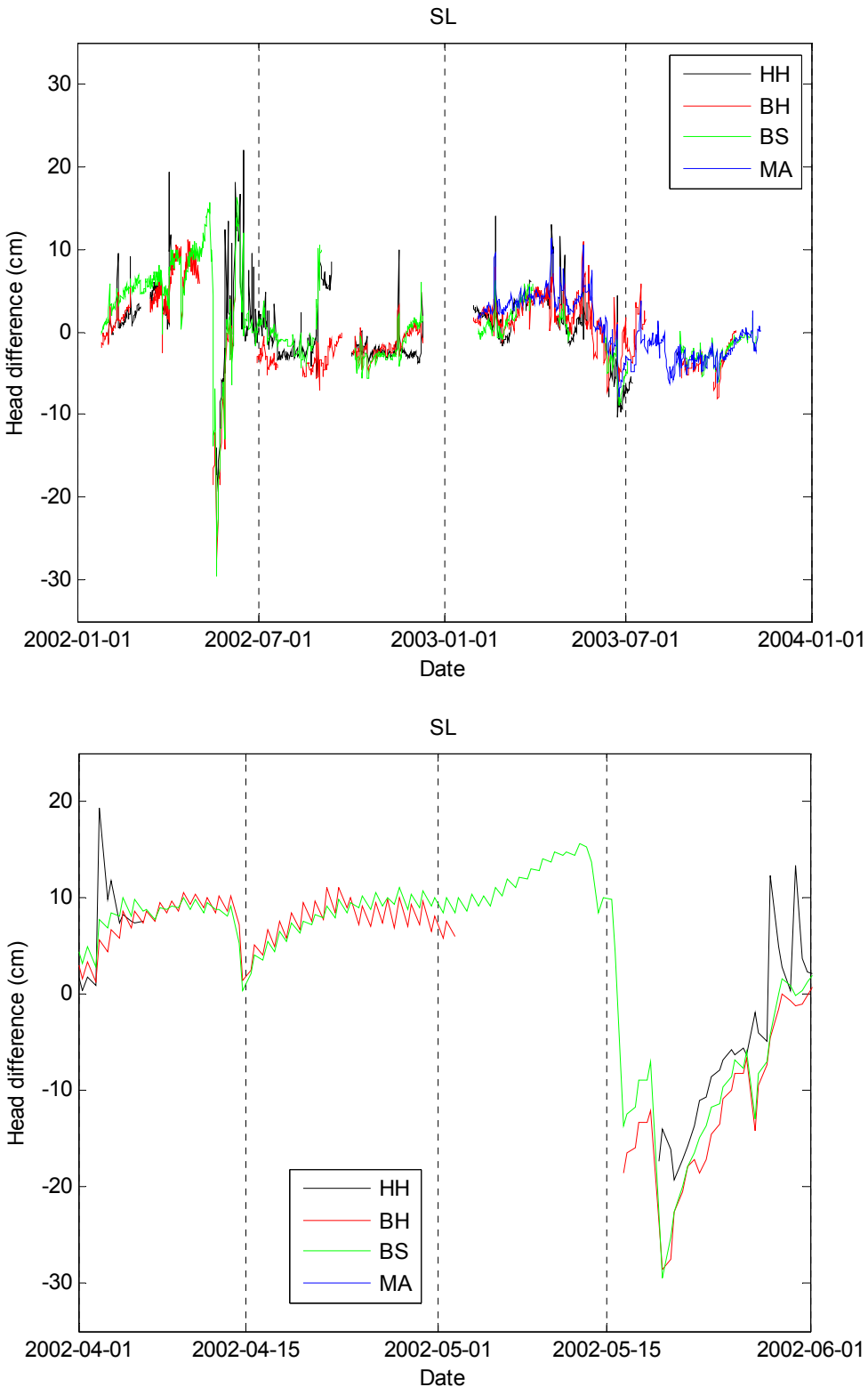

Figure A-78. Difference between the water table levels obtained from the model and from the field measurements in SL wells for the case K2. It is comparable to Figure A-76 for case K1.

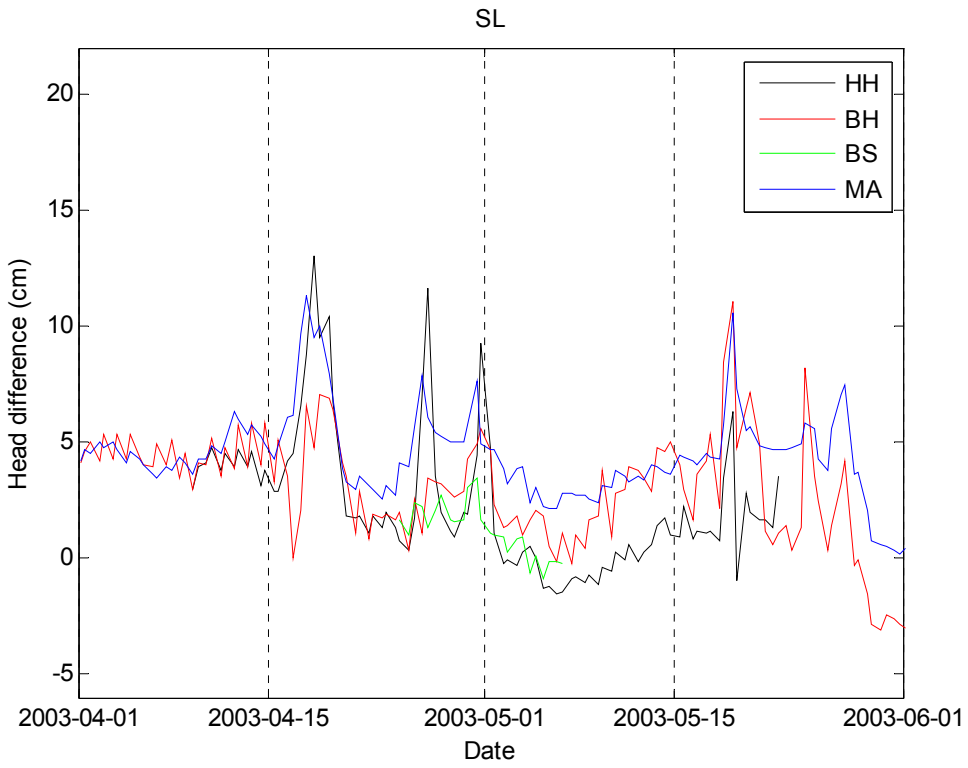

Figure A-78. Difference between the water table levels obtained from the model and from the field measurements in SL wells for the case K2. It is comparable to Figure A-76 for case K1. Continuation.

A4.2.6 Adjusting Several Parameters. Other Details

The cases listed in Table A-31 were obtained by following the minimum-searching procedure in Figure 61 after case 59. The sensitivity of overall error 2 to each parameter variations are plotted in Figure A-79. The tendency to reach a zero error change means that a local minimum is being approached. Notice that the maximum error changes are obtained by changing the rock conductivity using the step specified in Table 27 and the minimum error changes by modifying the rock porosity, which does not cause any error change. In general, if the error variation is high, the error change decreases monotonically and smoothly as the parameter varies. However, if the error change is low (about 1 micrometer), the dependence between error change and the parameter becomes noisy.

In order to make the minimum-searching procedure in Figure 61 more efficient, after case K129, the search was limited only to parameters that produce error variations higher than 1 micrometer and that are not oscillating around a value (changing sign in

step and therefore the direction of the searching). After case K197, a new case K198 was defined by interpolating the zero-error-change values in Figure 61 (see Table A-31). At this point, a small error in the computation of error 2 was fixed and also a new OLF leakance was saved in the OLF input file when the soil conductivity changes, which was omitted in previous cases. The last correction affects the error sensitivity to the soil conductivity, as shown Figure A-79. After case K288, the minimum-searching procedure was allowed to change parameters that produce error variations lower than 1 micrometer and also to reduce the step if the solution is around a local minimum and the error variations are higher than 1 micrometer.

The evolution of the overall error estimators during minimum-searching procedure is shown in Figure A-80 (black lines). As the procedure is minimizing directly the error 2, its decrease is more monotonic than the other overall errors, which also decrease at a longer scale. Only overall error 4 increases after case K400. All overall errors decrease faster at the beginning, where the error sensitivity to the parameters is higher. The detailed the evolution of error 2 for each well is also presented in Figure A-81. Notice that the errors for wells in the Marsh do not change appreciably while changing the GW parameters of the model, as expected.

The minimizing procedure was stopped on case K609, after reaching a local minimum. All the cases after case K588 were rejected even by using smaller steps. This does not mean necessarily that the absolute minimum for error 2 was reached. Thus, the space of the parameters was further explored by minimizing other errors, i.e., by changing the objective function to minimize.

Then, two separate minimum search procedures were performed in order to minimize the overall errors 3 and 4. The procedures start from the cases with the smallest overall error 3 (case K566) and error 4 (case K358). They were renamed as cases K2000 and K3000, respectively.

Both overall errors decreased up to a local minimum and the minimizing procedures were stopped in cases K2177 and K3159, respectively. Curiously, by minimizing error 3, new cases with lower overall errors 1 and 2 were found. So, minimization of error 2 restarted from case K2024 (renamed as K610) and also minimization of error 1 started from case K2030 (renamed as K1000).

Parameter	Veg. type	case K73	case K86	case K100	case K113	case K132	case K145	case K158	case K197	case K198	case K287	case K398	case K462
Leakance coefficient f_L on (79)	All	17.71	19.49	21.44	23.58	28.53	28.53	25.68	25.68	27.00	29.70	37.73	41.51
Soil conductivity HY, VHY (10^{-5} m/s)	All	1.77	1.95	2.14	2.36	2.85	3.14	3.45	4.17	2.60	0.73	0.73	0.59
Rock conductivity HY, VHY (10^{-3} m/s)	All	3.19	3.51	3.86	4.24	5.14	5.65	6.22	11.0	11.0	19.5	12.8	8.39
Soil porosity SF2	HH	0.55	0.56	0.57	0.58	0.59	0.59	0.58	0.58	0.58	0.58	0.61	0.59
	Others	0.89	0.88	0.87	0.86	0.84	0.83	0.82	0.76	0.73	0.60	0.54	0.50
Rock porosity SF2	All	0.20	0.20	0.20	0.20	0.20	0.20	0.20	0.20	0.20	0.20	0.20	0.20
VANAL (1/m)	All	2.74	2.73	2.72	2.71	2.69	2.68	2.67	2.61	2.60	2.54	2.49	2.51
VANBT	All	1.877	1.867	1.857	1.847	1.837	1.827	1.817	1.757	1.730	1.610	1.550	1.510
BROOK	All	2.6	2.5	2.4	2.3	2.2	2.1	2.0	1.5	2.0	2.2	1.6	1.2
T/ET	HH	0.91	0.92	0.93	0.94	0.95	0.96	0.97	0.97	0.97	0.99	0.98	0.99
	BH	0.81	0.82	0.83	0.84	0.85	0.86	0.87	0.92	0.94	0.96	0.98	0.99
	BS	0.66	0.66	0.66	0.67	0.67	0.67	0.67	0.67	0.70	0.73	0.76	0.76
	TS	0.51	0.52	0.53	0.54	0.55	0.56	0.57	0.59	0.60	0.63	0.65	0.67
	MA	0.11	0.12	0.13	0.14	0.14	0.15	0.16	0.17	0.17	0.20	0.21	0.22
Overall head error 1 (cm)	---	2.418	2.405	2.393	2.379	2.363	2.352	2.331	2.294	2.292	2.278	2.271	2.264
Overall head error 2 (cm)	---	4.105	4.066	4.033	4.004	3.957	3.937	3.919	3.853	3.838	3.793	3.775	3.758
Overall head error 3 (cm)	---	0.515	0.514	0.514	0.512	0.514	0.512	0.515	0.523	0.523	0.508	0.502	0.499
Overall head error 4 (cm)	---	1.507	1.492	1.480	1.471	1.463	1.461	1.460	1.464	1.460	1.460	1.444	1.463

Table A-31. Parameters adjusted while fitting water table well data after case K59.

Minimizing error 1 was stopped in case K1054, due to a lot of rejections after the last accepted case K1027. On the other hand, minimizing error 2 was stopped on case K829, after the last case accepted K728. While minimizing case 2, case K667 gives the current minimum value of error 1 and error 3. So, the procedure restarted minimizing error 3 on that case, renamed as K2178, which was stopped in case K2221 after the last case accepted K2206. Case K2190 gives the current minimum value for error 1, and the procedure of minimizing error 1 started again in that case, renamed as 1055. It was stopped in case K1132, after finding a local minimum at case K1095.

In parallel, a last attempt to explore the space parameters was conducted by starting to minimize error 4 far from the current case with its minimum error 4 value (K3135). So it is started in case K644 which is renamed as K3160. It was stopped in case K3239, after finding a local minimum in case K3233. The evolution of the four overall errors is presented in Figure A-80 by using different colors. The cases were renumbered in those graphs in order to have continuity at the starting case. The evolution of the parameters is also shown in Figure A-79 by using the same colors.

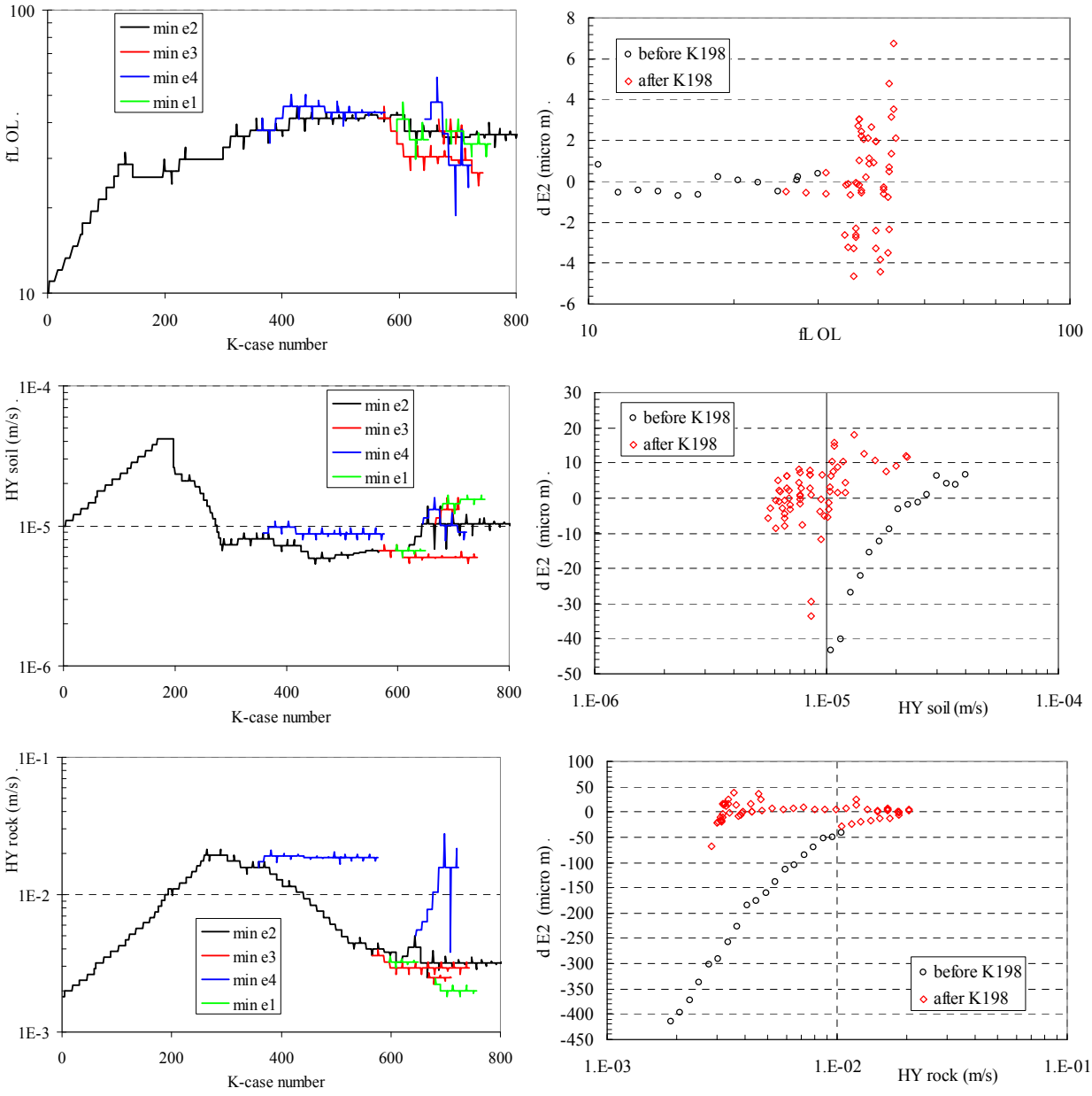

Figure A-79. Graphs for leakage coefficient and hydraulic conductivity in soil and rock. Figure continues and a detailed figure caption is at the end.

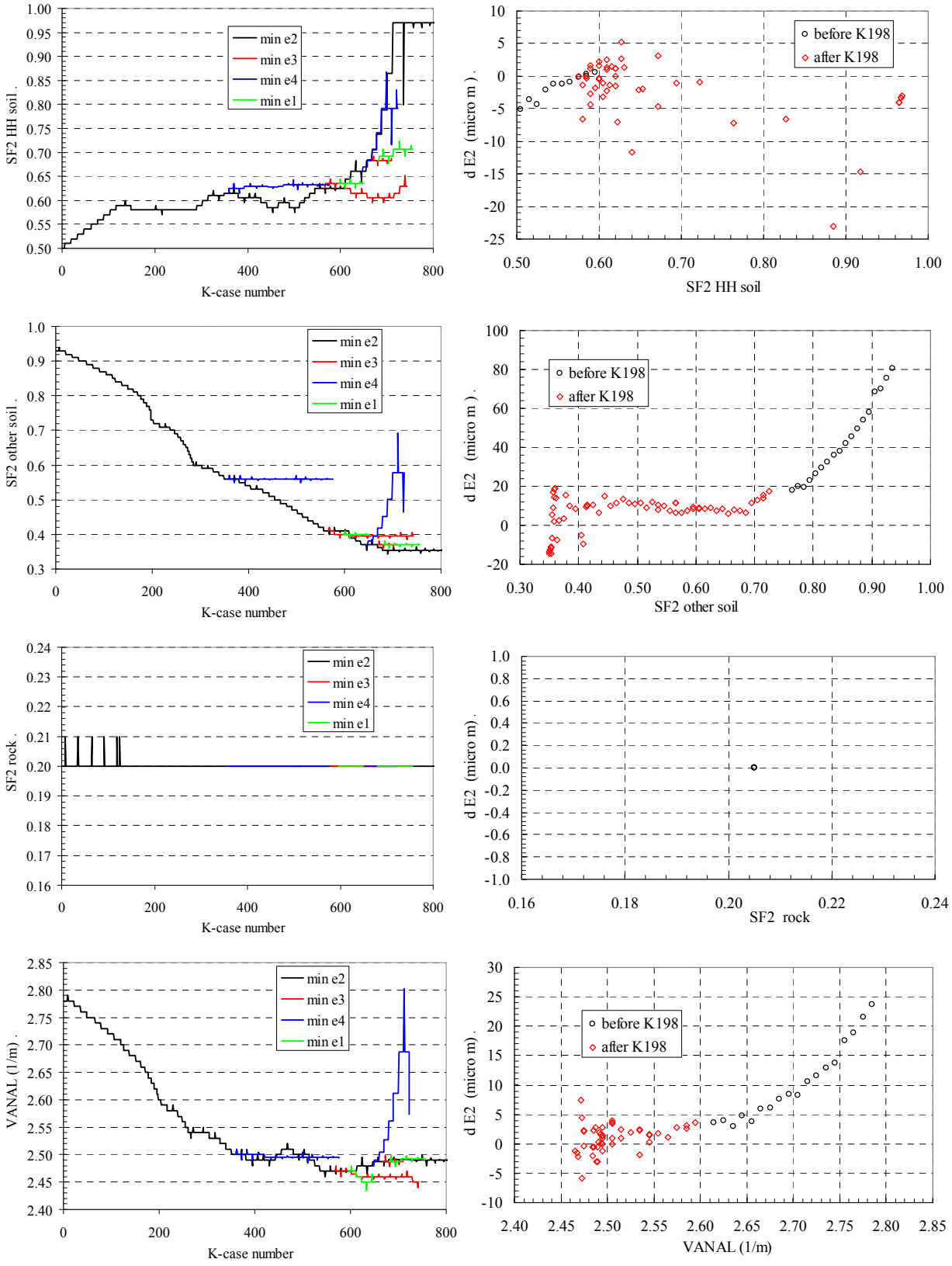

Figure A-79. Graphs for soil porosity in HH and other vegetation type areas and in rock, and for van Genuchten alpha. Figure continues and a detailed figure caption is at the end.

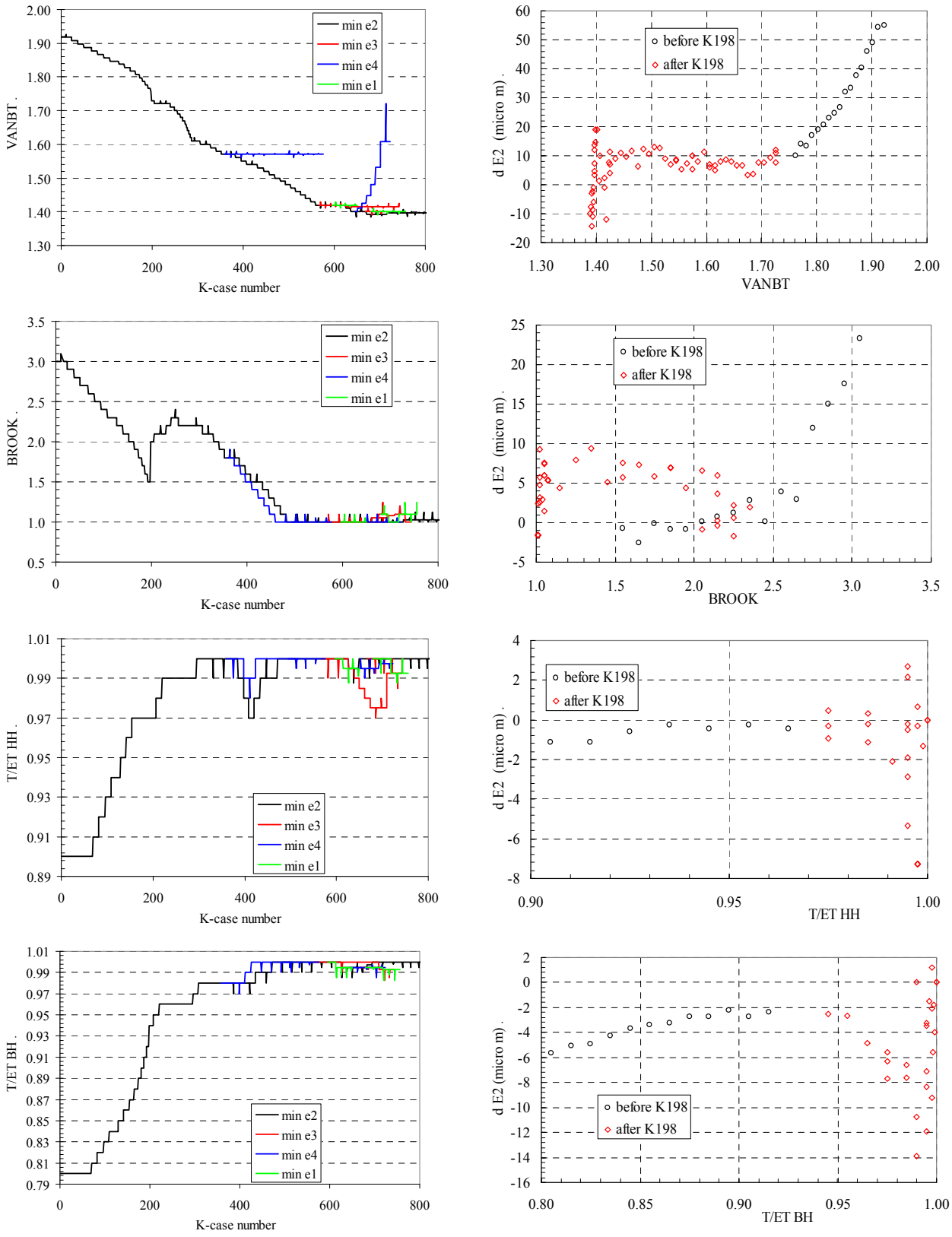

Figure A-79. Graphs for van Genuchten beta, Corey exponents and T/ET fractions. Figure continues and a detailed figure caption is at the end.

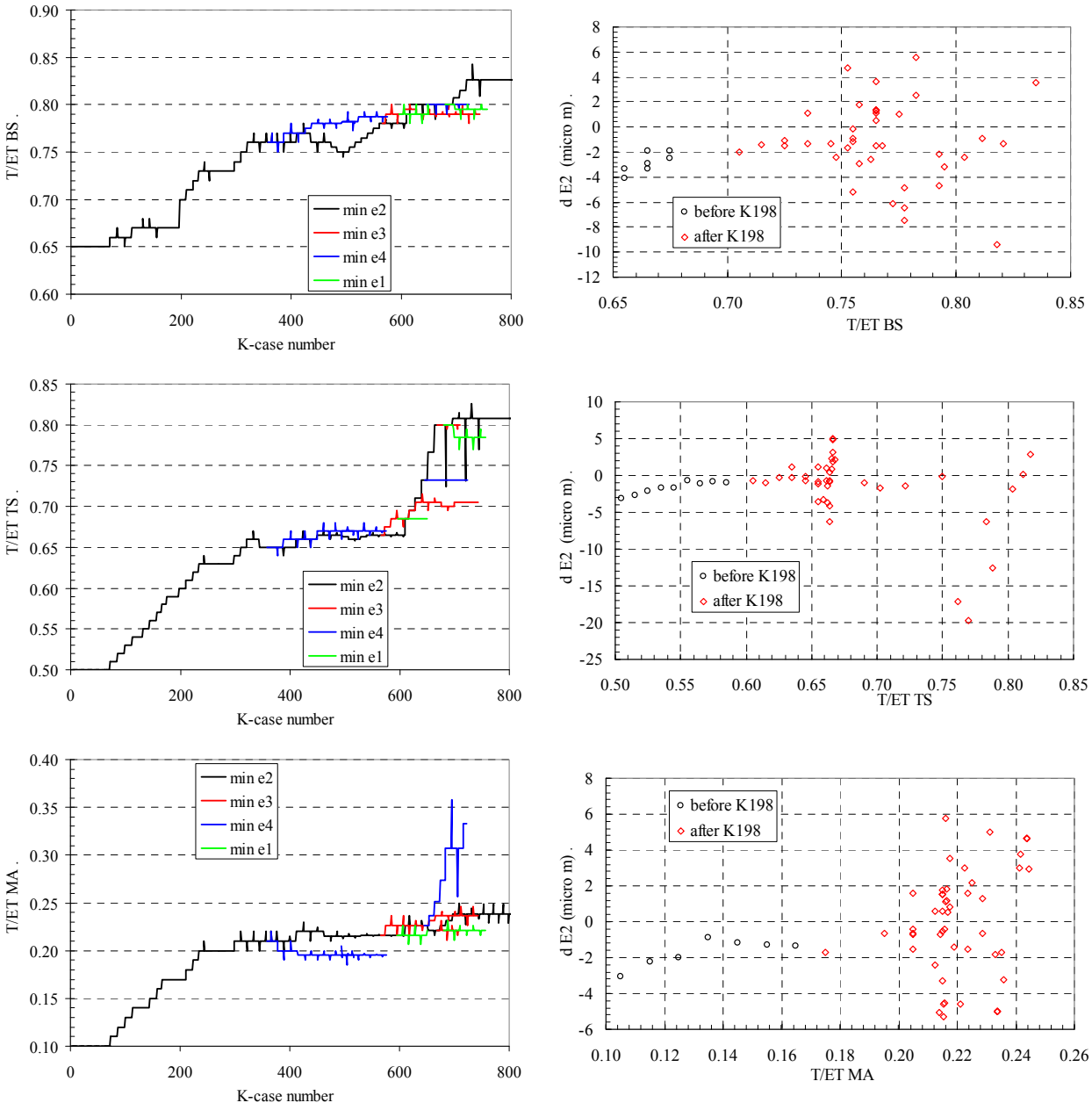

Figure A-79. On the left, the evolution of the parameters while minimizing different overall errors (different color lines). On the right, their corresponding error 2 variation while minimizing this error, obtained from positive steps (absolute or relative) of the given variable. The steps before case K288 are specified in Table 27, but after that are variable.

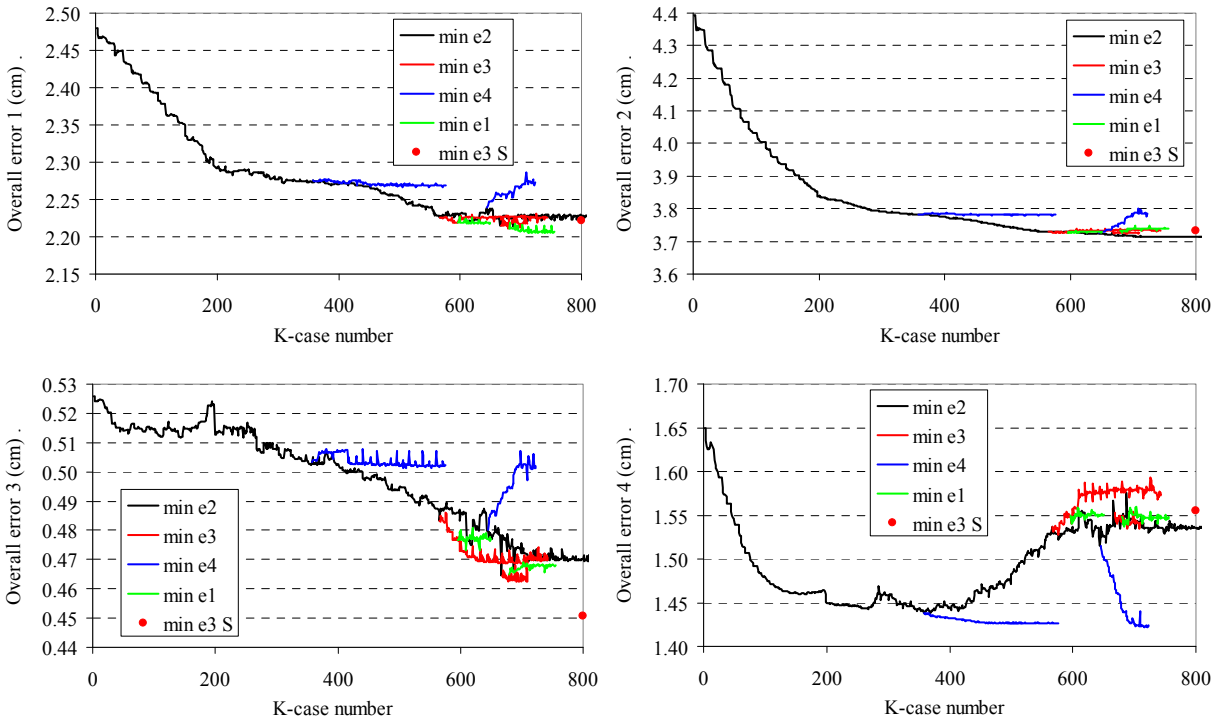

Figure A-80. Solid lines correspond to the evolution of the overall errors during minimum-searching procedure sketched in Figure 61. A different color is used depending on the error type to minimize. The red circle corresponds to the result of minimizing error 3 by changing the soil and rock layer elevation.

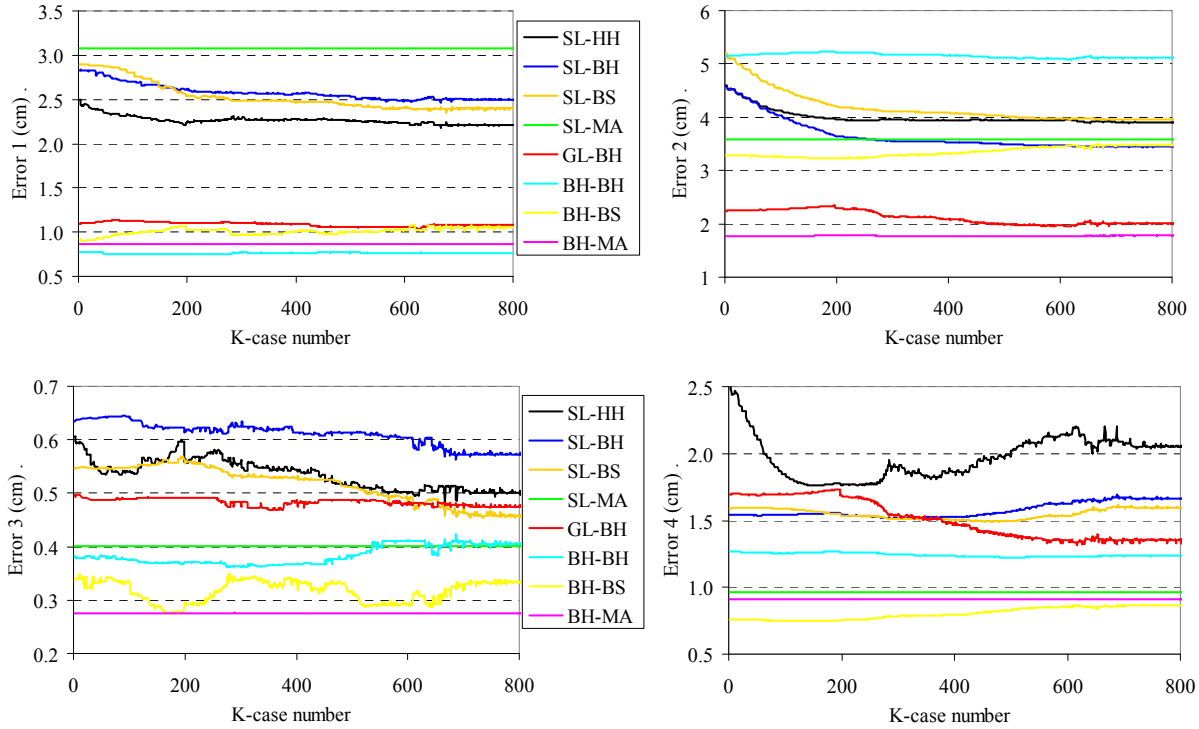

Figure A-81. Evolution of the error for different wells during the minimum-searching procedure.

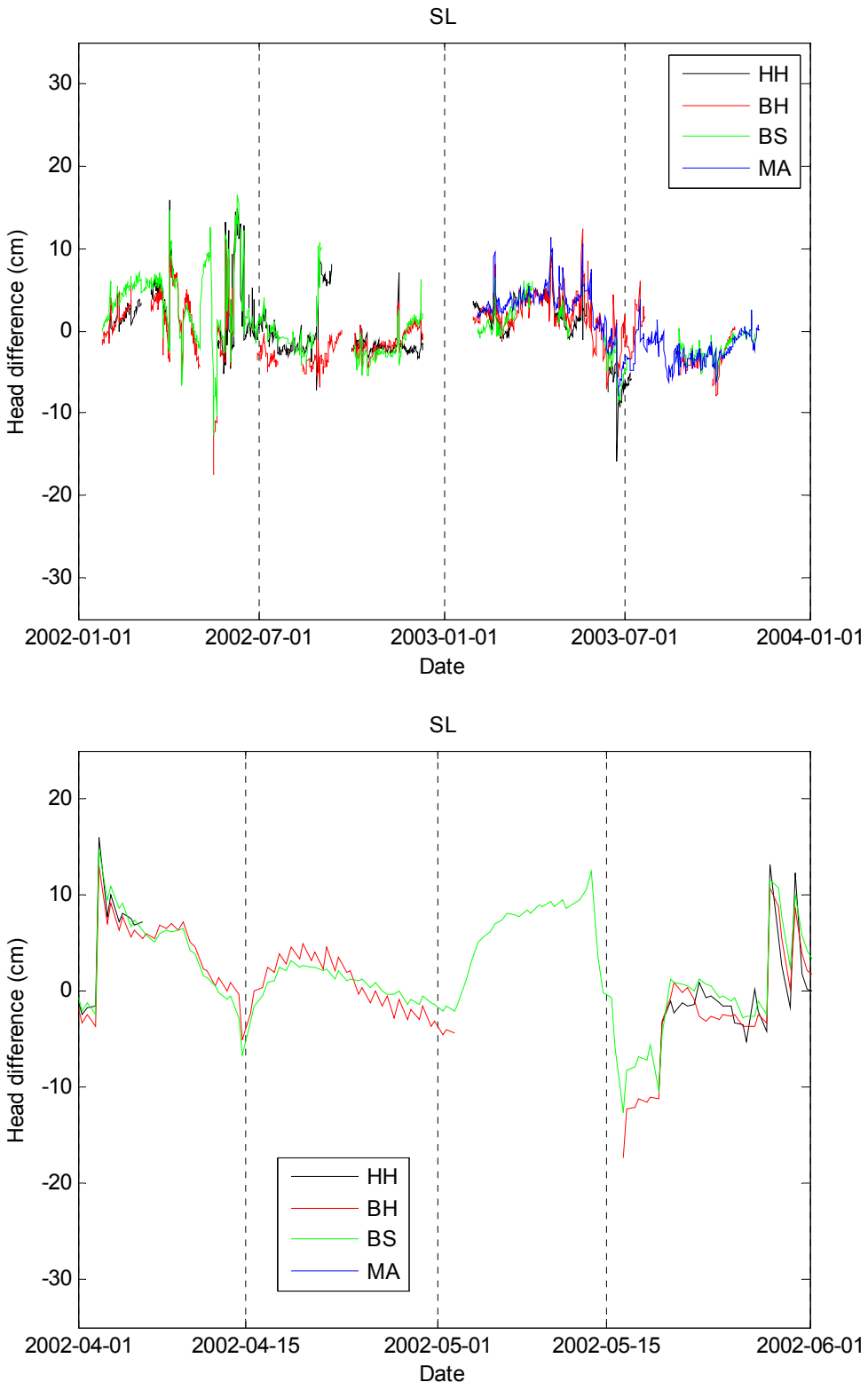

Figure A-82. Difference between the water table levels obtained from the model and from the field measurements in SL wells for case K2206. It is comparable to Figure A-78 for case K2.

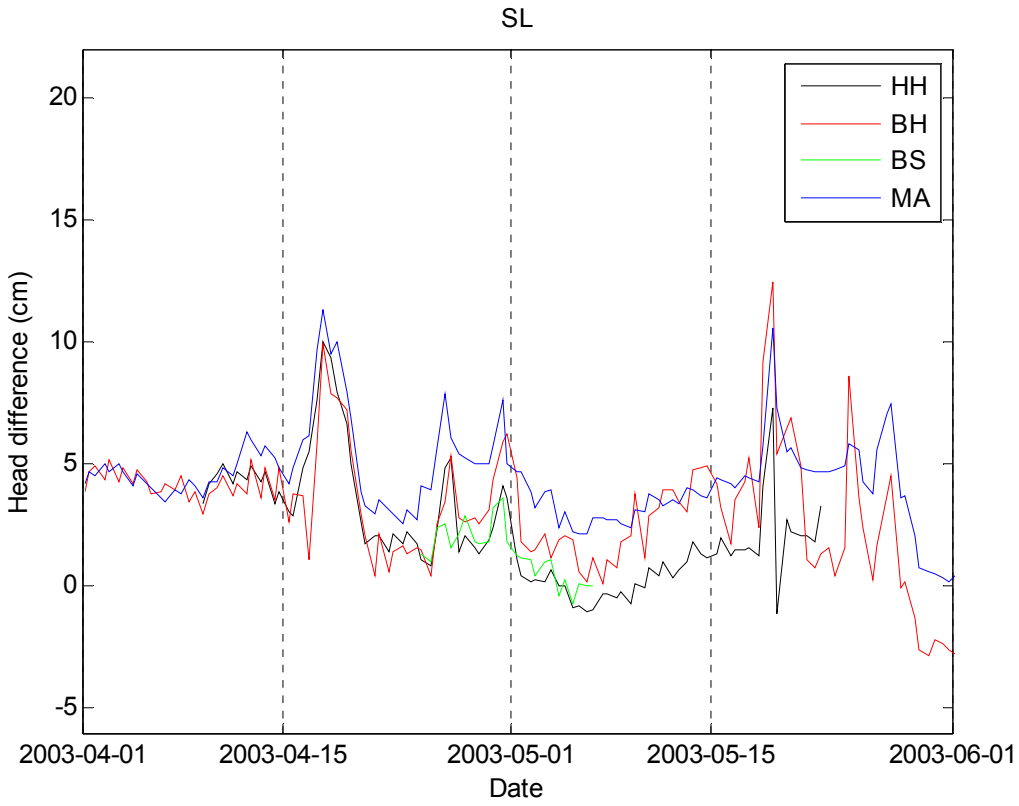

Figure A-82. Difference between the water table levels obtained from the model and from the field measurements in SL wells for case K2206. Continuation.

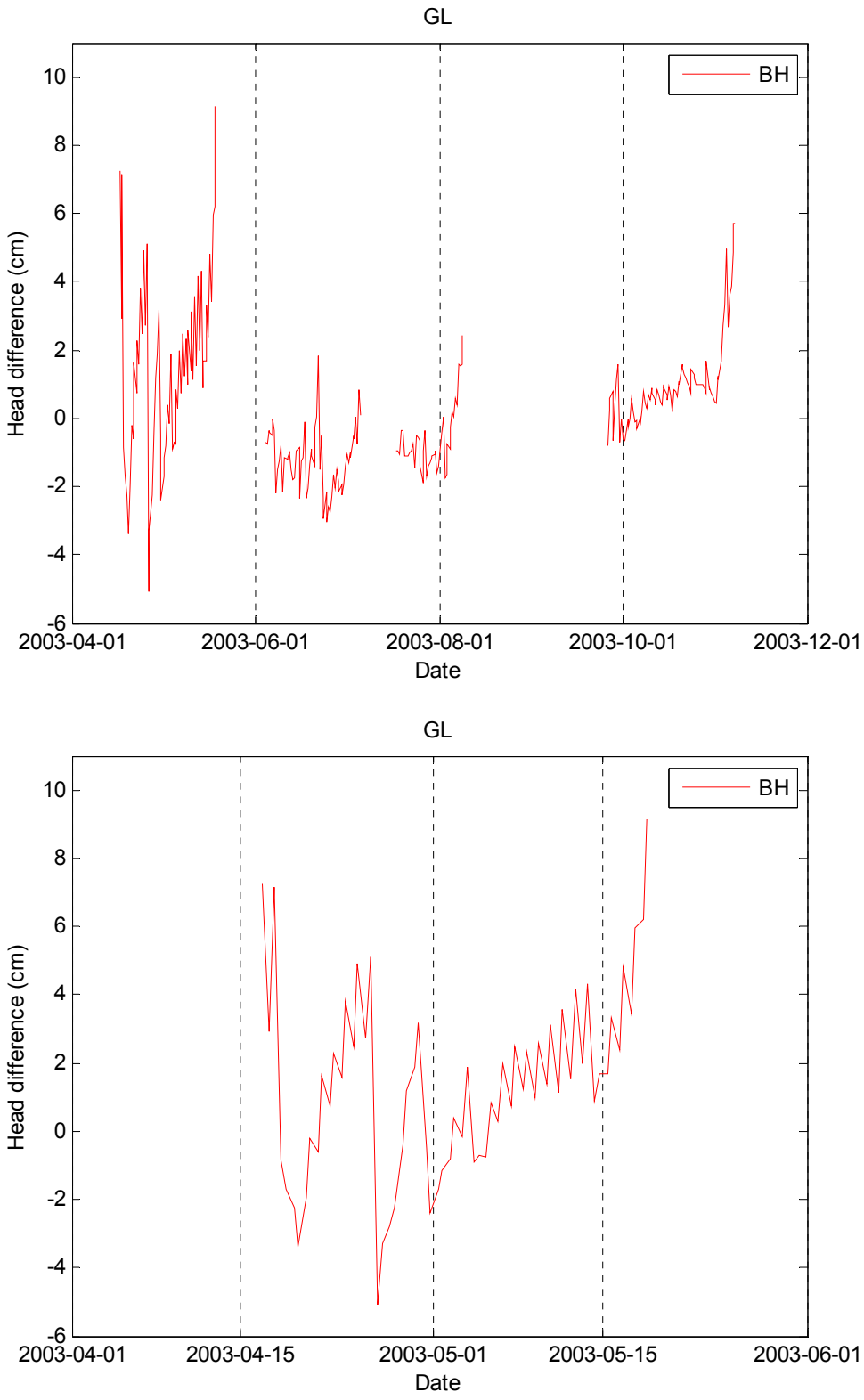

Figure A-83. Difference between the water table levels obtained from the model and from the field measurements in GL wells for case K2206. It is comparable to Figure A-74 for case K1.

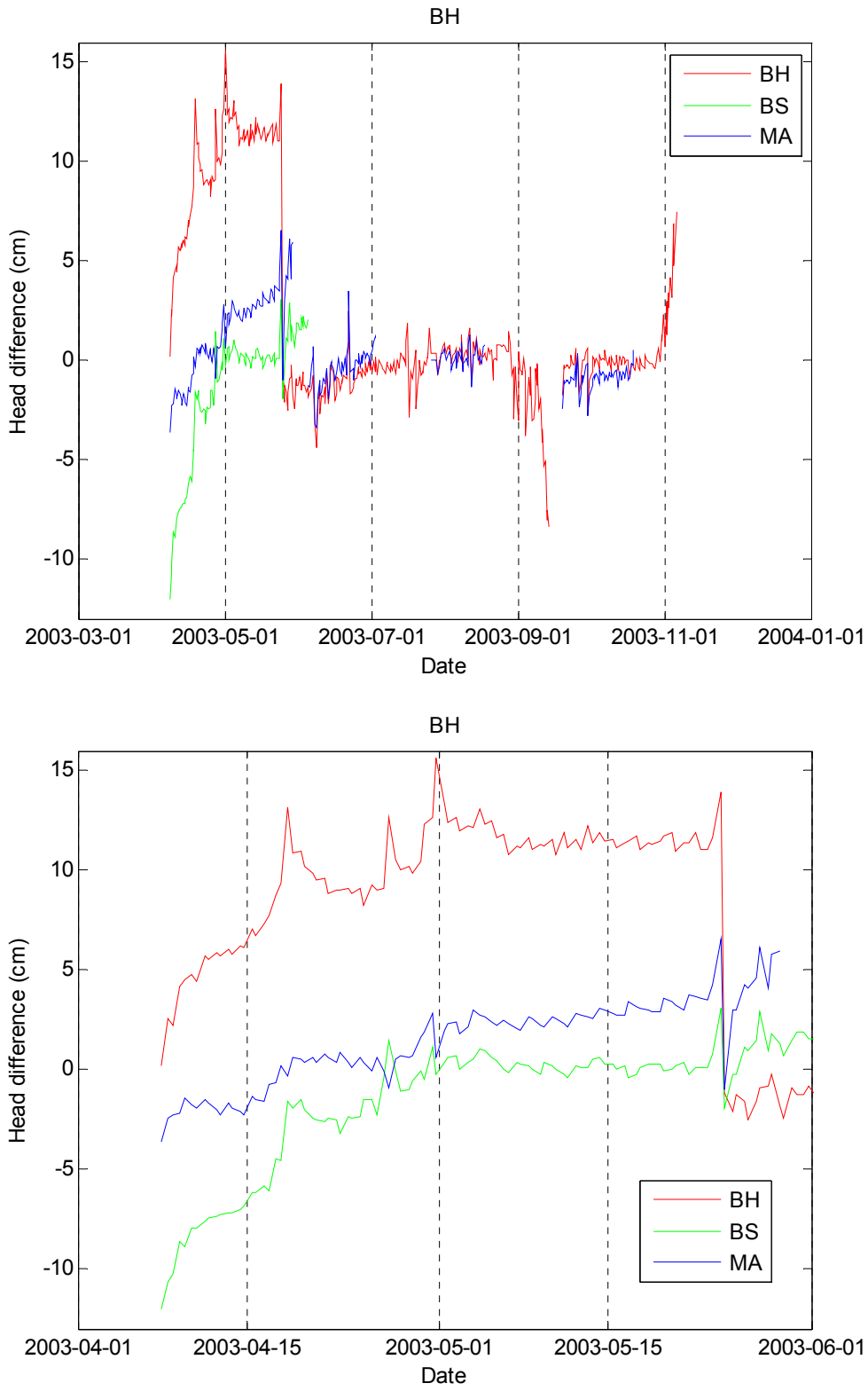

Figure A-84. Difference between the water table level from the model and from the field measurements in BH wells for case K2206. It is comparable to Figure A-75 for case K1.

A4.2.7 Adjusting Well Cell Elevations

Considering that the assumed soil and bedrock surface elevations can have up to a 15 cm deviation from their real value and keeping the restriction that the soil depth is not lower than 10 cm, those elevations were changed at each well cell in order to find the minimum error 3 for each tree island, which is similar to the overall error but excludes the other tree islands. This implies changes in the top and bottom elevation of the layers in the BCF file, the bottom elevation and the leakage coefficient in the OLF file and also the soil surface elevation in EVT file. The minimizing procedure here differs from the previous one illustrated in Figure 61, because the error in one tree island is minimized by changing the elevation of one well at a time. The procedure started in case K2206 described in Table 28, which was renamed as K4000.

TI	Well	Top soil elevation (m)		Top rock elevation (m)	
		Old	new	old	new
SL	HH	2.189	2.339	1.822	
	BH	1.522	1.461	0.857	0.885
	BS	1.414	1.489	0.788	0.938
	MA	1.300	1.403	0.800	0.650
GL	BH	1.401	1.382	0.136	0.230
BH	BH	1.534	1.571	0.688	0.725
	BS	1.388	1.528	-0.181	-0.266
	MA	1.319		1.071	1.108

Table A-32. Modification of the layer elevations in the well cells by minimizing error 3.

The initial and final elevation values are summarized in Table A-32. The evolution of the tree island errors are presented in Figure A-85. The best fitted case was renamed K4100 and the overall error is compared to the previous ones in Figure A-80. Figures comparing water table level from the model in case K4100 and from the field measurements can be found in Appendix A4.2.2.

In general, error 3 does not decrease appreciably by changing the soil and rock layer elevation at well cells. This may indicate that the predicted water table level of the well is influenced by the surrounding cells to some extent and not only by the cell where the well is located.

After the elevation at the well cells was modified, the mean layer surface

elevation and the total volume of the layer cells are computed for each vegetation type region in each tree island (see Table A-33).

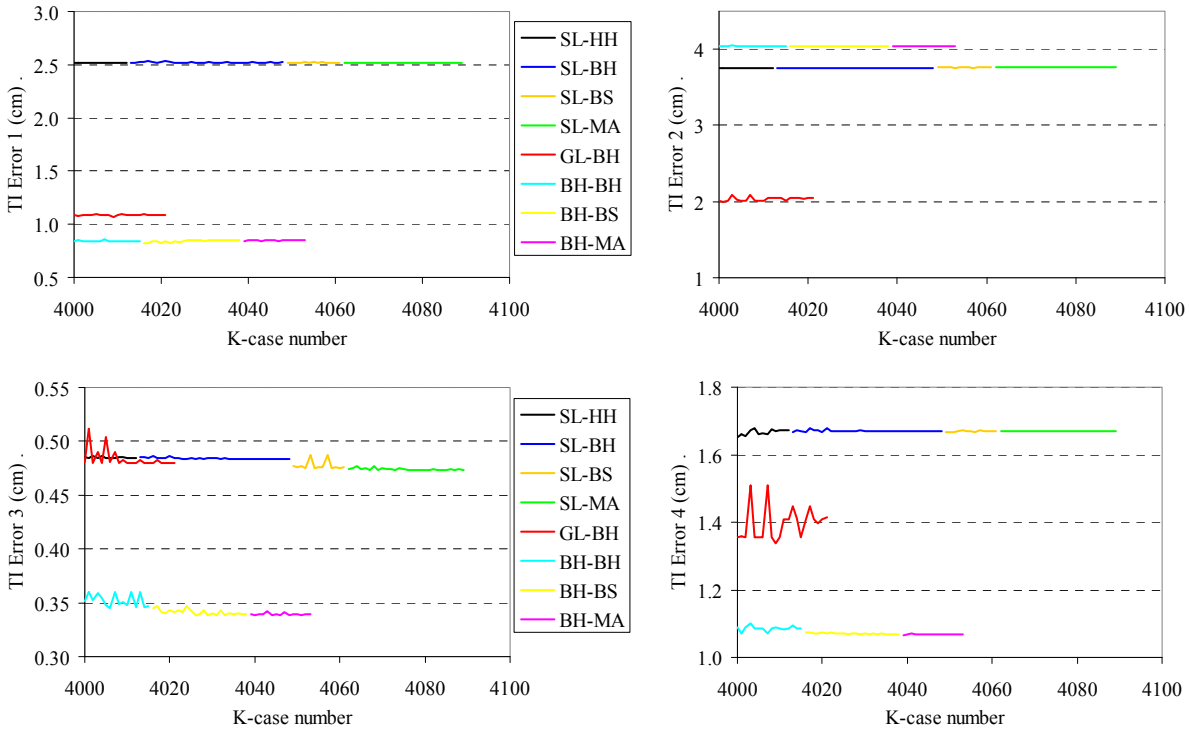

Figure A-85. Evolution of the tree island errors while changing surface elevations at different well cells trying to minimize TI error 3.

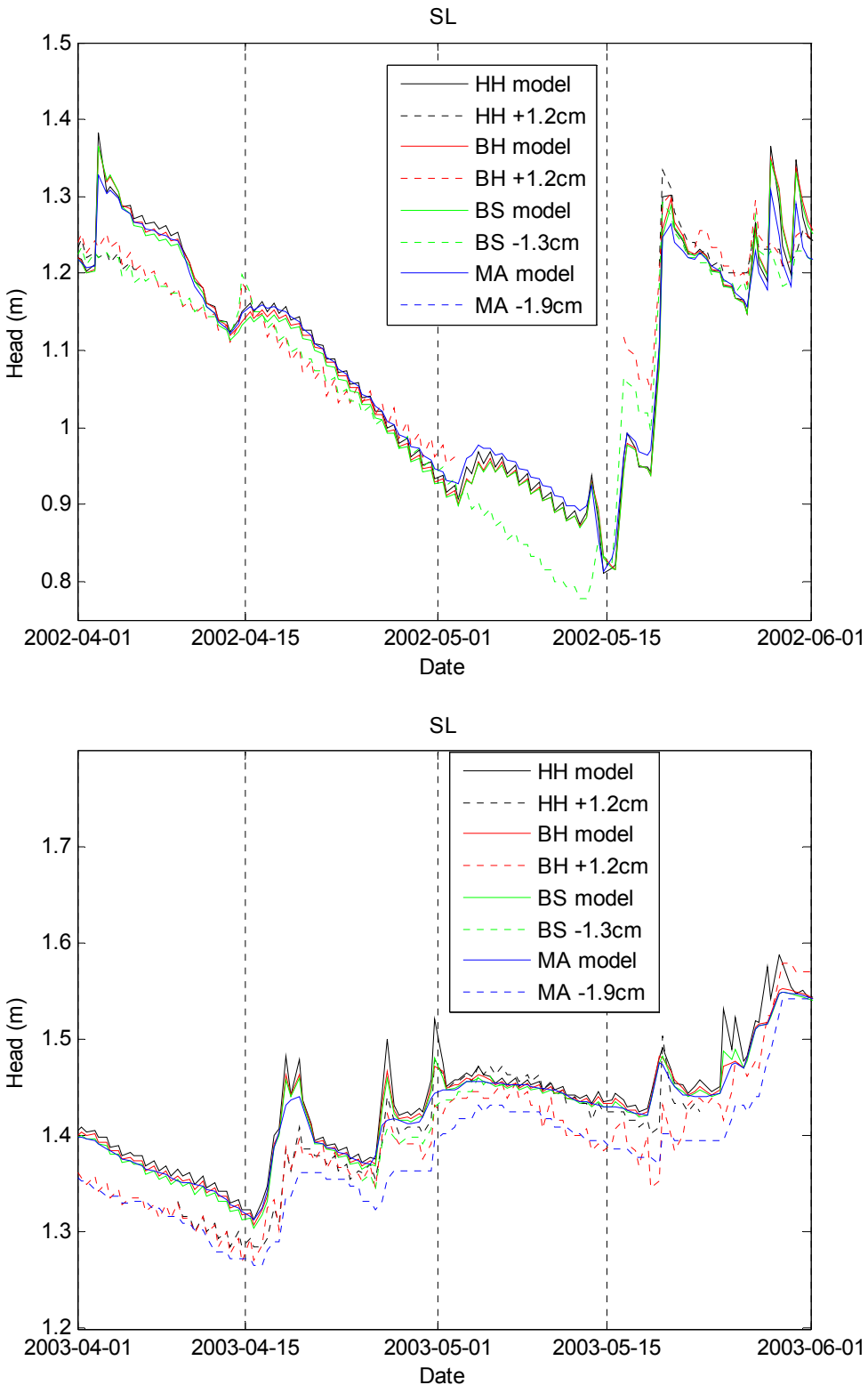

Figure A-86. Comparison between the water table level from the model and from the field measurements in SL wells for case K4100. It is comparable to Figure 62 for case K2206.

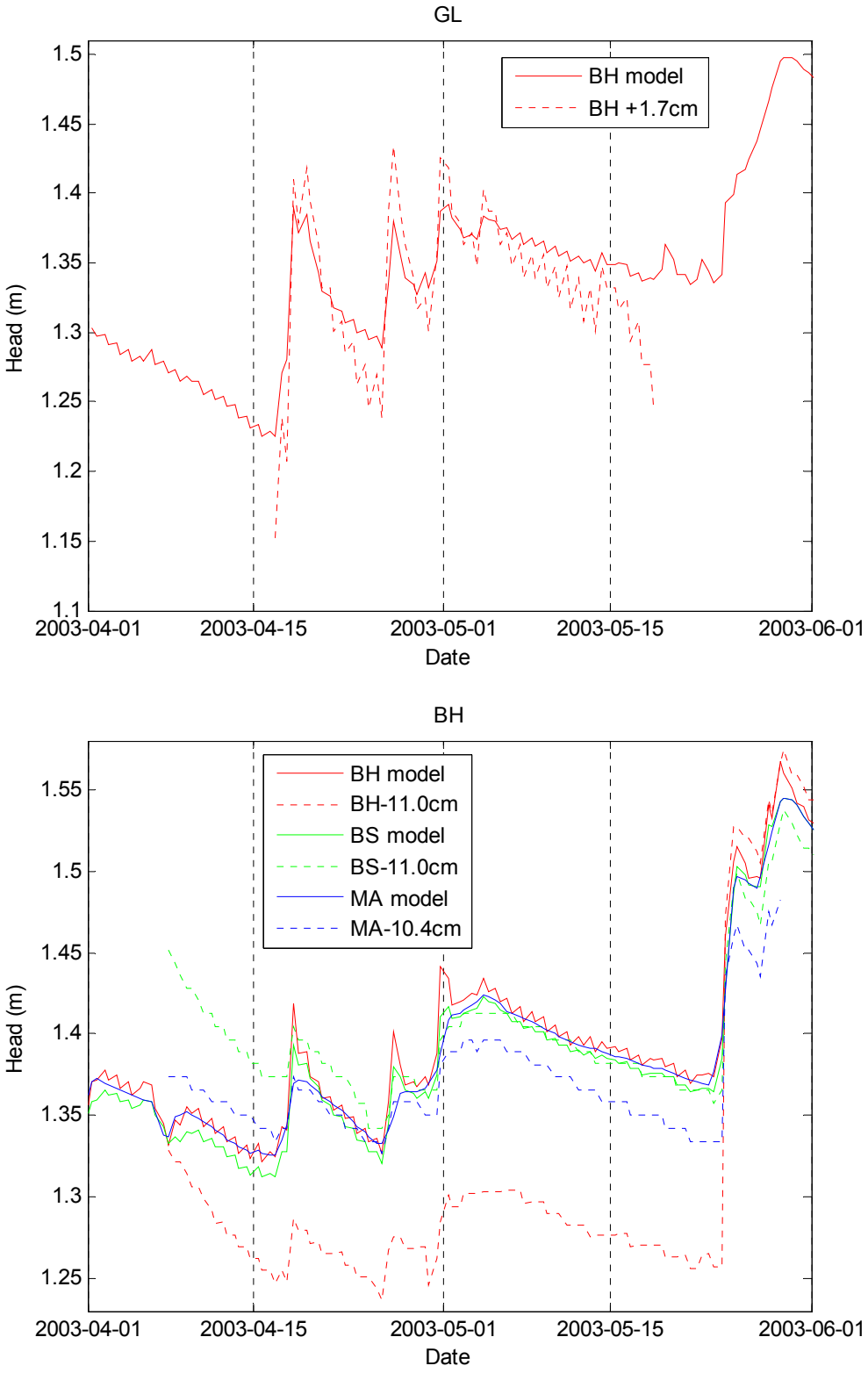

Figure A-87. Comparison between the water table level from the model and from the field measurements in GL and BH wells for case K4100. It is comparable to Figure 63 for case K2206.

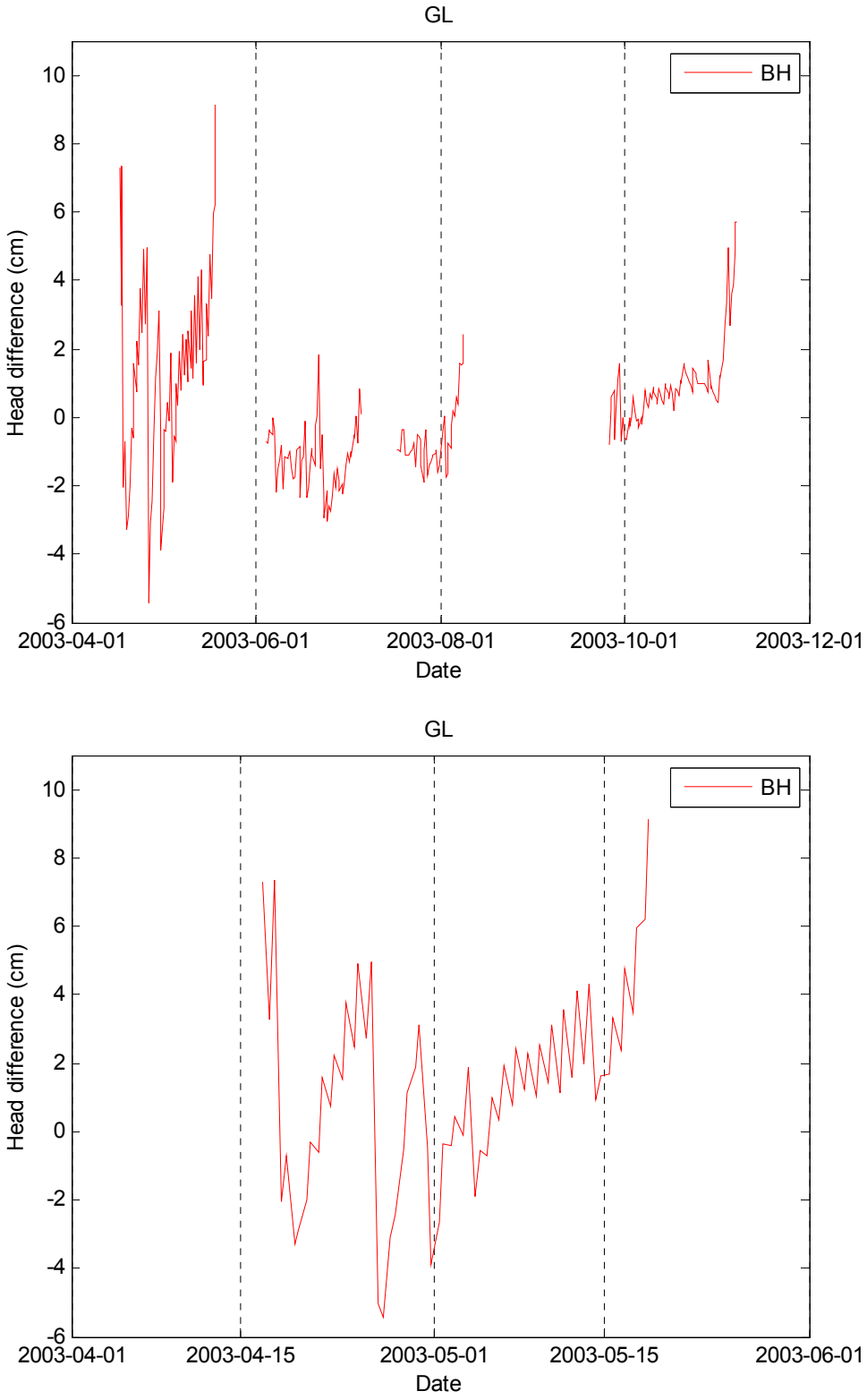

Figure A-88. Difference between the water table level from the model and from the field measurements in GL wells for case K4100. It is comparable to Figure A-83 for case K2206.

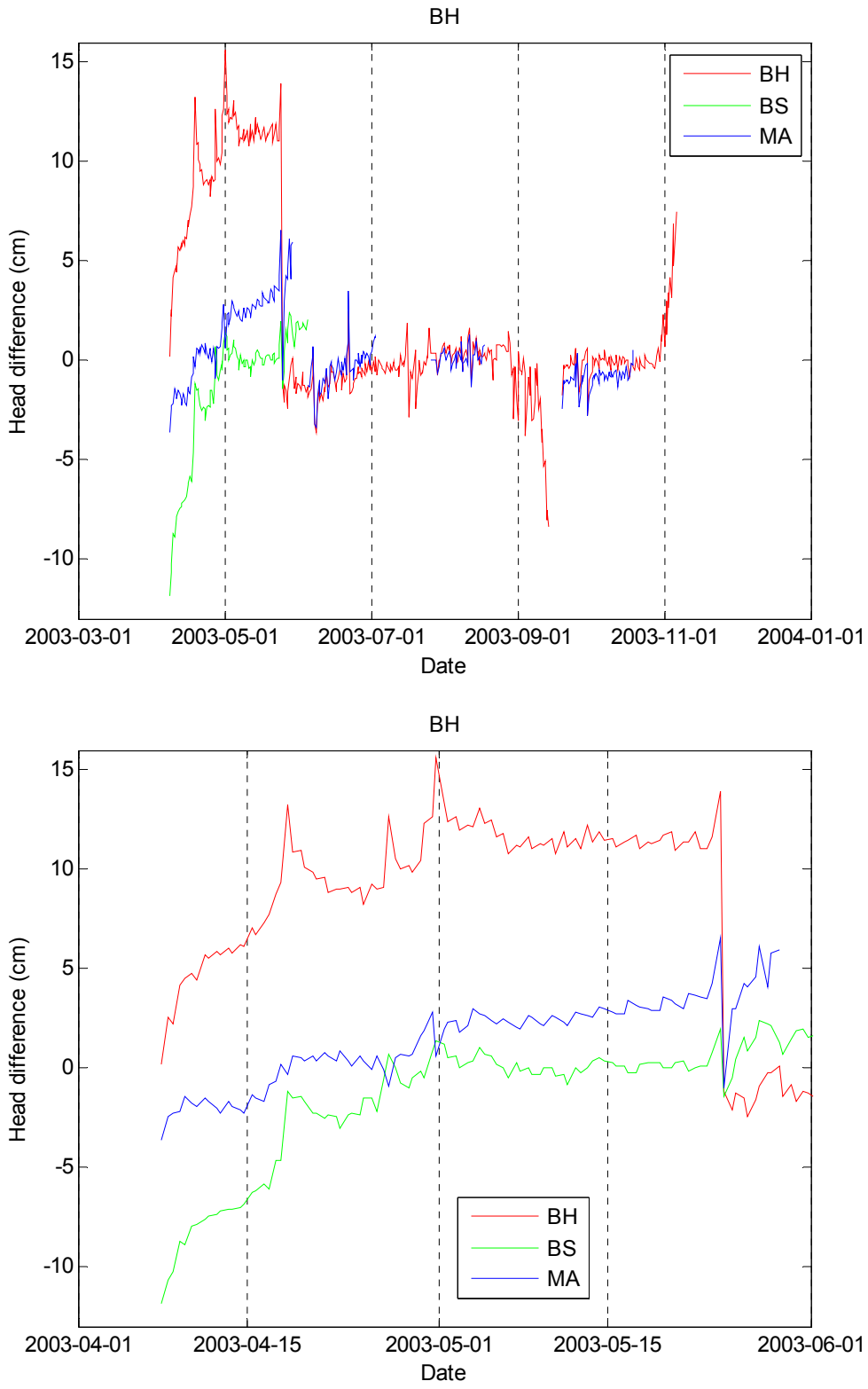

Figure A-89. Difference between the water table level from the model and from the field measurements in BH wells for case K4100. It is comparable to Figure A-84 for case K2206.

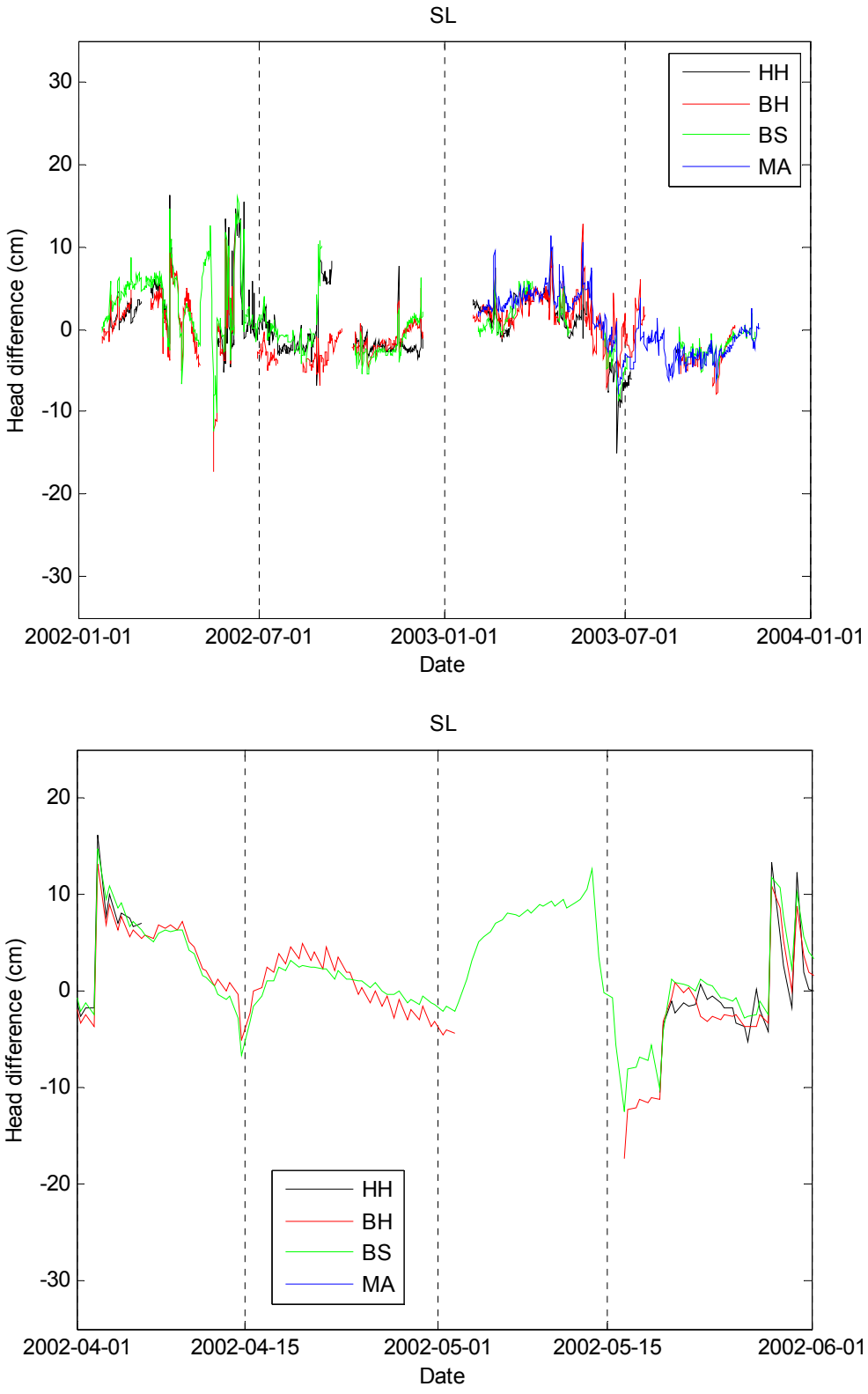

Figure A-90. Differences between the water table level from the model and from the field measurements in SL wells for case K4100. It is comparable to Figure A-82 for case K2206.

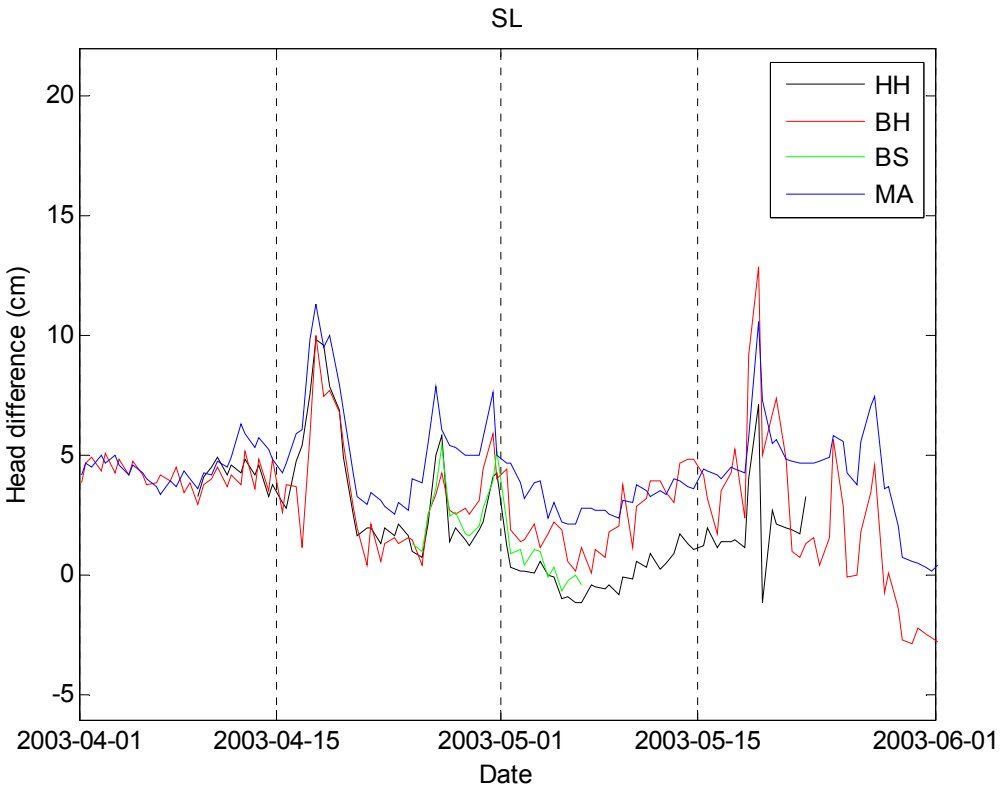

Figure A-90. Differences between the water table level from the model and from the field measurements in SL wells for case K4100. Continuation.

VT	Tree island	SL	GL	BH
MA	Mean soil surface elevation (m)	1.294	1.110	1.305
	Mean rock surface elevation (m)	0.801	0.225	0.999
	Horizontal area (m^2)	174917	104519	147375
	Volume of the soil layer cells (m^3)	86132	92517	45029
	Volume of the rock layer cells (m^3)	939908	501385	821041
TS	Mean soil surface elevation (m)	1.367	1.181	1.312
	Mean rock surface elevation (m)	0.821	0.192	0.956
	Horizontal area (m^2)	33342	38156	13825
	Volume of the soil layer cells (m^3)	18237	37744	4924
	Volume of the rock layer cells (m^3)	179795	181759	76420
BS	Mean soil surface elevation (m)	1.476	1.253	1.372
	Mean rock surface elevation (m)	0.819	0.161	0.847
	Horizontal area (m^2)	21700	9133	36008
	Volume of the soil layer cells (m^3)	14253	9977	18917
	Volume of the rock layer cells (m^3)	116993	43227	195120
BH	Mean soil surface elevation (m)	1.535	1.330	1.417
	Mean rock surface elevation (m)	1.054	0.160	0.919
	Horizontal area (m^2)	7142	81417	40192
	Volume of the soil layer cells (m^3)	3435	95262	20014
	Volume of the rock layer cells (m^3)	40178	385291	220705
HH	Mean soil surface elevation (m)	1.931	1.701	1.859
	Mean rock surface elevation (m)	1.639	1.006	1.379
	Horizontal area (m^2)	2900	6775	2600
	Volume of the soil layer cells (m^3)	847	4708	1249
	Volume of the rock layer cells (m^3)	18013	37789	15472

Table A-33. Layer mean surface elevation, horizontal area and layer cell volumes for each vegetation type in each tree island.

A4.3 Transport Parameter Calibration

In this section, additional details about the transport parameter calibration from Phosphorus spatial distribution are described.

A4.3.1 Model Setup. Additional Figures

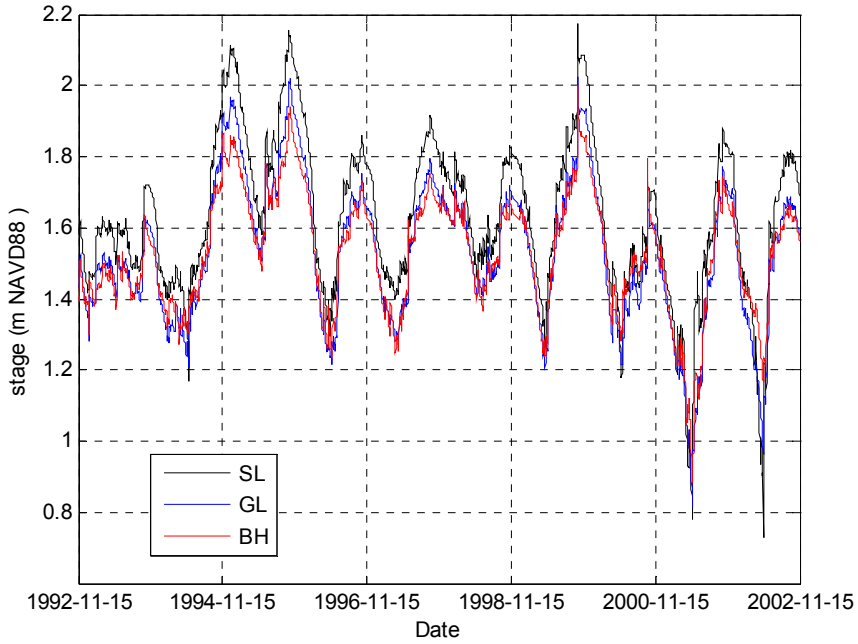

Figure A-91. Interpolated daily mean stages in the tree islands of Shark River Slough. This is a magnified view of Figure 25.

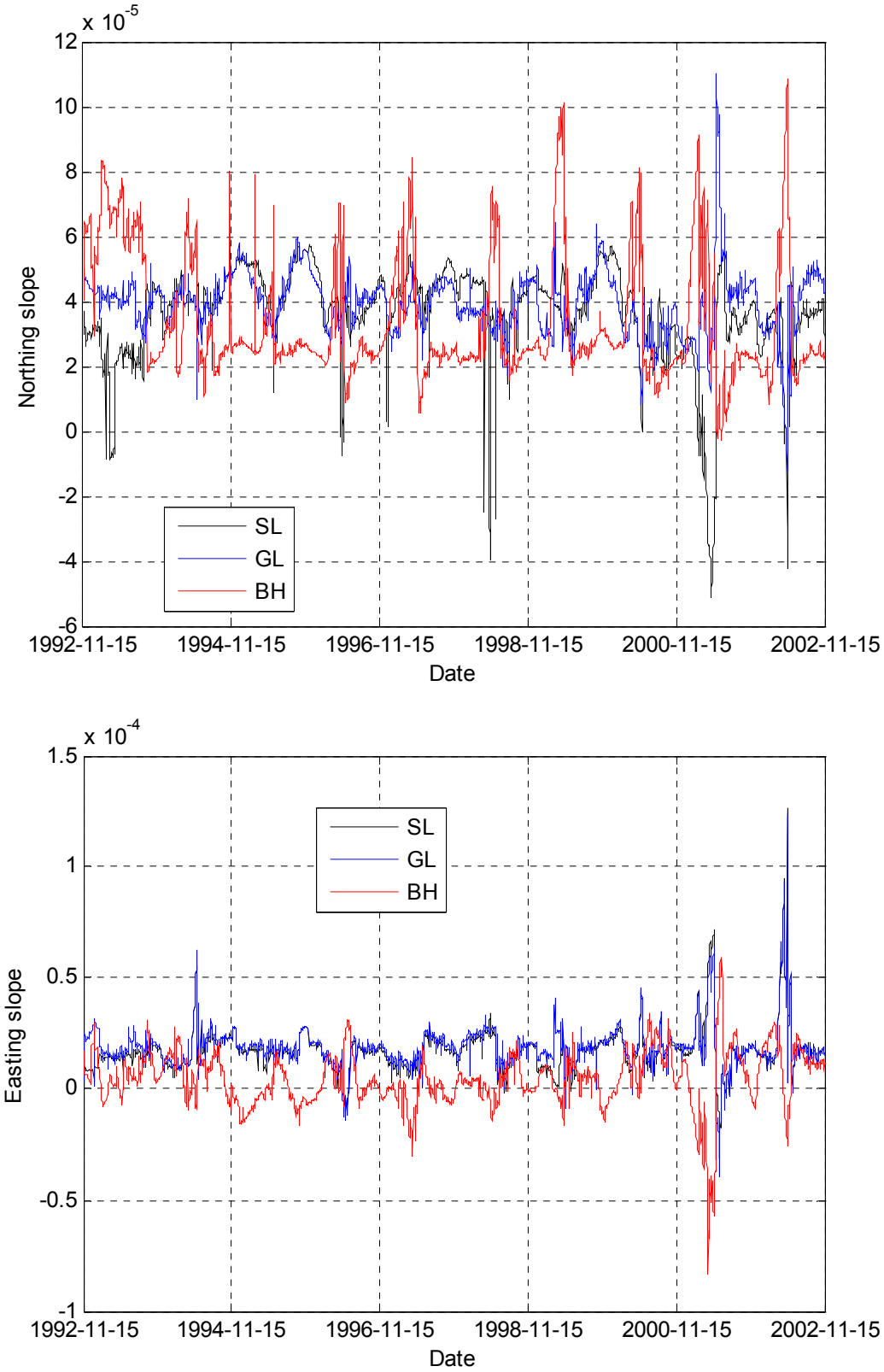

Figure A-92. Slopes obtained from the stage interpolation in the tree islands of Shark River Slough (magnified view of Figure 26).

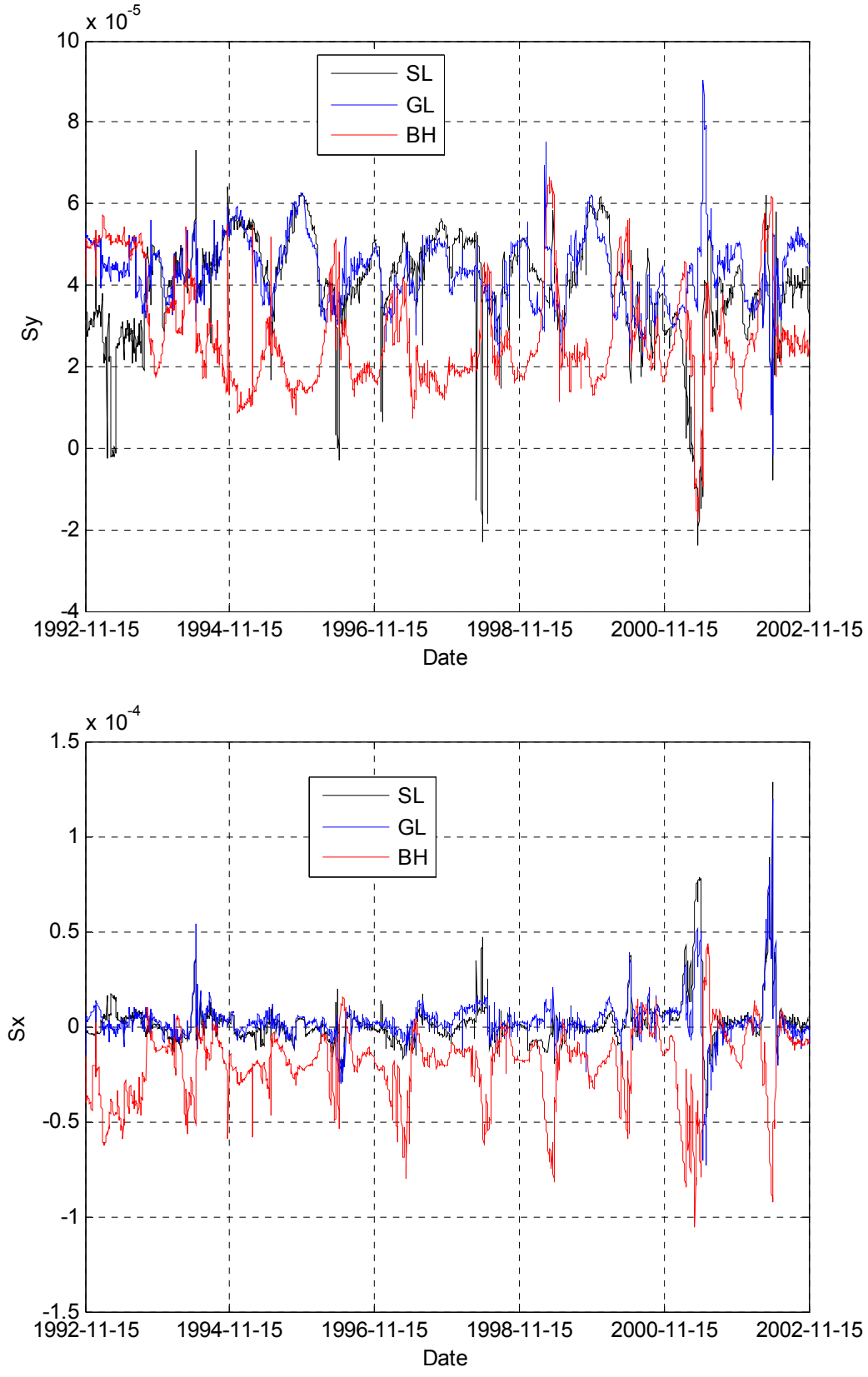

Figure A-93. Slopes in Figure A-92 in the rotated coordinate system of each tree island.

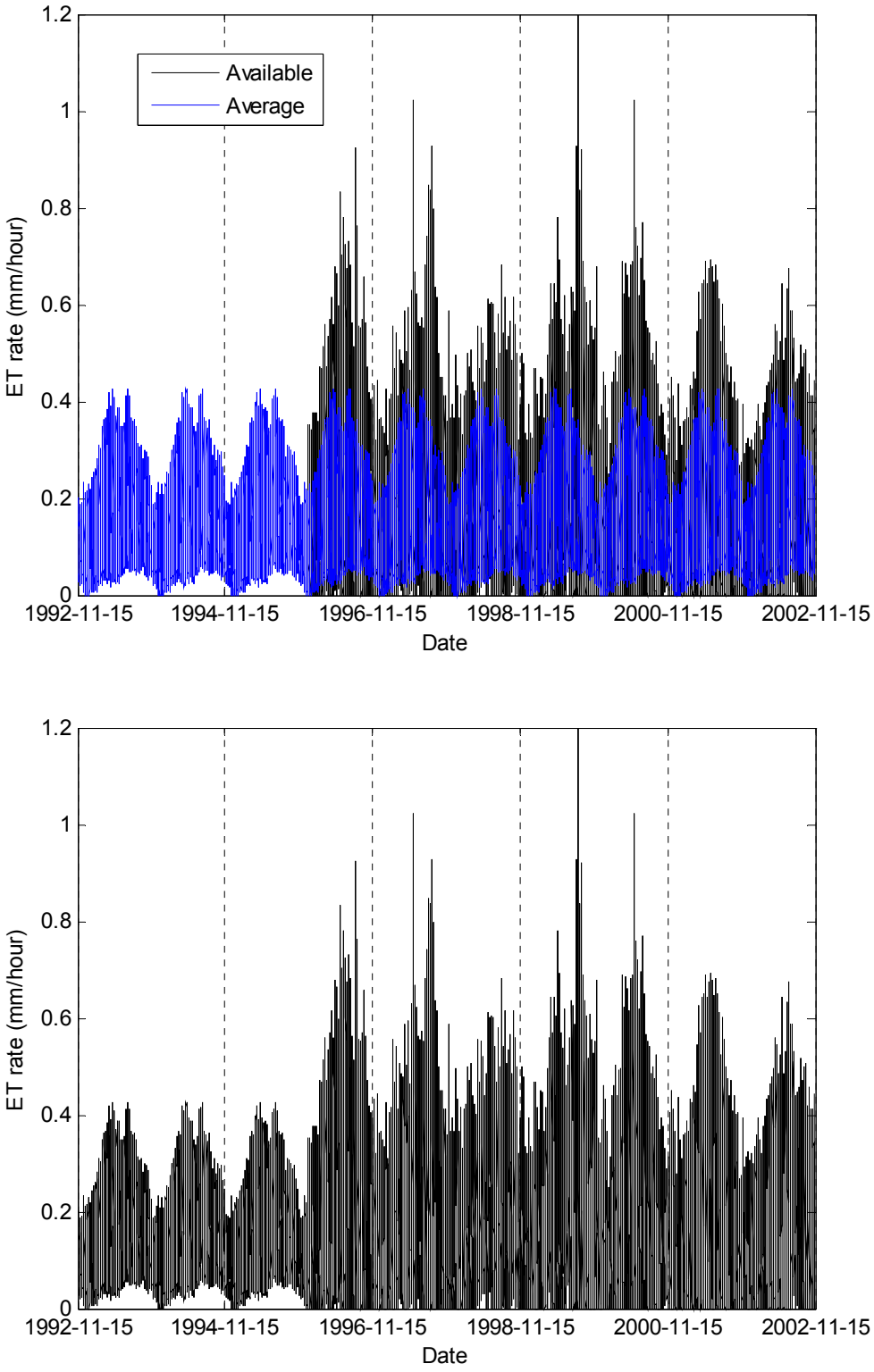

Figure A-94. ET hourly rates from years 1992 to 2002. Above, the available measured rates and the averaged ones. In the second graph, the composite curve assumed by substituting the missing measured rates with the averaged ones.

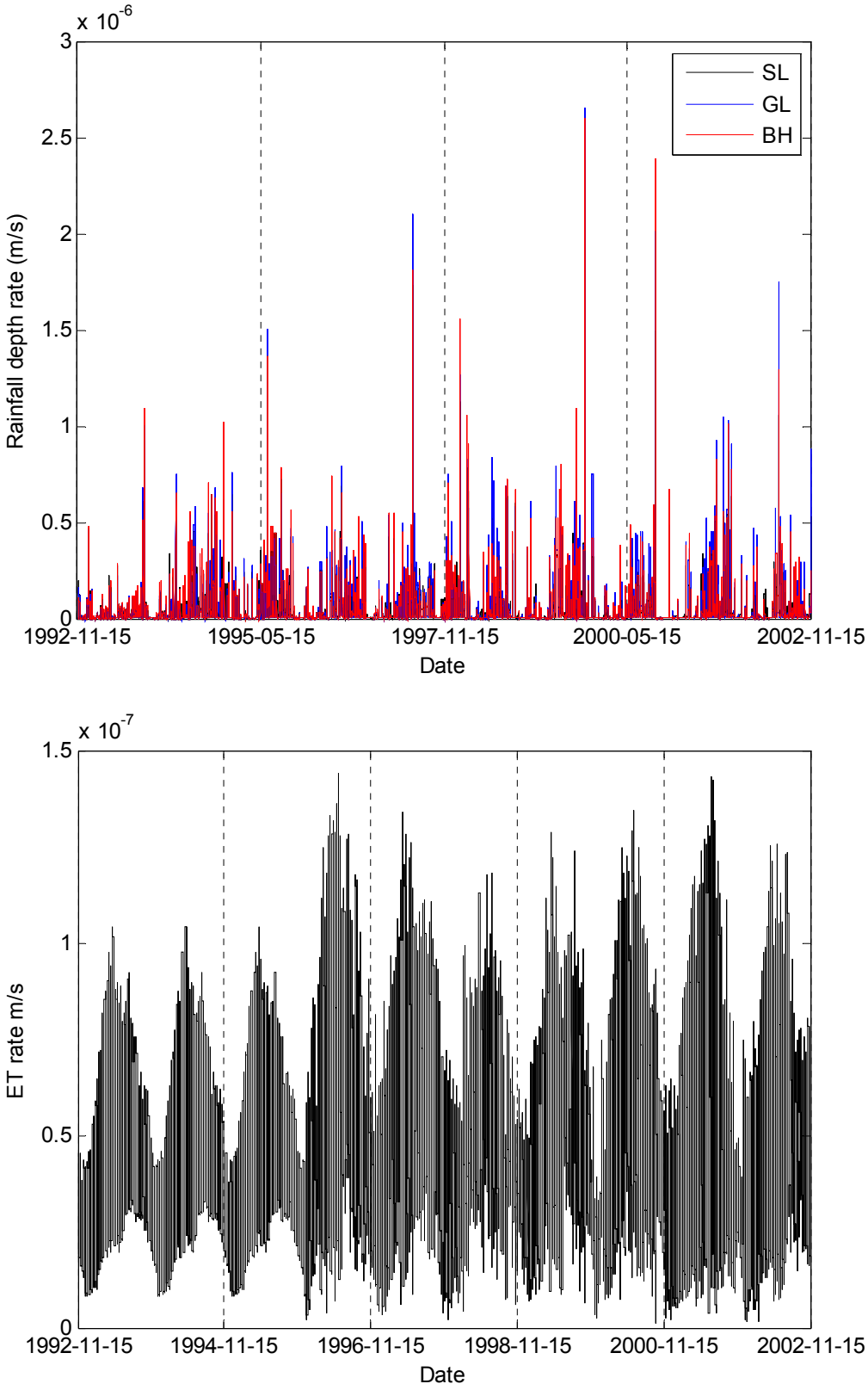

Figure A-95. Rainfall and ET rates specified for two stress periods every 24 hours.

A4.3.2 Using MODHMS. Additional Figures

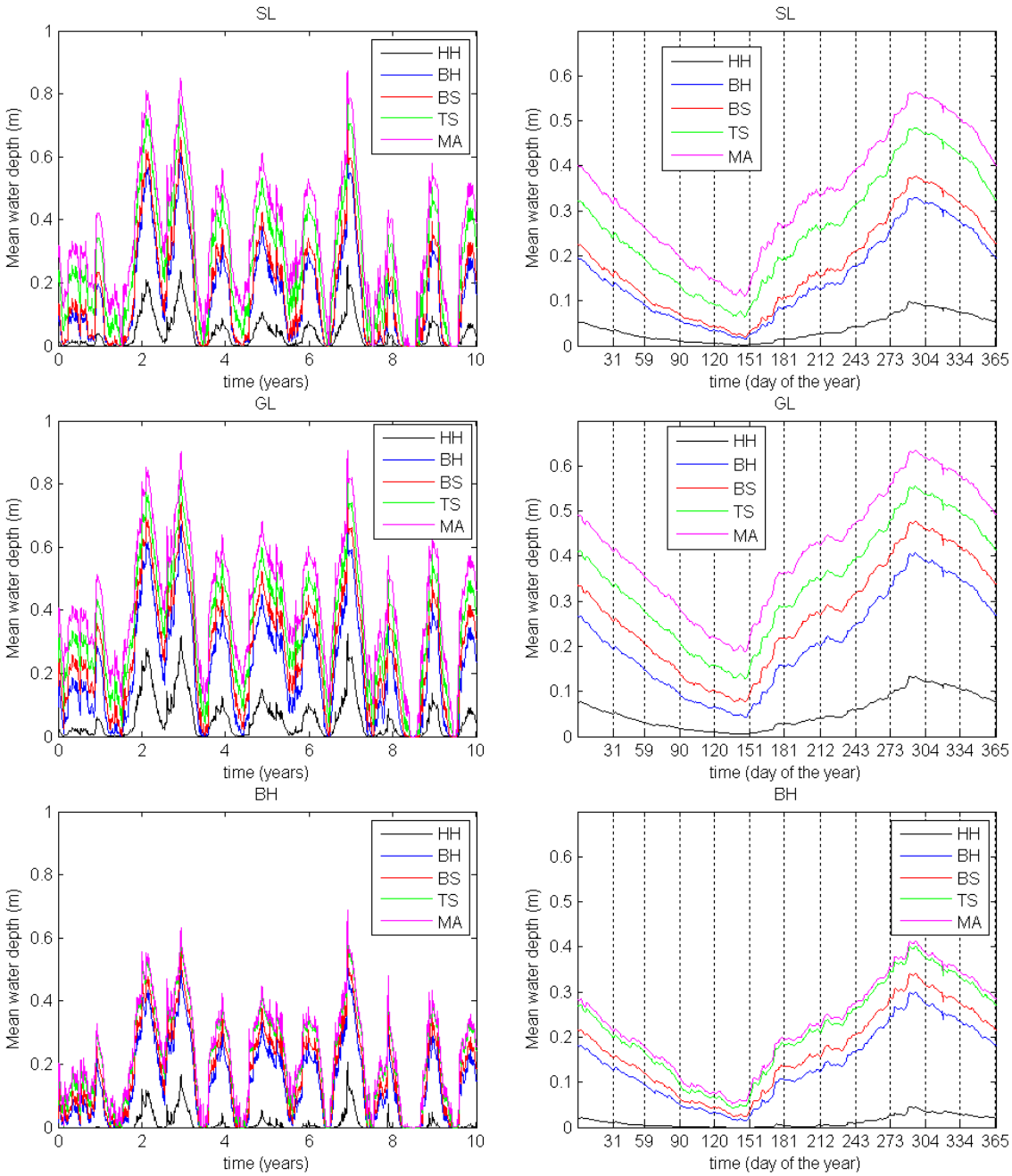

Figure A-96. On the left hand side, the evolution of the mean overland water depth averaged for each vegetation type area in case L1. On the right hand side, those values are averaged for each day of the year.

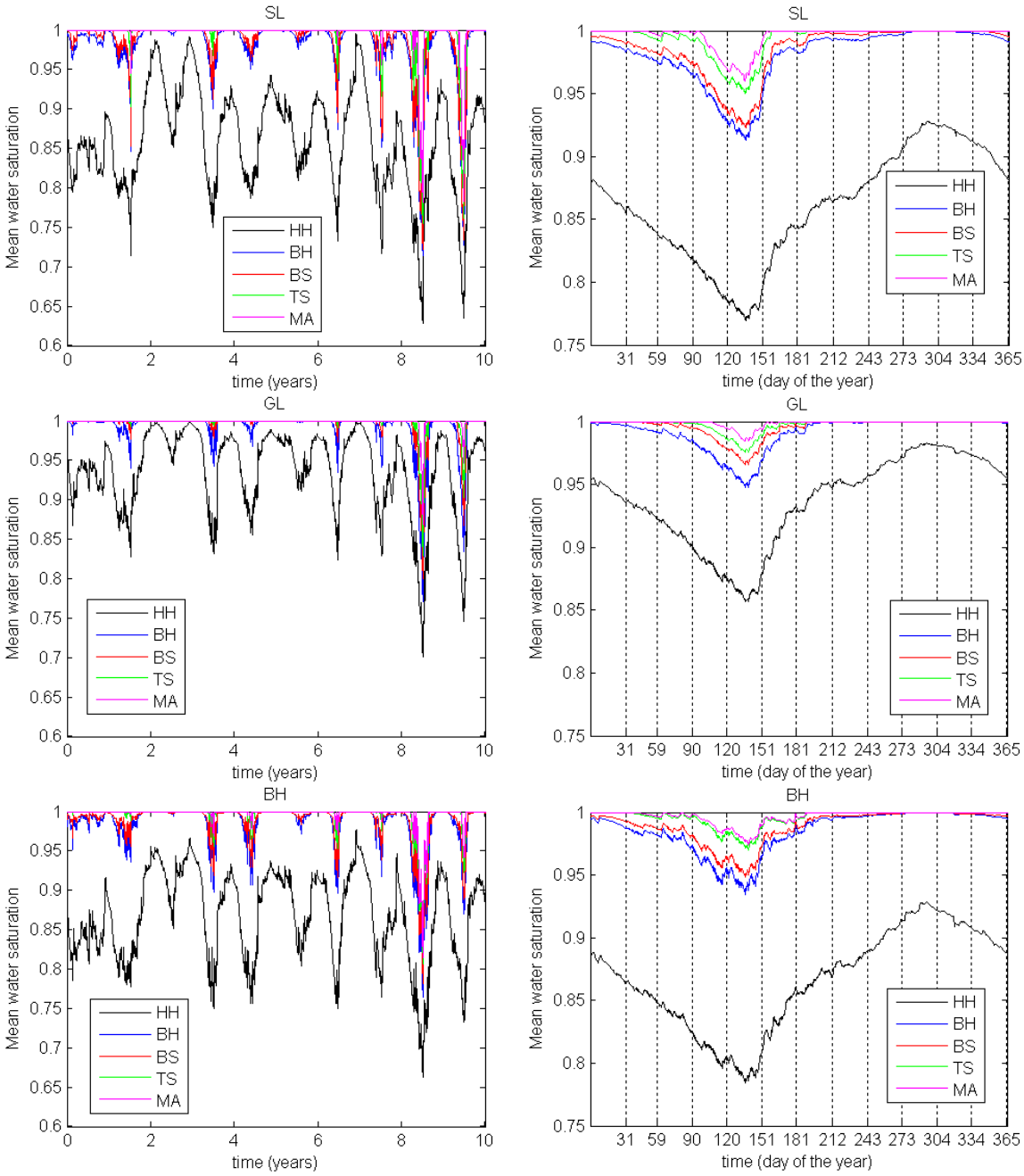

Figure A-97. On the left hand side, the evolution of the mean soil water saturation averaged for each vegetation type area in case L1. On the right hand side, those values are averaged for each day of the year.

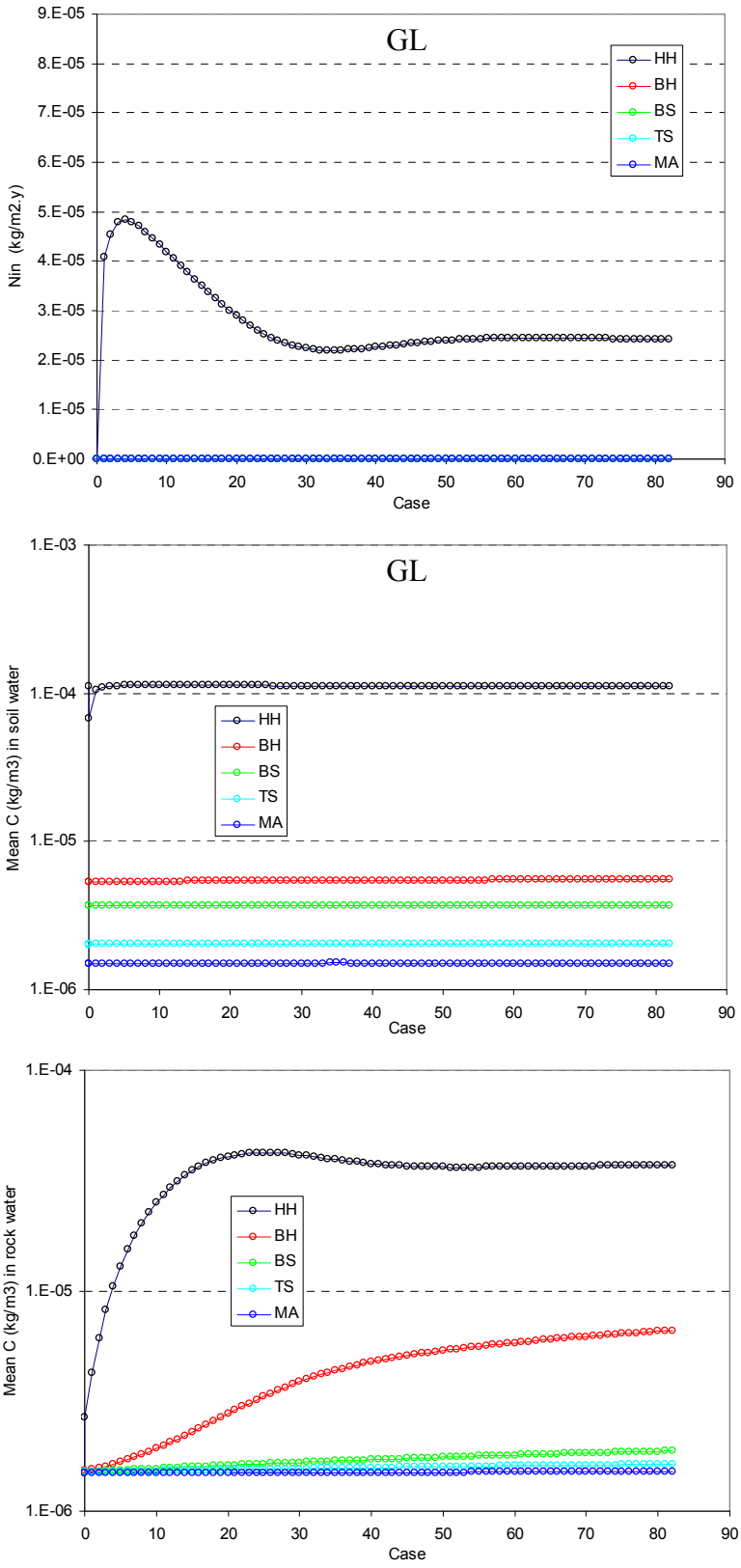

Figure A-98. Evolution of the fitted input rate (Nin) and mean concentrations in soil and rock during the iterative procedure for GL Tree Island.

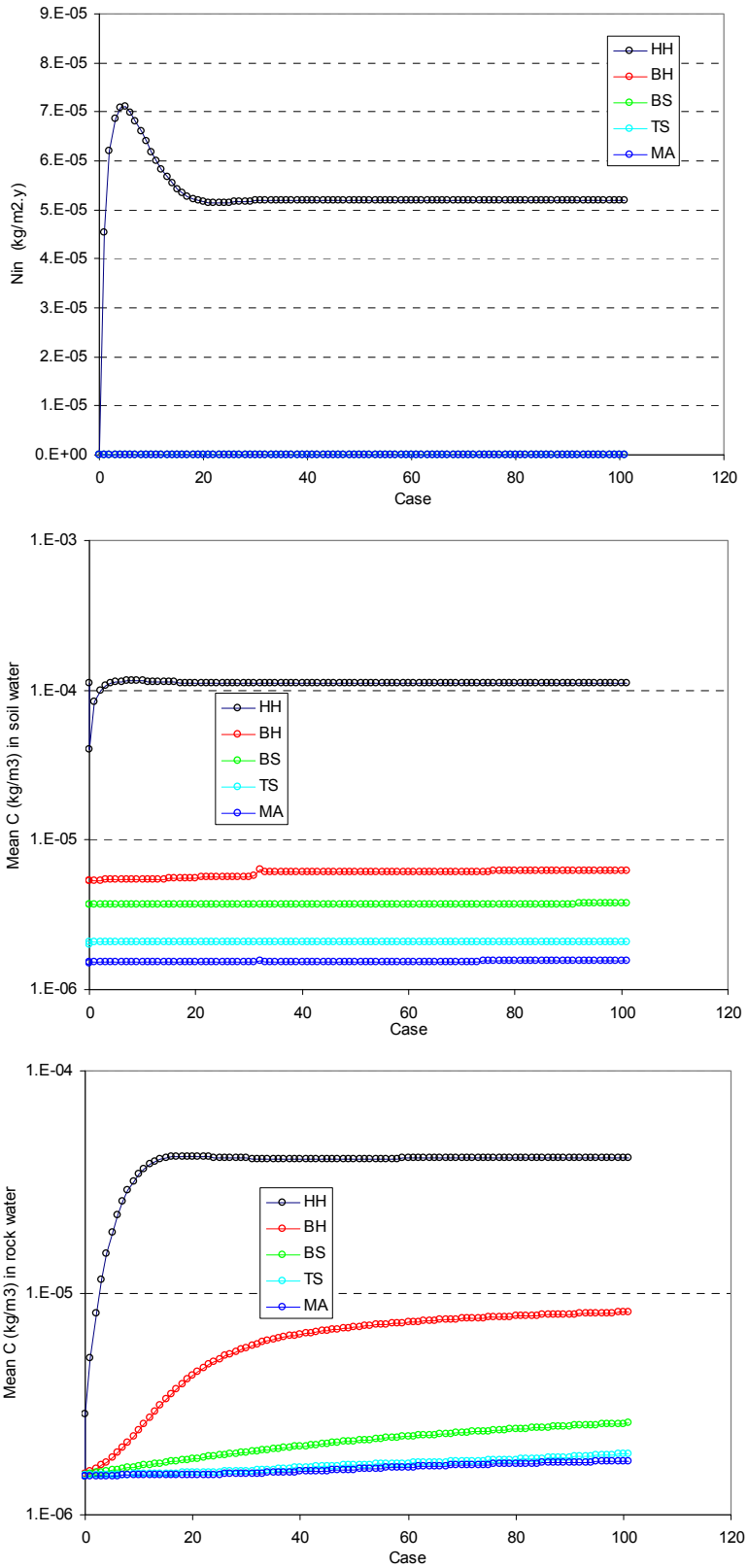

Figure A-99. Evolution of the fitted input rate (Nin) and mean concentrations in soil and rock during the iterative procedure for BH Tree Island.

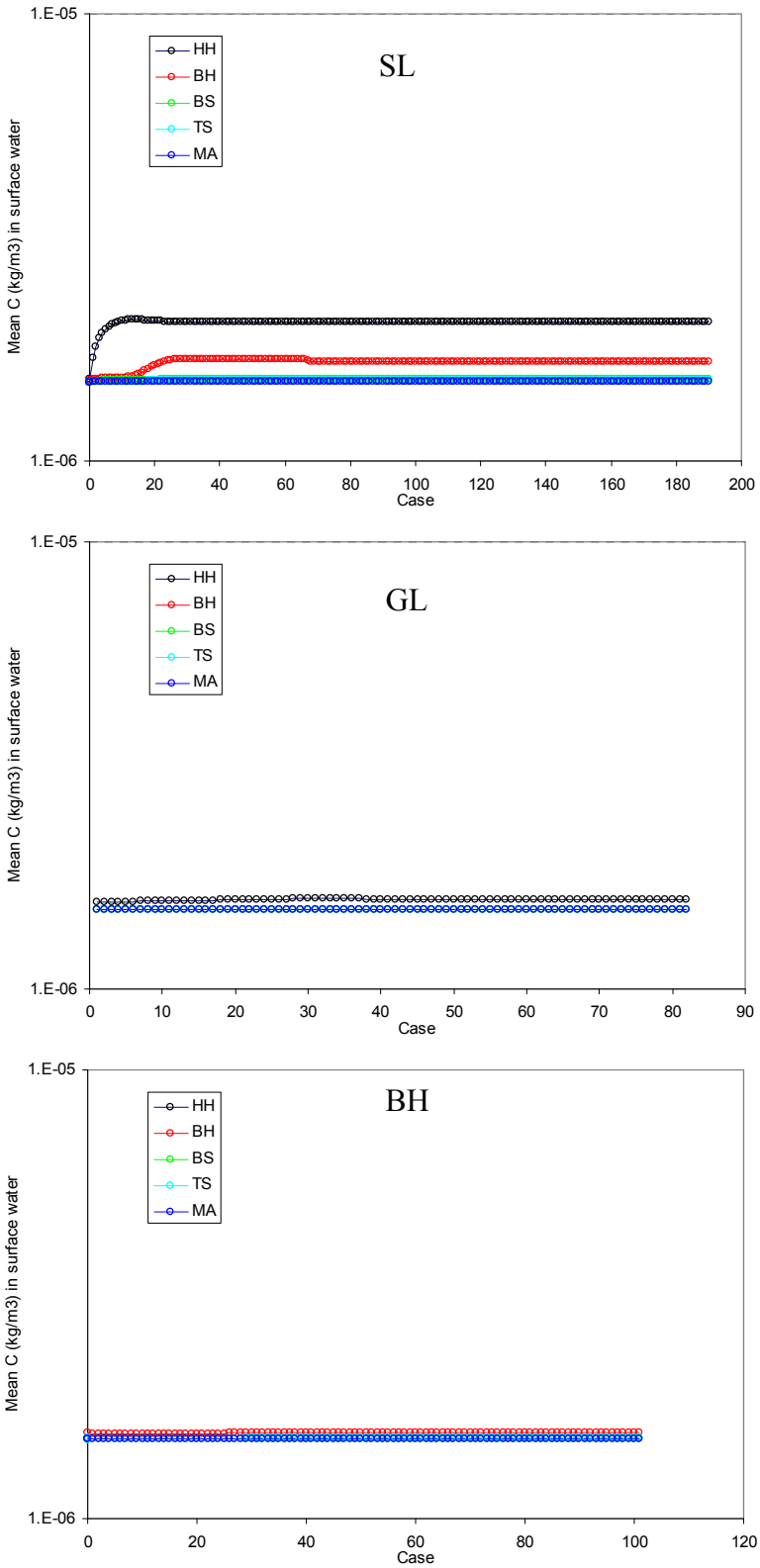

Figure A-100. Evolution of the mean surface water concentration while iterating.

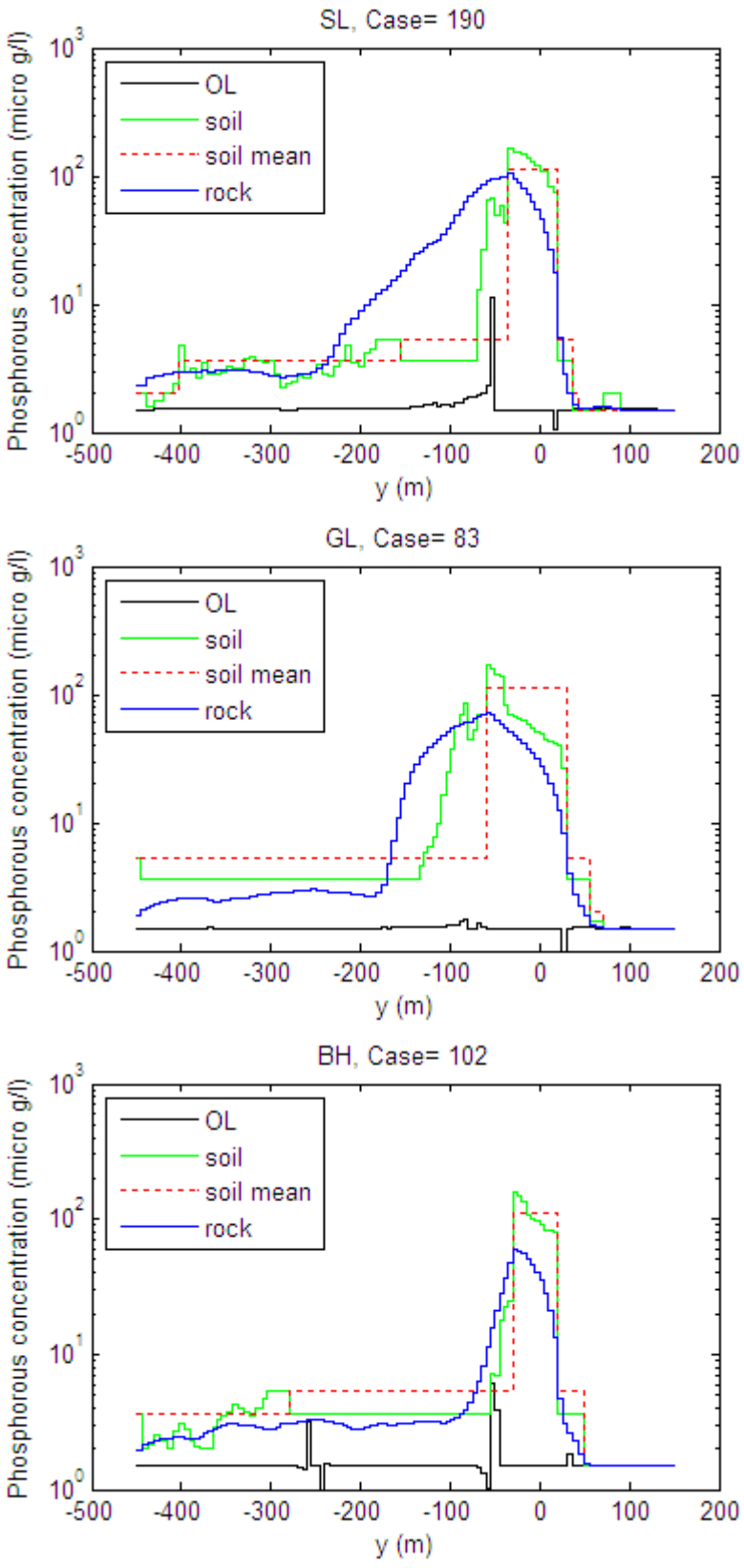

Figure A-101. Initial concentration along the tree island axes obtained from the last case run.

A4.3.3 Using the Developed Code. Additional Figures

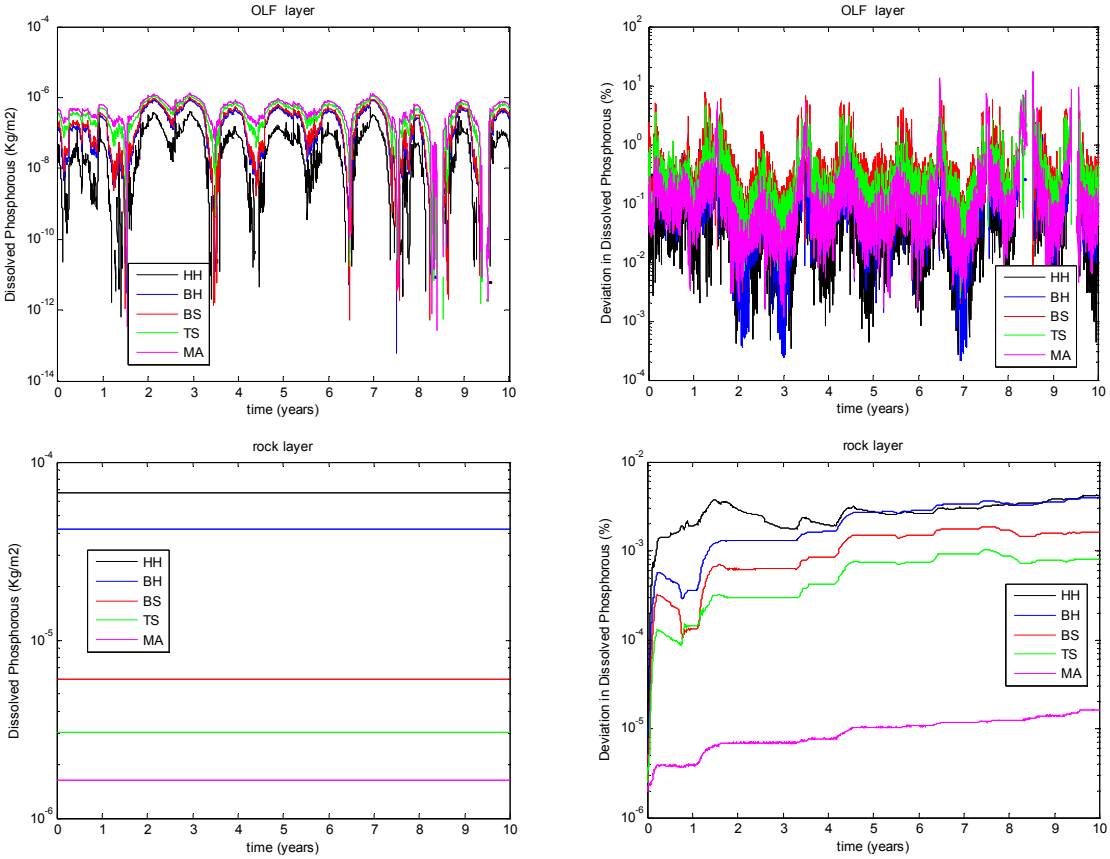

Figure A-102. On the left hand side, the 10-year evolution of the mass of dissolved Phosphorus in OL and rock layers, in different vegetation type areas of SL tree island, obtained from the MatLab code. On the right hand side, the deviations regarding the previous MODHMS results. It complements Figure 69.

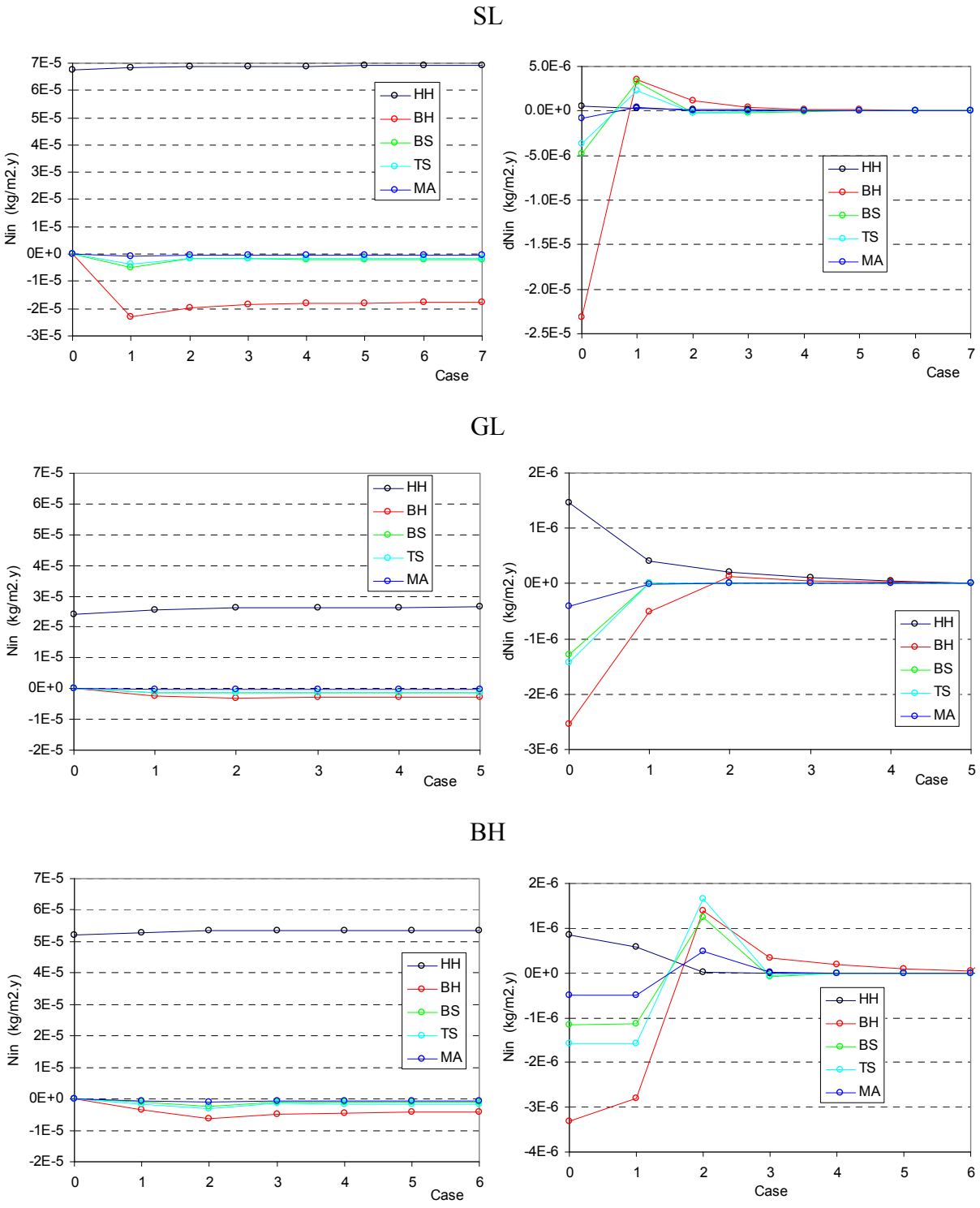

Figure A-103. Evolution of the external input rate and its variation while iterating in order to fit them for case L0.

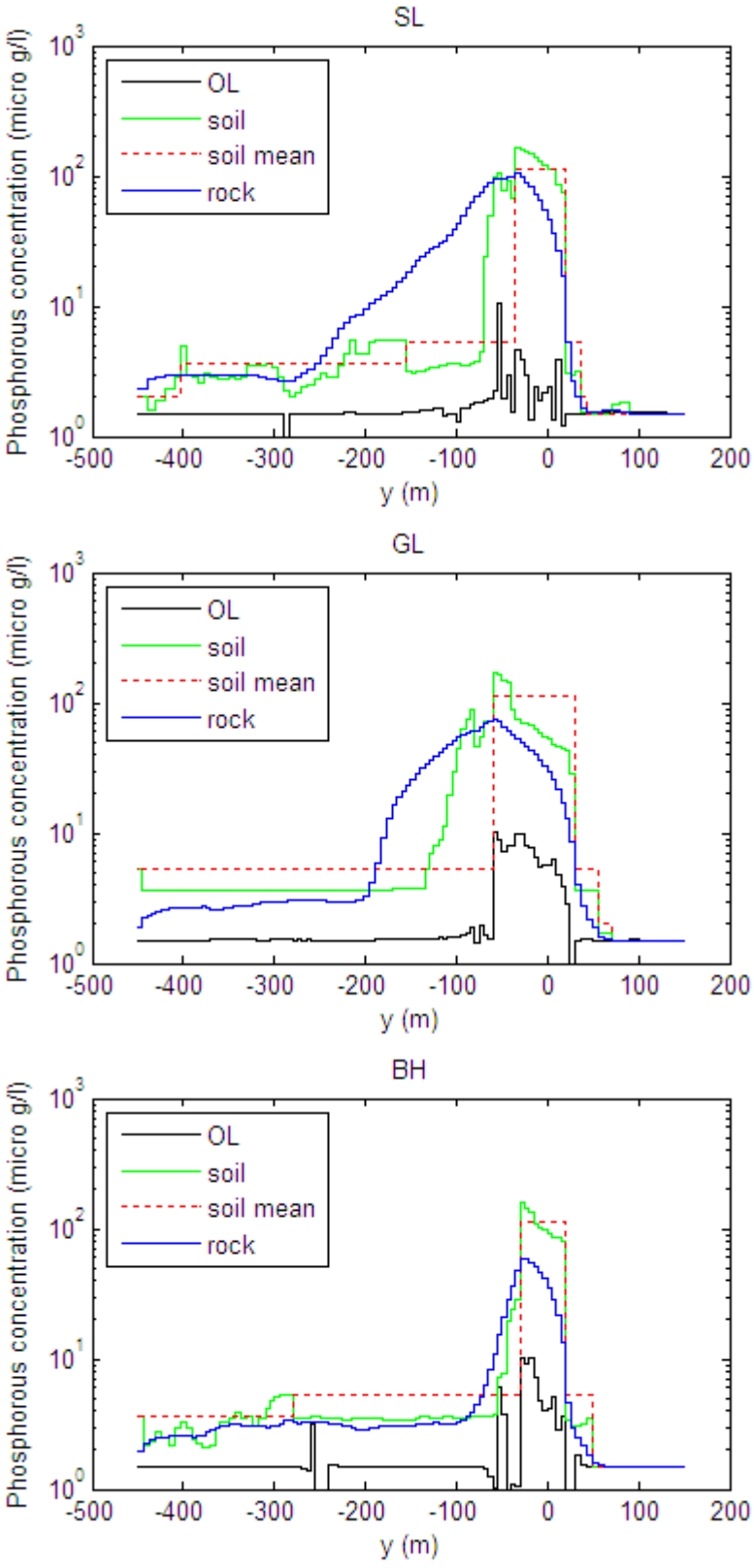

Figure A-104. Initial concentration along the tree island axes obtained from the last run for case L0.

Appendix 5. Addendum for Chapter 5

A5.1 Solving the Full Set of Equations

A5.1.1 Net Phosphorus Release Rate from Biomass. Additional Figures

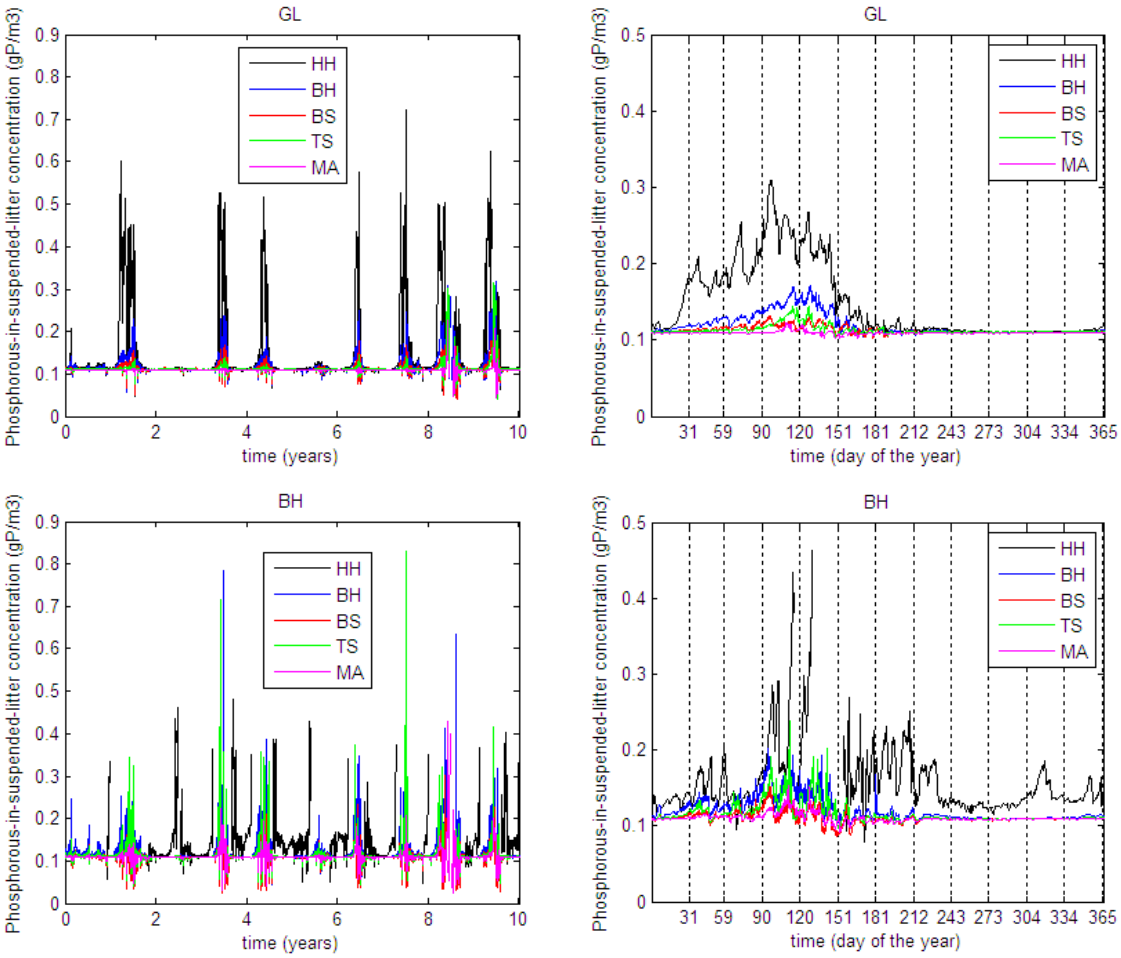

Figure A-105. On the left hand side, the evolution of the Phosphorus-in-suspended litter concentration (C_L) averaged for each vegetation type area in case L1. On the right hand side, those values are averaged for each day of the year. Complement to Figure 73.

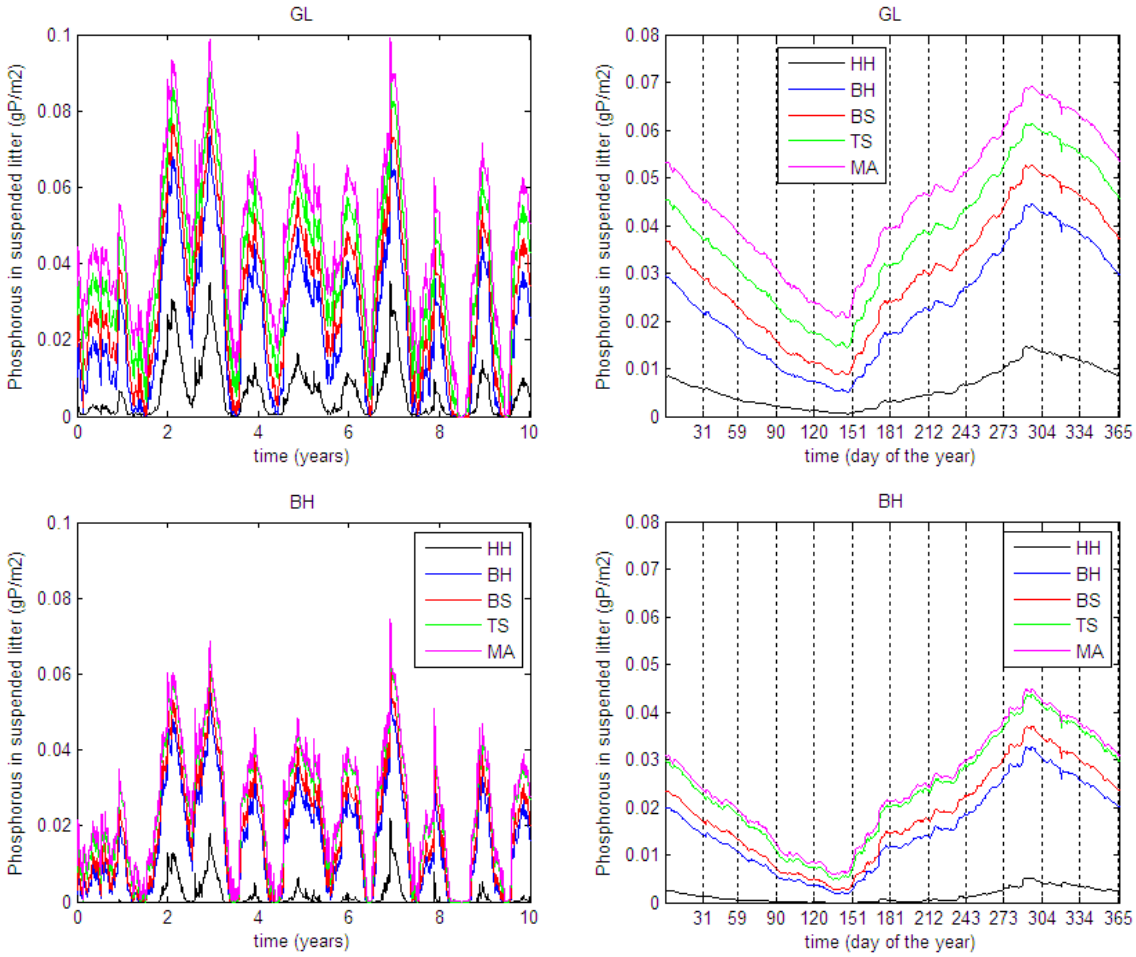

Figure A-106. On the left hand side, the evolution of the mass per unit area ($C_L h$) of Phosphorus in suspended litter averaged for each vegetation type area in case L1. On the right hand side, those values are averaged for each day of the year. Complement to Figure 74.

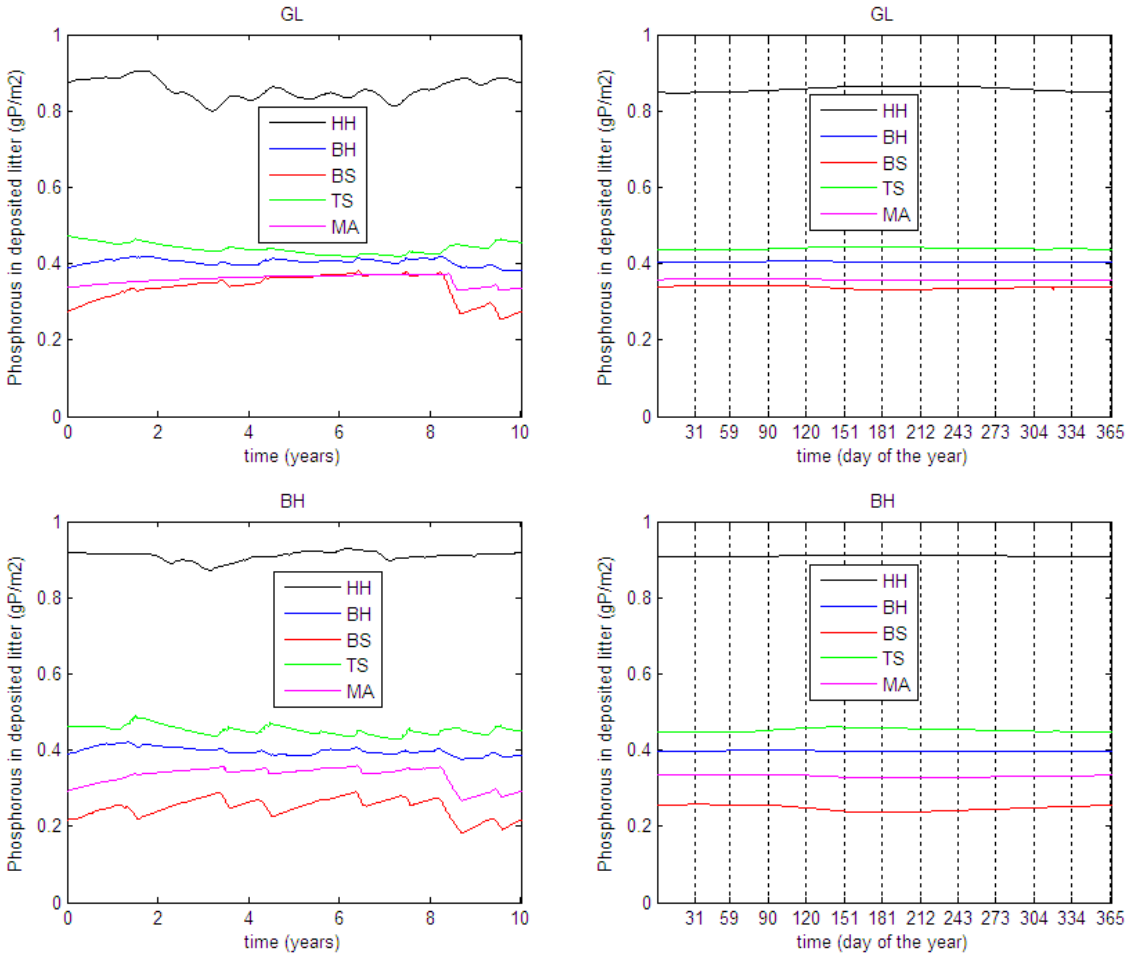

Figure A-107. On the left hand side, the evolution of the Phosphorus-in-deposited litter (L) averaged for each vegetation type area in case L1. On the right hand side, those values are averaged for each day of the year. Complement to Figure 75.

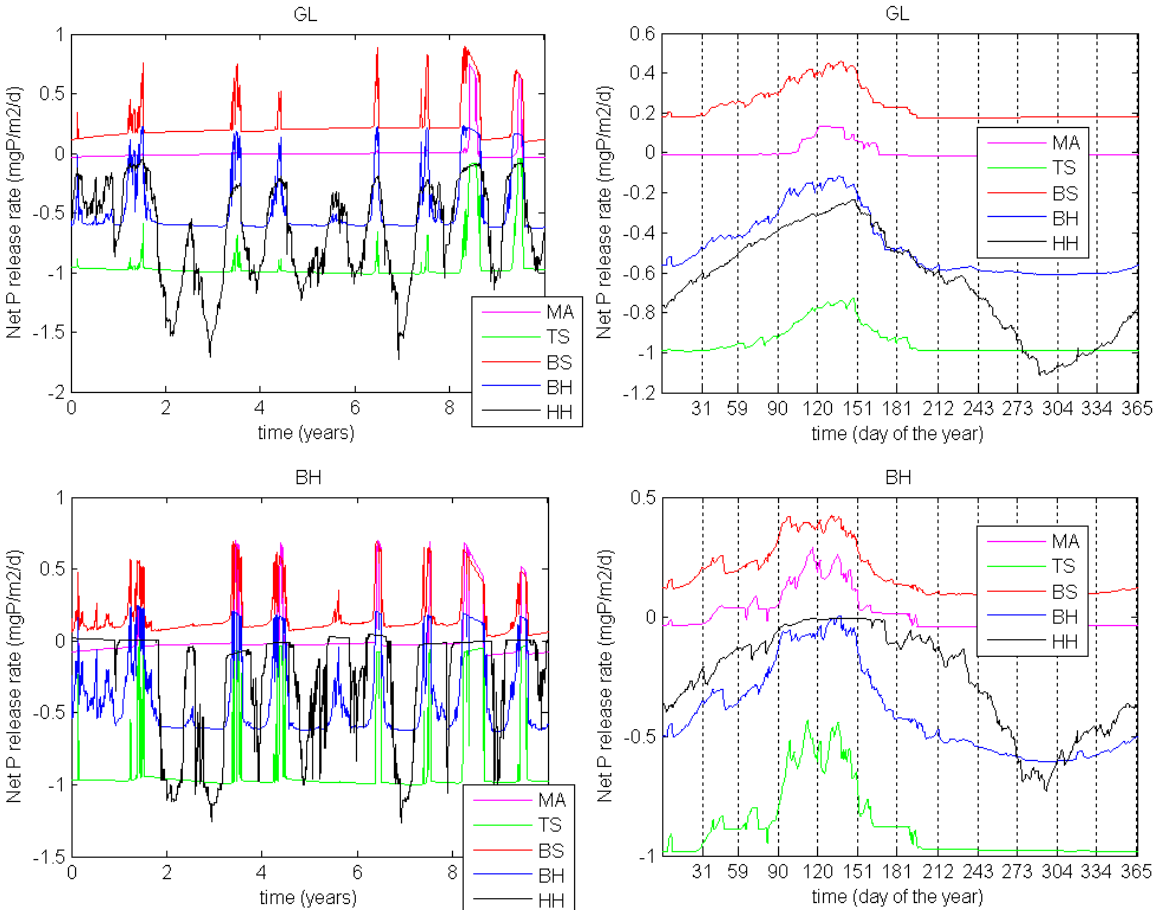

Figure A-108. On the left hand side, the evolution of the net release rate of Phosphorus (R_{dec} - ε_{Lprod}) averaged for each vegetation type area in case L1. On the right hand side, those values are averaged for each day of the year. Complement to Figure 76.

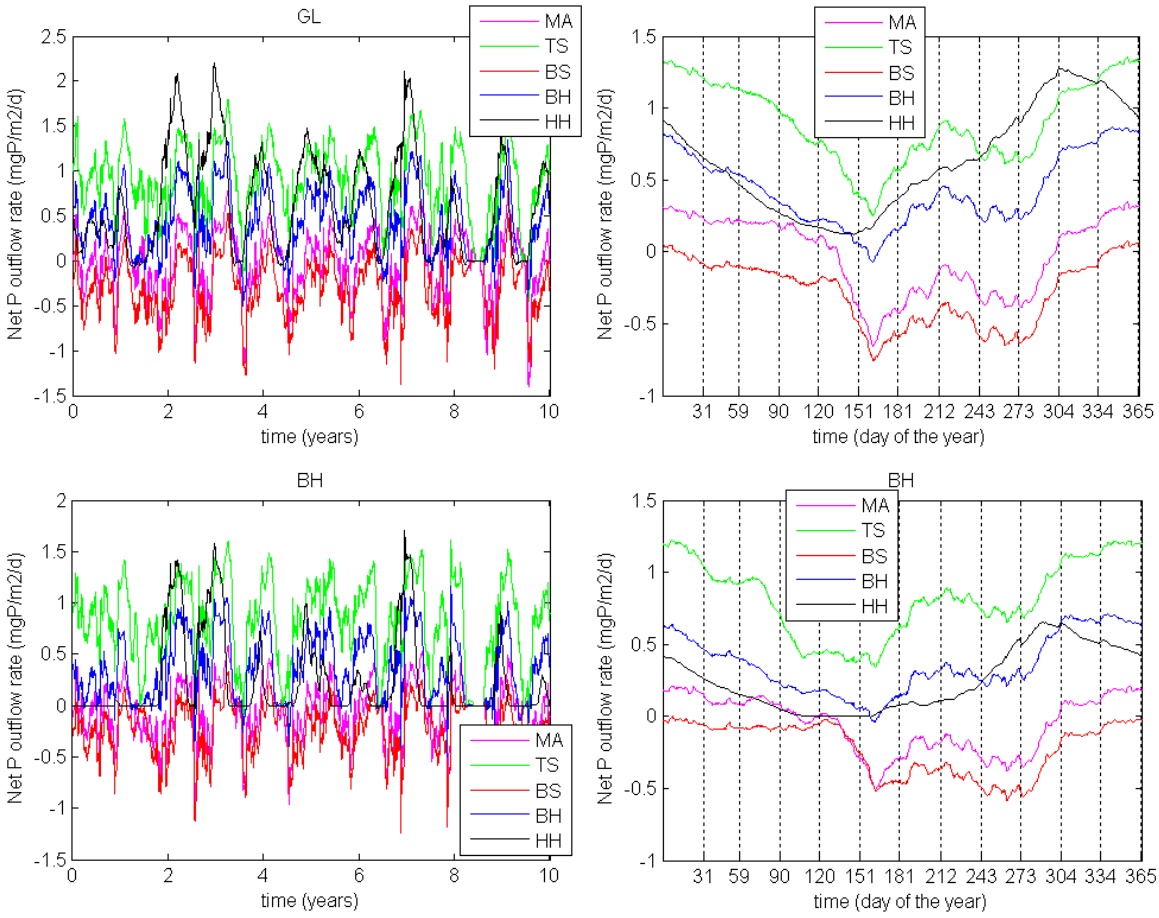

Figure A-109. On the left hand side, the evolution of the net outflow rate of Phosphorus averaged for each vegetation type area in case L1. On the right hand side, those values are averaged for each day of the year. In both cases, a running average with a 30-days window was performed. Complement to Figure 77.

A5.1.2 Estimation of External Input Rate. Additional Figures

Additional figures to section 5.1.2 are presented below.

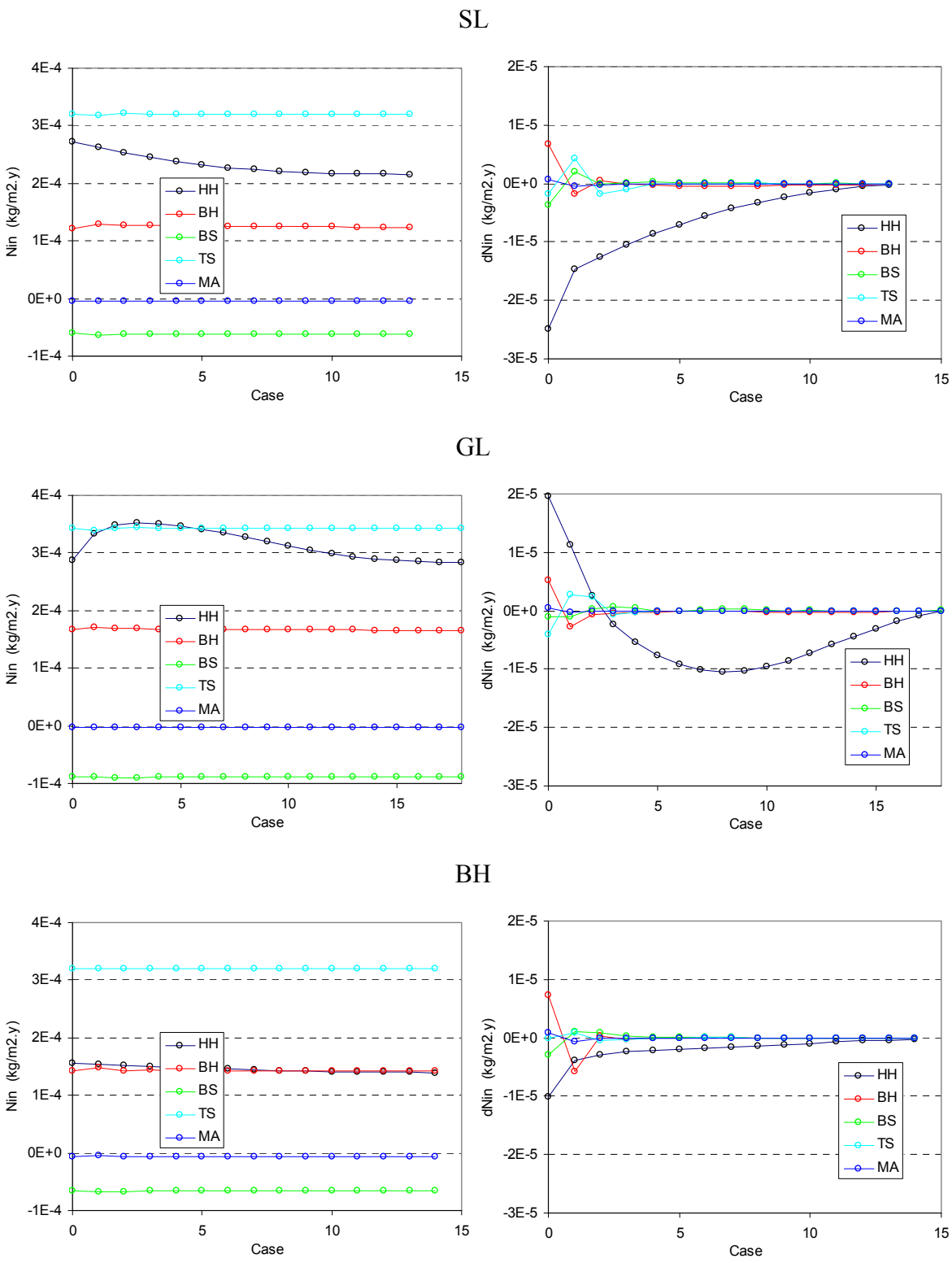

Figure A-110. Evolution of the external input rate and its variation while iterating in order to fit them for case L1.

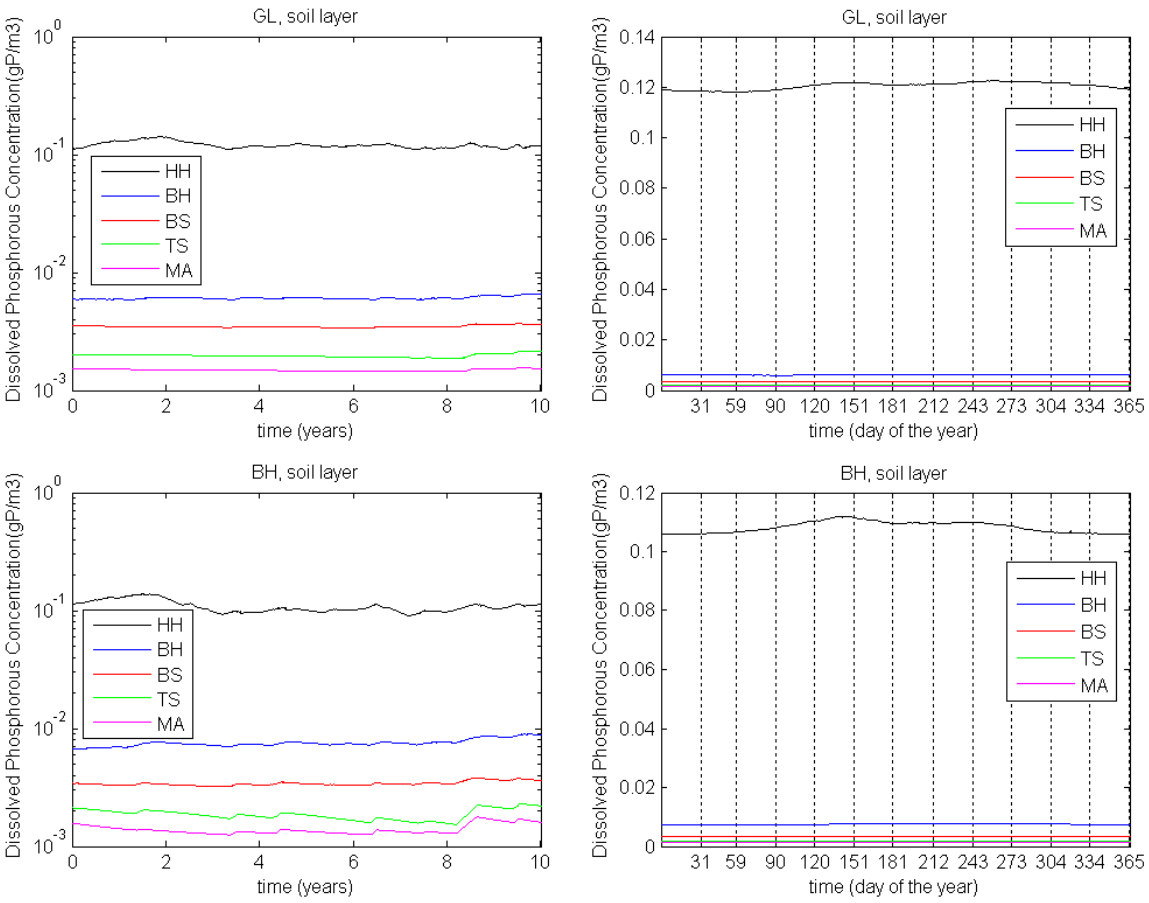

Figure A-111. On the left hand side, the evolution of the dissolved Phosphorus concentration (C) in soil layer averaged for each vegetation type area in case L1. On the right hand side, those values are averaged for each day of the year. Complement to Figure 80.

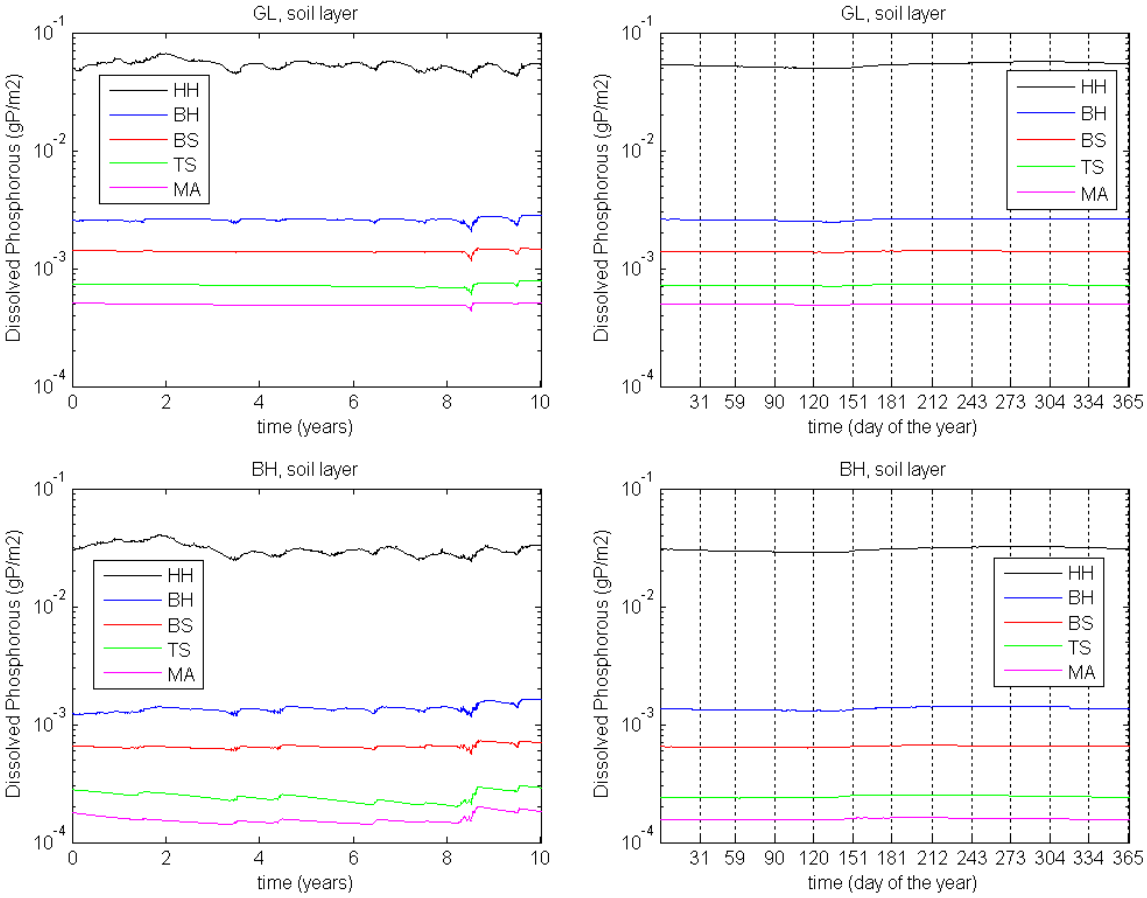

Figure A-112. On the left hand side, the evolution of the mass of dissolved Phosphorus per unit area (*Ch*) in soil layer averaged for each vegetation type area in case L1. On the right hand side, those values are averaged for each day of the year. Complement to Figure 81.

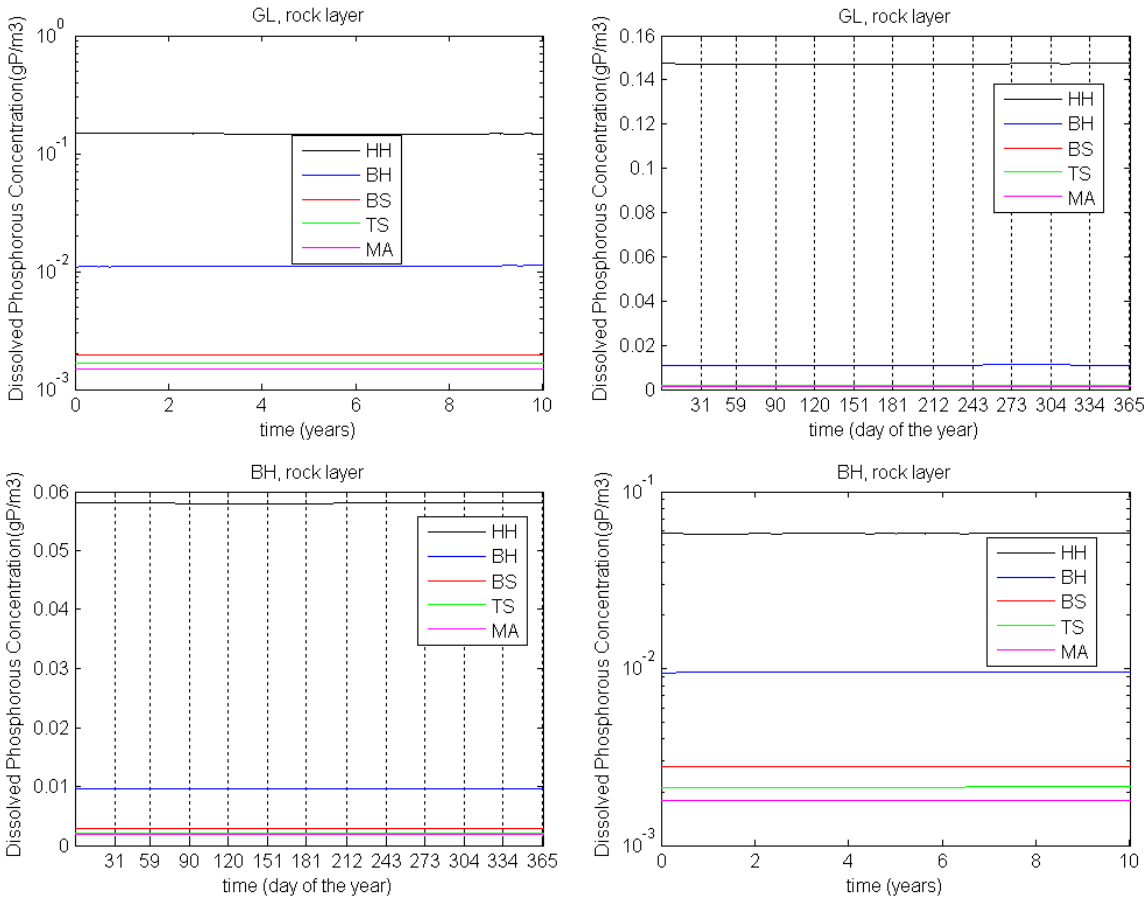

Figure A-113. On the left hand side, the evolution of the dissolved Phosphorus concentration (C) in rock layer averaged for each vegetation type area in case L1. On the right hand side, those values are averaged for each day of the year. Complement to Figure 82.

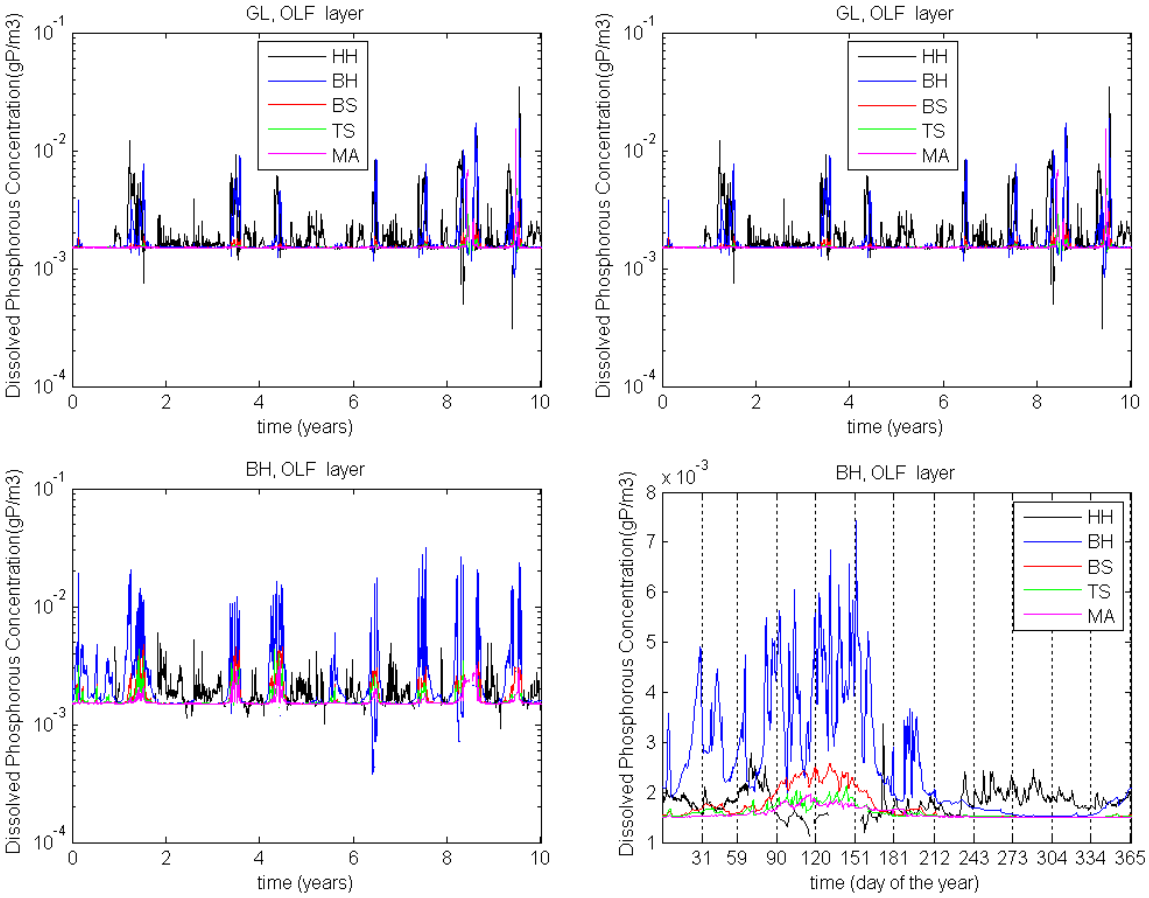

Figure A-114. On the left hand side, the evolution of the dissolved Phosphorus concentration (C) in OL layer averaged for each vegetation type area in case L1. On the right hand side, those values are averaged for each day of the year. Complement to Figure 83.

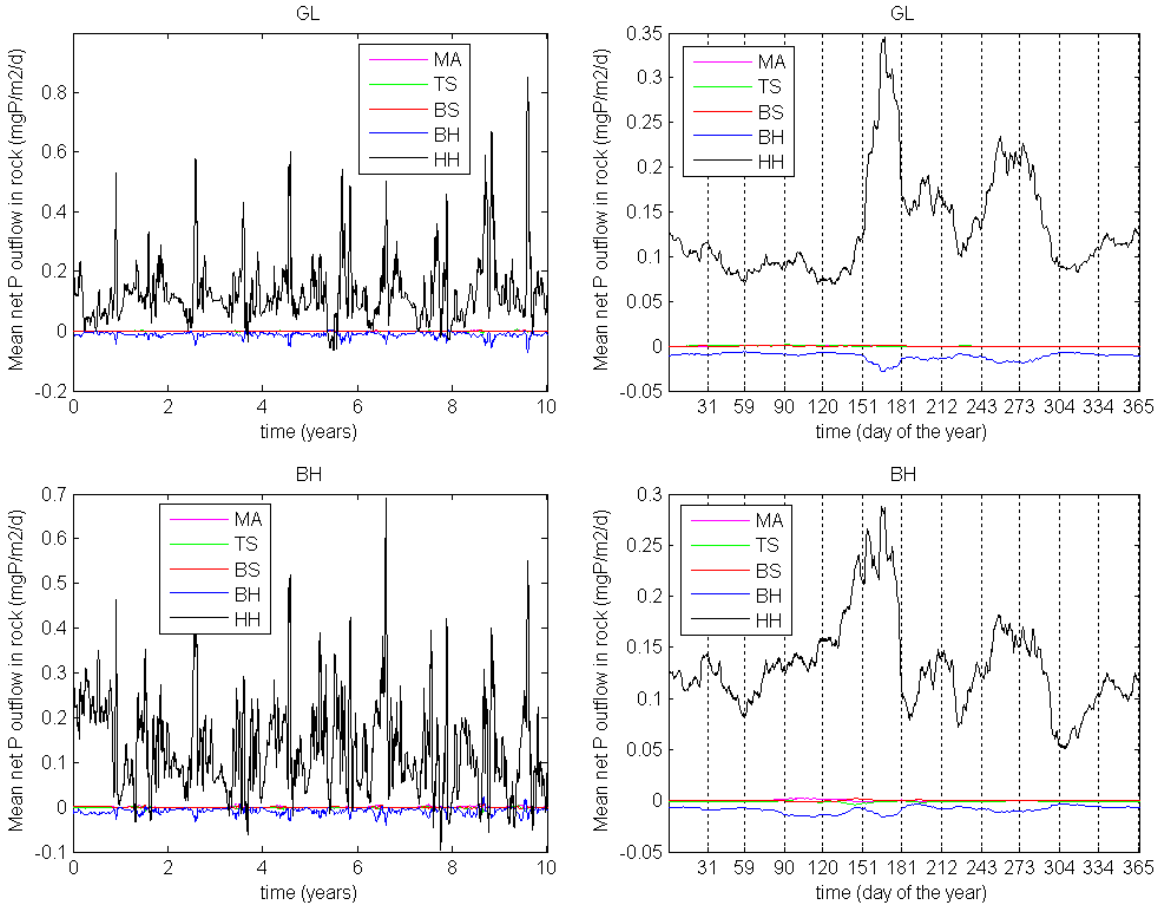

Figure A-115. On the left hand side, the evolution of the net dissolved Phosphorus outflow in the rock layer averaged for each vegetation type area in case L1. On the right hand side, those values are averaged for each day of the year. In both cases, a running average with a 15-days window was performed. Complement to Figure 84.

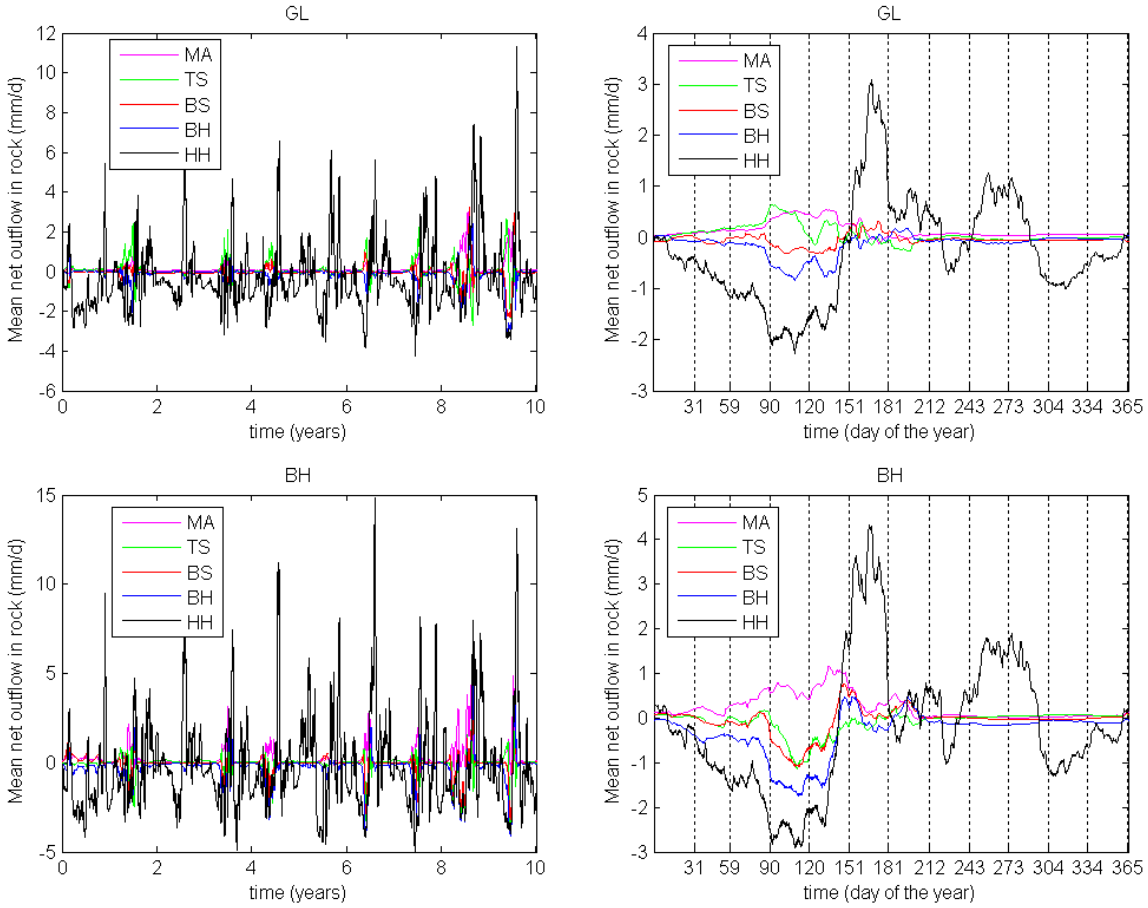

Figure A-116. On the left hand side, the evolution of the net water outflow in the rock layer averaged for each vegetation type area in case L1. On the right hand side, those values are averaged for each day of the year. In both cases, a running average with a 15-days window was performed. Complement to Figure 85.

A5.1.3 Additional Pool and Fluxes Figures

The following pool and fluxes diagrams were obtained from the final model (case L1) after a 10 year simulation for each tree island. Pool volume or mass values for each layer and vegetation type are presented in black and correspond to the end of the simulation. They are normalized by unit horizontal area and have units of in mm and in mgP/m^2 for water and Phosphorus, respectively. Volume and mass flux values are also presented and they correspond to annual averaged values over the ten years. Annual fluxes are also normalized by unit horizontal area and have units of mm/day and $mgP/m^2/day$ for water and Phosphorus, respectively. In the diagrams, blue is used for water, red for Phosphorus (dissolved or adsorbed) and green for Phosphorus in biomass (live or dead). Colored numbers inside the pools correspond to the 10-year annual change rates in the pools, which should be equal to the total incoming fluxes. The difference between those two values (volume or mass balance error per unit area and time) is shown in gray near by the pools. Solid arrows correspond to advective and diffusive fluxes and dashed arrows to processes and sources.

The diagrams are presented for SL, GL and BH tree islands, in that order. Inside each tree island, the diagrams are presented at each vegetation type area in the order HH, BH, BS, TS and MA. Most of the information in those diagrams has been previously presented in Figure 67, Figure 72 and Figure 79. The main difference here is that the diagrams looks similar to the conceptual model diagram in Figure 6 for each vegetation type area. Moreover, the diagram showing the total pools and fluxes for the whole tree island areas are also included.

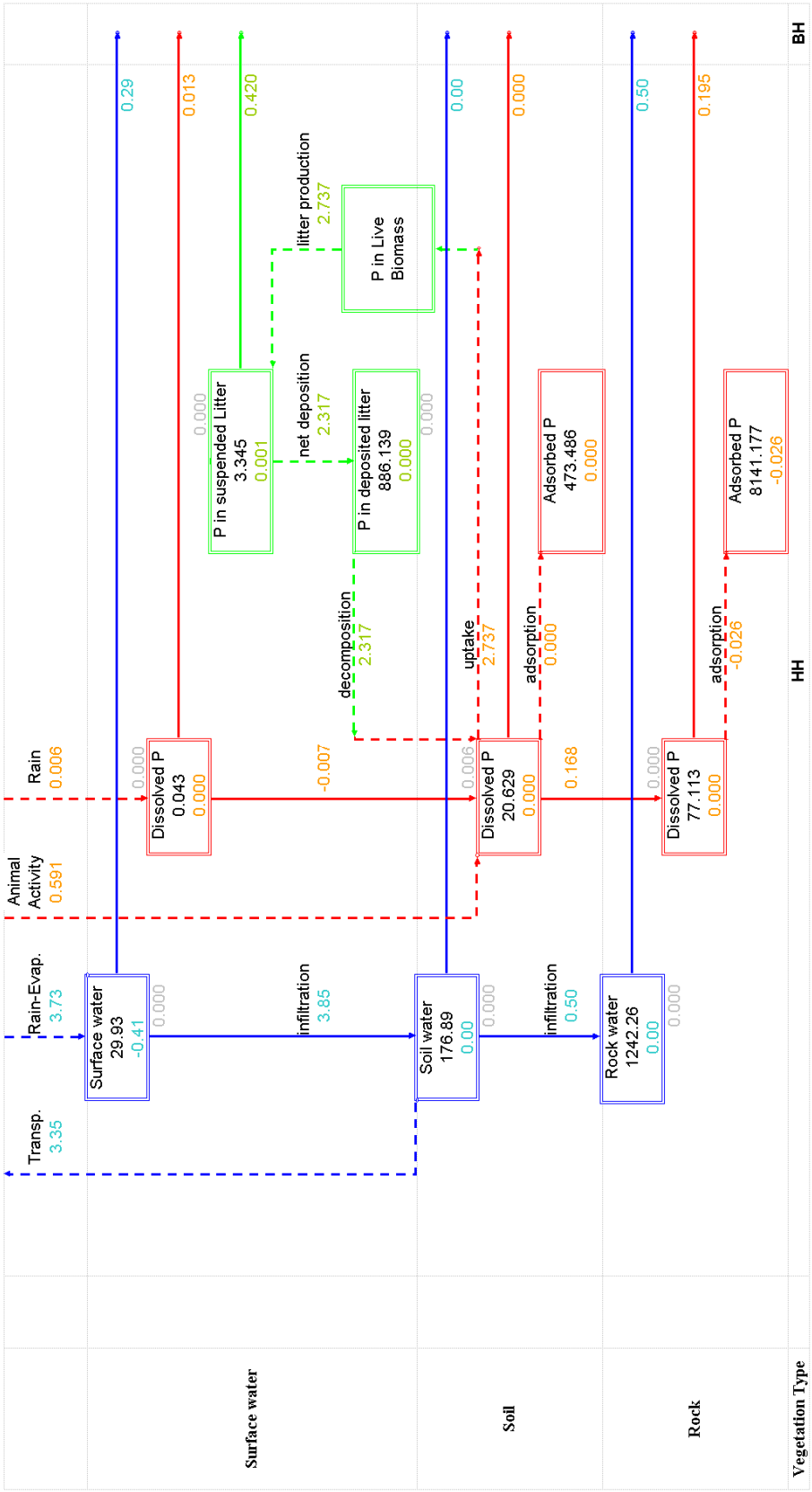

Figure A-117. Pools and fluxes representation for HH area in SL tree island.

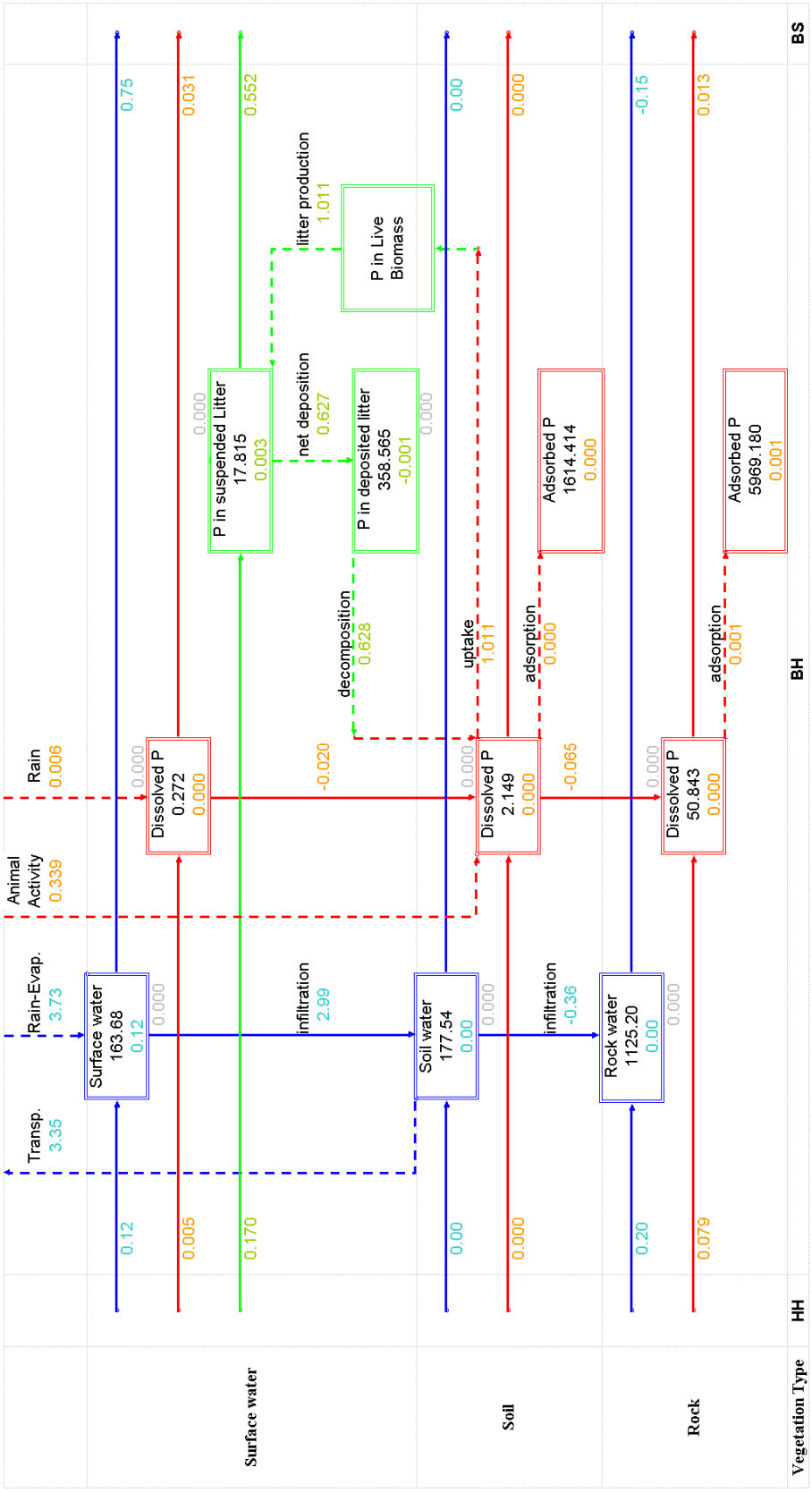

Figure A-118. Pools and fluxes representation for BH area in SL tree island.

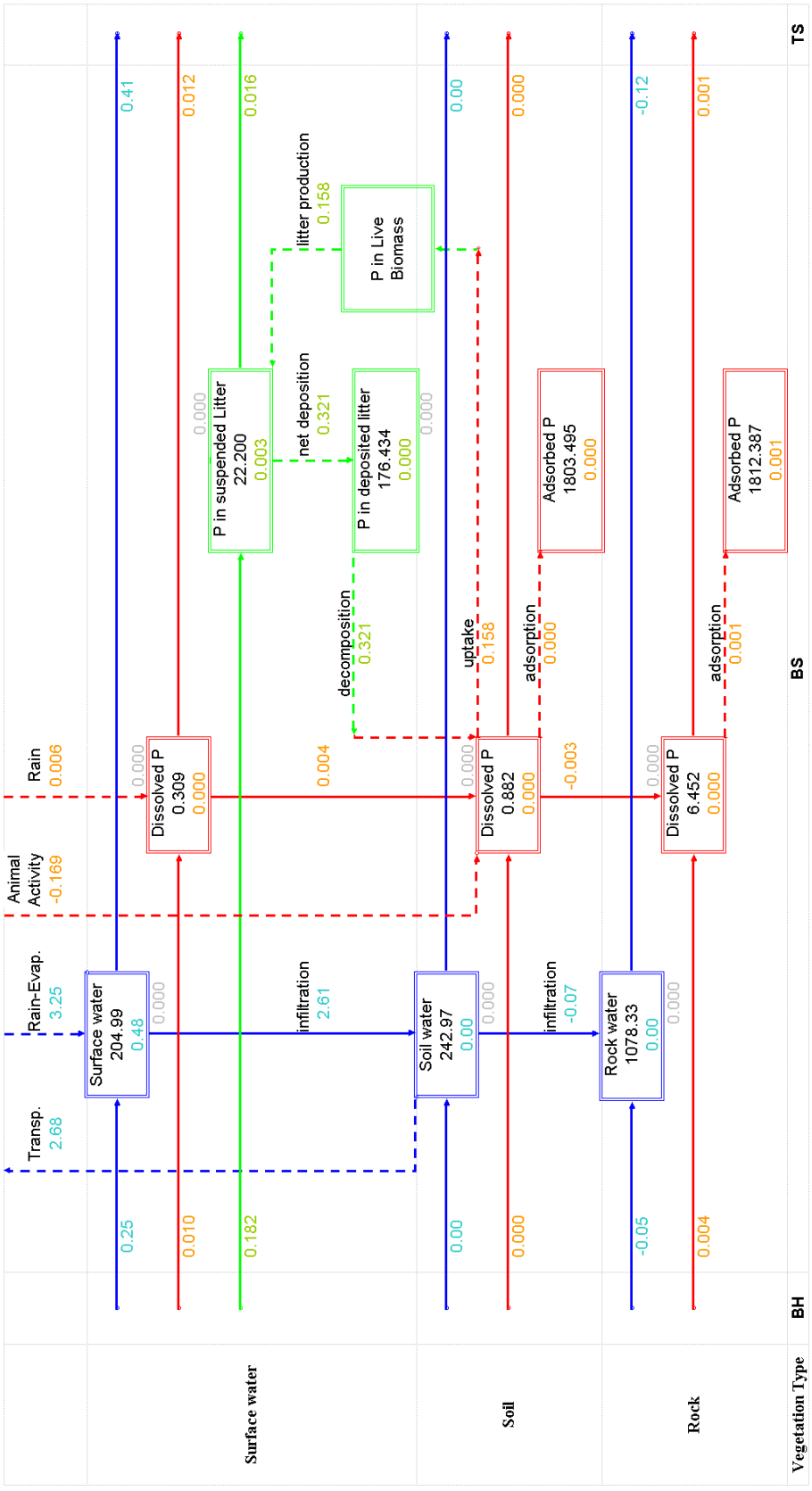

Figure A-119. Pools and fluxes representation for BS area in SL tree island.

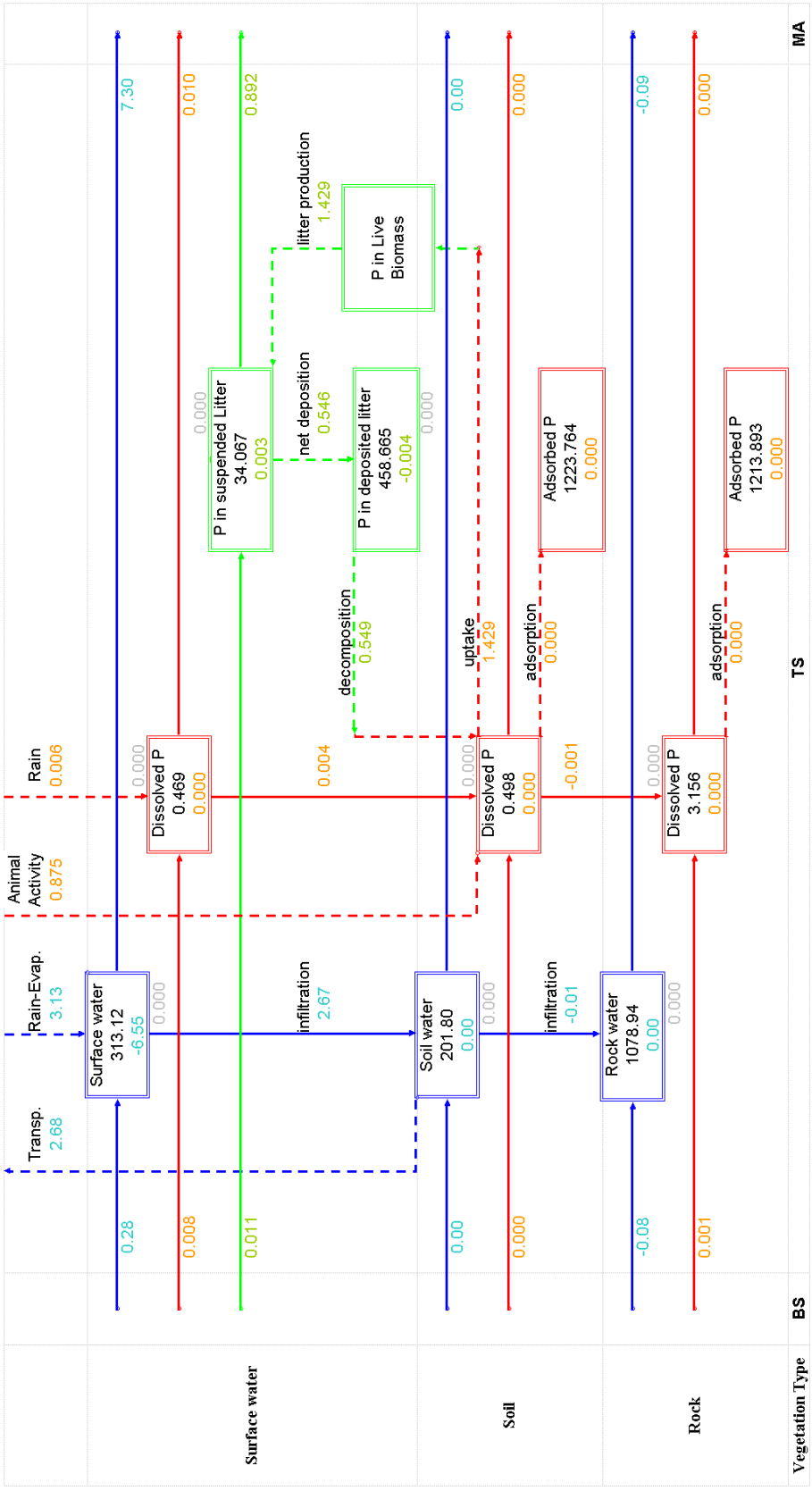

Figure A-120. Pools and fluxes representation for TS area in SL tree island.

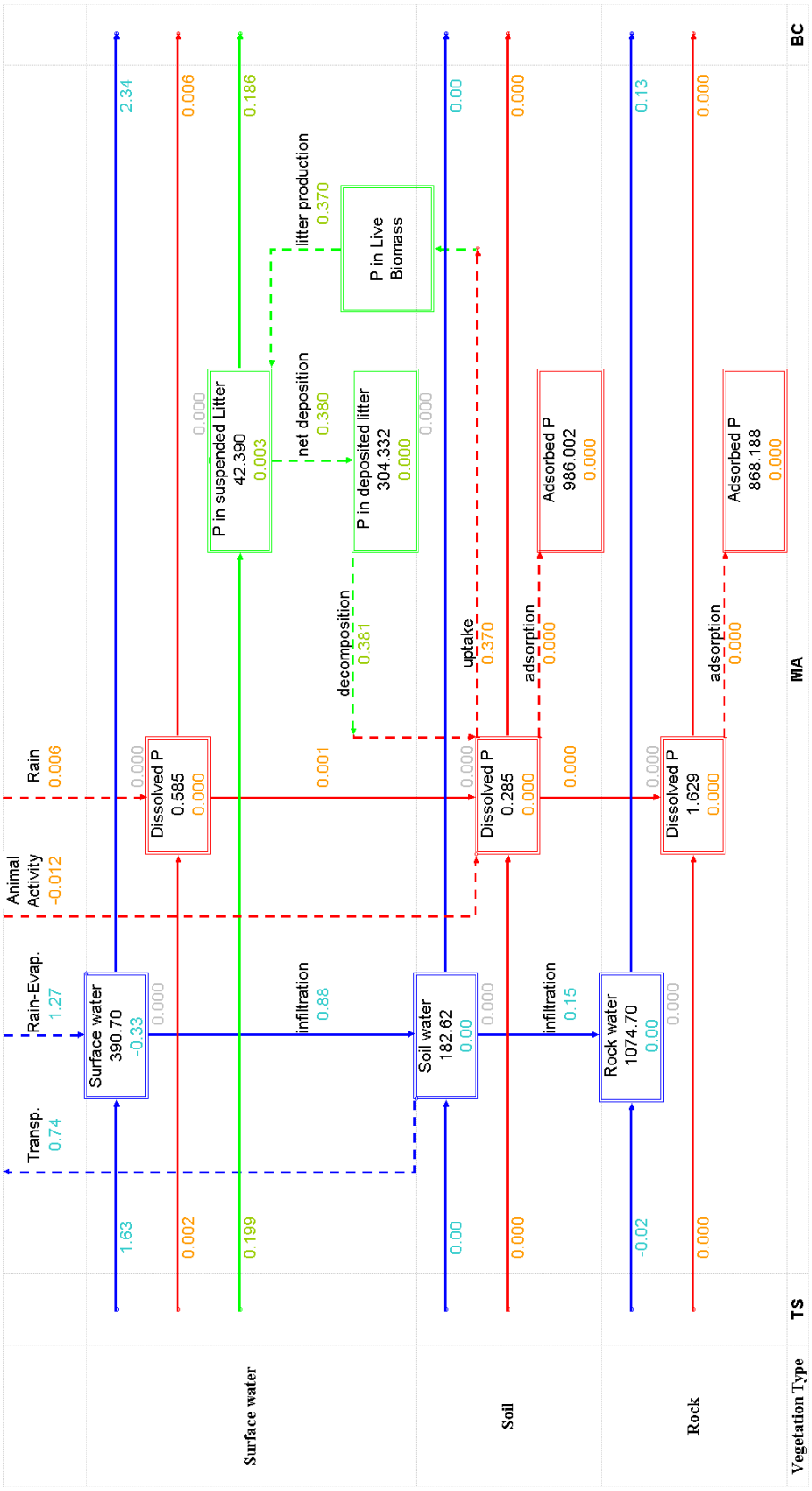

Figure A-121. Pools and fluxes representation for MA area in SL tree island.

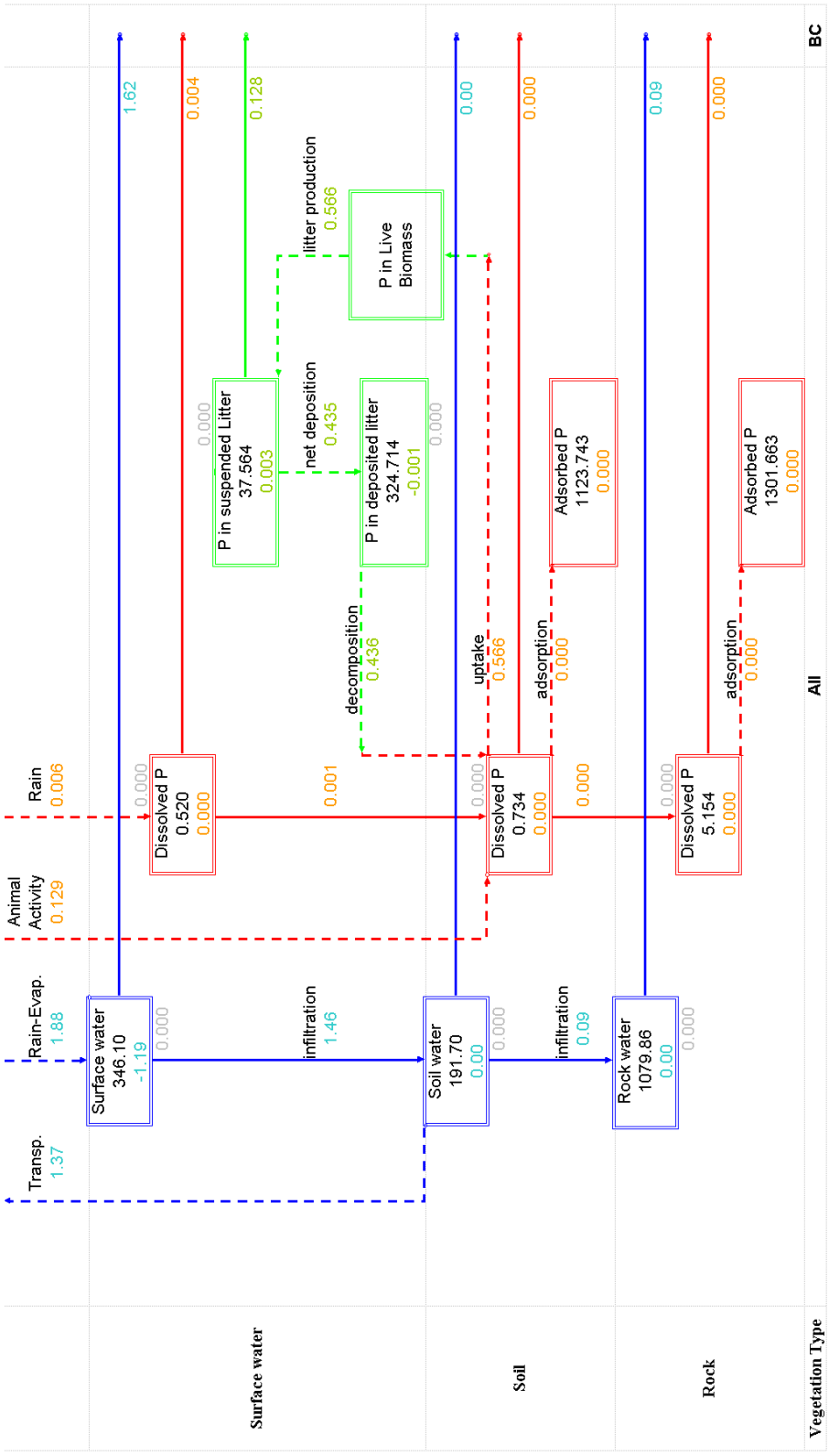

Figure A-122. Pools and fluxes representation for whole model area in SL tree island.

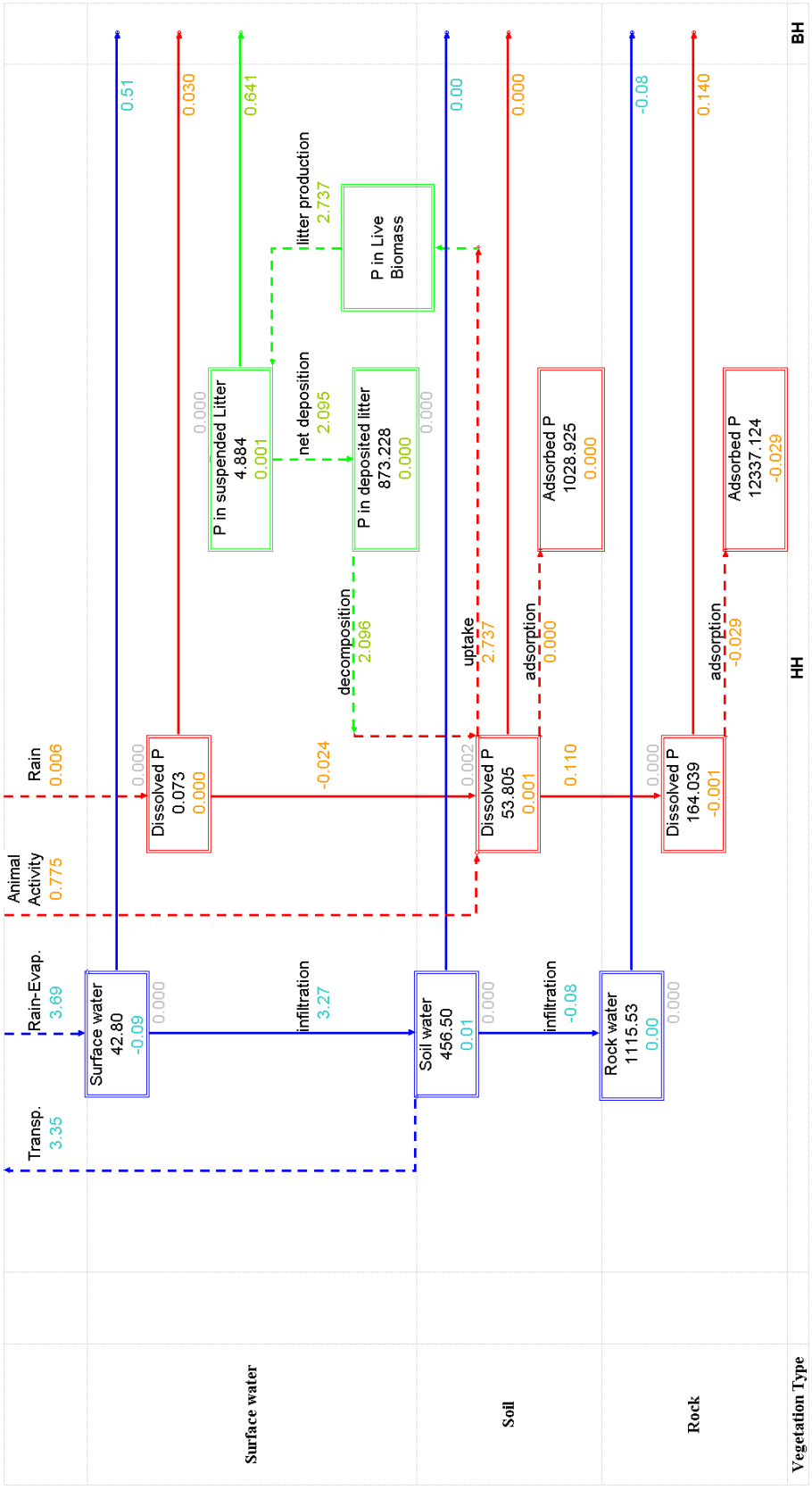

Figure A-123. Pools and fluxes representation for HH area in GL tree island.

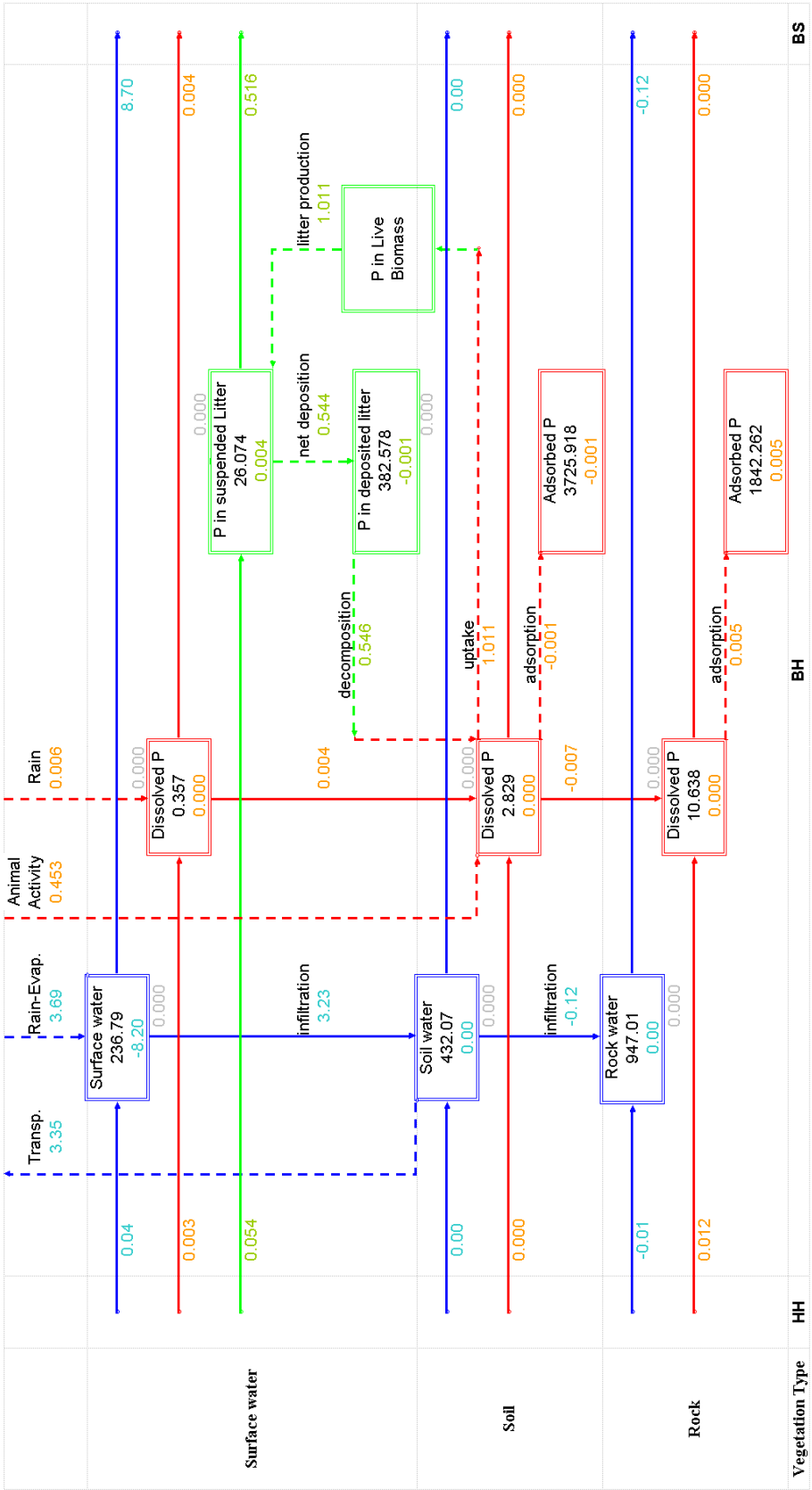

Figure A-124. Pools and fluxes representation for BH area in GL tree island.

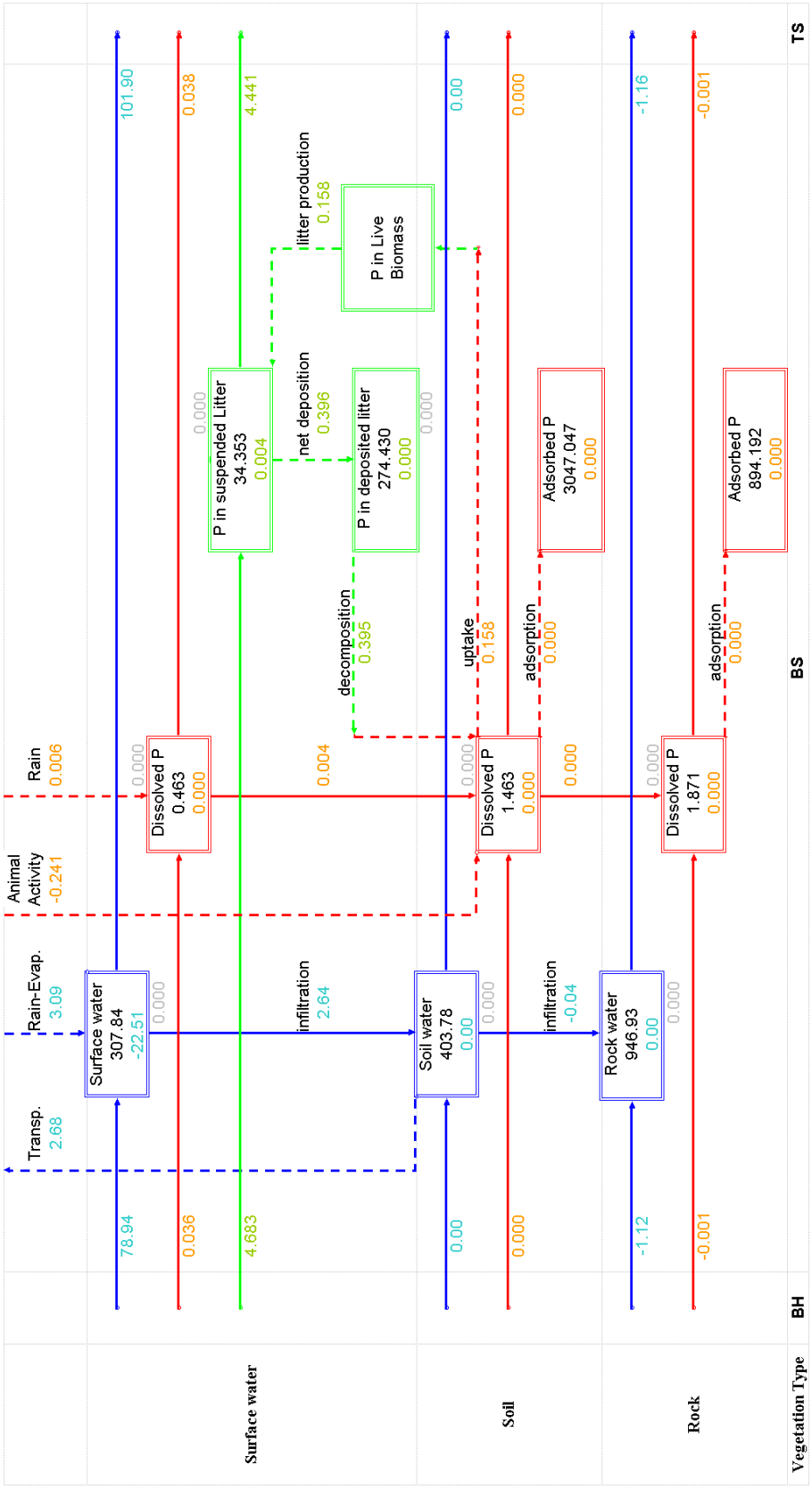

Figure A-125. Pools and fluxes representation for BS area in GL tree island.

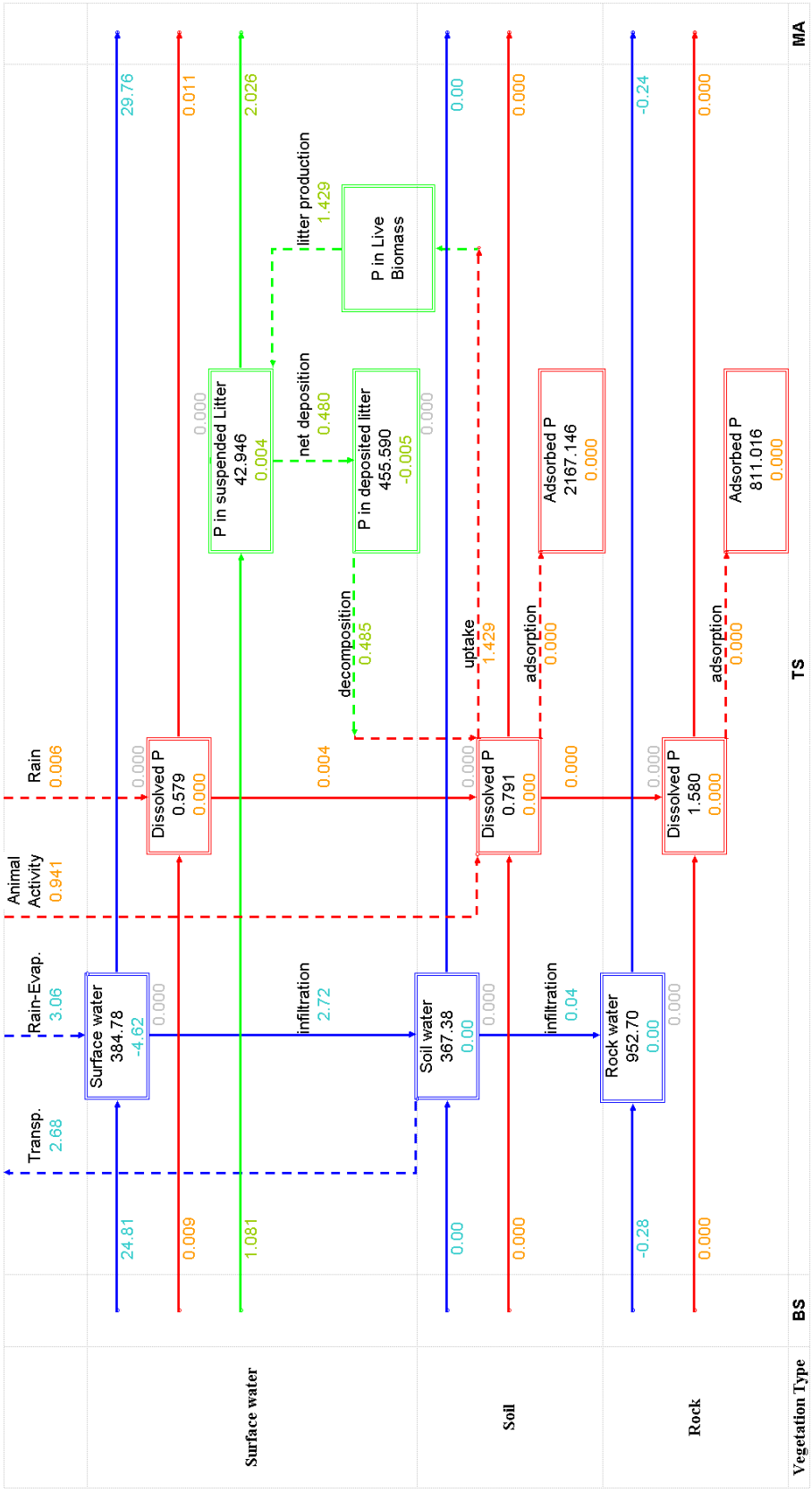

Figure A-126. Pools and fluxes representation for TS area in GL tree island.

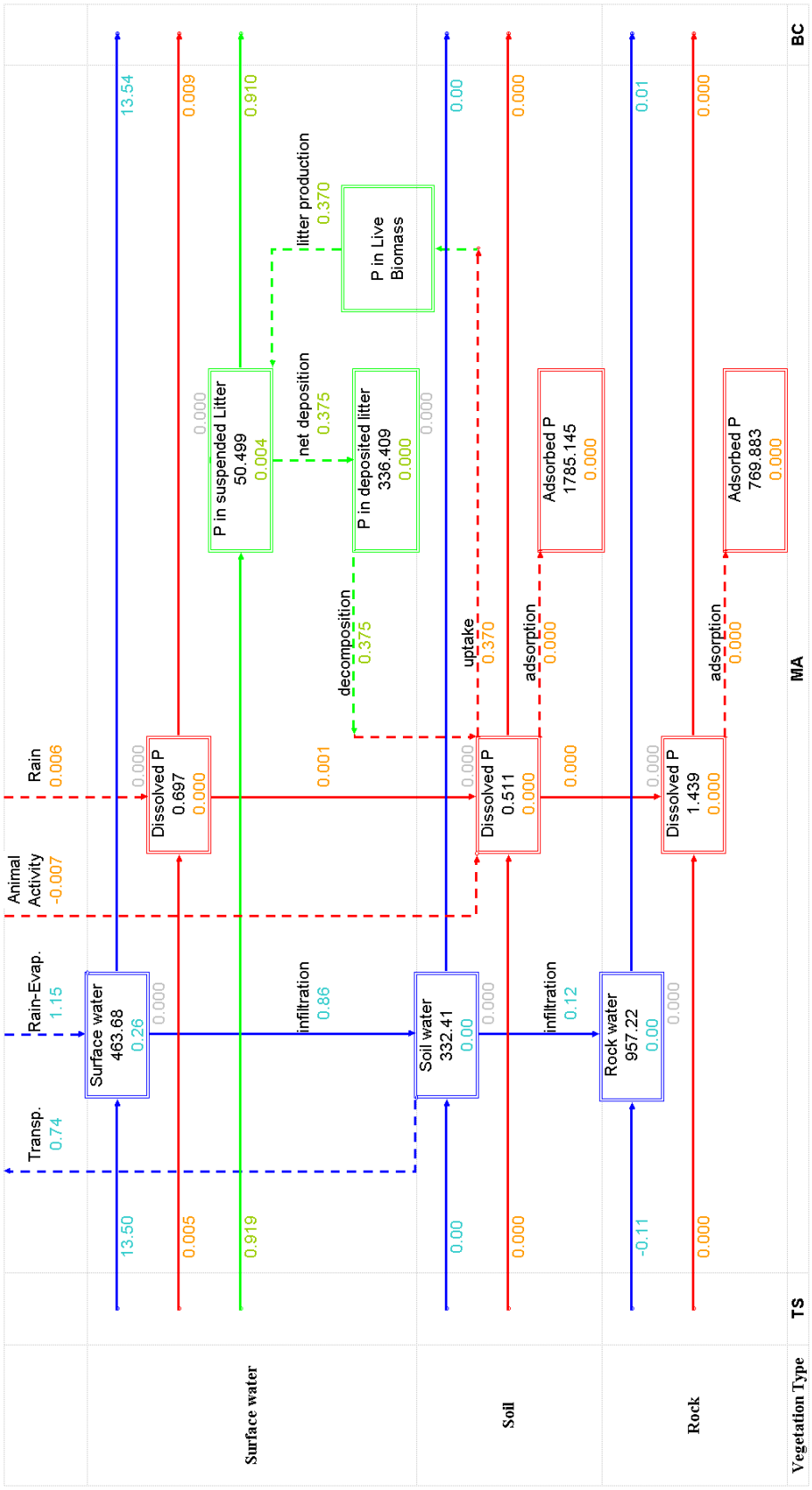

Figure A-127. Pools and fluxes representation for MA area in GL tree island.

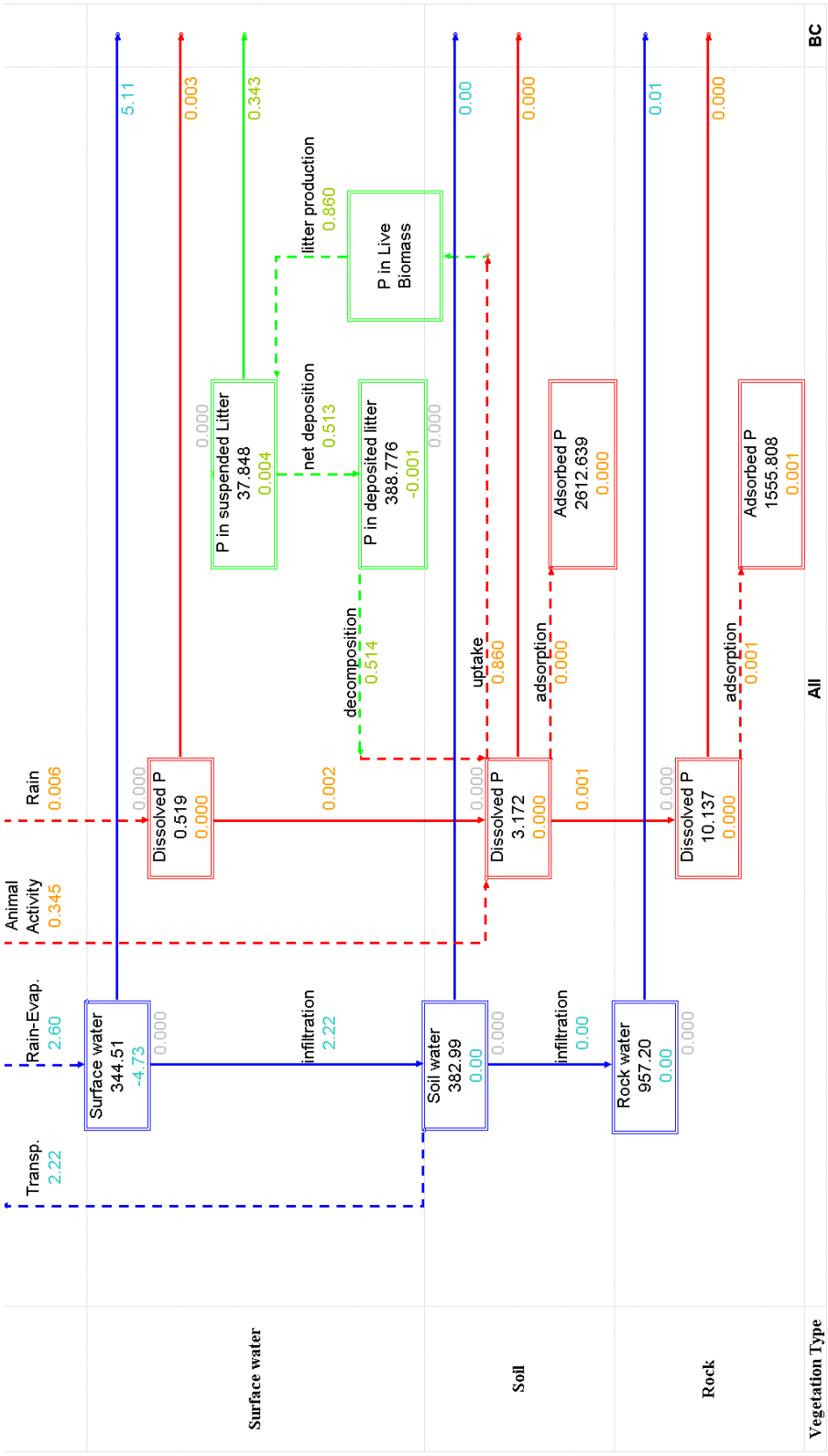

Figure A-128. Pools and fluxes representation for whole model area in GL tree island.

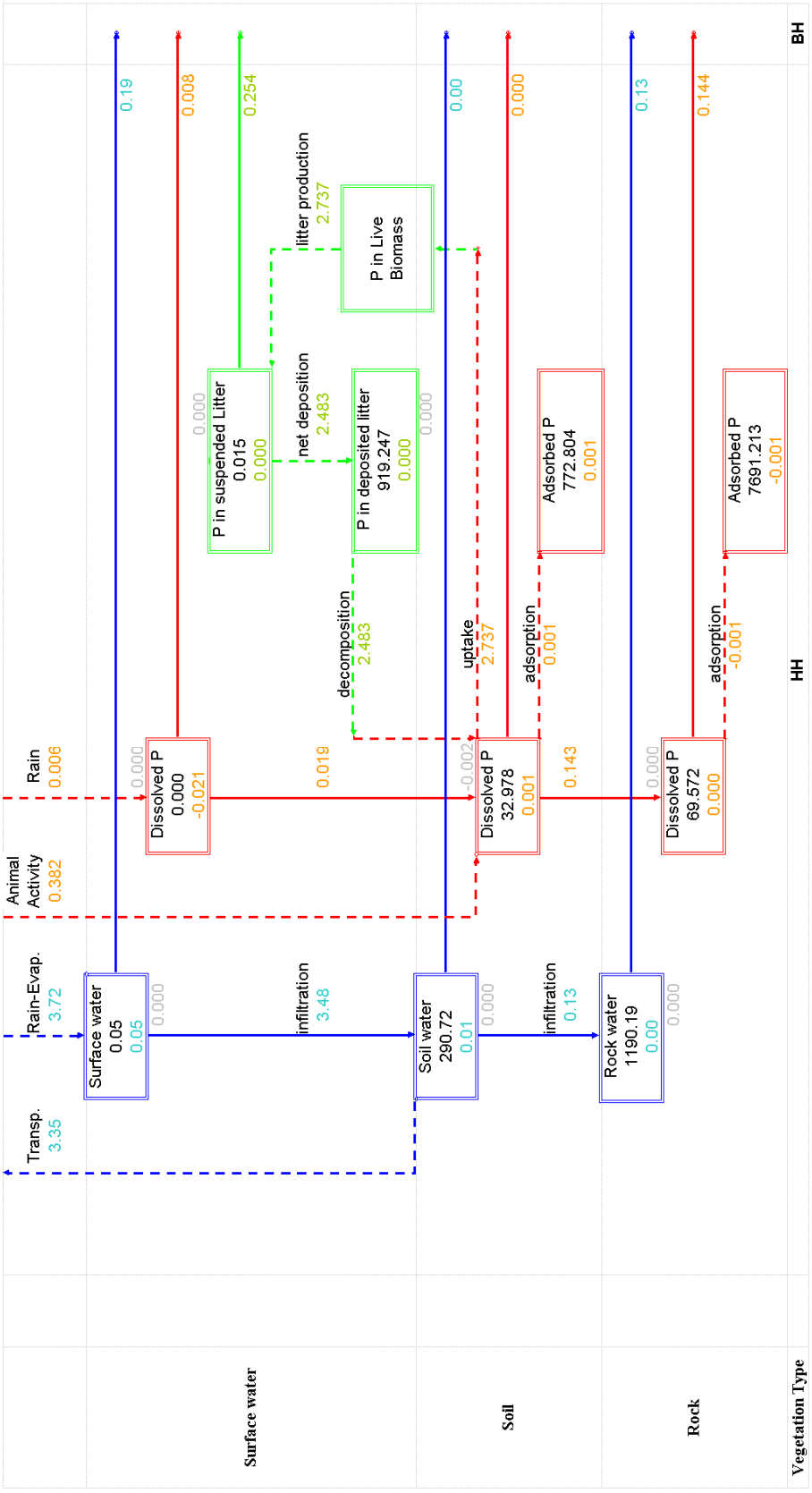

Figure A-129. Pools and fluxes representation for HH area in BH tree island.

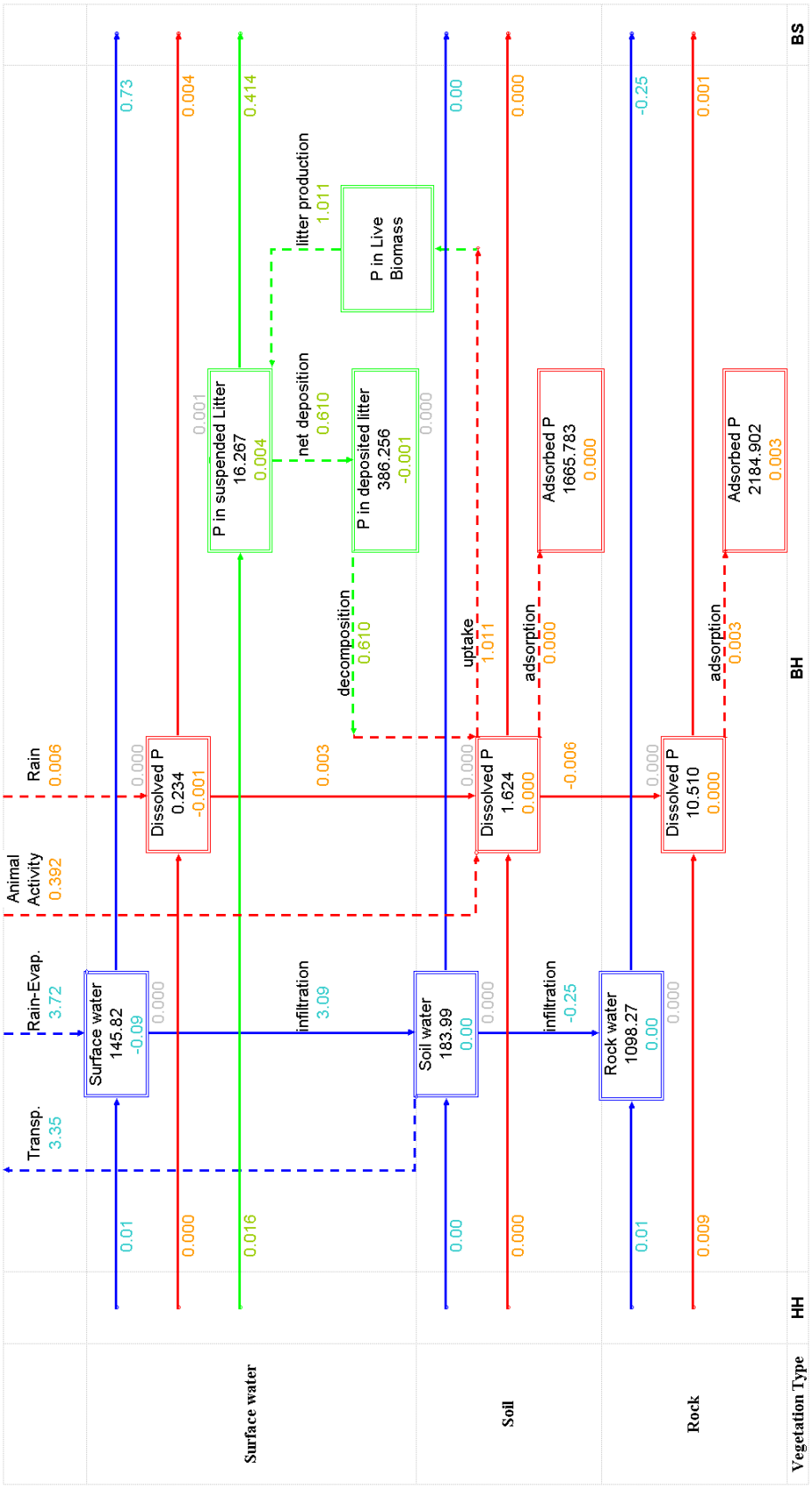

Figure A-130. Pools and fluxes representation for BH area in BH tree island.

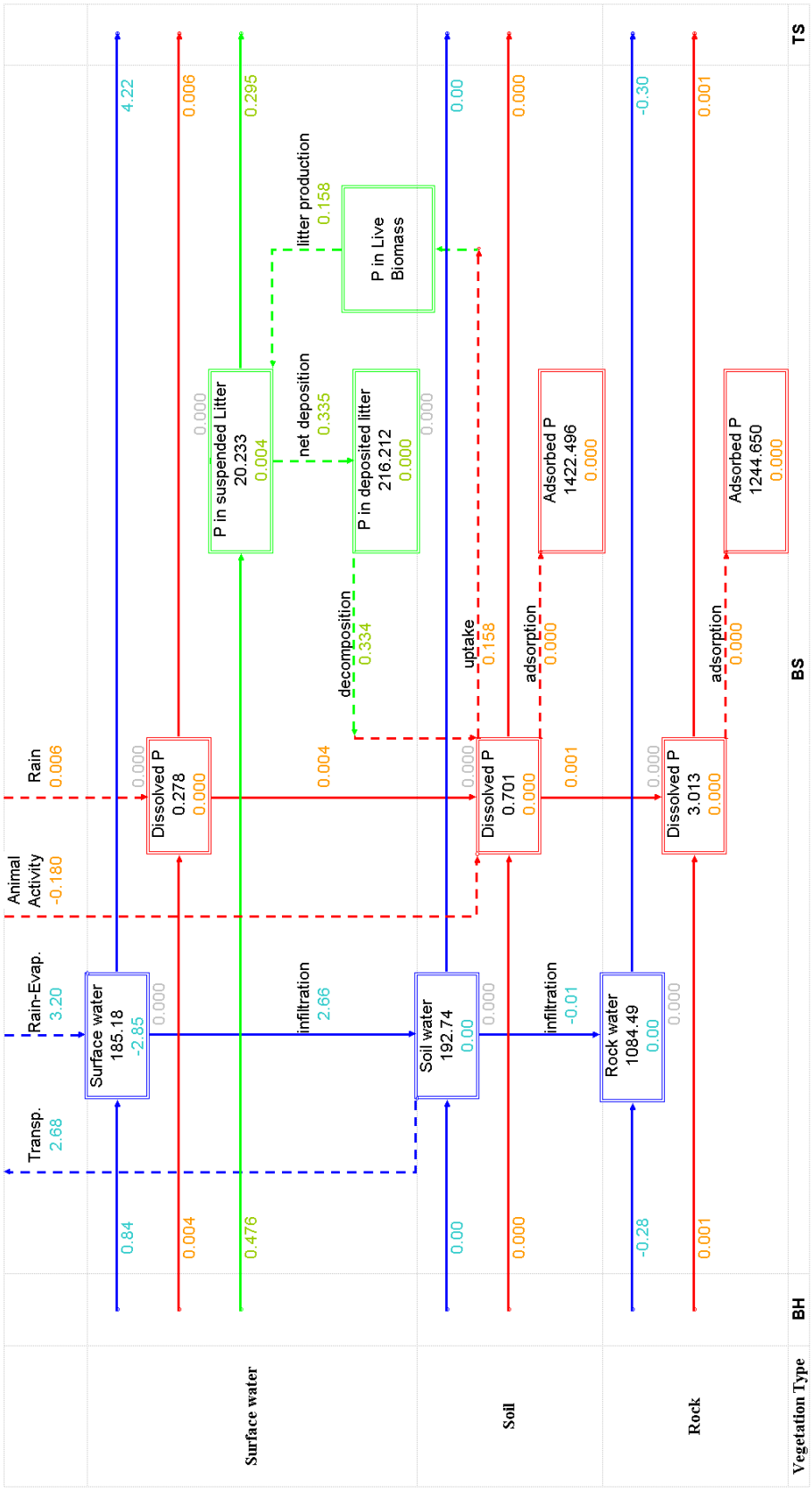

Figure A-131. Pools and fluxes representation for BS area in BH tree island.

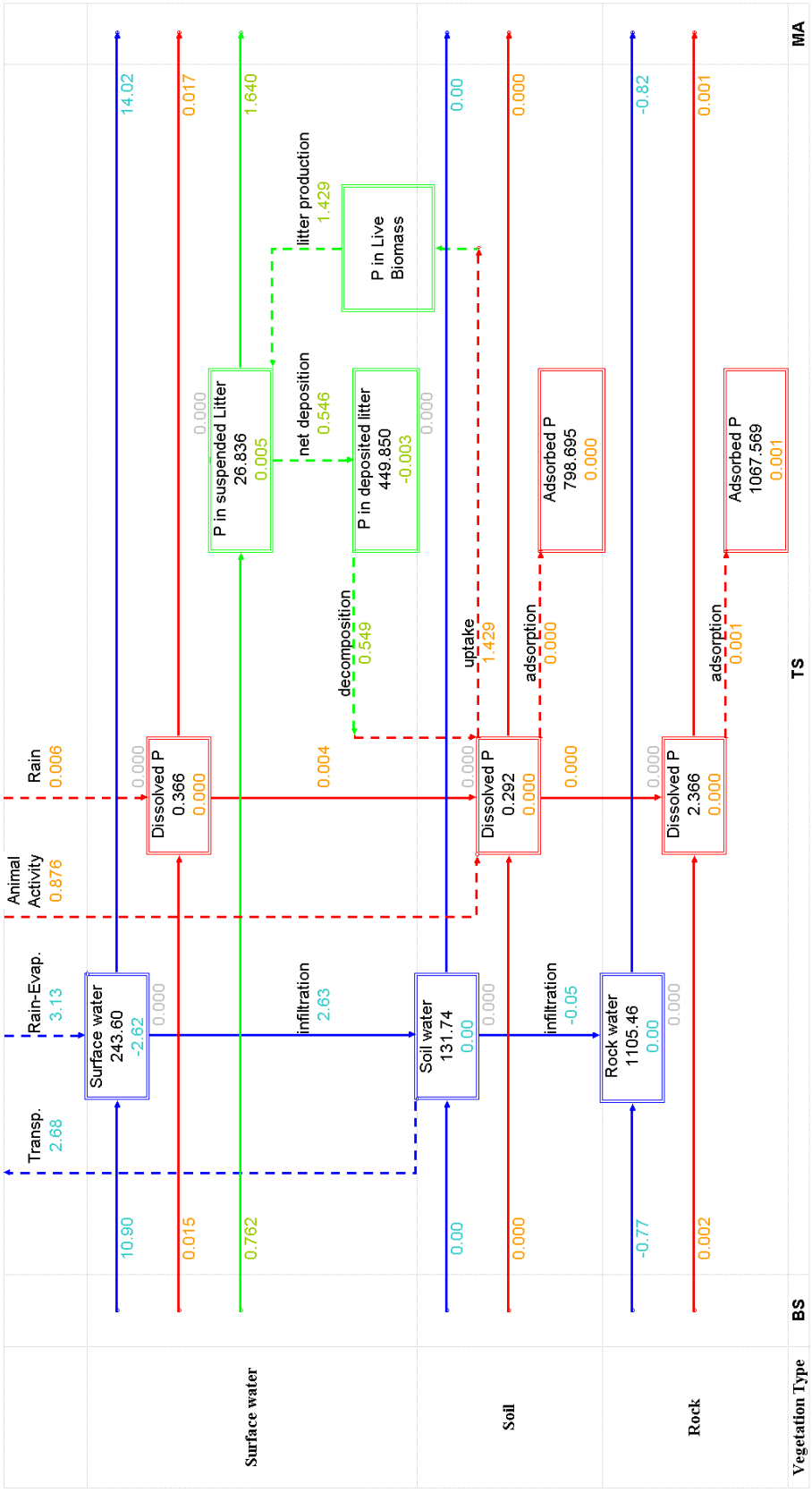

Figure A-132. Pools and fluxes representation for TS area in BH tree island.

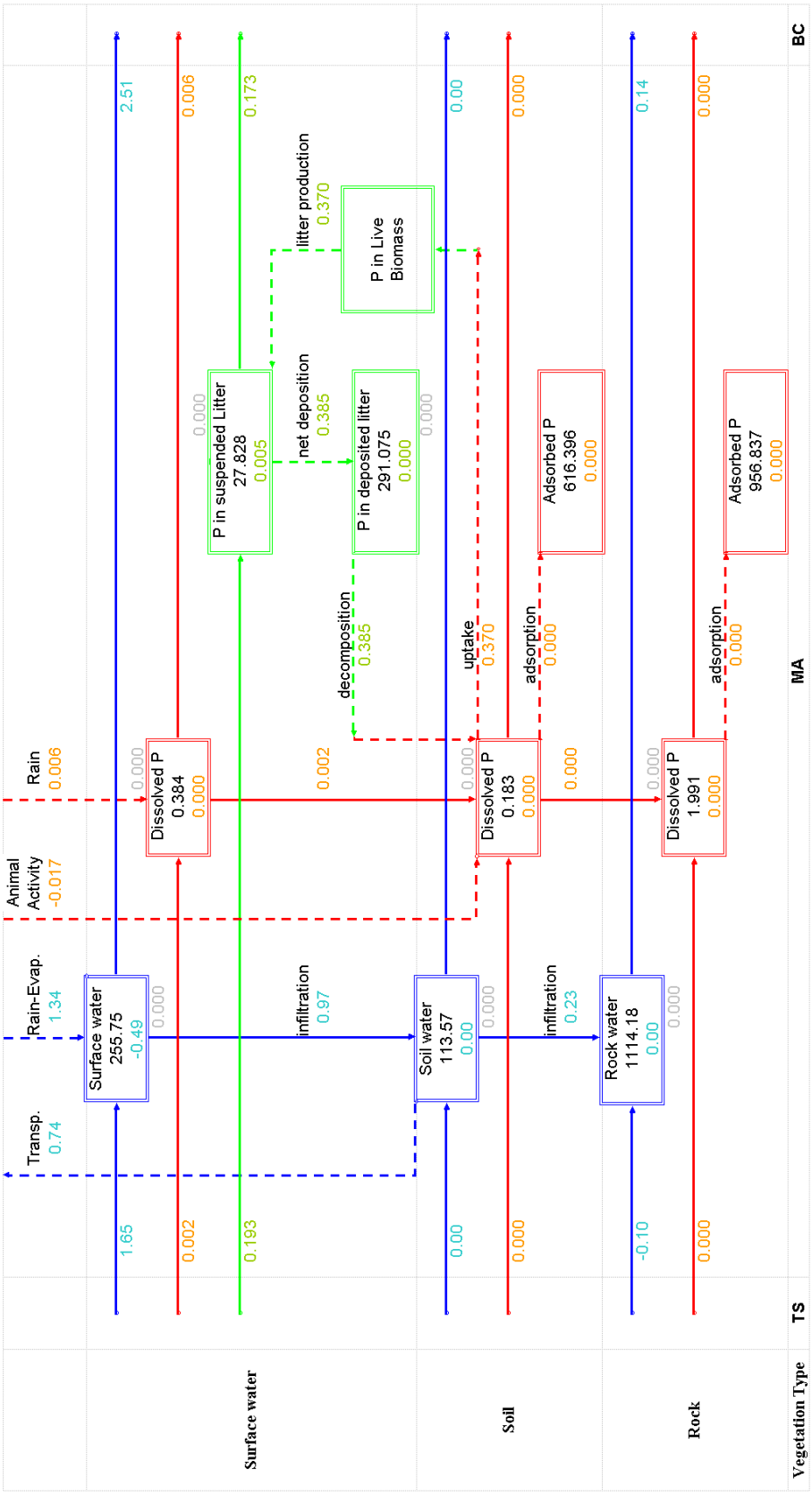

Figure A-133. Pools and fluxes representation for MA area in BH tree island.

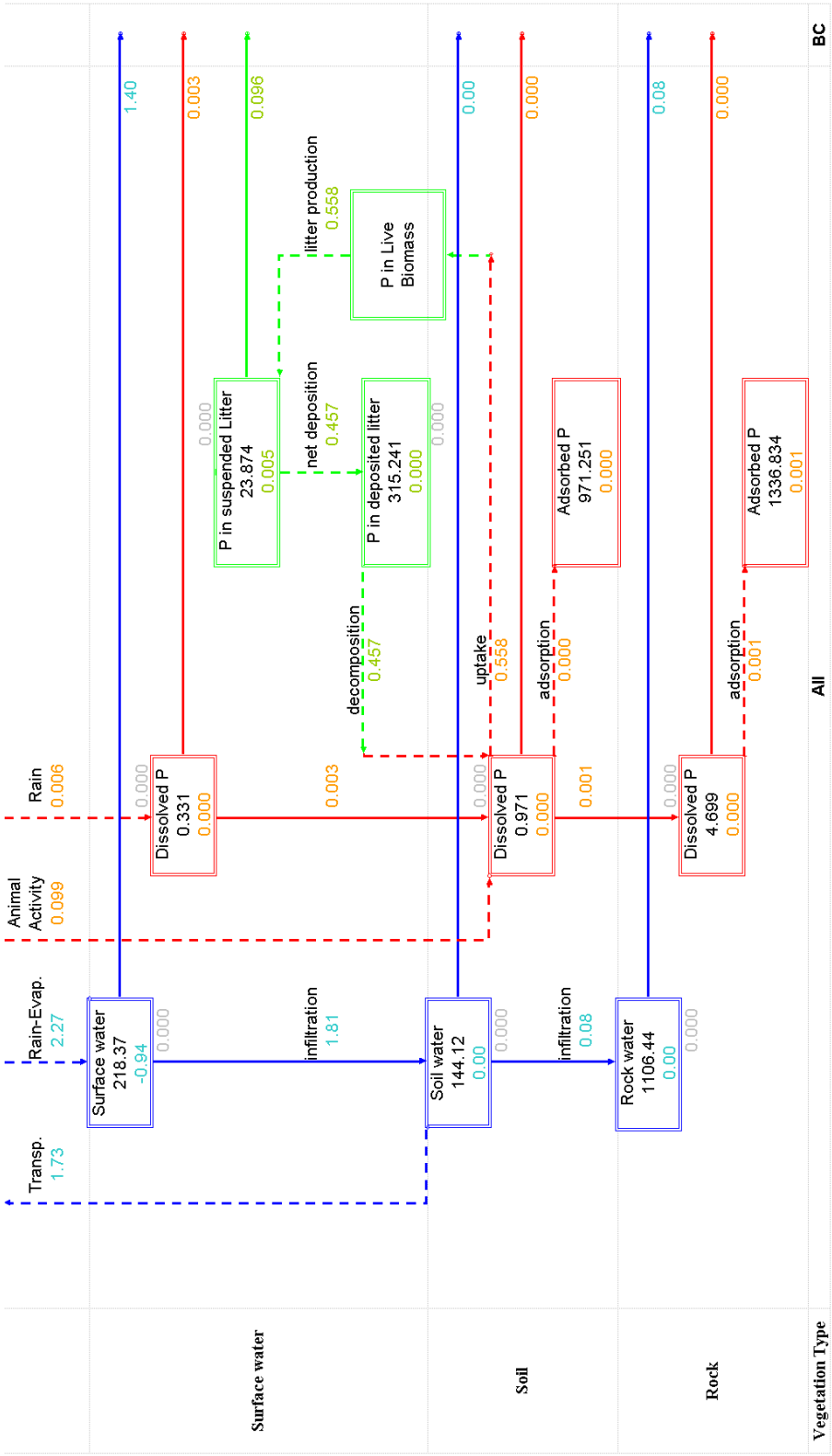

Figure A-134. Pools and fluxes representation for whole model area in BH tree island.

A5.1.4 Rainfall and ET Driven Fluxes. Additional Figures

Figures of this appendix section start in next page.

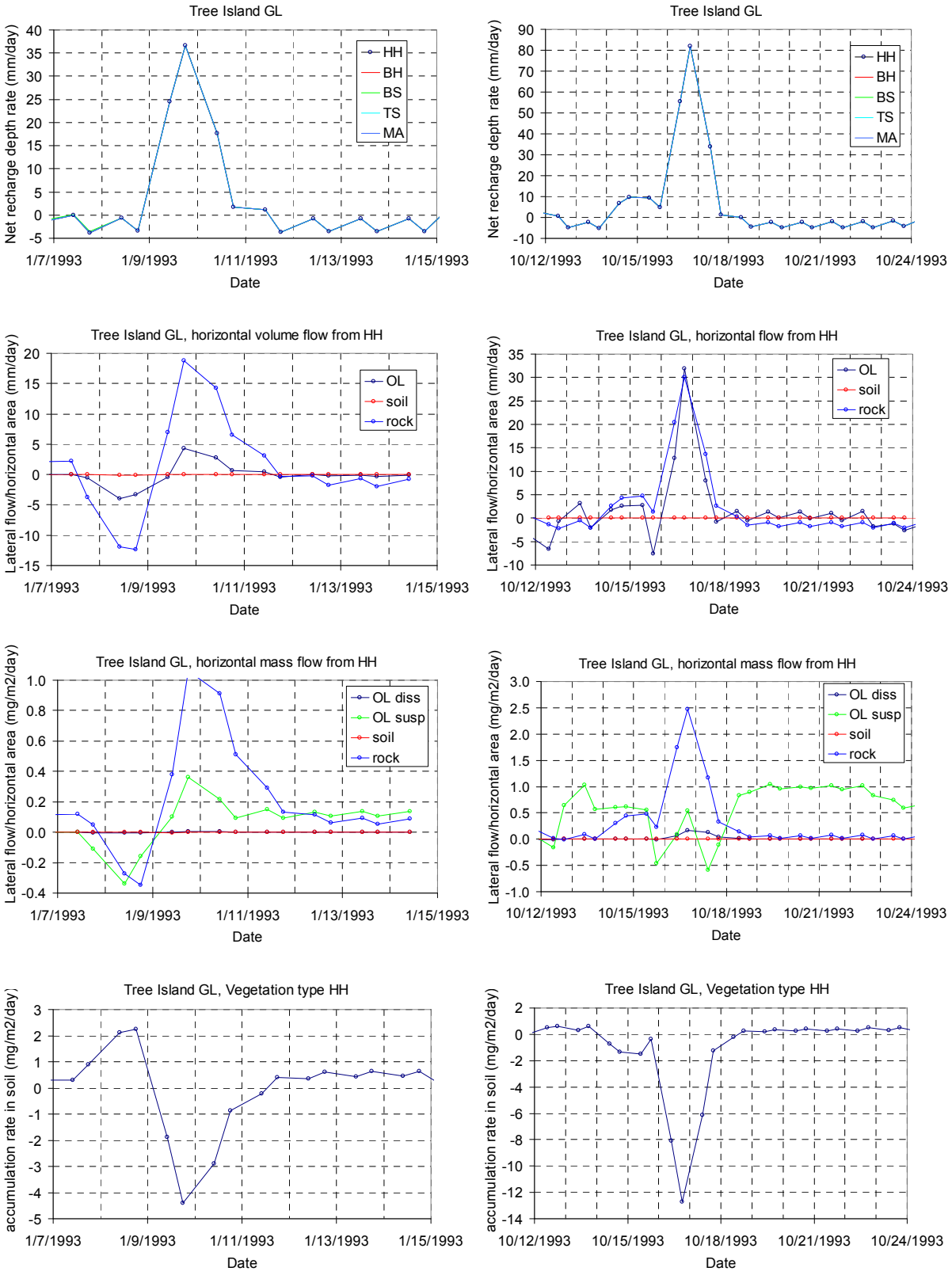

Figure A-135. Several plots showing the evolution of the variables at GL Tree Island around the rainfall events occurred on Jan 9, 1993 and Oct 16, 1993.

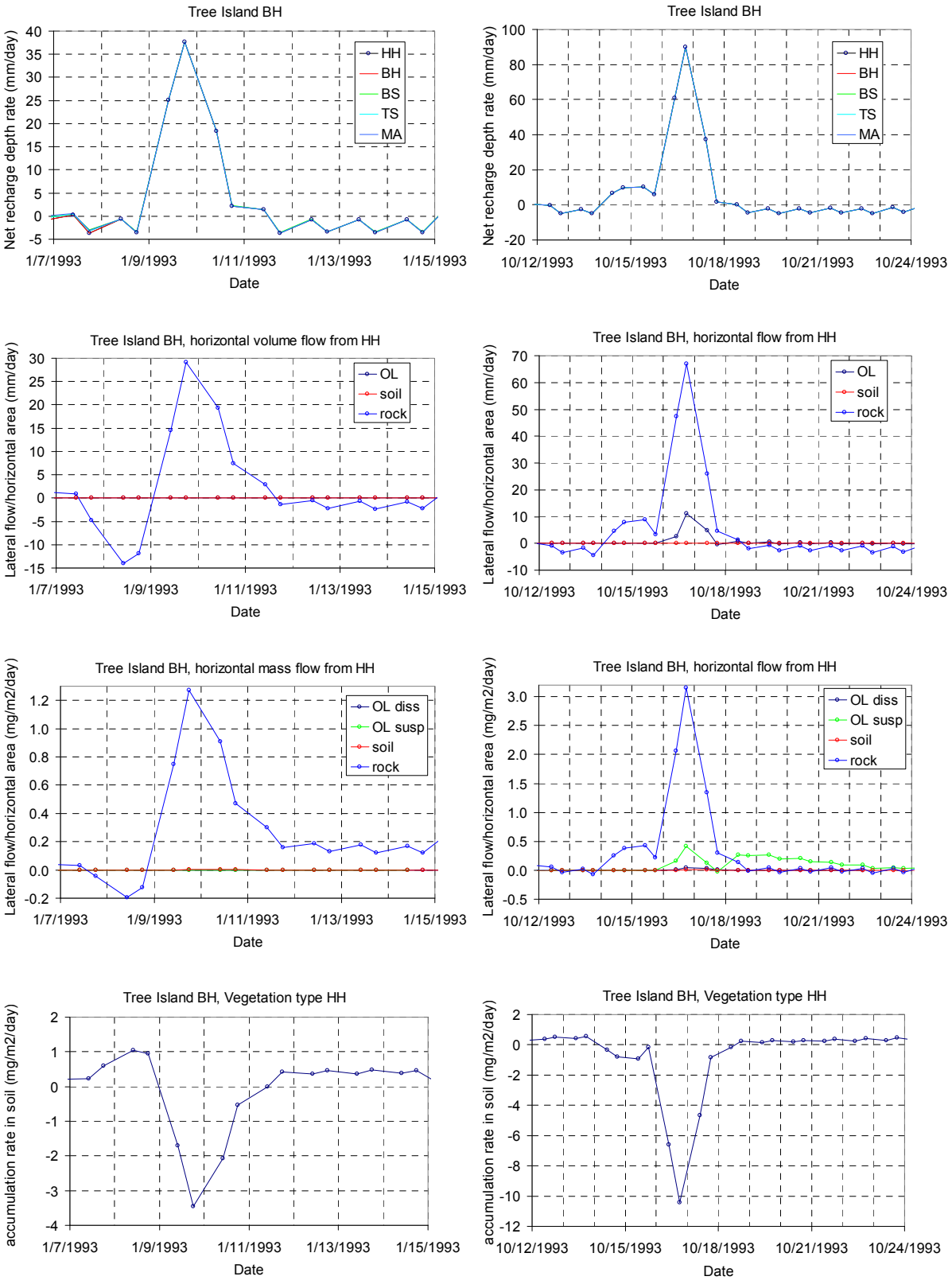

Figure A-136. Several plots showing the evolution of the variables at BH Tree Island around the rainfall events occurred on Jan 9, 1993 and Oct 16, 1993.

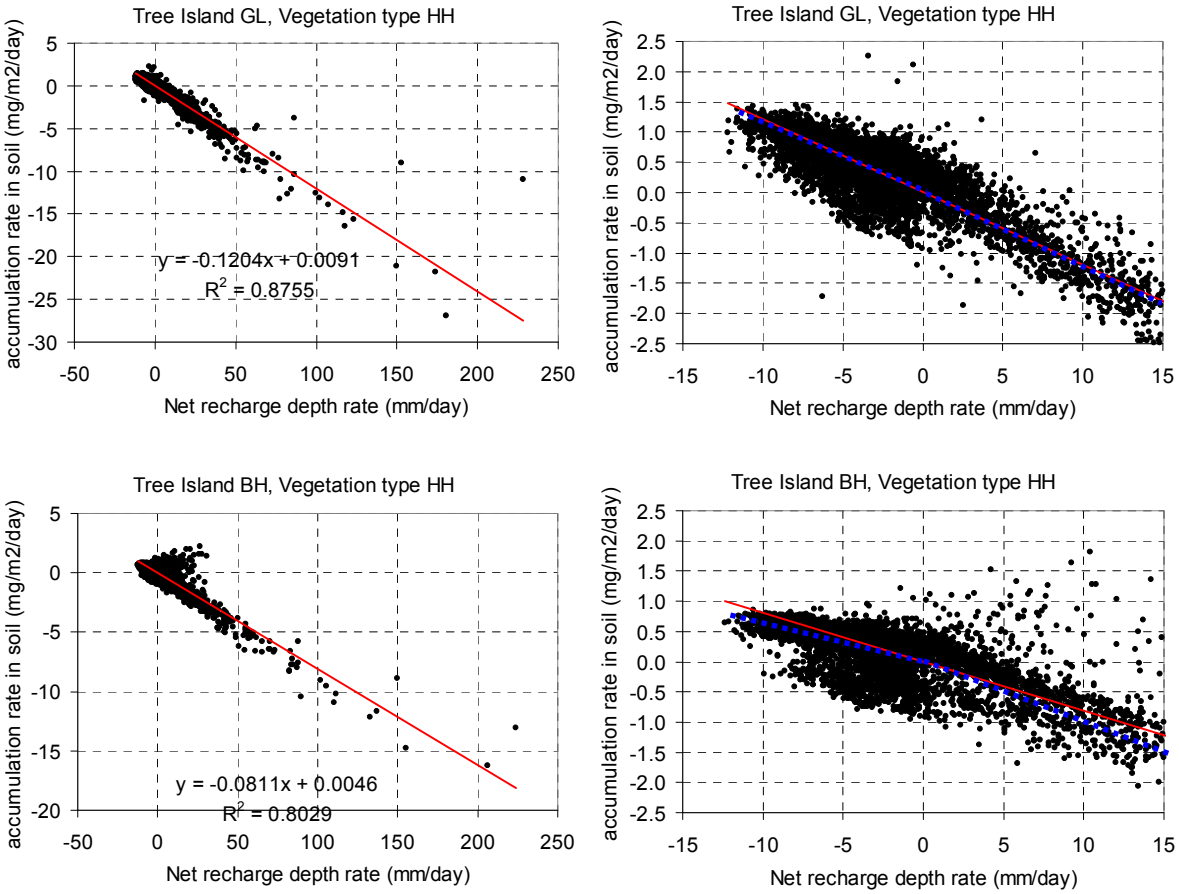

Figure A-137. Correlation between the accumulation rates of dissolved and adsorbed Phosphorus in soil layer at HH areas and the net recharge rate (rainfall – total ET rate). Complement to Figure 88.